

Ph.D. Thesis
Doctor of Philosophy

 **DTU Energy**
Department of Energy Conversion and Storage

SrTiO₃-based oxides: A versatile platform for emerging magnetic and electronic properties

Rasmus Tindal Dahm

Kgs. Lyngby 2023



**Section for Functional Oxides
Department of Energy Conversion and Storage
Technical University of Denmark**

DTU Lyngby campus
Anker Engelunds vej 101
2800 Kgs. Lyngby, Denmark
Building 310

Prof. Dr. Nini Pryds
Phone: +45 2219 5752
E-mail: nipr@dtu.dk

Summary

In a world of fast development where microelectronics has been a large and inevitable part of society, there has never been higher demand for new materials allowing new functionalities in electronic devices as there is today. Here, the metallic interface between the two insulators LaAlO_3 and SrTiO_3 opens up the field of oxide electronics due to the vast range of properties this heterostructure exhibits, as well as the ability to tune these properties. However, it remains an open question as to why the $\text{LaAlO}_3/\text{SrTiO}_3$ system can display such a versatile palette of physical properties, where, e.g., magnetism forms in the heterostructure despite the parent materials being nominally non-magnetic.

In this thesis, the focus is aimed at understanding how the interfacial magnetism and conductivity in SrTiO_3 -based heterostructures are influenced by fabrication methods, strain, and oxygen vacancy doping. The findings of this thesis improve our basic understanding of these heterostructures and stimulate exploration of new devices being utilized in integrated circuits used in new electronics.

In each chapter of the thesis, I highlight an important aspect for understanding the heterostructures. The thesis is constructed as follows.

Chapter 1 starts with a brief introduction to the SrTiO_3 -based system, which is the building block of the studied heterostructures.

Chapter 2 presents the applied experimental methods for fabricating the samples, which includes the termination procedures for substrate surfaces, film growth by pulsed laser deposition, and deposition monitoring by reflecting high energy electron diffraction, as well as characterization techniques such as magnetotransport used to investigate the materials in this study.

Chapter 3 describes the fabrication of freestanding oxide membranes. The methods used in this thesis typically rely on releasing thin oxide films using sacrificial interlayers and selective etching in addition to freestanding oxide membranes formed spontaneously during growth.

Chapter 4 describes the properties of the freestanding membranes that show the possibility of tweaking oxygen diffusion, but still preserve properties such as superconductivity in the freestanding form.

Chapter 5 deals with the magnetic properties of the SrTiO_3 -based system and the dependence on the deposition process and post-processing using annealing.

Chapter 6 describes the relationship between band structure and process parameters SrTiO_3 -based systems by surface treatment, annealing, Sr diffusion in anatase- $\text{TiO}_2/\text{SrTiO}_3$ and introduction of an additional buffer layer.

Chapter 7 concludes the thesis and provides an outlook.

Resumé

I en verden, hvor udviklingen af mikroelektronik er blevet en stor og uundgåelig del af samfundet, har der aldrig været større efterspørgsel efter nye materialer, som tillader nye funktioner i elektroniske enheder, end i dag. Her åbner den metalliske grænseflade mellem de to isolerende LaAlO_3 og SrTiO_3 op for området for oxid-baseret elektronik på grund af den store vifte af egenskaber, som denne heterostruktur viser, samt muligheden for at finjustere disse egenskaber. Det er dog stadig et åbent spørgsmål, hvorfor $\text{LaAlO}_3/\text{SrTiO}_3$ -systemet kan vise en sådan alsidig palet af fysiske egenskaber, hvor magnetisme f.eks. dannes i heterostrukturen, selvom de oprindelige materialer individuelt ikke er magnetiske.

I denne afhandling fokuserede jeg på at forstå, hvordan magnetismen og ledningsevnen i grænsefladen i SrTiO_3 -baserede heterostrukturer påvirkes af fremstillingsmetoder, strain og doping af ilt-vakancer. Fundene i denne afhandling forbedrer vores grundlæggende forståelse af disse heterostrukturer og stimulerer opdagelsen af nye enheder, som anvendes i integrerede kredsløb i ny elektronik.

I hvert kapitel i afhandlingen fremhæver jeg et vigtigt aspekt for at forstå heterostrukturerne. Afhandlingen er struktureret således:

Kapitel 1 begynder med en kort introduktion til SrTiO_3 -baserede systemer, som er byggestenene i de undersøgte heterostrukturer.

Kapitel 2 præsenterer de anvendte eksperimentelle metoder til fremstilling af prøverne, herunder fremgangsmåde for overfladeterminering af substraterne, film-deponering ved hjælp af pulserende laserdeponering og overvågning af deponeringen ved hjælp af refleksion af højenergielektron-diffraktion samt karakteriseringsmetoder som magnetotransport, der anvendes til at undersøge materialerne i dette studie.

Kapitel 3 beskriver fremstillingen af fritstående oxidmembraner. De metoder, der anvendes i denne afhandling, baserer sig typisk på frigivelse af tynde oxidfilm ved hjælp af et vandopløseligt mellemlag og selektiv ætsning samt fritstående oxidmembraner, der spontant dannes under groningen.

Kapitel 4 beskriver egenskaberne ved de fritstående membraner, der viser muligheden for at finjustere ilt-diffusion, men stadig bevare egenskaber som superledning i den fritstående form.

Kapitel 5 behandler de magnetiske egenskaber ved SrTiO_3 -baserede systemer og afhængigheden af deponeringsprocessen og efterbehandling ved høje temperaturer.

Kapitel 6 beskriver relationen mellem båndstruktur og procesparametre for SrTiO_3 -baserede systemer ved overfladebehandling, høje temperaturer, Sr-diffusion i anatase- $\text{TiO}_2/\text{SrTiO}_3$ og indførelse af et yderligere bufferlag.

Kapitel 7 konkluderer afhandlingen og giver en perspektivering.

Preface

This PhD thesis is submitted in the partial fulfilment of the requirements for acquiring the degree of Doctor of Philosophy at the Technical University of Denmark.

The content of this thesis is primarily based on collaborations between energy conversion and storage at the Technical University of Denmark, Center for Quantum Devices at University of Copenhagen, Swiss Light Source at Paul Scherrer Institute, Group for Ferroelectrics and Functional Oxides at École Polytechnique Fédérale de Lausanne, Institutes für Physik Martin-Luther-Universität Halle-Wittenberg. I have worked with various techniques, all with the common goal of understanding the physics SrTiO₃-based oxides.

Principal supervisor:

Prof. Nini Pryds, Technical University of Denmark

Co-supervisors:

Dr. Dennis Valbjørn Christensen, Technical University of Denmark

Prof. Vincenzo Esposito, Technical University of Denmark

Assessment committee:

Prof. Chang-Beom Eom, University of Wisconsin-Madison

Dr. Felix Gunkel, Forschungszentrum Jülich

Dr. Ivano Eligio Castelli (chairman), Technical University of Denmark

Kgs. Lyngby, January 9th, 2023



Rasmus Tindal Dahm

Acknowledgements

I would like to acknowledge the help, supports and collaboration from family, friends, co-workers, collaborators, and supervisors.

First, I would like to thank the head of department, Søren Linderoth and section leader Nini Pryds for the opportunity to make this PhD project possible. I would express my sincere gratitude to my principal supervisor Nini Pryds who, no matter the time of day, had time to discuss results and revise my manuscript; and my co-supervisor Dennis Valbjørn Christensen who always has time to help in the lab or engage in a scientific discussion. I would also like to express my deepest thanks to Daesung Park who has been a great help throughout my project whether it be help in the lab, theoretical level, or presenting of data. I would also like to express my appreciation towards Francesco Maria Chiabrera, Shinhee Yun Felix Trier and Daesung Park, whether that be guidance in the lab teaching me first-hand experience of theoretical knowledge with the pulsed laser deposition system and cryostat systems. I also want to thank Thomas Sand Jespersen for thoughtful discussions. During my stay at the Paul Scherrer Institute, I had the pleasure of meeting Milan Radovic and his team of brilliant scientists. Therefore, I would like to thank Milan Radovic, Hang Li, and Eduardo Bonini Guedes from the SIS beamline and Vladimi Stokov at the ADRESS beamline for introducing me to the synchrotron community and the very complex but important science that they do every day. A special thanks to my office mate from the beginning of my PhD, Ricci Schüsler Erlandsen, who was always up to for a chat and my more recent officemate Thor Hvid-Olsen.

I would also like to take the opportunity to thank the commitment committee Chang-Beom Eom, Felix Gunkel and Ivano Eligio Castelli for taking time out of their busy schedules to read and attend the defense of this thesis.

Lastly, I'd like to thank my family and Caroline Berndtsson, my beloved life partner, for all her support and taking care of the family situation in hectic times whether that be taking care of our daughter Olivia or preparing dinner for when I get home late after a long day at DTU.

Contents

Summary	i
Resumé.....	iii
Preface.....	v
Acknowledgements.....	vii
Contents	ix
List of acronyms & symbols	xiii
CHAPTER 1 Introduction to oxide electronics	1
1.1 Complex oxide	1
1.2 The physics of complex oxide.....	2
1.2.1 Crystal field theory	3
1.3 Perovskite: SrTiO ₃	4
1.3.1 Stability of the perovskite	5
1.3.2 SrTiO ₃ symmetry	6
1.3.3 Defects in SrTiO ₃	7
1.3.4 Selected properties of bulk SrTiO ₃ : superconductivity	8
1.4 SrTiO ₃ – based heterointerfaces	10
1.5 SrTiO ₃ – based heterointerfaces: properties.....	13
1.5.1 Lifshitz transition	13
1.5.2 Superconductivity in LaAlO ₃ /SrTiO ₃	14
1.5.3 Magnetism.....	16
1.5.4 Ordinary magnetoresistance.....	18
1.5.5 Ordinary and anomalous Hall effect	18
CHAPTER 2 Experimental.....	21
2.1 Sample preparation.....	21
2.1.1 Single termination procedure	21
2.1.2 TiO ₂ -terminated SrTiO ₃ of the current thesis	23
2.1.3 Film growth.....	25
2.1.4 Pulsed laser deposition.....	25
2.1.4.1 Laser fluence.....	26
2.1.4.2 Oxygen partial pressure	27
2.1.4.3 Reflection high-energy electron diffraction	28

2.2	Sample characterization	30
2.2.1	Transport measurement.....	30
2.2.2	Magnetometry	30
2.2.3	X-ray diffraction	32
2.2.4	Angle-resolved photoemission spectroscopy.....	32
CHAPTER 3 Fabrication of freestanding membranes.....		35
3.1	Freestanding membranes utilizing soluble sacrificial layer	36
3.1.1.1	Sacrificial buffer layer	37
3.1.2	Fabrication procedure of wet etch method.....	38
3.1.3	Characterization of stacked membranes	41
3.2	Freestanding membranes through controlled spalling	43
3.2.1	Spalling mechanism	43
3.2.2	As-grown spalled membrane size distribution.....	44
3.2.3	Controlled spalled membrane size distribution and fabrication	45
3.2.4	Membrane transferring.....	48
CHAPTER 4 Properties of freestanding membranes.....		51
4.1	Physical properties of moiré patterns in SrTiO ₃ membranes	51
4.2	Superconducting 2DEG in freestanding LaAlO ₃ /SrTiO ₃ membranes	52
4.2.1	Preparation of the device and ensuring good contact to the 2DEG	52
4.2.2	Temperature dependence	53
4.2.3	The superconducting phase in spalled membranes	54
CHAPTER 5 Magnetism in SrTiO ₃ -based structures.....		59
5.1	Controllable magnetism through growth pressure	59
5.2	Tuning SrTiO ₃ -based systems by oxygen vacancies.....	63
5.3	Magnetism in self-assembled LaAlO ₃ (1-x):LaBO ₃ (x)/SrTiO ₃ heterostructures	67
CHAPTER 6 The electronic structure of STO-based oxides.....		71
6.1	Creation and control of low dimensional states at SrTiO ₃ surface	71
6.2	The electronic structure of a-LAO/LMO/STO.....	75
6.3	The electronic structure of ion diffusion in TiO ₂ /SrTiO ₃	78
6.4	Electronic response to strain in SrTiO ₃ (001)	81
CHAPTER 7 Conclusions & outlook		85
APPENDIX A SrTiO ₃ TiO ₂ treatment protocol		87
A.1	Aqua regia TiO ₂ treatment	87
A.2	Buffered HF TiO ₂ treatment.....	88

APPENDIX B Appendix of papers.....	89
B.1 Published peer-reviewed articles	89
B.2 Articles accepted, submitted or under preparation	90
Bibliography	219

List of acronyms & symbols

Symbol	Quantity	Value
e	elementary charge	$1.602 \times 10^{-19} \text{ C}$
$h = 2\pi\hbar$	Planck's constant	$6.626 \times 10^{-34} \text{ J s}$
k_B	Boltzmann constant	$1.381 \times 10^{-23} \text{ J/K}$
μ_B	Bohr magneton	$9.274 \times 10^{-24} \text{ J/T}$
Φ_0	flux quantum	$2.01/mT (\mu\text{m})^2$

Physical constants

Acronym	Definition
2DEG	two-dimensional electron gas
AC	alternating current
ADF-STEM	annular dark-field scanning transmission microscopy
AFM	atomic force microscope
AHE	anomalous Hall effect
ARPES	angle-resolved photoemission spectroscopy
CAB	cellulose acetate butyrate
CB	conduction band
DC	direct current
DFT	density functional theory
EDC	energy distribution curve
EELS	electron energy loss spectroscopy
EPI	electron-phonon interactions
FFT	fast Fourier transformation
GL	Ginzberg-Landau
HRTEM	high-resolution transmission electron spectroscopy
IPA	isopropanol
LAO	LaAlO ₃
LBO	LaBO ₃
LMO	LaMnO ₃
MBE	molecular beam epitaxy
MD	molecular dynamics
MDE	momentum distribution curve
OHE	ordinary hall effect
PDMS	poly(dimethylsiloxane))
PLD	pulsed laser deposition
PMMA	poly(methyl methacrylate)
PT	pulse tube
RHEED	reflection high-energy electron diffraction

Acronym	Definition
RP	ruddlesden-popper
RSM	reciprocal space map
SAO	$\text{Sr}_3\text{Al}_2\text{O}_6$
SEM	scanning electron microscopy
SQUID	superconducting quantum interference device
SR	success rate
STO	SrTiO_3
SX-ARPES	soft x-ray angle-resolved photoemission spectroscopy
UHV	ultra-high vacuum
VB	valence band
vdP	van der pauw
VUV-ARPES	vacuum-ultraviolet angle-resolved photoemission spectroscopy
XPS	x-ray photo spectroscopy
XRD	x-ray diffraction

CHAPTER 1

Introduction to oxide electronics

1.1 Complex oxide

A fundamental understanding of materials is essential for creating new materials for energy, information, and electronic technology. Complex oxides are a widely used solid-state material class that contain oxygen and other elements, such as a transition metal in the case of transition metal oxides. This class of materials hosts a wide-range of exciting properties including ferroelectricity¹⁻⁴, ferromagnetism⁵⁻¹¹, multiferroicity¹²⁻¹⁴, high-temperature superconductivity¹⁵, colossal magnetoresistance¹⁶⁻¹⁹, and metal-to-insulator transitions^{20,21}. These exciting properties are due to the very strong correlation effects, leading to the coupling of the charge, spin, orbital, and lattice degrees of freedom^{22,23} (see Figure 1.1).

Emergent phenomena in condensed matter physics are the hallmark of many-body systems, and yet unraveling their nature remains one of the central challenges²⁴. With endless possible interactions, an interplay between the interactions can be the missing link in a percolative network of emergent phenomena. Traditionally, physicists and material scientists strive towards the philosophy of reductionism, where the properties of a single or few particles system is used to explain larger systems. However, this is not sufficient to

understand large complex correlated systems, as quoted by P.W. Anderson in 1972: “*The ability to reduce everything to simple fundamental laws does not imply the ability to start from those laws*”^{23,25,26}. As an analogy, it is almost impossible to construct worldly phenomena, such as the human body, starting from elementary particles and using just the fundamental laws.

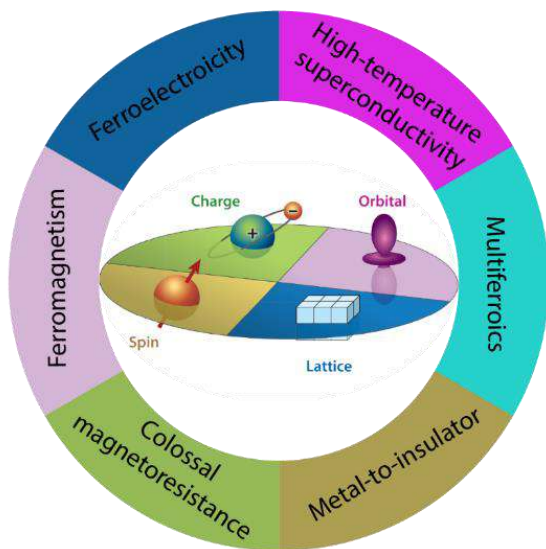


Figure 1.1. The complex correlation between charge, spin, orbital and lattice creates emerging phenomena in complex oxides and are responsible for the variety of properties such as ferroelectricity, ferromagnetism, high-temperature superconductors, multiferroics, Colossal magnetoresistance and metal-to-insulator transition. Figure adapted from reference [236].

Complex oxides have shown to be a great candidate for many technological applications²⁷ due to their wide and exciting range of properties. Owing to the complex nature of the interactions, we still failed to decisively identify the mechanism that generates the superconducting charge carriers even after decades of rigorous study. This is partially because we can no longer consider the electron in these systems as moving freely without interacting with each other, i.e., *electron gas*, but rather the

particles interact and “feel” each other in an *electron liquid* with many-body interactions such as the electron-electron or the electron-phonon interactions (EPI).

Although the understanding of such correlated systems is challenging, it also provides an opportunity for a complex metal oxide to exploit the coupling of spin, charge, and lattice degrees of freedom to create novel electronic²³ and spintronic devices²⁸ or even computing elements comparable to the neurons and synapses in the brain²⁹.

1.2 The physics of complex oxide

Complex oxides exhibit many spectacular magnetic and electrical properties, including high-temperature superconductivity and multiferroicity, making them particularly promising for a wide range of technology applications²⁷. This family of materials has crystal structures such as perovskite (ABO_3), rock salt (BO), and rutile (BO_2), to name a few. The most common formula for these materials is perovskite oxides ABO_3 structure. These materials are chemically very flexible, allowing for a wide degree of doping and elemental substitutions. Here, the A-site is usually occupied by a rare-earth and/or alkaline large cation that has 12-fold coordination with oxygen anions; the B site is positioned in the center of a corner-sharing octahedron formed by neighboring oxygen anions and is typically a transition metal, where most of the interesting physics occurs while O is the oxygen anion. Figure 1.2 shows the periodic table of elements with the transition metals highlighted in blue and post-transition metals highlighted in yellow, accounting for the B-side transition metal.

The properties of complex oxides depend on the ionic composition, but also the position and rotation of the ions relative to each other, i.e., the geometry of the ligands (oxygen in

1 H Hydrogen 1																	2 He Helium 4																	
3 Li Lithium 7	4 Be Beryllium 9																	5 B Boron 11	6 C Carbon 12	7 N Nitrogen 14	8 O Oxygen 16	9 F Fluorine 19	10 Ne Neon 20											
11 Na Sodium 23	12 Mg Magnesium 24																	13 Al Aluminum 27	14 Si Silicon 28	15 P Phosphorus 31	16 S Sulfur 32	17 Cl Chlorine 35.5	18 Ar Argon 40											
19 K Potassium 39	20 Ca Calcium 40	21 Sc Scandium 45	22 Ti Titanium 48	23 V Vanadium 51	24 Cr Chromium 52	25 Mn Manganese 55	26 Fe Iron 56	27 Co Cobalt 59	28 Ni Nickel 59	29 Cu Copper 64	30 Zn Zinc 65	31 Ga Gallium 70	32 Ge Germanium 73	33 As Arsenic 75	34 Se Selenium 79	35 Br Bromine 80	36 Kr Krypton 84																	
37 Rb Rubidium 85.5	38 Sr Strontium 88	39 Y Yttrium 89	40 Zr Zirconium 91	41 Nb Niobium 93	42 Mo Molybdenum 96	43 Tc Technetium 98	44 Ru Ruthenium 101	45 Rh Rhodium 103	46 Pd Palladium 106	47 Ag Silver 108	48 Cd Cadmium 112	49 In Indium 115	50 Sn Tin 119	51 Sb Antimony 122	52 Te Tellurium 128	53 I Iodine 127	54 Xe Xenon 131																	
55 Cs Cesium 133	56 Ba Barium 137																	72 Hf Hafnium 178.5	73 Ta Tantalum 181	74 W Tungsten 184	75 Re Rhenium 186	76 Os Osmium 190	77 Ir Iridium 192	78 Pt Platinum 195	79 Au Gold 197	80 Hg Mercury 201	81 Tl Thallium 204	82 Pb Lead 207	83 Bi Bismuth 209	84 Po Polonium	85 At Astatine	86 Rn Radon		
87 Fr Francium	88 Ra Radium	104 Rf Rutherfordium	105 Db Dubnium	106 Sg Seaborgium	107 Bh Bohrium	108 Hs Hassium	109 Mt Meitnerium	110 Ds Darmstadtium	111 Rg Roentgenium	112 Cn Copernicium	113 Nh Nihonium	114 Fl Flerovium	115 Mc Moscovium	116 Lv Livermorium	117 Ts Tennessine	118 Og Oganesson																		
																		57 La Lanthanum	58 Ce Cerium 140	59 Pr Praseodymium 141	60 Nd Neodymium 144	61 Pm Promethium	62 Sm Samarium 150	63 Eu Europium 152	64 Gd Gadolinium 157	65 Tb Terbium 159	66 Dy Dysprosium 162.5	67 Ho Holmium 165	68 Er Erbium 167	69 Tm Thulium 169	70 Yb Ytterbium 173	71 Lu Lutetium 175		
																		89 Ac Actinium	90 Th Thorium 232	91 Pa Protactinium 231	92 U Uranium 238	93 Np Neptunium	94 Pu Plutonium	95 Am Americium	96 Cm Curium	97 Bk Berkelium	98 Cf Californium	99 Es Einsteinium	100 Fm Fermium	101 Md Mendelevium	102 No Nobelium	103 Lr Lawrencium		

Figure 1.2. Periodic table of elements with transition metals and post transition metals highlighted in blue and yellow, respectively.

complex oxides) relative to the transition metal. The unusual properties of complex oxides are due to several factors:

- 1) The arrangement of ions within the unit cell
- 2) Electron correlation effects
- 3) The polarizability of oxygen

This will be discussed in more detail in the following section. To understand complex oxides, we need to consider first what makes the transition metal elements in the periodic table unique compared to their elemental colleagues. Transition metal elements are elements in the periodic table (see Figure 1.2) that correspond to the d levels filling and therefore are called d block elements. Transition metals are elements that have at least one partially filled d-orbital atom or otherwise can produce cations that have partially filled d-subshells. All the transition elements, apart from the first and the last, display various oxidation states, making them interesting from a functional perspective. Not only are they rich in properties, but they are also partly abundant, with Fe, Ti, Mn, Zr, V, and Cr being most commonly found while W, Au, Ag, and Pt are rarer³⁰.

1.2.1 Crystal field theory

Crystal field theory (CFT) describes the bonding interaction between transition metals and ligands³¹. It describes the effect of the attraction between the positive charge of the metal cation and the negative charge of the non-bonding electrons of the ligand. CFT successfully accounts for some magnetic properties, splitting of the orbitals, and colors of transition metal complexes, but it does not describe bonding.

The electrons in the d orbitals of the central metal ion are surrounded by an electric field created by the negatively charged ligands. Therefore, the d electrons closer to the ligands will have a higher energy than those further away, which results in the splitting of d-orbitals in energy. This splitting is affected by:

1. The nature of the metal ion
2. The metal's oxidation state (a higher oxidation state leads to a larger splitting)
3. The arrangement of the ligands around the metal ion
4. The nature of the ligands surrounding the metal ion

In an isolated atom or ion, all five d-orbitals (Figure 1.3) have degenerate electronic structure, meaning the energy levels of the 5-fold 3d orbitals have the same energy. However, when the transition metal ion is surrounded by ligands (oxygen), the d-orbital energy level splits into different energy levels. Crystal field theory describes the effect by considering the ligands' negative point charges that repel the d-orbital electrons, breaking the degeneracies of the electron orbital and creating an energy gap Δ_0 . When the d-orbital energy levels of a d-metal are split in an octahedral environment, the octahedral crystal field causes the d-orbitals to split into two energy levels, the low energy level t_{2g} and the

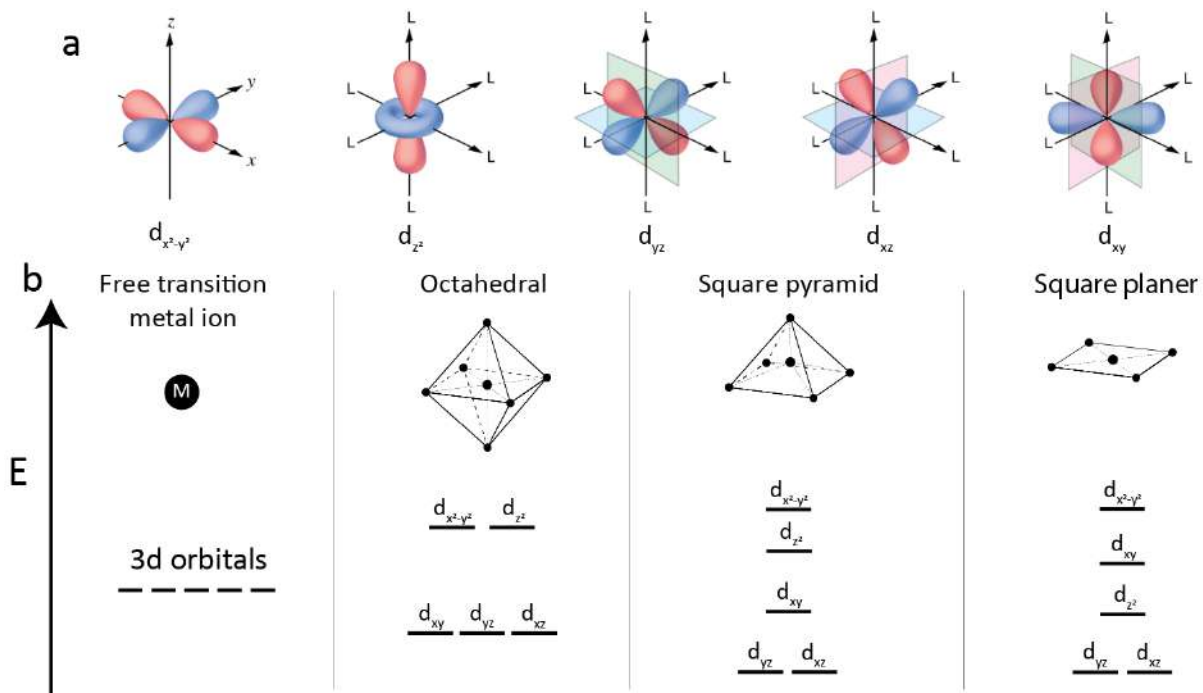


Figure 1.3. Illustration of the five possible d-orbitals of (a). $d_{x^2-y^2}$ and d_{z^2} are denoted as the e_g orbitals while the low energy d_{xy} , d_{yz} and d_{xz} are referred to as the t_{2g} orbitals. Figure adapted from reference [237]. b) Crystal field splitting for the three common structures: Octahedral, square pyramid and square planer, while the five d-orbitals in an isolated are degenerate.

high energy level e_g . The orbital energy depends on their shape (Figure 1.3a), where the non-axial orbitals d_{xy} , d_{yz} and d_{xz} are referred to as t_{2g} and the axial orbitals are referred to as e_g . This shows that the electrostatic repulsion from the ligands has a large effect on the properties, where the e_g orbitals pointing directly towards the ligands raise in energy, while the t_{2g} orbitals located in between lower the energy. As a result, the t_{2g} orbitals will be the first to be filled. If the pairing energy is smaller than Δ_0 , two electrons will occupy the same orbital according to Hund's rule ($\uparrow\downarrow$), referred to as low spin, while in the opposite situation, where the pairing energy is lower than Δ_0 , the electrons occupy all five orbitals before pairing the spin. In other words, in high-spin configuration, every orbital is first occupied by one electron before adding a second electron to any of them, just like with degenerate d-orbitals. In the low-spin configuration, the lower energy level is completely filled before the higher level is occupied. Properties such as color, magnetism, structure, stability, and reactivity depend on Δ_0 , and the pairing energy. The most common crystal fields found in complex oxides are the octahedral, tetrahedral pyramidal, and square planar as illustrated in Figure 1.3b.

1.3 Perovskite: SrTiO_3

Perovskite-type transition metal oxides display a vast variety of compositional and structural variations and, as a result, a wealth of interesting magnetic and electric behaviors³². Strontium titanate (SrTiO_3 or STO) has a perovskite structure like CaTiO_3 , the mineral from which the name was derived. The cation in STO is titanium (Ti), while strontium (Sr) is positioned at the corners of the unit cell. The TiO_6 -octahedral exhibits

covalent bonds, while Sr²⁺ and O²⁻ exhibit ionic bonds, which results in a mixed state of bonds. STO, with its lattice constant (3.905 Å)³³ (Figure 1.5a), provides an excellent lattice match to most materials with perovskite structure. For that reason, it is an excellent substrate for the epitaxial growth of many oxides' thin films^{34,35}.

1.3.1 Stability of the perovskite

With the effect of the oxygen ligands on the transition metal's band structure in mind, we will now consider distortion of the structure and what effect this will have on the electronic configuration. Structural deformations have been shown to greatly affect perovskite's electronic and magnetic properties³⁶. These types of distortions are typically provoked by stress³⁷ and change of temperature³⁸ that cause the octahedral to deform, ultimately causing rotation and tilting³⁹. This type of mechanical deformation opens a pathway for scientists to engineer properties.

In an ideal cubic perovskite structure (ABO₃), the atoms are just touching one another, the B–O distance is equal to $a/2$ and the A–O distance is $\sqrt{2}(a/2)$, where a is the cube unit cell length and the following relation between radii of ions holds: $R_A + R_O = \sqrt{2}(R_B + R_O)$. Goldschmidt⁴⁰ found that the perovskite structure is retained in ABO₃ compounds even when this relation is not exactly obeyed. The Goldschmidt tolerance factor, $t = \frac{r_A + r_O}{\sqrt{2}(r_B + r_O)}$, relate the ionic radii of the corner-sided A atoms, centered transition metal B atom and electronically stabilizing anions (in most cases oxygen). In general, materials with a tolerance factor of 0.9–1.0 have an ideal cubic structure^{40,41}. A tolerance factor of 0.71–0.9 results in a distorted perovskite structure with tilted octahedra⁴². Non-perovskite structures are formed when the tolerance factor is higher (>1) or lower (<0.71)⁴³. Examples of material larger than 1 ($t = 1.063$) is BaTiO₃ that favors a ferroelectric displacement, while CaTaO₃ ($t = 0.946$) favors an antiferroelectric displacement^{32,41,44}.

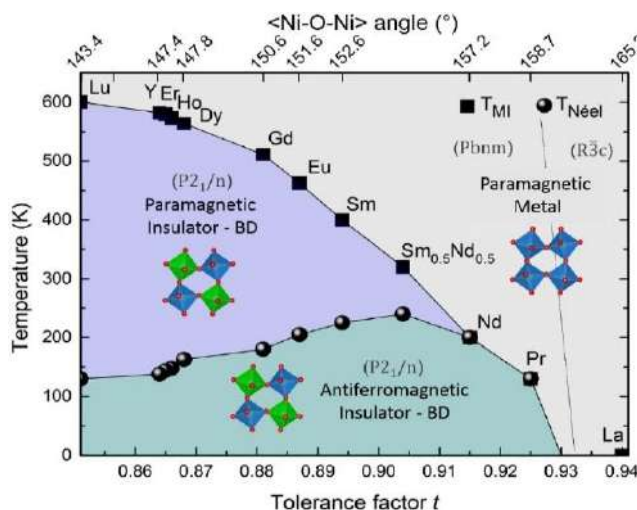


Figure 1.4. The Ni-O-Ni angle in nickelates plays an important role in structural distortion and has the ability to change the metal-to-insulator transition temperature. Figure adapted from reference [38].

The perovskite nickelate family is characterized by the chemical formula RNiO₃ where R is a trivalent rare earth R = La, Pr, Nd, Sm, Eu, Gd, Dy, Ho, Er, Y, and Lu. The physical and structural properties of these compounds are summarized in the phase diagram displayed in Figure 1.4³⁸, parameterized by temperature and tolerance factor. In this work, the evolution of the metal to insulating transition in the RNiO₃ can be correlated to the Goldschmidt tolerance factor. In addition to substituting the full number of A-side atoms, it is also possible to partially substitute the A-side atoms, diluting

the structure, and effectively doping the crystal. A pristine example is the $\text{La}_{2-x}\text{Sr}_x\text{CuO}_4$, where incorporating Sr induces a high-temperature superconducting phase⁴⁵ and the manganites, where doing LaMnO_3 (LMO) with the larger Sr obtaining $\text{La}_{2/3}\text{Sr}_{1/3}\text{MnO}_3$ strongly enhances the transport properties⁴⁶.

1.3.2 SrTiO_3 symmetry

At room temperature, STO is a cubic structure with space group $Pm\bar{3}m$ and a lattice parameter of 3.905 \AA ³³. STO is characterized by a Goldschmidt tolerance factor very close to unity.

The structure of STO is sensitive to temperature variations⁴⁷. Figure 1.5e shows that upon cooling to a temperature below $T_{\text{AFD}} = 105 \text{ K}$, the unit cell of the STO undergoes a phase transition from cubic to tetragonal, with an octahedral rotation angle of 2.1° and elongation of the cubic structure with a c/a ratio of 1.00056 ⁴⁸. Furthermore, below $\sim 105 \text{ K}$ upon crossing a domain boundary, the elongated crystal axis rotates by 90° resulting in the nucleation of twin structures creating a domain structure⁴⁹. STO has another second order phase transition that causes the tetragonality to saturate at a temperature of about $\sim 40 \text{ K}$ ⁵⁰.

The structure of STO is distorted from the ideal cubic structure, for example, under stress or a change in temperature. These two distortions manifest themselves as shown in Figure 1.5a-d³² either as “conventional” ferroelectric displacement (Figure 1.5b) of the ions from their symmetry position or as antiferrodistortive (AFD) rotation of the oxygen TiO_6 octahedral (Figure 1.5c) with an antiphase rotation of the neighboring octahedra’s.

In the limit of zero temperature where thermal fluctuations are absent, phase transition with respect to a non-thermal tuning parameter such as pressure and composition, can be driven purely by quantum fluctuations. In this region, the interplay between quantum and thermal fluctuations can lead to novel exotic phenomena such as quantum paraelectric transition⁵¹. Quantum paraelectric transition is another unique property of STO⁵² which was also found

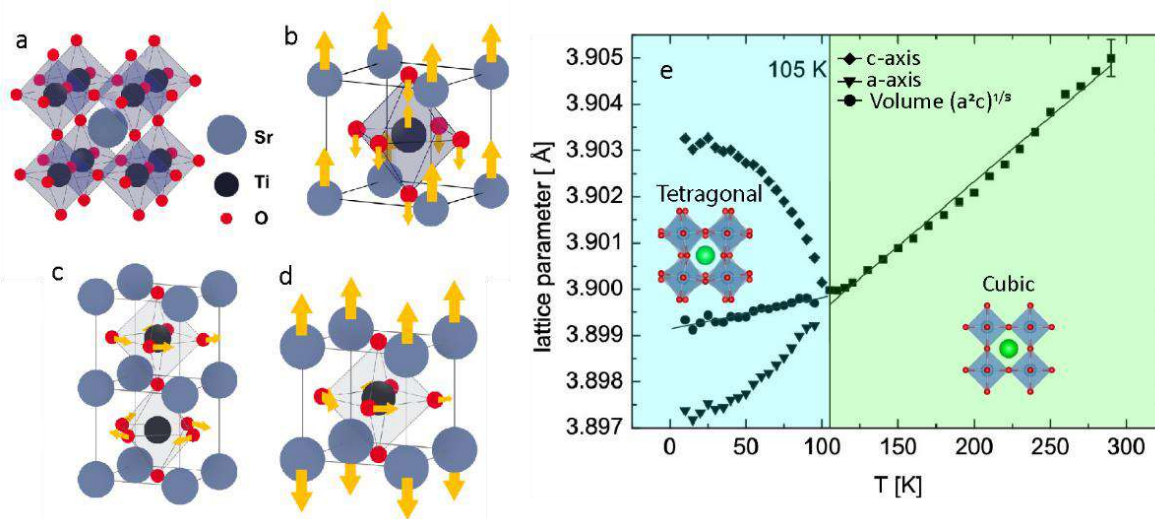


Figure 1.5. STO ranging from ideal cubic to different distorted scenarios. a) At room temperature STO is an ideal face-centered cubic $Pm\bar{3}m$. b) Ferroelectric distortion of STO. Figure adapted from [32]. e) STO structural phase diagram. Figures adapted from references [238,239].

in other systems, such as KTaO_3 ⁵³ and CaTiO_3 ⁵⁴. This occurs when a ferroelectric instability is stabilized by quantum fluctuations. The quantum fluctuations suppress the ferroelectric phase and are often associated with increasing in the dielectric constant⁵⁵.

At room temperature, STO already has a large dielectric constant of $\epsilon_{\text{STO}} = 300$, but this diverges to 20,000 at 4 K⁵² due to the quantum paraelectric transition. At low temperatures ($T < 0.5$ K), STO displays a striking superconductive behavior with low carrier concentration⁵⁶. It was found that substituting the ¹⁶O-isotope with the heavier ¹⁸O suppresses the quantum fluctuations, but also increases T_C for the superconducting phase⁵⁷. The competition for the formation of electron pairing and ferroelectricity, a mechanism known as quantum criticality in STO are still debated.

1.3.3 Defects in SrTiO₃

Understanding defect structure in STO is important to understand the various properties of STO. For example, STO is known as dielectric materials, however, if the materials are not treated carefully the formation of oxygen deficiency gives rise to electrical conductivity⁵⁸.

STO has both cation and anion point vacancies, as well as interstitial defects. For example, in thin films of STO, Ti and Sr vacancies^{8,59} have been observed with a relative concentration of $V_{\text{Ti}}/V_{\text{Sr}}$ depending on laser fluence during Pulsed laser deposition (PLD) film growth. The Ruddlesden-Popper (RP) phases of STO which have a $\text{Sr}_{n+1}\text{Ti}_n\text{O}_{3n+1}$ structure are another type of defect in STO⁶⁰ and have its simplest form for $n = 1$ (Sr_2TiO_4); it corresponds to the removal of a TiO_2 layer from the perovskite STO structure resulting in a double-layer of SrO.

Oxygen vacancies (V_{O}) are one of the most important factors in modifying the properties of STO and their effect cannot be ignored. The formation of V_{O} in STO is intimately related to the rich variety of physics phenomena, such as electrical⁶¹ and magnetic^{62–64} properties. A cardinal example is the high sheet carrier density at the heterointerfaces between LaAlO_3 (LAO) and STO^{9,65}. Another example are the optical properties of transparent STO which

can change the color from opaque white to blue⁶⁶. Therefore, a fundamental understanding of the role of V_{O} is an essential prerequisite for creating and/or establishing the physics and functionalities.

V_{O} are the most abundant intrinsic point defect in STO and they form as a result of a missing oxygen atom in the lattice shown in the following equation using the Kröger-Vink notation ($\text{O}_{\text{O}}^{\times}$ represents neutral oxygen atom in the lattice)⁶⁷.

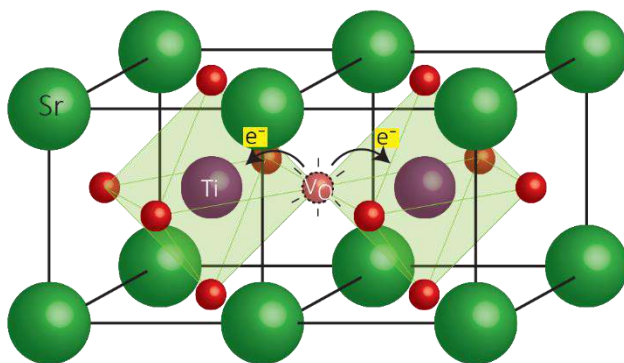
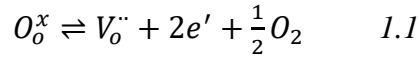


Figure 1.6. Oxygen vacancy in STO lattice. The oxygen vacancy reduces the valence charge of titanium from Ti^{4+} to Ti^{3+} by donating its electrons the neighboring Ti-atoms, although the OV can move in the crystal.



From the above equation, it is evident that there are two electrons (e') obtained from every $V_o^{\cdot\cdot}$ and that the oxygen vacancies carry a net positive charge, as indicated by two dots when the Kröger-Vink convention is used. This is important because these anion vacancies are responsible for a significant part of the multi-functionality of STO. While stoichiometric STO is electrically insulating, STO becomes metallic with a sufficiently high concentration of V_o and even shows superconductivity at low temperatures (< 300 mK)⁵⁶. The V_o can be easily manipulated with a wide range of variables, such as temperature⁶⁸, oxygen partial pressure (PO_2)⁶⁹, electrical field⁷⁰, and light⁷¹. V_o is often introduced in the crystal by annealing in oxygen reduced conditions (e.g. low oxygen atmosphere at sufficiently high temperatures), resulting in electrically n-type STO⁷². Each V_o dopes the sample with $2e^-$. However, these may be localized and not contribute to the conductivity but rather act as a magnetic impurity⁷³. The vacancies have also been shown to migrate under an electric field at elevated temperatures, resulting in a colored gradient⁷⁴. At $T = 295$ K the diffusion coefficient of V_o is $\sim 10^{-14} \text{ cm}^2 \text{ s}^{-1}$ while at $T = 1600$ K the diffusion coefficient is $\sim 10^{-4} \text{ cm}^2 \text{ s}^{-1}$. Figure 1.6 illustrates the formation of V_o and the contribution of the two electrons from the equation above to the Ti orbitals, reducing the Ti valance from Ti^{4+} to Ti^{3+} .

1.3.4 Selected properties of bulk $SrTiO_3$: superconductivity

Schooley et al.⁵⁶ reported a superconducting phase transition below 250 – 280 mK (**Figure 1.7**) in reduced STO. This was the first observation for superconductivity in the complex oxide and paved the way for the search for high T_c superconductors, but was it disregarded due to its very low transition temperature. Surprisingly, the superconductivity in STO exists with a very low carrier density of $5.5 \times 10^{17} \text{ cm}^{-3}$ with the transition temperature being tunable by varying the carrier density. This was a milestone since it had the tunable properties from a semiconductor to a superconductor. Such a superconducting transition was only discovered in traditional metals. When a material undergoes a superconducting phase transition, the electrons can move freely though the lattice without scattering, resulting in a state of zero resistance. This phenomenon was discovered in 1911 by the Dutch physicist Heike Kamerlingh Onnes, but it was not until 1957 that

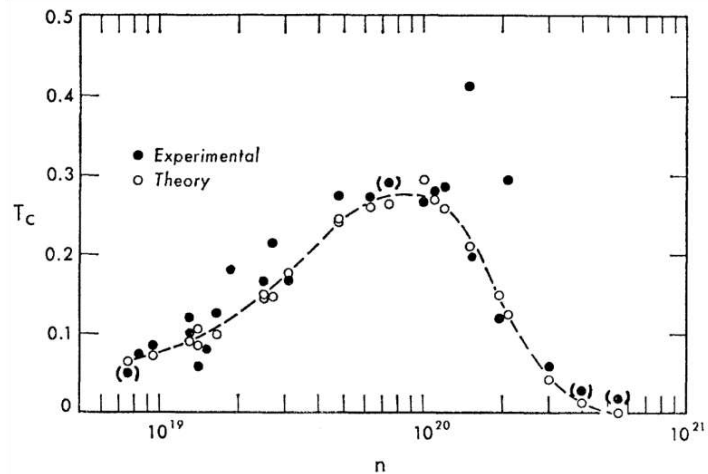


Figure 1.7. Critical temperature as function of carrier density for defect reduced STO. Reduced STO is possible to undergo a superconducting transition at low carrier density of $5.5 \times 10^{17} \text{ cm}^{-3}$, and has a peaking transition temperature of 250-280 mK. Figure adapted from reference [56].

a mechanism was proposed by Bardeen, Cooper and Schrieffer (BCS), which suggests that electrons condense into pairs. Superconductors are typically divided into two classes: type I and type II superconductors. Type I superconductors are described by the BCS theory, where two electrons form a pair near the Fermi energy. In 1950, Vitaly Ginzburg and Lev Landau suggested that a type II superconductor should form in homogeneous states in the presence of a strong magnetic field. This would form Abrikosov vortices⁷⁵, which are vortex-shaped flows of supercurrent where the length of the normal conducting vortex core is equal to the coherence length, ξ . The coherence length is smaller than the penetration depth, described by the GL parameter and will be discussed later. ξ describes the change in the order parameter over a length scale and is the size of a Cooper-pair. Solving the GL differential equation yields an expression for the coherence length⁷⁶:

$$\xi = \frac{\Phi_0}{2\sqrt{2}H_c(T)\lambda_{\text{eff}}(T)} \quad 1.2$$

where Φ_0 is the magnetic flux quantum and λ_{eff} is the effective penetration depth, which is the measured penetration depth. Type I and type II superconductors differ mainly by their response to an external magnetic field H . Applying a magnetic field to a type I superconductor will result in the field being expelled until reaching a critical field H_c where the superconducting state is destroyed. The expulsion of the magnetic field is known as the Meissner effect. The superconducting state is also sensitive to a current exceeding the critical current I_c , which is when the kinetic energy of the electrons is larger than the bonding energy of the cooper pair, thus energetically favorable to split up and terminate the superconducting state. The critical magnetic field and critical temperature are expressed by the following parabolic equation⁷⁶:

$$H_c(T) \approx H_c(0) \left[1 - \left(\frac{T}{T_c} \right)^2 \right] \quad 1.3$$

A type II superconductor has a critical field similar to a type I superconductor where the Meissner state is not broken and is a perfect diamagnet; however, exceeding that critical field will not destroy the superconducting properties, but rather hover into a mixed state. In this mixed state, part of the magnetic flux will penetrate the superconductor and pin the magnetic flux, creating superconducting vortices. These vortices are pinned to the penetrating field lines. To understand the mixed state, one should first consider the regime just above H_{c1} . In this state, the vortices are well-separated, and the circulating supercurrent around the normal core has a size equivalent to the penetration depth λ , while creating a moment of one unit of magnetic flux quantum $\Phi_0 \equiv \frac{hc}{e}$, while the normal conducting core has a size of the coherence length. A finite resistance begins to arise when exceeding H_{c1} . As H approaches H_{c2} , more field lines penetrate the superconducting material, resulting in more vortices being formed. As $H = H_{c1}$ the number of vortices in the material becomes so large that the vortices overlap, which results in a larger finite resistance and the mixed state transitions into a normal state.

Type I and II superconductors are also distinct by a parameter from Ginzburg-Landau theory⁷⁶. The Ginzburg-Landau parameter $\kappa = \lambda/\xi$ describes the ratio between penetration depth and the coherence length and has a positive surface energy for a type I superconductor where the $0 > \kappa > 1/\sqrt{2}$ and negative surface energy for a type II where

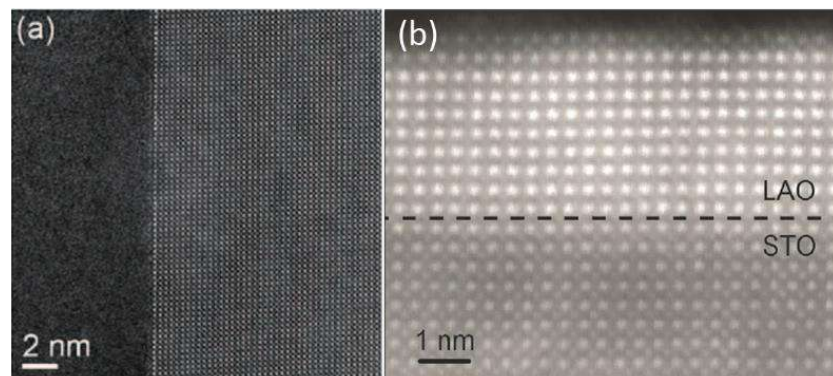
superconductor $\kappa > 1/\sqrt{2}$. Superconductivity in a 2D film is governed by the Berezinskii-Kosterlitz-Thouless (BKT) transition⁷⁷, which can be characterized by the temperature T_{BKT} . For $T < T_{\text{BKT}}$, vortex pairs with opposite signs are formed. At $T = 0$ and zero field, the system will seek the lowest energy which contains no vortices. As the temperature increases, the anti-parallel vortices are formed. At low enough temperatures these vortices are bound, but increasing the temperature will surpass the threshold and the vortices become free. The result of the free vortices is that they destroy the superconductivity, resulting in a finite resistance. Since the vortices are not superconducting in the center with a width of ξ , the film does not form vortices in presence of a parallel field, and the superconductivity is not destroyed as a result of vortex formation. Furthermore, since the film is thin, the Meissner effect does not have to expel a high quantity of field lines, and as a result, the parallel field is much larger than the perpendicular in a thin film.

1.4 SrTiO₃ – based heterointerfaces

Since the discovery of two-dimensional electron gas (2DEG) at the heterointerface between LAO and STO, a wide variety of emergent physical properties, such as superconductivity⁷⁸, magnetism⁹, and spin-orbital coupling⁷⁹, have been reported. These heterostructures are generally formed by depositing oxide thin films on STO substrates. The epitaxial template is a very important factor for the quality of the interface and the overall heterostructure. Epitaxial growth of oxide films provides a powerful pathway to create new states of matter at interfaces as a consequence of the interactions between the spin, charge, orbital, and lattice degrees of freedom. STO is a widely used substrate for the growth of functional oxide films as it is possible to obtain a single-terminated atomically flat surface utilizing selective wet-etching and annealing^{80,81}. Additionally, STO has a cubic lattice constant of $a = 3.905 \text{ \AA}$ that fits reasonably well with many possible top films⁸². Figure 1.8a shows an amorphous film on a STO single crystal, while an atomically abrupt interface between a 9 unit-cell LAO layer and STO substrate can be formed with atomical precision (Figure 1.8b). In the past three decades there has been an advance in techniques in thin film growth. Particularly, the controllable and precise characteristics of PLD allow the deposition of atomically flat oxide films and control the layer-by-layer growth. Other deposition methods have also been used, such as sputtering, molecular beam epitaxy (MBE) and atomic layer deposition (ALD).

Molecular beam epitaxy is not only suited for growing III-V semiconductor heterostructures, but has also found its place in the field of complex oxides. MBE is a low-

Figure 1.8. High-resolution transmission spectroscopy image of amorphous LAO/STO, displayed as crystalline STO substrate to the right with non-crystalline LAO on the left-hand side. Adapted from reference [240] (b) crystalline LAO (top) on STO (bottom) with a sharp interface. Figure adapted from reference [241].



energy deposition technique and is therefore able to avoid defects which are usually caused by high-energy species on the substrate. To overcome typically MBE growth conditions, i.e. the very low base pressure and high-temperature conditions for a growth of stoichiometric⁸³, a hybrid MBE technique utilizing a volatile organic compound binding the titanium substituting the solid titanium source. This results in opening the stoichiometric growth window significantly, and making STO growth more assessable^{83,84}.

Sputtering and *atomic layer deposition* are other deposition techniques which are also used for oxide film fabrication⁸⁵. They have advantages for large-area film deposition and high deposition rate compared to MBE and PLD techniques, which makes the techniques widely used in the industry.

Pulsed laser deposition is the most used technique for the deposition of a wide variety of oxides and STO-based interfaces. In PLD, a laser with a high-power density and narrow frequency bandwidth is used as a source for ablating desired materials. The ablated species are then transferred in its plasma state (plume) to the substrate. The description of PLD will be described in more detail in the following chapter.

The most commonly studied STO-based heterostructure is the crystalline LAO grown on the (100) surface of STO. The discovery of the 2DEG interface between two non-conducting large band gap insulators such as STO and LAO, was reported in 2004 by Ohtomo and Hwang⁸⁶. This extensive breakthrough led to numerous discoveries in the 2DEG in the following years^{32,87} which will be discussed in the following section. For that reason, it is tempting to quote the phrase “the interface is still the device”⁸⁸. Surprisingly, the interface conductivity is governed by a critical thickness of LAO²⁰. When 4 unit-cells of LAO is deposited, the interface changes from an insulating state to a conducting state. It is also possible to induce the conducting state in a 3 unit-cell thin film of LAO, by using an electrical field. The width of the interface in STO(001) is found to be confined and has a small spatial width of 1 nm⁸⁹, while in STO(111) is found to be much broader with a 3.3 nm⁹⁰.

The Ti 3d band of bare STO crystal is split into the low energy t_{2g} and higher energy e_g bands⁹¹ (see also chapter 2.1). However, during the growth of an epitaxial layer on STO such as LAO, this causes additional distortion on the octahedral caused by inversion symmetry breaking, splitting the orbitals further depending on the interfacial orientation⁹². The splitting sequence of the band depends not only on the type of the top layer but also on the STO orientation. For the STO(001)-oriented interface the e_g bands, i.e., d_{z^2} and the d_{yz}/d_{xz} are pushed to a higher energy state, while the t_{2g} bands, i.e., d_{xy} and $d_{x^2-y^2}$, perturbed to a lower energy state. On the other hand, the STO(111)-oriented interface, the t_{2g} splits into a_{1g} singlet and e'_g doublet, with a minimal energy difference⁹⁰.

The LAO/STO interface is a paradigm example, exhibiting conducting 2DEG, between two non-magnetic insulating metal oxides. In the (001) direction, two different interfaces can be formed between polar LAO, which consists of alternating $(\text{LaO})^+-(\text{AlO}_2)^-$ layers, and

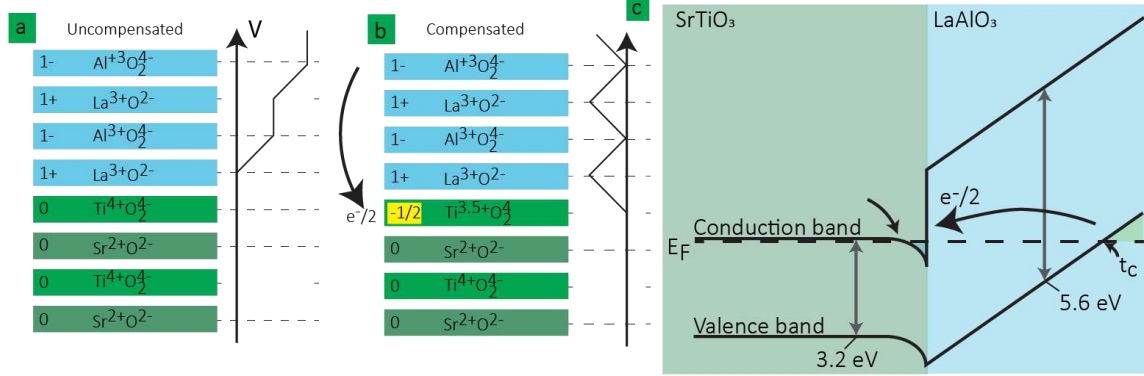


Figure 1.9. Polar catastrophe mechanism in LAO/STO. (a) Alternating layers of STO, $\text{Sr}^{2+}\text{O}^{2-}$ and $\text{Ti}^{4+}\text{O}_2^{4-}$ for uncompensated LAO film on STO, where (b) displays the half electron compensation from the surface to the interface. (c) band diagram of STO and LAO.

nonpolar SrTiO_3 , which consists of alternating $(\text{SrO})^0$ - $(\text{TiO}_2)^0$ layers. One is called *n*-type (i.e., LaO/TiO_2) and the other is called *p*-type (i.e., AlO_2/SrO).

At present, no single mechanism can fully explain the experimental observation of the interfacial conductivity in this LAO/STO system. For the formation of 2DEG at *n*-type interfaces, three main mechanisms have been suggested:

Polar catastrophe: A leading interpretation for the interfacial conductivity is based on the “*polar catastrophe*” mechanism⁹³. The polar stacking of the charged LAO atomic planes on the neutral STO planes gives rise to an electrostatic potential difference across the LAO film that increases proportionally to its thickness and therefore a sufficiently thick LAO film must be relaxed by an interfacial reconstruction. It was proposed that an electronic reconstruction may be the dominating effect, involving a transfer of electrons from LAO to STO, likely into the STO Ti *3d* conduction band close to the interface, thus giving rise to the interfacial conduction (Figure 1.9). Although this model seems to provide an appealing explanation for many important features of the observed phenomena, there are unresolved issues. Thus, a consensus on the correct physical interpretation has not yet been reached. One example of unresolved issues is the difference between the electronic carrier density measured in well-oxidized samples ($2 - 4 \times 10^{13} \text{ cm}^{-2}$) and that predicted by the polar catastrophe model ($3 \times 10^{14} \text{ cm}^{-2}$). A possible explanation for this “missing charge” problem is that part of the electrons injected into the interface are localized and therefore do not contribute to the conduction^{94,95}.

Oxygen vacancies: Polar catastrophe cannot solely explain the conductivity in the interface of LAO/STO. Other studies show that annealing STO at above 600 °C in vacuum⁹⁶ or growing LAO films on STO at different PO_2 changes the conductivity. Chen *et al.* even showed that the non-crystalline amorphous LAO heterostructure becomes conducting⁹⁵.

Cationic intermixing: A third mechanism to explain the conducting interface of LAO on STO is cationic intermixing, sometimes referred to as interdiffusion⁹⁷. It has been observed in the first few unit-cells of the interface⁹³. In the case of La_{Sr} defects, the La^{3+} effectively works as a dopant substituting the Sr^{2+} . This is caused by Ti^{4+} reducing to Ti^{3+} as an effect of compensation from nearby Ti-layers. Additionally, Zunger *et al.* realized that at a

thickness above the critical thickness of LAO (4 unit-cells) a spontaneous formation of oxygen on for surface of LAO appears⁹⁸.

Each mechanism represents one aspect of the interface physics and explains some experimental findings, but conflicts with a few others. None of the mechanisms explains the insulating nature of *p*-type interfaces. For interface magnetism, it was shown experimentally that the local magnetic moments are associated with Ti³⁺ ions⁹⁹. However, it is yet unclear whether such Ti³⁺ ions reside in STO, or LAO, or both near the interface.

1.5 SrTiO₃ – based heterointerfaces: properties

As explained earlier, the realization of an atomically abrupt interface is an important step to successfully obtaining new and exotic properties. Unlike the conventional semiconductor 2DEGs, electron gases at complex oxide interfaces involve many-body interactions and give rise to much richer exotic properties such as conduction⁸⁶, interfacial superconductivity⁷⁸, ferromagnetism⁹, and tunable metal-insulator transitions¹⁰⁰, to name but a few. It offers us the opportunity for a new generation of all-oxide electronic devices that can outperform their conventional analogs²⁷.

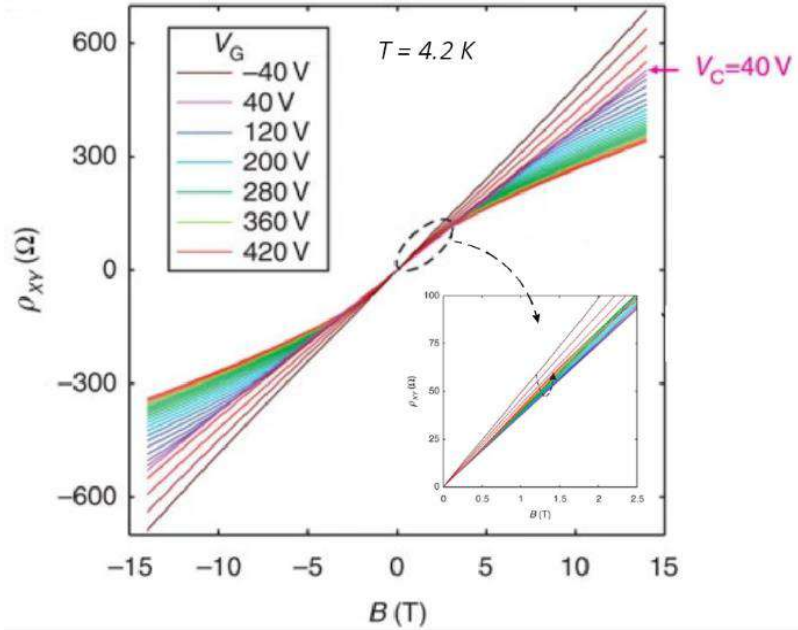
A primary area of current research is to control the states at the STO-based heterostructures through small external modifications, e.g., electrical, magnetic, thermal, or mechanical stimuli⁸⁷. Such a trigger impulse can push the system from one phase to the other, shift the phases to a higher temperature, and may also lead to novel properties that do not normally exist in nature and can only be stabilized in thin films. Additionally, if these oxide interfaces are to be used in future electronic devices, they must be able to be integrated with conventional Si circuits; this is also a subject of intensive research¹⁰¹.

In the following, I will concentrate only on the properties which are used in the current thesis; these are conductivity, superconductivity, and magnetism.

1.5.1 Lifshitz transition

The Lifshitz transition occurs when the carrier density exceeds the critical value from which new bands with different symmetry begin to populate^{102,103}. For STO with tetragonal symmetry below 105 K, the light d_{xy} band is split to lower energy (see Figure 1.3b), compared to the heavy d_{xz}/d_{yz} bands and therefore the d_{xy} band fills up first. Upon reaching the critical value at the band bottom of d_{xz}/d_{yz} (T_{Lifshitz}), multiple bands start occupying. This can be observed from Hall measurements. By tuning the electrical gate (tuning the carrier density), the Hall resistance shifts from a linear to a non-linear multiband resistance. This is due to exceeding the Lifshitz critical point, where both bands with multiple carrier masses contribute to the total Hall resistance¹⁰². Figure 1.10 displays an

Figure 1.10. Hall resistivity (ρ_{xy}) in presence of an external magnetic field. A single band conductor will show a linear response to the field, while a multiband with difference carrier densities and mobility will show a non-linear trace. The 2DEG reaches the Lifshitz transition at 40 V, going from single to multiband conduction. Figure adapted from reference [102].



example of LAO/STO interface electrostatically tuned with a back gate to tune the Fermi level with a Lifshitz transition at 40 V.

1.5.2 Superconductivity in LaAlO₃/SrTiO₃

Superconductivity has been found not only in reduced bulk STO, but also at the 2DEG-interface in LAO/STO heterostructures. Both show similar critical temperatures ($T_C < 300$ mK)⁷⁸. Similar to bulk STO, the 2DEG-interface in LAO/STO heterostructure is gate-tunable (carrier density), resulting in a dome-shaped superconducting phase with a transition temperature ranging from ~ 300 to 0 mK. It is a Berezinskii-Kosterlitz-Thouless (BKT) transition⁷⁷, that the superconductor is of the interface and not the bulk¹⁰⁴. This also means that the critical magnetic field is highly dependent on the direction of the field¹⁰⁵. It has been suggested that the maximum of the dome¹⁰², is the Lifshitz transition, meaning all three t_{2g} bands (d_{xy} , d_{xz} and d_{yz}) band resulting in multi-band interactions in the 2DEG. Additionally, the LAO/STO 2DEG has shown to coexisting superconducting and magnetic phase¹⁰⁶.

To obtain a basic understanding, the perpendicular fields, parallel fields, and coherence length will be discussed in this section. As described in chapter 1.3.4, the direction relative to the superconducting phase dictates the order of the critical field. The first field can be calculated from GL theory and is also referred to as the thermodynamic field.

$$H_{c1} = \frac{\Phi_0}{4\pi\lambda \ln(\kappa)} \quad 1.4$$

Increasing the magnetic field exceeds the thermodynamic field and results in field lines penetrating the superconductor. Since LAO/STO 2DEG is a type II superconductor¹⁰⁵, it has a second critical field. During the nucleation process in a bulk superconductor, field lines penetrate the solid, slowly turning it into a normal conductor when exceeding the second (and largest) critical field, given by⁷⁶:

$$H_{c2} = \frac{\Phi_0}{2\pi\xi^2(T)} \quad 1.5$$

This means that at a certain threshold the superconductor has been saturated with penetrated flux quantum. This happens when the number of vortices in the superconductor becomes large enough such that there is no more room for the vortices in the superconductor, thus resulting in the normal state conductance core of the vortices overlapping, which leads to a universal normal state conductance for the system. An intuitive understating of equation 1.5 is that, Φ_0 is the flux quantum and takes the value $2.01/\text{mT}(\mu\text{m})^2$, and since ξ is the length of the vortex core, H_{c2} relates the number of vortices to the size of the vortices in the superconductor. This illustrates that at a certain threshold there is no place for additional vortices. For a 2D superconductor, vortices can only be generated by the perpendicular field as an effect of the equation for the perpendicular field. The expression can also be rewritten in terms of the thermodynamic critical field $H_{c2} = \sqrt{2}\kappa H_c$ showing the nucleation field scales with the thermodynamic field. Since LAO/STO has a 2D superconducting nature, we need to consider the expression for the parallel critical field⁷⁶:

$$H_c = 2\sqrt{6} \frac{H_c \lambda}{d} \quad 1.6$$

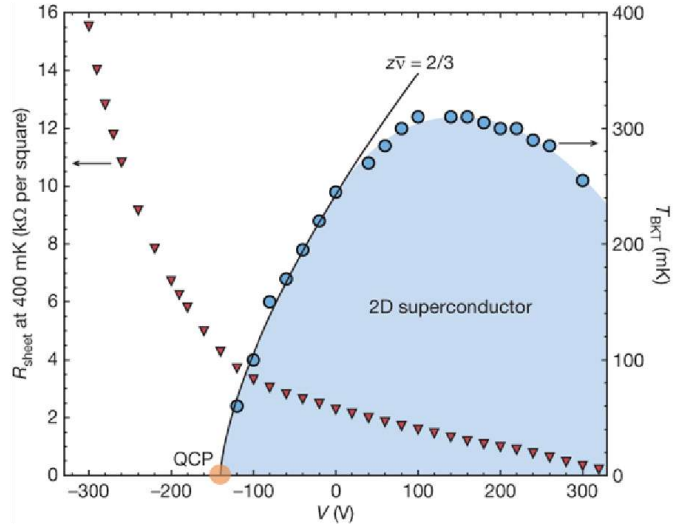
where λ is the London penetration depth, d is the thickness of the 2-dimensional superconducting state and H_c is the first critical field also referred to as the thermodynamic critical field for a bulk superconductor independent of shape and size. The parallel critical field can largely exceed the thermodynamic field if d/λ is small, since the diamagnetic energy for a given field is much smaller for a thin film compared to a bulk superconductor and is therefore able to maintain the superconducting state for a larger field¹⁰⁵.

Combining the parallel and nucleation fields with the coherence length, we can obtain an expression for the thickness d of the 2D superconducting film. This is done by substituting the coherence length into the equation for the perpendicular field and then substituting the expression for the second critical field into the critical parallel film, resulting in the expression:

$$d = \sqrt{\frac{6\Phi_0 H_c^{\perp}}{\pi(H_{c\parallel})^2}} \quad 1.7$$

From this equation, it is possible to estimate the effective thickness, d , from measurements of the perpendicular and parallel fields, which is used in order to estimate the carrier density. Superconductivity at STO-based 2DEGs is found at temperatures below ~ 300 mK⁷⁸. The two-dimensional confinement of the mobile carriers makes it easy to tune its density and in turn the conductance by the field effect. An interesting feature of the superconducting phase of LAO/STO interface is the ability to electrostatically tune the carrier density allowing an on/off switching of superconducting phase transition, thus being able to switch between an insulating and superconducting state exceeding the quantum phase transition (QPT). A phase diagram showing the different phases of LAO/STO by Cavaglia et al.¹⁰⁷ is shown in Figure 1.11. As the phase diagram shows, an applied gate

Figure 1.11. LAO/STO 2DEG gate tunable superconducting phase transition. Left axis (red triangles) displays the sheet resistance with respect to gate tuning in the normal regime at 400 mK, while the right axis (blue circles) displays the BKT transition temperature with respect to gate voltage. The maximum transition temperature is found at ~ 300 mK at the top of the dome where the Lifshitz transition occur. Figure adapted from reference [107]



voltage between -300 V and 320 V changes the normal state sheet resistance by two orders of magnitude, but also tunes the critical temperature of the superconducting transition temperature. At the largest negative gate voltage, where the electron density is smallest, the resistance is largest. As the electron density is increased, the resistance drops. At $R_s \sim 4.5$ k Ω the electrons condense into a superconducting phase. Remarkably, the transition Resistance (R_c) is surprisingly close to the quantum resistance for bosons with $2e$ charge, where $R_Q = \frac{h}{4e^2} = 6.45$ k Ω . If one would keep increasing the gate voltage, the differential R_s becomes smaller, but T_{BKT} increases to a maximum of ~ 310 mK before it starts dropping again, resulting in a dome structure of the superconducting phase diagram.

1.5.3 Magnetism

LAO and STO are both non-magnetic band insulating materials, therefore, the first result by Brinkman et al.⁹ in 2007 of a magnetic interface between the two materials was surprising. The report shows that in the temperature dependence of the sheet resistance, there was a Kondo-like minimum followed by a saturating upturn in the resistance associated with Kondo scatterings.

Magnetization measurements have been carried out by a wide range of direct and indirect methods, including SQUID magnetometry⁸, scanning SQUID magnetometry⁷, torque magnetometry¹⁰⁶, x-ray magnetic circular dichroism^{11,99} and indirect transport studies such as magnetoresistance⁹ and anomalous Hall effect^{6,108}

Utilizing SQUID, Ariando et al.¹⁰⁹ reported that the LAO/STO interface displays a large negative magnetization below 60 K from zero field cooling, with an applied field of 0.1 kOe, indicating a diamagnetic response. However, in the field-cooled data, the magnetization increases significantly, indicating a paramagnetic response. After subtracting the diamagnetic and paramagnetic components, the sample also showed a ferromagnetic hysteresis loop persisting even at room temperature¹⁰⁹.

The ferromagnetic phase depends on the concentration of itinerant carriers n_e and localized moments n_m leading to three possible states³²: (1) if $n_m \gg n_e$ the system will become a non-magnetic insulator since the concentration of the localized moments will be too large;

(2) if $n_m \simeq n_e$ the phase will be a ferromagnetic insulator since the mobile carriers will be just enough to carry the moment and support the long-range ferromagnetic order; (3) if $n_m \ll n_e$ it will be a Kondo conductor without ferromagnetic long order range, since the system will be flooded with itinerant carriers suppressing the ferromagnetic signal. Realizing the need for itinerant electrons to carry the moment, and unpaired spin in non-degenerate $3d$ orbitals allowing for exchange mechanism allows us to set up two criteria for a realization of a ferromagnetic ordered state¹¹⁰:

1. The electrons that are transferred to the otherwise empty titanium $3d$ band modify the valence state from Ti^{4+} to Ti^{3+} thus resulting in an orbital reconstruction from $[\text{Ar}]3d^0$ to $[\text{Ar}]3d^1$.
2. There should be no $3d$ orbital degeneracy, where the d_{xy} and $d_{x^2-y^2}$ are pushed below the d_{yz}/d_{xz} and d_{z^2} , respectively.

The LAO/STO heterostructure meets exactly these criteria, realizing an orbital reconstruction such that the d_{xy} orbital is pushed 26 meV below d_{yz}/d_{xz} and the electron transferred to the interface preferentially will occupy the d_{xy} orbital⁹⁹. These electrons carry a spin and are able to undergo a ferromagnetic ordering. Therefore, it is crucial for the heterostructure to be conducting (4 unit-cells for LAO) in order to achieve the ferromagnetic phase¹¹¹.

The question arises of where the measured magnetism is located at the interface. Techniques such as SQUID magnetometry and scanning SQUID magnetometry do not distinguish the interface from the surface and the middle part of the LAO film. However, X-ray magnetic circular dichroism at the Ti $L_{2,3}$ edge is able to establish more direct proof that the magnetism originates from the Ti^{3+} exchange mechanism⁹⁹.

Does the magnetism originate from impurities within the substrate? The impurity level (Co, Ni, Fe) varies across vendors but is in ppm level⁶⁸. This means that there will be a background magnetization originating from the impurities; however, it was shown by Rice et al.⁵ and many others¹¹²⁻¹¹⁵ that the magnetism is related to the oxygen vacancies level.

Other defects have also been shown to be the reason for the observed magnetism. The magnetic response of A-site Sr-vacancies manifests itself in indirect anomalous Hall effects measurements¹⁰⁸. More prominent defect is the acceptor-like B-site cation vacancy that has also been shown to massively affect the magnetic properties. A study by D. S. Park et al.¹¹⁶ showed that in both homostructure STO/STO and the heterostructure LAO/STO samples grown with varying Al-concentration, showing that the B-site cation film significantly increases the overall magnetization, likely caused by a compensating antisite defect mechanism. This laid the groundwork for further studies, including off-stoichiometric studies to improve the magnetization in these systems.

There have been a wide range of studies on different STO-based heterostructures which show magnetism, such as $\text{LaAlO}_3/\text{Co-SrTiO}_3$ and $\text{LaAlO}_3/\text{Fe-SrTiO}_3$ ¹⁰, introducing a

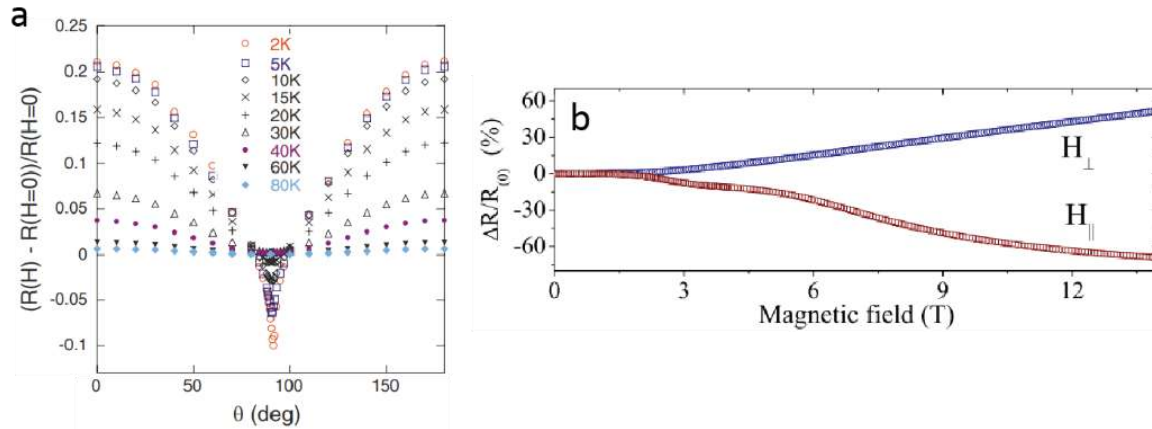


Figure 1.12. The magnetoresistance angle dependency for in LAO/STO systems a) The magnetoresistance as a function of θ at a field of 8 T, stepping in temperatures. Figure adapted from reference [16]. b) The magneto resistance as function of magnetic field for both in-plane and out-of-plane orientated field, shows different sign depending on the orientation of the field. Figure adapted from reference [122].

ferromagnetic buffer layer such as EuTiO_3 or BaFe_3 at the LAO/STO interface to induce spin-polarized electrons by magnetic proximity effect^{117,118}, EuO/SrTiO_3 , MAl_2O_4 [$\text{M} = \text{Ni}, \text{Co}$]/ SrTiO_3 ^{119,120} and GAO/STO ¹²¹. Applying external strain to STO-based heterostructures has been shown to influence the ferromagnetic domain structures^{7,121}. This has been shown with scanning SQUID that by applying stress to the surface of the sample with the tip, it is possible to alter the orientation and magnitude.

1.5.4 Ordinary magnetoresistance

Measuring the resistance in a longitudinal configuration under the influence of an external magnetic field, changes the resistance with respect to the field strength. This is known as magnetoresistance (MR) and is defined as a relative change in the resistance upon applying a magnetic field:

$$MR = \frac{R(B) - R(B=0)}{R(B=0)} \quad 1.8$$

A signature of the LAO/STO magnetoresistance is the anisotropy dependent^{16,122}. This means that the direction of the external magnetic field will result in both positive and negative magnetoresistance for out-of-plane and in-plane perpendicular to the current flow directions (Figure 1.12b), respectively. The strong anisotropy is associated with magnetic scattering from the temperature dependency as an effect of the magnetic ordering temperature dependency.

Another effect that can typically be seen in LAO/STO magnetoresistance is the weak anti-localization¹²³, manifesting itself at a negative correction of the resistivity, and is associated with the spin-orbit coupling¹²³.

1.5.5 Ordinary and anomalous Hall effect

When we apply current between two electrodes and simultaneously apply a magnetic field, it will cause the electrons to deflect to one side as a result of the Lorentz force – this is the ordinary Hall effect (OHE). The signal that we are picking up between the electrodes is

linearly dependent on the magnetic field, and the slope of the line tells us how many electrons we have. The OHE provides a direct method for experimentally probing the nature of the carriers and finding out whether they are holes or electrons, depending on the direction of the deflected, realized as a positive or negative R_{xy} vs B slope, carrier density and mobility.

In the simplest picture, the slope is linear, and the sheet carrier density can be subtracted by $n_s = \frac{IB}{eV_H}$, where B/V_H is the slope of the hall resistance vs. field. This enables us to calculate the charge mobility $\mu_e = \frac{1}{en_s\rho_{xx}}$. One can tune these carriers with an electrostatic gate, and the 2DEG of STO/LAO, for example, shows variation of multiple carriers¹⁰². This is realized as shown in Figure 1.10 with gate tuning the Fermi level and resulting in a non-linear Hall resistance. In this case, the simple model for the sheet carrier mobility needs the additional term including the multicarrier^{102,124}:

$$R_{xy}^{2e} = -\frac{1}{e} \frac{\left(\frac{n_1\mu_1^2}{1 + \mu_1^2 B^2} + \frac{n_2\mu_2^2}{1 + \mu_2^2 B^2} \right)}{\left(\frac{n_1\mu_1}{1 + \mu_1^2 B^2} + \frac{n_2\mu_2}{1 + \mu_2^2 B^2} \right)^2 + \left(\frac{n_1\mu_1^2}{1 + \mu_1^2 B^2} + \frac{n_2\mu_2^2}{1 + \mu_2^2 B^2} \right) B^2}$$

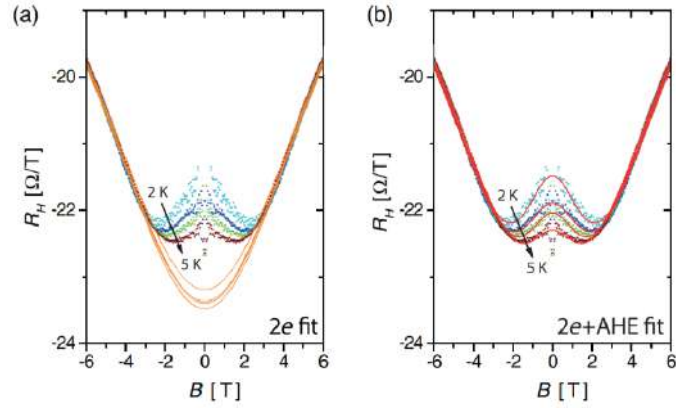
Here the subscripts 1 and 2 reflect the two carriers with different charge carriers and densities originating from the two-band contribution to the overall Hall resistance.

In 2DEG magnetic interfaces, such as the case in STO-based interfaces, the itinerant electrons interact with the magnetic moments, showing a non-linear relationship between the transverse resistance (R_{xy}) vs. magnetic field (B) – it is a signature of Anomalous Hall Effect (AHE) (existence of magnetism in the film). The AHE originates from the carriers carrying a different spin that are spin-polarized, resulting in an imbalanced population of accumulated spins in the opposite direction of the sample¹²⁵. The total hall resistance is thus given by:

$$R_{xy} = R_{xy}^{\text{OHE}} + R_{xy}^{\text{AHE}} = R_{xy}^{\text{OHE}} + R_0^{\text{AHE}} M_z(B)$$

where $M_z(B)$ represents a spontaneous magnetization in the out-of-plane direction and R_0^{AHE} is the saturated resistance. The AHE manifests itself as an increase in the resistance at a small applied external magnetic field but saturates quickly with the field. This is shown in Figure 1.13 where the Hall coefficient $R_H = \left(\frac{R_{xy}}{B} \right)$ at ± 6 T at temperatures ranging from 2 – 5 K for NdGaO₃/SrTiO₃ films. It is evident from Figure 1.13a that one should include the AHE contribution, while in Figure 1.13b implements also the magnetic scatterings in the fit line, only at small fields.

Figure 1.13. Hall coefficient R_H (R_{xy}/B) at $\pm 6 T$. Different color corresponds to different temperature ranging from 2 – 5 K. (a) Fit according to $2e$ model not taking the anomalous contribution into account. (b) Same data displayed with $2e$ model with the additional AHE. Figure adapted with permission from [108].



Typically, the anomalous hall signal is described with a Langevin function¹⁰⁸, therefore, one can rewrite the following: $R_{xy}^{AHE} = R_0^{AHE} \tanh \frac{B}{B_c}$. Plotting this gives the s-shaped data. It is important to keep in mind that the AHE is not a direct way to measure the magnetization, but rather an indirect approach taking spin deflection into account. Nonetheless, it is still possible to obtain information such as the Curie temperature from the 2DEG.

CHAPTER 2

Experimental

2.1 Sample preparation

Surface termination is known to play an important role in determining the physical properties of materials. Achieving high-quality STO-based heterostructure depends very much on the way we prepare our samples. The typical sample fabrication steps are displayed in Figure 2.1. The starting point is a single crystal of STO, where the surface is often double terminated with SrO and TiO₂. The surface of the STO is then etched and thermally annealed to obtain a single terminated TiO₂ surface with well-defined terraces. A uniform and well-defined terminated surface is the prerequisite for achieving high-quality films. These steps are crucial for achieving a high-quality and reproducible sample; hence a detailed description of the termination is made in this section. Although this thesis will mainly consider non-patterned films, it is also possible to create a patterned 2DEG, e.g., a Hall bar, but utilizing a selective etch with a mask that could either be hard or soft or a shadow mask, during deposition^{126–128}.

2.1.1 Single termination procedure

Achieving atomically flat single TiO₂-terminated STO substrates require a two-step treatment: (1) a chemical etch including both DI-water treatment to promote hydroxylation of the topmost SrO layer at the surface of as-received STO¹²⁹ prior to the acidic etch, followed by (2) thermal annealing for recrystallization. For epitaxial film growth, the surface properties of the substrate materials are critical not only with respect to lattice

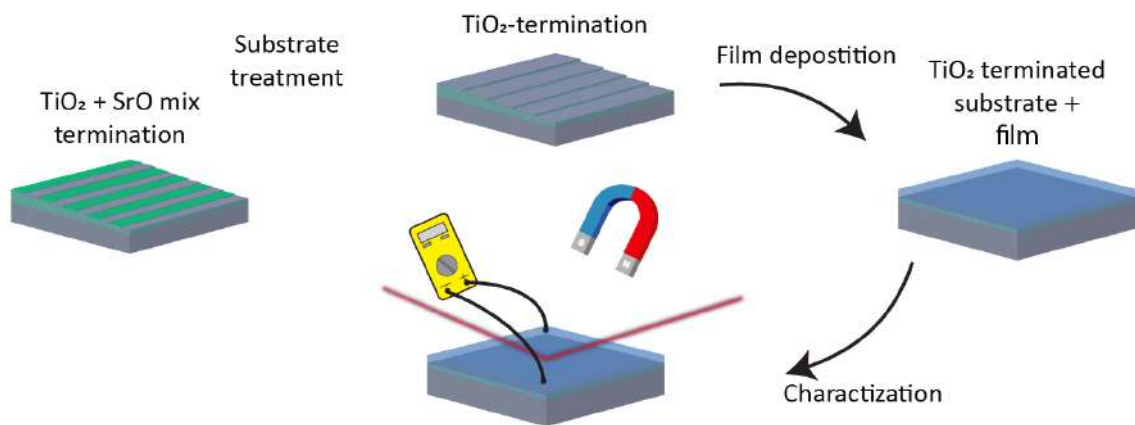


Figure 2.1. Fabricating a STO based hetero- and homostructure are typically realized in these steps: 1. mixed terminating as-received substrates are chemically etched and annealed to achieve single TiO₂-termination. Film deposition, followed by characterization.

mismatch and resulting film strain but also the miscut angle and step-terrace structure at the surface of the substrates may influence the formation of discontinuities or distinct line-defects in the film plane. The terrace width is related to the miscut angle α of the substrate through $w = a / \tan \alpha$, where $a = 3.905 \text{ \AA}$ is the unit-cell height of STO. Commercial STO single crystal substrates are supplied with well-defined crystal orientations, (100), (111), and (110) and with either one or two sides polished and with a given miscut angle. The ideal step height is one unit cell high (3.905 \AA) and the terrace width range is typical about $70 - 500 \text{ nm}$, corresponding to miscut angles of $\alpha = 0.3^\circ - 0.05^\circ$. By increasing the substrate miscut angle, we could systematically reduce the terrace width and thereby increase the density of steps at the surface. A uniform height profile of the terraces is of importance – this will be shown in the following chapter. Achieving a single TiO_2 -terminated can be made in one of the following ways:

Buffered hydrofluoric acid (BHF): Kawasaki's pioneering work⁸⁰ showed that a simple chemical etch can remove SrO for TiO_2 single termination of the substrate surface. Before annealing the STO wafer the post-etch is a crucial step to obtaining well-defined long-order terrace structures¹³⁰. The process was further optimized by introducing a DI-water before the chemical etching to promote strontium hydroxide complex formation that is more easily etched with the chemical etch. Detailed procedure on how to treat the STO single crystal using Buffered HF is given in Appendix A.

Aqua regia: The 'Arkansas' method developed by M. Kareev et al.⁸¹ at the University of Arkansas showed that using a chemical solution of 3:1 HCl-HNO₃ solution would result in similar TiO_2 termination at the surface of STO substrate as the STO surface made by using the conventional BHF method. The advantages of the method are both the safety aspect and fewer oxygen vacancies during the substrate treatment process compared to the highly corrosive BHF method¹³¹. However, there is inconsistency in terms of the aqua regia which has to be mixed every time. This is because nitrosyl chloride (NOCl) and chlorine Cl₂ fume and thus decrease its potency in time while BHF is a premixed solution bought from the vendor.

Thermal annealing: In order to achieve long-ordered well-defined terraces at the surface of STO substrate, thermal annealing in O₂ atmosphere is required after etching to achieve atomic reconstruction. The annealing temperature is crucial; for example, annealing at too high temperatures causes a Sr segregation on the surface^{66,132}. This results in an undesired mixed termination after the acid and thermal annealing process¹³³ Figure. 2.2b is an AFM topography image of the surface of the as-received STO substrate which is rather flat with no defined step-terrace structure¹³². Figure 2.2a shows a typical AFM topography of an STO substrate after etching, but prior to the thermal annealing process. Figure 2.2c shows the surface after annealing. It is clearly visible that straight and quasi-uniformly structured terraces of the single TiO_2 -terminated surface exist after the thermal treatment.

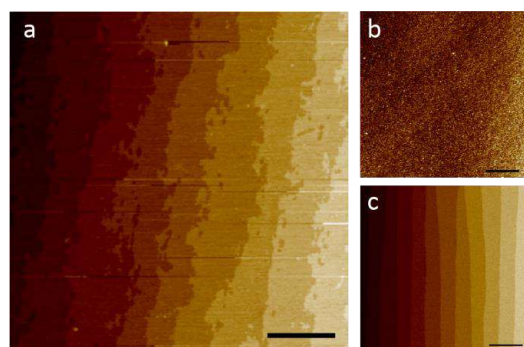


Figure 2.2. a) Etched STO before annealing. The rough terraces are typical before a thermal annealing and a surface reconstruction takes place. b) A as received substrate from supplier B with no treatment shows a flat surface. c) Annealing the sample will create a reconstruction of the surface make long-ranged well-defined terraces. Scale bars in (a) and (b) are 400 nm and bar in (c) is 2 μm .

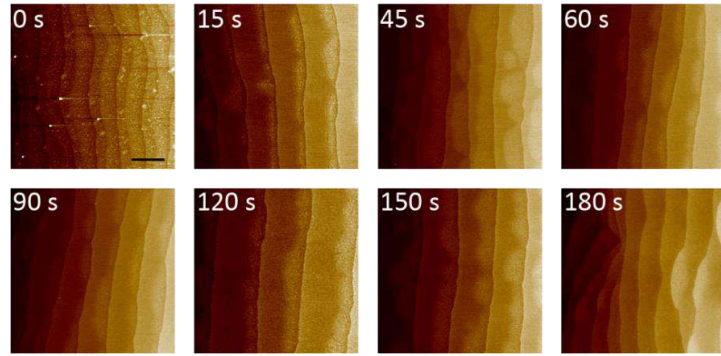
SrO-terminated SrTiO_3 : In contrast, obtaining a singly SrO-terminated STO has shown to be more challenging, as there is currently no selective wet etch for TiO_2 . This has led the way for alternative routes for obtaining such termination. One of the strategies¹³⁴ is to get SrO-terminated STO by deposition of a SrO monolayer on a TiO_2 -terminated STO by using a real-time reflection high-energy electron diffraction (RHEED)-assisted PLD technique. Also, it was found¹³⁵ that when the STO substrates are annealed in air at high temperature (1300 °C), Sr diffuses out from the bulk. This results in progressive SrO enrichment of the topmost surface up to 100% SrO, maintaining remarkably atomically flat perovskite-layered surfaces.

2.1.2 TiO_2 -terminated SrTiO_3 of the current thesis

In order to establish a well-defined and controlled single TiO_2 surface termination, an optimization of the surface termination took place. After the standard etching procedure using - 3:1:16 (HCl(37%):HNO₃(66%):H₂O) commonly known as Aqua Regia. The substrate is then annealed in a tube furnace at 1000 °C for 1 hour in O₂ flow with a ramping rate starting from room temperature of 1.67 °C/minute. Single crystal STO substrates, supplied by our main two suppliers: (1) the German-based CrysTec GmbH Kristalltechnologie (supplier A) and (2) the Japanese Shinkosha Co., Ltd (supplier B), were investigated.

The aqua regia treatment has the advantage of being much more environmentally friendly and safer to work with, compared to the BHF treatment process. Therefore, over the years we have chosen to work with aqua regia and do so also in this thesis. However, recently we have experienced inconsistency in the surface termination; where we normally would achieve quasi-uniform single TiO_2 -terminated surfaces following the otherwise well-used procedure. We now see mixed TiO_2 - and SrO terminations at the recently treated substrates, evident from a half unit-cell height profile utilizing AFM. Therefore, to obtain the singly TiO_2 -terminated surface, I have studied both the effect of acid concentration and etch time in aqua regia on the surface termination. To study the effect of the corrosiveness of the acid's ability to controlled etch the hydroxylated SrO (from the DI water treatment prior to chemical etching) I have chosen different concentrations: (1) a diluted (3:1:32); (2) normal (3:1:16), and (3:1:8) concentrated solutions following the procedure shown in Appendix A. However, by changing the concentration and following the otherwise same procedure of elevated DI water sonication for 20 minutes and 20 minutes in the acid while sonicating at the same temperature as the water treatment, we did not see a noticeable difference of the

Figure 2.3. Substrates from CrysTec GmbH Kristalltechnologie fabricated following BHF treatment with varying etching times from 0 seconds to 3 minutes. The AFM topography images reveals double SrO and TiO₂ termination on the surface for all the samples.



surface. Therefore, the acid concentration in the selected range does not seem to be the problem, whether the acid is not sufficiently strong or too strong. It is well-known that a high-temperature profile can cause SrO to segregate to the surface¹³⁵. Therefore, we have also performed temperature variation studies ranging between 950, 1000 (normally used), and 1050°C using the normal concentrated acid procedure. Again, there is no significant change in the tomography. We cannot tell whether we need to increase the temperatures further to establish a full surface reconstruction or if we would have to lower the temperature further to avoid SrO-segregation on the surface. Refining the surface TiO₂-terminated procedure is very time-consuming, and therefore, to save time, we moved our focus to the most recognized and well-used etchant for TiO₂-terminated STO, the BHF. To overcome the absence of well-defined single terminated terraces originating from the acid treatment, we decided to use the BHF method. We therefore used 6:1 (NH₄F:HF) BHF solution (from Merck). We used the etching protocol described as detailed in Appendix A. The only parameter that we varied was the etching time. This was done on both substrates from suppliers A and B (also to investigate the effect of the single crystal quality) as shown in Figures 2.3 and 2.4, respectively. All the samples have been treated in the same way. Thus, the samples denoted by 0 seconds (not acid-etched) have also been submerged in DI water and annealed in the same manner as the sample e.g., at 60 seconds. Figure 2.3 shows AFM images of the surface of the treated STO as a function of etching time (0 seconds to 3 minutes). The non-etched sample (0 s) has a clear half step termination where the surface is covered with both SrO or TiO₂. Annealing for 15 seconds seems to “agglomerate” the SrO-terminated regions, i.e., the region with the “light” contrast, however, a long etching time of up to 150 seconds does not seem to change the ratio between the SrO and the TiO₂. From this set of data, there does not seem to be a clear trend on whether the etching time plays a major role in the final termination of the STO surface. Etching the substrate has an effect regardless of the etching time. To investigate whether this was a characteristic of a certain substrate batch, we compared the results with other batches but also other suppliers. Figure 2.4 shows AFM topography with corresponding phase images of STO (from supplier B) for different etching times ranging from 0 to 60 seconds.

Surprisingly, the surface from supplier B is remarkably different compared to the substrates from supplier A. Etching these substrates revealed that substrates begin to show signs of over-etching after 30 seconds determined by comparing the height profiles. Nonetheless, the terraces were found to have well-defined widths and clear and sharp edges. The phase images displayed in Figure 2.4b show regions with more explicit phase contrast that are

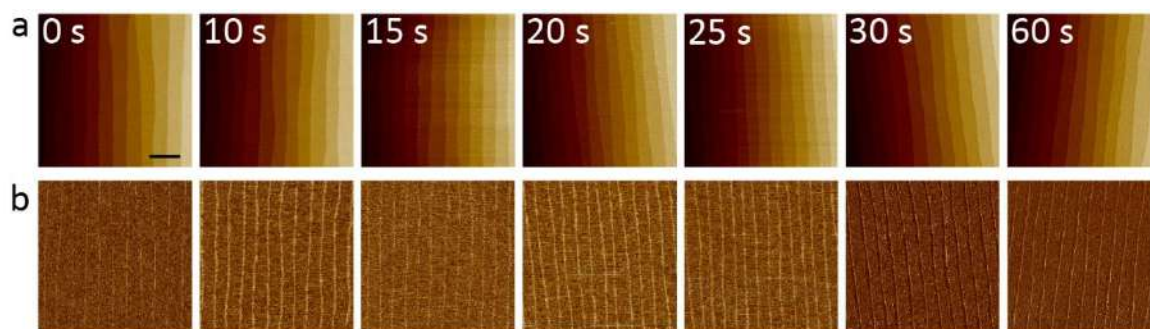


Figure 2.4. ST0 substrates from Shinkosha (supplier B) following the BHF procedure varying the etch time from the non-etched 0 second to the 60 second etched substrate. a) The topography image of the sample, b) shows the phase image of the sample. The non-etched samples are perfectly TiO_2 -terminated confirmed with electrical characterizations, while etching results in a less ideal surface, showing an over etching at 30 seconds at the step of the terrace.

typically associated with different surface termination due to changes in the composition and friction. The minor contrast in the phase images at the edges of these terraces can, of course, be traces of SrO, but this is not clear. Therefore, from these findings, the best surface termination was achieved without etching, but purely through a thermal annealing process. To verify the nature of the termination, we have grown a LAO film on the substrate that should only be conducting with a TiO_2 -termination; the resistance was found to be in the order of $100 \text{ k}\Omega$ with a 2-point measurement at room temperature, manifesting that the majority of the surface is TiO_2 -terminated. Due to the time constraints and the need for a well-defined sample for the proceeding experiments, we decided to use the samples received from supplier B. Furthermore, we did not try to replicate the treatment utilizing aqua regia on the substrates from supplier B owing to the lack of time. This could be a future experiment to test.

2.1.3 Film growth

In this thesis work, I used the PLD as a main deposition technique to fabricate my film samples. PLD is a widely used technique for functional oxide growth owing to its high flexibility and controllability including film growth kinetics, film thickness, and stoichiometry of desired materials. Other methods, such as molecular beam epitaxy (MBE), are also suited for the growth of complex oxides. However, they require significantly higher temperatures and vacuum; although a recent development in the MBE, namely the hybrid MBE⁸⁴ lowers the required temperatures and vacuum needed to access the stoichiometric window. A recent development of the PLD is the metal-organic PLD¹³⁶ that utilizes a metal-organic precursor (e.g., titanium tetraisopropoxide) atmosphere in the PLD and ablation of a target (e.g., SrO) forming a film (STO) with a reduced cation point defect concentration compared to traditional PLD techniques. In the following section, details of PLD as a film growth method will be presented.

2.1.4 Pulsed laser deposition

PLD offers a simple process involving the ablation of a target material with a pulsed 248 nm KrF excimer laser (used in our lab), subsequently forming a plasma plume aimed

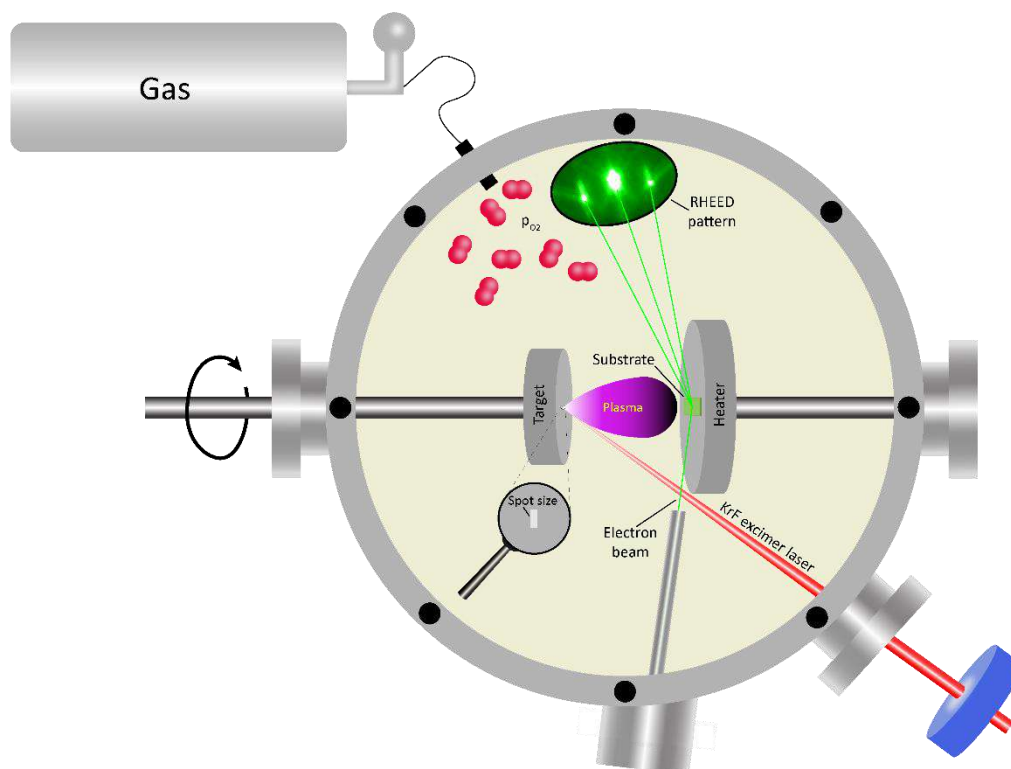


Figure 2.5. Pulsed laser deposition with a KrF excimer laser setup with RHEED to monitor the film deposition. A rotating target is shot by a focused pulsing laser, ablating material towards a substrate with the possibility of heating. An electron beam aimed at the substrate deflects the electron beam creating a real time *in-situ* RHEED pattern allowing to monitor the film thickness and quality. The chamber pressure is controlled and monitored with turbo pumps and gas inlet allowing control of the partial pressure in the chamber.

towards a substrate where the film begins growing (see Figure 2.5). Despite the simple principles, the process offers a high level of complexity. The process involves a large number of variable parameters such as laser fluence, laser spot size, target composition, laser wavelength, laser frequency, background gas, partial pressure during the process, target-to-substrate distance, and substrate temperature. All these parameters can have an impact on the plume and adatom dynamics at the substrate surface. They are often overlapped and interrelated with each other as interdependent parameters. Controlling the epitaxial film growth can be monitored in real time by employing RHEED. In my thesis, the two main parameters that I varied were laser fluence and PO_2 , while keeping the other parameters constant.

2.1.4.1 Laser fluence

Laser fluence is an important parameter which is often overseen and describes the relationship between laser energy and the focused spot size on the target, $F = \frac{E [J]}{A [cm^2]}$. The PLD laser fluence strongly influences the kinetic energy of the ablated species and therefore affects the adatom composition and mobility at the substrate surface, therefore dictating the ablation rate and film thickness¹³⁷. The kinetic energy becomes especially important in the growth of complex compounds; as a result of an inadequate laser fluence it will preferentially ablate certain elements over others, which results in a non-stoichiometric

film^{116,137–140}. It should also be noted that the ablation of a certain element happens surpassing a threshold ablation energy. An example is the control of the stoichiometry of LAO and STO films^{116,139,140}. In the case of STO and LAO, a preferential ablation of Ti/Al (Sr/La) can be induced by increasing (decreasing) laser fluence, leading to the formation of Sr/La-(Ti/Al-) deficient STO and LAO films and therefore to different films/interfaces properties. Since the accurate control of laser fluence was of absolute importance in the current thesis for the determination of the magnetism at the interface⁸, the fluence was measured carefully in each deposition. The laser energy was measured outside the chamber prior to each film growth using a 2D power meter. Nonetheless, it is inevitable that during the ablation, excess material will also ablate and be deposited on the laser entrance window, therefore the energy of the laser beam reaching the substrate is not the same as the one measured outside the chamber. During my thesis I ensured that the value of the fluence was based on the energy measured inside the chamber on the substrate

Spot size: Acquiring the preferred laser fluence can be done either by changing the laser energy or the spot size. The preferred way is to vary the laser energy at a fixed spot size. If the spot size changes, the number of elements ablated from the target changes too, consequently affecting the growth rate. In a study by H. N. Lee et al.¹⁴¹ the authors show that by diminishing the spot size from 7.7 mm² to 0.4 mm², and maintaining the laser fluence, the number of pulses required for a single unit cell went from 7 to 200 pulses for growing STO homoepitaxial heterostructure. Additionally, changing the laser spot size can affect the kinetic energy of the species arriving at the substrate surface.

The spot size used in this thesis is 1.75 mm², measured using an optical paper clamped to the target position in the PLD. To change the fluence, we fixed the spot size, to ensure a consistent growth rate and avoid variations in the amount of oxygen vacancies originating from a change in the spot size¹⁴¹. For each deposition, the laser energy was measured outside the chamber right before entering the PLD chamber. As an effect of depositions in the chamber, it is inevitable that the window will be contaminated in time, thus lowering the actual energy inside the chamber. To avoid this, we regularly opened the chamber to measure the energy both inside and outside. This allowed us to know the energy from measuring outside.

2.1.4.2 Oxygen partial pressure

The background gas and type of gas in the PLD chamber are perhaps two of the most important features for controlling the growth and the resultant properties of the final films. The most commonly used gasses used in a PLD chamber are oxygen, nitrogen, argon, and methane. The gas controls the kinetics of the arriving species thus controlling and incorporating other species in the film e.g., oxygen. The plasma plume is a direct indicator (besides the film) that the growth changes character varying the pressure and gas^{142,143}.

Choosing the exact background pressure is not by any means a trivial process and requires systematic investigation to reach the best solution. By changing the partial pressure, the plume dynamics greatly change and can be categorized into three regimes¹⁴⁴: (1) a vacuum-like regime at low pressure (see Figure. 2.6a); (2) a transition regime where the plume splits and forms two ionic concentrated areas (see Figure. 2.6b); and (3) a diffusion regime where

the ablated particles diffuse away from the plume (see Figure. 2.6c). When the mean free path of the species in the plume is longer than the target-to-substrate distance, i.e., the target species does not scatter on the background gas, it is defined as a vacuum-like regime¹⁴⁵. That said, there can still be scatterings within the plasma plume for more complex target materials. Where the scattered elements in the

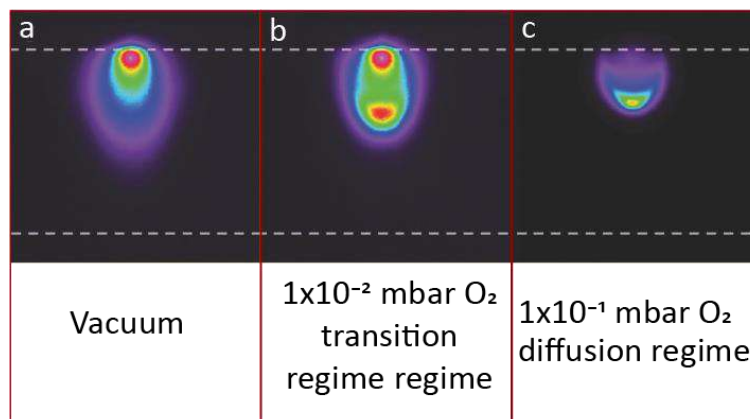


Figure 2.6. ICCD image after $1 \mu s$ of ablation in a) vacuum b) 1×10^{-2} mbar and c) 1×10^{-1} mbar O_2 background gas without substrate heating. The plume is extracted from the upper part towards the lower. Figure adapted from reference [137].

plume have different arrival times on the substrate due to the elements having a different sizes, this scatters differently on the background gas, resulting in a longer time-of-flight before arriving at the surface of the substrate. The transition regime is defined as the regime where the mean free path is smaller than the target-to-substrate. This dictates the film composition, i.e., light elements, are more prone to scatter compared to heavier elements. As an example, strontium is ~ 1.8 times heavier than titanium, thus Ti scatters more frequently. In the diffusion regime, the elements arrive on the substrate simultaneously, thus forming a homogeneous film; however, it tends to be very porous. The diffusion regime requires high partial pressure, e.g., 1×10^{-1} mbar of O_2 and Ar and has a slow expansion¹³⁷.

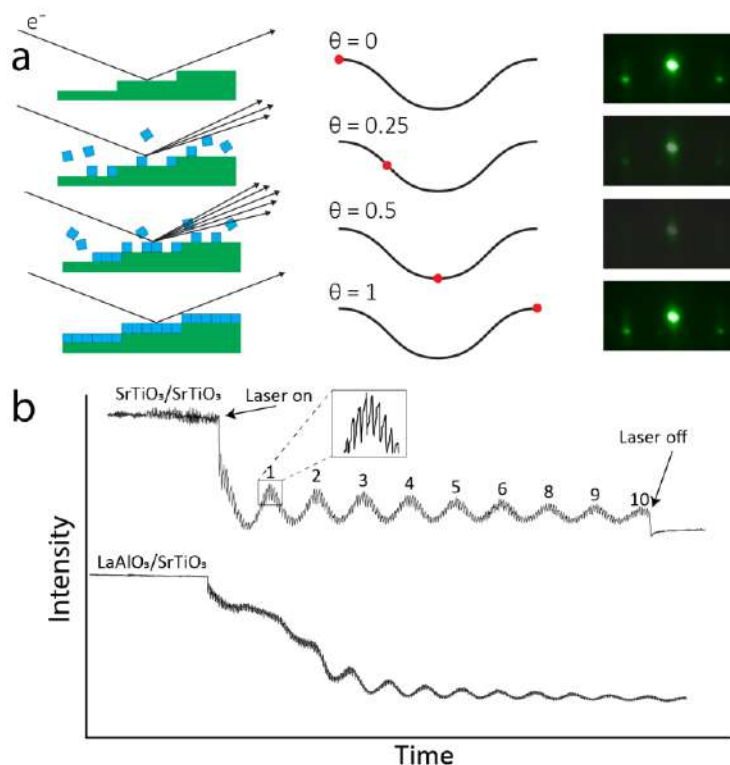
2.1.4.3 Reflection high-energy electron diffraction

During the growth of my films, I have constantly used RHEED to monitor the films' thicknesses and terminations. The RHEED system consists of a high-energy electron beam (10-50 keV) arriving at the surface of the sample at a low angle and diffracting from it. The electron beam arrives at the surface with a gracing angle (0.1° - 0.5°), allowing the electrons to penetrate and probe only the topmost surface layer (1-2 nm)¹⁴⁶. The scattered electrons are collected by a phosphorus screen displaying a RHEED pattern as illustrated in Figure 2.5. The growth of a thin film can be categorized into three modes:

1. *Frank-van der Merwe*; that is, a layer-by-layer growth, where the growth of one layer is completed before the next one starts¹⁴⁷.
2. *Volmer-Weber*; where the material grows in islands mode¹⁴⁸.
3. *Stranski-Krastanov*; this is a combination of layer-by-layer and island growth modes¹⁴⁹.

The principle of the RHEED is illustrated in Figure 2.7. The detected intensity of the specular spot in RHEED during the deposition is monitored. When the incoming angle and outgoing angle of the electron beam are equal, the reflected beam is called the specular beam and its spot is the specular spot, which is always enhanced in intensity by constructive

Figure 2.7. Illustration of film deposition with Reflective high-energy electron diffraction schematic with starting at $\theta = 0$ to 1 referring to start and finish for a full unit-cell film with corresponding RHEED pattern, with the most illuminated pattern being a complete unit cell and least bright being the halfway deposited unit cell. Bottom image displays RHEED oscillations for STO homostructures and LAO/STO heterostructure. Insert displays the oscillations caused by pulsed, and therefore are spaced with the repetition rate.



interference. During crystal growth in a layer-by-layer mode, the first atomic layer grows by making 2D islands, then the islands grow laterally and eventually connect with each other to complete the new atomic layer. Thus, the surface temporally becomes a stepped surface during the growth. This process can be monitored by utilizing the intensity change of the specular spot as mentioned above. The intensity should oscillate as shown in Figure 2.7a during the layer growth. The period of the oscillation corresponds to the completion of the growth of a single atomic layer. Therefore, just by counting the number of intensity oscillations of the specular spot in RHEED during the crystal growth, one can know the number of atomic layers grown. Then, one can control the thickness of the grown layer with the precision of one-atomic-layer thickness.

The RHEED oscillations of STO grown on TiO₂-terminated STO are displayed in Figure 2.7b. The LAO on TiO₂-terminated STO will have a sharp decrease in RHEED intensity in the first LAO unit-cells (see Figure 2.7b bottom panel). This can be explained by the difference in the growth alignment of STO which is perfectly matched in comparison with the LAO on STO, which does not fully match the substrate. As a result of the difference in the c-axis length between STO unit-cell (3.905 Å) and the deposited STO film unit cell (3.791 Å), a realignment for optimal RHEED oscillations¹⁵⁰ is required, which is illustrated in Figure 2.7 bottom oscillation.

2.2 Sample characterization

In this thesis, I have used various techniques to characterize the samples. These include transport measurement setup, magnetometry, and structural characterization with X-rays.

2.2.1 Transport measurement

As I discussed in the introduction, many of the physical properties of the materials, such as the ferromagnetic and superconducting phase, needed to be characterized and in the following section I will briefly discuss the techniques used in my thesis.

Closed cycle cryostat: Traditionally, cooling materials to cryogenic temperatures was achieved using liquid helium or nitrogen. However, a simpler approach is to use a cryocooler. A cryocooler requires a helium compressor that requires power and cooling water to operate. There are two types of cryocoolers, the Grifford McMahon cryocooler, and the Pulsed Tube (PT) cryocooler. The system used in this thesis utilized PT cryocoolers. The PT cryocoolers have no cold moving parts, which makes them advantageous in terms of noise and requires less service. The cooling itself takes place in the cryocooler through a controlled expansion of the compressed helium gas. The magnetotransport measurements in Article VIII were carried out in a CRYOGENIC cryogen-free measurement system with the temperature ranging from RT to 2 K and perpendicular magnetic fields up to ± 16 T.

$^3\text{He}/^4\text{He}$ dilution refrigerator: To reach the necessary temperature of around ~ 300 mK for LAO/STO to be superconducting, the electron transport measurements were performed in an Oxford Triton $^3\text{He}/^4\text{He}$ dilution refrigerator with a base temperature of ~ 15 mK. The principles of the dilution refrigerator are the formation of a phase boundary between the ^3He -rich *concentrated phase* and ^3He -poor *diluted phases* that occur at 870 mK. In a mixing chamber, two phases of ^3He - ^4He , the concentrated and diluted, are in a state of equilibrium separated by a phase boundary with the concentrated phase on top of the diluted. Pumping the ^3He from the diluted phase to the concentrated phase is an endothermic process, that is the heart of the base temperature of the sample stage, as this process will be the driver for the cooling power (23). The Oxford Triton used in this thesis is equipped with a vector magnetic allowing for field at $B_{x/y} = 1$ T and $B_z = 6$ T. The transport data in Article IV was collected with a Triton dilution refrigerator system from Cryofree, Oxford Instruments. The temperature was controlled with a Lakeshore Cryotronics instrument Model 372 AC Resistance Bridge and Temperature Controller. AC excitations were sourced with a SR830 DSP lock-in amplifier with a $10^5:1$ AC voltage divider. The DC bias was sourced with a NI PXI-r4461 digital-to-analog converter. The drain was connected to an I-V converted from Physics Basel SP983 IF3602.

2.2.2 Magnetometry

There are several methods for probing the magnetic properties of a sample. In this thesis, both superconducting quantum interference device (SQUID) and vibrating sample magnetometer (VSM) have been utilized. Both systems measure the same property, but on a fundamentally different basis

VSM works by vibrating the sample perpendicular to a uniform magnetic field, taking advantage of Faraday's law of inductance. The vibrating magnetized sample introduces perturbations in the external magnetic field induced by electromagnetic coils. The magnetic flux perturbation is measured with pickup coils surrounding the sample, generating an electromotive force that depends on (1) the amplitude and frequency of the vibration, (2) an external magnetic field, and (3) the magnetization of the sample. Setting the vibration and amplitude as a fixed parameter when measuring a ferromagnet, the resulting data provides a picture of the magnetization in a dynamic external field¹⁵¹. For LAO/STO and STO/STO, the magnetization saturates around 3 kOe (300 mT), thus an external field in the order of ± 5 kOe. The VSM setup used in this thesis is from Physical Property Measurement System (PPMS) and has a detection limit of 6×10^{-7} emu, enough to measure the magnetic moment in LAO/STO and STO/STO, which exceeds a few μ emu. Due to geometrical limitations, the samples measured in the VSM are in the order of 2.5×5 mm² and only the in-plane magnetization is measured. The magnetization data in Article X was collected with a physical property measurement system from Quantum Design VSM setup.

SQUID combines the two physical phenomena of flux quantization and Josephson effect. The flux quantization requires the magnetic flux included by a superconducting loop to be quantized with the unit of a flux quantum ($\Phi_0 = h/2e$). The Josephson effect is the tunneling of Cooper pair through an insulating barrier separating the two superconductors. The DC SQUID consists of two Josephson junctions in parallel in a superconducting loop and has a current bias. When the pick-up loop experiences an increasing flux e.g., from the samples that are magnetized from an external field, the voltage oscillates with a period of a Φ_0 , from where the magnetization of the samples is measured¹⁵². The magnetic SQUID measurements were performed by Quantum Design SQUID Magnetometer with the samples mounted at different orientations to measure the in-plane (100) and out-of-plane (001) crystallographic directions. The magnetization data in Articles V, VIII, and X was collected with a this SQUID. Unlike the VSM-setup, it is possible to measure both in-plane and out-of-plane magnetization, where for the LAO/STO interface, the out-of-plane magnetization is roughly of a factor 2 larger compared to the in-plane magnetization¹¹⁶.

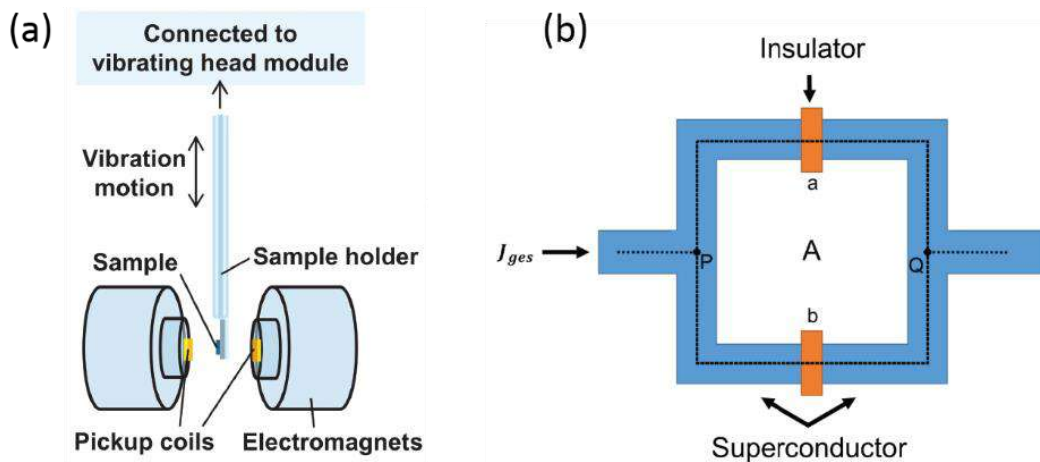


Figure 2.8. a) Schematic of vibrating sample magnetometry. A sample vibrating perpendicular to the applied magnetic field induced by perpendicular orientated electromagnets. Pickup coils surrounding the sample detects the magnetic flux perturbations. b) DC superconducting quantum interference device take advantage of the two Josephson junctions with an applied current bias to detect the magnetic flux from the sample. Figure (a) adapted from reference [151] and figure (b) adapted from reference [152].

2.2.3 X-ray diffraction

X-ray diffraction (XRD) is primarily used for the characterization of material properties such as the crystal structure, lattice size, and strain of the grown films. From Bragg's law, it is possible to derive the lattice constant from the 2θ , while producing a reciprocal space map (RSM) that introduces the tilting ω , to create a 2d map around a discrete Bragg peak. The diffractometers used in this thesis to study the structural properties of the grown film were a high-resolution Bruker D8 Discover diffractometer with monochromatic Cu $K\alpha 1$ radiation ($\lambda = 1.54056 \text{ \AA}$).

2.2.4 Angle-resolved photoemission spectroscopy

Angle-resolved photoemission spectroscopy (ARPES) is based on the photoelectric effect, experimentally discovered first in 1887 by Heinrich Hertz¹⁵³ and later described by Albert Einstein in 1905¹⁵⁴. The photoemission effect describes the emission of electrons from a material by light as an effect of energy transfer from the photon to the emitted electron. ARPES uses kinetic energy in the form of intensity and angle from the emitted electrons, to deduce information about the binding energy and momentum of the surface of the material. This makes ARPES suited for determining and describing the band structure of a solid surface material. For a more detailed description of ARPES, the reader is referred to the reference^{155,156}.

A simplified model that is commonly used in the ARPES community to describe the photoelectric emission process is the three-step model:

1. Optical excitation of the electron in the solid.
2. Transportation of the photoexcited electron to the sample surface.
3. Escape of the photoexcited electron from the surface to the vacuum.

The emitted electron to the vacuum follows the energy conservation law that describes the kinetic energy E_{kin} through $E_{kin} = h\nu - \phi - E_{bin}$, where $h\nu$ is the photon energy from the monochromatic light source, ϕ is the work function describing the energy that an electron needs to escape the surface area in the range of 4-5 eV¹⁵⁶ for Ti-terminated Nb doped SrTiO₃ (Nb:STO), and E_{bin} is the binding energy of the electron to the nucleus.

ARPES is a highly surface-sensitive technique. Utilizing the excitation energy by varying the photon energy ($h\nu$) changes the electron inelastic mean free path (IEMP); that is,

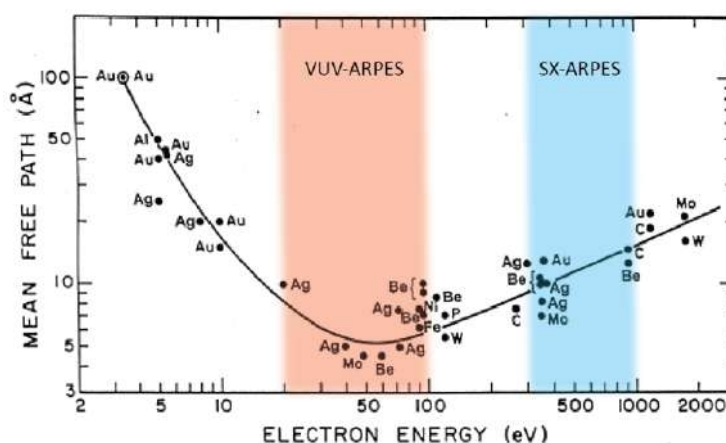


Figure 2.9. Universal curve describing the mean free path of the excited electron before it scatters at marked energy regions corresponding to ultraviolet ARPES and soft X-ray ARPES. Figure adapted from reference [242].

the mean length the electron travels before it scatters. This allows us to engineer the probing depths, for example, UV-ARPES is in the range of 20-100 nm probes 5-7 Å within the surface, while soft x-ray AREPS ranges between 300-1000 eV probing 8-20 Å. The probing depth is described by the universal curve (Figure 2.9) linking the photon energy with the mean free path of photoexcited electrons. After the electrons leave the solid, the surrounding environment has a high importance, as it affects the mean-free path. Therefore, the ARPES method was only developed after the ultra-high vacuum in the 1960's technologies became available. The vacuum used with ARPES is usually in the order of 10^{-11} mbar. By collecting the emitted electrons utilizing a hemispherical electron analyzer, it is possible to measure the kinetic energy and momentum of the photoemitted electrons. Introducing an angle between the analyzer and the sample, achieved in this thesis by tilting the sample, it is possible to analyze the wave-vector in k-space using the equations:

$$k_x = \frac{\sqrt{2mE_{\text{kin}}}}{\hbar} \sin(\theta) \cos(\alpha) \quad 2.1$$

$$k_y = \frac{\sqrt{2mE_{\text{kin}}}}{\hbar} \cos(\theta) \sin(\alpha) \quad 2.2$$

$$k_z = \frac{1}{\hbar} \sqrt{2m(E_{\text{kin}} \cos^2 \theta + V_0)} \quad 2.3$$

Here, the θ and α are the tilting angles of the sample and V_0 is the sum of the work function and energy of the band bottom, known as the inner potential. For a more detailed discussion of the expression and how it is determined, several detailed reviews are given in Refs. ¹⁵⁵⁻¹⁵⁷. For a 2D electronic state, there is no dispersion with the perpendicular k_z . The band dispersion will change as a function of the photon energy, where k_x and k_y are probed with a fixed photon energy, tilting the sample along the x and y axes. This can be achieved by tuning the incident photon energy, changing the momentum along the surface or the film's surface (k_z).

The ARPES data in this thesis has been collected at the Paul Scherrer Institute (PSI) at Swiss Light Source (SLS) at the Surface/Interface Spectroscopy (SIS) end station and Advanced REsonance Spectroscopies (ADRESS) end station for the SX-ARPES characterizations.

CHAPTER 3

Fabrication of freestanding membranes

This chapter will focus on the fabrication of freestanding membranes utilizing two different approaches:

- (i) Detachment of active membranes from STO by employing a water-sacrificial layer.
- (ii) Stress-mediated detachment of lattice-mismatched LAO films from STO as a spalling approach.

This chapter will be based mainly on Articles I, II, and III in appendix B. Typically, complex oxide thin films are epitaxially grown by employing well-established growth conditions and by controlling the distinct material interfaces at the atomic level. Although these methods are well established, they have limitations in epitaxy, which possess a restricted degree of freedom in terms of integration, manipulation, and utilization:

1. Heteroepitaxy usually works for a limited set of material systems with similar crystal structures, lattice parameters, and crystallographic orientations.
2. When epitaxial films are grown on single-crystalline substrates, the properties of ultrathin films are largely affected by interacting with the underlying substrates.
3. During the high-temperature growth of epitaxial films, it is inevitable to have a mixture of the two layers. This causes atomic diffusion/exchange, e.g., cationic intermixing¹⁵⁸ which are detrimental effects for the study of truly sharp interfaces.
4. Epitaxial film growth typically requires sufficiently high temperatures, which also limit the integration of materials that are stable in low-temperature environments, or which are thermodynamically unstable when in contact with each other.

Addressing these limitations, new methods have been attempted by bridging the realm of epitaxially grown complex oxides and low-dimensional Van der Waals (vdW) material systems. The idea of creating freestanding membranes based on semiconducting materials was first demonstrated 25 years ago^{159,160}. Recently, different strategies for fabricating freestanding thin film membranes have been explored: (i) freestanding thin films utilizing a soluble sacrificial layer^{161,162}; (ii) mechanical exfoliation of epitaxial oxide films¹⁶³; (iii) self-formed freestanding thin films through spalling^{101,164,165} (see Figure 3.1). In the following section, I will discuss two experimental works which have been done for the fabrication of freestanding oxide membranes by employing a water-soluble sacrificial layer (e.g. $\text{Sr}_3\text{Al}_2\text{O}_6$) and for self-forming freestanding oxide membranes.

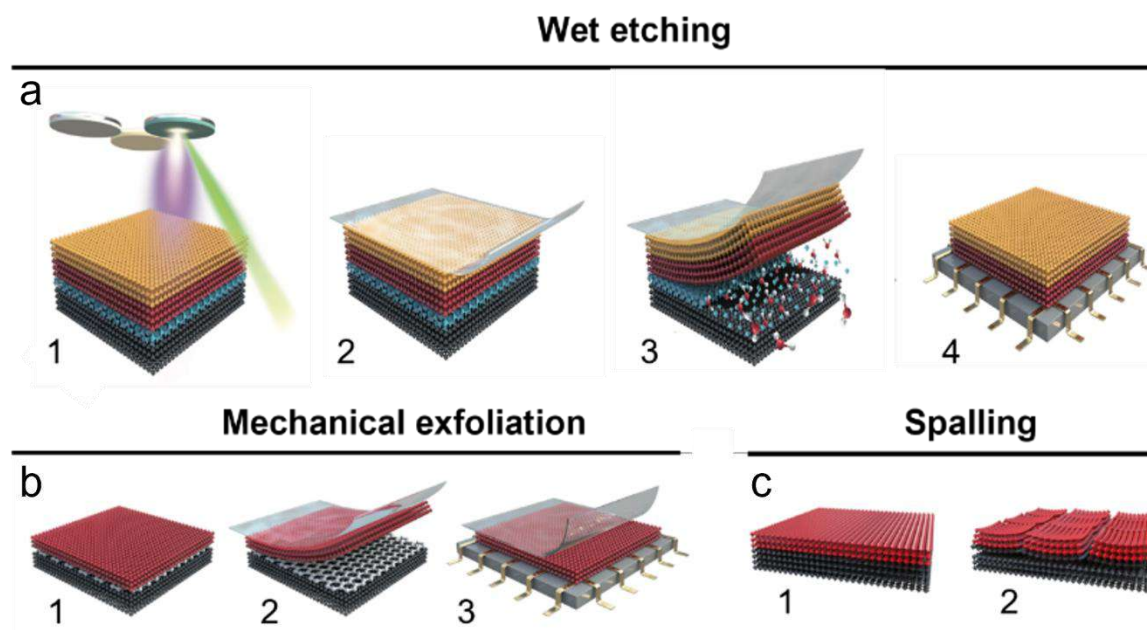


Figure 3.1. Schematics for different freestanding thin film fabrication methods. a) Wet etching method: the growth of a sacrificial layer before growing a target thin film layer on a substrate. A top polymer layer is used attached to the surface and transferred to an etchant liquid to dissolve the sacrificial layer b) Mechanical exfoliation method: a film is deposited on a 2D material and cleave the active layer from the 2D material mechanically. c) Self-formed freestanding thin film membrane through spalling: a lattice-mismatched layer is deposit onto a brittle substrate, resulting in spontaneously forming fragmented flakes.

3.1 Freestanding membranes utilizing soluble sacrificial layer

Fabrication of freestanding membranes and stacking the membranes on top of each other by using soluble sacrificial layers is a new and promising technology. This approach involves several fabrication steps which will be discussed below. Some of the questions are the followings:

1. Can we release and transfer a large-scale area of oxide membranes with minimum fractures?
2. Can we stack these membranes on top of each other?
3. Do the membranes form bonds when they are stacked together?

To answer these questions, we have fabricated a series of freestanding oxide membranes by following the overall steps of (1) thin-film preparation, (2) lift-off, (3) transfer, and (4) stacking. The method is described in Article II. Since lattice and structural mismatches between the grown film and the sacrificial layer significantly affect the properties of the grown film layer, a suitable sacrificial layer should be carefully selected in terms of the lattice parameter. In the following experiments, STO has been used as the grown film material, which will become the freestanding membrane.

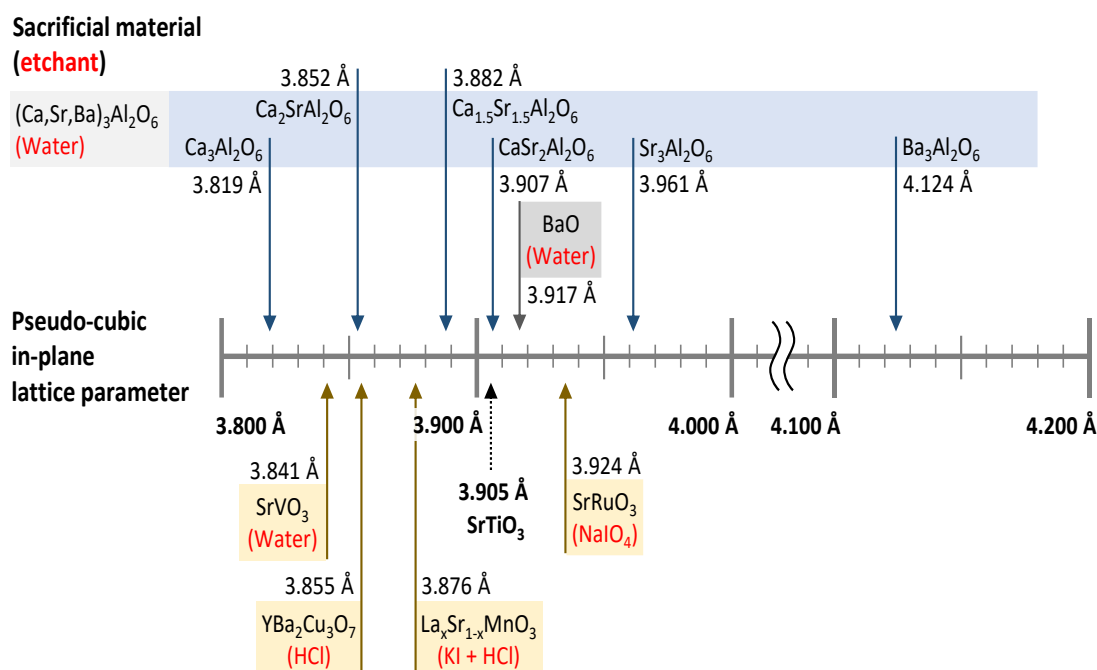


Figure 3.2. Sacrificial materials compatible with perovskite oxides in respect of lattice match. Pseudo-cubic in-plane lattice parameter of the Sacrificial material with the common template substrate STO (black dashed line) showcased to displays lattice parameter compatibility. The uppermost water-soluble sacrificial materials shown with a blue arrow are of the family $(\text{Ca}, \text{Sr}, \text{Ba})_3\text{Al}_2\text{O}_6$ ranging in lattice parameter from 3.819 Å with 100 % Ca to 4.124 Å with 100 % Ba. The lowermost materials have the perovskite structure. The etchant is written with red text.

3.1.1.1 Sacrificial buffer layer

A sacrificial layer should possess the following properties: (i) facilitating a facile epitaxial growth on perovskite oxides with multiple crystal orientations, and (ii) presenting volatile and selective etching compatibility towards a liquid etchant. Figure 3.2 illustrate the pseudo-cubic in-plane lattice parameters for several sacrificial materials. The sacrificial materials include the majority of water-soluble materials and a few exceptions such as $\text{La}_x\text{Sr}_{1-x}\text{MnO}_3$ that dissolves in a solution of potassium iodide and hydrochloric acid. The family of $(\text{Ca}, \text{Sr}, \text{Ba})_3\text{Al}_2\text{O}_6$ has a cubic unit cell (space group $Pa\bar{3}$) and is widely used as a sacrificial layer for the growth of freestanding oxide membranes owing to their water-solubility and growth compatibility with perovskite substrates and films within the range shown in Figure 3.2. Controlling the ratio between Ca and Sr (Ca/Sr), the lattice parameter of the compound can be continuously tuned between a value of 3.819 Å (100% Ca) to 3.961 Å (100% Sr). Substitution of Sr with Ba can lead to a lattice parameter of 4.142 Å (100 % Ba). However, the mismatch between the layers is not the only parameter. For example, $\text{CaSr}_2\text{Al}_2\text{O}_6$ has nearly perfect lattice match with STO with only 0.5 % lattice mismatch, and therefore should in principle be the most suitable sacrificial layer. However, since the Ca ions are small compared to Sr, it can cause structural distortion¹⁶⁶. For this reason, the use of $\text{Sr}_3\text{Al}_2\text{O}_6$ (SAO) without Ca is a better candidate as a sacrificial layer for SrTiO_3 . SAO has a lattice constant of 15.844 Å matching 4 unit-cells of STO ($a_{\text{SAO}}/4 = 3.961 \text{ Å}$). Therefore, it gives a lattice mismatch of 1.4 % with STO, which is significantly larger than for the case of doping the structure with Ca,

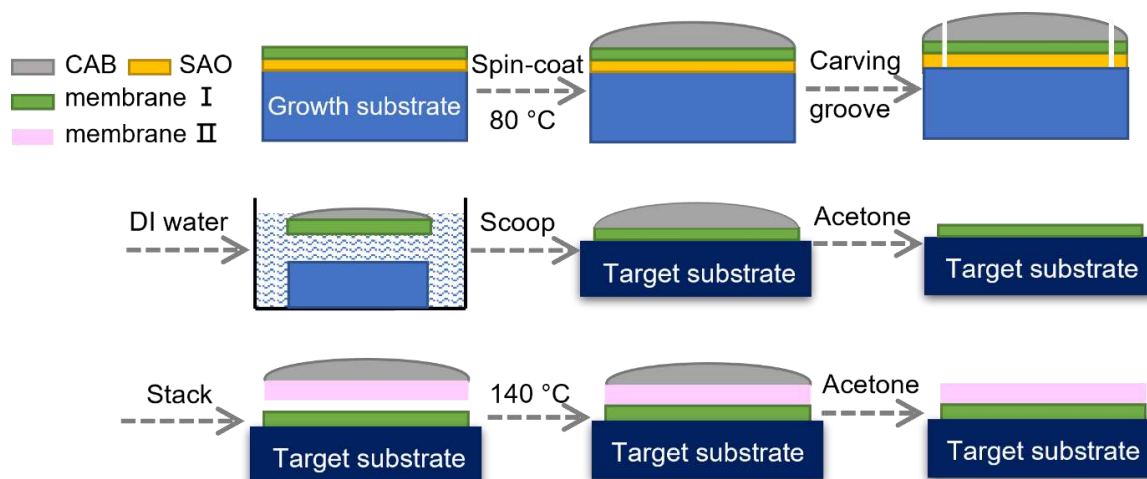


Figure 3.3. Schematic illustration of the fabrication process to produce freestanding membrane utilizing the wet etch method with a water-soluble sacrificial layer SAO. SAO and the target film are grown on a STO substrate followed by spin-coating of a supporting CAB layer and groove carving. The SAO interlayer is dissolved in DI water and the freestanding membranes is scooped to a target substrate and the CAB film is dissolved. The process is repeated on additional membrane II that is stacked on the first membrane I and heated at 140 °C for 15 minutes followed dissolving of the remaining support layer on membrane II.

$\text{CaSr}_2\text{Al}_2\text{O}_6$. However, the lattice mismatch is still much smaller compared to the lattice mismatch of $\sim 3\%$ between canonical LAO and STO heterostructure. It is worth mentioning that since the film is deposited at elevated temperatures (700 – 900 °C) and low PO_2 (10^{-6} – 10^{-5} mbar) cationic intermixing has been observed¹⁶⁷. This should be taken into account when using these material compositions as it may cause the films to be water-insoluble¹⁶⁸. For that reason, the solubility of the sacrificial layer is often only tuned by substituting Sr or Ba for Ca due to an increase in the thermodynamic driving force for the cation hydration^{161,169}. For example, it takes 5-10 minutes to dissolve a 16 nm $\text{Ba}_3\text{Al}_2\text{O}_6$ interlayer, while it takes as much as 1 day to dissolve a similar SAO interlayer¹⁶¹. The thickness of the sacrificial layer also plays an important role in the dissolving time. While it takes 1 day to dissolve a 9 nm SAO interlayer, it takes only 5 minutes to dissolve a 90 nm¹⁶⁹. The thickness of the sacrificial layer used in these experiments is 10 nm. While DI water dissolves the sacrificial layer, it may also dissolve some target materials (the materials grown on the sacrificial layer). Ferroelectric BaTiO_3 (not used in this study) is an example of where water interacts with the surface of the membrane, which can lead to the displacement of Ti ions in the TiO_2 plane and surface cation vacancies caused by the hydroxylation of Ba-O bonds in the first BaO layer^{170,171}.

3.1.2 Fabrication procedure of wet etch method

The fabrication of a freestanding membrane with a water-soluble sacrificial layer can be divided into a three-step process, followed by stacking of the membranes.

Thin-Film preparation: The water-soluble sacrificial buffer layer was grown on TiO_2 -terminated STO(001) substrate by PLD at 750 °C in PO_2 of 10^{-5} mbar. The thickness of SAO was controlled by RHEED (Figure 3.5a). Following the growth of SAO, the STO was subsequently grown on the sacrificial layer at 700 °C in partial pressure inside the chamber

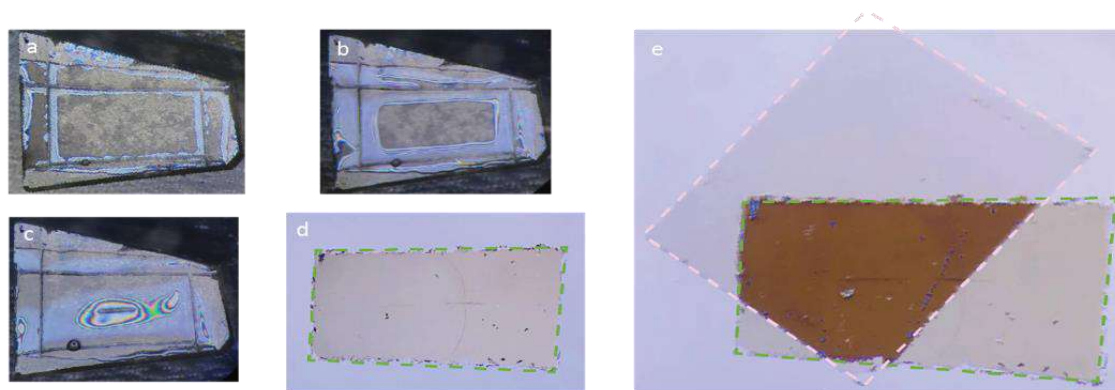


Figure 3.4. Optical microscopy images of the transferring process of the STO membrane from the STO-template to the target substrate. a-c) The dissolving process of SAO in water after immersing (a) till completely dissolved (c). d) The STO membranes transferred to the target substrate. e) Another STO membranes (pink dashed square) stacked on the initial STO membrane (green dashed square).

of 5×10^{-4} mbar. The growth of STO was also monitored by RHEED (see Figure 3.5b). These conditions are crucial to achieving a high-quality fabrication of the sacrificial interlayer and realizing an epitaxial film. Here, we had chosen SAO as a sacrificial layer due to its good lattice mismatch to STO. The as-grown STO film shows high growth quality, which was manifested by the formation of terraces, as observed by AFM, see Figure 3.5c.

Lift-off: Detaching the sacrificial layer and target film from the STO substrate was achieved by applying a support layer of cellulose acetate butyrate (CAB, 20 g/100 ml in ethyl acetate). The CAB was spin-coated on the surface of the STO film and subsequently heated at 80 °C for 5 minutes to solidify the polymer (See Figure 3.3). Compared to other polymers such as poly(methyl methacrylate) (PMMA) and poly(dimethylsiloxane) (PDMS), CAB has advantages owing to its physical and chemical properties, i.e., better tunable adhesion to oxides, a high modulus, high flexibility, and high solubility in acetone. It is important to note that the flexibility comes from the fact that Young's modulus decreases with temperature. For this reason, the polymer layer is softened at elevated temperatures, making it easier to spread out over the surface for the stabilization of the membrane.

Employing the CAB supporter is important to avoid crinkling and folding of the freestanding membrane during the etching-and-release process¹⁷². Spin-coating CAM on a grown STO film also causes the deposition of CAB on the sidewalls of the film. This hampers the water-soluble interlayer to be exposed to the water. Therefore, to allow the dissolving of the sacrificial layer, grooves are carved into the sample surface before immersing in DI water (see Figure 3.3). This gives additional benefits for determining the geometry of the membranes by designing the grooves. Figure 3.4a-c shows the process of dissolving the sacrificial layer of the CAB/STO/SAO/STO stack where (a) shows the as-immersed membrane, (b) shows the intermediate dissolving of SAO, and (c) shows the almost fully dissolved sacrificial layer.

Transfer: After dissolving the sacrificial interlayer, the freestanding film with the CAB supporter is released from the substrate and scooped up from the water. And, they are transferred to target substrates, e.g., TiN, Si, or other oxides. To remove the CAB

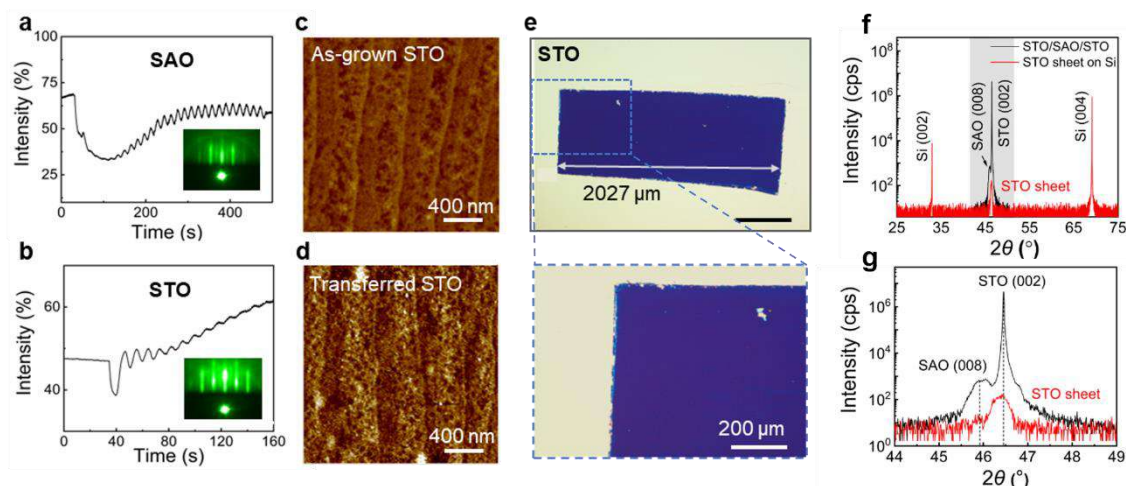


Figure 3.5. a) The time dependent RHEED oscillations and pattern of 10 nm SAO interlayer. b) The early stage of RHEED oscillations of 30 nm STO with corresponding pattern. c,d) AFM topography image of the as-grown (c) STO and the transferred STO membrane (d). e) Optical microscope image of a millimeter scale 30 nm thick STO freestanding membrane transferred on a TiN/Si substrate with corresponding magnification of the upper left edge. The scalebar in (e) is 500 μm. f,g) XRD of the STO/SAO films before (f) and after (g) transfer where (g) is a magnification of the grey area in (f).

supporting layer, the substrate with the transferred freestanding oxide film is immersed in acetone and cleaned with 2-propanol (IPA). Figure 3.4d shows an example of a transferred membrane.

Stacking: To transfer the second freestanding layer to the first freestanding layer placed on a target substrate, the edges of the second freestanding membrane are often curled. Therefore, IPA is used to fix the corners of the second layer to the target substrate, whereas another fresh CAB film is used to cover the stacked membranes. To achieve good contact between the freestanding layers, they are heated at 140 °C for 15 min and finally immersed in acetone to dissolve the CAB layer. In order to avoid contamination between the layers which can affect the adhesion, hybridization, and interactions between the two oxide membrane layers, post-annealing in a tube furnace at 500 °C in oxygen atmosphere is carried out to remove possible organic hydrocarbon contamination from the interface. Figure 3.4e shows an optical image of the stacked membranes.

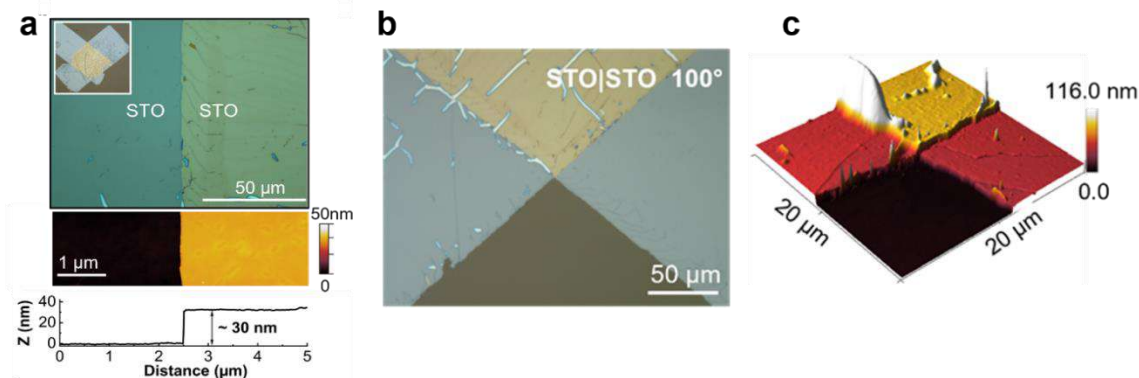


Figure 3.6. a,b) Optical microscope image of the stacked STO membranes, which corresponding height profile obtained from AFM in (a). The STO membranes in (b) have been stacked with an angle of 100° relative to each other. c) The stacked heterostructure is forming an overlapping region displayed by the yellow color in the AFM 3D image.

Following the processes described above, we fabricated a large-scale membrane (> 2 mm) with a minimum of fractures (Figure 3.5e). The RHEED intensity and pattern for the growth of a water-soluble sacrificial SAO interlayer (~ 10 nm-thick) show clear intensity oscillations during the film growth and a streaky pattern after the film growth. The RHEED patterns indicate a high-quality STO film growth with clear intensity oscillations for the first unit cells. AFM topography ($2 \times 2 \mu\text{m}^2$) image shows that the STO film layer remains the step-terrace surface structure before and after transferring the membrane (Figure 3.5c,d). XRD confirms a single-crystalline STO(001) film before and after transferring the film (Figure 3.5f,g). The (002) STO peak remained at the same position both before and after the transfer although the peak broadened after the transfer due to its 2D nature.

3.1.3 Characterization of stacked membranes

Here, the remaining question is whether we could stack the films on top of each other while achieving them with crack-free and chemical bonds. This section will focus on developing the quality of the membranes after stacking them and investigating their atomic/chemical bonding driven by a simple stacking approach. Figure 3.6 shows a successful stacking of STO membranes. The inset of Figure 3.6a shows a low-magnification optical image for the stacked membranes. It indicates that it is possible to achieve a large area of membranes. However, stacking the membranes create wrinkles in the overlapping region of the top freestanding layer due to stress from the bottom membranes and the top polymer used to stack the top membrane. AFM image for the surface morphology of the stacked membranes

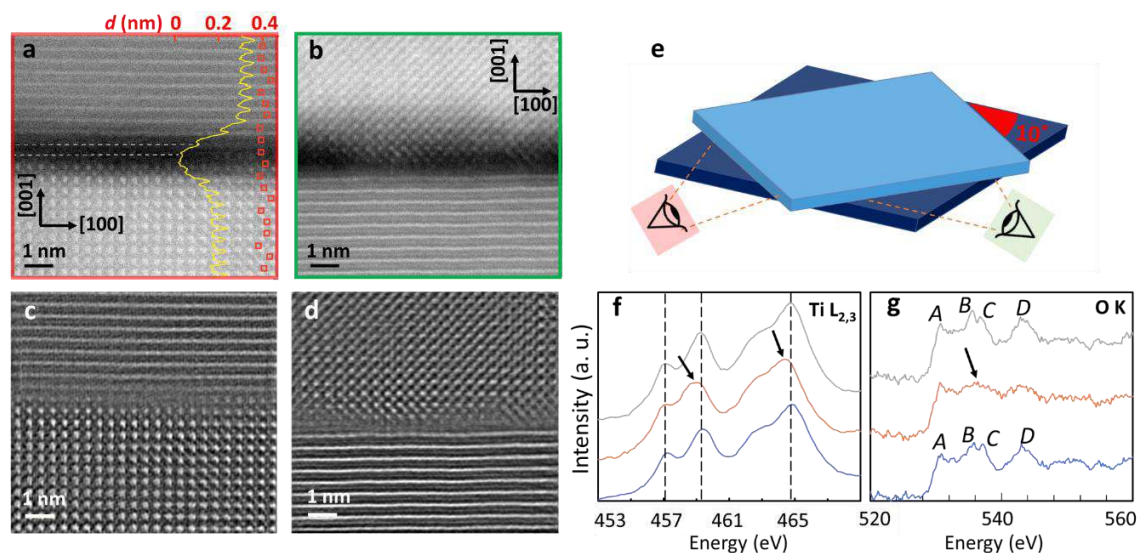


Figure 3.7. a,b) Atomic-resolution ADF-STEM images of the interfacial area of the STO/STO stacked membrane of the lower film (a) and the upper film (b) orientated in the (010) axis, respectively, by tilting the sample 10.5° around the (001) axis. The yellow profile displays the intensity, the red squares represent the Sr atomic columns, and the white dashed line marks the interface. c,d) FFT of (a) and (b). e) Schematic illustration of the membranes with probing orientation in (a) and (b). f) HAADF-STEM of a 4° twisted STO/STO grain boundary with the upper film aligned in the (010) axis. f,g) EELS signal of the Ti $L_{2,3}$ edge (f) and O-K edge (g) captured at the bottom membrane (blue line), the interfacial area of the two membranes (orange line) and the top membrane (grey line). The dashed lines in (f) indicates the t_{2g} and e_g states to displays the shift in e_g . The peaks A, B, C, and D in (g) displays the broadening of the B in the interface associated with O 2p hybridization.

shows that the height between the two membranes was ~ 30 nm - equivalent to the thickness obtained by RHEED oscillations. This also indicates that the two membranes are closely connected/bounded without additional height difference. Moreover, stacking the membranes gives the possibility to vary the angle between the layers (twisting). Figure 3.6b,c shows a stack of STO membranes with an angle of 100° (or 10° , depending on the viewpoint). The twisted angle was confirmed by an XRD φ -scan showing the 4-fold degeneracy of STO with a twin peak with a 10.4° spacing angle between them, corresponding to the angle observed from the optical microscope. To examine the interface between the two membranes, we used annular dark field scanning transmission electron microscopy (ADF-STEM) (see Figure. 3.7) The ADF-STEM image displays the interfacial area between the two membranes at two different angles (Figure 3.7a,b) illustrated in Figure 3.7e. Due to the probing angle in Figure 3.7a-d the two membranes are displayed as either dots or lines due to a twisted angle of the top membrane of 10.4° . Figure 3.6c,d shows the fast Fourier transformation (FFT) of Figure 3.6a,b. The crystal structure of the STO membrane can be recognized from the ADF-STEM data and the atomic positions of Sr and Ti can be well resolved. Identifying the interface area, some regions show direct bonding between the membranes, whereas the dark regions observed at the interfaces in our stack are similar to those seen previously in STO bicrystals, which correspond to dislocation cores. Similar observations were made by L. A. Hughes et al.¹⁷³, who stacked two single crystals of STO together with a spark plasma sintering (SPS) apparatus applying a pressure of 120-140 MPa followed by a twisting of the crystals (Figure 3.8). Our cross-section observations are in good agreement with the results of L. A. Hughes et al. Here, the dark regions in the interface denoted with arrows are explained by dislocation cores created by stacking faults consisting of Ti-O layers.

The elemental valence state near the interface was studied with electron energy loss spectroscopy (EELS) at the Ti-L_{2,3} and O-K edges at different regions of the homostructure STO membrane. The spectra were recorded in the bottom STO membrane (blue line, Figure 3.7 f.g), the dark region interface (orange line, Figure 3.7f.g), and the top STO membrane (grey line, Figure 3.7f.g). The two bulk areas away from the interface show a 2.2 eV crystal

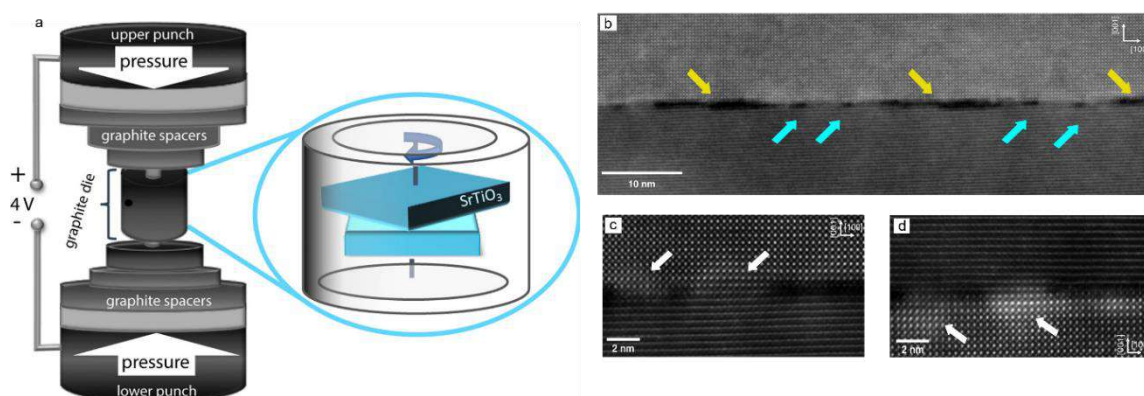


Figure 3.8. Method and grain boundary results of pressing a STO substrates with substantial pressure onto another STO substrate and then twisting it achieved by L. A. Hughes and K. van Benthem (15). a) Schematic illustration of the SPS apparatus used to pressure and twist two STO with 120-140 MPa. b) HAADF-STEM image of a 4° (100) twist grain boundary. The upper half crystal is orientated in the (010) and the lower half-crystal is tilted around the (001) axis by 4° . Yellow and blue arrow denotes shorter and longer defects, respectively. c,d) HAADF-STEM images captured at the same area with the upper half crystal in the (100) grain boundary for (c) and (010) for (d). Figures adapted from reference [173].

field splitting in the Ti- $L_{2,3}$ between the Ti $3d t_{2g}$ and e_g states, while the O-K edge shows four peaks denoted A, B, C, and D corresponding to local O $2p$ hybridization with the Ti $3d$ states. The Ti- $L_{2,3}$ edge in the interface region is shifted 0.4 eV and the B peak broadens and merges with the C peak in the O-K edge spectra. This indicates a partial reduction of the Ti^{4+} to Ti^{3+} as a compensation mechanism for oxygen or strontium vacancies¹⁷³, strongly indicating interactions between the membranes. Remarkably, this shows that we were able to form atomic bonds between the membranes simply by placing the membranes on top of each other, followed by a post-annealing at 650 °C in O_2 atmosphere, and we did not need to apply high pressure as seen in earlier studies.

3.2 Freestanding membranes through controlled spalling

An alternative approach to achieve freestanding membranes is by depositing a biaxially tensile-strained epitaxial film on a largely lattice-mismatched substrate. For example, by depositing a sufficiently thick LAO film on STO, fractures appear in the STO substrate, resulting in a release of membranes that contain a bilayer of LAO/STO.

3.2.1 Spalling mechanism

This method relies on the deposition of a strained top film on a brittle lattice-mismatched crystal and handles the layer to peel off the membrane. It was first successfully demonstrated on semiconductors such as silicon, germanium nitride, and III-V semiconductors^{174–176}. The spalling process relies on depositing a tensile-strained top layer on the crystal/wafer of interest under sufficient stress and sufficient bonding strength. Thus, the crystal experiences cracks that propagate through the crystal. This fracture mode is

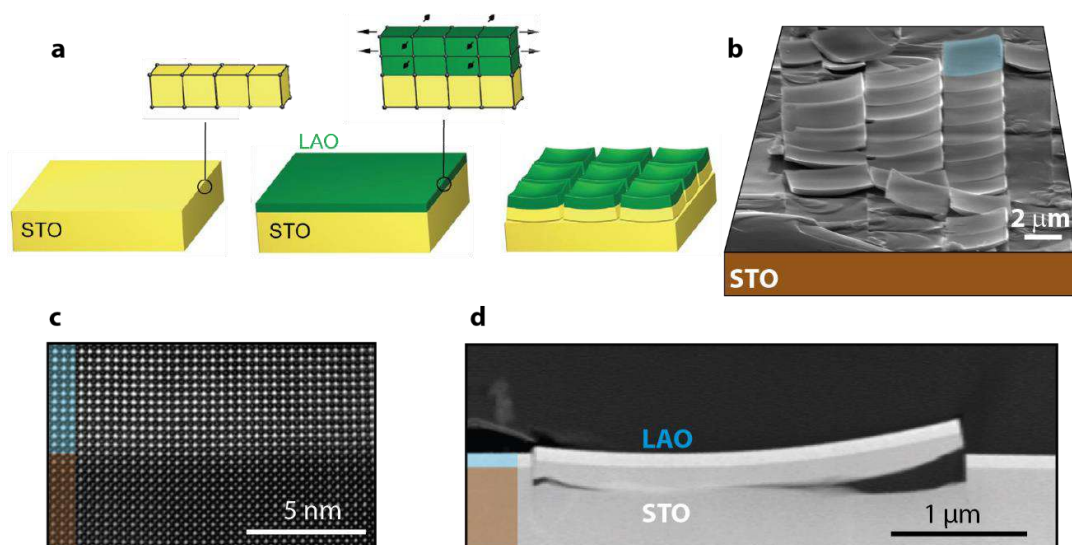


Figure 3.9. a) Schematic representation of the spalling mechanism in LAO/STO membranes. b) SEM image of the surface of a LAO/STO membranes after the spalling with membranes still located on the growth substrate with size around 2 μm . c) in-plane SEM image of a membrane with a clear contrast difference displaying both the STO bottom fragment from the substrate and the LAO top film. d) HRTEM cross section image of a membrane displaying the pristine interface is preserved after the spalling with LAO on the top and STO on the bottom.

known as spalling and relies on a stable propagation of the fracture mode parallel to the substrate at the equilibrium depth where the shear stress is minimized. The process is based on a self-correction. For a crack too close to the surface, the crystal above the crack contracts upon fracture, and the crack propagation is deflected downward. Conversely, for a very deep crack in the substrate, the top layer expands upon fracture due to the curvature of the membrane, and instead, the crack is deflected upwards¹⁷⁷. The resulting steady-state crack propagation is thus parallel to the surface at a depth that depends on the mechanical properties of the crystals. The basic idea of this mechanism is illustrated in Figure 3.9a,d. Experimental observations show that the thickness of the STO fragment stripped away from the substrate correlates with the film thickness or is slightly larger¹⁷⁶. This process was first described by J. W. Hutchinson and Z. Suo in 1999¹⁷⁷ and was realized on the canonical LAO/STO system reported in 2020¹⁶⁴. The LAO film was grown at 730 °C in 2×10^{-2} PO₂ with a fluence of 2-2.5 J/cm² with post-annealing at 500 °C in 50 mbar oxygen for 1 hour before cooling with the same pressure. The spalling formation of a bicrystal such as LAO/STO is carried out in three stages: 1) the initial strained sample from the lattice mismatch does not show membrane formatting during the growth; 2) during the growth, the sample goes into an intermediate state where it develops cracks in the STO as observed as a sudden intensity drop in the RHEED oscillations, which would continue even with the laser being turned off, and is ascribed to the surface strain relaxing, by forming cracks; 3) upon exposure to air, the sample develops membranes in a mosaic-like structure. It was shown that the spalling of the surface is achieved with film thickness ranging from 28-180 nm of LAO. For more details on membrane formation, the reader is encouraged to see the paper by Sambri et al.¹⁶⁴.

3.2.2 As-grown spalled membrane size distribution

The initial spalling of the membranes originates from an uncontrolled spalling of the surface in approximately rectangular membranes along the crystal axis (100) and (010) with the lateral sized D_y and D_x . To understand the lateral size distribution, we manually measured 451 membranes from three different areas of the sample (Figure 3.10b). Figure 3.10a shows an example of the image used to measure the size. We note that all the membranes on the sample have a curvature as a result of the bilayer heterostructure. Combining the results of the lateral size in a sharp peak at $\sim 1.9 \mu\text{m}$ with a very sharp distinct peak (Figure 3.8c), indicating that the size distribution is mostly uniform. The self-spalling of the LAO/STO membrane fracture is driven by strain energy distribution in the LAO/STO heterosystem. This means that it is very unlikely that larger membranes would be found because a larger strain may break the membranes into smaller ones.

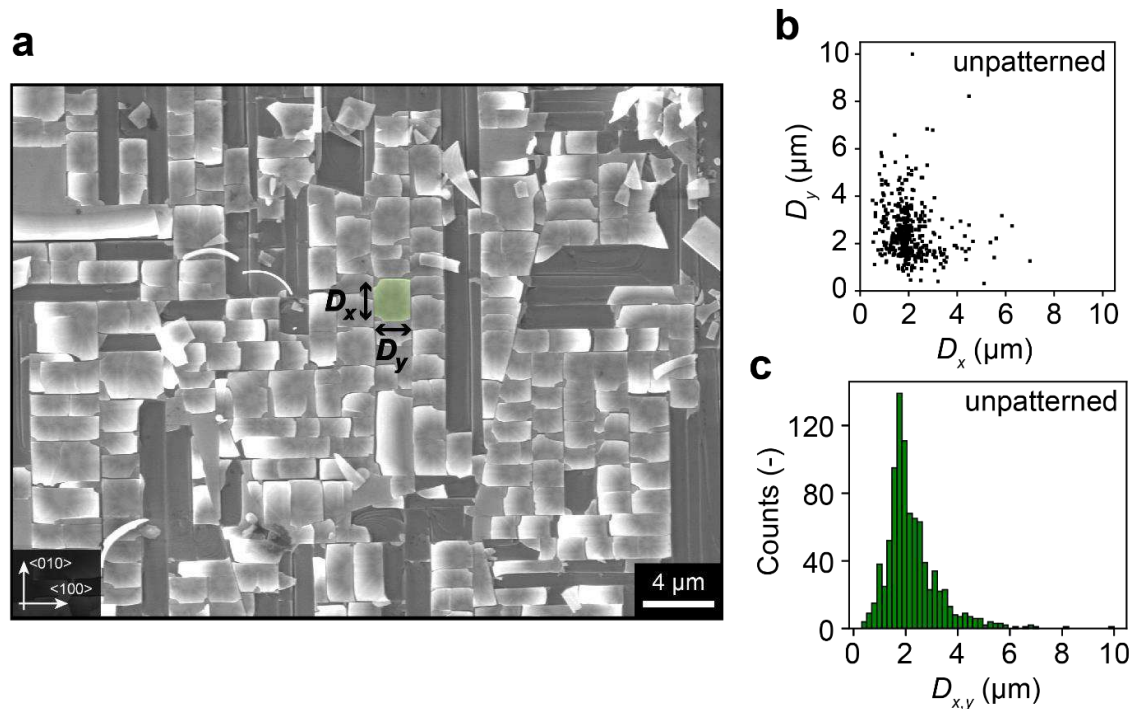


Figure 3.10. a) SEM image of the surface, showing the spontaneous spalling and membrane formation of a as-grown sample with 70 nm LAO. b) Distribution of the lateral size (D_x, D_y) of the membranes. The data points have been collected on multiple SEM images. No correlation was found between D_x and D_y . c) the overall size distribution of the membranes plotted as a histogram with preferential size of 1~ 1.9 μm .

3.2.3 Controlled spalled membrane size distribution and fabrication

For spalling used with conventional semiconductors, the initial fractures are triggered by a discontinuity appearing at the edges of the stressor layer¹⁷⁶. For that reason, we have investigated the possibility of controlling the spalling of LAO/STO by introducing many small edges shaped by a patterned substrate, and by controlling the position of the fractures by a topological discontinuity.

The schematic illustration of the patterning is illustrated in Figure 3.11a, where TiO_2 -terminated STO substrates were covered in a ~ 900 nm electron beam resist, followed by electron beam lithography and development to open the resist at the arrays of the square regions. The trenches are 250 nm wide and have a depth of 20 nm (Figure 3.11d from the white dashed line in (d)). We varied the square size from 0.5-20 μm allowing us to understand whether there is an optimal size for the membranes or whether we are able to fabricate membranes larger compared to the uncontrolled spalling. This allowed us to understand whether the strain in significantly smaller membranes was sufficient to create the membranes. To create the trenches, we utilized Argon milling. Ar^+ ion bombardment was earlier shown to form V_O in STO¹⁷⁸, therefore we tested whether 6 minutes of bombardment utilizing - that is, the time we used to mill the trenches with a current of 23 mA and voltage of 600 V - would cause the STO to be electrically conducting, which turned out not to be the case. Figure 3.11b,c show a patterning of the substrate with well-defined trenches. The step-terrace structure of the unpatterned part of the squares is well preserved for the deposition of the stressor LAO layer.

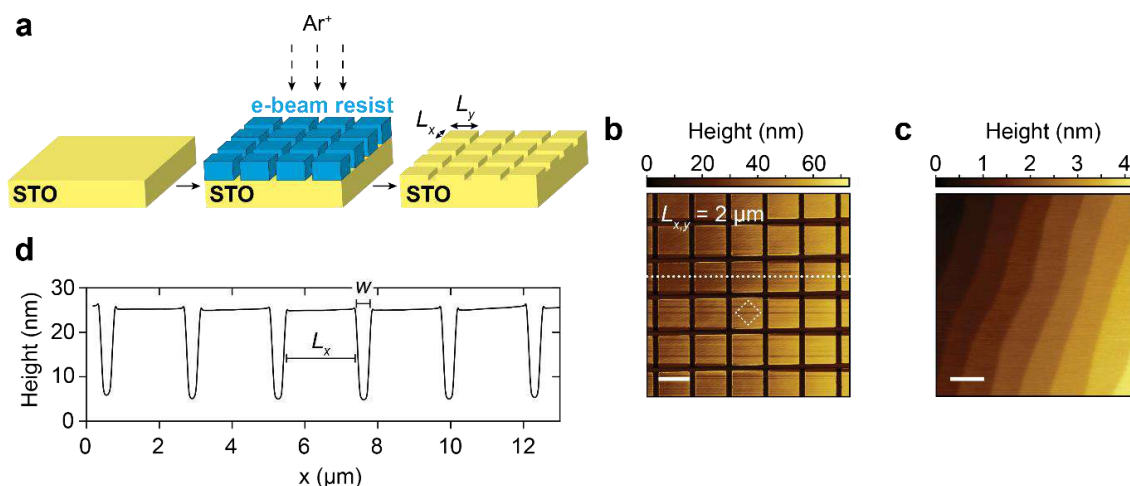


Figure 3.11. a) Schematic illustration of the surface patterning by argon ions bombardment with Kaufman ion milling. A patterned electron resist is used as mask to direct the argon beam. b) AFM topography image of the STO substrate after the argon milling and resist stripping. The lateral size ($L_{x,y}$) is $2 \mu\text{m}$ equal to the scalebar in the image. White dashed square is the magnification in (c) displaying the terrace structure and the white dashed line is the height profile shown in (d) showing an average trench depth of 20 nm and trench width of 250 μm .

The deposition of LAO shows the formation of LAO/STO membranes spalling along the intended pattern (Figure 3.12). However, the membranes do not cover all of the intended area. In the regime smaller than the unpatterned membranes ($L_{x,y} = 0.5 - 2 \mu\text{m}$), only a few membranes formed, associated with the strain relaxation at the edges of the patterned area, thus indicating that there is a threshold for spontaneous spalling which may be ascribed to the pattern but also the thickness of the stressor LAO layer. Figure 3.13a-c shows no spalled membranes, while Figure 3.13e-h shows spalled membranes with large areas. For that reason, the size of the membranes patterned with the size $L_{x,y} = 0.5 - 2 \mu\text{m}$ are excluded from the analysis in Figure 3.13.

For the membranes in the patterned field with $L_{x,y} = 4 - 20 \mu\text{m}$, we manually measured the size of 1146 membranes imaged by SEM distributed throughout the sample. The distribution of the membranes is plotted in Figure 3.13. It is worth mentioning that since

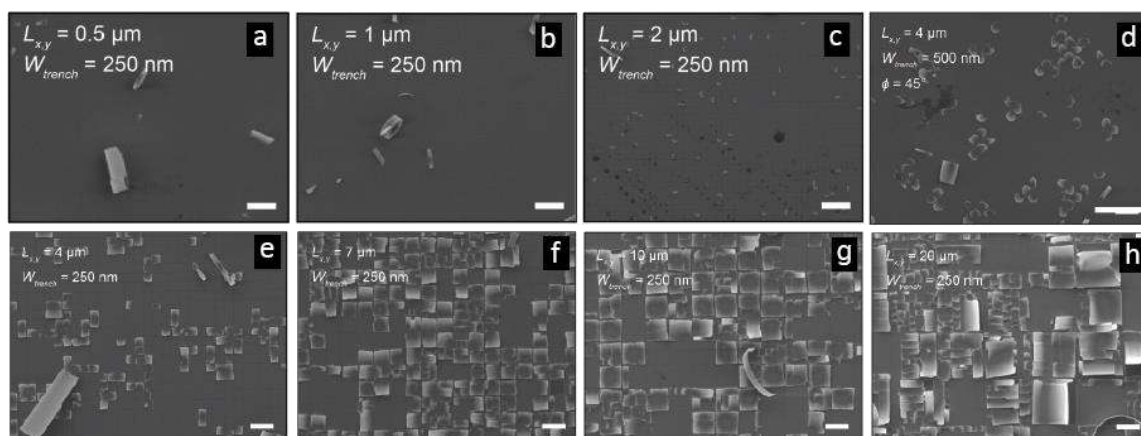


Figure 3.12. SEM images of patterned STO with 70 nm LAO. a-c) $L_{x,y} = 0.5 - 2 \mu\text{m}$ shows no spalled membranes. d) The patterning orientation has been rotated 45° with $L_{x,y} = 4 \mu\text{m}$. e-h) $L_{x,y} = 4 - 20 \mu\text{m}$ show clearly spalled membranes. These images are examples of the imaged used to count the membranes in Figure 3.13.

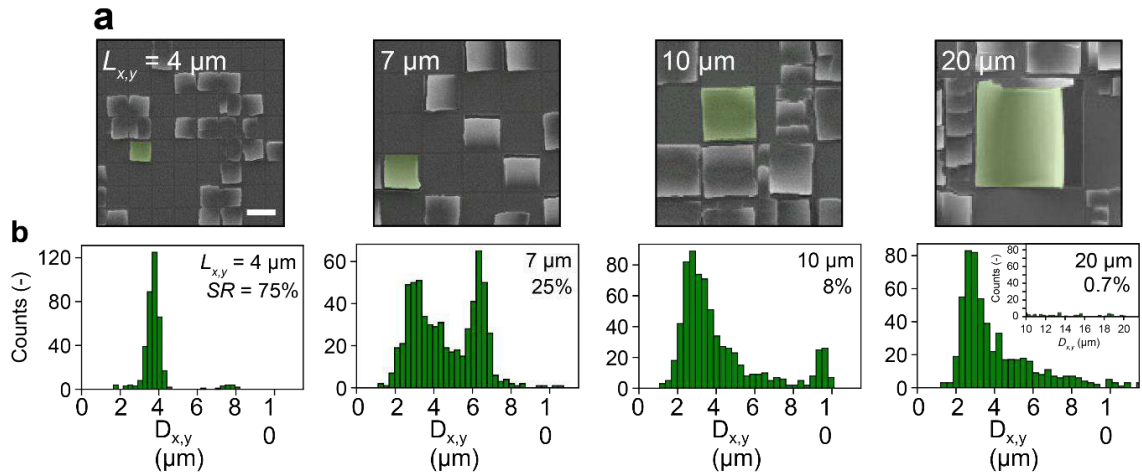


Figure 3.13. a) SEM images of $L_{x,y} = 4, 7, 10$ and $20 \mu\text{m}$ with a spalled membrane false colored to illustrate an intact spalled membrane contributing to the spalling statistics. b) Histogram of the lateral size $D_{x,y}$ corresponding to the membranes in (a).

we measured the samples from top-down scanning electron microscopy (SEM) images, we did not consider the fact that the curvature changes the area. For $L_{x,y} = 4 \mu\text{m}$, the LAO/STO membranes displayed a narrow size distribution that closely matched the intended patterned size. However, a small but significantly narrow distribution of membranes was found at $L_{x,y} \sim 8 \mu\text{m}$, i.e., twice the size of the narrow population. For $L_{x,y} = 7 \mu\text{m}$, the size distribution shows two distinct populations: one corresponding to the intended $7 \mu\text{m}$ and one half the size of $L_{x,y} = 7$ at $\sim 3.5 \mu\text{m}$. Nonetheless, it is clear, that the membranes were still affected by the trenches since the spalling was achieved with sizes significantly larger than the unpatterned spalling $\sim 1.9 \mu\text{m}$. For $L_{x,y} = 10$ and $20 \mu\text{m}$, the likelihood of forming membranes corresponding to the intended $L_{x,y}$ is small, but the membranes rather reduced in size and approached the as-grown membranes. Both for $L_{x,y} = 10$ and $20 \mu\text{m}$, only very few membranes were observed in the size we aimed at, with $L_{x,y} = 20 \mu\text{m}$ being significantly smaller than $L_{x,y} = 10 \mu\text{m}$, with the data shown in the insert in Figure 3.13b. This method shows that there is a clear lower and upper limit manifesting itself when the size of the patterned size becomes much larger than the average size of the unpatterned membranes, e.g. $L_{x,y} = 10$ and $20 \mu\text{m}$, and they start to break into smaller pieces. To get an idea of the rate of the membranes that have spalled following the designed pattern, we used the success rate (SR), defined as the fraction of membranes $D_{x,y}$ from the histogram in figure 3.10 (unpatterned) and figure 3.13 (patterned) with a dimension window of $\pm 0.25 \mu\text{m}$ that was the same size as the width of the trenches (definition A). The SR monotonously decreased from SR of 75 % (2.7 %) for $L_{x,y} = 4 \mu\text{m}$ to 0.7 % (0.0 %) for $L_{x,y} = 20 \mu\text{m}$ for the patterned and unpatterned samples, respectively. This clearly shows that the spalling of membranes within the designed frame significantly increased compared to uncontrolled spalling. For the membranes at $L_{x,y} = 4, 7,$ and $10 \mu\text{m}$ in particular, the fraction of membranes spalling with respect to the design was significantly larger. We noted that for the large membranes ($L_{x,y} = 10$ and $20 \mu\text{m}$), this definition was not sufficient to describe the actual picture. A membrane designed to fit a $L_{x,y} = 20 \mu\text{m}$ that breaks into many smaller pieces drive the fraction of spalled $D_{x,y} = 20 \mu\text{m}$ down. We

$L_{x,y}$ (μm)	4 (μm)	7 (μm)	10 (μm)	20 (μm)
SR unpatterned	2.7 %	0.3 %	0.1 %	0.0 %
SR patterned definition A	75 %	25 %	8 %	0.7 %
SR patterned definition B	~10 %	~25 %	~20 %	~5 %

Table 3.1. The SR of unpatterned and patterned membranes is defined from the fraction of the spalled membranes in the histogram in figure 3.10 and 3.13 with the dimensions $D_{x,y}$ within $\pm 0.25 \mu\text{m}$ (i.e. the trench width) of the defined pattern. Whereas definition A takes the size of the spalled membrane and compares it to a fragment of the total amount of membranes, definition B relates the area covered by correctly spalled membranes with respect to the total image area.

addressed this issue by considering an alternative definition of the SR, where the area was covered by correctly spalled membranes with respect to the total imaged area (definition B). This definition is insensitive to the failures such as the membranes failing to fracture, or the membranes subdividing into smaller membranes. Table 3.1 shows a significant difference in the SR of the two definitions, where the failure for the smaller membranes is mainly due to membranes not forming, whereas for $L_{x,y} = 10$ and $20 \mu\text{m}$ definition B segregates the large number of membranes counted from the area of a few grid spaces for the large membranes. The above analysis indicates that the membranes can be spalled along the intended patterns and it was possible for all the grid's sizes. The histograms in Figure 3.10 and 3.13 give a quantitative analysis of the fraction of spalling efficiency. Obviously, the SR would be 100 % in both definitions if every pattern spalled membranes in the designed size.

The SEM image for the unpatterned membranes clearly shows that, in the case of uncontrolled growth, the natural fracture direction is along the (100)/(010) high-symmetry direction (Figure 3.10a). This symmetry was also used to control the spalling in figure 3.1-3.13. However, we dedicated an area on the sample to understand whether the membranes would always spall in the crystal orientation or whether it was possible to make more complex shapes. For that reason, we rotated the pattern with 45° , i.e., (110)/1-10) direction with respect to the design used. The rotated pattern is shown in Figure 3.12d, from which it is clear that although a significant fraction of the membranes showed cracks along the (100)/(010) direction, the membranes also fractured along the patterned trenches, showing that the pre-patterned growth method was feasible for controlling the growth that was not along the naturally (100)/(010) crystal orientation.

3.2.4 Membrane transferring

With the ability to control the film growth, we also demonstrated with the perspective of the self-formed membranes with patterning techniques feasible for electronic devices, that we can transfer the size-controlled membranes utilizing a micromanipulator onto a SiO_2/Si substrate (Figure 3.14). Three different membranes $L_{x,y} = 7, 10$ and $20 \mu\text{m}$ were transferred to the substrate with existing alignment marks used for lithography techniques. With this degree of freedom, it was possible to realize, it was not only possible to move a single membrane for device fabrication, but it was also possible to move several membranes for more complex device combination functionalities of different oxide heterostructures within the same circuit. The membranes were sufficiently clamped to the

substrate for device fabrication by vdW forces, although for device fabrication, the membranes were further fixed to the substrate due to the metal deposition, clamping the membranes.

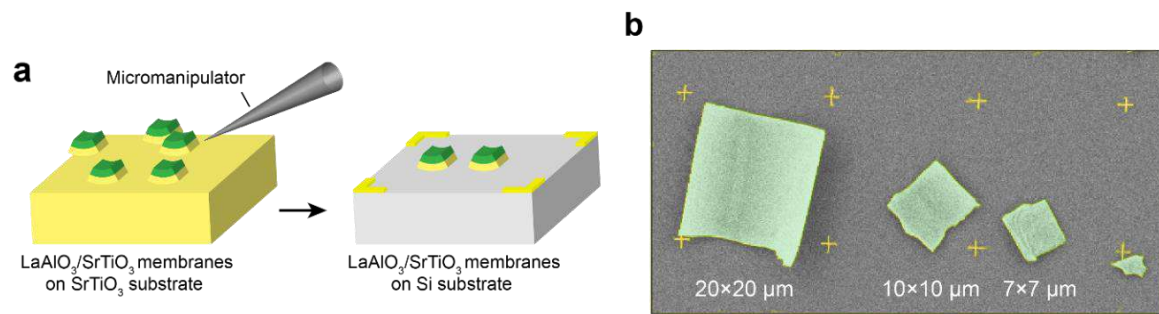


Figure 3.14. a) Transferring method of a spalled LAO/STO from the patterned growth substrate to the SiO₂/Si substrate utilizing a micromanipulator, where vdW forces are sufficient to clamp the membrane to the substrate. b) SEM micrograph of membranes transferred to the SiO₂/Si substrate between prepatterned alignment marks.

CHAPTER 4

Properties of freestanding membranes

In the previous chapter, I discussed possible fabrication techniques that I used to achieve freestanding membranes. Releasing the homo- and heterostructure films from bulk or thin film templates and transferring them onto other substrates can open doors for emerging phenomena through a new degree of freedom often used in 2D materials, but now to be utilized with complex oxides. This chapter will focus on the properties of these membranes both theoretically from ab-initio calculations, but also from transport properties. This chapter will be based mainly on article IV and part of article II.

4.1 Physical properties of moiré patterns in SrTiO₃ membranes

With the ability to create freestanding complex oxide membranes, the door is opened for emerging properties arising from stacking, creating an interference pattern from crystal structures with identical structures with a twisted angle with respect to each other, also known as moiré patterns. Molecular Dynamics (MD) calculations show that the twisting of two STO freestanding membranes with respect to each other yields anisotropic oxygen ion diffusion behavior in the near interface region of STO/STO, which is otherwise isotropic in bulk (001) STO. Figure 4.1a shows the calculated tracer diffusion coefficient for oxygen (D^*) as a function of the twist angle. The tracer diffusion coefficient for oxygen (D^*) is the slope of the calculated Mean-squared displacements (MSD) for oxygen ion migration in bulk (001)-STO as a function of time. This is calculated by finding the distance oxygen diffuses at a certain time at 1600 K, and changes with a twisting angle (Figure 4.1c,d). The sudden increase in the tracer diffusion relative to the twist angle between the two layers is referred to as the magic angle, where D^* changed at specific angles, and is noted in the figure as θ_1/θ_1^* , θ_2/θ_2^* , etc. Note that due to the cubic structure of STO, D^* and the activation energy (E_a) are symmetric around 45°. Since the diffusion of oxygen vacancy is a thermally activated process, the temperature dependence of oxygen vacancy diffusivity can be expressed by an Arrhenius relationship where the diffusion constant is proportional to the E_a from which the activation energy can be extracted (Figure 4.1e). This variation of diffusivity is consistent with the overall E_a for oxygen diffusion which increased with the increasing twist angle. E_a is tuned remarkably from 0.6 to 1.2 eV as the twist angle changes from 0° to 45°. The phenomenon is attributed to the relative rotation between layers, which forms a periodic moiré potential in the material system affecting the diffusion path and resulting in lattice site preference for the diffusion of oxygen vacancies. The vacancy environment (including their electrons and holes), remains almost immobile below room temperature but can move at higher temperatures due to the thermally activated processes involving oxygen diffusion and vacancy migration. Together with the experimental observations in chapter 3.1.3 on the enhanced oxygen vacancy concentration at the twisted

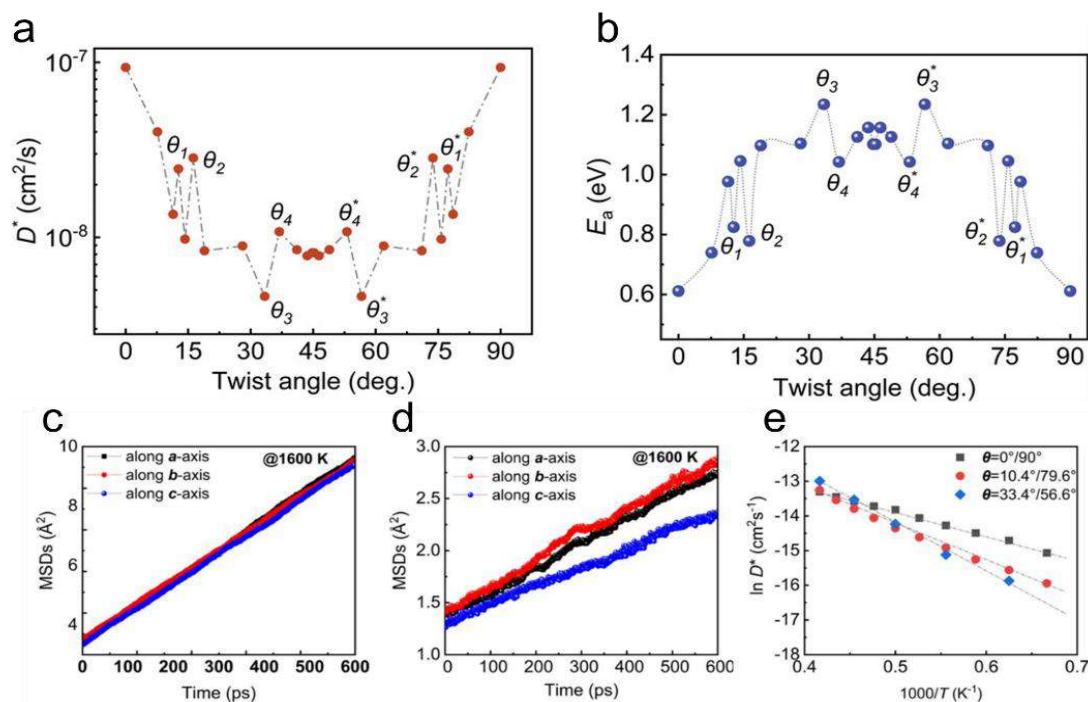


Figure 4.1. ab-initio calculations of the tracer diffusion coefficient (D^*) for oxygen ions as a function of the twist angle (a) and the activation energy (E_a) for oxygen ion migration with respect to the twist angle. The calculations have been carried out at elevated temperatures of 1200 K. c) Mean-squared displacements (MSDs) for oxygen ion migration in bulk (001)-STO at a typical temperature of 1600 K. d) Mean-squared displacements (MSDs) for oxygen ion migration in twisted STO/STO ($\theta/\theta^* = 33.4^\circ/56.6^\circ$). e) Arrhenius plots for STO/STO with different twisting angles. Note that $\theta/\theta^* = 0^\circ/90^\circ$ corresponds to bulk STO.

STO/STO interface from the EELS data, this shows that twisting freestanding thin films would be a valuable synthetic strategy for manipulating the diffusion properties of oxygen vacancies in perovskite oxide thin films using twisted membranes. This makes these freestanding membranes interesting for designing novel functional energy materials and devices for cutting-edge electronic and energy-related technologies.

4.2 Superconducting 2DEG in freestanding LaAlO₃/SrTiO₃ membranes

The state-of-the-art techniques to fabricate freestanding membranes utilizing the sacrificial wet etch approach described in chapter 3.1.2 may be a larger part of futures device fabrication; however, so far, it has not been possible to create freestanding LAO/STO membranes that are conducting. Following the alternative approach described in chapter 3, we have been able to fabricate membranes that are not only conducting but also preserve properties such as superconductivity seen in the traditionally thin film deposition approach.

4.2.1 Preparation of the device and ensuring good contact to the 2DEG

One of the challenges in the preparation of any device using a membrane is to ensure good electrical ohmic contact to the buried interface with the least possible contact resistance.

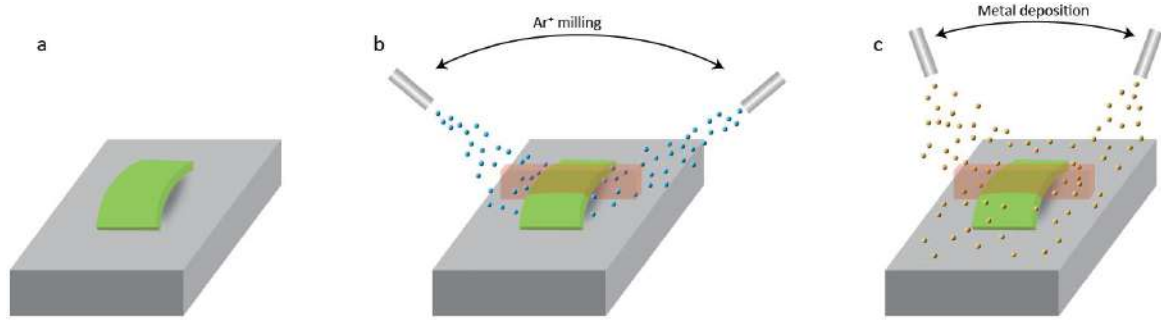


Figure 4.2. Schematic illustration of the membrane contacting. a) A LAO/STO membrane is deposited on the substrate, preferably bending down wards for a more easily accessible contacting. b) Ar⁺ milling with an angle of $\pm 50^\circ$ on both sides of the membrane to enhance the probability for contacting. c) Ti/Au deposition with an angle of $\pm 20^\circ$ on both side of the membrane.

This is partially due to the thick size of the LAO film on the STO, meaning that simply depositing metal on the surface does not bridge the 2DEG to the contacting electrodes. Therefore, to prepare the electrical contacts for the spalled membranes, individual LAO/STO membranes were transferred onto a Si substrate. This is achieved by utilizing the tip of either a clean room wipe or a micromanipulator to a SiO₂/Si⁺⁺ substrate with pre-patterned electrodes and alignment marks used with lithography methods. A ~ 900 nm trilayer of e-beam was spin-coated, exposed with lithography, and developed to open the resist for the metal deposition that serves as electrodes for the membrane. Before the metal deposition, a brief Ar⁺ milling with an angle of 50° was employed at the edges of the membrane. The metal electrodes were evaporated in the same chamber as the argon milling consisting of Ti/Au deposited with an angle of 20° . The employed angle was to ensure contact with the side of the membranes, where the 2DEG is exposed. The remaining resist and metal were removed with a lift-off in warm N-methyl-2-pyrrolidone. Figure 4.3 shows an AFM micrograph with the corresponding height profile of a device example displaying a device with metal contacts. The curvature of the membranes is preserved after the metal evaporation and has a radius of curvature of $\sim 5 \mu\text{m}$ derived from the height profile.

4.2.2 Temperature dependence

A total of 50 devices of two-terminal were fabricated where 23 of the devices showed low conductivity at room temperature, and the rest showed resistance in M Ω -range, presumably

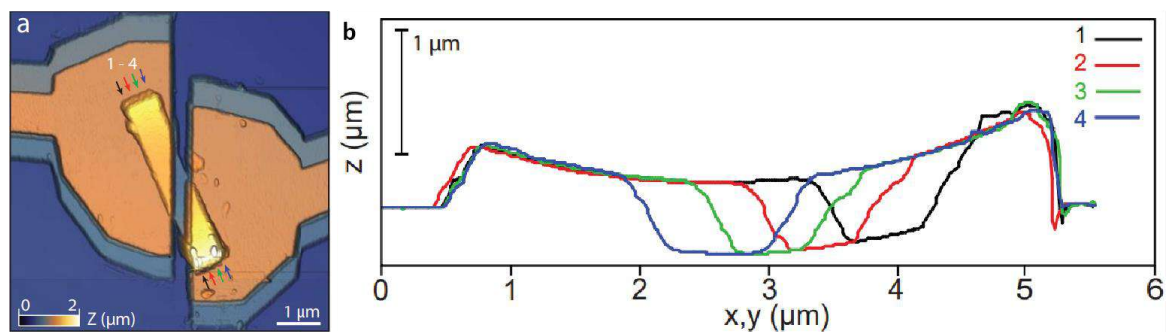


Figure 4.3. Atomic force microscopy topography of a membrane device, displaying a membrane clamped below metal (Ti/Au) electrodes. Colored arrows display the height profiles in (b). The height profile confirms the curvature of the membranes after metal deposition. The radius of curvature is $\sim 5 \mu\text{m}$.

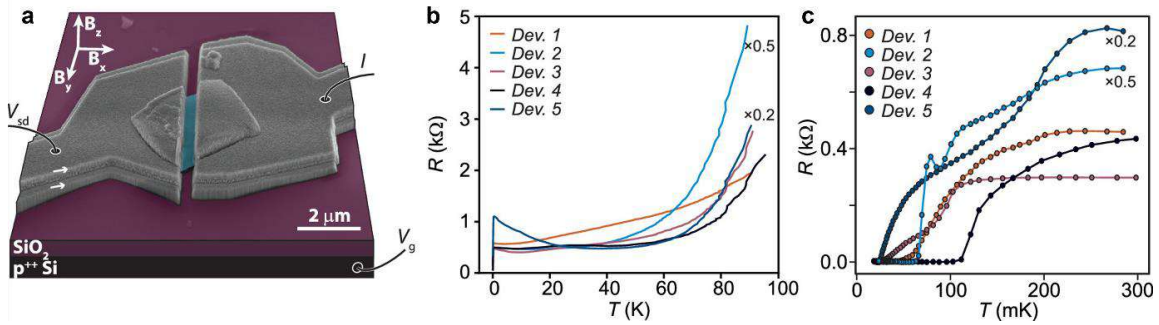


Figure 4.4. a) Tilt-view SEM image of an as-grown (non-patterned) LAO/STO micromembrane device (false colored). b) Two-terminal resistance vs. temperature dependence for five devices showing metallic behavior. c) Low temperature regime of (b) showing the superconducting transition. The resistance of the cryostat filters and membrane/interface have been subtracted. Device 2 and 5 have been scaled for clarity by 0.5 and 0.2, respectively.

due to bad contacting of the 2DEG. Out of the 23 conducting devices, 5 devices (devices 1-5) were selected for more detailed transport measurements. The measurements were performed in a dilute refrigerator system described in chapter 2.2.1. Due to limitations in the fabrication process where metal deposition requires an angled metal evaporation, preferably from two sides to ensure contact (see Figure 4.2). However, utilizing this method only allows for a very small contact area presumably resulting in a small device yield i.e., by only creating a two-terminal and not a four-terminal device, we are able to make devices more reliably. Therefore, the transport-characterized devices in this thesis have a two-terminal configuration. An example of such a device can be seen in Figure 4.4a displaying an SEM image of the device. The double steps in the metal layer originates from the angled deposition from either side of the membrane with two materials (Ti/Au). The two-point resistance as a function of temperature is shown in Figure 4.4b-c, where (b) is the full range and (c) shows a magnification of the low-temperature region. There is a distinct resistance drop across all the samples, consistent with the emerging superconducting phase at these temperatures. The obvious dissimilar superconducting phase transitions with temperature and its nonhomogeneous transitions have been seen before in bulk LAO/STO systems^{78,79} and was layer attributed to the superconducting phase being spread in puddles that have an individual superconducting transition temperature, which also seems to be the case for the membranes¹⁷⁹. Given that the 2DEG in the membranes is buried 70 nm from the surface, much deeper than that in bulk samples of < 6 nm^{78,180-182}, this result suggests that the origin of the inhomogeneity is intrinsic^{183,184} and is not associated with surface adsorbates. Also, strain in LAO/STO can modulate the interface density¹⁸⁵ and a nonhomogeneous strain profile in the membranes could lead to spatial variations.

4.2.3 The superconducting phase in spalled membranes

The superconducting state was measured utilizing an external magnetic field with the spatial orientation (B_x , B_y , and B_z) shown in Figure 4.5a, where B_x and B_y are the in-plane applied magnetic fields and B_z is the out-of-plane applied field relative to the current. Figure 4.5a-c shows the resistance as a function of the temperature at a fixed magnetic field for device 4. The field was increased in steps of 50 mT per measurement. There is a clear appearance of the different critical temperatures between the devices and the

nonmonotonous transitions between the devices. This is seen in previous studies of superconductivity in LAO/STO interfaces^{78,79}, where the behavior in the mesoscopic system is caused by a charge imbalance arising from the inhomogeneous phase transition¹⁸⁶. This picture supports the spatially inhomogeneous superconducting phase in the membranes. Defining the superconducting transition as the $0.95 \times R_N$, where R_N is the normal state conductance, and plotting the field as a function of the critical temperature yield, gives a figure as shown in Figure 4.5d. The dots represent the data from Figure 4.5a-c, and the solid lines are the GL relation $H_c(T)/H_c(0) = 1 - [1 - (T/T_c(0))^2]$, where $T_c(0)$ is the critical temperature at zero fields and the critical field at $T = 0$. These values were estimated for all of the five devices, but for device 4 we also performed additional gating measurements, see Figure 4.5b,c. Device 4 displays a critical field and temperature dependence, where $T_c(0) = 246$ mK, $H_c^x(0) = 831$ mT, $H_c^y(0) = 1335$ mT, and $H_c^z(0) = 165$ mT. We note that the critical parallel fields for H_c^x and H_c^y , with respect to the substrate surface, are all different. This behavior is consistent with the curvature of the membrane due to different areal rejection of the field (Messiner effect) depending on the in-plane orientation of the field. Since the membrane is bending either up or down, the magnetic field lines either meet a small or large rejection depending on whether the membrane is orientated with the bending edge parallel or perpendicular to the field line, respectively. To estimate the characteristic coherence length (ξ) and the effective thickness of the superconducting layer, we take the largest in-plane value, since this is the closest estimate of the parallel field to the membrane. The perpendicular critical field (H_c^z) is not, on the other hand, expected to be affected by the orientation, therefore we can use this value. For more details regarding the expression for the coherence length and thickness, the reader is encouraged to revisit chapter 1.5.2. We also found that the definition for the superconducting phase transition does not affect the values significantly. For device 5 the $R(T_c) = 0.9R_N$ give T_c and H_c values of $T_c = 196$ mK, $H_c^{x/y/z}(0) = 648/1815/191$ mT, respectively.

Figure 4.6b shows a contour map of the differential resistance vs the current (I) and the temperature (T). The zero-resistance state illustrated as blue, extends up to ~ 200 mK, and in Figure 4.6c the extracted temperature dependence of the critical current is shown along with a fit to the GL mean field result $I_c^{\text{GL}}(t) = I_c(0)(1 - t^2)^{3/2}(1 + t^2)^{1/2}$ where $t = T/T_c^{\text{GL}}$, $T_c^{\text{GL}} = 145$ mK, and $I_c(0) = 108$ nA. The fit captures the trend reasonably well but drops to zero more abruptly than in the experiment. The reason for this discrepancy is unknown. A key aspect of the LAO/STO membrane system is the susceptibility to electrostatic gating, which merges the functionality of strong correlations with the

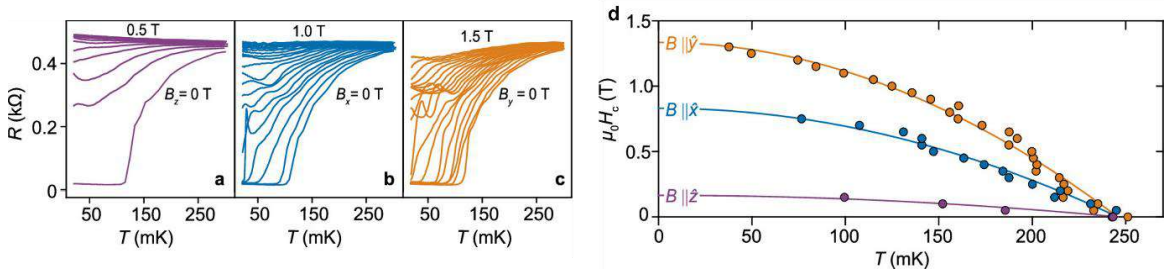
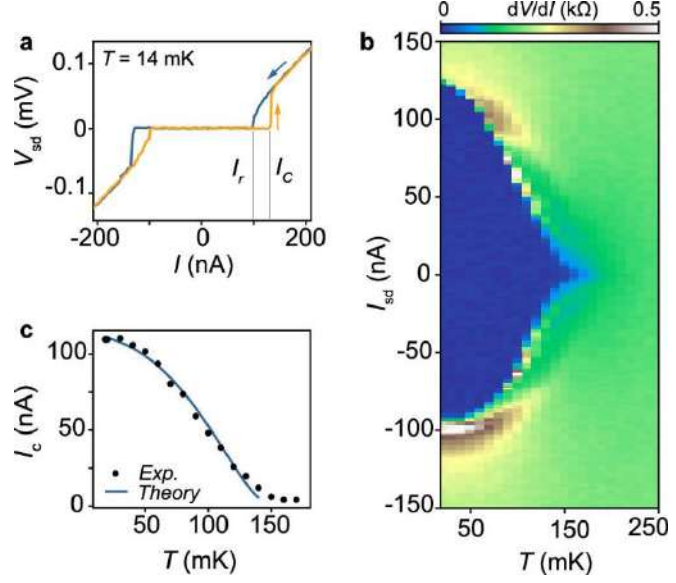


Figure 4.5. a-c) Resistance as a function of temperature at fixed fields ranging from 0-0.5 T for (a), 0-1 T for (b), and 0-1.5 T for (c). The shown device is 4. The field was increased in steps of 50 mT. d) Critical field ($\mu_0 H_c$) as a function of temperature. The solid line represents a fit of the Ginzburg-Landau theory fitted to the superconducting transition in (a-c) defined as $0.95 \times R_N$.

Figure 4.6. a) DC bias voltage (V_{sd}) for device 4 as a function of current (I). The orange and blue lines represent the up and down trace, respectively. There is a clear difference in the critical current (I_c) and the retrapping current (I_r). b) Color map of the resistance (dV/dI) as function of current (I) and temperature (T). The blue zero resistance state vanished around 200 mK to a normal state conductance illustrated as green color. c) Critical current as function of temperature extracted from (b) (dots) fitted with Ginzburg-Landau theory (solid line).



tunability of semiconductors. For thin films LAO/STO heterostructures, the tuning of the carrier density by backgating²⁰ and topgating¹⁸⁷ has been well established, allowing

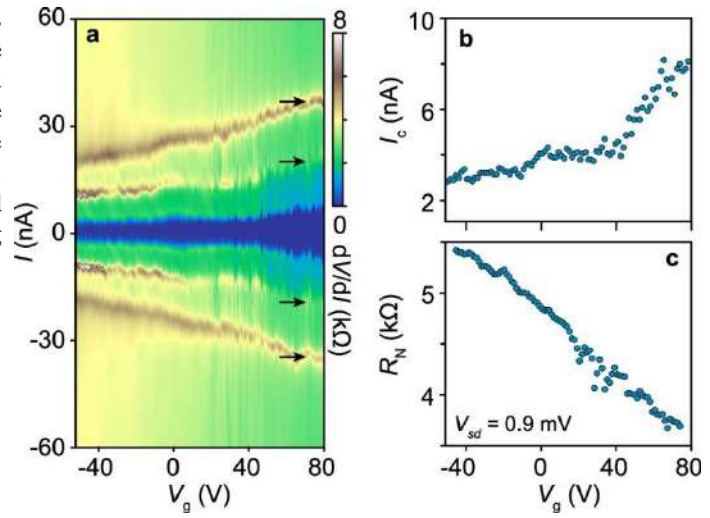
the tuning of the superconducting transition temperature^{107,188,189}. For the measurement of Devices 3 and 4, unfortunately, the backgate was not connected, and instead, device 5 was measured in a separate cooldown to previously shown measurements. Figure 4.7a shows dV/dI vs V_g and I for device 5 measured in a separate cooldown with the zero-resistance region illustrated by a dark blue color widening with increasing V_g . The corresponding extracted gate dependence of the critical current $I_c(V_g)$ and normal state resistance $R_N(V_g)$, respectively, where R_N extracted from the normal region conductance. The critical current in Figure 4.7b clearly illustrates the opening in Figure 4.7a. The behavior of the normal state conductance is consistent with a superconducting 2DEG following the same trend of conventional LAO/STO in the underdoped regime.

Due to the fact that we were using only two-terminal configuration, we were not able to perform Hall measurements to obtain the carrier mobility and density of these devices. However, since our results showed a superconducting state very similar to that of the conventional LAO/STO, the values of T_c and the gate dependence places the devices as being slightly underdoped with respect to the maximum of the dome-shaped superconducting phase shown in Figure 1.11. From this, we estimate the carrier density of $n_s \approx 1 \times 10^{13} \text{cm}^{-2}$ for devices 1-4 with $R_s \approx 1 \text{k}\Omega/\square$ with the typical mobility of $\mu \sim 1000 \text{cm}^2/\text{Vs}$. We stress that this is only an estimate and should be considered only as indirect indication that the membranes behave similarly to a conventional LAO/STO heterointerface. This is surprising, since these membranes show properties identical to what can be expected from conventional LAO/STO heterointerfaces, given the fact that these membranes have very large strain ($\sim 2\%$) and strain gradients ($\sim 10^5 \text{m}^{-1}$) in the membranes¹⁶⁴.

In summary, using Si/SiO₂ as a substrate, we fabricated electrical devices based on LAO/STO membrane. We reported measurements of the low-temperature characteristics, demonstrating the presence of a superconducting phase that shows the two-dimensional character of the electron system in the freestanding heterostructure membranes. The critical

supercurrent density and the temperature dependence were found to be similar to values reported for macroscopic LAO/STO samples.

Figure 4.7. a) Differential resistance as function of applied DC current and gate voltage for device 5. B) The extracted critical current (I_c) as function of gate voltage from (a). c) Normal state conductance as function of gate voltage. The resistance is conductance is extracted at high bias outside the superconducting and step region.



CHAPTER 5

Magnetism in SrTiO₃-based structures

This chapter deals with magnetism in STO and STO-based heterostructures. By controlling the PO₂ of the environment as well as the annealing temperature, it was possible to control the stoichiometry of the films and thereby the magnetic responds of the films. Another approach is diluting the LAO films with LaBO₃ (LBO) during the growth as a way to create a magnetic 2D/3D system on STO, where vertically aligned LBO pillars were formed on 2DEG films displaying a highly anisotropic magnetic response. This chapter is a review of the papers in appendix V, IX and X.

5.1 Controllable magnetism though growth pressure

The origin of magnetism in STO has been frequently debated over the last decades, and the presence of oxygen vacancies defects has been widely considered as one of the main contributors to magnetization: Oxygen vacancies allow the partial reduction of Ti⁴⁺ into magnetically active Ti³⁺. A few examples of some of the proposed mechanisms are listed here: Coey *et al.* suggested that the origin of ferromagnetism in reduced STO was either due to direct exchange interactions between V_O and the molecular orbitals of valence electrons of surrounding Ti ions or due to a Stoner-type spin-splitting of the Ti 3*d* band for ferromagnetically coupled electrons⁶⁸. However, Brovko and Tosatti¹⁹⁰ reported theoretical results suggesting that an isolated oxygen vacancy defect in STO only stabilizes states with low or zero total magnetization, since the two Ti spins facing each other across the V_O are antiferromagnetically coupled via strong direct exchange interaction. Doenning and Pentcheva⁹⁴ demonstrated that in LAO/STO heterostructures, Ti *d*_{xy} bands could be dominantly magnetized via magnetic double-exchange interactions between Ti³⁺ and Ti⁴⁺ when a tensile in-plane strain is induced in TiO₆ octahedra and the electron doping level is below $7 \times 10^{14} \text{ cm}^{-2}$. However, this electron doping level (0.5*e* per Ti) per STO monolayer is hard to achieve practically when considering that Ti *d*_{xy} orbital polarization in a *c*-axis compressed STO is purely induced by a high V_O concentration of ~25 at. % as a V_O sublattice.

In this work, we demonstrate tunable magnetic properties of homoepitaxial STO thin films by controlling both cation off-stoichiometry (V_{Ti}) and V_O contents using PLD. Our results show that PO₂ strongly influences the growth dynamics and the magnetization of the films. As described in chapter 2.1.4, a preferential ablation of Ti (Sr) in STO can be induced by increasing (decreasing) laser fluence, leading to the formation of Sr-(Ti-) deficient STO films. Since the kinetic energy of the arriving species is highly affected by the background pressure in the chamber during the PLD process, a suitable balance between the laser fluence and background gas is essential^{137,191}. To do this we have grown various samples

at different PO₂ values at 5×10^{-2} , 1×10^{-2} , 5×10^{-4} , and 5×10^{-6} mbar with film thickness kept constant at around 25-26 nm and were cooled in O₂-rich atmosphere (200 mbar). Defects typically resulted in lattice expansion and a charge rearrangement in STO, leading to lattice symmetry breaking (electric polarization), followed by an electronic reconstruction and crystal field splitting (e.g., splitting of degenerate Ti 3d orbitals into a relative energy scheme that follows $d_{xz}/d_{yz} < d_{xy} < d_{z^2} < d_{x^2-y^2}$)^{192,193}. Therefore, we performed high-resolution XRD 2θ - ω patterns of oxidized STO films, grown on STO(001), as a function of PO₂, to observe any indication for lattice expansion. Figure 5.1a shows the XRD spectra showing that the oxidized films were grown epitaxially and possess thickness fringes. The STO film grown at PO₂ = 5×10^{-2} mbar shows almost identical 2θ (001) peak positions to those of the STO homo-substrate with well-defined thickness fringes. This indicates low out-of-plane strain ($x_z = +0.19\%$) in the film and an excellent crystal quality. When PO₂ was decreased to PO₂ = 5×10^{-4} mbar, a continuous shift of the out-of-plane STO(001) peaks toward lower 2θ values was found. This revealed an increase in the c-axis lattice parameter to a value of $c = 3.95 \text{ \AA}$ ($x_z = +1.15\%$), as shown in Figure 5.1c. The RSM maps in Figure 5.1b show the strain distribution of the two STO films (PO₂ = 5×10^{-2} and 5×10^{-4} mbar) at the (103) reflection. This shows that the in-plane lattice spacing for both films is coherently aligned with the in-plane spacing of the underlying STO substrates ($a = 3.905 \text{ \AA}$), while the c-axis lattice parameter was found to increase with PO₂. We have measured the magnetization of the samples such that we can compare the out-of-plane lattice expansion with the measured magnetic hysteresis loop can compare the out-of-plane lattice expansion with the measured magnetic hysteresis loop.

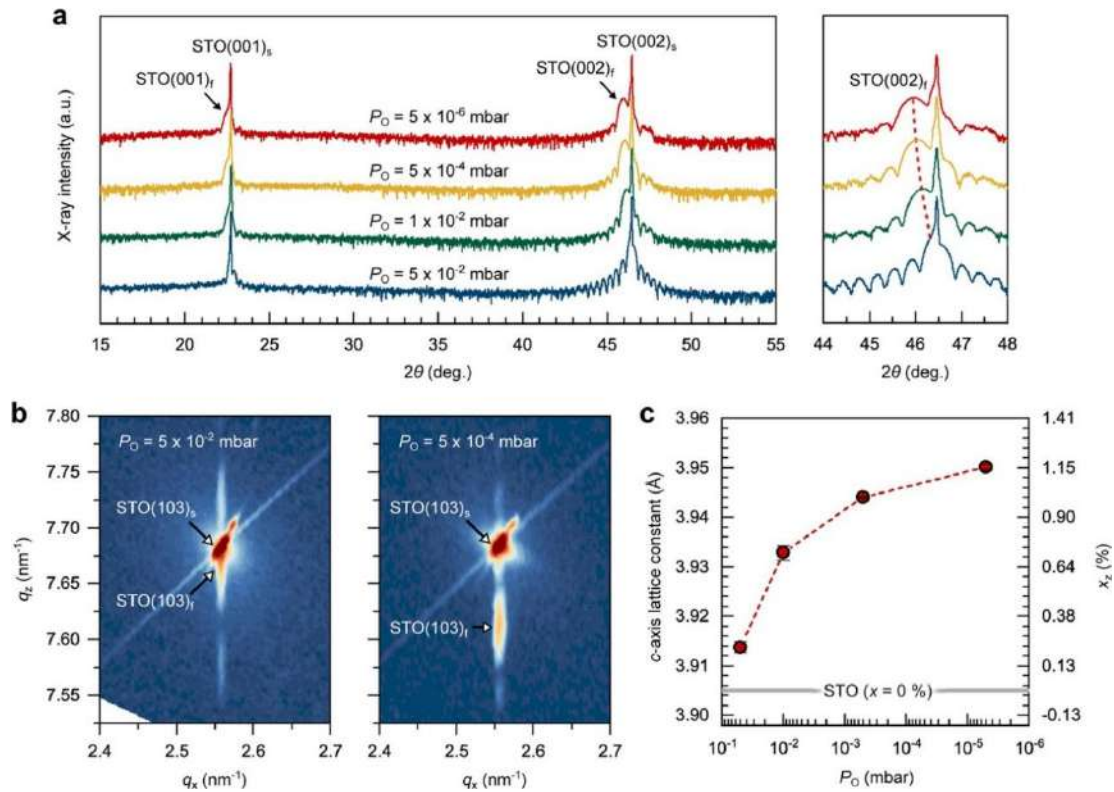


Figure 5.1. a) XRD 2θ - ω for four STO film grown at various PO (5×10^{-2} , 1×10^{-2} , 5×10^{-4} , and 5×10^{-6} mbar). The right panel shows a magnification of film and substrate at STO(002). b) RSM near STO(103) reflection for STO films grown at PO = 5×10^{-2} and 5×10^{-4} mbar. c) c-axis lattice constant expansion as function of growth PO₂.

Figure 5.2 displays the magnetic hysteresis loop of the STO films measured with SQUID (described in chapter 2.2.2.) at 5 K as a function of PO_2 . The measured hysteresis loops were corrected by subtracting the constant diamagnetic and paramagnetic background from the instrument's accessory. The results show a notable increase in the magnetization with decreasing PO_2 . The saturation magnetic moment of the films continuously increases up to $14 \mu\text{emu}$ ($56 \mu\text{emu}/\text{cm}^2$), as the growth pressure is decreased to a value of $PO_2 = 5 \times 10^{-4}$ mbar. The enhanced magnetism at low PO_2 can be understood through the rise of cation off-stoichiometry (Ti deficiency) in the films since V_O would not be sufficient to create such a large magnetization (more on that in chapter 5.2).

The O and Ti ions neighboring a V_{Ti} site became spin-polarized through charge rearrangement, yielding a μ_B/V_{Ti} of 0.48. Furthermore, we considered the effect of A-site Sr (2+) vacancies on the magnetism of STO. An A-site vacancy defect contributes to a relatively weak magnetization of $m < 0.07 \mu_B/V_{Sr}$ in STO due to its much less effective charge rearrangement⁸: (i) Only two electrons can contribute to the oxygen atoms adjacent to a Sr vacancy site and (ii) a Sr vacant site has a relatively large distance (2.76 \AA) to the 12 nearest oxygens as compared to that (1.95 \AA) of a Ti vacant site. Also, an isolated V_O when stabilized in STO produces a very weak magnetism ($0.003 \mu_B/V_O$) without significant exchange interaction with the neighboring Ti atoms (e.g., a magnetization of Ti d_{xy} bands). This is consistent with previous reports¹⁹⁰. Paring the oxygen and titanium vacancies (i.e., the vacancies are neighbors), our calculations clarify that the large measured magnetization is produced by the $V_{Ti}-V_O$ pair due to (i) a more energetically stable formation (smaller charge screening effect) in the STO system with a tendency to pair the oppositely charged defects [when comparing the charge screening effect of STO with a singular V_{Ti} through relaxation and the largely varied magnetization ($4 \mu_B/V_{Ti} \rightarrow 0.48 \mu_B/V_{Ti}$)], (ii) a higher dispersive nature of the induced magnetic moment over the lattice atoms, and (iii) an effective magnetic coupling with a shorter distance ($3.5a$) between the vacant defect pairs. This trend is also in good agreement with our experimental results, where a sample cooled in the same PO_2 , and therefore still having V_O , increased the magnetization by a factor of ~ 3.5 compared to the oxidized samples (for more details see Article V).

In conclusion, we have demonstrated that the magnetic properties of engineered STO thin films can be effectively tuned by PLD film growth parameters (interdependent parameters of laser fluence and PO_2) by controlling the concentration of cation vacancies, anion vacancies, and their complex defects. Our results show that B-site cation vacancies, V_{Ti} ,

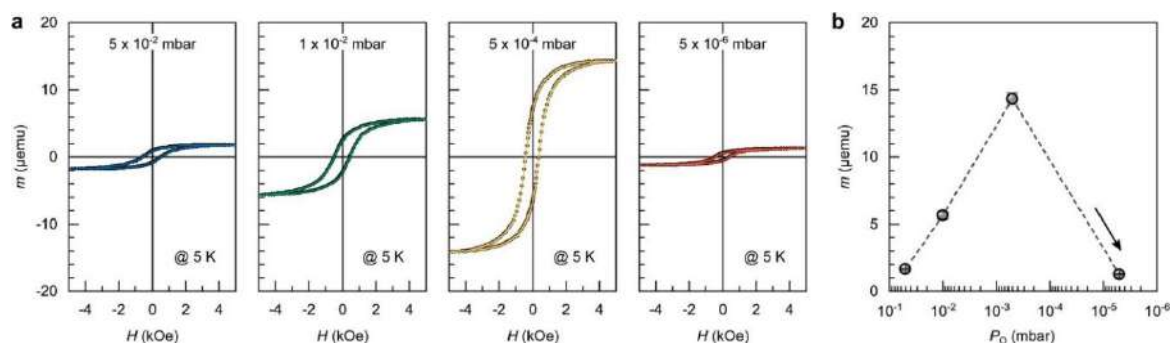


Figure 5.2. a) Magnetic hysteresis loop of the STO films measured at 5 K. b) variation in the magnetic moment derived from the saturation level as function of PO_2 .

not only contribute to the magnetization of STO but also promote the incorporation of oppositely charged V_O into the B-site cation deficient STO for the formation of the V_{Ti} - V_O pairs. This greatly increases the magnetization and stability of the system and has been demonstrated both experimentally and theoretically.

5.2 Tuning SrTiO₃-based systems by oxygen vacancies

Magnetism in band insulating ABO₃ perovskite strontium titanate, STO, and the related systems, is an important physical property for potential oxide spin-based electronics such as sensors and memories¹⁹⁴. Chemical modification, e.g., substitutional magnetic element doping (Co, Cr, and Fe)^{195–197} and defect engineering^{68,116} has been widely utilized to create and control the magnetism in STO systems. A widely accepted magnetic reservoir in STO is the oxygen vacancy, which is the most abundant intrinsic point defect. Despite substantial work on the related chemical and electrical properties in STO^{32,87,91}, its magnetic contribution has not been fully experimentally manifested and is yet to be explored, due to unstable and weak magnetic signals.

Here, this work demonstrates a tunable magnetism in STO-based systems, i.e., a STO single crystal, a STO/STO homostructure, and a stoichiometric LAO/STO heterostructure, by controlling the content of oxygen vacancies. The effect of oxygen vacancies on the magnetization of the samples was systematically determined by conducting continuous thermal annealing processes in different temperatures (200 – 700 °C) and atmospheres (in O₂ and in vacuum). Our results clearly exhibit a tunable magnetism in the STO-based systems by controlling oxygen deficiency: (i) the magnetization of all the as-prepared samples is almost similar with saturation moments of ~5 - 7 μemu; (ii) a significant reduction (~70 - 80 %) in the magnetization of all the STO-based materials when V_O are sufficiently compensated by a thermal annealing, driven at 700 °C in O₂; and (iii) the magnetization of all the samples were turned back to/over the initial values when the samples were subsequently annealed in an O-reducing condition at the same temperature.

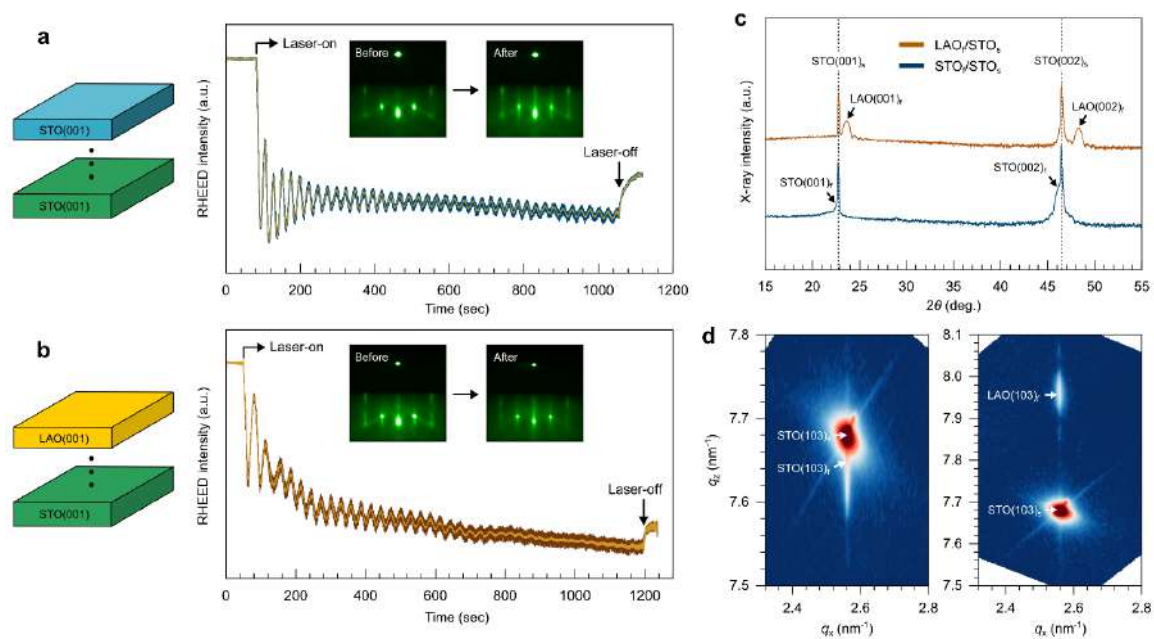


Figure 5.3. a,b) RHEED intensity profiles for the STO (a) and LAO (b) films grown on STO(001), recorded during PLD film growth. The insets show the RHEED patterns before and after film growth. c) XRD θ - 2θ patterns for the grown STO and LAO films on STO(001). d) reciprocal space mapping around (103) reflection of STO.

This work provides not only direct experimental evidence for the oxygen vacancy-induced magnetism in STO, but also gives insights for understanding the correlated electronic and magnetic properties of STO-based homo/heterosystems.

To investigate the effect of oxygen vacancy on the magnetic properties of STO-based systems, three different STO-based samples were prepared: (i) a reduced TiO₂-terminated STO(001) single crystal, treated at 700 °C in PO₂ = 5 × 10⁻⁴ mbar; (ii) a stoichiometric STO film on TiO₂-terminated STO(001); and (iii) a stoichiometric-like LAO film on TiO₂-terminated STO(001). The volume of the STO single crystal substrate used in this work was 5 × 5 × 0.5 (z) mm³. The epitaxial STO and LAO films were grown by PLD at 700 °C in an PO₂ of 5 × 10⁻⁴ mbar and were cooled down to room temperature in the same film growth pressure. Both films were grown by using laser fluence of ~1.5 J/cm². The thickness of both films was controlled by RHEED during film growth and remained almost consistent with approximately 15 nm (see Figure 5.3a,b).

Figure 5.3c shows XRD θ - 2θ scans for the as-grown STO and LAO films grown on STO(001). The results indicate that the *c*-axis parameters of the epitaxially grown STO(001) and LAO(001) films are 3.920 Å and 3.765 Å, respectively. This corresponds to the out-of-plane strain of the grown STO, and LAO films are approximately +0.3 % and -0.7 % with respect to their bulk cubic (/pseudo cubic) parameters. RSM further indicates that the in-plane lattice spacing of both films are coherently matched with that of the STO substrate (Figure 5.3d).

To examine the magnetic properties of the samples, a VSM system was employed. Careful data corrections (subtraction of diamagnetic background caused by instrumental accessories, e.g., a sample holder and a low temperature glue) were made before sample measurement. Moreover, the accuracy of measured data for the samples was determined by comparing magnetic data of the same samples, collected by SQUID in MLU, Germany (not

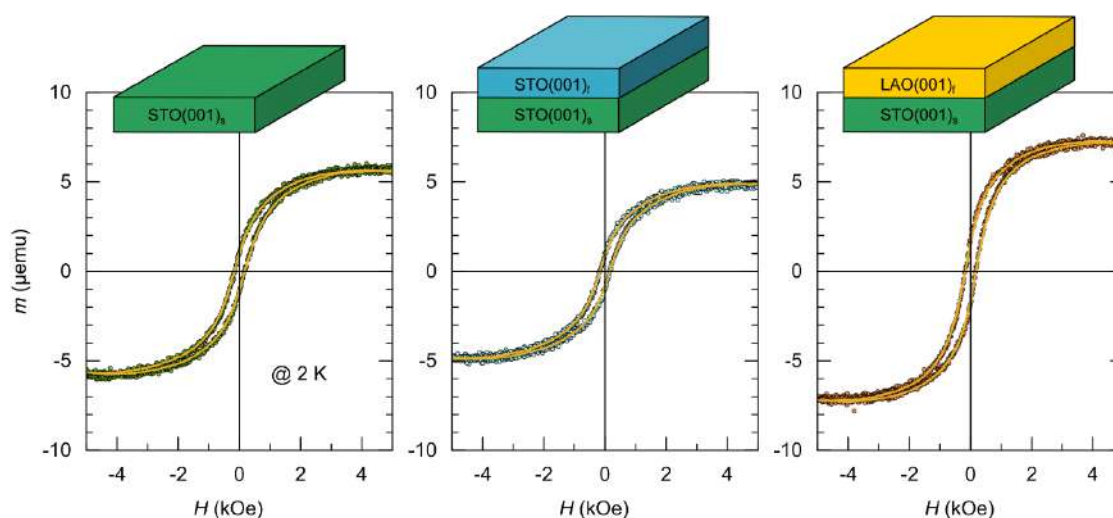


Figure 5.4. The 2 K magnetic hysteresis loops of the as-prepared samples: a treated STO substrate in 5 × 10⁻⁴ mbar at 700 °C (left), a 15 nm-thick STO film grown on STO(001) in 5 × 10⁻⁴ mbar 700 °C (middle), and a 15 nm-thick LAO film grown on STO(001) in 5 × 10⁻⁴ mbar at 700 °C.

shown here). We confirmed that magnetic data measured in two different places are identical and thus the VSM data is highly reliable.

Figure 5.4 shows the 2 K magnetic hysteresis loops of the samples, measured by applying external magnetic fields in ± 5 kOe range along the in-plane direction of the samples. All the samples exhibit clear ferromagnetic hysteresis behaviors. Almost similar saturation magnetic moment ($m_s \sim 5 - 7 \mu\text{emu}$), remanence ($m_r/m_s \sim 18 - 20\%$), and coercive fields ($H_c \sim 150 - 180$ Oe) for the as-prepared samples were found. This reveals the same magnetic nature for all samples regardless of the upper STO and LAO layers. Such a weak magnetic response with $m_s < 10 \mu\text{emu}$ has been typically observed in STO-based systems, e.g., reduced STO and conductive LAO/STO interfaces¹¹⁶. The origin of the ferromagnetism in reduced STO has been proposed by the effect of oxygen vacancies as they could allow the partial reduction of Ti^{4+} into magnetically active Ti^{3+} . Possible magnetic solutions, e.g., oxygen defect-mediated magnetic ordering and/or localized unpaired Ti *d*-band electron spins through exchange coupling of itinerant carriers, have been proposed^{68,198,199}. Since, in this work, all the as-prepared samples (treated or grown in 5×10^{-4} mbar) are partially oxygen-reduced, it was predicted that oxygen vacancy would play a common role in creating the magnetic properties of all the samples.

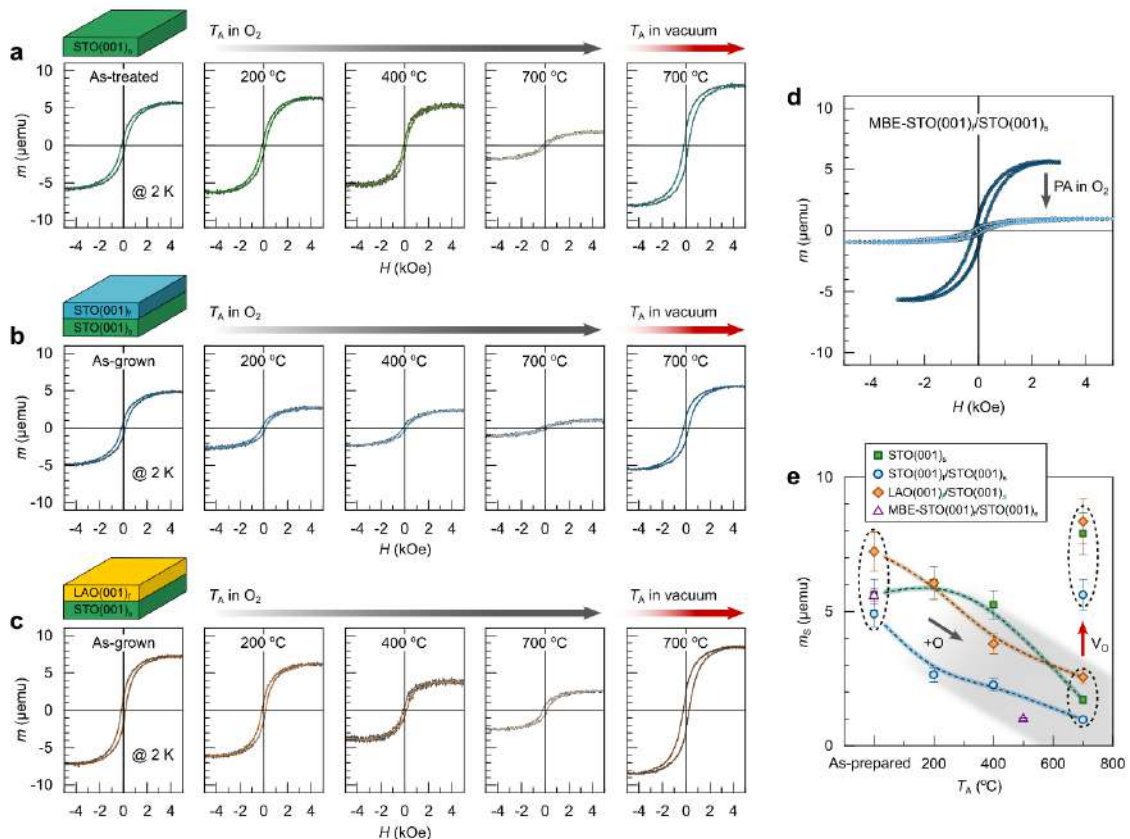


Figure 5.5. a,b,c) The 2 K magnetic hysteresis loops of the STO single crystal, STO/STO, LAO/STO samples as a function of T_A . All the samples were annealed in O₂ by varying T_A up to 700 °C and the same samples were subsequently annealed in vacuum at 700 °C. d) The 5 K magnetic hysteresis loop of the MBE-grown STO film (20 nm thick) on STO(001) before and after PA. e) A comparison for the measured magnetic moment of the samples with different PA conditions.

To verify the effect of oxygen vacancies on the magnetic properties of the samples, ex-situ post annealing (PA) work was carried out. Firstly, all the samples were subsequently annealed in common magnetic reservoir in the samples is oxygen vacancy as it can be thermodynamically reactive with and compensated by additional oxygen as $\frac{1}{2}\text{O}_2 + \text{V}_\text{O}$. Moreover, a similar large reduction (approximately ~80 %) in the magnetization of a stoichiometric-like STO film grown on STO(001) by molecular beam epitaxy (performed in University of Minnesota, USA) was found after O₂ annealing at 500 °C for 1 hour (Figure 5.5d). To further confirm the effect, we annealed the samples in vacuum at 700 °C for 2 hours. The results clearly exhibited that the magnetization of all the samples turned back to increase, similarly to those for the as-prepared samples. All the measured m_s for the samples are listed in Figure 5.5e.

In summary, this work provides experimental evidence that oxygen vacancy acts as a common magnetic reservoir in STO-based systems with a limited range of $m_s < 10 \mu\text{emu}$. This means that the magnetization of STO-based systems can be effectively tuned by controlling oxygen vacancy in-and-out processes. Experimentally, future quantitative work is indeed required to establish the relationship between the concentration of oxygen vacancies versus the magnetization of STO or the related systems.

5.3 Magnetism in self-assembled $\text{LaAlO}_3(1-x):\text{LaBO}_3(x)/\text{SrTiO}_3$ heterostructures

Here, we demonstrate an interface engineering of complex oxide nanocomposite thin film heterostructure, $\text{LaAlO}_3(1-x):\text{LaBO}_3(x)$ (LABO) nanocomposite films deposited on STO(001), using a self-assembly approach to control the electric and magnetic landscape. Our results show that a unique 2D layer-by-layer growth mechanism yields atomically abrupt crystal interfaces where vertically aligned magnetic structures are spontaneously formed in the LABO/STO heterostructures (see Figure 5.6f). This transition is primarily driven by the change in the composition ratio. The presence of such structural transition in this material system leads to the coexistence of a low-dimensional high-mobility electron gas and magnetism ordering. The LABO composite thin films with composition of $0 \leq x \leq 10\%$ were grown on TiO_2 -terminated STO(001) substrates with PLD, as schematically shown in Figure 5.6a with thickness kept between 22 and 25 nm.

The film is grown on a TiO_2 -terminated STO(001) monitored with RHEED for both the growth of LAO (bottom) and LABO top, shown in Figure 5.6b. For the LAO film, a steady 2D growth mode was observed, resulting in streak RHEED pattern after the growth. In contrast, the LABO film growth showed a transition from 2D to 3D film growth transition around 10-12 unit-cells resulting in a spotty RHEED pattern. To obtain insights for the film growth characteristics of the LABO films with varying x , RSM was performed for the LAO and LABO films around the STO(113) reflections as shown in Figure 5.6c. The RSM shows that the in-plane LAO($hh0$) for the undoped LAO film (~ 25 nm thick) is constrained along the STO($hh0$), yielding a positive strain of approximately +3.0%, while the out-of-plane ($00l$) shows a negative strain of $\sim 0.8\%$ to compensate for the in-plane strain. In contrast,

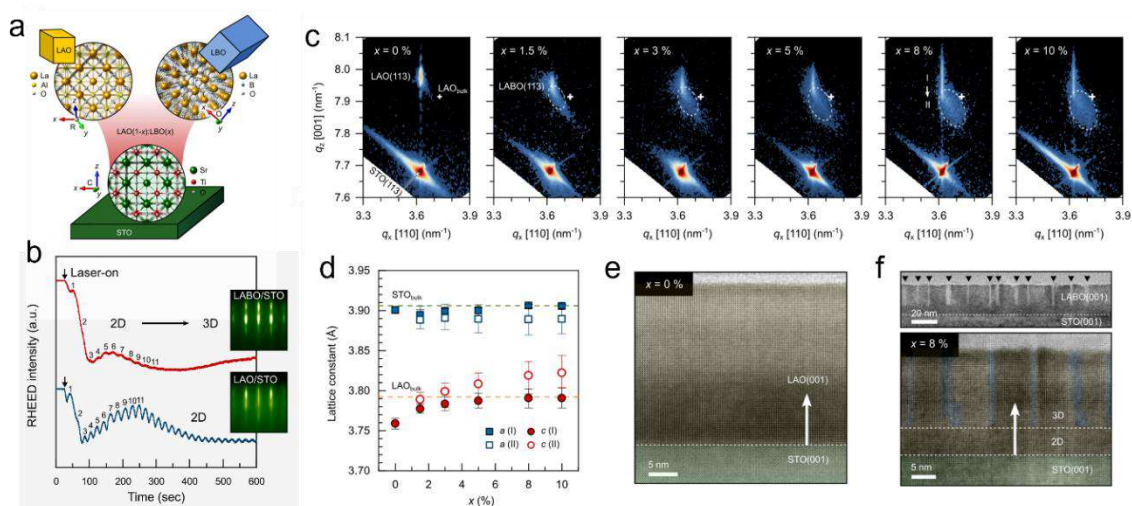


Figure 5.6. a) Schematic illustration of the LABO nanocomposite film growth containing rhombohedral $\text{LaO}(1-x)$ and orthorhombic $\text{LBO}(x)$ grown on cubic STO(001). b) RHEED oscillations and pattern of LABO (top) and LABO (bottom) growth. c) RSM of the nanocomposite film as function of x measured at the (113) reflection of STO. d) The a - and c -axis lattice constant of the nanocomposite films as function of x for both region (I) and (II). e) Cross-sectional high-resolution STEM image along (100) direction for the LAO/STO film. f) Cross-sectional TEM (upper panel) and HR-STEM (lower panel) images of the LABO ($x = 8\%$) nanocomposite film on STO(001).

the RSM for the LABO nanocomposite films shows a development of two reflections of the films varying with composition x . Assigning these two reflections: (I) a film region that is coherently constrained with the in-plane STO parameter, (II) a region that moves away from the in-plane STO. The nanocomposite film (LABO) with lower concentration of LBO ($x \leq 5\%$) shows a partial in-plane strain relaxation of region (I) seen from the spot coherent to the substrate; however, region (II) has a developing intensity with higher composition x . Upon x increasing above $x \geq 8\%$, the reflections separate into two regions: streak and a broad peak. While the streak represents the strain gradient of the 2D coherent film perfectly aligned with the in-plane STO, the out-of-plane c -lattice constant increases with x , while still aligned perfectly along the in-plane axis with the underlying STO substrate, also shown in Figure 5.6d. This is different from the normal LAO/STO, where the elastic deformation of a coherent LAO layer has a Poisson ratio of 0.24³⁵. This can be seen in the light of the tensile in-plane strain of LAO, which will be compensated by compressive out-of-plane strain, resulting in the LAO having a reduced thickness (≤ 20 unit-cells)²⁰⁰. However, in this work we observe that the in-plane and out-of-plane strains of the coherent layer (I) in the nanocomposite ($x \geq 8\%$) films are almost only tensile strained in-plane relative to bulk LAO. This means that the out-of-plane of the continuously developed coherent layer is oppositely constrained (c -axis lattice elongation) in the LABO nanocomposite films maintaining the in-plane matching with the underlying STO. Figure 5.6e illustrates a cross-sectional high-angle annular dark field (HAADF) STEM image of the undoped LAO(001) film grown on STO(001). As expected, we see a layer-by-layer epitaxial growth of the 26 nm-thick undoped LAO($x = 0$) (001) film layer on STO(001). In contrast, we found that the LABO film ($x = 8\%$) shows vertically aligned stripes (1.5 – 2 nm width) with visible contrast (atomic z -contrast) as shown in the HAADF-STEM images in Figure 5.6f, whereas $x < 8$ we did not see the vertically aligned stripes (see Article VIII). An intriguing observation is magnetism in the LABO/STO heterostructures. Figure 5.7a illustrates the magnetic hysteresis loops of the samples as a function of x , measured along the in-plane direction ($H^{\parallel}, (100)$) at 5 K. No ferromagnetic response was found in a bare TiO₂-terminated

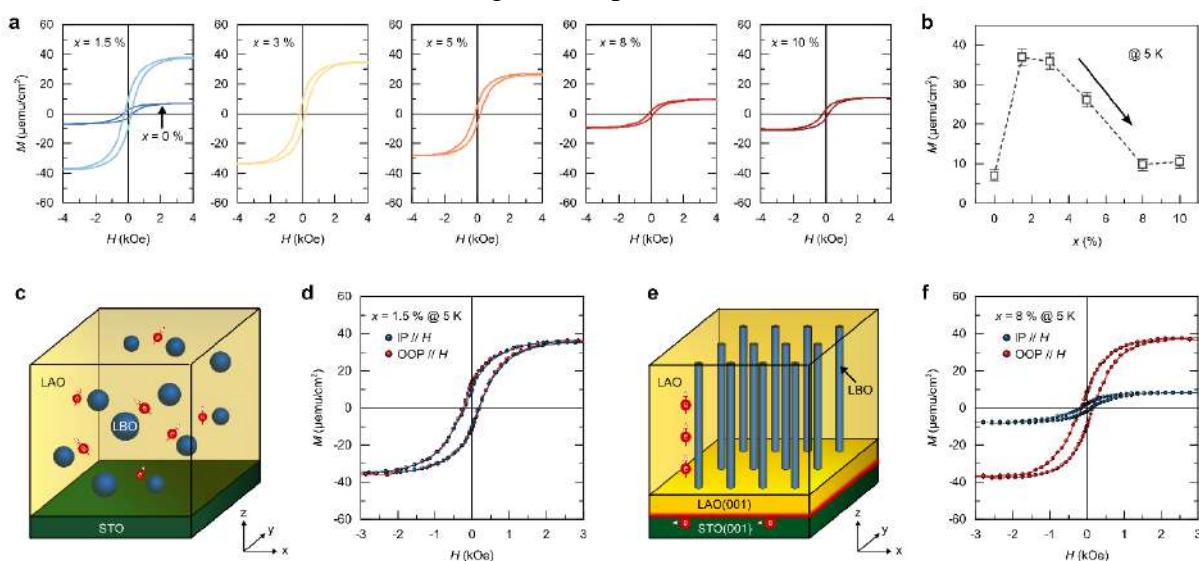


Figure 5.7. a) In-plane magnetic hysteresis loop of the LABO films as function of x ($= 0\%$, 1.5% , 3% , 5% , 8% , and 10%) measured at 5 K. b) variation in the in-plane saturation magnetization as a function of x . c,d) In-plane and out-of-plane magnetization of $x = 1.5\%$ measured at 5 K (d) displaying randomly distributed moments in the film (c). e,f) In-plane and out-of-plane magnetization of $x = 8\%$ measured at 5 K (f) displaying moments aligned with the LBO nanopillars (e).

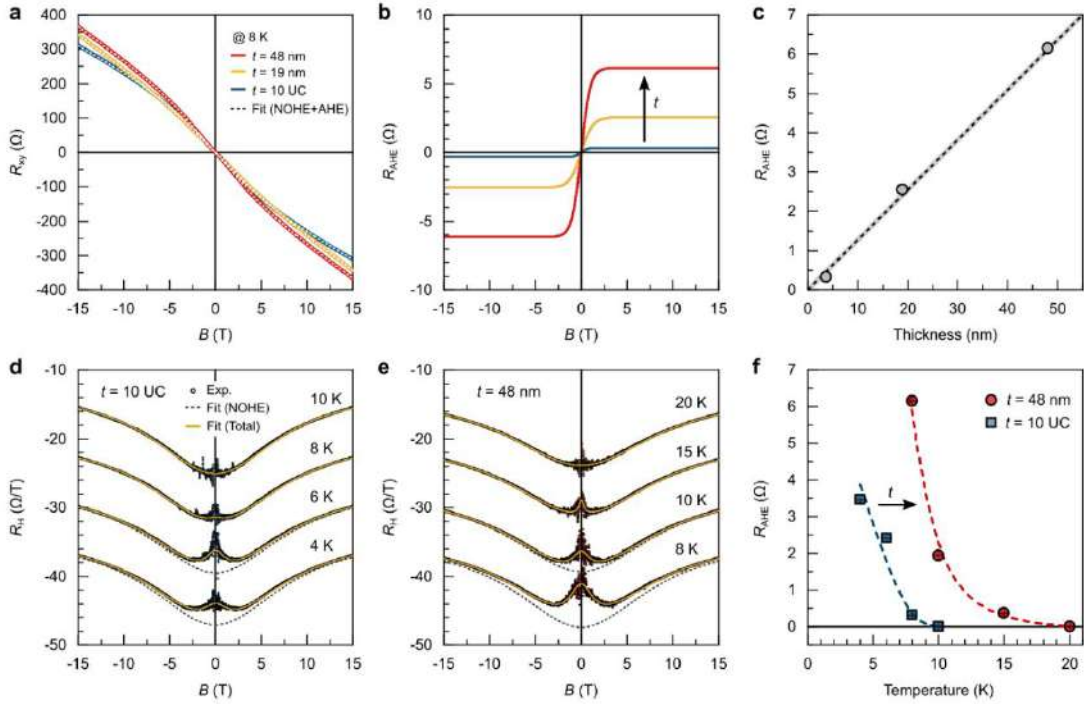


Figure 5.8. a) Hall resistance R_{xy} of LABO ($x = 10\%$) at 8 K as function of thickness ($t = 10$ unit-cells, 19 nm and 48 nm). R_{xy} is fitted by deconvoluting nonlinear ordinary Hall effect (NOHE) and non-hysteretic anomalous Hall effect (AHE). b) The deconvoluted AHE resistance (R_{AHE}) of the samples shown as a Langevin function. c) Thickness dependent R_{AHE} at 8 K. d,e) Temperature dependence of R_{AHE} of the 10 unit-cell and 48 nm samples. The experimental data is fitted to NOHE and AHE. f) Temperature dependence of R_{AHE} for the two samples in (d) and (e).

substrate, showing that magnetization is only achieved in the presence of the film. To compare the magnetization, Figure 5.7b shows the in-plane saturation magnetization as a function of x . The in-plane saturation magnetization of the samples ($x \geq 8\%$) decreases towards the value of the undoped LAO/STO sample (Figure 5.7b). We have further measured two nanocomposite samples ($x = 1.5\%$ and 8%) along both the in-plane ($H^{\parallel}(100)$) and out-of-plane ($H^{\perp}(001)$), with the results shown in Figure 5.7c-f. There is no variation in the magnetization of the nanocomposite sample when $x = 1.5\%$ due to randomly distributed magnetic moments in the film. In contrast, the out-of-plane magnetization was found to be $\sim 30 \mu\text{emu}/\text{cm}^2$ in the nanocomposite sample ($x = 8\%$) resulting in a 5 times stronger magnetization compared to the in-plane magnetization. Therefore, a magnetic anisotropic structure is generated as a result of the formation of the mixed 2D-3D LABO/STO heterostructures ($x \geq 8\%$). The origin of the preferential out-of-plane magnetism in the self-assembled 2D-3D LABO/STO heterostructure has been experimentally and theoretically proposed to be the presence of boron interstitials which are placed near the vertical LAO:LBO interfaces (see Article VIII).

Based on the out-of-plane magnetism results of the LABO/STO heterostructures, we have further performed magnetotransport measurements for the sample with high LBO content ($x = 10\%$). Figure 5.8a shows the 8 K Hall resistance (R_{xy}) of the LABO/STO heterostructures as a function of the thickness of LABO film layers ($t = 10$ unit-cells, 19 nm, 48 nm), measured by applying external magnetic fields up to $B = \pm 16$ T. The low-temperature R_{xy} data were fitted by using a two-band model due to the non-linearity of the hall resistance (Figure 5.8a) due to high- and low-mobility electrons. The derivative of

dR_H/dB shows a clear increase in the low-field non-linearity of R_H across the zero-field associated with the AHE^{102,108}. The result shows a clear increase of R_{AHE} with increasing thickness of magnetic LABO upper layer (see Figure 5.8c) and that the magnitude of the extracted AHE strongly depends on the temperature (Figure 5.8d-f). This indicates that, in the 2D-3D LABO/STO heterostructures, the observed magnetoelectric coupling effects stem from a magnetic proximity of the LABO film layer to the 2DEG at the LAO/STO interface. Therefore, the transport results affirm that the spontaneously formed 2D-3D LABO/STO heterostructure generates an emergent magnetoelectric coupling effect, which can be effectively tuned by the thickness of the nanocomposite overlayer.

In conclusion, we demonstrate magnetism and electromagnetic coupling in a self-assembled 2D-3D LABO/STO heterostructure, which can be evoked by the composition of two constituent oxide phases, LAO and LBO. Finding an appropriate composition of LBO is a key parameter for driving the spontaneous transition from 2D to 3D structure - in this work, the spontaneous structural transition happened at composition of $x \geq 8$ %. The formation of atomically defined horizontal 2D-LAO/STO and vertical 3D-LAO/LBO interfaces leads to the coexistence of a 2DEG and tunable magnetic ordering. Hence, the self-assembled 2D-3D LABO/STO heterostructure generates an emergent magnetoelectric coupling effects, resulting in the appearance of AHE with a film thickness dependence. This work paves the way for designing oxide nanocomposite heterostructures via a self-assembly approach with multifunctional coupled phenomena

CHAPTER 6

The electronic structure of STO-based oxides

This chapter deals with the relationship between band structure and the process parameters such as surface treatment, annealing, strain, or additional a buffer layer. The reviews in this chapter are based on the papers VI, VII, and IX found in the appendix of this thesis.

6.1 Creation and control of low dimensional states at SrTiO₃ surface

The octahedral crystal field in the cubic single crystal STO splits the Ti 3*d* orbitals to *t*_{2*g*} and *e*_g subbands, with degenerate *t*_{2*g*} states at the Γ point and the *e*_g states lying at higher binding energies. The degeneracy and the lower dimensionality of the electronic bands can be lifted by structural relaxation and reconstructions at the STO surface²⁰¹. Additionally, the band structure in bare STO can be modified by temperature change^{202–205} and surface termination^{134,206,207}. ARPES studies on a nominally TiO₂-terminated STO single crystal^{72,201,208,209} display the typical electronic structures of STO consisting of shallow *d*_{xz}/*d*_{yz} bands and deep *d*_{xy} subbands – a fingerprint of most STO-based systems (see also chapter 1.2). Interestingly, a single band was observed in the epitaxial-grown SrO layer on TiO₂-terminated STO²⁰⁶ and a recent study of SrO-capped STO systems exhibited the absence of electronic states near E_F ²¹⁰.

This subchapter describes the experimental results of sputtering and annealing effect on the surface region of TiO₂-terminated Nb doped STO investigated by ARPES. The STO were subjected to three different treatments as follows: 1) "as-received" substrate; 2) 5 minutes of Ar sputtering followed by annealing in ultra-high vacuum (UHV) at 700 °C for one hour; and 3) high-temperature annealing at 800 °C for 2 hours in UHV. We used ARPES to study the surface band structure and XPS to characterize the core levels of the sample at each stage.

Figure 6.1 shows the electronic structure of the STO surface measured by ARPES in the three stages (#1, #2, and #3) described above (Figures 6.1a-c). The ARPES data was obtained using circular polarized (C+) light that allows both in-plane *d*_{xy} and out-of-plane *d*_{xz}/*d*_{yz} orbitals at the STO surface to be probed. The electronic structures of STO in stages #1, #2, and #3 after 100 minutes of irradiation along the Γ -X crystal direction are shown in Figure 6.1a-c. The band characters of stages #1 to #3 are displayed by in-plane Fermi surface (FS) maps and *k*_z maps (Figure 6.1j-l). For stages, #1 and #3 (Figure 6.1 j,l), the in-plane FSs consist of one circular electron pocket and two intersecting ellipsoidal electron pockets centered at Γ , which are typical for the STO(001) surface. The *d*_{yz} and *d*_{xz} bands

for stages #1 and #3 show a quasi-3D characteristic, while the d_{xy} band shows a two-dimensional (2D) character (Figure 6.1j,l). Stage #2 only shows a single circular electron pocket centered around Γ with a 2D character, i.e., there is no dispersion in the k_z direction (Figure 6.1k).

Figure 6.2a,b shows XPS spectra of the STO sample in all three stages study the core levels of the sample of Sr $3d$, Ti $3p$, and Ti $2p$ with photon energies in the VUV (170eV; surface sensitive) and soft X-ray (750 eV; more bulk sensitive) ranges. The core levels of Ti are located at the peaks at $E_B \sim 38$ eV for the $3p$ (Figure 6.2a) and at $E_B \sim 459$ eV for the $2p$ (Figure 6.2b) for the Ti^{4+} ions, whereas the shoulder peaks at $E_B \sim 35$ eV and at $E_B \sim 457$ eV belong to the Ti^{3+} ions. The Ti^{3+} seems to increase in stage #3, which most likely happens due to the vacuum annealing at high temperatures. However, the Sr $3d$ core levels of the surface state show a significant intensity decrease after sputtering and annealing (#2) (see Figure 6.2c). The data from the soft X-rays (Figure 6.2b) suggests that decrease in the spectral weight of Sr is a surface effect. The VUV-XPS data shows that the spectral weight of Sr at the surface is significantly increased (Figure 6.2a). Also, the data shows that the multi-peak nature of the Sr $3d$ core in STO splits into a multippeak structure in stage #3,

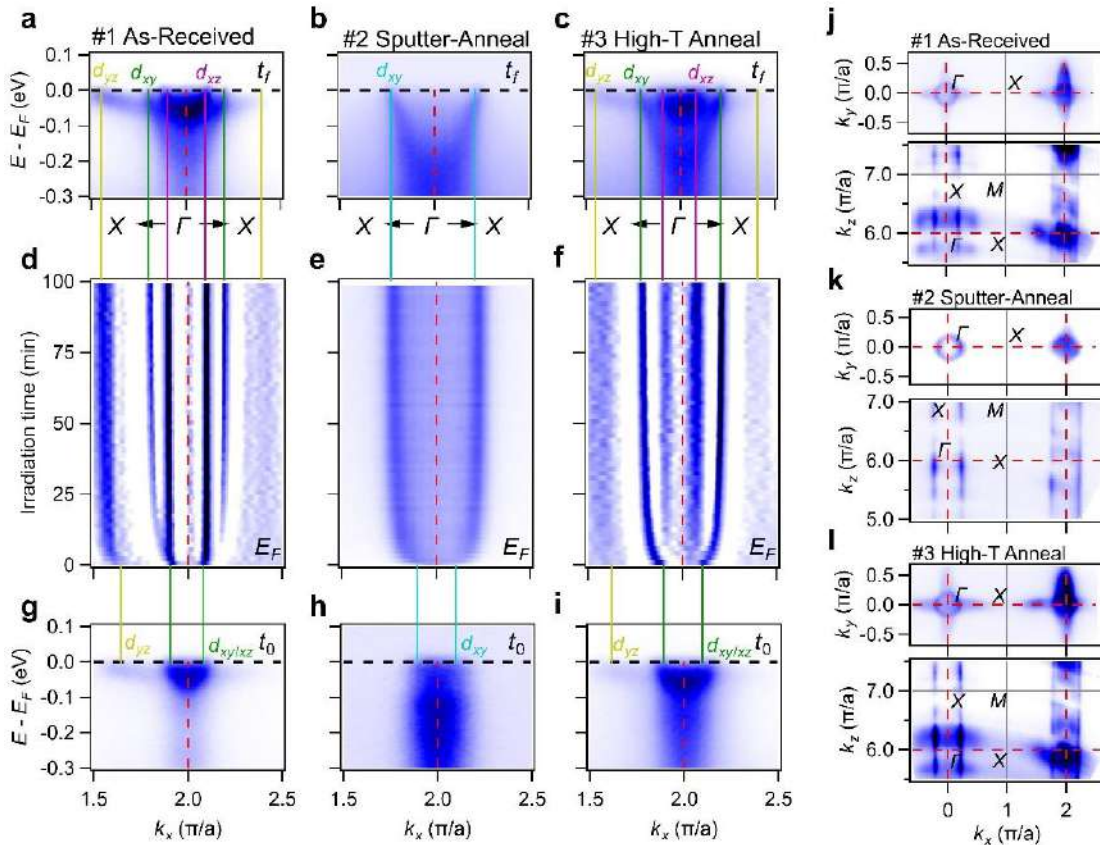


Figure 6.1. a-c) ARPES intensity cuts of as-received (stage #1), sputter-annealed (stage #2), and high temperature annealed (stage #3) STO wafers, respectively, after saturating the carrier density by irradiation (t_f). d-f) k -resolved ARPES maps at E_F of stages #1 to #3, respectively, as a function of VUV irradiation time. e) Intensity map, and (d,f) are horizontal 2nd derivative maps. g-i) ARPES intensity cuts of stages #1 to #3 measured at a fresh spot and acquired within 2 minutes of VUV-irradiation (t_0), respectively. Green, pink, cyan and yellow lines mark the k_F of d_{xy} , d_{xz} , d_{xy} in #2, and d_{yz} bands, respectively. j-l) Fermi surface maps of the ΓXY plane (upper) by in-plane mapping and the ΓXZ plane (lower) by $h\nu$ -dependent mapping of stage #1 to #3, respectively. Grey solid lines mark the BZ boundary and red dashed lines show the high-symmetry lines. Figure (a-i) and the upper panel of (j-l) are measured at 85 eV. All figures are measured with circular polarized (C+) light.

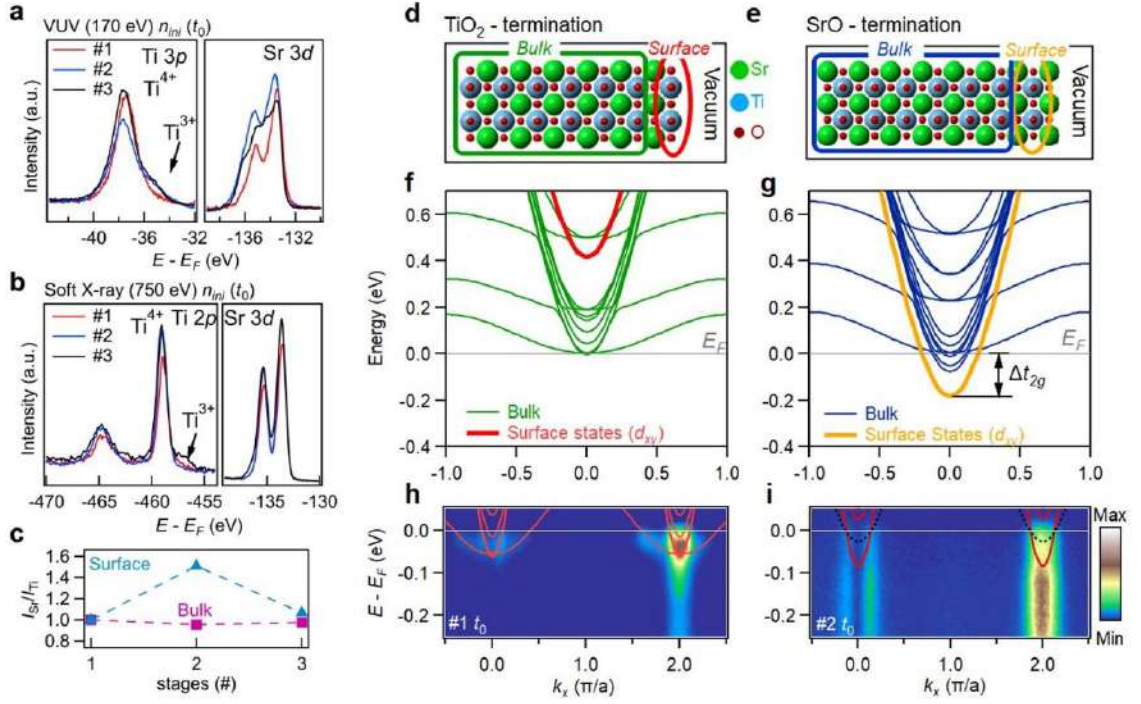


Figure 6.2. a,b) Core-level of Ti $3p$ and Sr $3d$ orbitals measured at $h\nu = 170$ eV at the initial carrier density of the three stages (t_0). b) Core-level of Ti $2p$ and Sr $3d$ orbitals measured at 750 eV at the initial carrier densities of the three stages (t_0). c) Calculated spectral weight ratio of Sr/Ti extracted from (a) and (b), and normalized to the ratio of the as-received STO wafer (#1). d-e) Relaxed $2 \times 2 \times 7$ STO slabs of TiO₂-termination and SrO-termination, respectively. Red/orange ellipses and dark green/blue squares mark the superficial TiO₂ layer and the bulk of two models, respectively. Green, blue, and red spheres represent the Sr, Ti, and O atoms, respectively. f,g)- Calculated electronic band structures of TiO₂- and SrO- terminated STO models as presented in (a) and (b), respectively. The red and orange curve in (f) and (g) highlights the d_{xy} band from the first TiO₂ layer. h,i) ARPES intensity cuts of as-received (#1) and sputter-annealed (#2) STO wafer at t_0 , plotted with calculated band structures in (f) and (g), respectively. The dashed black curves in (f) show the fitted d_{xy} bands.

indicating that there is a chemically distinct Sr species after the surface rearrangement. Comparing the spectral weight of the XPS data provides a quantitative analysis of the changes between the different stages. Figure 6.2c show the normalized value of the different stages, i.e., comparison of surface and bulk. The ratio I_{Sr}/I_{Ti} of the bulk-like region (soft X-ray extracted) remains nearly unchanged (see pink dash line in Figure 6.2), while the surface region (VUV-extracted) increases by about 50% from stage #1 to stage #2 and decreases again to the starting value in stage #3 (blue dashed line in Figure 6.2). Thus indicating that annealing and sputtering result in an enrichment of Sr on the surface of the single STO terminated TiO₂ crystal.

To get an understanding of the band reconstruction, we used DFT to calculate the TiO₂- and SrO- terminated STO to understand the two possible consequences of the surface termination (Figure 6.2d,e). We define Δt_{2g} as the energy difference (band splitting) between the lowest d_{xy} and d_{xz}/d_{yz} states from the first TiO₂ layer. This allows us to compare the ARPES data with the slab calculations. The calculations show that the value of Δt_{2g} is negligible for the TiO₂-terminated slab, see Figure 6.2f. In contrast, the SrO-terminated slab shows that the d_{xy} -band derived from the TiO₂ layer below the surface terminated SrO shifts ~ 150 meV downwards, thus generating a tetragonal symmetry splitting of the t_{2g} bands, see Figure 6.2g. This split is much larger than the fitted data measured in figure 6.2i for stage #2, where the dashed band (black) represents the fitted data and the solid lines

(red) are the calculated bands. A possible explanation is the large effective mass of the observed band at t_0 caused by strong EPI, which we did not consider in these calculations. When E_F is set according to the experimental value of k_F (Figure 6.2h,i), only the surface d_{xy} band crosses E_F for stage #2, while the remaining bands are unoccupied, thus showing only a single-band state in stage #2 in agreement with the ARPES data in Figure 6.1b. This shows that the surface termination of STO has a clear effect on the surface electronic reconstruction. V_O may still affect the system, causing a transfer from the 2D to 3D electronic state, as seen in other systems²¹¹ and as also indicated in stage #3 showing a quasi-3D state after heavy annealing at 800 °C for 2 hours. Annealing the sample typically induced V_O , however, it was reported that the SrO-terminated surface completely prevents the formation of V_O at the surface²¹². Nonetheless, our ARPES and DFT data validate that the Sr-enriched STO(001) surface is characterized by the intrinsic splitting of the t_{2g} states and the surface state, causing a pure 2D electronic structure.

In summary, employing systematic XPS measurements, we show that combining Ar sputtering and UHV annealing modifies the STO surface composition, transforming nominally TiO_2 -terminated to SrO-enriched surface. Utilizing ARPES with first principle DFT calculations shows that a Sr-enrichment on the surface of STO (001) by sputtering and annealing results in a surface where only the d_{xy} state persists, yielding a pure 2D electronic state.

6.2 The electronic structure of a-LAO/LMO/STO

For STO-based 2DEGs, the typical carrier mobility is around $1000 \text{ cm}^2 \text{ V}^{-1} \text{ s}^{-1}$ at low temperatures^{213,214}, where the experiment in this section has been carried out at 12 K. Recent studies show that carrier mobility can be significantly enhanced by deliberate surface or interface engineering^{180,213,215–219} by introducing buffer layers, controlled surface preparation, alternative top- films (e.g., $\gamma\text{-Al}_2\text{O}_3/\text{STO}$), and Mn doping the LAO film. For example, by insertion of a single unit cell of epitaxial LMO at the interface between amorphous-LaAlO₃ (a-LAO) and STO substrate (a-LAO/LMO/STO)²¹⁷, the mobility exceeds $70,000 \text{ cm}^2 \text{ V}^{-1} \text{ s}^{-1}$ at 2 K. The electrons of the d_{xy} orbitals, contributing to the most carrier concentration, are strongly confined near the surface/interface of STO, forming quasi-2D subbands (Figure 6.3a), known as the light band with low effective mass, while d_{xz}/d_{yz} orbitals construct heavy bands with large effective mass while their wave functions extend deep into the bulk STO, resulting in quasi-3D character²⁰¹. It is believed that it is due to Mn³⁺ at the buffer layer which acts as an electron sink in the perovskite structure, by decreasing the carrier density of 2DEG on the STO side through interfacial charge transfer²¹⁷. To understand the electronic band structure of this system, we have used SX-ARPES to identify both the heterostructure without the buffer layer and the LMO-buffered a-LAO/STO systems. Soft X-rays are suitable for systems where the interfacial 2DEG locates at the interface underneath the capping layer, normally for capping layers which are thicker than 1.6 nm. Here, the photoelectrons have an escape depth sufficiently larger than a few Å to a few nm as described by the universal curve (see Figure 2.9), which is sufficiently large to probe buried interfaces^{193,220–224}.

We first identified the FS maps and band dispersions for *a*-LAO/STO heterointerfaces with and without the LMO buffer layer. Figure 6.4c,e shows a circular electron pocket located

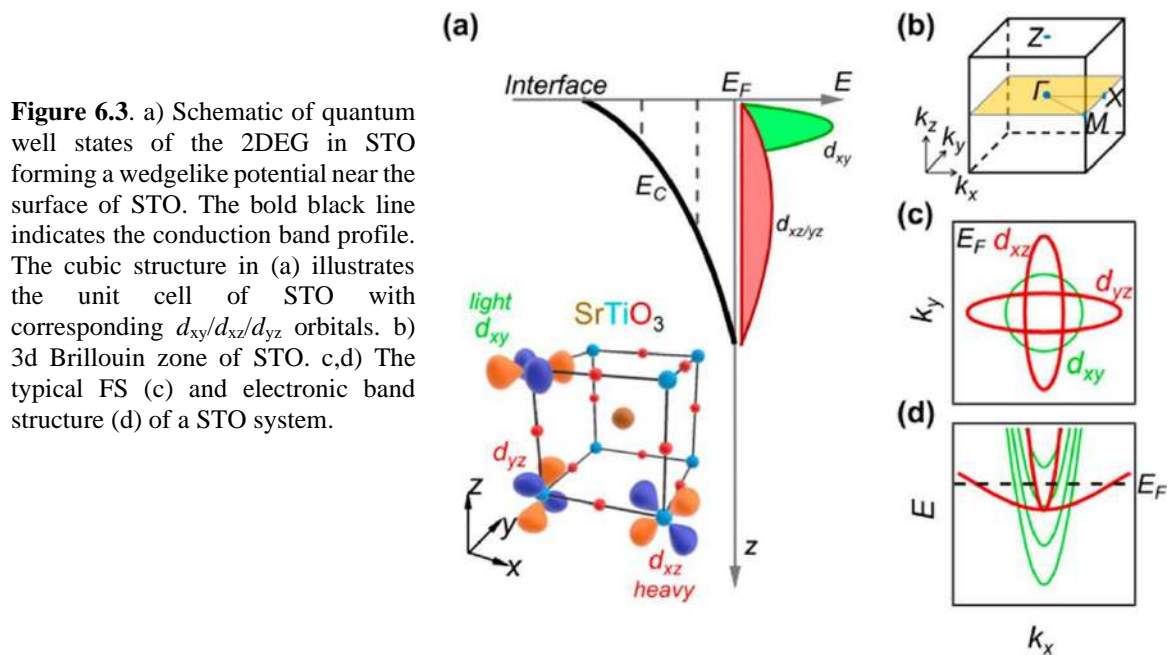


Figure 6.3. a) Schematic of quantum well states of the 2DEG in STO forming a wedgelike potential near the surface of STO. The bold black line indicates the conduction band profile. The cubic structure in (a) illustrates the unit cell of STO with corresponding $d_{xy}/d_{xz}/d_{yz}$ orbitals. b) 3d Brillouin zone of STO. c,d) The typical FS (c) and electronic band structure (d) of a STO system.

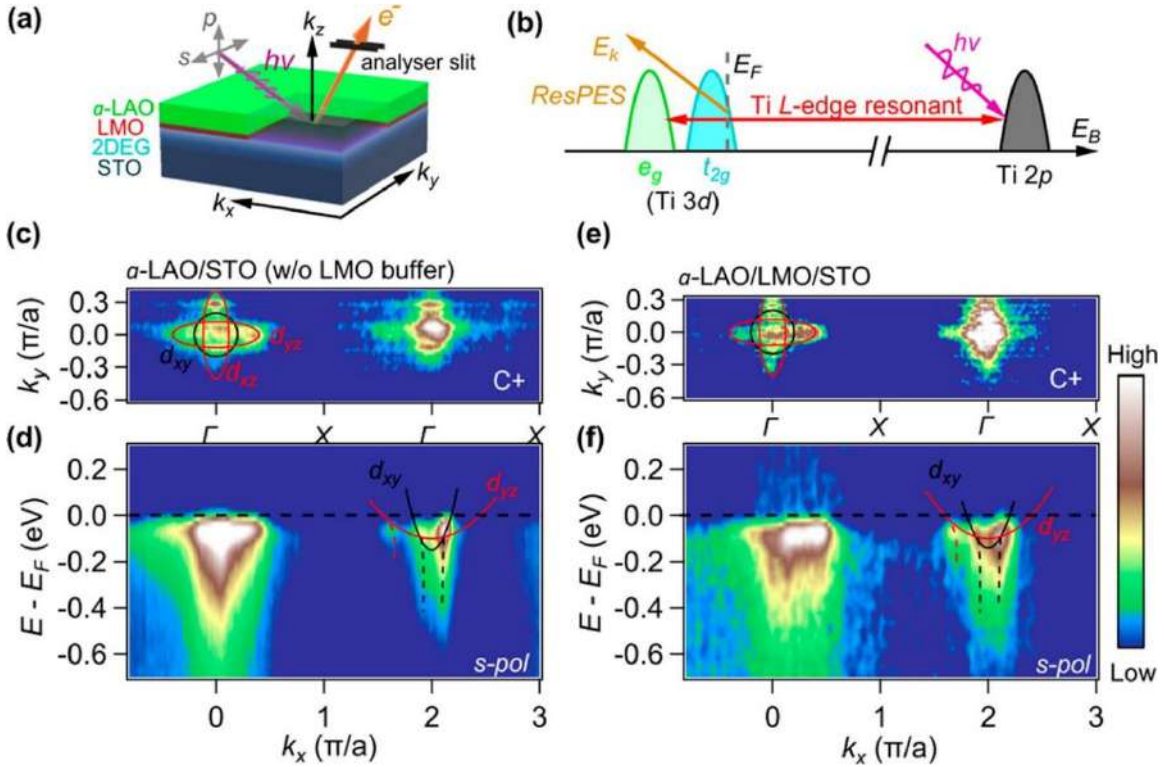


Figure 6.4. a) Schematic of the modulated delta doped a-LAO/LMO/STO system with the experimental geometry for the ARPES measurement illustrated. b) illustration of the resonant photoemission process in STO 2DEG systems. c,e) Fermi surface map with C+ polarization of a-LAO/STO (c) and a-LAO/LMO/STO ($t_{LMO}=1$ uc) at the Fermi surface in $k_z = 0$ plane. The black circle and red eclipse are a guide for the eye for the Fermi surface of d_{xy} and d_{xz}/d_{yz} orbitals, respectively.

at the center of the Brillouin zone (BZ) and two other intersecting elliptical electron pockets aligned along the k_x and k_y directions (the ΓX direction in the BZ (Figure 6.3b)). A typical FS pattern of the STO-based 2DEG systems is measured in Figure 6.3c²⁰¹.

From Figure 6.4d,f we can identify the light d_{xy} bands and heavy d_{yz} bands near the second Γ -point for both the a-LAO/STO and a-LAO/LMO/STO samples, marked as parabola to guide the eye. The k_F used to fit the parabolas is determined by the intensity peaks of the momentum distribution curve (MDC) at E_F . In an alternative approach for systems with narrow bands such as this, where the energy resolution is low, k_F is extracted using the extremes of MDC gradient (dI/dk_x), which gives a higher accuracy^{225,226}. Using this method, it is evident that there is a small decrease in the k_F and carrier density of $k_F^{xy/yz}$ (\AA^{-1}) = 0.14/0.38 and 0.16/0.35 for a-LAO/STO and a-LAO/LMO STO, respectively, although these changes are relatively small compared to conventional crystalline LAO/STO with $k_F^{xy/yz}$ (\AA^{-1}) of 0.15/0.33. Nonetheless, these results are in good agreement with conventional STO-based systems, where the Ti t_{2g} bands are reconstructed at the interface forming deep d_{xy} subbands and shallow d_{xz}/d_{yz} bands, as shown in the illustration in Figure 6.3d. This behavior of deep d_{xy} subbands and shallow d_{xz}/d_{yz} bands comes from the confined quantum well states with the bent band profiles near the surface region (see Figure 6.3a), which is typically estimated by the binding energies of Ti 2p orbitals.

STO-based systems have shown a sensitivity toward exposure to X-ray beam irradiation^{201,208,223}. For that reason, we have performed k-resolved intensity maps as a

function of beam irradiation time at E_F for both samples to examine this effect. The sample with the LMO buffer layer was only slightly affected by the irradiation time. This suggests that: 1) the introduction of the LMO spacer suppresses the formation of V_O in the buffered sample; and 2) although the beam irradiation induces in-gap states in buffered samples, the photogenerated extra carriers are most likely transferred to the manganite buffer layer instead of 2DEG conduction layer.

Finally, we found that the EPI is strongly suppressed in the system with the buffered LMO film. The EPI often results in the polaronic nature of the interfacial charge carriers that increase their effective mass²¹⁸. The tail below the high-intensity (brown) region is associated with the EPI (the second BZ in Figure 6.4d,f). The intense spot near E_F (brown spot at $k_x = 2\pi/a$ in Figure 6.3d,f) is the quasiparticle (QP) (i.e., electron interactions in a many-body-system), and the intensity at higher binding energies below the QP reflect the EPI strength. Since the EPI suppresses the carrier mobility due to scattering, this is an important feature. Performing energy distribution curve (see Article VI) shows that the relative distance between the QP to the peaks (humps) at lower binding energies increases from 33% in a-LAO/STO to 46% in a-LAO/LMO/STO. As the EPI strength is related to the QP residual weight²²¹, the increase in the residual weight suggests a decrease in the EPI strength.

In summary, SX-ARPES, were used to analyze the electronic structure of the a-LAO/LMO/STO. We found that a nontrivial feature of weakened EPI strength was associated with a decrease in the formation of V_O . The combination of (1) an unexpected irradiation-robust band structure, and (2) a significantly reduced EPI strength on the STO side, which is absent in the nonbuffered interface^{193,220} could account for the extreme mobility of the buffered oxide heterostructures. These combined effects of a reduction of the carrier density, the suppression of defect concentration of V_O , as well as the decrease in the EPI strength on the STO side, could account for the high mobility of the buffered oxide heterostructures.

6.3 The electronic structure of ion diffusion in TiO₂/SrTiO₃

In this work, we studied the electronic structure of anatase-TiO₂ deposited on single crystal STO doped Nb (a-TO/STO:Nb) heterostructure. Utilizing ARPES, we observed a band modulation in the a-TO/STO induced by vacuum annealing. Through high-temperature annealing process, Sr ions from the STO underwent a thermal diffusion, migrating to the upper a-TiO₂ film, thus resulting in the TiO₂ resembling the STO band structure that consists of deep d_{xy} and shallow d_{xz}/d_{yz} bands. To study this, we grew 5 nm Anatase TiO₂ films on a 0.5 Nb doped STO (001) substrate. The samples were studied in three stages: 1) as-grown sample; 2) vacuum annealing at 700 °C for 1 hour to remove contaminations from the sample after exposure to air; and 3) vacuum annealing at 800 °C for 1 hour.

The electronic structure and FS of the a-TO/STO sample are shown in Figure 6.5a-h. We note that the 2nd BZ (at $k_x = 2\pi/a$) seen in Figure 6.5a-c,e,g is much stronger than the first BZ but take advantage of both as they show light different features e.g., the circular d_{xy} electron pocket is clearer in #3 in the first BZ compared to the second zone. Nonetheless, the BZ zones are inherently not different around the Γ -point due to the periodicity of the Bloch waves in the crystal. The electronic structure of the as-grown (#1, see Figure 6.5a) and low-temperature annealed (#2, see Figure 6.5b) sample show only one occupied band (d_{xy}). The difference in the electronic structure between stages #1 and #2 is the increased data quality of stage #2, owing to the annealing process cleaning the surface of the film. Annealing the sample for an additional 1 hour at 800 °C (#3, see Figure 6.5c), showed that the band bottom of d_{xy} extended to higher binding energies at ~ 0.3 eV, and an additional two shallow d_{xz}/d_{yz} bands emerged at the E_F . The electronic structure in stage #3 (Figure 6.5c) remarkably resembles the electronic structure of pure STO.

Considering the FS of stage #2 (and #1), the in-plane image shows only one circular electron pocket centered at the Γ -point shown in Figure 6.5d as well as dispersion along k_z (Figure 6.5e), consistent with the FS of TiO₂ films in former studies^{201,227} (Figure 6.5h). In contrast, the FS in stage #3 after annealing reveals the formation of only one circular and two intersecting elliptical electron pockets centered at the Γ -point (Figure 6.5f), which belongs to the deep d_{xy} and shallow d_{xz}/d_{yz} bands, see Figure 6.5c. The circular band additionally shows a linear dispersion along k_z , while the shallow elliptical bands show 3D features in the k_z direction centered at the Γ -points (Figure 6.5e,g). These FS features in stage #3 and band dispersion along Γ -X are very similar to the electronic band structure of STO surface^{201,204}. This finding implies that annealing the a-TO/STO at sufficiently high temperatures can cause a phase transition from a-TiO₂ band structure to a similar band structure of STO. The core level spectra of Ti 2*p* and Sr 3*d* from XPS measurements for the three samples' stages are displayed in Figure 6.6a,b. The core level intensity curves are normalized to the background for better comparison. Although we see a small Sr 3*d* signal marked by the blue arrow in Figure 6.6a in stages #1 (red line) and #2 (blue line), they are probably due to the Sr migration during the fabrication process. The intensity of Ti 2*p* orbitals in stage #2 increases rapidly after low-temperature annealing (Figure 6.6a), likely to be due to surface cleaning improving the ARPES spectra signal, and also enhancing the intensity of the Ti³⁺ shoulder peak ($E_B \sim -454$ eV) associated with V_O (Figure 6.6a). After

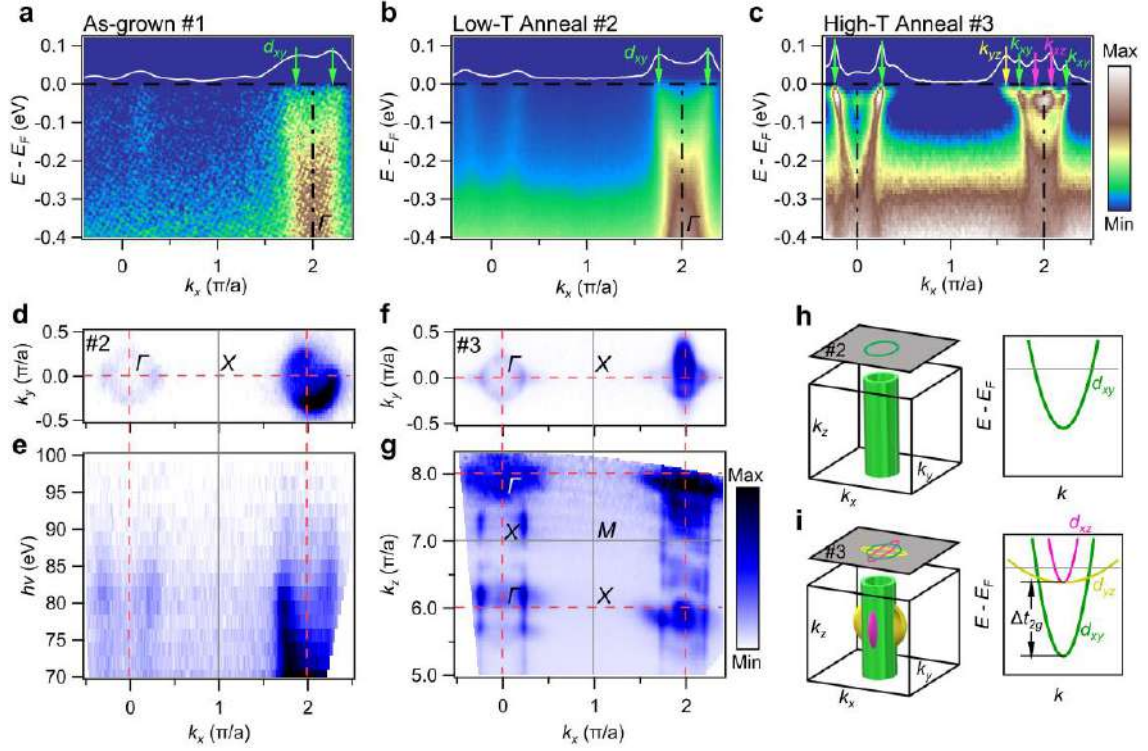
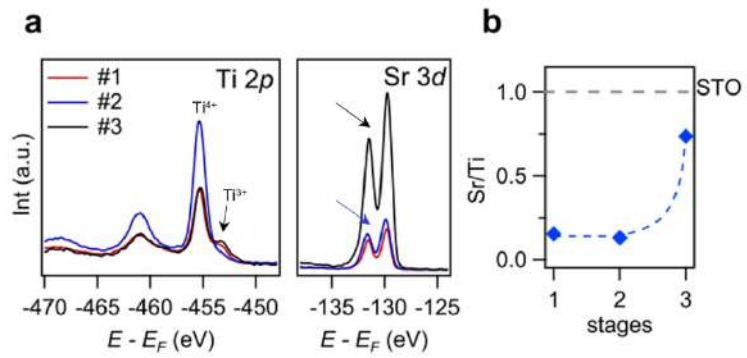


Figure 6.5. a-c ARPES intensity cuts of as-received (stage #1), low-temperature annealing (stage #2), high temperature annealed (stage #3) of the a-TiO₂/STO sample, respectively. d-g Fermi surface maps of the Γ XY plane (upper) by in-plane mapping and the Γ XZ plane (lower) by $h\nu$ -dependent mapping of stage #2 (d, e) and #3 (f, g). h,i) The electron pocket in the BZ of stage #1 and #2 (h) and stage #3 (i).

high-temperature annealing, the intensity of Ti $2p$ orbitals in stage #2 decreases, while the Sr $3d$ orbital intensity increases significantly (Figure 6.6a). This suggests that a large amount of Sr diffuses into the TiO₂ layer, resulting in an elemental ratio similar to that of the STO substrate. To demonstrate this more clearly, we show the spectral weight ratio of Sr $3d$ and Ti $2p$ in all three stages (Figure 6.6b), where $I_{\text{Sr}}/I_{\text{Ti}} = 1$ refers to an ordinary STO substrate. The as-grown non-annealed and low-temperature annealed stages have an $I_{\text{Sr}}/I_{\text{Ti}}$ -ratio of 0.14, thus showing that there is only a limited amount of Sr in the a-TiO₂ film due to the reasons mentioned above. In contrast, high-temperature annealing increased the ratio to ~ 0.7 , i.e., the TiO₂ film approaches an Sr-poor STO film on the surface, presumably caused by Sr diffusion from the substrate to the thin film during the high-temperature annealing.

In conclusion, the as-grown a-TiO₂/STO has a deep d_{xy} band. The low-temperature annealed a-TiO₂/STO has a single circular d_{xy} electron pocket and 3D features in the k_z direction. High-temperature annealing causes the sample surface to resemble the STO surface band structure, while the core spectra of Ti $2p$ and Sr $3d$ show that the $I_{\text{Sr}}/I_{\text{Ti}}$ ratio approaches that of a perfect STO crystal.

Figure 6.6. a) Core-level of Ti $2p$ and Sr $3d$ orbitals normalized to the background for all three stages measured at 750 eV. b) I_{Sr}/I_{Ti} ratio of the spectral weight with grey dashed line representing the Sr/Ti ratio of a perfect STO crystal.



6.4 Electronic response to strain in SrTiO₃ (001)

A wide range of external stimuli are widely used to affect the properties of STO-based structures⁸⁷. The relatively large splitting between the light d_{xy} and heavy d_{xz}/d_{yz} bands^{201,204} suggest that deviations from the cubic (or slightly tetragonal when at low temperatures) structure might occur at the surface region. It has already been shown that an La-doped STO film under uniaxial stress³⁷ can enhance electron mobility by a remarkable 300 %, indicating that strain could be an effective way to tune the properties.

We prepared two samples of 2 wt. % Nb-doped STO(001), one that had not been annealed (called N-A) and one that had been annealed (called A-STO) at 500 °C for 1 hour in oxygen-rich conditions to avoid formation of V_O. To investigate the effect of strain, we used a homemade bending device that works by a screw pushing a cylindrical part of the bender that subsequently induces strain on the substrate, as shown schematically in Figure 6.7(a-b). The cylinder displacement and thus the strain is controlled by turning a screw with a conical tip, which serves as a wedge³⁷. To calibrate the strain profile of the STO slab, we measured the height profile change as a function strain using Cyberscan Vantage optical profilometer on a 500 μm thick 5x10 mm² STO slab. The resulting data, as shown in Figure 6.7c, fits to parabolas of the form $y = ax^2 + bx + c$, where $C = 2a$ is the maximum curvature i.e., the maximum achievable strain. The profilometry data shows that the STO wafer bends around its shorter symmetry axes. We estimated the strain by multiplying the curvature (C) by half the thickness of the wafer $S = C \cdot t/2$ ³⁷. The maximum strain as a function of the maximum height is displayed in Figure 6.7d, for all the strained orientations. To investigate the strain with respect to the orientation, we performed finite element simulations utilizing COMSOL Multiphysics (Figure 6.7e-g). This showed that the bent STO substrate in the in-plane long direction between the clamped regions is expanded in the x-direction (Figure 6.7e). To compensate for the expansion in the x-direction, the out-of-plane axis (z-direction in the figure) experiences compressive strain (to ensure constant volume). In contrast, the short side of the sample, which is the in-plane axis (y in the figure), is only negligibly affected compared to the two other orientations. The same bender was specially designed and modified to serve as a sample holder for the ARPES measurements (Figure 6.7b). The ARPES spectrum which is collected at 20 K showed no states at the Fermi level during the initial exposure, but new states developed throughout the measurements as a function of time, developing parabolic dispersion when the intensity was saturated. The ARPES data obtained with $h\nu = 85$ eV C+ polarized light is shown in Figure 6.8, and were all obtained at the saturated state. The panels (a-f) display the data for the non-annealed sample, while the panels (g-l) show the band structure for the annealed sample. Panels (b, e, h, k) and (c, f, I, l) display the dispersion map without and with an applied force, respectively. The maximum strain before the sample broke was roughly estimated to 0.1%. Since the strain originated from the displacement, and the displacement was tuned by turning the screw, we cannot know the exact displacement without measuring it with the profilometer, thus the estimate comes from how much we turned the screw. The photon energy and polarization were chosen carefully such that it is possible to measure the band structure corresponding to the Γ -point, while the C+ polarization allows us to capture contribution from all the manifold t_{2g} orbitals²⁰¹. We note that the intensity varies across BZ, arising from matrix element effects, i.e., modulations of the spectral intensity

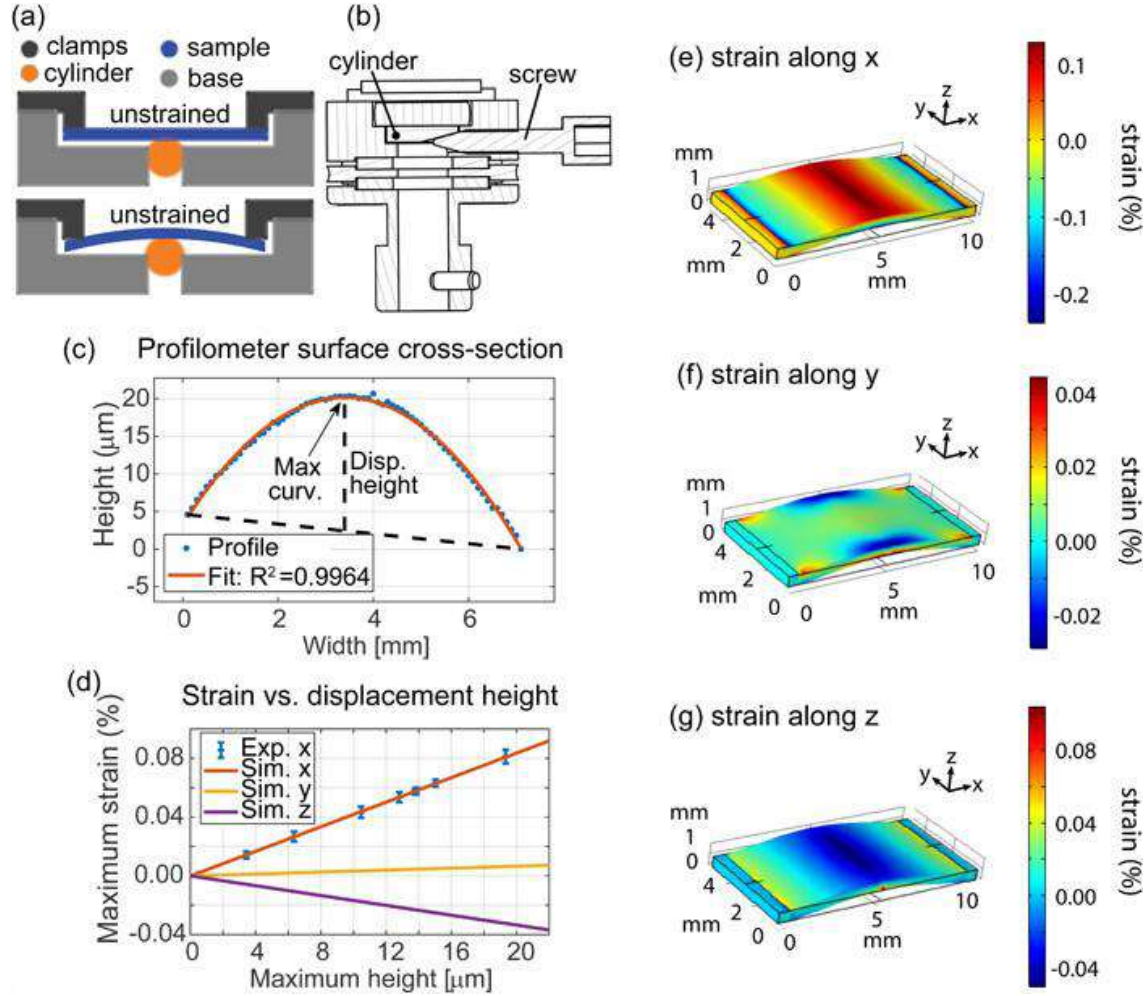


Figure 6.7. a) Schematic of the strain device. A cendred ball pushed upwards in the middle of the sample clamped at the sides forcing the sample to bend. b) Cross section drawing of the strain device showing that by turning a screw forces the ball upwards. c) Profilometer measurements of a strained slap (blue dots) to a parabola $y = ax^2 + bx + c$ (red solid line) with the maximum height being $C = 2a$. d) Displacement converted to strain for x, y, and z orientations following $S = C * t/2$. e-g) x, y, and z strain obtained utilizing finite element method on a 500 μm STO slap with fixed edges. The center of the slap has a displacement of 30 μm .

caused by the dependence of the ARPES data on photon energy and experimental geometry^{201,204,208}. In particular, the bottom of the d_{yz} band and the outer d_{xy} band are easily seen around the first Γ -point at the first BZ, while the bottom of the d_{xy}/d_{xz} bands are very clear around the second Γ -point²⁰¹. Thus, the measurements were performed around both the first and second Γ -points. The respective band dispersion maps in Figure 6.8 were obtained along Γ -X at $k_y = 0$, represented by the horizontal line in the FS maps in Figure 6.8a,d,g,j. The $d_{xy}/d_{xz}/d_{yz}$ bands remain degenerate for the non-annealed sample, resembling the bulk conducting the band. However, for the annealed sample the d_{xy} bands shift downwards ~ 180 eV to lower binding energies. The band structure of the non-annealed and annealed samples indicates that the adsorbents passivate the surface and prevent the formation of the 2DEG, whereas it can be fully developed at a clean surface. Careful analysis of the Fermi wave vector k_F and of the splitting value between d_{xy} and d_{yz} bands can only confirm that no change in the conduction band is observed within the experimental resolution (around 10 meV) for either the non-annealed or the annealed

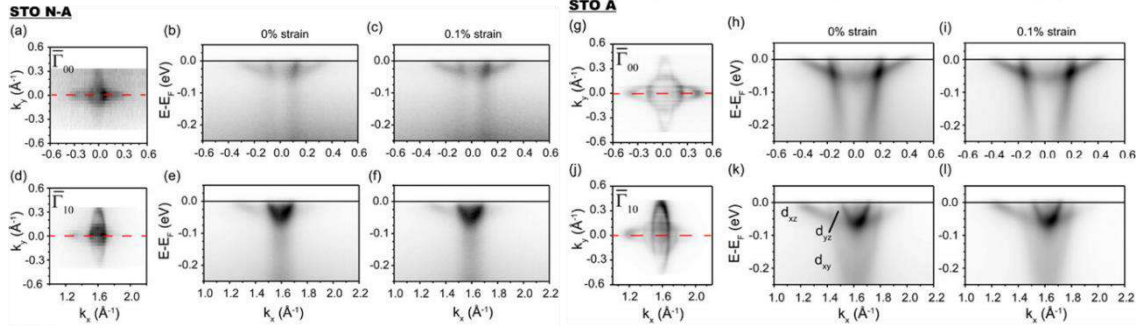


Figure 6.8. APRES data of nonannealed STO (001) (STO N-A) (a-f) and annealed STO (001) (STO A) (g-l), collected around the first and second Γ -point along the Γ -X direction. a,d,g,j) The FS of N-A sample (a,d), and A sample (g,j). The corresponding conducting bands are collected along the red line in the FS map for both no strained, N-A sample (b) and (e), and A sample (h) and (k). The same maps for strained N-A (c) and (f) and A samples (i) and (l).

samples upon bending. This finding also suggests that a strain of 0.1 % is too small to clearly distinguish the conducting band of STO. That said, from the valence band spectra, we observed a shift in the spectral weight of the in-gap state redistributing from -5 to -7 eV at only 0.1% strain for the annealed sample, while the non-annealed did not show such a change. This may arise from the fact that the in-gap states have earlier been associated with point defects in the crystal^{228–231} which may give rise to localized electronic states or induce the formation of small polarons, quasiparticles arising due to strong, short-range EPI, which show a typical binding energy of 1 eV^{232–235}. The fact that we do not observe a change in the d_{xy} band with strain in the ARPES data is also confirmed with our DFT calculations (see Article VII) where we calculated a sample with 0.2% along the x-direction and -0.1% along the z-direction, which shows a slightly increased Δt_{2g} of 7 meV that may not be possible to detect within the experimental resolution, and therefore DFT shows shift in the d_{xy} that we cannot detect with the experimental setup.

In conclusion, by combining the experimental external strainer in combination with ARPES supported by DFT calculations, we have examined the consequences of applied strain on the electronic structure of the STO(001) surface on both the as-received non-annealed and annealed STO surfaces. We were able to apply 0.1 % strain before the sample cracked; however, this level of in-plane tensile strain shows no influence on the electronic structure of the low-dimensional states, but is enough to sensibly alter the in-gap states. We utilized DFT to compare the splitting energy showing that our ARPES measurements are consistent with DFT calculations, however, to see a large change in the band structure, it requires heteroepitaxial growth to apply significant strain in the order of 2-3 %.

CHAPTER 7

Conclusions & outlook

The conducting interface between the insulating oxides LaAlO₃ (LAO) and SrTiO₃ (STO) displays numerous physical phenomena that can be tuned by fabrication parameters, post-treatment, and external stimuli. Here, I report some of the main results which show how the interfacial magnetism and conductivity in SrTiO₃-based heterostructures are influenced by fabrication methods, strain, and oxygen vacancy doping.

Oxide-based freestanding membranes have the potential to become the preferred candidates for next-generation oxide materials coupling the high selectivity to the high functionality of these materials. Here, we provide a new way to assemble both similar and dissimilar freestanding oxide membranes via artificial stacking and twisting and demonstrate that these stacks are indeed heterostructures with atomic bonds formed at the interfaces. Additionally, I have shown that LAO/STO membranes formed by spalling exhibit properties which are comparable to their counterpart LAO/STO thin film, i.e., the existence of a superconducting phase persists in these membranes.

We further demonstrated that the magnetic properties of engineered STO thin films can be effectively tuned by PLD film growth parameters (interdependent parameters of laser fluence and P_{O₂}) by controlling the concentration of cation vacancies, anion vacancies, and their complex defects. We have also demonstrated a self-assembly of combined 2D and 3D nanocomposite heterostructure, which can be evoked by the composition of two constituent oxide phases. To obtain this structural transition, it was essential to control the ratio between two distinct crystal components, LAO and LBO. The formation of atomically defined horizontal 2D-LAO/STO and vertical 3D-LAO/LBO interfaces in this system leads to the coexistence of a 2DEG and a tunable magnetic ordering.

Understanding the electronic band structure of STO-based heterostructure is crucial for understanding the transport properties of the material. We have used ARPES to understand the electron mobility enhancement on the a-LAO/LMO/STO with a single unit-cell of LMO between a-LAO/STO. The ARPES results reveal a nontrivial feature of weakened EPI strength concomitant with decreased formation of oxygen vacancies. The combination of these effects could explain the mobility enhancement. By using a custom-made device to bend and, consequently, generate a strain we have tested STO-based materials with ARPES. We have shown that the in-gap states are tunable with strain, while band structure modifications require heteroepitaxial growth. This provides a practical guidepost for engineering the properties of STO under the application of strain.

Possible future work: The ability to detach the STO membrane from its epitaxial host substrate and strain it opens opportunities for further work. This could be used in conjunction with strain which showed an enhance the mobility with increasing strain, but this time one can apply much

larger strain values. Utilizing the LAO/STO spalled membranes can also potentially be used as a platform for Josephson junctions. By changing the contacting metal (Ti/Au), e.g., to Al which has a higher superconducting transition temperature than LAO/STO and can potentially show novel physics not seen in LAO/STO. Another interesting experiment is investigating the strain energy in spalled membranes, and exploring whether it is possible to achieve larger (or smaller) membranes by changing the top film to a smaller lattice mismatch (or larger) with STO.

APPENDIX A

SrTiO₃ TiO₂ treatment protocol

A.1 Aqua regia TiO₂ treatment

Chemical treatment

1. Preheat water in an ultrasonic bath to 70 °C (7/8 filled).
2. Immerse substrate in EtOH and sonicate for 5 min. at RT followed by drying and defect/dirt inspection.
3. Repeat step 2 with acetone.
4. Immerse substrate in milli-Q water (or de-ionized water) and sonicate for 20 min. at 70 °C followed by drying and defect/dirt inspection.
5. Prepare an 3:1:16 HCl(37%) : HNO₃(66%) : H₂O(milli – Q) acid solution (e.g. 9mL:3mL:48mL for a total of 60mL) by adding HCl slowly to HNO₃ (and not vice versa). Let it be for 5 min. See below for info about the aqua regia acid solution*. Immerse substrate in acid solution and ultrasonicate for 20 min at 70 °C and transfer directly to water (step 6). Clean alumina oven boxes with the acid solution.
6. Immerse substrate in milli-Q water (or de-ionized water) and sonicate for 30 s. at RT followed by drying and defect/dirt inspection.

Annealing in tube furnace

1. Place tube in furnace with ≈13 cm of each tube-end outside the furnace. Check the thermocouple with corresponding plug in the rear end reaches 50 cm into the tube.
2. Place substrate in alumina boxes and insert the box close to thermocouple in the center of the furnace. Set the flowrate of oxygen through the tube to ≈10 (arbitrary units) with 5-10 bubbles per second in the bubble-bottle (with 500 ml water).
3. Bake substrate by ramping 100 °C/h to 1000 °C in tube furnace and hold for 1 h then ramp to 25 °C at 100 °C/h.

* Information about aqua regia:

- HNO₃ (aq) + 3HCl (aq) → NOCl (g) + 2H₂O (l) + Cl₂ (g), which is usually used for dissolving noble metals.
- Always make it fresh as it decomposes into 3 toxic gases, which makes it less effective:
2NOCl (g) → 2NO (g) + Cl₂ (g) ; 2NO (g) + O₂ (g) → 2NO₂(g)
- Do not use a closed container (due to the gas production) and keep away even small amounts of organic material as it might cause explosion

A.2 Buffered HF TiO₂ treatment

Personal protective equipment: Acid apron, acid shoes, BHF gloves, face mask

Equipment needed: Glass beakers, 3 Teflon beakers, Teflon tray, Teflon dipper/Tweezer, N₂ gun, ultrasonicated.

Chemical Treatment

Cleaning:

1. **Immerse the substrates in acetone** and sonicate for 3 minutes at RT.
2. Without drying, **Immerse the substrates in IPA** and sonicate for 3 minutes at RT followed by drying and defect/dirt inspection.

Sr(OH)₂ formation:

3. **Immerse** substrate in **mili-Q water** (or de-ionized water) and sonicate for 2 min at RT followed by drying and defect/dirt inspection.

BHF Etching:

4. **Prepare** the etch by pouring BHF in the smallest **Teflon beaker** such that it will cover the samples and **mili-Q water** (or de-ionized water in the **two larger beakers**. Fill the larger beakers with 6/8 water to assure a large dilution of BHF. Place the Teflon tray underneath the Teflon beakers.
5. **Immerse** the substrates in **BHF** utilizing the Teflon dipper for **1:30 minutes**. **Transfer the substrates** to the middle-sized Teflon beaker for 5 seconds to stop the etch followed by transferring the substrates to the largest beaker Teflon for 20 seconds.

Cleaning afterward:

6. **Immerse the substrates in acetone** and sonicate for 3 minutes at RT.
7. Without drying, **Immerse the substrates in IPA** and sonicate for 3 minutes at RT followed by drying and defect/dirt inspection.

Annealing in a tube furnace

1. **Place** the tube in a furnace with ≈ 13 cm of each tube end outside the furnace. Check the thermocouple with the corresponding plug in the rear end reaches 50 cm into the tube.
2. **Place** the substrate in alumina boxes and insert the box close to the thermocouple **in the center of the furnace**. Set the flow rate of oxygen through the tube to ≈ 10 (arbitrary units) with 5-10 bubbles per second in the bubble bottle (with 500 ml water).
3. **Bake the substrate** by ramping 100 °C/h to 1000 °C in the tube furnace and hold for 1 h then ramp to 25 °C at 100 °C/h.

APPENDIX **B**

Appendix of papers

B.1 Published peer-reviewed articles

- I** F. M. Chiabrera, S. Yun, Y. Li, **R. T. Dahm**, H. Zhang, C. K. Kirchert, D. V. Christensen, F. Trier, T. S. Jespersen & N. Pryds. Freestanding perovskite oxide films: Synthesis, challenges, and properties. *Annalen der Physik*, **534** (9), 2200084 (2022).
- II** Y. Li, C. Xiang, F. M. Chiabrera, S. Yun, H. Zhang, D. J. Kelly, **R. T. Dahm**, C. K. Kirchert, T. E. L. Cozannet, F. Trier, D. V. Christensen, T. J. Booth, S. B. Simonsen & N. Pryds. Stacking and twisting of freestanding complex oxide thin films. *Advanced Materials*, **34** (38), 2203187 (2022).
- III** **R. T. Dahm**, R. Erlandsen, F. Trier, A. Sambri, E. D. Gennaro, A. Guarino, L. Stampfer, D. V. Christensen, F. M. Granozio & T. S. Jespersen. Size-controlled spalling of LaAlO₃/SrTiO₃ micromembranes. *ACS applied materials & interfaces*, **13** (10), 12341-12346 (2021).
- IV** R. Erlandsen, **R. T. Dahm**, F. Trier, M. Scuderi, E. D. Gennaro, A. Sambri, C. K. Kirchert, N. Pryds, F. M. Granozio & T. S. Jespersen. A Two-Dimensional Superconducting Electron Gas in Freestanding LaAlO₃/SrTiO₃ Micromembranes. *Nano Letters*, **22** (12), 4758–4764 (2022).
- V** A. D. Rata, J. Herrero-Martin, I. V. Maznichenko, F. M. Chiabrera, **R. T. Dahm**, S. Ostanin, D. Lee, B. Jalan, P. Buczek, I. Mertig, A. Ernst, A. M. Ionescu, K. Dörr, N. Pryds & D.-S. Park. Defect-induced magnetism in homoepitaxial SrTiO₃. *APL materials*, **10** (9), 091108 (2022).
- VI** H. Li, Y. Gan, M. A. Husanu, **R. T. Dahm**, D. V. Christensen, M. Radovic, J. Sun, M. Shi, B. Shen, N. Pryds, & Y. Chen. Robust Electronic Structure of Manganite-Buffered Oxide Interfaces with Extreme Mobility Enhancement. *ACS Nano* **16** (4), 6437–6443 (2022).
- VII** E. B. Guedes, T. W. Jensen, M. Naamneh, A. Chikina, **R. T. Dahm**, S. Yun, F. M. Chiabrera, N. C. Plumb, J. H. Dil, M. Shi, D. V. Christensen, W. H. Brito, N. Pryds, & M. Radović. Disclosing the response of the surface electronic structure in SrTiO₃ (001) to strain. *Journal of Vacuum Science & Technology A: Vacuum, Surfaces, and Films*, **40** (1), 013213 (2022).

B.2 Articles accepted, submitted or under preparation

- VIII** D.-S. Park, A. D. Rata, **R. T. Dahm**, K. Chu, Y. Gan, I. V. Maznichenko, S. Ostanin, F. Trier, H. Baik, W. S. Choi, C.-J. Choi, Y. Kim, G. J. Rees, H. Gíslason, P. Buczek, I. Mertig, A. Ionescu, A. Ernst, K. Dörr P. Muralt & N. Pryds. Controlled Electronic and Magnetic Landscape in Self-Assembled Complex Oxide Heterostructures. Submitted to *ADV. Materials*.
- IX** H. Li, W. H. Brito, E. B. Guedes, A. Chikina, **R. T. Dahm**, D. V. Christensen, S. Yun, F. M. Chiabrera, N. C. Plumb, M. Shi, N. Pryds & M. Radović. Reconstruction of low dimensional electronic states by altering the chemical arrangement at the SrTiO₃ surface. Manuscript under preparation.
- X** **R. T. Dahm**, N. Pryds & D.-S. Park. Tuning the interface magnetism in SrTiO₃-based oxides. Manuscript under preparation.
- XI** H. Li, **R. T. Dahm**, W. H. Brito, E. B. Guedes, A. Chikina, D. V. Christensen, S. Yun, F. M. Chiabrera, N. C. Plumb, M. Shi, N. Pryds & M. Radović. Tailoring the Electronic Structures of Titanium Oxide Thin Films by Ion Diffusion. Manuscript under preparation.

F. M. Chiabrera, S. Yun, Y. Li, **R. T. Dahm**, *et al.*
Freestanding perovskite oxide films: Synthesis, challenges
and properties
Annalen der Physik **534**, 2200084 (2022)



Pulsed laser deposition beamline

Freestanding Perovskite Oxide Films: Synthesis, Challenges, and Properties

Francesco M. Chiabrera, Shinhee Yun, Ying Li, Rasmus T. Dahm, Haiwu Zhang, Charline K. R. Kirchert, Dennis V. Christensen, Felix Trier, Thomas S. Jespersen, and Nini Pryds*

In this review paper, recent progress in the fabrication, transfer, and fundamental physical properties of freestanding oxide perovskite thin films is discussed. First, the main strategies for the synthesis and transfer of freestanding perovskite thin films are analyzed. In this initial section, particular attention is devoted to the use of water-soluble $(\text{Ca,Sr,Ba})_3\text{Al}_2\text{O}_6$ thin films as sacrificial layers, one of the most promising techniques for the fabrication of perovskite membranes. The main functionalities that have been observed in freestanding perovskite thin films are then reviewed. In doing so, the authors begin by describing the emergence of new phenomena in ultrathin perovskite membranes when released from the substrate. They then move on to a summary of the functional properties that are observed in freestanding perovskite membranes under the application of strain. Indeed, freestanding thin films offer the unique possibility to actively control the strain state far beyond what can be observed with traditional methods, allowing the investigation of the profound interplay between structural and electronic properties in oxides. Overall, this review highlights the potential of oxide-based freestanding thin films to become the preferred platform for the study of novel functionalities in perovskite oxide materials.

1. Introduction

In December of 1959 Richard Feynman proposed in his famous lecture “There’s Plenty of Room at the Bottom” that layered heterostructures could host properties and phenomena not present in the constituent materials alone.^[1] Nearly 63 years later this statement is still relevant. After decades of progress in the field, conventional 2D materials—such as graphene and transition-metal dichalcogenides—as well as advanced methods for the synthesis of these materials into layered structures have been widely investigated.^[2,3] Despite the large number of oxides that occur in 2D layered crystal structures, ultrathin freestanding oxides were only recently identified as one of the future directions in ceramics by a recent National Science Foundation workshop.^[4] Here, we review the recent progress in the fabrication, transfer, and fundamental physical properties of freestanding oxide perovskite thin films.


Transition metal oxides thin films constitute an exciting class of electronic and ionic materials with a plethora of functionalities, including superconductivity, ferro-, pyro-, and piezoelectricity, ferromagnetism, and multiferroicity.^[5–7] This richness arises from a strong interaction between the charge, orbital, spin, and structural properties, which enables the realization of functional devices with functionalities beyond those possible with standard semiconductors. Perovskites represent one of the most important crystal structures among transition metal oxides.

This crystal structure has the general formula ABO_3 and includes an octahedron of oxygen ions surrounding each B-site cation. Materials with the perovskite structure may have a highly symmetric cubic lattice, which when distorted can induce tilting and rotation of the oxygen octahedra. The tilted and rotated octahedra may in turn dictate the dielectric, magnetic, optical, and catalytic properties of the perovskites. The properties of oxides in general, and of perovskites in particular, are closely coupled to their lattice. Breaking the lattice symmetry can therefore result in prominent changes in the material’s properties. This is particularly the case when two oxides form a heterointerface, where completely different electronic and ionic properties emerge at

F. M. Chiabrera, S. Yun, Y. Li, R. T. Dahm, H. Zhang, C. K. R. Kirchert, D. V. Christensen, F. Trier, T. S. Jespersen, N. Pryds
Department of Energy Conversion and Storage
Denmark University of Technology (DTU)
Fysikvej 310, Kongens Lyngby 2800, Denmark
E-mail: nipr@dtu.dk

Y. Li

The State Key Laboratory of Refractories and Metallurgy, Collaborative Innovation Center for Advanced Steels, International Research Institute for Steel Technology, Faculty of Science
Wuhan University of Science and Technology
Wuhan 430081, China

 The ORCID identification number(s) for the author(s) of this article can be found under <https://doi.org/10.1002/andp.202200084>

© 2022 The Authors. Annalen der Physik published by Wiley-VCH GmbH. This is an open access article under the terms of the Creative Commons Attribution-NonCommercial-NoDerivs License, which permits use and distribution in any medium, provided the original work is properly cited, the use is non-commercial and no modifications or adaptations are made.

DOI: 10.1002/andp.202200084

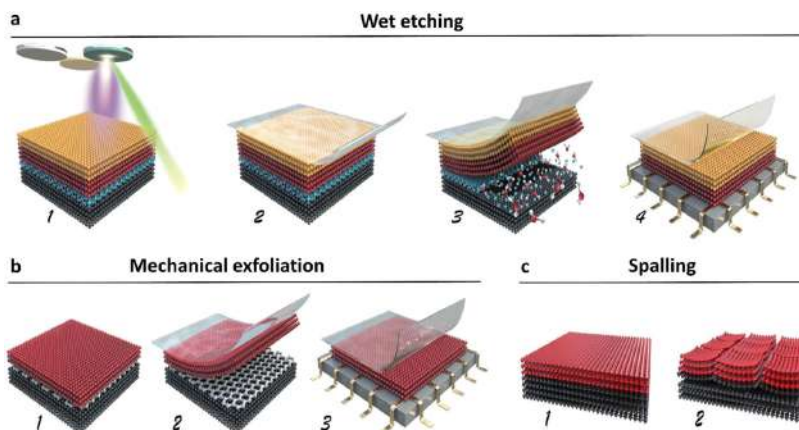


Figure 1. Fabrication of single-crystal free-standing thin films, a) wet etching of sacrificial layers: 1) Deposition of the sacrificial layer and the target thin films, 2) application of a polymer on the film for easing the transfer process, 3) dissolution of the sacrificial layer with a liquid etchant, and 4) transfer of the layer onto another substrate. b) Mechanical exfoliation method: 1) Deposition of target thin film onto a 2D material, 2) cleavage of the deposited layer and 3) transfer onto another substrate. c) Self-formed freestanding thin films through spalling: 1) deposition the film (e.g., LaAlO_3) onto a substrate (e.g., SrTiO_3), and 2) forming fragmented flakes above a critical thickness.

the interface. Traditionally, these complex oxide thin-films and interfaces are grown epitaxially with a well-regulated growth scheme and atomic-level control over the material interfaces and substrate surfaces. However, these methods have fundamental limitations that prevent an unrestricted manipulation, integration, and utilization of these materials owing to the fact that:

- 1) Heteroepitaxy only works for a limited set of material systems with similar crystal structures, lattice orientations, and lattice parameters.
- 2) Epitaxial films are clamped by the substrate with the properties of the ultrathin films often affected by substrate interactions
- 3) During the high-temperature growth of epitaxial films, it is inevitable to have a mixture of the two layers leading to cationic interdiffusion,^[8] which prevents the study of truly sharp interphases.
- 4) Epitaxial growth typically requires elevated temperatures, often preventing the integration of materials which are stable in different environments or which are thermodynamically unstable when in contact with each other.

Recently, new methods have been developed, bridging the realms of epitaxial complex oxides and low-dimensional van der Waals (vdW) materials systems. By replicating concepts previously developed in semiconductor technology,^[9,10] the realization of freestanding perovskite films was demonstrated. Through controllable weakening of epitaxial crystals and epitaxial water-soluble sacrificial crystal layers, it is now possible to detach ultrathin complex oxide crystals (i.e., typically 50–100 nm but in principle can be of any thickness above one unit cell^[11]) from their substrate to realize freestanding thin films. Different strategies for fabricating freestanding layers have been demonstrated as illustrated in **Figure 1**: 1) Freestanding thin films using wet etching of sacrificial layers;^[12,13] 2) Mechanical exfoliation method of

epitaxial oxide crystals;^[14] and 3) Self-formed freestanding thin films through spalling.^[15,16] Recently, heterostructures have also been fabricated by stacking membranes directly.^[14] These results demonstrate an exciting general approach for producing freestanding thin films and multilayers. The membranes can be made of functional perovskite oxides and transferred directly onto any substrate, thus bypassing the limitations of conventional epitaxy.^[17] Moreover, freestanding thin films have been shown to display different functionalities when released from their substrate, thus presenting a new playground for investigating fundamental properties into large regimes of strain and strain gradients. This broadly defined field is rapidly developing and this review paper is aimed at describing the current state of the art of freestanding perovskite oxide: their synthesis, fabrication, transfer, and functional properties. Finally, the review will also provide an outlook on the current state.

2. Fabrication of Single-Crystal Freestanding Thin Films

In this section, the most common methods for fabricating freestanding perovskite membranes are reviewed. We will focus on the methods that allow achieving of high-quality single-crystal oxide thin films: wet etching of sacrificial layers, mechanical exfoliation of epitaxial oxide crystals, and self-formed freestanding thin films through spalling.

2.1. Wet Etching of Sacrificial Layers

Wet etching release/epitaxial lift-off is emerging as one of the most reliable methods for obtaining high-quality single-crystal of freestanding perovskite oxides.^[12,18] In this method, the perovskite oxide of interest is grown on top of a sacrificial layer which

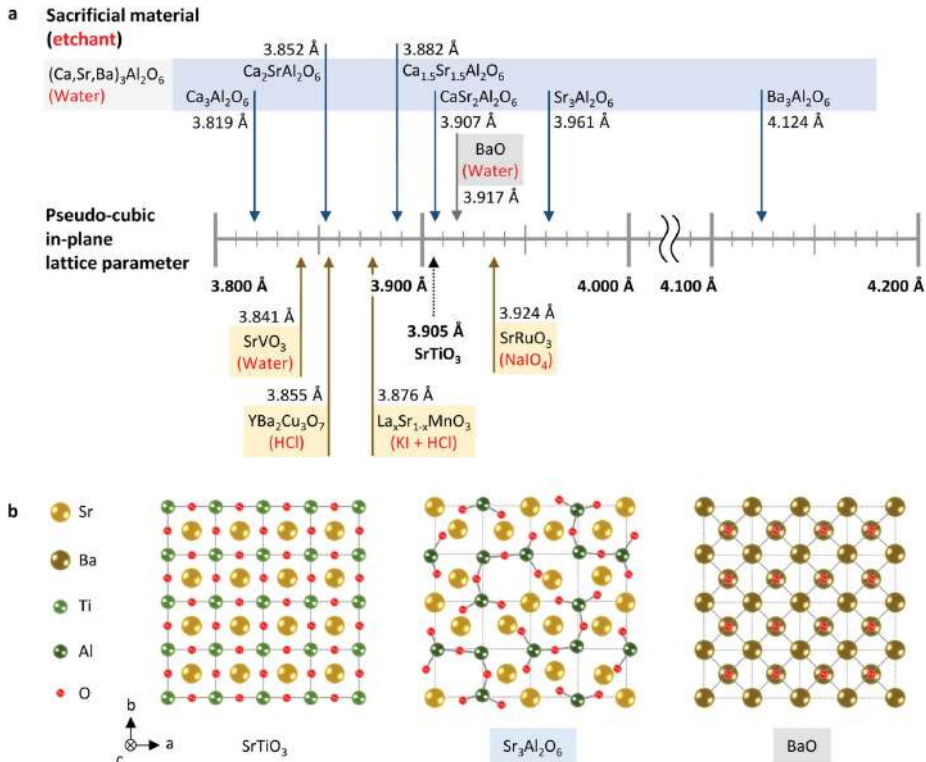


Figure 2. Sacrificial materials compatible with perovskite oxides. a) Pseudo-cubic in-plane lattice parameters of sacrificial materials with the representative perovskite oxide ($SrTiO_3$ indicated by a black dashed arrow). Each etchant is written in red inside parenthesis. The blue arrow represents the family of $(Ca,Sr,Ba)_3Al_2O_6$, and the brown arrow does perovskite oxide or layered perovskite oxide. The grey arrow indicates metal oxide with a rock salt structure. b) Schematic of crystal structures for $SrTiO_3$, $Sr_3Al_2O_6$, and BaO projected onto the $(001)_{pc}$ plane. Note that $SrTiO_3$, $Sr_3Al_2O_6$, and BaO are displayed as 1×1 , 4×4 , and $2\sqrt{2} \times 2\sqrt{2}$ unit cells, respectively.

is then dissolved by selective etching, releasing the freestanding membrane (Figure 1a). An ideal sacrificial layer should thus: 1) present a facile epitaxial growth on perovskite oxide substrates with custom orientation, 2) allow a coherent epitaxial growth of perovskite oxide films, and 3) present a high selectivity toward the liquid etchant. In the following, the main sacrificial layers proposed in the literature and the main transfer methods are reviewed.

2.1.1. $(Ca,Sr,Ba)_3Al_2O_6$

The family $(Ca,Sr,Ba)_3Al_2O_6$ has been largely used as sacrificial layer for growing perovskite oxides due to a facile dissolution in water and to a good structural and chemical compatibility with perovskite oxides.^[12,19–23] For example, $Sr_3Al_2O_6$ (SAO) possesses a cubic unit cell (space group $Pa\bar{3}$) with lattice constant equal to 3.961 Å, consisting of Sr ions and AlO_4 tetrahedra.^[24] This structure resembles quite well four unit cells of many perovskite oxides ($a_{SAO}/4 = 3.961$ Å) and the epitaxial growth is allowed by a 75% match of the oxygen sublattice of the two structures, see

Figure 2b. For this reason, SAO was extensively used as sacrificial layer for the growth of a variety of epitaxial perovskite thin films, as listed in **Table 1**. Using pulsed laser deposition (PLD) or molecular beam epitaxy (MBE), perovskite oxide membranes were grown on SAO in a layer-by-layer mode, attested by clear reflection high energy electron diffraction oscillations.^[12,25] Structural characterizations of ultrathin membranes revealed that the crystallinity of the layers remains close to the seed films down to few unit cells.^[11,26] It is worth noticing that the epitaxial relation between SAO sacrificial layers and other perovskite oxides is not limited to the (001) orientation, but also extends to other crystallographic orientations. As an example, single-crystal (110) - and (111) -oriented membranes of $SrRuO_3$ (SRO) and $La_{0.67}Sr_{0.33}MnO_3$ were successfully grown on SAO sacrificial layer and transferred onto arbitrary substrates.^[27,28]

Interestingly, by controlling the ratio between Ca, Sr, and Ba the reduced lattice parameter of $(Ca,Sr,Ba)_3Al_2O_6$ can be continuously tuned from 3.819 Å (100% Ca) to 4.124 Å (100% Ba) (Figure 2a).^[57,56] For example, $Ca_2SrAl_2O_6$ was used as a seed sacrificial layer for $La_{0.7}Ca_{0.3}MnO_3$ growth due to the nearly perfect lattice match ($<0.1\%$).^[55] The minimization lattice mismatches

Table 1. (Ca,Sr,Ba)₃Al₂O₆ as sacrificial layers in literature.

Material	Synthesis method	Sacrificial layer						
		Synthesis condition	Target material	Substrate	Transfer method	Etchant, temperature, time	Comments	
Sr ₃ Al ₂ O ₆	PLD	<i>T</i>	670–900 °C	SrTiO ₃ ^[12,19–23]	SrTiO ₃	PDMS	Water	(Ca,Sr,Ba) ₃ Al ₂ O ₆ Tunable lattice parameter
		<i>P</i> _{O₂}	1.0 × 10 ⁻⁶ – ~0.27 mbar	La _x Sr _{1-x} MnO ₃ ^[19,28,58]	(001)	PMMA	RT	
				BaTiO ₃ ^[59–63]	SrTiO ₃	PPC/PMMA	5 m	
		or		BiFeO ₃ ^[64,65]	(110)	PET/PMMA	(~90 nm)	
		<i>P</i> _{Ar}	~6.7 × 10 ⁻⁶ mbar	SrRuO ₃ ^[27,60]	SrTiO ₃	PPC/PDMS	1 h	
		<i>E</i>	0.8–2.0 J·cm ⁻²	LaNiO ₃ ^[66]	(111)	PET/PDMS	(~50 nm)	
				BiMnO ₃ ^[67]		PET/ PEDOT:PSS	1 d	
				Sr ₂ IrO ₄ ^[68]		PI tape	(~9 nm)	
				Fe ₃ O ₄ ^[69,70]		PET		
				CeO ₂ ^[71]		epoxy		
		La _{0.7} Ca _{0.3} MnO ₃ ^[72]		Photoresist				
		[(La _{0.7} Sr _{0.3} MnO ₃) ₅ (SrTiO ₃) ₅] _{<i>n</i>} ^[12,19,35]						
		BaTiO ₃ /La _{0.7} Sr _{0.3} MnO ₃ ^[73]						
		BaTiO ₃ /La _{0.7} Sr _{0.3} MnO ₃ /BaTiO ₃ ^[13]						
		LaAlO ₃ /YBa ₂ Cu ₃ O _{7-x} /LaAlO ₃ ^[74]						
		La _{0.7} Sr _{0.3} MnO ₃ /BiFeO ₃ ^[75]						
		BiFeO ₃ /La _{0.67} Sr _{0.33} MnO ₃ ^[76]						
		BaTiO ₃ -CoFe ₂ O ₄ ^[77]						
	MBE	<i>T</i>	750–950 °C	SrTiO ₃ ^[11,78]	SrTiO ₃	PI tape		
		<i>P</i> _{O₂}	1.29 × 10 ⁻¹¹ – 1.33 × 10 ⁻⁶ mbar	BiFeO ₃ ^[79]	(001)	PEN/epoxy		
				PbTiO ₃ ^[25]				
Sr ₂ CaAl ₂ O ₆	PLD	<i>T</i>	710 °C	SrTiO ₃ ^[32]		PPC	Water	
		<i>P</i> _{Ar}	~5.3 × 10 ⁻⁶ mbar	n-SrTiO ₃ /n-PbTiO ₃ /n-SrTiO ₃ ^[33]		PMMA	RT	
		<i>E</i>	1.35 J·cm ⁻²	[(PbTiO ₃) ₁₆ /(SrTiO ₃) ₁₆] ^[33]			-	
Sr _{1.5} Ca _{1.5} Al ₂ O ₆	PLD	<i>T</i>	700 °C	SrRuO ₃ ^[34]		PDMS	Water	
		<i>P</i> _{O₂}	2 × 10 ⁻³ mbar				RT	
		<i>E</i>	2.0 J·cm ⁻²				12 h	
SrCa ₂ Al ₂ O ₆	PLD	<i>T</i>	700 °C	La _{0.7} Ca _{0.3} MnO ₃ ^[31]		PPC/PMMA	Water	
		<i>P</i> _{O₂}	~6.7 × 10 ⁻⁶ mbar				RT	
		<i>E</i>	1.25 J·cm ⁻²				-	
Ba ₃ Al ₂ O ₆	PLD	<i>T</i>	850 °C	La:BaSnO ₃ ^[30]		PPC/PDMS	Water	
		<i>P</i> _{O₂}	~1.3 × 10 ⁻⁷ mbar				RT	
		<i>E</i>	1.5 J·cm ⁻²				5–10 m	
		<i>P</i> _{O₂}	~0.08 mbar					

The synthesis method of each sacrificial thin film is shown along with synthesis conditions, substrates, and etching conditions; In the table, *T*, *P*_{O₂}, *P*_{Ar}, and *E* indicate the synthesis temperature, pressure of oxygen gas, pressure of argon gas, and laser energy density, respectively; The list of perovskite oxide membranes obtained, the substrate, and the transfer method are also shown; In the column of etching condition, water and RT represent deionized water and room temperature; d, h, and m denote days, hours, and minutes, respectively.

can largely improve the quality of the released membranes by hindering the formation of cracks,^[55] which has motivated the exploration of sacrificial layers such as Ca₂SrAl₂O₆ (3.852 Å), Ca_{1.5}Sr_{1.5}Al₂O₆ (3.882 Å), Sr₂CaAl₂O₆ (3.907 Å), and Ba₃Al₂O₆ (4.124 Å).^[56,55,52–54] However, small Ca ions can make more distorted geometries leading to less structural compatibility with perovskites and reduced water solubility.^[57]

Table 1 presents a list of references where (Ca,Sr,Ba)₃Al₂O₆ was used as sacrificial layer for obtaining oxide membranes, along with the synthesis method and the main synthesis conditions used in literature. It is interesting to note that in order to achieve a good crystal quality, SAO sacrificial layers are usually grown at high temperatures (700–900 °C) and low oxygen partial pressure (10⁻⁶–10⁻⁵ mbar). Nevertheless, it was observed that, at these temperatures,

cationic interdiffusion between the sacrificial and the functional layer can occur, especially along misfit dislocations or vertically extended defects.^[44] As a matter of example, cationic intermixing between SAO and La_{0.7}Sr_{0.3}MnO₃ thin films at 900 °C may cause a phase transformation of the sacrificial layer, making it water-insoluble.^[19] Interestingly, Baek et al. showed that the inclusion of a few-unit-cells of SrTiO₃ (STO) between the SAO and La_{0.7}Sr_{0.3}MnO₃ entirely blocks Mn and La diffusion into the sacrificial layer and avoids the structural transformation, preserving the water solubility.^[19] Moreover, 6 u.c. of STO capping layer was also found to protect the sacrificial layer from air humidity, making this heterostructure a practical template for ex situ epitaxial growth using other techniques.^[58]

(Ca,Sr,Ba)₃Al₂O₆ can be immersed in deionized water at room temperature to dissolve the sacrificial layer and release

Table 2. The experimental information of other oxides as sacrificial layers.

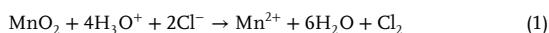
Sacrificial layer			Target material	Substrate	Transfer method	Etchant, temperature, time	Comments
Material	Synthesis method	Synthesis condition					
La _{0.7} Sr _{0.3} MnO ₃	PLD	<i>T</i> 650–800 °C	PbZr _{0.2} Ti _{0.8} O ₃ ^[40–44]	SrTiO ₃	PMMA	KI + HCl solution	-
La _{0.67} Sr _{0.33} MnO ₃		<i>P</i> _{O₂} ~0.03–2.7 mbar <i>E</i> 1.0–2.0 J·cm ⁻²	[(CaTiO ₃) _{<i>n</i>} (SrTiO ₃) _{<i>n</i>}] ₆ ^[40] BiFeO ₃ /SrRuO ₃ ^[40] LiFe ₂ O ₈ ^[46] SrRuO ₃ /BaTiO ₃ /SrRuO ₃ ^[45] Ba _{1-x} Sr _x RuO ₃ /Ba _{1-x} Sr _x TiO ₃ / Ba _{1-x} Sr _x RuO ₃ ^[45] BaTiO ₃ ^[47]	(001) GdScO ₃ (110)	PS/PMMA PI tape PPC/PDMS	- 1 d	
SrRuO ₃	PLD	<i>T</i> 600–615 °C <i>P</i> _{O₂} 0.1–0.12 mbar <i>E</i> 1.5 J·cm ⁻²	La _{0.7} Sr _{0.3} MnO ₃ ^[48] LaAlO ₃ /SrTiO ₃ ^[49]	SrTiO ₃ (001)	PDMS	NaIO ₄ (0.4 M) RT Few h - 2 d	-
SrVO ₃	PLD	<i>T</i> 760 °C <i>P</i> _{O₂} 1.2 × 10 ⁻⁶ mbar	SrTiO ₃ ^[50]		PDMS PET/silicon film	Water 50 °C 5 d	Small lattice parameter
YBa ₂ Cu ₃ O ₇	PLD	<i>T</i> 750 °C <i>P</i> _{O₂} ~0.08 mbar	SrRuO ₃ ^[80] La _{0.7} Sr _{0.3} MnO ₃ ^[80,81]		PMMA	HCl (0.6%) - Few m	Short etching time
SrCoO _{2.5}	PLD	<i>T</i> 750 °C <i>P</i> _{O₂} ~0.13 mbar <i>E</i> 1.1 J·cm ⁻²	SrRuO ₃ ^[53]	SrTiO ₃ (001) SrTiO ₃ (110) SrTiO ₃ (111)	PDMS	Vinegar, 36% CH ₃ COOH and carbonated drinks RT - 3–10 m	
BaO	PLD	<i>T</i> 400 °C <i>P</i> _{O₂} ~1.3 × 10 ⁻⁵ mbar <i>E</i> -	BaTiO ₃ /SrTiO ₃ ^[54]	SrTiO ₃ (001)	PET/PDMS	Water - > 10 h	Epitaxial growth on SrTiO ₃ (001)
MgO	PLD	<i>T</i> 600 °C <i>P</i> _{O₂} ~2.7 × 10 ⁻² mbar <i>E</i> -	CaFe ₂ O ₄ ^[55]	SrTiO ₃ (001)	PS	(NH ₄) ₂ SO ₄ (10%) 80 °C 12 h	-

The synthesis method for each sacrificial material is shown with synthesis conditions, target material, substrate, transfer method, and etching conditions; In the table, *T*, *P*_{O₂}, *P*_{Ar}, and *E* indicate the synthesis temperature, pressure of oxygen gas, pressure of argon gas, and laser energy density, respectively; In the column of etching condition, water and RT represent deionized water and room temperature; d, h, and m denote days, hours, and minutes, respectively.

the freestanding membranes. The time it takes to remove the (Ca,Sr,Ba)₃Al₂O₆ sacrificial layer depends on the composition and the thickness of the sacrificial layer, see Table 1. In the case of Ca₃Al₂O₆, the sacrificial layer is weakly soluble in water because of the strong Ca–O bonding.^[59] However, the solubility can be tuned by substituting Sr or Ba for Ca, which increases the thermodynamic driving force for the cation hydration.^[12,56,54] For example, it takes 5–10 min to fully dissolve the 16 nm thick Ba₃Al₂O₆ layer while it takes around 1 day for SAO of similar thickness (Table 1).^[56] Regarding the thickness dependence, the sacrificial layer dissolving time is reduced as the thickness of the layer increases. For the SAO, it takes 1 day (5 min) to dissolve a film thickness of 9 nm (90 nm).^[12] Last, it is worthwhile to mention that target materials might also react with water, for example, BaTiO₃ (BTO), which could lead to Ti ion displacements in the TiO₂ plane and surface oxygen vacancies due to the hydroxylation of the first BaO layer.^[60,61] Therefore, care should be taken when choosing the sacrificial layers and the target material.

2.1.2. Perovskite Oxides and Other Oxides

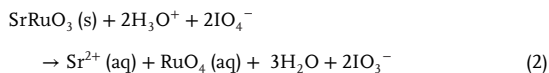
Perovskite oxides such as La_xSr_{1-x}MnO₃ (LSMO),^[62–69] SRO,^[70,71] SrVO₃ (SVO),^[72] have also been demonstrated as sacrificial layers, see Table 2. Compared with the complex crystal structure of the (Ca,Sr,Ba)₃Al₂O₆, these sacrificial layers have in most cases the same structure as the target perovskite films, which could potentially help in preserving the in-plane orientation and retain the structural quality of the transferred film. In the case of LSMO sacrificial layer, the chemical reaction for selective etching of LSMO is based on the reduction of the insoluble Mn⁴⁺ to soluble Mn²⁺ by Cl⁻ according to the following reaction^[73]



However, if Mn⁴⁺ is not completely reduced, insoluble MnO₂ precipitates are left behind. As a matter of example, Elan-govan et al. have grown BTO/LSMO heterostructure on STO

(001) to realize BTO freestanding membranes.^[69] The single-crystalline BTO film was released by selective etching of the LSMO in an aqueous solution of KI + HCl + H₂O. Negligible chemical etching of BTO was observed due to the much faster etch rate of LSMO with respect to BTO.

Dissolving of SRO is realized by oxidizing RuO₂ into volatile RuO₄ within aqueous solution:



Weber et al. have investigated the etching rate of SRO with different etchants and selected NaIO₄ solution with a suitable etching rate (2 nm s⁻¹) and near-neutral pH.^[79] Using this approach, Pesquera et al. grew LSMO epitaxially on STO mediated by an SRO sacrificial layer, which was subsequently dissolved by selective etching without damaging the LSMO film.^[70] This approach is also used to fabricate single-crystalline freestanding membranes of LAO/STO heterostructures and directly integrated the membrane on sapphire substrate via vdW stacking.^[71]

SrVO₃ is another sacrificial layer candidate, which is suitable for the growth of a wide spectrum of perovskites due to its cubic structure (*a* = 3.84 Å). Compared with LSMO or SRO that requires complex etchants, SVO can be dissolved in water.^[72] This material would expand the choice of water-soluble materials especially for those materials that are not chemically stable against stronger acids. However, special caution is needed because SVO is toxic.

Recently, SrCoO_{2.5} (SCO) has been also proposed as generic sacrificial layer for a facile epitaxy of perovskite oxides thin films.^[76] SCO presents a brownmillerite structure with an in-plane lattice parameter close to the STO (*a* = 3.90 Å) and can be epitaxially grown on many perovskite substrates with different crystallographic orientations. Moreover, SCO can be dissolved in weak acetic acid solutions, in vinegar and in common carbonated drinks, which allows a safe transfer process of perovskite membranes.

Beside perovskite oxides, metal oxides were also proposed as sacrificial layers, such as BaO,^[77] MgO,^[78] ZnO,^[80] and VO₂.^[81] BaO has a rock salt structure with a lattice parameter of 5.539 Å. The lattice mismatch with STO is small (0.31%) as a result of the 45° rotation when coherently grown on the STO (001) substrate, see Figure 2b.^[77] Takahashi and Lippmaa have fabricated BTO/STO freestanding membranes using BaO as a sacrificial layer.^[77] This BaO sacrificial layer was dissolved by water after 10 h as a result of the reaction between BaO and water: BaO + H₂O → Ba(OH)₂. Various combination of the sacrificial layer and etchant have been developed, for example, MgO, ZnO, and VO₂, and were used to fabricate non-perovskite oxides, such as CaFe₂O₄, VO₂, and TiO₂.^[77,78,80,81] However, such sacrificial layers are not suitable to fabricate freestanding membranes with a perovskite structure due to the large lattice mismatch.

2.1.3. Transfer Methods for Freestanding Oxide Thin Films

The transfer and manipulation of single-crystals membranes is an essential part of wet etching methods, since the integrity and

quality of the membrane is largely affected by the releasing process and handling techniques.^[31,42,82] Common methods used for perovskite oxides membranes mimics the well-developed wet transfer process of 2D vdW materials, such as graphene^[83,84] and TMDC,^[85,86] and generally involve three major steps: lifting off the film, stamping the free-standing film onto the desired substrate and last, removing the stamp layer (also called support layer). **Figure 3** shows the main strategies adopted in literature for transfer and manipulation of perovskite oxide membranes.

The first step is the etching process where the oxide film is detached from the growth substrate by selectively etching the sacrificial layer, as described above (see Table 1 for the list of etchants and optimized condition for each sacrificial layer). To prevent crinkling and folding of the free-standing membranes during the etching release process,^[82] a common way is to cover a support layer on the oxide membrane to facilitate the lifting off and follow-up transferring, just as polymer-supported is used for transfer of graphene.^[84] Many polymer materials have been developed and used as support layers, considering the merits of flexibility, mechanical strength, and adhesive contact, such as polyimide (PI) tape, polydimethylsiloxane (PDMS),^[11,12,82,87] polymethyl-methacrylate (PMMA),^[20,62] polystyrene (PS), or the combination of these materials, like polypropylene carbonate (PPC)-PDMS stack^[13,62,87] and PI sheet with PPC layer.^[52,67]

PMMA, which is most commonly used in transferring of chemical-vapor-deposited graphene,^[38,84] has also found a wide application in the transfer of oxide membrane.^[20,62,42] PMMA can be easily coated on the oxide surface, and washed away by acetone once the transfer is completed, see Figure 3a. However, the polymer residues and the contamination associated with this process are always hard to be removed.^[88] Moreover, it was found that the PMMA on the oxide stack may not be fully in contact with the transfer substrate, which can result in unattached regions that tend to form bubbles and ripples or in the cracking of the membrane during the dissolving process of PMMA.^[42,83] Zhang et al. has introduced a frame structure consisting of polyethylene terephthalate (PET) and PMMA to stamp the SRO film, achieving a high yield transfer rate without macroscopic cracking.^[42]

Thermal release polymer sheets such as PDMS have been also explored as candidates for support layers, see Figure 3b. Instead of chemically etching in the final step, the polymer can be handily released by heating up to 70 °C, which facilitates the removal of residues and the membrane cleanliness.^[12] However, cracks and tears can be introduced inevitably when peeling off PDMS from the membrane, making it difficult to obtain continuous membranes.^[82] A two-layer structure was also designed to improve this method, for example, PPC-PDMS stack.^[13,62,87]

Scotch tape, like PI tape, has been used to transfer large area oxide membranes through adhesion, see Figure 3c.^[28,68] However, the downside of this method is that it is impossible to remove the adhesive tape from the membrane at the final step. Steady transfer operation should be guaranteed, otherwise the freestanding membrane may easily bend and crack.

A support-free transfer method was also proposed by Gu et al.,^[31] see Figure 3d. In their work, they showed that crack-free membranes of SRO and BTO could be obtained by scooping the freestanding membranes floating on the surface of the solvent after the dissolution of the sacrificial layer. Interestingly, in their

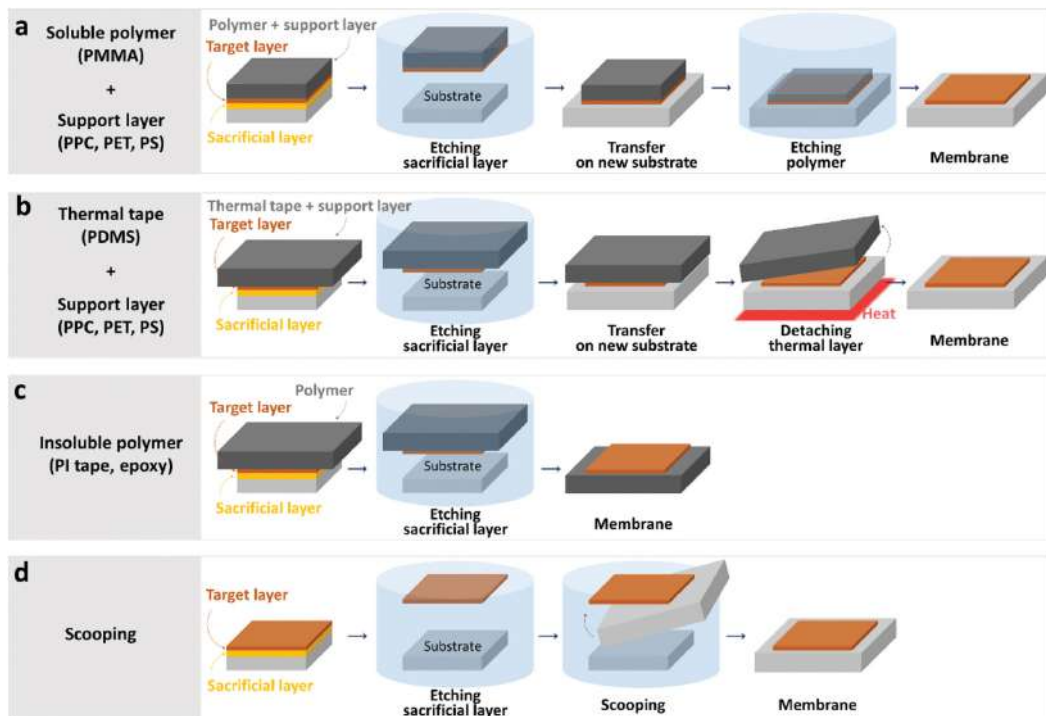


Figure 3. Sketch of the main transfer strategies used for the release and transfer of perovskite oxide membranes via wet etching method: a) Soluble polymer, b) Thermal tape, c) Insoluble polymer and d) Scooping of the floating membrane.

work they also showed that the substrate, after the membrane releasing, could be reused for other depositions.

The enormous progress in the development of 2D materials transfer such as graphene and TMDs over the last decades, can be a good starting point for successfully and fast progress of transfer methods for perovskite oxide membranes. The polymer-assisted transfer method has been demonstrated to yield a single-crystal oxide membrane with macroscopic dimensions (hundreds of micrometers to millimeters). However, considering the hardness and brittleness of oxide membranes, as well as the issues such as cracks, wrinkles, trapped bubbles, and polymer residues, the question of how to develop techniques for transferring single-crystal oxide membranes with sufficient size, as-grown uniformity, and high-quality onto arbitrary substrate remains a key challenge.

2.2. Mechanical Exfoliation

In the last few years, the quest for flexible oxide electronics has motivated the development of mechanical exfoliation methods for integrating oxide thin films into complex devices.^[89] Mechanical exfoliation is a technique based on the deposition of target thin film onto a 2D layered material, followed by the cleavage of the deposited layer along the heterointerface (Figure 1b).^[90] 2D layered materials are structures characterized by weak bonds be-

tween the constitutive layers. This allows thinning the 2D-layered substrate along these planes, reducing progressively its thickness and increasing its flexibility, eventually achieving membranes. Moreover, the integration of well-ordered epitaxial structure into 2D layered substrates can be achieved even for dissimilar crystalline structure, through quasi-van der Waals (qvW) epitaxy.^[91–93] In traditional epitaxy, strong chemical bonds between the thin film and the substrate determine the orientation and structural characteristics of the layers, intrinsically limiting the choice of substrates materials. Indeed, when the lattice constants of the substrates strongly differ from the thin films, structural dislocations or random orientation of grains tend to appear in the layers, in order to minimize the elastic strain energy of the system. On the contrary, vdW epitaxy consists in the creation of weak bonds between the film and the substrate, which allows the growth of relaxed and epitaxial thin layers with unrelated orientation with the substrate.^[94–96] The deposition of 3D structures on 2D layered materials can take place through the qvW epitaxy, a mixed behavior based on the initial creation of an interface with vdW bonds followed by traditional homoepitaxial growth of the layer.^[97] The weak interaction between the oxide layers and the substrates offers the opportunity of creating freestanding membranes by exfoliating the top layers.^[98]

A characteristic example of 2D-layered material used for the integration of perovskite oxide is mica, a large family of phyllosilicate minerals possessing a monoclinic structure

layered along the 001 plane. Mica possesses general formula $X_2Y_nZ_8O_{20}(OH,F)_4$, where X, Y and Z are the interlayer cation (e.g., K and Na), the octahedrally coordinated atom (e.g., Al and Mg) and the tetrahedral coordinated element (Si, Al, etc.), respectively. The most commonly used micas for the thin film integration are the muscovite ($n = 4$, e.g., $KAl_2(Si_3Al)O_{10}(OH)_2$) and the phlogopite ($n = 6$, e.g., $KMg_3(Si_3Al)O_{10}F_2$).^[93] Mica is emerging as one of the most interesting substrates for flexible electronic, due to its superior mechanical properties and its good compatibility with oxides' deposition processes.^[92,93] The epitaxial growth of perovskite oxides on Mica has been generally interpreted in the light of qvdW epitaxy.^[91–93,99] Nevertheless, Lu et al.^[100] recently showed that strong bonds can be formed at the interface between phlogopite mica and STO thin films deposited by PLD, resulting in the epitaxial relation $\{111\}_{STO}||\{001\}_{mica}$ (in-plane $\langle 110 \rangle_{STO}||\langle 100 \rangle_{mica}$ and $\langle 112 \rangle_{STO}||\langle 010 \rangle_{mica}$), see **Figure 4**. Despite the different cationic rearrangements of these orientations, the epitaxial match is allowed by an almost identical rearrangement of the oxygen sublattices of the two compounds.^[100] A similar (111) orientation was also observed for other perovskites thin films deposited on mica (001), such as SRO/BTO,^[101] SrVO₃,^[102] Eu-doped 0.94Bi_{0.5}Na_{0.5}TiO₂–0.06BaTiO₃,^[99] CaVO₃/STO,^[103] and La_{0.7}Sr_{0.3}MnO₃/STO.^[104] Nevertheless, other types of orientations and even polycrystalline thin films are reported in literature for perovskite oxides deposited on mica substrates.^[105–107] In this sense, Ko et al. found that the PbZrO₃/SRO heterostructure tends to develop multiple orientations if directly grown on muscovite mica, while well-oriented (111) thin films can be obtained by the insertion of a 1-nm-thick CoFe₂O₄ seeding layer.^[108] These results show that different types of crystallographic orientations and bonding can be expected at the perovskite/mica interface. The possibility of cleaving La_{0.7}Sr_{0.3}MnO₃ thin films from mica substrates was demonstrated by Zhang et al.^[98] In their work, the authors showed that polycrystalline LSMO thin films could be easily peeled off by muscovite mica due to the weak interaction between the film and the substrate. Additionally, mica can be cleaved along the weak bonded constitutive planes after the thin film deposition, increasing the flexibility of the structure and allowing the study of bending strain effect on the perovskite layers (see Section 4.2).^[93,101]

Another promising 2D material that can be used for the mechanical exfoliation of perovskite oxide thin films is graphene. Lee et al. showed that STO thin films with predominant (001) orientation can be directly grown on graphene covered SiO₂/Si substrates by PLD.^[109] The thermal oxidation of graphene can be avoided during the film growth by using low oxygen partial pressure ($\approx 10^{-6}$ mbar). The interface between the STO and the graphene is characterized by moderate bonding, as suggested by the presence of moderate lattice strain in the oxide layer.^[109] Interestingly, Kum et al. showed that graphene can be used as a universal mechanical exfoliation method for obtaining freestanding oxides thin films.^[114] In their work, the authors showed that epitaxial STO (001) thin films can be grown on double-layer graphene-coated STO (001) single-crystals through remote epitaxy, a mechanism based on the semitransparency of the graphene layer to the atomic potential fields of the STO substrate. Moreover, the thin films can be transferred to other substrates thanks to the weak bonds between graphene and the perovskite layer. These results show that graphene-based remote epitaxy has emerged

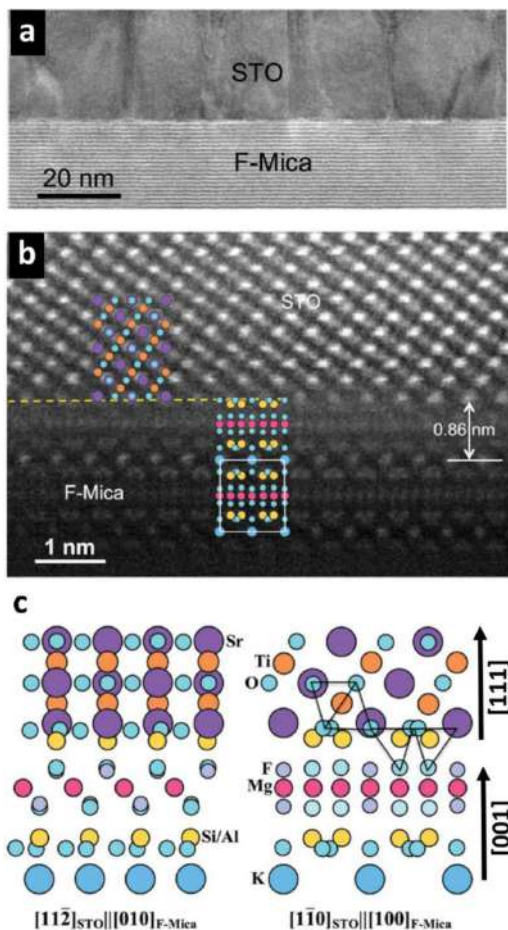


Figure 4. Epitaxial growth of SrTiO₃ on Mica. a) Low magnification TEM and b) STEM high angle angular dark field image of an STO thin film grown on Mica. c) Reconstruction of the epitaxial relation and reconstruction of the interface between the (001) mica and the (111) STO thin films. The epitaxial relation is ensured by a similar arrangement of the oxygen sublattice. Reproduced under terms of the CC-BY 4.0 license.^[100] Copyright 2020, Wiley-VCH.

as a promising method for obtain large area freestanding thin films.

2.3. Self-Formed Freestanding Films through Spalling

As an alternative to the method based on sacrificial layers and epitaxial liftoff^[110] freestanding membranes of brittle crystals can be produced by inducing and controlling the fracture mode known as spalling. The basic mechanisms and elements of the technique are illustrated in Figure 1c: A tensile strained top layer is deposited on the crystal/wafer of interest and under sufficient stress and sufficient bonding strength, the crystal will form

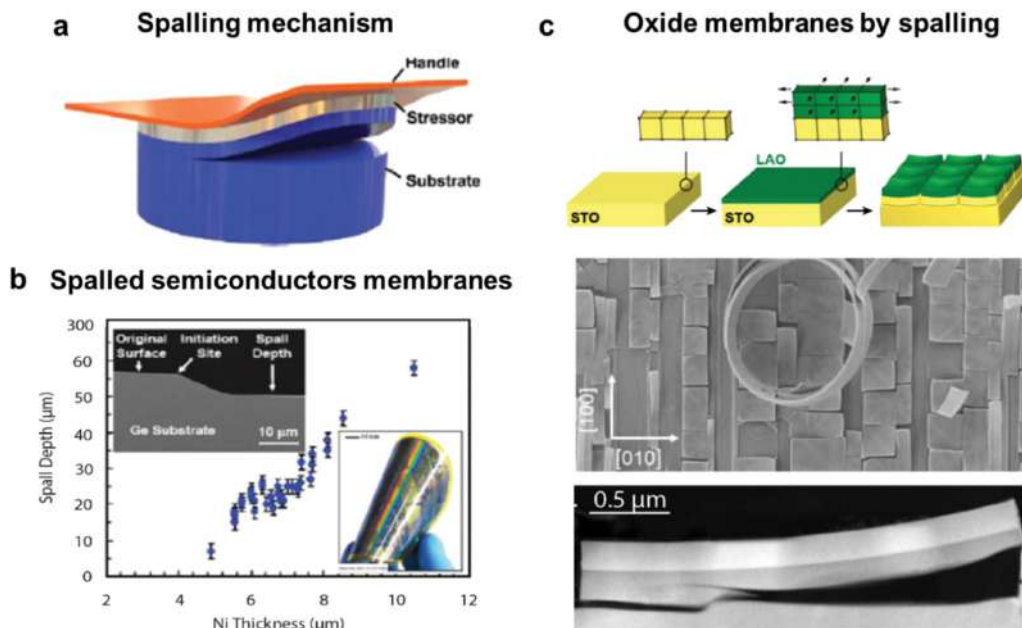


Figure 5. Self-formed membranes through spalling. a) Illustration of the spalling mechanism. b) Evolution of the spalling depth of the fracture plane as a function of the thickness of the stressor for Ge single-crystals. c) Schematic representation and SEM images of spalling mechanism of LAO thin films deposited on STO (001). a,b) Reproduced under terms of the CC-BY license from Bedell et al., 2013, IOP Science. The inset of (b) is adapted with permission.^[115] Copyright 2013, American Chemical Society. c) Top panel reproduced with permission.^[16] Copyright 2021, American Chemical Society. Bottom two panels reproduced with permission.^[15] Copyright 2020, Wiley-VCH.

cracks which propagate through the crystal. Different types of substrate fractures may occur, the most familiar being the vertical cracking through the entire crystal leading to breaking of the wafers. However, under certain conditions of tensile strained top-layers on brittle crystals, the interplay of the shear- and opening-stress at the tip of a crack may direct the propagation parallel to the surface at a stable depth. This fracture mode is known as spalling and relies on a stable propagation of the fracture mode parallel to the substrate at the equilibrium depth where the shear stress is minimized. The process is self-correcting: for a crack too close to the surface, the crystal above the crack will contract upon fracturing and the crack propagation is deflected downward. Conversely, for a crack very deep in the substrate the top layer will expand upon fracture due to the curvature of the membrane and the crack is instead deflected upwards.^[111] The resulting steady-state crack propagation is thus parallel to the surface at a depth that depends on the mechanical properties of the crystals. The phenomenon and its mechanism was first analyzed in detail by Hutchinson et al.^[111] It is important to note that the mechanism is purely mechanical, that is, it does not require defects, inhomogeneities, or anisotropies and applies in general for material combinations with the required mechanical properties.

Substrate spalling has been investigated for the realization of semiconductor membranes. Dross et al.^[112] obtained silicon membranes of areas up to 25 cm² and thicknesses of 30–50 microns by deposition/bonding of Ag and Al films on silicon and inducing the strain by the difference in the coefficients of

thermal expansion upon cooling the sample after annealing. The metal film was then selectively etched and the high-quality spalled silicon films were used to fabricate functional solar cells. The method has been generalized and optimized, including the introduction of flexible handle layers to support and control the initiation of the fracturing rather than the spontaneous spalling of early works. Wafer scale spalled membranes of germanium, nitrides, and III–V compounds have been successfully produced^[113,114] and also the release of free-standing semiconductor membranes containing functional elements and electronic devices and circuits have been demonstrated as a viable route toward flexible electronics.^[115,116] The thickness of the spalled membranes depends on the mechanical properties, stresses, and thicknesses^[113] of both the target crystal, the stressor material and possible handle-layers. For example, for the same materials, there is an approximately linear relationship between the thickness of the stressor and the depth of the fracture plane (see Figure 5b). This enables good control of the spalling process and thicknesses from hundreds of angstroms to hundreds of micrometers have been achieved.^[117] No fundamental barrier seems to hinder spalling of films of only a few nanometers.

Until now, the spalling method has been developed in the context of semiconductors, however, recently, the viability of the method was demonstrated also for oxides.^[15] Epitaxial LAO/STO heterostructures with 70–100 nm LAO top layers were grown by PLD, and the LAO/STO lattice mismatch LAO experiences

tensile epitaxial needed for activating the spalling process. No handle layers were used to direct the fracturing and provide mechanical support of the membrane, which resulted in a combination of vertical and spalling fracturing, leaving a mosaic of micrometer scaled membranes on the sample surface (Figure 5c). As expected for the spalling process, the parallel fracture occurred below the tensile LAO and each membrane contains an LAO/STO interface. Dahm et al.^[16] showed that by pre-patterning of the growth substrate using lithography and ion milling, the lateral locations of cracks can be controlled. This procedure enabled the controlled formation of free-standing LAO/STO micro membranes with sizes from 2 to 20 μm . Also, by mechanical micro-manipulation individual membranes were transferred to silicon substrates and electrical devices were fabricated using lithography.^[16]

3. Emerging Functionalities in Freestanding Perovskite Thin Films

Perovskite oxide thin films present several functional properties that have allowed their usage in sensors, actuators, surface acoustic wave devices, and memory devices to name a few.^[5–7] The continued advancement of oxides in potential applications is however often hampered by the lack of epitaxial integration with important technological platforms such as silicon and flexible materials like PET. Freestanding oxide membranes, on the other hand, provide the possibility to combine oxide perovskite with other materials by means of mechanical transfer (stamping). This possibility has led to significant advances in the field, for example, with demonstration of freestanding $\text{LaAlO}_3/\text{STO}$ membranes on silicon substrates that contain a 2D electron gas exhibiting also superconductivity at low temperature.^[15,16] Another important prospect of freestanding membranes is the emergence of different functionalities when compared with the substrate-clamped counterpart. This section will cover representative seminal works where new functional properties not found in the substrate-supported thin film have arisen.

3.1. Surface-Induced Changes in the Electronic and Structural Properties

Transitioning from an as-grown to a freestanding state will naturally force the membranes to undergo structural changes, for example, due to the large surface to volume ratio. Ji et al.^[11] synthesized high-quality freestanding BiFeO_3 films with MBE using the method of Lu et al.^[12] They discovered that ultrathin freestanding BFO films show a structural transition from rhombohedral-like phase to tetragonal-like phase when the clamping effect of the substrate is removed, see Figure 6a. This effect is especially observed in 3 u.c. thick BFO membranes, where the significant increase of the lattice parameter yielded to a c/a ratio of 1.22 and a polarization of $140 \mu\text{C cm}^{-2}$ in the out-of-plane direction.^[11] This stands in sharp contrast to the bulk rhombohedral BiFeO_3 ,^[118] which only reaches a polarization of $100 \mu\text{C cm}^{-2}$ and c/a ratio of 1. Through first principle calculation, they proposed that the large c/a ratio originates from the displacement of Fe from the centrosymmetric position in the tetragonal phase of ultrathin BFO membranes not clamped by the substrate.^[11]

Enhanced tetragonality was also observed in ultrathin freestanding STO thin films by Chiu et al.^[119] In their work, the authors showed that STO thin films below 10 nm undergo through a transformation from cubic to tetragonal structure when released from the substrate. This phase is characterized by a displacement of Ti atoms from the TiO_6 octahedron center and by the appearance of delocalized electrons. A modification of the electronic and magnetic properties was also observed in other perovskites membranes when released from the substrate. Lu et al. showed that ultrathin freestanding LaMnO_3 thin films display an exotic soft ferromagnetism along both in-plane and out-of plane direction for thicknesses below 4 nm.^[120] This phenomenon, not present in the substrate-supported thin films, is originated by a symmetrical reduction of Mn oxidation state near the membrane's surface, induced by a protonation of the material during the wet releasing process, which reduces the magnetic anisotropy and leads to the appearance of multidirectional soft ferromagnetism. These works show that surface effects in ultrathin perovskite oxide membranes may give rise to functional properties absent in the substrate-supported thin films.

3.2. Enhanced Elasticity and Flexibility

Perovskite oxides in bulk form are usually very brittle and only withstand small tensile strains before fracture.^[121] Because of this, conventional oxide thin films grown epitaxially on bulk crystal substrates are tough and very difficult to manipulate mechanically without causing crystal fracturing. However, when the oxide film is released from its epitaxial host by one of the strategies described in this review, it becomes far more flexible.^[22,30] Indeed, it was shown that single-crystal perovskite membranes can sustain extremely large tensile strain before breaking.^[22,69,30,35,38,122] In particular, Harbola et al. showed that in single-crystal membranes of STO the tensile strain strength can be as high as 6%, almost an order of magnitude more than in bulk form.^[22] A non-monotonic change of the Young modulus in nanometric membranes of STO was also observed, due to a competitive behavior of surface elasticity and strain gradient elasticity.^[23] Moreover, ferroelectric freestanding perovskite thin films display superelasticity and ultraflexibility at the nanoscale, due to a continuous rotation of the polarization direction and to local phase transformations that avoid mechanical failure.^[69,30,35,38,122] More details about this phenomenon and about the effects of strain in freestanding perovskite oxides will be discussed in Section 4 of this work.

3.3. Suppression of Mechanical Interaction with the Substrate

Freestanding oxide thin films are characterized by a suppression of the mechanical interaction with the substrate (i.e., absence of the clamping effect). This effect may be particularly relevant in ferroelectric materials, where the clamping effect controls the movement of ferroelastic domain walls and limits the piezoelectric response.^[123] Bakaul et al. studied the evolution of ferroelectric domain walls in PZT freestanding thin films.^[64] A decrease from two to three orders of magnitude of domain wall velocity was found after the substrate removal. However, this variation does not origin directly from the alteration of the epitaxial

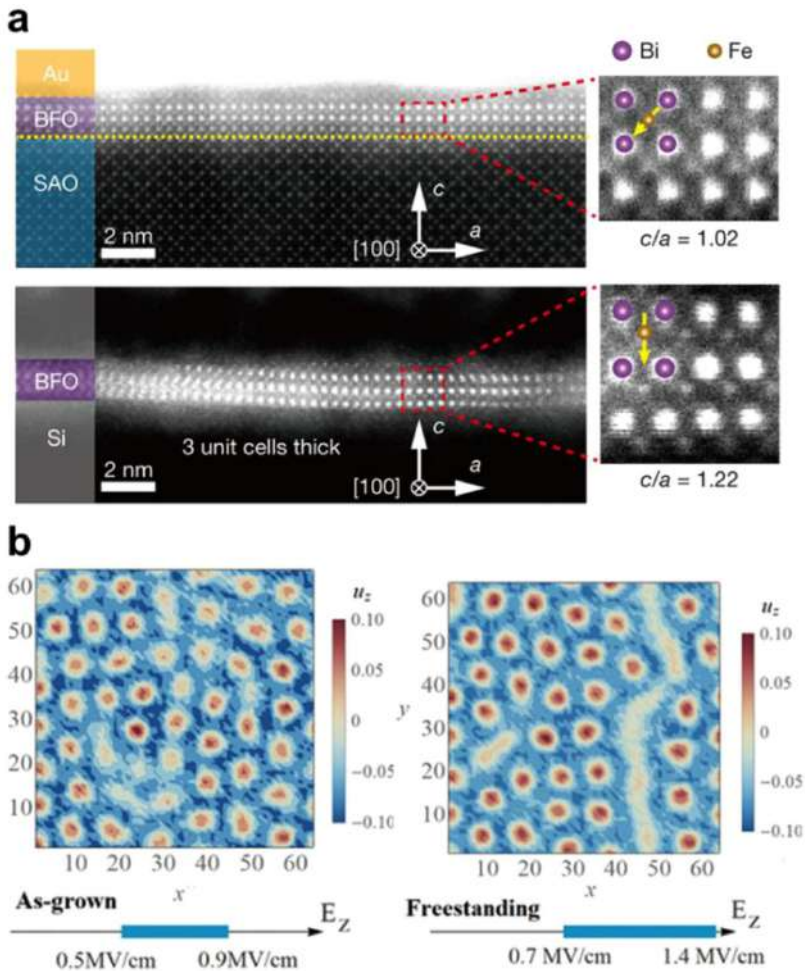


Figure 6. a) Giant out of plane polarization in freestanding BiFeO_3 thin films below 3 u.c. TEM images shows a large tetragonality and a large out of plane displacement of the Fe atoms after the releasing process. Reproduced with permission.^[11] Copyright 2019, Springer Nature. b) Ferroelectric bubble domain in PZT/STO/PZT freestanding membranes. The panel shows the comparison between the out-of-plane polarization component for as grown and freestanding thin films. Reproduced with permission.^[65] Copyright 2020, Wiley-VCH.

landscape, but rather from the formation of mesoscopic ripples, generated to release the compressive strain during the membrane fabrication. On the contrary, Pesquera et al. showed that high-quality freestanding BTO membranes sandwiched between SRO thin films electrodes present lower coercive fields and faster domain dynamics compared to substrate-clamped epitaxial BTO.^[67] The origin of this change of behavior lies in a reduction of the elastic energy needed for the creation of 90° domain boundaries in membranes upon the substrate removal, favoring the polarization switching of the ferroelectric freestanding thin films.^[67]

The possibility of completely detaching the film from the substrate can also give rise to the formation of exotic ferroelectric topologies. Saidur et al. showed that ferroelectric bubble domains

can be stabilized in freestanding PZT/STO/PZT heterostructure membranes.^[65] These type of ferroelectric topological objects are typically seen as a precursor to electrical skyrmions, which have been shown to arise in ferroelectric–dielectric–ferroelectric heterostructures epitaxially clamped to flat oxide surfaces.^[124,125] Comparing the as-grown to the freestanding PZT/STO/PZT system, first principle-based effective Hamiltonian simulations shows that the stress in the free freestanding membranes increases the energy range and the domain size that stabilize the formation of skyrmion bubbles, due to a reduction of the homogeneous strain, see Figure 6b.^[65] Additionally, Li et al. observed a radical transformation of the polarization direction in $\text{PbTiO}_3/\text{STO}$ superlattice with a SRO bottom electrode when released from its substrate.^[126] Interestingly, the variation of the

polarization direction in the superlattice drove the membrane to curl up into microtubes, in order to minimize the overall elastic energy. These results show that the suppression of the mechanical interaction with the substrates may influence the polarization dynamics of ferroelectric perovskite oxides.

3.4. 2D Free-Standing Perovskite Oxides

Finally, it is worth mentioning the last advances in the synthesis of perovskite oxides approaching the 2D limit. Hong et al. found that ultrathin membranes of STO below 5 u.c. undergo through a crystalline to amorphous transition when released from the substrate.^[20] The collapse of the crystalline order was interpreted in the frame of the Berezinskii–Kosterlitz–Thouless transition, which predicts the proliferation of dislocations below a critical thickness, hindering the long-range crystallinity.^[20] Nevertheless, Ji et al. recently showed the possibility of synthesizing single-crystal STO and BiFeO₃ down to 1 unit cell, with a good long range crystallinity observed by TEM.^[111] These results pave the way to the study of interfacial and 2D phenomena in perovskite oxides thin films.^[127]

4. Strain Control in Freestanding Perovskite Oxide Thin Films

The profound interplay between structural and electronic properties is one of the most interesting strategy for discovering and control functionalities in perovskite oxides.^[128–131] Epitaxial perovskite thin films and heterostructures are largely influenced by strain, especially when the thicknesses of the films are only a few unit cells.^[132,133] Indeed, perovskites are well known for their strong coupling between structural distortions and physical properties due to the centrally coordinated octahedra bond flexibility, which allows for a multitude of distortions from the ideal highly symmetric structure.^[5] The traditional method for investigating strain effects is based on the epitaxial growth on lattice-mismatched substrates, which results in the generation of misfit strain in the layers. This method, however, limits the maximum achievable strain before structural relaxation of the layers takes place and hinders a deterministic study of the strain effect on the functional properties.^[134] Moreover, epitaxial growth of thin films usually requires high temperature conditions, favoring the formation of chemical defects (e.g., oxygen vacancies) and cationic interdiffusion with the substrate.^[135] For example, tensile strain reduces the formation energy of oxygen vacancies during growth, which largely modifies the electronic structure and hinders an isolated study of structural effects on the functional properties.^[136–138] Additionally, the presence of the oxide substrate, order of magnitudes thicker than the thin film, may impede the measurements of some functionalities, such as the probe of in-plane ionic conductivity in oxygen ionic conductors.^[139] For overcoming these limitations, new strategies must be pursued.

Freestanding thin films are emerging as a new platform for investigating extremely large and tunable strain states in perovskite oxides. The most common strategies for controlling lattice strain in thin membranes are 1) multilayer epitaxy of freestanding thin

films, 2) mechanical bending, and 3) mechanical stretching (see Figure 7). In the following, we review these methods, highlighting the main advantages and drawbacks.

4.1. Multilayer Epitaxy in Freestanding Films

Epitaxial strain in multilayer membranes was recently proposed by Pesquera et al. as an alternative method for controlling the strain state of oxide thin films by tuning the lattice mismatch of the multilayers' components.^[67] In a single material membrane, the misfit strain imposed by the substrate vanishes in the release process and the layer tends to adopt the bulk equilibrium lattice parameter. In a multilayer epitaxial membrane, the releasing procedure will remove the substrate constraint but the lattice misfit among the layers will determine a residual strain state in the films. Considering the simple case of an oxide thin film epitaxially sandwiched between two symmetrical layers, the lattice mismatch between the components will drive a force with opposite directions on the internal (P) and the external layers (−P/2), see Figure 7a. Considering a planar stress condition and no bending of the trilayer membrane, the equilibrium in-plane strain of the internal layer can be calculated as^[140]

$$\epsilon_i = \frac{u_M}{1 + \frac{t_i}{2t_e} \cdot \frac{M_i}{M_e}} \quad (3)$$

where t_i and M_i are the thickness and biaxial modulus of the internal layer, t_e and M_e the thickness and biaxial modulus of the external ones, and u_m the misfit strain between the in-plane lattice parameters of the internal and external thin films ($u_m = \frac{a_i - a_e}{a_i}$). Figure 7b shows the equilibrium in-plane strain of a trilayer membrane calculated as a function of the layers thickness ratio for different bulk misfit strains. The results show that the in-plane strain can be progressively tuned by varying the thickness of the external layers, with a trend that depends on the mechanical properties of the layers. Using this approach, Pesquera et al. achieved the control of the tetragonality of compressive strained ferroelectric BTO sandwiched between Ba_{1-x}Sr_xRuO₃ electrodes.^[67] Their results show that a deterministic control of the Curie temperature, remanent polarization, and coercive field can be obtained in BTO through compressive strain.

Overall, the main advantage of this method is the possibility of continuously controlling the strain state of oxides by varying the thickness or the composition of the layers. Moreover, a facile measurement of out of plane electrical properties can be achieved by depositing metallic oxides as external layers. Nevertheless, the driving force for the generation of in-plane strain remains the lattice mismatch between the layers, which bears the typical disadvantages of traditional substrate-induced misfit strain and limits its application to oxides that can be coherently grown on each other.

4.2. Mechanical Bending

Mechanical bending is the most common way employed in literature to actively control the strain in oxide thin film.^[141] Two main types of strategies were developed: 1) bending of layers supported

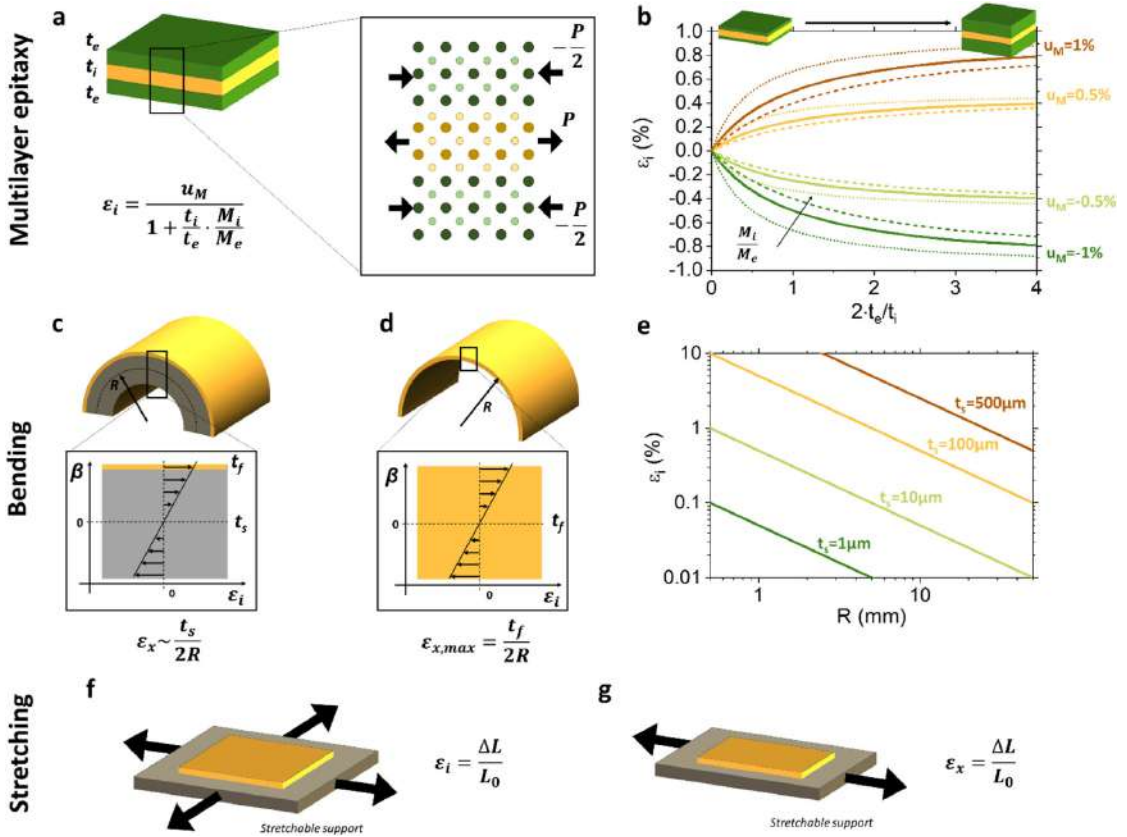


Figure 7. Schematic representation of the main strategies for strain tuning in oxide membranes. a) Sketch of a trilayer epitaxial membrane displaying strain due to lattice mismatch between the layers. b) Evolution of the strain in a symmetrical trilayer as a function of the layers thicknesses, for different misfit strains (u_M) and elastic Moduli ratios (M_i/M_e). Schematic representation of the distribution of strain states in a c) supported and d) self-standing membrane subjected to mechanical bending. e) Maximum bending strain calculated for a supported membrane under different radius of curvature (R) and for different substrates thicknesses (t_s). Sketch of the f) biaxial and g) uniaxial strain achievable in a membrane under mechanical stretching.

on a flexible or curved substrate (Figure 7c) and 2) bending of self-standing thin films (Figure 7d). In both cases, bending generates an in-plane strain, ϵ_x , along the bending direction proportional to the distance, b , from the neutral plane:

$$\epsilon_x = \frac{\beta}{R} \quad (4)$$

where R is the radius of curvature of neutral plane. Tensile strain develops for a convex bending mode while compressive strain for a concave one. In a multicomponent system, the neutral plane position depends on the thicknesses (t_i) and the mechanical properties of the constituent layers (with Young's modulus E_i). The general expression for a multilayer structure with n components is^[142]

$$\beta = \frac{\sum_{i=1}^n E_i t_i ((\sum_{j=1}^n t_j) - t_i/2)}{\sum_{i=1}^n E_i t_i} \quad (5)$$

In the case of a single oxide membrane supported on a thick flexible substrate ($t_s \gg t_f$, where t_s and t_f are the thicknesses of the support and the film, respectively), the strain in the thin film can be approximated as:

$$\epsilon_x = \frac{t_s}{2R} \quad (6)$$

Along the other directions (i.e., out of plane and perpendicular to the bending direction) a biaxial strain with opposite sign of ϵ_x develop, proportional to the Poisson coefficient.^[78] Figure 7e shows the expected strain in a supported-membrane as a function of the bending radius for different substrate thicknesses. One can note that larger strains are achievable by choosing thicker substrates but the ultimate strain will largely depend on the fracture point of the support, that is, the compressive and tensile strength.^[93,142] For example, muscovite mica substrates, one of the most promising support for flexible electronics,^[93]

can withstand a tensile strain up to $\approx 0.3\%$ upon bending (for thickness between 15 and 85 μm).^[143]

The mechanical bending strategy has been largely adopted for the study of the strain effect on transport and magnetic properties of perovskite membranes. Liu et al. found that the magnetic properties of SRO thin films deposited on muscovite mica are very sensitive to mechanical strain.^[101] Upon bending, they observed a large variation of the Curie temperature, saturated magnetic moment, and coercive field. An increase of saturated moment from 1.2 to 3.2 μB per Ru was measured for a compression strain of -0.3% and was attributed to a spin state transition from low to high spin taking place under compressive in-plane strain. Li et al. also observed a significant effect of bending strain on the electrical resistivity of SRO thin films.^[144] In their work, a decrease (increase) of resistivity of -26.05% (1.75%) was observed for a compressive strain of -0.25% (tensile, $+0.25\%$). The decrease of resistivity upon compression originates from an increase of the Ru—O—Ru bond angle and by a rise of the density of state near the Fermi level, as probed by Raman and X-ray photoelectron spectroscopy. LSMO thin films are also known to give rise to a variation of resistivity^[106] and magnetization^[145,146] upon mechanical bending. In particular, Yao et al. showed that outward bending in LaMnO_3 thin films generates a significant modification of the oxygen octahedra and Mn—O—Mn bonds, which induces a larger overlap between the Mn and O orbitals and a significant enhancement of saturation magnetization (92%) and of Curie temperature (123–130 K).^[146] Similarly, strain effects on the electrical resistivity have been reported also for other perovskites oxides such as SrVO_3 and $\text{BaNb}_{0.5}\text{Ti}_{0.5}\text{O}_3$.^[103,105] It is also worth noting that bending strain may affect other functional properties of perovskite oxides thin films, such as the photoluminescence intensity of Pr-doped $\text{Ba}_{0.85}\text{Ca}_{0.15}\text{Ti}_{0.9}\text{Zr}_{0.1}\text{O}_3$ thin films.^[147]

The opportunity of dynamically tuning of ferroelectric and dielectric properties in ferroelectric supported thin films through mechanical bending was demonstrated by Ko et al.^[143] In their work, the authors showed that BTO thin films on Mica substrates undergo a transformation from ferroelectric tetragonal to paraelectric cubic structure for both inward and outward bending mode, hindering the out of plane ferroelectric polarization. The results were used to build a mechanically controlled ferroelectric transistor, where the conductivity of the top electrode (Al-doped ZnO) can be modulated by the variation of ferroelectric polarization of the underlying BTO, controlled through the bending mechanism. Zhao et al. explored the multiferroic properties of (Fe)/BTO membranes on PDMS substrate during mechanical bending.^[33] They found that the compressive strain enhances the ferromagnetic resonance of the Fe layer along the out-of-plane direction, due to a variation of the electric field at the Fe₂/BTO interface tuned by the rotation of ferroelectric domains.

Mechanical bending also introduces a strain gradient in the structure, equal to $\frac{d\epsilon}{d\beta} = 1/R$ (see ⁷c). In perovskite oxides, strain gradients can give rise to the generation of electric fields, through the flexoelectric effect.^[48] Guo et al. showed that ferroelectric BiFeO_3 membranes on PDMS withstand significant strain gradients during the mechanical bending, which can be used to modulate the photovoltage and photocurrent generated in the layers.^[48] Jiang et al. also show the flexoelectric control of the photoconductivity in $\text{LaFeO}_3/\text{LaNiO}_3$ heterostructures on muscovite mica,

where a continuous change of short-circuit current density upon bending was reported.^[148]

In the case of a self-standing membrane (Figure 7d), the position of the neutral plane will be equal to half its thickness ($b_f = t_f/2$, where t_f is the thicknesses of the film) and the strain in the outer/inner surfaces can be written as: $\epsilon_x = t_f/2R$. Clearly, compared to the substrate supported membranes, the radius of curvature needs to be significant smaller for achieving similar strains, which can be accomplished by the use of nanomanipulators^[35] or by other external stimuli^[69] in scanning or transmission electron microscopies. As commented in Section 3.2, the study of ferroelectric self-sustained membranes subjected to large bending strain showed that these ceramic materials, generally considered brittle in bulk, possesses superelasticity and ultraflexibility at the nanoscale.^[69,30,35,38,122] Dong et al. first showed that single-crystalline ferroelectric BTO membrane can withstand a remarkable tensile strain of 10% without breaking.^[30] The origin of this superelasticity was found to lie in a continuous rotation of the polarization direction in BTO membranes, which efficiently avoid mismatch stress and delay the membrane failure. Peng et al. found also that multiferroic BiFeO_3 membranes displays superelasticity, due to a reversible rhombohedral–tetragonal phase transition taking place in the most strained regions.^[35] Such superior flexibility can also be observed in periodic wrinkles that can be formed during the membranes releasing and transfer process.^[122]

Overall, mechanical bending emerges as a reliable strategy to investigate strain effects on perovskite oxide membrane. The ability to actively control the strain state in the same sample by controlling the radius of curvature allows a systematic and precise study of the variation of functional properties. The limitations of this method for substrate-supported thin films mainly arise from the limited strain that can be imposed without affecting the mechanical properties of the support, while for self-standing membranes from the requirements of nanomanipulators needed to achieve large strain states.

4.3. Mechanical Stretching

Mechanical stretching of single-crystal perovskite membranes is emerging as a new fascinating strategy to study the functional properties of perovskite oxides under tensile strain. This technique is based on the deposition of single-crystal thin films on a sacrificial layer and the subsequent transfer of the membrane on a flexible polymer (see Section 2.1.2), such as PI^[55,52] or PET.^[25] The support can then be stretched in a biaxial or uniaxial mode by micro-manipulators (see Figure 7f,g, respectively), producing a tensile strain in the structure equal to $\epsilon_1 = \Delta L/L_0$, where ΔL and L_0 are the elongation and the initial length, respectively.^[149] The adhesion between the thick polymer and the nanometric membrane allows the transfer of the strain state from the support to the thin film. As commented in Section 3.3, it was shown that freestanding perovskite thin films can withstand extremely large tensile strain before breaking, allowing the investigation of strain states not achievable in bulk and substrate-supported perovskite oxides.^[22,23,69,30,35,38,122]

The mechanical stretching method was first used by Hong et al. to study the magnetotransport properties of

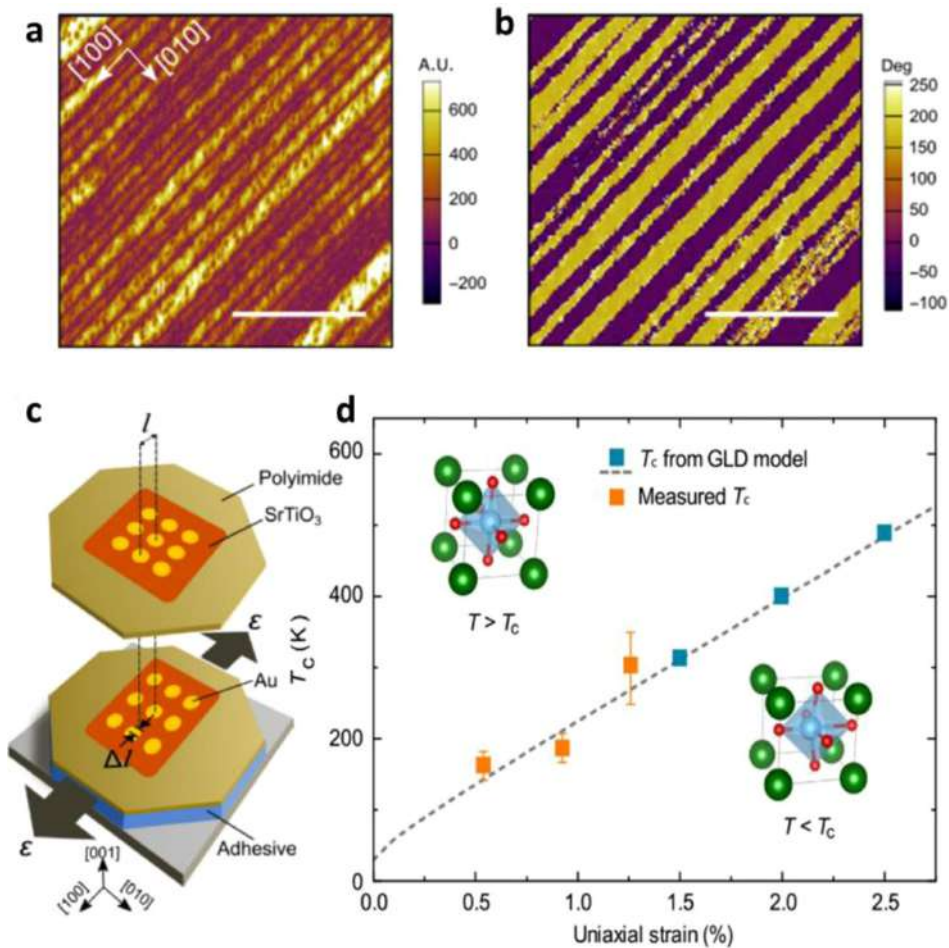


Figure 8. Strain-induced ferroelectricity in STO membranes. Piezoelectric force microscopy a) amplitude and b) phase measured for STO membranes under 2% uniaxial strain, showing the appearance of in-plane ferroelectric domains. c) Schematic of the uniaxial strain application on STO membranes. d) Ferroelectric transition temperature (T_c) measured in STO membranes as a function of uniaxial strain and predicted by numerical models. Reproduced under terms of the CC-BY license.^[52] Copyright 2020, Springer Nature.

$\text{La}_{0.7}\text{Ca}_{0.3}\text{MnO}_3$ under extreme uniaxial and biaxial tensile strain (8% and 5%, respectively).^[55] They found that strain promoted a transition from ferromagnetic metal to antiferromagnetic insulator, evidenced by orders of magnitude increase of resistivity at low temperature. The antiferromagnetic state is characterized by a charge/orbital ordering consisting in alternating Jahn–Teller-distorted Mn^{3+}O_6 octahedra and Mn^{4+}O_6 , and can be quenched by the application of magnetic fields. Mechanical stretching was also employed for controlling the domain orientation in ferroelectric PbTiO_3 membranes and to induce room temperature ferroelectricity in STO membranes.^[25,52] In particular, Xu et al. showed that tensile strain can linearly increase the ferroelectric transition temperature of STO, giving rise to the creation of in-plane polarized 180° domain structure aligned along the strain direction, see **Figure 8**.^[52] The

ability to manipulate the polarization direction through strain was also exploited by Zang et al. to engineer the interfacial thermal resistance in self standing Al/BiFeO_3 membranes.^[51] In their work, the variation of polarization direction in ferroelectric BiFeO_3 through strain gave rise to a redistribution of the charge at the interface and eventually, through electron–phonon coupling, to a modification of the interface thermal resistance.

Overall, mechanical stretching appears as a promising method for tuning tensile strain of perovskite oxide membrane. The main advantage of this strategy is the possibility of controlling the strain state on the very same sample and the enormous strain that can be achieved. Nevertheless, due to the flexibility of the stretchable support, only tensile strain can be applied, which hinders the study of compressive strain states.

5. Outlook

Oxide-based freestanding membranes have the potentials to become the preferred candidates to next-generation oxide materials coupling the high selectivity to high functionality of these materials. However, it is not expected that the uptake of oxide-based freestanding membranes may occur in the short term, as novel fabrication, releasing and transferring processes needed to be further developed to take the full advantages of the oxides. Several approaches have been reported in this review paper for synthesizing, transferring, and measuring the freestanding oxide properties. What is still needed in the short term is the understanding of how to transfer large defect-free membrane size. Freestanding oxides show already unique properties and hence have significant potential for further new discoveries making them both interesting and challenging research subjects. Continuous development of operando probes and their combination as well as theoretical tools will help addressing the urgent questions regarding the relation between the freestanding oxide chemistry and their properties. Stacking, twisting, gate-modulating, and optically exciting have opened up a new field in 2D materials with promising ways in which unexpected strong correlations, topological, and symmetry-induced phenomena have been discovered. This, however, has never been tried before in oxide freestanding membranes and can lead to progress in synthesis, experimental tools, and potential new properties as well as applications of these materials. Finally, the rich science revealed so far in 2D moiré superlattice solids can be expected to remain an important source of stimulating scientific discoveries in freestanding oxide membranes. These directions could lead to new science, engineering, and application discoveries in atomically designed freestanding oxide materials.

Acknowledgements

F.M.C., D.V.C., and N.P. acknowledge the funding from Villum Fonden for the NEED project (00027993). Y.L. acknowledges the support by the National Natural Science Foundation of China (Grant No. 11704292), and gratefully acknowledges financial support from China Scholarship Council (Grant No. 201908420153). F.T. acknowledges support by research grant 37338 (SANSIT) from Villum Fonden. N.P. acknowledges the funding from the Danish Council for Independent Research Technology and Production Sciences for the DFF Research Project 3 PILOT (Grant No. 00069B) and the Novo Nordisk Foundation “Challenge programme 2021 – Smart Nanomaterials for Applications in Life-Science” BIO-MAG (Grant No. NNF21OC0066526).

Conflict of Interest

The authors declare no conflict of interest.

Keywords

freestanding thin films, lattice strain, perovskite oxides, sacrificial layers, ultrathin membranes

Received: February 28, 2022

Revised: May 9, 2022

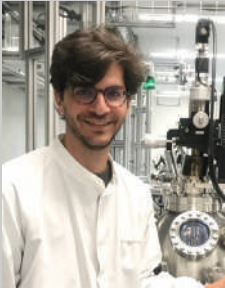
Published online:

- [1] R. P. Feynman, *Eng. Sci.* **1960**, 23, 22.
- [2] A. Chaves, J. G. Azadani, H. Alsalmán, D. R. da Costa, R. Frisenda, A. J. Chaves, S. H. Song, Y. D. Kim, D. He, J. Zhou, A. Castellanos-Gomez, F. M. Peeters, Z. Liu, C. L. Hinkle, S. H. Oh, P. D. Ye, S. J. Koester, Y. H. Lee, P. Avouris, X. Wang, T. Low, *npj 2D Mater. Appl.* **2020**, 4, 29.
- [3] M. Zeng, Y. Xiao, J. Liu, K. Yang, L. Fu, *Chem. Rev.* **2018**, 118, 6236.
- [4] K. T. Faber, T. Asefa, M. Backhaus-Ricoult, R. Brow, J. Y. Chan, S. Dillon, W. G. Fahrenholtz, M. W. Finnis, J. E. Garay, R. E. García, Y. Gogotsi, S. M. Haile, J. Halloran, J. Hu, L. Huang, S. D. Jacobsen, E. Lara-Curzio, J. LeBeau, W. E. Lee, C. G. Levi, I. Levin, J. A. Lewis, D. M. Lipkin, K. Lu, J. Luo, J. P. Maria, L. W. Martin, S. Martin, G. Messing, A. Navrotsky, et al., *J. Am. Ceram. Soc.* **2017**, 100, 1777.
- [5] D. V. Christensen, F. Trier, W. Niu, Y. Gan, Y. Zhang, T. S. Jespersen, Y. Chen, N. Pryds, *Adv. Mater. Interfaces* **2019**, 6, 1900772.
- [6] A. Tarancón, N. Pryds, *Adv. Mater. Interfaces* **2019**, 6, 1900990.
- [7] M. Coll, J. Fontcuberta, M. Althammer, M. Bibes, H. Boschker, A. Calleja, G. Cheng, M. Cuoco, R. Dittmann, B. Dkhil, I. El Baggari, M. Fanciulli, I. Fina, E. Fortunato, C. Frontera, S. Fujita, V. Garcia, S. T. B. Goennenwein, C. G. Granqvist, J. Grollier, R. Gross, A. Hagfeldt, G. Herranz, K. Hono, E. Houwman, M. Huijben, A. Kalaboukhov, D. J. Keeble, G. Koster, L. F. Kourkoutis, et al., *Appl. Surf. Sci.* **2019**, 482, 1.
- [8] S. A. Chambers, *Surf. Sci.* **2011**, 605, 1133.
- [9] M. Bruel, *Nucl. Instrum. Methods Phys. Res., Sect. B* **1996**, 108, 313.
- [10] W. S. Wong, T. Sands, N. W. Cheung, *Appl. Phys. Lett.* **1998**, 72, 599.
- [11] D. Ji, S. Cai, T. R. Paudel, H. Sun, C. Zhang, L. Han, Y. Wei, Y. Zang, M. Gu, Y. Zhang, W. Gao, H. Huan, W. Guo, D. Wu, Z. Gu, E. Y. Tsybal, P. Wang, Y. Nie, X. Pan, *Nature* **2019**, 570, 87.
- [12] D. Lu, D. J. Baek, S. S. Hong, L. F. Kourkoutis, Y. Hikita, H. Y. Hwang, *Nat. Mater.* **2016**, 15, 1255.
- [13] D. Lu, S. Crossley, R. Xu, Y. Hikita, H. Y. Hwang, *Nano Lett.* **2019**, 19, 3999.
- [14] H. S. Kum, H. Lee, S. Kim, S. Lindemann, W. Kong, K. Qiao, P. Chen, J. Irwin, J. H. Lee, S. Xie, S. Subramanian, J. Shim, S. H. Bae, C. Choi, L. Ranno, S. Seo, S. Lee, J. Bauer, H. Li, K. Lee, J. A. Robinson, C. A. Ross, D. G. Schlom, M. S. Rzchowski, C. B. Eom, J. Kim, *Nature* **2020**, 578, 75.
- [15] A. Sambri, M. Scuderi, A. Guarino, E. Di Gennaro, R. Erlandsen, R. T. Dahm, A. V. Björklig, D. V. Christensen, R. Di Capua, B. D. Ventura, U. S. di Uccio, S. Mirabella, G. Nicotra, C. Spinella, T. S. Jespersen, F. M. Granozio, *Adv. Funct. Mater.* **2020**, 30, 1909964.
- [16] R. T. Dahm, R. Erlandsen, F. Trier, A. Sambri, E. Di Gennaro, A. Guarino, L. Stampfer, D. V. Christensen, F. M. Granozio, T. S. Jespersen, *ACS Appl. Mater. Interfaces* **2021**, 13, 12341.
- [17] S. J. Skinner, J. A. Kilner, *Mater. Today* **2003**, 6, 30.
- [18] Y. Zhang, C. Ma, X. Lu, M. Liu, *Mater. Horiz.* **2019**, 6, 911.
- [19] D. J. Baek, D. Lu, Y. Hikita, H. Y. Hwang, L. F. Kourkoutis, *ACS Appl. Mater. Interfaces* **2017**, 9, 54.
- [20] S. S. Hong, J. H. Yu, D. Lu, A. F. Marshall, Y. Hikita, Y. Cui, H. Y. Hwang, *Sci. Adv.* **2017**, 3, eaao5173.
- [21] D. Davidovikj, D. J. Groenendijk, A. M. R. V. L. Monteiro, A. Dijkhoff, D. Afanasiev, M. Šiškins, M. Lee, Y. Huang, E. van Heumen, H. S. J. van der Zant, A. D. Caviglia, P. G. Steeneken, *Commun. Phys.* **2020**, 3, 163.
- [22] V. Harbola, R. Xu, S. Crossley, P. Singh, H. Y. Hwang, *Appl. Phys. Lett.* **2021**, 119, 053102.
- [23] V. Harbola, S. Crossley, S. S. Hong, D. Lu, Y. A. Birkhölzer, Y. Hikita, H. Y. Hwang, *Nano Lett.* **2021**, 21, 2470.
- [24] J. A. Alonso, I. Rasines, J. L. Soubeyroux, *Inorg. Chem.* **1990**, 29, 4768.
- [25] L. Han, Y. Fang, Y. Zhao, Y. Zang, Z. Gu, Y. Nie, X. Pan, *Adv. Mater. Interfaces* **2020**, 7, 1901604.

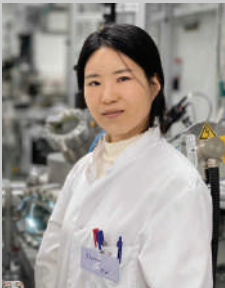
- [26] S. Cai, Y. Lun, D. Ji, L. Han, C. Guo, Y. Zang, S. Gao, Y. Wei, M. Gu, C. Zhang, Z. Gu, X. Wang, C. Addiego, D. Fang, Y. Nie, J. Hong, P. Wang, X. Pan, **2020**, arXiv:2009.03177.
- [27] P. T. P. Le, J. E. ten Elshof, G. Koster, *Sci. Rep.* **2021**, *11*, 12435.
- [28] Z. Lu, J. Liu, J. Feng, X. Zheng, L. H. Yang, C. Ge, K. J. Jin, Z. Wang, R. W. Li, *APL Mater.* **2020**, *8*, 051105.
- [29] H. Wang, L. Shen, T. Duan, C. Ma, C. Cao, C. Jiang, X. Lu, H. Sun, M. Liu, *ACS Appl. Mater. Interfaces* **2019**, *11*, 22677.
- [30] G. Dong, S. Li, M. Yao, Z. Zhou, Y. Q. Zhang, X. Han, Z. Luo, J. Yao, B. Peng, Z. Hu, H. Huang, T. Jia, J. Li, W. Ren, Z. G. Ye, X. Ding, J. Sun, C. W. Nan, L. Q. Chen, J. Li, M. Liu, *Science* **2019**, *366*, 475.
- [31] K. Gu, T. Katayama, S. Yasui, A. Chikamatsu, S. Yasuhara, M. Itoh, T. Hasegawa, *Adv. Funct. Mater.* **2020**, *30*, 2001236.
- [32] R. Li, Y. Xu, J. Song, P. Wang, C. Li, D. Wu, *Appl. Phys. Lett.* **2020**, *116*, 222904.
- [33] Y. Zhao, R. Peng, Y. Guo, Z. Liu, Y. Dong, S. Zhao, Y. Li, G. Dong, Y. Hu, J. Zhang, Y. Peng, T. Yang, B. Tian, Y. Zhao, Z. Zhou, Z. Jiang, Z. Luo, M. Liu, *Adv. Funct. Mater.* **2021**, *31*, 2009376.
- [34] T. Wang, R. C. Peng, W. Peng, G. Dong, C. Zhou, S. Yang, Z. Zhou, M. Liu, *Adv. Funct. Mater.* **2021**, *32*, 2108496.
- [35] B. Peng, R. C. Peng, Y. Q. Zhang, G. Dong, Z. Zhou, Y. Zhou, T. Li, Z. Liu, Z. Luo, S. Wang, Y. Xia, R. Qiu, X. Cheng, F. Xue, Z. Hu, W. Ren, Z. G. Ye, L. Q. Chen, Z. Shan, T. Min, M. Liu, *Sci. Adv.* **2020**, *6*, eaba5847.
- [36] Z. Zhao, A. Abdelsamie, R. Guo, S. Shi, J. Zhao, W. Lin, K. Sun, J. Wang, J. Wang, X. Yan, J. Chen, *Nano Res.* **2021**, *15*, 2682.
- [37] B. Wang, Y. Wu, X. Chen, Q. Han, Y. Chen, H. Wei, B. Cao, *Chem. Phys. Lett.* **2022**, *787*, 139207.
- [38] C. Jin, Y. Zhu, X. Li, F. An, W. Han, Q. Liu, S. Hu, Y. Ji, Z. Xu, S. Hu, M. Ye, G. Zhong, M. Gu, L. Chen, *Adv. Sci.* **2021**, *8*, 2102178.
- [39] S. Shrestha, M. Coile, M. Zhu, M. Sourji, J. Kim, R. Pandey, J. W. Brill, J. Hwang, J. W. Kim, A. Seo, *ACS Appl. Nano Mater.* **2020**, *3*, 6310.
- [40] F. An, K. Qu, G. Zhong, Y. Dong, W. Ming, M. Zi, Z. Liu, Y. Wang, B. Qi, Z. Ding, J. Xu, Z. Luo, X. Gao, S. Xie, P. Gao, J. Li, *Adv. Funct. Mater.* **2020**, *30*, 2003495.
- [41] W. Hou, M. Yao, R. Qiu, Z. Wang, Z. Zhou, K. Shi, J. Pan, M. Liu, J. Hu, *J. Alloys Compd.* **2021**, *887*, 161470.
- [42] B. Zhang, C. Yun, J. L. MacManus-Driscoll, *Nano-Micro Lett.* **2021**, *13*, 39.
- [43] J. Park, J. H. Shin, K. Song, Y. J. Kim, H. B. Jang, H. Lee, H. S. Sim, C. H. Yang, *Appl. Phys. Lett.* **2020**, *116*, 022401.
- [44] D. J. Baek, D. Lu, Y. Hikita, H. Y. Hwang, L. F. Kourkoutis, *APL Mater.* **2017**, *5*, 096108.
- [45] Z. D. Luo, J. J. P. Peters, A. M. Sanchez, M. Alexe, *ACS Appl. Mater. Interfaces* **2019**, *11*, 23313.
- [46] Z. Chen, B. Y. Wang, B. H. Goodge, D. Lu, S. S. Hong, D. Li, L. F. Kourkoutis, Y. Hikita, H. Y. Hwang, *Phys. Rev. Mater.* **2019**, *3*, 060801(R).
- [47] C. Jin, Y. Zhu, W. Han, Q. Liu, S. Hu, Y. Ji, Z. Xu, S. Hu, M. Ye, L. Chen, *Appl. Phys. Lett.* **2020**, *117*, 252902.
- [48] R. Guo, L. You, W. Lin, A. Abdelsamie, X. Shu, G. Zhou, S. Chen, L. Liu, X. Yan, J. Wang, J. Chen, *Nat. Commun.* **2020**, *11*, 2571.
- [49] G. Zhong, F. An, K. Qu, Y. Dong, Z. Yang, L. Dai, S. Xie, R. Huang, Z. Luo, J. Li, *Small* **2022**, *18*, 2104213.
- [50] H. Y. Sun, C. C. Zhang, J. M. Song, J. H. Gu, T. W. Zhang, Y. P. Zang, Y. F. Li, Z. B. Gu, P. Wang, Y. F. Nie, *Thin Solid Films* **2020**, *697*, 137815.
- [51] Y. Zang, C. Di, Z. Geng, X. Yan, D. Ji, N. Zheng, X. Jiang, H. Fu, J. Wang, W. Guo, H. Sun, L. Han, Y. Zhou, Z. Gu, D. Kong, H. Aramberri, C. Cazorla, F. Iñiguez, R. Rurali, L. Chen, J. Zhou, D. Wu, M. Lu, Y. Nie, Y. Chen, X. Pan, *Adv. Mater.* **2021**, *34*, 2105778.
- [52] R. Xu, J. Huang, E. S. Barnard, S. S. Hong, P. Singh, E. K. Wong, T. Jansen, V. Harbola, J. Xiao, B. Y. Wang, S. Crossley, D. Lu, S. Liu, H. Y. Hwang, *Nat. Commun.* **2020**, *11*, 3141.
- [53] Y.-T. Shao, S. Das, Z. Hong, R. Xu, S. Chandrika, F. Gómez-Ortiz, P. García-Fernández, L.-Q. Chen, H. Hwang, J. Junquera, L. Martin, R. Ramesh, D. Muller, *Microsc. Microanal.* **2021**, *27*, 348.
- [54] Z. Lu, Y. Yang, L. Wen, J. Feng, B. Lao, X. Zheng, S. Li, K. Zhao, B. Cao, Z. Ren, D. Song, H. Du, Y. Guo, Z. Zhong, X. Hao, Z. Wang, R.-W. Li, *npj Flexible Electron.* **2021**, *6*, 9.
- [55] S. S. Hong, M. Gu, M. Verma, V. Harbola, B. Y. Wang, D. Lu, A. Vailonias, Y. Hikita, R. Pentcheva, J. M. Rondinelli, H. Y. Hwang, *Science* **2020**, *368*, 71.
- [56] P. Singh, A. Swartz, D. Lu, S. S. Hong, K. Lee, A. F. Marshall, K. Nishio, Y. Hikita, H. Y. Hwang, *ACS Appl. Electron. Mater.* **2019**, *1*, 1269.
- [57] A. K. Prodjosantoso, B. J. Kennedy, B. A. Hunter, *Aust. J. Chem.* **2000**, *53*, 195.
- [58] D. Li, C. Adamo, B. Y. Wang, H. Yoon, Z. Chen, S. S. Hong, D. Lu, Y. Cui, Y. Hikita, H. Y. Hwang, *Nano Lett.* **2021**, *21*, 4454.
- [59] J. W. Bullard, H. M. Jennings, R. A. Livingston, A. Nonat, G. W. Scherer, J. S. Schweitzer, K. L. Scrivener, J. J. Thomas, *Cem. Concr. Res.* **2011**, *41*, 1208.
- [60] J. Shin, V. B. Nascimento, G. Geneste, J. Rundgren, E. W. Plummer, B. Dkhil, S. V. Kalinin, A. P. Baddorf, *Nano Lett.* **2009**, *9*, 3720.
- [61] X. Li, Y. Bai, B. C. Wang, Y. J. Su, *J. Appl. Phys.* **2015**, *118*, 094104.
- [62] S. R. Bakaul, C. R. Serrao, M. Lee, C. W. Yeung, A. Sarker, S. L. Hsu, A. K. Yadav, L. Dedon, L. You, A. I. Khan, J. D. Clarkson, C. Hu, R. Ramesh, S. Salahuddin, *Nat. Commun.* **2016**, *7*, 10547.
- [63] S. R. Bakaul, C. R. Serrao, O. Lee, Z. Lu, A. Yadav, C. Carraro, R. Maboudian, R. Ramesh, S. Salahuddin, *Adv. Mater.* **2017**, *29*, 1605699.
- [64] S. R. Bakaul, J. Kim, S. Hong, M. J. Cherukara, T. Zhou, L. Stan, C. R. Serrao, S. Salahuddin, A. K. Petford-Long, D. D. Fong, M. V. Holt, *Adv. Mater.* **2020**, *32*, 1907036.
- [65] S. R. Bakaul, S. Prokhorenko, Q. Zhang, Y. Nahas, Y. Hu, A. Petford-Long, L. Bellaiche, N. Valanoor, *Adv. Mater.* **2021**, *33*, 2105432.
- [66] S. R. Bakaul, *AIP Adv.* **2021**, *11*, 115310.
- [67] D. Pesquera, E. Parsonnet, A. Qualls, R. Xu, A. J. Gubser, J. Kim, Y. Jiang, G. Velarde, Y. L. Huang, H. Y. Hwang, R. Ramesh, L. W. Martin, *Adv. Mater.* **2020**, *32*, 2003780.
- [68] L. Shen, L. Wu, Q. Sheng, C. Ma, Y. Zhang, L. Lu, J. Ma, J. Ma, J. Bian, Y. Yang, A. Chen, X. Lu, M. Liu, H. Wang, C. L. Jia, *Adv. Mater.* **2017**, *29*, 1702411.
- [69] H. Elangovan, M. Barzilay, S. Seremi, N. Cohen, Y. Jiang, L. W. Martin, Y. Ivry, *ACS Nano* **2020**, *14*, 5053.
- [70] D. Pesquera, E. Khestanova, M. Ghidini, S. Zhang, A. P. Rooney, F. Maccherozzi, P. Riego, S. Farokhipoor, J. Kim, X. Moya, M. E. Vickers, N. A. Stelmashenko, S. J. Haigh, S. S. Dhesi, N. D. Mathur, *Nat. Commun.* **2020**, *11*, 3190.
- [71] K. Eom, M. Yu, J. Seo, D. Yang, H. Lee, J. W. Lee, P. Irvin, S. H. Oh, J. Levy, C. B. Eom, *Sci. Adv.* **2021**, *7*, eabh1284.
- [72] Y. Bourlier, B. Bérimi, M. Frégnaux, A. Fouchet, D. Aureau, Y. Dumont, *ACS Appl. Mater. Interfaces* **2020**, *12*, 8466.
- [73] N. Wiberg, E. Wiberg, A. Holleman, *Lehrbuch Der Anorganischen Chemie*, Walter de Gruyter GmbH & Co KG, location, Berlin **1995**.
- [74] Y. W. Chang, P. C. Wu, J. B. Yi, Y. C. Liu, Y. Chou, Y. C. Chou, J. C. Yang, *Nanoscale Res. Lett.* **2020**, *15*, 172.
- [75] C. C. Chiu, Y. W. Chang, Y. C. Shao, Y. C. Liu, J. M. Lee, S. W. Huang, W. Yang, J. Guo, F. M. F. de Groot, J. C. Yang, Y. De Chuang, *Sci. Rep.* **2021**, *11*, 5250.
- [76] H. Peng, N. Lu, S. Yang, Y. Lyu, Z. Liu, Y. Bu, S. Shen, M. Li, Z. Li, L. Gao, S. Lu, M. Wang, H. Cao, H. Zhou, P. Gao, H. Chen, P. Yu, *Adv. Funct. Mater.* **2022**, <https://doi.org/10.1002/adfm.202111907>
- [77] R. Takahashi, M. Lippmaa, *ACS Appl. Mater. Interfaces* **2020**, *12*, 25042.
- [78] Y. Zhang, L. Shen, M. Liu, X. Li, X. Lu, L. Lu, C. Ma, C. You, A. Chen, C. Huang, L. Chen, M. Alexe, C. L. Jia, *ACS Nano* **2017**, *11*, 8002.

- [79] D. Weber, R. Vofely, Y. Chen, Y. Mourzina, U. Poppe, *Thin Solid Films* **2013**, 533, 43.
- [80] X. Li, Z. Yin, X. Zhang, Y. Wang, D. Wang, M. Gao, J. Meng, J. Wu, J. You, *Adv. Mater. Technol.* **2019**, 4, 1800695.
- [81] D. K. Lee, Y. Park, H. Sim, J. Park, Y. Kim, G. Y. Kim, C. B. Eom, S. Y. Choi, J. Son, *Nat. Commun.* **2021**, 12, 5019.
- [82] Q. Wang, H. Fang, D. Wang, J. Wang, N. Zhang, B. He, W. Lü, *Crystals* **2020**, 10, 733.
- [83] J. Kang, D. Shin, S. Bae, B. H. Hong, *Nanoscale* **2012**, 4, 5527.
- [84] J. W. Suk, A. Kitt, C. W. Magnuson, Y. Hao, S. Ahmed, J. An, A. K. Swan, B. B. Goldberg, R. S. Ruoff, *ACS Nano* **2011**, 5, 6916.
- [85] F. Liu, W. Wu, Y. Bai, S. H. Chae, Q. Li, J. Wang, J. Hone, X. Y. Zhu, *Science* **2020**, 367, 903.
- [86] M. Sharma, A. Singh, R. Singh, *ACS Appl. Nano Mater.* **2020**, 3, 4445.
- [87] Y. Qi, J. Kim, T. D. Nguyen, B. Lisko, P. K. Purohit, M. C. McAlpine, *Nano Lett.* **2011**, 11, 1331.
- [88] Y. Chen, X. L. Gong, J. G. Gai, *Adv. Sci.* **2016**, 3, 1500343.
- [89] M. Yao, Y. Cheng, Z. Zhou, M. Liu, *J. Mater. Chem. C* **2019**, 8, 14.
- [90] P. C. Wu, Y. H. Chu, *J. Mater. Chem. C* **2018**, 6, 6102.
- [91] Y. H. Chu, *npj Quantum Mater.* **2017**, 2, 67.
- [92] Y. Bitla, Y. H. Chu, *Nanoscale* **2020**, 12, 18523.
- [93] Y. Bitla, Y. H. Chu, *FlatChem* **2017**, 3, 26.
- [94] A. Koma, *J. Cryst. Growth* **1999**, 201, 236.
- [95] A. Koma, K. Yoshimura, *Surf. Sci.* **1986**, 174, 556.
- [96] A. Koma, K. Ueno, K. Saiki, *J. Cryst. Growth* **1991**, 111, 1029.
- [97] J. Y. Hwang, Y. M. Kim, K. H. Lee, H. Ohta, S. W. Kim, *Nano Lett.* **2017**, 17, 6140.
- [98] C. Zhang, S. Ding, K. Qiao, J. Li, Z. Li, Z. Yin, J. Sun, J. Wang, T. Zhao, F. Hu, B. Shen, *ACS Appl. Mater. Interfaces* **2021**, 13, 28442.
- [99] M. Zheng, X. Y. Li, H. Ni, X. M. Li, J. Gao, *J. Mater. Chem. C* **2019**, 7, 8310.
- [100] L. Lu, Y. Dai, H. Du, M. Liu, J. Wu, Y. Zhang, Z. Liang, S. Raza, D. Wang, C. L. Jia, *Adv. Mater. Interfaces* **2020**, 7, 1901265.
- [101] J. Liu, Y. Feng, R. Tang, R. Zhao, J. Gao, D. Shi, H. Yang, *Adv. Electron. Mater.* **2018**, 4, 1700522.
- [102] J. Liu, S. Liu, Y. Wu, *J. Alloys Compd.* **2022**, 895, 162725.
- [103] R. Xu, X. Zhang, D. Zhang, J. Liu, J. Lu, R. Zhao, Y. Ji, F. Qian, H. Wang, J. Fan, W. Li, H. Yang, *J. Alloys Compd.* **2022**, 890, 161897.
- [104] W. Hou, S. Zhao, T. Wang, M. Yao, W. Su, Z. Hu, Z. Zhou, M. Liu, *Appl. Surf. Sci.* **2021**, 563, 150074.
- [105] C. Yang, M. Guo, D. Gao, W. He, J. Feng, A. Zhang, Z. Fan, D. Chen, M. Zeng, S. Wu, J. Gao, C. F. Guo, G. Zhou, X. Lu, J. Liu, *Adv. Mater. Technol.* **2019**, 4, 1900578.
- [106] M. Guo, C. Yang, D. Gao, Q. Li, A. Zhang, J. Feng, H. Yang, R. Tao, Z. Fan, M. Zeng, G. Zhou, X. Lu, J. M. Liu, *J. Mater. Sci. Technol.* **2020**, 44, 42.
- [107] Y. Yang, G. Yuan, Z. Yan, Y. Wang, X. Lu, J. M. Liu, *Adv. Mater.* **2017**, 29, 1700425.
- [108] D. L. Ko, T. Hsin, Y. H. Lai, S. Z. Ho, Y. Zheng, R. Huang, H. Pan, Y. C. Chen, Y. H. Chu, *Nano Energy* **2021**, 87, 106149.
- [109] S. A. Lee, J. Y. Hwang, E. S. Km, S. W. Kim, W. S. Choi, *ACS Appl. Mater. Interfaces* **2017**, 9, 3246.
- [110] J. J. Schermer, P. Mulder, G. J. Bauhuis, M. M. A. J. Voncken, J. Van Deelen, E. Haverkamp, P. K. Larsen, *Phys. Status Solidi A* **2005**, 202, 501.
- [111] J. W. Hutchinson, Z. Suo, *Adv. Appl. Mech.* **1991**, 29, 63.
- [112] F. Dross, J. Robbelein, B. Vandeveld, E. Van Kerschaver, I. Gordon, G. Beaucarne, J. Poortmans, *Appl. Phys. A: Mater. Sci. Process.* **2007**, 89, 149.
- [113] S. W. Bedell, K. Fogel, P. Lauro, D. Shahrjerdi, J. A. Ott, D. Sadana, *J. Phys. D: Appl. Phys.* **2013**, 46, 152002.
- [114] S. W. Bedell, P. Lauro, J. A. Ott, K. Fogel, D. K. Sadana, *J. Appl. Phys.* **2017**, 122, 025103.
- [115] D. Shahrjerdi, S. W. Bedell, *Nano Lett.* **2013**, 13, 315.
- [116] N. Li, S. Bedell, H. Hu, S. J. Han, X. H. Liu, K. Saenger, D. Sadana, *Adv. Mater.* **2017**, 29, 1606638.
- [117] S. W. Bedell, D. Shahrjerdi, B. Hekmatshoar, K. Fogel, P. A. Lauro, J. A. Ott, N. Sosa, D. Sadana, *IEEE J. Photovoltaics* **2012**, 2, 141.
- [118] D. Lebeugle, D. Colson, A. Forget, M. Viret, *Appl. Phys. Lett.* **2007**, 91, 022907.
- [119] C. C. Chiu, S. Z. Ho, J. M. Lee, Y. C. Shao, Y. Shen, Y. C. Liu, Y. W. Chang, Y. Z. Zheng, R. Huang, C. F. Chang, C. Y. Kuo, C. G. Duan, S. W. Huang, J. C. Yang, Y. De Chuang, *Nano Lett.* **2022**, 22, 1580.
- [120] Q. Lu, Z. Liu, Q. Yang, H. Cao, P. Balakrishnan, Q. Wang, L. Cheng, Y. Lu, J.-M. Zuo, H. Zhou, P. Quarterman, S. Muramoto, A. J. Grutter, H. Chen, X. Zhai, *ACS Nano* **2022**, 16, 7580.
- [121] P. Gumbsch, S. Taeri-Baghdarani, D. Brunner, W. Sigle, M. Rühle, *Phys. Rev. Lett.* **2001**, 87, 085505.
- [122] G. Dong, S. Li, T. Li, H. Wu, T. Nan, X. Wang, H. Liu, Y. Cheng, Y. Zhou, W. Qu, Y. Zhao, B. Peng, Z. Wang, Z. Hu, Z. Luo, W. Ren, S. J. Pennycook, J. Li, J. Sun, Z. G. Ye, Z. Jiang, Z. Zhou, X. Ding, T. Min, M. Liu, *Adv. Mater.* **2020**, 32, 2004477.
- [123] V. Nagarajan, A. Roytburd, A. Stanishevsky, S. Prasertchoung, T. Zhao, L. Chen, J. Melngailis, O. Auciello, R. Ramesh, *Nat. Mater.* **2003**, 2, 43.
- [124] Q. Zhang, L. Xie, G. Liu, S. Prokhorenko, Y. Nahas, X. Pan, L. Bellaiche, A. Gruverman, N. Valanoor, *Adv. Mater.* **2017**, 29, 1702375.
- [125] S. Das, Y. L. Tang, Z. Hong, M. A. P. Gonçalves, M. R. McCarter, C. Klewe, K. X. Nguyen, F. Gómez-Ortiz, P. Shafer, E. Arenholz, V. A. Stoica, S. L. Hsu, B. Wang, C. Ophus, J. F. Liu, C. T. Nelson, S. Saremi, B. Prasad, A. B. Mei, D. G. Schlom, J. ñiguez, P. García-Fernández, D. A. Muller, L. Q. Chen, J. Junquera, L. W. Martin, R. Ramesh, *Nature* **2019**, 568, 368.
- [126] Y. Li, E. Zatterin, M. Conroy, A. Pylpypets, F. Borodavka, D. J. Groenendijk, E. Lesne, A. J. Clancy, M. Hadjimichael, Q. Ramasse, A. Caviglia, J. Hlinka, U. Bangert, S. Leake, P. Zubko, *Adv. Mater.* **2022**, 34, 2106826.
- [127] D. M. Juraschek, P. Narang, *Nano Lett.* **2021**, 21, 5098.
- [128] E. B. Guedes, T. W. Jensen, M. Naamneh, A. Chikina, R. T. Dahm, S. Yun, F. M. Chiabrera, N. C. Plumb, J. H. Dil, M. Shi, D. V. Christensen, W. H. Brito, N. Pryds, M. Radović, *J. Vac. Sci. Technol., A* **2022**, 40, 013213.
- [129] J. M. Rondinelli, N. A. Spaldin, *Adv. Mater.* **2011**, 23, 3363.
- [130] D. Sando, *J. Phys.: Condens. Matter* **2022**, 34, 153001.
- [131] J. Hwang, Z. Feng, N. Charles, X. R. Wang, D. Lee, K. A. Stoerzinger, S. Mui, R. R. Rao, D. Lee, R. Jacobs, D. Morgan, Y. Shao-Horn, *Mater. Today* **2019**, 31, 100.
- [132] A. Biswas, Y. H. Jeong, in *Epitaxy* (Ed: M. Zhong), Intech Open, London **2018**.
- [133] A. D. Caviglia, R. Scherwitzl, P. Popovich, W. Hu, H. Bromberger, R. Singla, M. Mitrano, M. C. Hoffmann, S. Kaiser, P. Zubko, S. Gariglio, J. M. Triscone, M. Först, A. Cavalleri, *Phys. Rev. Lett.* **2012**, 108, 136801.
- [134] A. Fluri, C. W. Schneider, D. Pergolesi, *In Situ Stress Measurements of Metal Oxide Thin Films*, Elsevier Inc., New York **2018**.
- [135] L. Qiao, K. H. L. Zhang, M. E. Bowden, T. Varga, V. Shutthanandan, R. Colby, Y. Du, B. Kabius, P. V. Sushko, M. D. Biegalski, S. A. Chambers, *Adv. Funct. Mater.* **2013**, 23, 2953.
- [136] J. R. Petrie, H. Jeon, S. C. Barron, T. L. Meyer, H. N. Lee, *J. Am. Chem. Soc.* **2016**, 138, 7252.
- [137] T. Mayeshiba, D. Morgan, *Solid State Ionics* **2017**, 311, 105.
- [138] F. Gunkel, D. V. Christensen, Y. Z. Chen, N. Pryds, *Appl. Phys. Lett.* **2020**, 116, 120505.
- [139] A. Fluri, D. Pergolesi, V. Roddatis, A. Wokaun, T. Lippert, *Nat. Commun.* **2016**, 7, 10692.
- [140] P. M. Mooney, G. M. Cohen, J. O. Chu, C. E. Murray, *Appl. Phys. Lett.* **2004**, 84, 1093.

- [141] X. Chen, W. Mi, J. *Mater. Chem. C* **2021**, 9, 9400.
- [142] L. Mao, Q. Meng, A. Ahmad, Z. Wei, *Adv. Energy Mater.* **2017**, 7, 1700535.
- [143] D. L. Ko, M. F. Tsai, J. W. Chen, P. W. Shao, Y. Z. Tan, J. J. Wang, S. Z. Ho, Y. H. Lai, Y. L. Chueh, Y. C. Chen, D. P. Tsai, L. Q. Chen, Y. H. Chu, *Sci. Adv.* **2020**, 6, eaaz3180.
- [144] Y. Li, P. Zhou, Y. Qi, T. Zhang, *J. Am. Ceram. Soc.* **2021**, 105, 2038.
- [145] J. Huang, H. H. Wang, X. Sun, X. Zhang, H. H. Wang, *ACS Appl. Mater. Interfaces* **2018**, 10, 42698.
- [146] H. Yao, K. Jin, Z. Yang, Q. Zhang, W. Ren, S. Xu, M. Yang, L. Gu, E. J. Guo, C. Ge, C. Wang, X. Xu, D. Zhang, G. Yang, *Adv. Mater. Interfaces* **2021**, 8, 2101499.
- [147] M. Zheng, H. Sun, K. W. Kwok, *NPG Asia Mater* **2019**, 11, 52.
- [148] Z. Jiang, Z. Xu, Z. Xi, Y. Yang, M. Wu, Y. Li, X. Li, Q. Wang, C. Li, D. Wu, Z. Wen, *J. Mater.* **2021**, 8, 281.
- [149] C. W. Hicks, M. E. Barber, S. D. Edkins, D. O. Brodsky, A. P. Mackenzie, *Rev. Sci. Instrum.* **2014**, 85, 065003.



Francesco Chiabrera holds a M.Sc. in energy and nuclear engineering from the Polytechnic of Turin and a Ph.D. in nanoscience from the University of Barcelona. He has carried out Ph.D. research at the Catalonia Institute for Energy Research (IREC) in interface-dominated oxide thin films for energy storage and conversion. From 2020, he joined as postdoc in the group of Functional Oxide, Technical University of Denmark, where he is currently studying emerging functionalities in freestanding oxide thin-films for energy and information technology.



Shinhee Yun is currently working in the group of Functional Oxide (FOX) in the Department of Energy Conversion and Storage, the Technical University of Denmark as a postdoc. She was born in South Korea in 1989 and received a Ph.D. degree from the Department of Physics, Korea Advanced Institute of Science and Technology in 2020. In the same year, she joined FOX. Her research interests include flexoelectricity for sustainable energy and related functionalities as nanodevices.

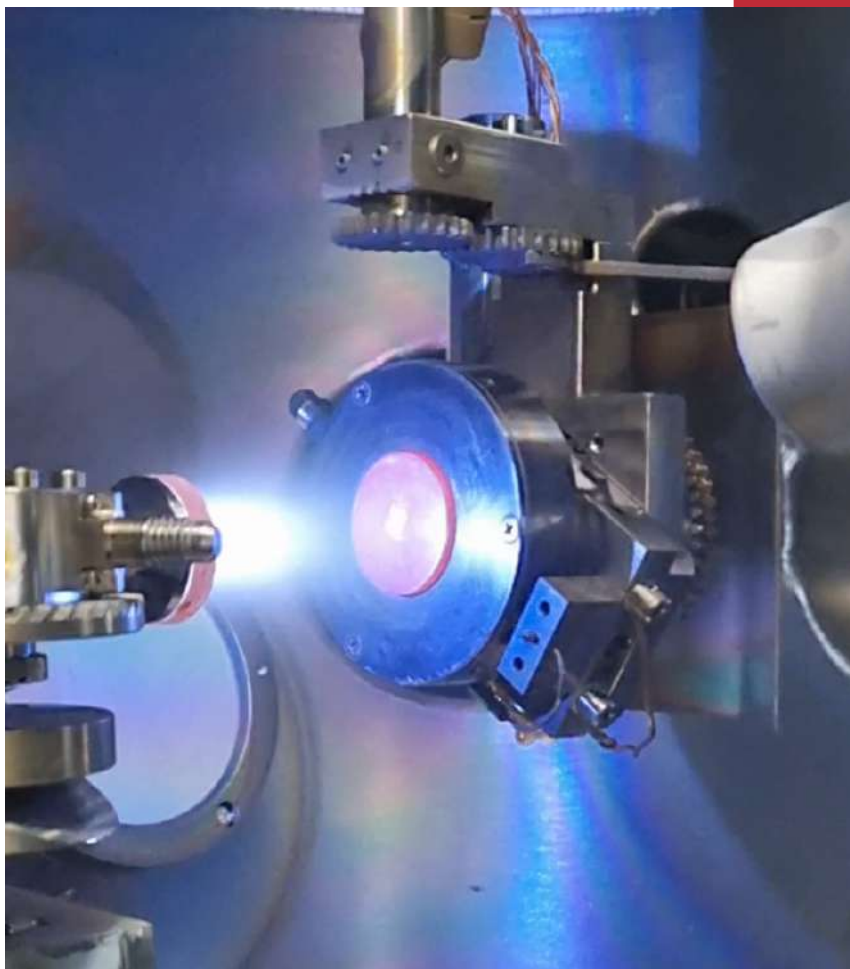


Thomas Sand Jespersen received his Ph.D. in 2007 from the Niels Bohr Institute, University of Copenhagen, Denmark on the topics of scanning probe characterization and electron transport in nanoscale semiconductors. Since 2012 he is an associate professor at Niels Bohr Institute focusing on experimental studies of correlated phenomena in oxide heterostructures and quantum transport and developments of semiconductor/superconductor epitaxial hybrid nanomaterials. Since 2021, he is a professor at the Technical University of Denmark, Department of Energy.



Nini Pryds is professor and heading the research section 'Functional Oxide' at the Department of Energy Conversion and Storage, The Technical University of Denmark (DTU), where he is leading a group of 35+ researchers working in the field of complex oxide thin films for applications in a wide range of energy and information technologies. He made major contributions in emerging disciplines such as nanoionics and iontronics, dealing with the design and control of interface-related phenomena in fast ionic and electronic conductors. His main interest is aimed at exploring how broken symmetries at interfaces affect magnetic, electronic, and ionic properties.

Y. Li, C. Xiang, F. M. Chiabrena, S. Yun, H. Zhang, D. J. Kelly,
R. T. Dahm, *et al.*
Stacking and twisting of freestanding complex oxide thin films
Advanced materials **34**, 2203187 (2022)



Pulsed laser deposition in action

Stacking and Twisting of Freestanding Complex Oxide Thin Films

Ying Li,* Cheng Xiang, Francesco M. Chiabrera, Shinhee Yun, Haiwu Zhang,* Daniel J. Kelly, Rasmus T. Dahm, Charline K. R. Kirchert, Thomas E. Le Cozannet, Felix Trier, Dennis V. Christensen, Timothy J. Booth, Søren B. Simonsen, Shima Kadkhodazadeh, Thomas S. Jespersen, and Nini Pryds*

The integration of dissimilar materials in heterostructures has long been a cornerstone of modern materials science—seminal examples are 2D materials and van der Waals heterostructures. Recently, new methods have been developed that enable the realization of ultrathin freestanding oxide films approaching the 2D limit. Oxides offer new degrees of freedom, due to the strong electronic interactions, especially the 3d orbital electrons, which give rise to rich exotic phases. Inspired by this progress, a new platform for assembling freestanding oxide thin films with different materials and orientations into artificial stacks with heterointerfaces is developed. It is shown that the oxide stacks can be tailored by controlling the stacking sequences, as well as the twist angle between the constituent layers with atomically sharp interfaces, leading to distinct moiré patterns in the transmission electron microscopy images of the full stacks. Stacking and twisting is recognized as a key degree of structural freedom in 2D materials but, until now, has never been realized for oxide materials. This approach opens unexplored avenues for fabricating artificial 3D oxide stacking heterostructures with freestanding membranes across a broad range of complex oxide crystal structures with functionalities not available in conventional 2D materials.

information, and energy applications. By stacking different 2D layered materials with different in-plane rotation angles between them, a large set of van der Waals (vdW) heterostructures can be created enabling the exploration of novel applications and the discovery of new phenomena.^[1–5]

A very interesting subgroup of functional materials is the complex metal oxides (e.g., transitional metal oxides, rare-earth oxides, etc.), which display a large range of appealing properties, both for electronics and the important field of ionic devices.^[6–11] The complex metal oxide heterointerfaces give rise to a plethora of novel phenomena not present in the individual parent compounds, and have motivated extensive research efforts in the fields of superconductivity,^[9] thermoelectricity,^[10] and ferromagnetism among many others.^[11] Complex oxide thin films can be grown epitaxially with a well-regulated growth scheme and atomic-level control over the material interfaces and


substrate surfaces. However, these growth methods have fundamental limitations that prevent the unrestricted manipulation, integration, and utilization of these materials: 1) heterointerfaces typically rely on epitaxy, which only occurs for a relatively

1. Introduction

The ability to create materials with predetermined properties has been one of the key elements for modern electronics,

Y. Li, F. M. Chiabrera, S. Yun, H. Zhang, R. T. Dahm, C. K. R. Kirchert, T. E. L. Cozannet, F. Trier, D. V. Christensen, S. B. Simonsen, T. S. Jespersen, N. Pryds
Department of Energy Conversion and Storage
Technical University of Denmark (DTU)
Fysikvej, 310, Kgs. Lyngby 2800, Denmark
E-mail: liying89@wust.edu.cn; haizh@dtu.dk; nipr@dtu.dk

Y. Li
Hubei Province Key Laboratory of Systems Science
in Metallurgical Process
Faculty of Science
Wuhan University of Science and Technology
Wuhan 430081, P. R. China
C. Xiang, T. J. Booth
Department of Physics
Centre for Nanostructured Graphene (CNG)
Technical University of Denmark (DTU)
Fysikvej, 309, Kgs. Lyngby 2800, Denmark
D. J. Kelly, S. Kadkhodazadeh
DTU Nanolab
Technical University of Denmark (DTU)
Fysikvej, 307, Kgs. Lyngby 2800, Denmark

 The ORCID identification number(s) for the author(s) of this article can be found under <https://doi.org/10.1002/adma.202203187>.

© 2022 The Authors. Advanced Materials published by Wiley-VCH GmbH. This is an open access article under the terms of the Creative Commons Attribution-NonCommercial-NoDerivs License, which permits use and distribution in any medium, provided the original work is properly cited, the use is non-commercial and no modifications or adaptations are made.

DOI: 10.1002/adma.202203187

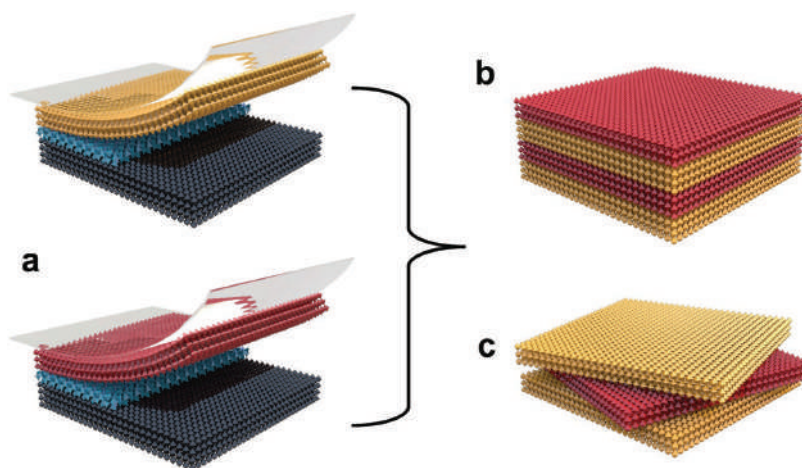


Figure 1. Schematic illustration of the fabrication and assembly of freestanding oxide membranes into artificial stacks with heterointerfaces by transfer method. a) Release of the freestanding oxide membranes (yellow, red) by dissolving the sacrificial layer (blue), b) stack of freestanding films, c) twisting the vertically stacked films.

limited set of material systems with similar lattice parameters; 2) epitaxial films are clamped by the substrate, which will constrain some important properties;^[12,13] 3) interfacial intermixing of two layers at high-temperature deposition can lead to cationic interdiffusion,^[14] which prevents the formation of atomically abrupt interfaces; and 4) there are limitations on the integration of materials with different thermodynamic stability conditions.

Recently, new methods have been developed enabling the detachment of ultra-thin complex oxide crystals from their substrate to realize freestanding oxide thin films.^[15–28] The methods typically rely on: 1) controllable weakening of epitaxial crystals;^[16] 2) releasing thin oxide films using sacrificial interlayers and selective etching (Figure 1a);^[17] and 3) self-formed freestanding oxide thin films.^[18] These innovative approaches, especially the sacrificial interlayer etching method, have produced a broad range of new freestanding oxide films of, e.g., cubic SrTiO₃,^[19] BaTiO₃,^[20] BiFeO₃,^[21] SrRuO₃,^[22] pseudocubic La_{0.7}Ca_{0.3}MnO₃,^[23] La_{0.7}Sr_{0.3}MnO₃,^[24] fluorite CeO₂,^[25] BaTiO₃/La_{0.7}Sr_{0.3}MnO₃ bilayers,^[26] La_{0.7}Sr_{0.3}MnO₃/BiFeO₃ bilayers,^[27] as well as (La_{0.7}Sr_{0.3}MnO₃)_n/(SrTiO₃)_n superlattices.^[17] These freestanding films and multilayers exhibit a wide range of exciting physical and chemical properties combined with the option of transferring them onto arbitrary substrates, thus bypassing the epitaxial roadblock.

Although many novel functionalities have been recently discovered in the freestanding oxide membranes,^[17,19,22–26] the assembling and stacking of these oxide thin films directly into heterostructures has not been shown yet. The properties and potential applications of such oxide heterostructures are fundamentally different from conventional 2D heterostructures and will allow, e.g., the design of new material systems (e.g., perovskite, spinel, and garnet structures) that address the overarching challenges of the next generation of energy technologies. Moreover, fabricating large-area freestanding films, free of cracks and defects remains challenging.^[17,19–26] In this work, we refine the epitaxial lift-off methods using sacrificial layers

to produce high quality, large, and uniform areas of perovskite SrTiO₃ (STO) and fluorite Gd-doped CeO₂ (Ce_{0.8}Gd_{0.2}O_{1.9}, CGO) freestanding films—two oxide representatives of semiconductor and ionic electrolytes. Further, we demonstrate a route for the fabrication and stacking of atomically controlled freestanding oxide layers of different composition and lattice parameter, see Figure 1b. Finally, inspired by breakthroughs in magic-angle graphene and twisted van der Waals heterostructures,^[1–5] we create the first oxide artificial heterostructures with a controlled twist angle between the crystallographic axes of the constituent layers (Figure 1c). The results provide a new degree of freedom for the design and engineering of oxide heterostructures and interfaces.

2. Results and Discussions

Freestanding oxide membranes were fabricated by growing single-crystal (001)-oriented STO and CGO with thicknesses ranging from 10 to 60 nm on a water-soluble Sr₃Al₂O₆ (SAO) sacrificial buffer layer by pulsed laser deposition (PLD) on (001)-STO substrate (see the Experimental Section). Since the high quality of SAO interlayer is essential for the growth and detachment of the upper film from the substrate, the growth and thickness of the films were monitored by reflection high-energy electron diffraction (RHEED). Layer-by-layer growth was achieved for both the SAO and STO layers, as highlighted in Figure 2a,b by the presence of clear oscillations in the intensity of the RHEED spots. The high quality and crystallinity of the oxide films were further confirmed by atomic force microscopy (AFM, Figure 2c and Figure S3, Supporting Information), X-ray diffraction (XRD, Figures S3 and S6, Supporting Information), and high-resolution transmission electron microscopy (HRTEM) below.

The first challenge we targeted was the epitaxial release and transfer of large areas of oxide membranes with high yield and minimal defects.^[25] For 2D materials, the maximum lateral size of exfoliated single layer flakes varies from a few

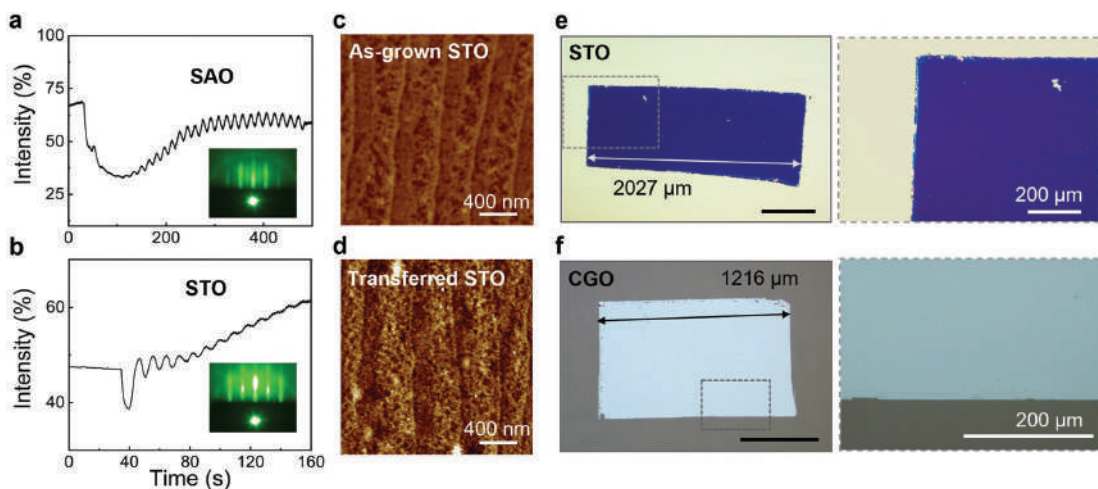


Figure 2. a) The time-dependent RHEED intensity oscillations and pattern of the SAO (10 nm) interlayer. b) The early stages of RHEED intensity oscillations and pattern of the upper STO film (30 nm). c,d) AFM images of the terraced morphology of STO films before and after transferring. The RMS is 0.184 and 0.215 nm. e,f) Optical microscopy images of the millimeter-scale 30 nm-thick STO and 40 nm-thick CGO freestanding films transferred on TiN/Si and single-crystal sapphire, respectively. Scale bar: 500 μm . High-magnification images of the corresponding area are outlined in the dotted boxes in (e) and (f).

micrometers to several tens of centimeters, while for freestanding oxide films, the sizes of the complete area without tearing or breaking were limited to a few hundreds of micrometers.^[19,21,23,25] In this study, we employed polymeric cellulose acetate butyrate (CAB) applied by spin-coating to support and transfer the substrate-free oxide film,^[29] replacing the most common stamp materials of poly(methyl methacrylate) (PMMA) and poly(dimethylsiloxane) (PDMS) (see the Experimental Section and Figure S1 in the Supporting Information for the transfer process).^[25,28,30] CAB has some advantages over PMMA or PDMS, owing to its desirable physical and chemical properties, such as better tunable adhesion to oxides, high modulus, flexibility and negligible chemical residues after dissolution in acetone.^[31] Utilizing the CAB polymer, we succeeded in exfoliating and subsequently transferring millimeter-sized, single-crystalline membranes of STO and CGO onto different substrates. Examples of transferring 1.2–2.0 mm lateralized STO and CGO onto TiN-coated silicon wafer (TiN/Si) and single-crystal sapphire, respectively, are shown in Figure 2e,f. Cracks, bubbles, and tearings are the most common types of fabrication process-induced defects in transferred materials. Using our methodology, we demonstrated a versatile approach, where homogenous crystalline membranes with large lateral size (>2000 μm , see Figure S2, Supporting Information) can be fabricated and transferred. Defects mostly appear at the edges, which is attributed to the stress during the releasing of the support layer (Figure 2e,f and Figure S2, Supporting Information). Moreover, AFM images show that the STO film retains terraced morphology at the microscale before and after the transfer (Figure 2c,d and Figures S3 and S6, Supporting Information), and the single-crystallinity of the transferred films was further confirmed by XRD (Figures S3 and S6, Supporting Information), scanning transmission electron microscopy (STEM, Figure 5

and Figure S7, Supporting Information), and HRTEM (Figure 6 and Figure S9, Supporting Information).

Transferring such large-area single-crystal oxide films with nearly perfect quality is the striking characteristic of this work, which is essential for the follow-up stacking and twisting of membranes. Using a micromanipulator, we align two freestanding films together on a hot target substrate ($\approx 140^\circ\text{C}$) to form a stable stack (see Experimental Section and Figure S1, Supporting Information). This transfer method represents a simple and effective way to produce stacked oxide heterostructures. We developed a “fixed corner” strategy by applying isopropyl alcohol (IPA) droplets to partially dissolve and fix the position of the top oxide layer with CAB covering layer. This strategy ensures that the top oxide layer does not slide, fold, or shrink in the stacking process, and also increases the contact area between adjacent layers (see the Experimental Section). The presence of contaminants at the interface between the oxide layers is another important issue in the fabrication of stacked oxide heterostructures, since it can affect the adhesion, hybridization, and interactions between the layers of the stack. Post-annealing was carried out at 650°C to remove possible hydrocarbon contamination, and samples were subsequently kept under a protective atmosphere of N_2 .

Figure 3 shows the successful stacking of single-crystal freestanding layers of CGO/CGO (Figure 3a), STO/STO (Figure 3b) as well as STO/CGO (Figure 3c). The insets in Figure 3a–c show the low-magnification images of the stacks, and demonstrate the feasibility of stacking large areas of freestanding oxide thin films. Some wrinklings of the top layer—caused by stresses generated by the bottom layer and top polymer layer can be observed in the overlapping region. AFM images of the surface morphology of the stacks after annealing together with the line profiles show that the thickness of the upper oxide layer

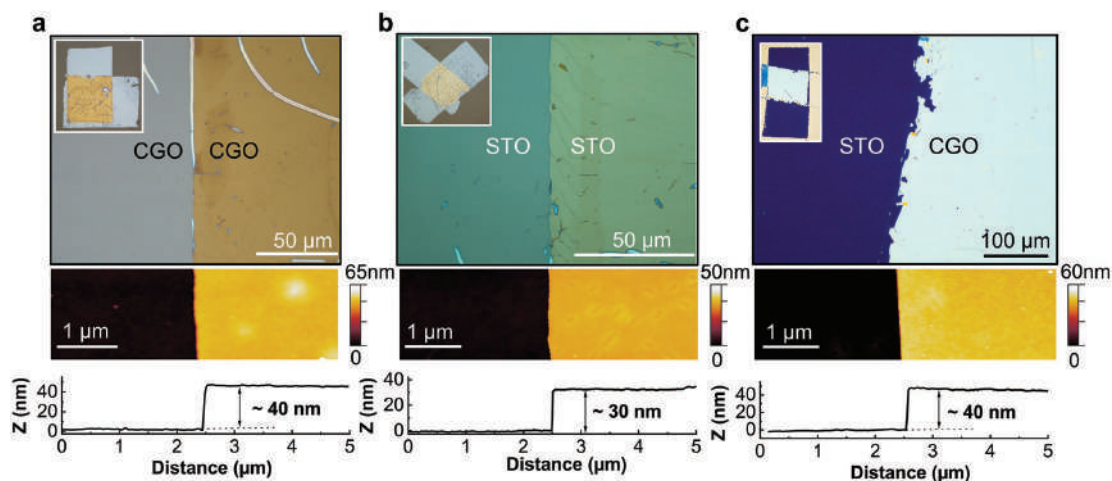


Figure 3. a–c) Optical microscopy images of the bilayers of CGO (40 nm)/CGO (40 nm) (a), STO (30 nm)/STO (30 nm) (b), and STO (30 nm)/CGO (40 nm) (c). The inset figures represent the low-magnification images of the oxide films stack transferred on target substrates. The panels below (a–c) show AFM images of the step edge of the oxide stacks with the line profiles indicating the thickness and flatness.

corresponds well to that determined by the RHEED oscillations. The surface morphology of the stacked STO membranes retains step-and-terrace features (Supporting Information, Figure S6). The line scans across the step edge show that the surface areas are flat within 5 μm , indicating the two layers of membranes are closely joined together without any notable “distance” between the layers. Our first-principle calculation results show that depending on the specific material stacking sequence and termination, the equilibrium structures can be stabilized with different interfacial distances, which correspond to the balances between the inter- and intralayer interactions (Note S4 and Figure S4, Supporting Information).

Twisted layers provide an additional degree of freedom to overcome the symmetry restrictions imposed by forming heterostructures using conventional epitaxial growth. A celebrated example is given by 2D material heterostructures consisting of graphene or transition metal dichalcogenides, where a slight rotation radically changes the properties and can lead to exotic physical behavior.^[1–5,32–35] There has been a large interest in those 2D materials but such twisting in freestanding oxide films has never been explored before. Here, **Figure 4** shows the control of the twist angle in the artificially stacked oxide bilayers by sequential transferring and stacking of freestanding oxide films with various rotational alignment, e.g., CGO/CGO with 90° twist angle (Figure 4a,d), CGO/CGO with 45° (Figure 4b,e), and STO/STO with 100° (Figure 4c,f). The twist angle between the stacked oxide layers was estimated from the edge orientation of the layers and confirmed by XRD (Note S5, Figures S5 and S6, Supporting Information). The stacks with large size (>1200 μm) are found to be stable (insets in Figure 3 and Figure 4a–c) after high-temperature annealing. AFM images of the twisted stacks with clear edges are shown in Figure 4d–f. It is clear from these twisted bilayer images that a well-defined rotation angle can be achieved.

The fabrication of freestanding oxide membranes into artificially twisted stacks enables the search for exotic new

physics and novel device functionalities. The cross-section of our stacked heterostructure composed of STO/STO has been characterized with annular dark-field scanning transmission electron microscopy (ADF-STEM). **Figure 5** shows an ADF-STEM image of 10° (equivalent to 80° or 100° twist angle due to symmetry) twisted STO/STO stack with a clean and well-defined interface oriented along the [010] zone-axis. No indication of any effect of a wrinkling phenomenon was observed at the twisted interfaces (see Supporting Information, Figure S7). Tilting the sample 10.5° around the [001] axis orients the top STO layer to [010] zone axis (Figure 5a,b), which is in good agreement with the results from XRD ($\approx 10.4^\circ$) and the geometric estimation ($\approx 10.0^\circ$) (Supporting Information, Figure S6). Fast Fourier transform (FFT) mask filtering was applied to the images in Figure 5a,b to clearly visualize the interfacial region of ≈ 1.0 nm thick between the two STO layers (Figure 5c,d). The crystal structure of STO is identified, and the atomic positions of Sr and Ti can be well resolved. Notably, the ADF-STEM images show some regions, where the two crystals appear to be directly bonded. This is confirmed by analyzing the intensity profile of the images along the [001] direction, and the interplanar distance $d_{(001)}$ between consecutive Sr atomic columns (see inset in Figure 5a, $d_{(001)} \sim 0.4$ nm), which demonstrates an uninterrupted and well-defined profile.

The observations of bright regions interspaced by darker regions at the interface of STO/STO stack (Figure 5a,b and Figure S7d, Supporting Information) are in excellent agreement with what has been reported earlier in artificially assembled 4° twisted STO bicrystals, in which the bonding between layers was achieved at a temperature of 800 °C for 20 min with an applied pressure of 120–140 MPa.^[36] The dark regions observed at the interfaces in our stack are similar to those seen previously in STO bicrystals, which correspond to dislocation cores.^[36] The possibility of tuning the dislocation network at the interface by twisting can, e.g., open new opportunities to

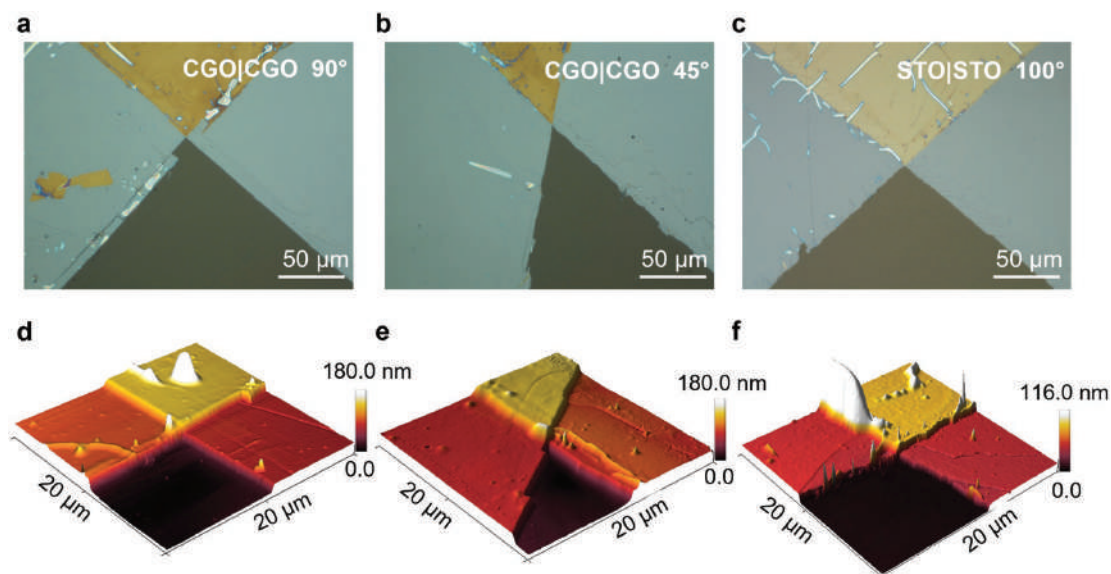


Figure 4. a–c) Optical microscopy images of the bilayers of CGO/CGO with twist angle of 90° (a), CGO/CGO with twist angle of 45° (b), STO/STO with twist angle of 100° (c). The stacked heterostructure is formed in the overlapping regions, which corresponds to the yellow frame in AFM 3D images in (d)–(f).

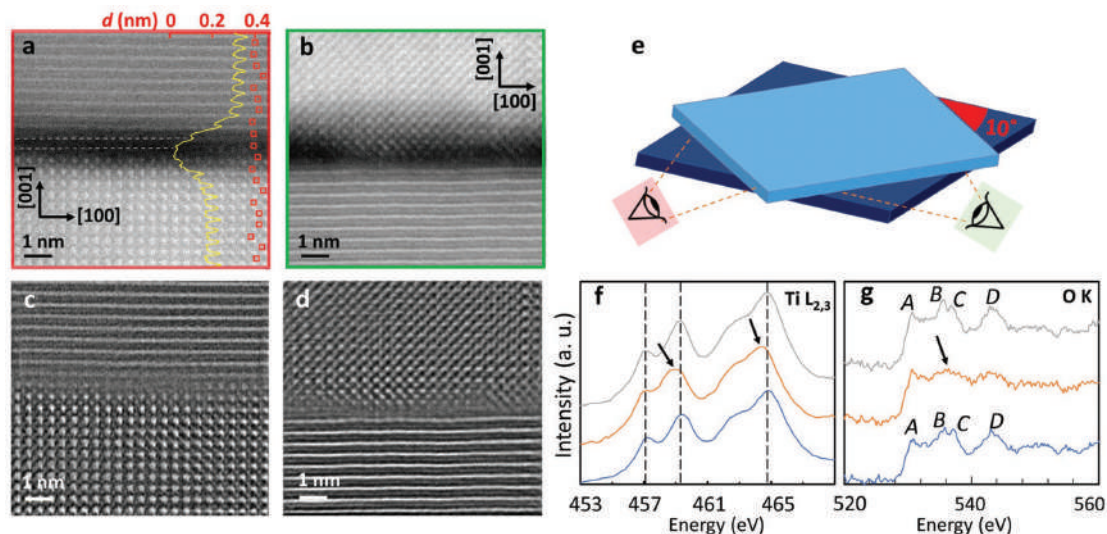


Figure 5. a,b) Atomic-resolution ADF-STEM images of the interfacial area of the 10° (or 100°) twist STO/STO stack with the lower film (a) and the upper film (b) oriented to the $[010]$ zone-axis, respectively, by tilting the specimen 10.5° around the $[001]$ axis. The intensity profile (yellow line) is plotted together with the distance $d_{(001)}$ between consecutive Sr atomic columns (red squares), as resolved in the image. The white dashed lines mark the interface. c,d) Respective inverse FFT images of (a) and (b), after applying mask filtering to the FFT. e) Schematic illustration of the membranes. f,g) EELS signal showing the Ti- $L_{2,3}$ (f) and O-K (g) edges recorded from the bottom layer STO (in blue), the dark region at the interface between the two STO layers (in orange) and the top layer STO (in gray). The shift in the $L_{2,3}$ peaks of the Ti edge and the flattening of the second peak in the O-K edge (peak B) are marked with arrows.

tune the ionic conductivity at interfaces, which is crucial for a wide range of energy technologies,^[37] ranging from fuel cells to batteries and catalysis, to name a few. Carbon residues from the transfer process were found at the interface similar to what is often observed in stacks of 2D materials (Supporting Information, Figure S8).^[38] Remarkably, our observations show that atomic bonds could form at the interfaces without the need to apply high pressure and high temperature but only by “placing” the layers on top of each other and post-annealing at 650 °C. Density functional theory calculations confirm that certain termination configurations influence the formation of the atomic bonds (Figure S4, Supporting Information).

We further studied the elemental valence state near the interface with electron energy loss spectroscopy (EELS). The EELS profiles of Ti-L_{2,3} and O-K edges were collected from different regions in the STO/STO stack (Figure 5f,g). The Ti-L_{2,3} edges recorded from the bulk area away from the interface show the typical crystal field splitting of 2.2 eV between the Ti 3d t_{2g} and e_g states, and the O-K edges exhibit four main peaks (labeled as A, B, C, and D in Figure 5g), which correspond to local O 2p hybridization with the Ti 3d states. In the selected dark region at the interface, the Ti-L_{2,3} edge displays a 0.4 eV shift (indicated by the arrows in Figure 5f), and the second peak (labeled as B) of the O-K edge broadens and is less distinct (Figure 5g). These

results are in agreement with a partial reduction of the Ti⁴⁺ into Ti³⁺ cations at the interface to compensate the oxygen and/or Sr vacancies, as commonly found at the core of STO grain boundaries.^[39] The results highlight again the possibility of tuning the interfacial dislocation network by stacking and twisting in order to design and enhance the ionic conductivity at the interface.

In relation to twisted heterostructures, moiré superlattices are drawing tremendous interest as a new area to explore the emergence of new properties in 2D layered materials, e.g., moiré phonons,^[32] moiré excitons,^[33] unconventional superconductivity,^[34] or Mott insulators.^[35] Such superlattices are material-specific to form different long-wave moiré patterns. However, the implementation has so far been limited to graphene and 2D materials. Further work is needed to clarify whether interactions between the twisted oxide heterostructures can lead to moiré-related phenomena. It is worth mentioning, however, that the moiré superlattice could be visualized in our stacked oxide films using HRTEM (Figure 6 and Figure S9, Supporting Information). Figure 6a presents a typical HRTEM image of the STO (10 nm)/STO (10 nm) stack composed of two (001)-oriented STO films twisted by 18° on a TEM grid (see the Experimental Section about the transfer method). In Figure 6a, typical lattice fringes can be observed (area in red box) corresponding to the single-layer STO membrane, while the darker

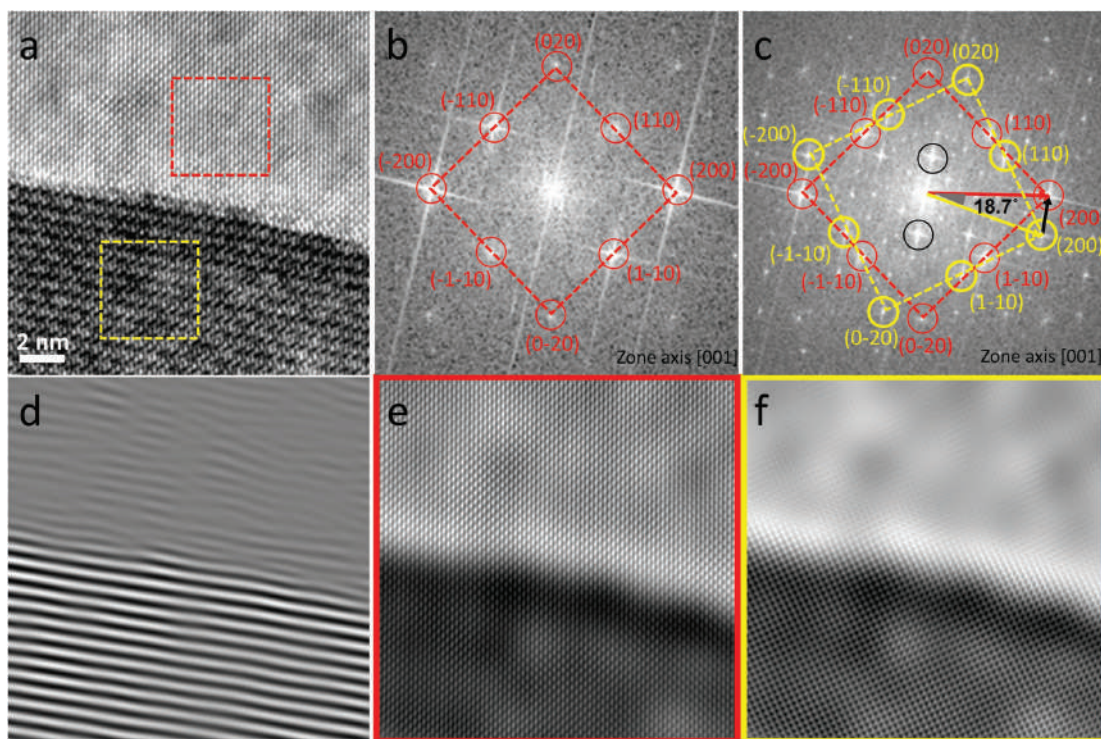


Figure 6. a) The HRTEM image with moiré fringes of the STO/STO stack. b,c) The FFT of the single-layer STO (marked in red box) and the stack area (marked in yellow box) in (a). The Miller indices are indicated for the most intense spots. d) The inverse FFT of the spots circled in black in (c). e,f) The inverse FFT of the spots circled in red and yellow in (c), corresponding to the bottom layer (red box) and upper layer (yellow box) in image (a), respectively.

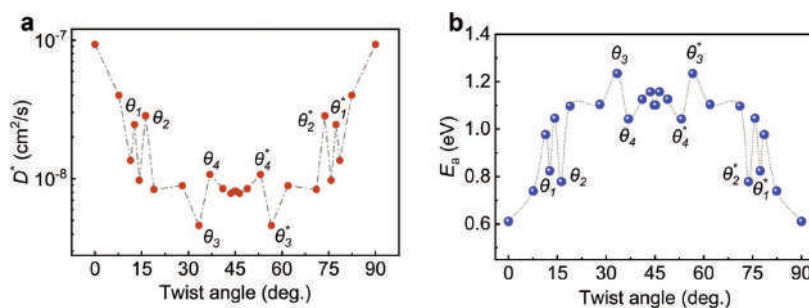


Figure 7. a) Tracer diffusion coefficient (D^*) for oxygen ions as a function of twist angle. b) Activation energy for oxygen ion migration as a function of twist angle. All the calculations in (a) were carried out at 1200 K (see the Experimental Section).

region (due to mass-thickness contrast) with a moiré pattern indicates the overlapping area of STO/STO stack. The FFT of the single-layer STO region is shown in Figure 6b, in which the most intense spots circled in red can be marked with the Miller indices of cubic STO (space group $Pm\bar{3}m$), verifying the single crystallinity and high quality of STO films. On the other hand, in Figure 6c, the FFT of the stacked area in Figure 6a (area in yellow box) is more complex. Two sets of spots circled in red and yellow and their inverse FFT in Figure 6e,f verify the overlapping of two STO films with a misorientation. In Figure 6c, two particularly intense spots (in black circles) are found close to the central spot, which correspond to the moiré fringes with a real space distance $d_{\text{moiré}} \approx 0.6$ nm (see the inverse FFT in Figure 6d). The rotation of the scattering vectors of (200) lattice plane in Figure 6c gives the twist angle of $\theta = 18.7^\circ$. Alternatively, θ is found to be 18.4° deduced from moiré fringes (Experimental Section, Equation (1)), consistent with the results obtained from scattering vectors.

Our demonstrated twisting method allows us to tune the properties of stacked multilayer structures on a larger scale than ever before. Here, we show the strength of twisted freestanding oxide materials via oxygen migration which occurs by a vacancy mechanism. Our molecular dynamic (MD) calculations (see the Experimental Section) reveal that “twisting” yields anisotropic oxygen ion diffusion behavior in the near interface region of STO/STO stack with twist angle θ , which otherwise is isotropic in bulk (001)-STO (Supporting Information, Figure S11). Figure 7a shows the calculated tracer diffusion coefficient for oxygen (D^*) as a function of twist angle. The angle of twist between the two layers has the so-called “magic” angle where D^* changed at specific angles (e.g., θ_1/θ_1^* , θ_2/θ_2^* , etc., note that $\theta^* = 90^\circ - \theta$ due to the symmetry). This variation of diffusivity is consistent with the overall activation energy for oxygen diffusion which increased with the increasing twist angle, i.e., from 0.6 to 1.1 eV as the twist angle changes from 0° to 45° , respectively (Figure 7b and Figure S11c, Supporting Information).^[40] The phenomenon is attributed to the relative rotation between layers, which form a periodic moiré potential in the material system affecting the diffusion path and resulting in lattice site preference for diffusion of oxygen vacancies. These results, together with the experimental observation of enhanced oxygen vacancy concentration at the twisted STO/STO interface deduced from the Ti-L_{2,3} edges in EELS (see Figure 5f),

suggest that twisting freestanding thin films would be a valuable synthetic strategy to manipulate the diffusion properties of oxygen vacancies in perovskite oxide thin films. Like many other discoveries of fundamental physical phenomena, we expect that these results will provide a new degree of freedom for designing novel functional energy materials and devices for cutting-edge electronic and energy-related technologies.

3. Conclusion

We provide a new way to assemble similar/dissimilar freestanding oxide membranes via artificial stacking and twisting, and demonstrate that these stacks are indeed heterostructures with atomic bonds formed at the interfaces. The most prominent novelties of our discoveries are: 1) we put forward a new topic on stacking a variety of freestanding oxide thin films into artificial oxide heterostructures, and show experimentally that we can assemble a stack of freestanding oxide thin films with different compositions. Compared with traditional epitaxial heterostructures, the stacking of the freestanding oxide thin films does not require lattice-matching, allowing layers with different lattice symmetries and atomic spacings to be stacked. 2) We show that we can control the twist angle between layers in the stack. Consequently, moiré patterns were observed by HRTEM, which verify the overlap and twist angle of the stacked oxide membranes. Such stacking and twisting has been recently recognized as a new degree of structural freedom in van der Waals heterostructure based on 2D materials but has never been demonstrated for freestanding oxide materials. 3) The cross-sectional STEM imaging and analysis of the oxide stack confirm that in the interface region, the two oxide crystals are directly bonded forming an oxide heterostructure, instead of a simple stack. We showed theoretically that the oxygen ion diffusion coefficient in the oxide stacks can be significantly tuned by twisting. The ground-breaking potential of stacking and twisting of oxide heterostructures stems from the strong degree of freedom available to design artificial freestanding heterointerfaces. The ability to modulate the interfacial properties of the stack via layer selectivity and twisting opens the possibility for integrating these structures in electronics with silicon-based architectures inducing moiré superlattice engineering, flexible, magnetic, or superconducting materials.

4. Experimental Section

Thin-Film Preparation: SrTiO₃ (STO) and Ce_{0.8}Gd_{0.2}O_{1.9} (CGO) films with various thicknesses were grown epitaxially on a water-soluble Sr₃Al₂O₆ (SAO) sacrificial buffer layer on a (001)-oriented STO substrate by PLD using a KrF ($\lambda = 248$ nm) excimer laser. First, the (001)-oriented SAO sacrificial layer was deposited on (001)-STO substrate at 750 °C with an oxygen pressure of 10⁻⁵ mbar. Subsequently, the STO and CGO films were grown on SAO at 700 °C with an oxygen pressure of 5 × 10⁻⁴ and 5 × 10⁻³ mbar, respectively. Such conditions were crucial to fabricate high-quality SAO interlayer and guarantee the elemental ratio of 3:2:6 in the SAO film, to promote its water solubility. The laser energy density was 2.2 J cm⁻². The repetition rate was 1 Hz. The growth process of the films was monitored by RHEED.

The Lift-Off, Transfer, and Stacking Process of Oxide Thin Films: Cellulose acetate butyrate (CAB) is used as the support layer (20 g/100 mL in ethyl acetate). SAO acted as the sacrificial layer which was first deposited on the substrate as indicated above. The sample was spin-coated with CAB and subsequently heated at 80 °C for 5 min. Then grooves were carved on the sample surface and the whole sample was immersed into deionized (DI) water at room temperature for 2 h. After the freestanding oxide film together with the CAB was released from the substrate by dissolving the SAO, it was scooped up and transferred to the target substrate. This was followed by immersing the target substrate and the freestanding oxide in acetone to remove the CAB layer and clean it with IPA. This procedure was repeated using an optical microscope and a micromanipulator to release the second layer onto the bottom layer with a target twist angle. Then IPA was used to partly dissolve and fix the four corners of second layer. Another fresh CAB film was used to cover the stack, again fixed by IPA at the corners. The assembled stack was heated at 140 °C for 15 min and finally soaked in acetone to remove the CAB. The membranes and stacks were post-annealed at 650 °C in oxygen and protected in N₂ (Figure S1 in the Supporting Information shows the detailed sequence of the transferring and stacking).

TEM Measurement and Analysis: HRTEM was performed using a Titan Analytical 80–300ST TEM operated at 300 kV. The oxide membranes with CAB support layer were transferred onto the TEM grid (Si₃N₄ microporous TEM window grid with 2.0 μm pores). The grid and the stack were then immersed in acetone for 30 min to dissolve the CAB. Critical point drying in CO₂ was used to substitute the organic solvent. The TEM sample holder and samples were plasma cleaned for 2 min immediately before insertion in the microscope to remove any carbon contamination on the sample surface. The exact twist angle θ of the stacked freestanding oxide films on the TEM grid was determined in two different ways: a) measuring the twist angle between the two scattering vectors directly from an FFT and b) using the moiré fringes following the equation^[41]

$$d_{\text{moiré}} = \frac{d}{2\sin(\theta/2)} \quad (1)$$

where $d_{\text{moiré}}$ is the corresponding real space distance of the moiré fringes and d is the lattice spacing corresponding to the scattering vector (200). In Figure 6, $d_{\text{moiré}} = 0.60$ nm, and $d_{(200)} = 1.95$ Å, which gives $\theta = 18.4^\circ$, consistent with the previous calculation result of 18.7° from method (a).

Morphology and Structure Characterization: The surface images, morphology, and crystal structures of sample are examined by the optical microscope (Nikon, ECLIPSE, L200N), AFM (Dimension Icon, Bruker), and XRD device (Rigaku, Smartlab).

Cross-Sectional STEM Measurement and Analysis: Specimens of the oxide stack were prepared using focused ion beam (FIB) milling. Prior to the preparation, a thin layer of Au (a few nanometers) was deposited on the surface of the sample to minimize charging. The region, where a thin lamella was fabricated from, was additionally covered with 1 μm of Pt in order to protect the sample from FIB-induced damage. A cross-sectional lamella with thickness of ≈80 nm was produced by FIB milling with Ga⁺ ions at 30 kV and currents in the range 9 nA to 48 pA. STEM images were recorded using an FEI 80–300 kV Titan TEM instrument equipped with an aberration corrector on the probe forming lenses. The microscope

was operated at 300 kV. The electron probe convergence semiangle and size were ≈18 mrad and 0.1 nm, respectively, and the images were recorded with an annular dark-field inner collection semiangle of 40 mrad. The distance between consecutive Sr planes was determined by applying the function “peakfinder” in Matlab to the intensity profile obtained from the images. The EELS data was acquired using a Gatan GIF Tridium spectrometer. A spectrometer collection semiangle of ≈20 mrad was used and the EELS measurements had an energy resolution of 0.8 eV. The background signal in the EELS spectra was removed after fitting with a power-law model.

Theoretical Calculations: The first-principle calculations were performed using GBRV ultrasoft pseudopotential with the generalized gradient approximation Perdew–Burke–Ernzerhof functional.^[42] The predicted lattice parameter (3.8996 Å) of the relaxed structure agreed well with the experimental data for bulk STO of 3.901 Å.^[43] A 2 × 2 × 2 repetition of the five-atom unit cell of STO was used to mimic the freestanding oxide thin films. The vdW-DF2 correction was used to take into account the interactions between the two blocks and this was implemented in the Quantum ESPRESSO package.^[44–48] To avoid the interaction between periodic images, a large fixed simulation box was used (40 Å along the out-of-plane direction). The Brillouin zone was sampled with a 4 × 4 × 1 Γ -centered Monkhorst k-point mesh. The lattice energy was optimized until the force on each atom was less than 1.0 × 10⁻⁴ eV Å⁻¹. The cutoff for plane-wave and charge density was 40 and 160 Ry, respectively.

MD simulations were performed to investigate the oxygen ion diffusion in twisted systems. The interatomic interactions were described using the rigid-ion potentials

$$V_{ij} = \frac{z_i z_j e^2}{r} + D_{ij} \left\{ \left[1 - e^{-a_i(r-r_0)} \right]^2 - 1 \right\} + \frac{C_{ij}}{r^{12}} \quad (2)$$

where the first-, second-, and third term describes the long-range Coulomb interactions, the short-range interactions (Morse potential), and the repulsive interactions, respectively. The potential parameters were directly taken from Pedone et al.^[49]

The MD simulations for bulk STO were performed using a 16 × 16 × 16 repetition of the five-atom unit cell, containing 20 480 atoms. For the twisted systems, the in-plane lattice parameter was twist angle-dependent. Therefore, an $N \times N \times 8$ repetition was used for the top and the bottom layers (e.g., $N \times N \times 16$ in total), where N denotes the repetition along the in-plane direction and varies between 1 and 8. Figures S12 and S13 in the Supporting Information schematically show the crystal structures for typical twist angles. Such large supercells enable good statistics for the calculations. The oxygen vacancies were introduced randomly by removing oxygen ions at random positions, where the site fraction was fixed at 1%. Such oxygen vacancies were compensated by reducing the charge of all the Ti cations. The activation energy (ΔE) of the oxygen vacancies was obtained by fitting the Arrhenius plot (see Supporting Information). The model for bulk STO was verified with the values taken from the literature (Supporting Information, Figure S10). All the MD simulations were performed for the SrO-TiO₂ configuration, which was the most stable configuration as indicated in the Supporting Information, Figure S4. The systems were first equilibrated in the *NPT* ensemble average for at least 300 ps, followed by the production run for at least 600 ps in the *NVT* ensemble. The temperature and pressure were controlled by the Nose-Hoover thermostat (barostat), as implemented in LAMMPS.^[50] The tracer diffusion coefficient (D^*) was obtained from a mean square displacements analysis by summing the diffusion along the a , b , and c -axes using: $\langle r^2 \rangle = 6D^*t + B$, where t is the time and B describes the thermal vibrations. The robustness of the simulations was confirmed by repeating the calculations multiple times.

Supporting Information

Supporting Information is available from the Wiley Online Library or from the author.

Acknowledgements

N.P. acknowledges the support of The European Commission for the Grant 80127 (Biomings, FET-OPEN), N.P., T.S.J., and D.V.C. acknowledge the support of Novo Nordisk Foundation Challenge Programme 2021: Smart nanomaterials for applications in life-science, BIOMAG Grant NNF21OC0066526. Y.L. acknowledges the support by the National Natural Science Foundation of China (grant no. 11704292), and gratefully acknowledges the financial support from China Scholarship Council (grant no. 201908420153) and the supported by Hubei Province Key Laboratory of Systems Science in Metallurgical Process (Wuhan University of Science and Technology). T.S.J. acknowledges support by Research Grant 00013157 from VILLUM FONDEN and DFF-7014-00132 from the Danish Council for Independent Research. F.T. acknowledges support by research Grant 37338 (SANSIT) from VILLUM FONDEN. C.X. acknowledges the support by China Scholarship Council (grant no. 201906240046), T.J.B. acknowledges the support of the VILLUM FONDEN (IonGate), and C.X., D.J.K., and T.J.B. acknowledge the support of the Danish National Research Foundation (DNRF) Center for Nanostructured Graphene (DNRF103).

Conflict of Interest

The authors declare no conflict of interest.

Data Availability Statement

The data that support the findings of this study are available from the corresponding author upon reasonable request.

Keywords

freestanding films, moiré superlattice, oxide thin film, stacking, twisting

Received: April 8, 2022

Revised: July 26, 2022

Published online: August 22, 2022

- [1] Y. Cao, V. Fatemi, S. Fang, K. Watanabe, T. Taniguchi, E. Kaxiras, P. Jarillo-Herrero, *Nature* **2018**, *556*, 43.
- [2] Y. Cao, V. Fatemi, A. Demir, S. Fang, S. L. Tomarken, J. Y. Luo, J. D. Sanchez-Yamagishi, K. Watanabe, T. Taniguchi, E. Kaxiras, R. C. Ashoori, P. Jarillo-Herrero, *Nature* **2018**, *556*, 80.
- [3] Y. Liu, Y. Huang, X. Duan, *Nature* **2019**, *567*, 323.
- [4] L. Wang, E. M. Shih, A. Ghiotto, L. Xian, D. A. Rhodes, C. Tan, M. Claassen, D. M. Kennes, Y. Bai, B. Kim, K. Watanabe, T. Taniguchi, X. Zhu, J. Hone, A. Rubio, A. N. Pasupathy, C. R. Dean, *Nat. Mater.* **2020**, *19*, 861.
- [5] T. I. Andersen, G. Scuri, A. Sushko, K. De Greve, J. Sung, Y. Zhou, D. S. Wild, R. J. Gelly, H. Heo, D. Bérubé, A. Y. Joe, L. A. Jauregui, K. Watanabe, T. Taniguchi, P. Kim, H. Park, M. D. Lukin, *Nat. Mater.* **2021**, *20*, 480.
- [6] H. Su, S. Jaffer, H. Yu, *Energy Storage Mater.* **2016**, *5*, 116.
- [7] A. Tarancón, N. Pryds, *Adv. Mater. Interfaces* **2019**, *6*, 1900990.
- [8] C. Ahn, A. Cavalleri, A. Georges, S. Ismail-Beigi, A. J. Millis, J. M. Triscone, *Nat. Mater.* **2021**, *20*, 1462.
- [9] C. Richter, H. Boschker, W. Dietsche, E. Fillis-Tsirakis, R. Jany, F. Loder, L. F. Kourkoutis, D. A. Muller, J. R. Kirtley, C. W. Schneider, J. Mannhart, *Nature* **2013**, *502*, 528.
- [10] Y. Q. Zhang, H. Ohta, in *2D Nanomaterials for Energy Applications*, (Ed.: S. Zafeirotas), Elsevier, New York **2020**, pp. 209–225.
- [11] A. Brinkman, M. Huijben, M. Van Zalk, J. Huijben, U. Zeitler, J. C. Maan, W. G. Van Der Wiel, G. Rijnders, D. H. A. Blank, H. Hilgenkamp, *Nat. Mater.* **2007**, *6*, 493.
- [12] S. R. Bakaul, J. Kim, S. Hong, M. J. Cherukara, T. Zhou, L. Stan, C. R. Serrao, S. Salahuddin, A. K. Petford-Long, D. D. Fong, M. V. Holt, *Adv. Mater.* **2020**, *32*, 1907036.
- [13] D. Pesquera, E. Parsonnet, A. Qualls, R. Xu, A. J. Gubser, J. Kim, Y. Jiang, G. Velarde, Y. L. Huang, H. Y. Hwang, R. Ramesh, L. W. Martin, *Adv. Mater.* **2020**, *32*, 2003780.
- [14] S. A. Chambers, M. H. Engelhard, V. Shutthanandan, Z. Zhu, T. C. Droubay, L. Qiao, P. V. Sushko, T. Feng, H. D. Lee, T. Gustafsson, E. Garfunkel, A. B. Shah, J. M. Zuo, Q. M. Ramasse, *Surf. Sci. Rep.* **2010**, *65*, 317.
- [15] D. X. Ji, S. Cai, T. R. Paudel, H. Sun, C. Zhang, L. Han, Y. Wei, Y. Zang, M. Gu, Y. Zhang, W. Gao, H. Huyan, W. Guo, D. Wu, Z. Gu, E. Y. Tsymlab, P. Wang, Y. Nie, X. Pan, *Nature* **2019**, *570*, 87.
- [16] L. Lu, Y. Dai, H. Du, M. Liu, J. Wu, Y. Zhang, Z. Liang, S. Raza, D. Wang, C. L. Jia, *Adv. Mater. Interfaces* **2020**, *7*, 1901265.
- [17] D. Lu, D. J. Baek, S. S. Hong, L. F. Kourkoutis, Y. Hikita, H. Y. Hwang, *Nat. Mater.* **2016**, *15*, 1255.
- [18] R. T. Dahm, R. Erlandsen, F. Trier, A. Sambri, E. Di Gennaro, A. Guarino, L. Stampfer, D. V. Christensen, F. M. Granozio, T. S. Jespersen, *ACS Appl. Mater. Interfaces* **2021**, *13*, 12341.
- [19] R. J. Xu, J. Huang, E. S. Barnard, S. S. Hong, P. Singh, E. K. Wong, T. Jansen, V. Harbola, J. Xiao, B. Y. Wang, S. Crossley, D. Lu, S. Liu, H. Y. Hwang, *Nat. Commun.* **2020**, *11*, 3141.
- [20] H. Elangovan, M. Barzilay, S. Seremi, N. Cohen, Y. Jiang, L. W. Martin, Y. Ivry, *ACS Nano* **2020**, *14*, 5053.
- [21] Z. Zhao, A. Abdelsamie, R. Guo, S. Shi, J. Zhao, W. Lin, K. Sun, J. Wang, J. Wang, X. Yan, J. Chen, *Nano Res.* **2022**, *15*, 2682.
- [22] P. T. P. Le, J. E. ten Elshof, G. Koster, *Sci. Rep.* **2021**, *11*, 12435.
- [23] S. S. Hong, M. Gu, M. Verma, V. Harbola, B. Y. Wang, D. Lu, A. Vailionis, Y. Hikita, R. Pentcheva, J. M. Rondinelli, H. Y. Hwang, *Science* **2020**, *368*, 71.
- [24] Z. X. Lu, J. Liu, J. Feng, X. Zheng, L. H. Yang, C. Ge, K. J. Jin, Z. Wang, R. W. Li, *APL Mater.* **2020**, *8*, 051105.
- [25] B. W. Zhang, C. Yun, J. L. MacManus-Driscoll, *Nano-Micro Lett.* **2021**, *13*, 39.
- [26] Z. D. Luo, J. J. P. Peters, A. M. Sanchez, M. Alexe, *ACS Appl. Mater. Interfaces* **2019**, *11*, 23313.
- [27] C. Jin, Y. Zhu, W. Han, Q. Liu, S. Hu, Y. Ji, Z. Xu, S. Hu, M. Ye, L. Chen, *Appl. Phys. Lett.* **2020**, *117*, 252902.
- [28] F. M. Chiabrera, S. Yun, Y. Li, R. T. Dahm, H. Zhang, C. K. R. Kirchert, D. V. Christensen, F. Trier, T. S. Jespersen, N. Pryds, *Ann. Phys.* **2022**, <https://doi.org/10.1002/andp.202200084>.
- [29] G. F. Schneider, V. E. Calado, H. Zandbergen, L. M. K. Vandersypen, C. Dekker, *Nano Lett.* **2010**, *10*, 1912.
- [30] X. Li, Y. W. Zhu, W. W. Cai, M. Borysiak, B. Han, D. Chen, R. D. Piner, L. Colombo, R. S. Ruoff, *Nano Lett.* **2009**, *9*, 4359.
- [31] K. J. Edgar, C. M. Buchanan, J. S. Debenham, P. A. Rundquist, B. D. Seiler, M. C. Shelton, T. Dindall, *Prog. Polym. Sci.* **2001**, *26*, 1605.
- [32] M. Lin, Q. Tan, J. Wu, X. Chen, J. Wang, Y. Pan, X. Zhang, X. Cong, J. Zhang, W. Ji, P. Hu, K. Liu, P. Tan, *ACS Nano* **2018**, *12*, 8770.
- [33] H. Yu, G. Liu, J. Tang, X. Xu, W. Yao, *Sci. Adv.* **2017**, *3*, e1701696.
- [34] Y. Cao, J. M. Park, K. Watanabe, T. Taniguchi, P. Jarillo-Herrero, *Nature* **2021**, *595*, 526.
- [35] T. Li, S. Jiang, L. Li, Y. Zhang, K. Kang, J. Zhu, K. Watanabe, T. Taniguchi, D. Chowdhury, L. Fu, J. Shan, K. F. Mak, *Nature* **2021**, *597*, 350.
- [36] L. A. Hughes, K. van Benthem, *J. Am. Ceram. Soc.* **2019**, *102*, 578.
- [37] M. D. Armstrong, K. W. Lan, Y. W. Guo, N. H. Perry, *ACS Nano* **2021**, *15*, 9211.
- [38] S. J. Haigh, A. Gholinia, R. Jalil, S. Romani, L. Britnell, D. C. Elias, K. S. Novoselov, L. A. Ponomarenko, A. K. Geim, R. Gorbachev, *Nat. Mater.* **2012**, *11*, 764.

- [39] C. Yang, Y. Wang, W. Sigle, P. A. van Aken, *Nano Lett.* **2021**, *21*, 9138.
- [40] F. Cordero, *Mater. Sci. Eng., A* **2009**, *521–522*, 77.
- [41] D. B. Williams, C. B. Carter, *Transmission Electron Microscopy: A Textbook for Materials Science*, Springer US, Boston, MA, USA **2009**.
- [42] K. F. Garrity, J. W. Bennett, K. M. Rabe, D. Vanderbilt, *Comput. Mater. Sci.* **2014**, *81*, 446.
- [43] Yu. Abramov, V. G. Tsirel'son, V. E. Zavodnik, S. A. Ivanov, I. D. Brown, *Acta Crystallogr., Sect. B: Struct. Sci., Cryst. Eng. Mater.* **1995**, *B51*, 942.
- [44] T. Thonhauser, S. Zuluaga, C. A. Arter, K. Berland, E. Schröder, P. Hylgaard, *Phys. Rev. Lett.* **2015**, *115*, 136402.
- [45] P. Giannozzi, O. Andreussi, T. Brumme, O. Bunau, M. Buongiorno, M. Calandra, R. Car, C. Cavazzoni, D. Ceresoli, M. Cococcioni, P. Giannozzi, O. Andreussi, T. Brumme, O. Bunau, M. B. Nardelli, P. Giannozzi, O. Andreussi, T. Brumme, O. Bunau, M. Buongiorno, M. Calandra, R. Car, C. Cavazzoni, D. Ceresoli, M. Cococcioni, *J. Phys.: Condens. Matter* **2017**, *29*, 465901.
- [46] P. Giannozzi, S. Baroni, N. Bonini, M. Calandra, R. Car, C. Cavazzoni, D. Ceresoli, G. L. Chiarotti, M. Cococcioni, I. Dabo, A. Dal Corso, S. De Gironcoli, S. Fabris, G. Fratesi, R. Gebauer, U. Gerstmann, C. Gougoussis, A. Kokalj, M. Lazzeri, L. Martin-Samos, N. Marzari, F. Mauri, R. Mazzarello, S. Paolini, A. Pasquarello, L. Paulatto, C. Sbraccia, S. Scandolo, G. Sclauzero, A. P. Seitsonen, et al., *J. Phys.: Condens. Matter* **2009**, *21*, 395502.
- [47] T. Thonhauser, V. R. Cooper, S. Li, A. Puzder, P. Hylgaard, D. C. Langreth, *Phys. Rev. B* **2007**, *76*, 125112.
- [48] K. Berland, V. R. Cooper, K. Lee, E. Schröder, T. Thonhauser, P. Hylgaard, B. I. Lundqvist, *Rep. Prog. Phys.* **2015**, *78*, 066501.
- [49] A. Pedone, A. G. M., M. C. Menziani, A. N. Cormack, U. A. Segre, *J. Phys. Chem. B* **2006**, *110*, 11780.
- [50] S. Plimpton, *J. Comput. Phys.* **1995**, *117*, 1.

R. T. Dahm, *et al.*

Size-controlled spalling of $\text{LaAlO}_3/\text{SrTiO}_3$ micromembranes
ACS applied materials & interfaces **13**, 12341-12346 (2021)



Shinkosha SrTiO_3 substrate

Size-Controlled Spalling of LaAlO₃/SrTiO₃ Micromembranes

Rasmus T. Dahm, Ricci Erlandsen, Felix Trier, Alessia Sambri, Emiliano Di Gennaro, Anita Guarino, Lukas Stampfer, Dennis V. Christensen, Fabio Miletto Granozio, and Thomas S. Jespersen*

Cite This: *ACS Appl. Mater. Interfaces* 2021, 13, 12341–12346

Read Online

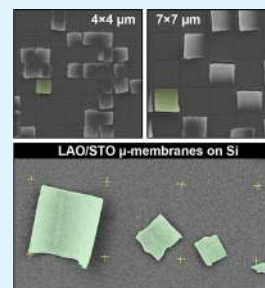
ACCESS |

Metrics & More

Article Recommendations

Supporting Information

ABSTRACT: The ability to form freestanding oxide membranes of nanoscale thickness is of great interest for enabling material functionality and for integrating oxides in flexible electronic and photonic technologies. Recently, a route has been demonstrated for forming conducting heterostructure membranes of LaAlO₃ and SrTiO₃, the canonical system for oxide electronics. In this route, the epitaxial growth of LaAlO₃ on SrTiO₃ resulted in a strained state that relaxed by producing freestanding membranes with random sizes and locations. Here, we extend the method to enable self-formed LaAlO₃/SrTiO₃ micromembranes with control over membrane position, their lateral sizes from 2 to 20 μm, and with controlled transfer to other substrates of choice. This method opens up the possibility to study and use the two-dimensional electron gas in LaAlO₃/SrTiO₃ membranes for advanced device concepts.



KEYWORDS: LaAlO₃/SrTiO₃, two-dimensional electron gas, freestanding oxide membranes, flexible electronics, thin-film spalling, micro manipulation

INTRODUCTION

The realization and characterization of freestanding epitaxial oxide layers has recently received significant attention due to potential applications in flexible electronics and photonics.^{1,2} The membrane geometry allows for the integration of oxide functional materials in technologically important platforms, such as silicon or flexible polyethylene terephthalate (PET), where conventional epitaxial integration is challenging.^{3–5} Most excitingly, however, the membrane properties may be significantly altered compared to the bulk counterpart, offering new opportunities for functional devices. Examples include enhanced ferromagnetic properties for La_{1–x}Sr_xMnO₃ membranes⁶ and a giant flexoelectric response in freestanding BiFeO₃ and SrTiO₃ films.⁷ Recent advances toward single unit cell oxide membranes even join these systems to the family of two-dimensional materials alongside graphene and transition-metal dichalcogenides.^{8,9}

Most studies of freestanding oxide membranes have relied on the deposition of the oxide layer of interest in sacrificial epitaxial layers such as La_{1–x}Sr_xMnO₃ or Sr₃Al₂O₆, which subsequently can be dissolved in KI/HCl and water, respectively, to lift-off the oxide membrane.^{3,11}

Using this approach, it has not yet been possible to realize freestanding membranes of the conducting heterostructure LaAlO₃/SrTiO₃ (LAO/STO), which is the canonical system for emergent electronic phases in oxides.^{12–14} An alternative approach for the formation of thin membranes, which obviates the need for a sacrificial layer and etching, is that of controlled spalling. This method relies on the deposition of a stressor

layer and a flexible handle-layer to controllably delaminate the surface layers of a brittle crystal and has been successfully used to release membranes from wafer scale semiconductors such as silicon, germanium, nitrides, and III–V compounds.^{15–17} The spalling process relies on a stable fracture mode where a crack propagates parallel to the substrate at the equilibrium depth where the shear stress is minimized. The process self-corrects such that, for a crack very close to the surface, the top layer contracts and the crack tip is deflected downward; conversely, for a crack very deep in the substrate, the top layer will expand upon fracture due to the curvature and the crack is instead deflected upward. The details of the crack propagation are reviewed in ref 18. In ref 10, some of us reported the spontaneous spalling of self-formed micrometer sized membranes of LAO/STO employing the lattice mismatched LAO top layer as the stressor layer. The process is schematically illustrated in Figure 1a, and a scanning electron microscope (SEM) micrograph of a typical sample is shown in Figure 1b. Depending on the LAO thickness, the thicknesses of the micro membranes were ~140–200 nm, and importantly, the interface conductivity remains intact after membrane release and transfer to a silicon platform. This creates qualitatively new

Received: December 5, 2020

Accepted: February 22, 2021

Published: March 4, 2021



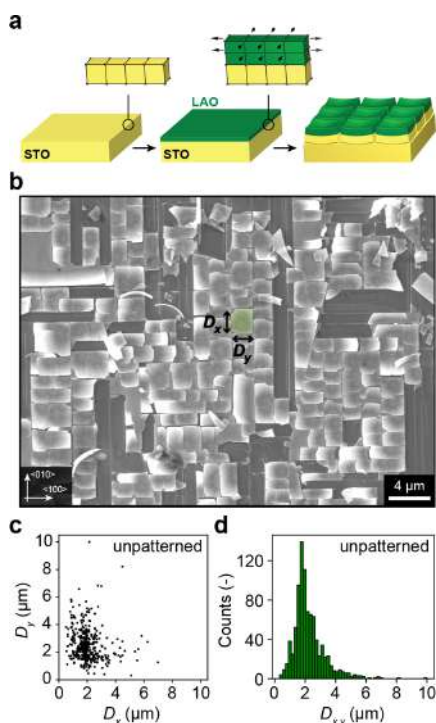


Figure 1. (a) Schematic illustration of the spontaneous (LAO/STO) membrane spalling. Adapted with permission from ref 10. Copyright 2020 John Wiley & Sons. (b) Scanning electron microscope (SEM) image showing the spontaneously formed LAO/STO membranes of an as-grown sample with 70 nm LAO. (c) Distribution of lateral sizes (D_x , D_y) of membranes. No correlation is found between D_x and D_y , and panel (d) shows the overall size distribution ($D_{x,y}$) displaying a clear preference for membranes with lateral sizes around $\sim 1.9 \mu\text{m}$.

opportunities for oxide electronics allowing for integration with conventional semiconductor electronics and semiconductor processing. Furthermore, since each LAO/STO growth results in millions of individual membranes sufficient for multiple device generations, the results greatly improve the opportunities for device optimization and reproducibility. The proof-of-concept developed in ref 10 relies on the spontaneous spalling of the surface and results in membranes of random sizes forming at random positions and subsequent uncontrolled transfer to silicon.

Here, we extend this work by introducing a new concept for pregrowth substrate preparation allowing for control of where the LAO/STO membranes form on the substrate as well as their individual lateral dimensions. Further, we demonstrate controlled manipulation of individual LAO/STO micromembranes onto silicon substrates.

RESULTS AND DISCUSSION

Initially, we considered the as-grown, uncontrolled, spontaneously spalled LAO/STO sample with 70 nm LAO shown in Figure 1b. The sample surface is fractured into approximately rectangular membranes with edges parallel to the [100] and [010] crystal directions of STO and lateral dimensions D_x , D_y .

We note that all membranes in Figure 1b and throughout this work exhibit curvature. This is a consequence of the different lattice spacings of LAO and STO and thus directly confirms that all the membranes host the LAO/STO heterostructure and not just the LAO top film. The sizes of all 451 imaged membranes from three different regions of the sample were manually measured, and the size distribution can be seen in Figure 1c. No linear statistical correlation was found between D_x and D_y , and the combined distribution of the lateral membrane dimension ($D_{x,y}$)—i.e., the distance between spontaneous surface fracture events—is shown in Figure 1d having an average of $\sim 1.9 \mu\text{m}$. Consequently, the average membrane area and circumference follow distributions peaked at $4.5 \mu\text{m}^2$ and $\sim 8 \mu\text{m}$, respectively (see the Supporting Information (SI) Figures S1 and S2). The distribution in Figure 1d, having a sharply peaked mean around $\sim 1.9 \mu\text{m}$ and a low probability for larger and smaller dimensions, reflects that the driving force for membrane fracturing—the energy associated with the strain—increases with the lateral size. This makes it unlikely to find very large membranes as these will internally fracture and subdivide as a consequence of the energy balance between the membrane strain and the membrane surface energy.^{18–20}

For conventional spalling of semiconductors, the initial fracturing is triggered by a discontinuity appearing at the edges of the stressor layer.¹⁵ Here, we instead investigated the possibility of controlling the position of fractures by topographic discontinuities predefined in the growth substrate. The process is schematically illustrated in Figure 2a and relies on a combination of lithography and Ar^+ -ion milling to define trenches in the STO substrate prior to LAO deposition. Each STO substrate was patterned with multiple $200 \times 200 \mu\text{m}^2$ fields, each consisting of a grid of 250 nm wide trenches milled to a depth of 20 nm. The trench grid thus outlines an array of square regions of pristine STO surfaces ready for epitaxially strained growth. The dimensions of the squares $L_{x,y} = 0.5\text{--}20 \mu\text{m}$ were varied between each field, and Figure 2b–d show typical characteristics of a $L_{x,y} = 2 \mu\text{m}$ field before growth. As detailed in the Experimental Section, milling parameters were carefully chosen to prevent the substrate conductivity caused by the Ar^+ -ion bombardment, and resist-stripping and surface cleaning procedures were optimized to ensure that the patterned STO surface displayed TiO_2 -terminated terrace structures (Figure 2c) facilitating the epitaxial growth of LAO.

Figure 3a shows typical scanning electron micrographs of patterned samples after the growth of 70 nm of LAO¹⁰ (see Figure S3 for additional images). The clear directed formation of LAO/STO micromembranes following the intended substrate pattern was observed for all fields, proving the viability of the concept. However, membranes did not form at all the intended positions, indicating that the patterned surface discontinuity can be further optimized to trigger surface fractures more efficiently. For fields with $L_{x,y} = 0.5\text{--}2 \mu\text{m}$, which is equal to or smaller than the average unpatterned membrane size shown in Figure 1d, only very few free-standing membranes were found. We associate this with strain relaxation at the edges of the pattern and an elastic energy of the small membranes below the threshold for spontaneous spalling. This thus sets a lower limit on the size of controlled membranes; however, we expect that this limit will depend on the pattern and the LAO thickness; these smallest membrane patterns are excluded from the analysis below.

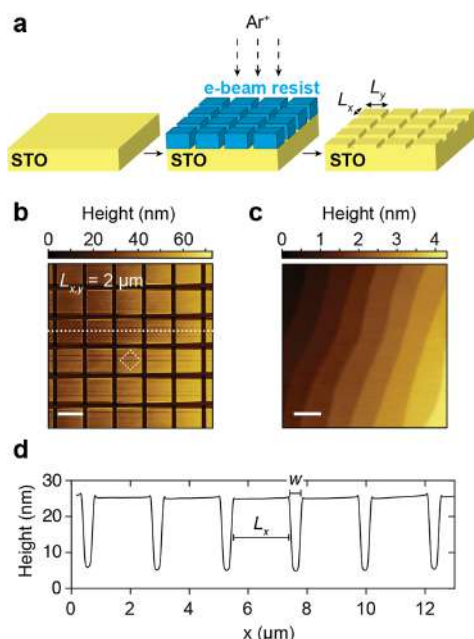


Figure 2. (a) Schematic illustration of the surface patterning by Ar^+ -ion milling. (b) Atomic force microscopy (AFM) topography map of the STO surface following Ar^+ -ion milling and cleaning procedures for a field with $L_{xy} = 2 \mu\text{m}$ squares (scale bar is $2 \mu\text{m}$). The dashed square and line correspond to the zoomed image in c and height profile in d, respectively. (c) High-resolution AFM image of the area in b showing clear terraces characteristic of clean TiO_2 -terminated STO (scale bar is 200 nm). (d) Height profile along the dashed line in b, which shows an average milled depth of 20 nm and a trench width of $w = 250 \text{ nm}$.

For the fields with $L_{xy} = 4\text{--}20 \mu\text{m}$, 1146 membranes were imaged by SEM and manually counted using the same procedure as that for Figure 1 (see SI Figure S4). The resulting membrane size distributions, D_{xy} , for each patterned grid size (L_{xy}) are presented in Figure 3b. For $L_{xy} = 4 \mu\text{m}$, the LAO/STO membranes clearly display a narrow size distribution closely matching the patterned size. A smaller but significant population of membranes also appears with lateral sizes around $D_{xy} \sim 8 \mu\text{m}$, i.e., twice the patterned L_{xy} due to two neighboring membranes remaining merged. For $L_{xy} = 7 \mu\text{m}$, a different behavior is apparent: the size distribution shows two characteristic populations—one corresponding to the intended patterned size of $7 \mu\text{m}$ and one of the smaller sizes around $\sim 3.5 \mu\text{m}$ corresponding internally to the fracture of the patterned squares. By comparing the size distribution of the as-grown sample in Figure 1b where the average size was around $\sim 1.9 \mu\text{m}$, it is clear that these internally fractured membranes are affected by the proximity of the trenches to dictate their resulting larger size. As the patterned square size is increased to $L_{xy} = 10$ and $20 \mu\text{m}$, it is clear that the likelihood of forming correspondingly large membranes is reduced while the population of smaller internally fractured membranes increases. For $L_{xy} = 20 \mu\text{m}$, the distribution approaches that of the as-grown sample with an average lateral size around $\sim 2.5 \mu\text{m}$, and only very few membranes of the intended size were observed (see inset in the lower panel of Figure 3b). Thus, this

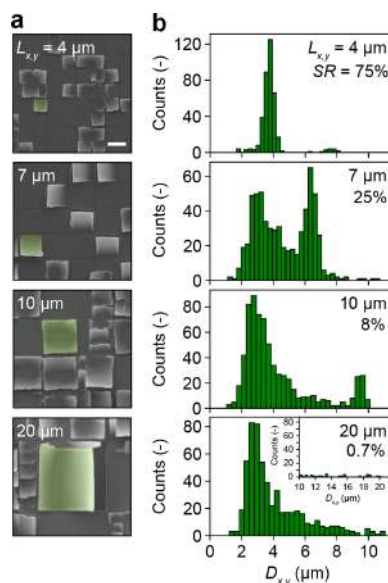


Figure 3. (a) Representative SEM images of the different patterned sizes investigated with $L_{xy} = 4\text{--}20 \mu\text{m}$. Scale bar corresponds to $5 \mu\text{m}$. (b) Size distributions (D_{xy}) of membranes measured in SEM for each L_{xy} investigated, with success rate (SR) indicated for each. For smaller patterned sizes, the resulting membranes appear with a size close to the intended. As the patterned size is increased, smaller membranes are formed as a result of internal fracture inside the patterned square that ultimately approaches the as-grown membrane size distribution.

method has both an upper and lower limit for the size control, with the yield of intentionally sized membranes reducing as the pattern sizes become much larger than the average $1.9 \mu\text{m}$. Also stated on the respective panels of Figure 3b is the success rate (SR), defined as the fraction of spalled membranes with dimensions D_{xy} within $\pm 0.25 \mu\text{m}$ (i.e., the trench width) of the defined pattern dimensions L_{xy} out of the total number of membranes. With this definition—reflecting the peak area of the distributions—the success rate decreases monotonously from 75% for the $4 \mu\text{m}$ pattern to 25%, 8%, and 0.7% for the 7, 10, and $20 \mu\text{m}$ patterns, respectively. This is clearly significant compared to the unpatterned sample (Figure 1c) where the corresponding SR for the same sizes would be 2.7%, 0.3%, 0.1%, and 0.0%. This is also consistent with a direct inspection of SEM images, which confirm that membranes found with the intended sizes indeed result almost exclusively from directed formation along the milled pattern and not random spalling, which occasionally has a similar size. An alternative definition of SR is the area covered by correctly spalled membranes with respect to the total imaged area. This definition is insensitive to the failure mode (e.g., whether membranes failed to fracture at all or the degree to which a patterned membrane subdivided). With this definition, the corresponding success rates are $\sim 10\%$, 25%, 20%, and 5% for $L_{xy} = 4, 7, 10,$ and $20 \mu\text{m}$. The failure mode for the smaller membranes are thus primarily due to intended membranes not forming at all, while for $L = 20 \mu\text{m}$, a sizable fraction of the number of possible membranes did form, although a large number of smaller membranes is also present. We note that both definitions of SR would yield 100% in the

case of perfect controlled spalling, and we expect that the numbers can be greatly improved in the future by optimizing the patterning and growth parameters. To summarize, for all grid sizes, membranes were found and were spalled along the intended pattern. While this serves as proof of the concept, the histograms in Figure 3b quantify its efficiency as discussed above.

As clearly seen in the scanning electron micrographs of the uncontrolled membrane growth in Figure 1b, the natural fracture direction is along the [100]/[010] high-symmetry directions, and these were also chosen for the orientation of the control patterns in Figures 2 and 3. To investigate the possibility of generating complex membrane shapes following other directions, a trench pattern was fabricated along [110]/[1-10], i.e., rotated by 45° with respect to the design in Figures 2 and 3. The resulting membranes are shown in SI Figure S5. While a significant fraction of membranes shows internal cracks or corners truncated along [100]/[010], the pregrowth patterning method is clearly feasible for also directing fractures along directions not along the naturally preferred [100]/[010].

Lastly, to demonstrate the perspectives of the self-formed membranes and the present patterning technique for electronic devices, we show in Figure 4 the results of the controlled

geometries, the membranes are further fixed by contact materials. We also note that the micromanipulator technique will allow for the routine transfer of the membranes to any substrate and will expand the possible heteromaterial combinations. We expect that entire arrays of membranes may be simultaneously transferred, keeping their mutual distances, by adapting the techniques of polydimethylsiloxane (PDMS) stamping developed for the assembly of van der Waals heterostructures.

CONCLUSION

To conclude, we have demonstrated a proof-of-principle for the directed spalling and size control of conducting LAO/STO heterostructure membranes. The method relies on patterning the stress discontinuities in the LAO/STO epitaxial heterostructure by locally altering the growth substrate using argon milling prior to the growth. The size control is constricted by an upper and lower limit with respect to the yield and reproducibility of membranes. We also demonstrate the capability of direction fracture formation along directions different from [100]/[010] otherwise strongly preferred without the pregrowth patterning. Lastly, we show that the membranes can be manipulated in a controllable manner with a micromanipulator needle and transferred onto a silicon substrate. Preliminary results (Figure S5) suggest that extending the trench width may increase the yield, and we expect that a systematic variation of all the design parameters (trench width, depth, etc.) as well as LAO thickness will allow for significant improvement of the yield and extend the method toward more complex structures. We note further that the membranes exhibit thickness variations determined by the propagation of the crack tip during spalling. At a distance from the edge that exceeds the thickness, the unevenness is not expected to depend on the nature of the crack triggering (spontaneous vs controlled), and although no systematic study has been done, no significant differences have been observed compared to the previous work of ref 10. Thickness variations may, however, be related to the speed of the spalling process, and we expect that, by introducing a sacrificial handling/straining layer onto the heterostructure stack, our method may be improved both toward membranes of larger lateral size and more uniform thickness.

EXPERIMENTAL SECTION

LAO with a thickness of 70 nm, used for both unpatterned and pregrowth patterned spalled micromembranes, was grown by pulsed laser deposition (PLD) on TiO₂-terminated (001) STO substrates heated to 730 °C at an oxygen background pressure of 2×10^{-2} mbar. The LAO was ablated from a single crystal target with a KrF excimer laser at a repetition rate of 3 Hz and a laser fluence around 2.5 J/cm². The laser pulse width was 20 ns, the ablation spot area was 0.78 mm², and the angle of incidence was 45°. The target–substrate distance was in all depositions fixed to 37 mm. Following LAO growth, the samples were annealed at 500 °C in 50 mbar oxygen for 1 h, before cooling to room temperature under the same oxygen partial pressure.

To prepare the pregrowth patterned sample for electron-beam lithography, the sample was first rinsed in acetone and isopropanol and finally dried with N₂. In order to direct the Ar⁺-milling, the sample was prepared with a ~900 nm trilayer e-beam resist stack consisting of copolymer El6, Czar 13%, and a decharging top-layer of Espacer 300Z. The resist stack was exposed and developed using standard conditions. The Ar⁺-milling was carried out with a Kaufman ion source using a beam voltage of 600 V and a beam current of 23 mA. Using these beam conditions, the sample was milled for 6 min.

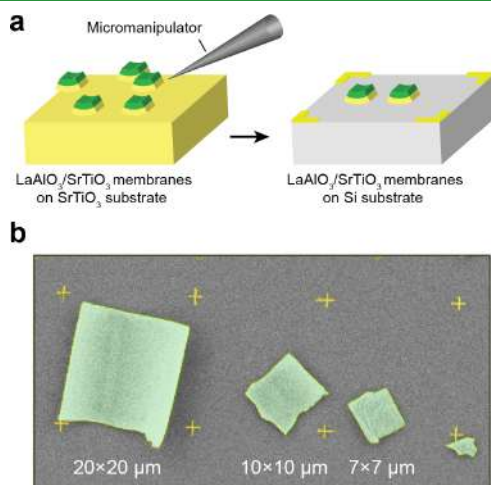


Figure 4. (a) Schematic illustration of the controllable manipulation and transfer of LAO/STO membranes with a micromanipulator needle onto a silicon substrate. (b) SEM image of transferred membranes arranged into a row on the prepatterned silicon substrate.

membrane transfer onto a SiO₂/Si substrate by means of a micromanipulator (see Experimental Section for details). Four individual membranes were selected on different patterning fields of the growth substrate and transferred and arranged on a Si/SiO₂ substrate with respect to an existing alignment grid. This degree of control shows the feasibility of this patterning method for realizing unique device principles involving the LAO/STO interface two-dimensional electron gas or for devices combining functionalities of different oxide heterostructures in the same circuit. We note that, despite the curvature, the membranes are sufficiently clamped to the substrate by van der Waals forces to allow for standard device fabrication procedures (resist spinning, etc.). In device

The remaining resist was stripped with *N*-methyl-2-pyrrolidone (NMP), and organic residues were removed by oxygen plasma ashing.

Individual LAO/STO membranes were transferred from the growth substrate to the silicon substrate in a home-built setup having a programmable motorized stage (*x,y,z*) + rotation where the growth source substrate and the silicon target substrates are placed. In addition, the system was equipped with an Eppendorf *x,y,z* manipulator equipped with a 0.1 μm disposable tungsten needle. The system was integrated into a long working-distance optical microscope, and nanostructures can routinely be picked-up from the source substrate and deposited on the target substrate with an accuracy of less than 1 μm .

■ ASSOCIATED CONTENT

Supporting Information

The Supporting Information is available free of charge at <https://pubs.acs.org/doi/10.1021/acsami.0c21612>.

Figures of histograms of membrane area and circumference, SEM images, and recorded sizes (D_x , D_y) of all membranes investigated (PDF)

■ AUTHOR INFORMATION

Corresponding Author

Thomas S. Jespersen – Center for Quantum Devices, Niels Bohr Institute, University of Copenhagen, 2100 Copenhagen, Denmark; Department of Energy Conversion and Storage, Technical University of Denmark, 2800 Kgs. Lyngby, Denmark; orcid.org/0000-0002-7879-976X; Email: tsand@nbi.ku.dk

Authors

Rasmus T. Dahm – Center for Quantum Devices, Niels Bohr Institute, University of Copenhagen, 2100 Copenhagen, Denmark; Department of Energy Conversion and Storage, Technical University of Denmark, 2800 Kgs. Lyngby, Denmark

Ricci Erlandsen – Center for Quantum Devices, Niels Bohr Institute, University of Copenhagen, 2100 Copenhagen, Denmark; Department of Energy Conversion and Storage, Technical University of Denmark, 2800 Kgs. Lyngby, Denmark

Felix Trier – Center for Quantum Devices, Niels Bohr Institute, University of Copenhagen, 2100 Copenhagen, Denmark; orcid.org/0000-0003-0228-0635

Alessia Sambri – CNR-SPIN, Complesso Universitario di Monte S. Angelo, Via Cintia 80126, Naples, Italy

Emiliano Di Gennaro – Dipartimento di Fisica “E. Pancini”, Compl. Univ. di Monte S. Angelo, Università di Napoli “Federico II”, Via Cintia 80126, Napoli, Italy; orcid.org/0000-0003-4231-9776

Anita Guarino – Department of Physical Sciences and Technologies of Matter, CNR-DSFTM NFFA Trieste Area Science Park, 34149 Trieste, Italy

Lukas Stampfer – Center for Quantum Devices, Niels Bohr Institute, University of Copenhagen, 2100 Copenhagen, Denmark

Dennis V. Christensen – Department of Energy Conversion and Storage, Technical University of Denmark, 2800 Kgs. Lyngby, Denmark

Fabio Miletto Granozio – CNR-SPIN, Complesso Universitario di Monte S. Angelo, Via Cintia 80126, Naples, Italy; orcid.org/0000-0002-9417-7848

Complete contact information is available at:

<https://pubs.acs.org/10.1021/acsami.0c21612>

Notes

The authors declare no competing financial interest.

■ ACKNOWLEDGMENTS

This research was supported by the Danish National Research Foundation. T.S.J. acknowledges support by Research Grant 00013157 from VILLUM FONDEN and DFF-7014-00132 from the Danish Council for Independent Research. A.S., E.D.G., A.G., and F.M.G. acknowledge funding from the project QUANTOX (QUANTum Technologies with 2D-OXides) of QuantERA ERA-NET Cofund in Quantum Technologies (Grant Agreement N. 731473) implemented within 10th European Union’s Horizon 2020 Programme and MIUR PRIN 2017 (Grant Nos. 20177SL7HC “TOPSPIN” and 2017YCTB59 “TWEET”).

■ REFERENCES

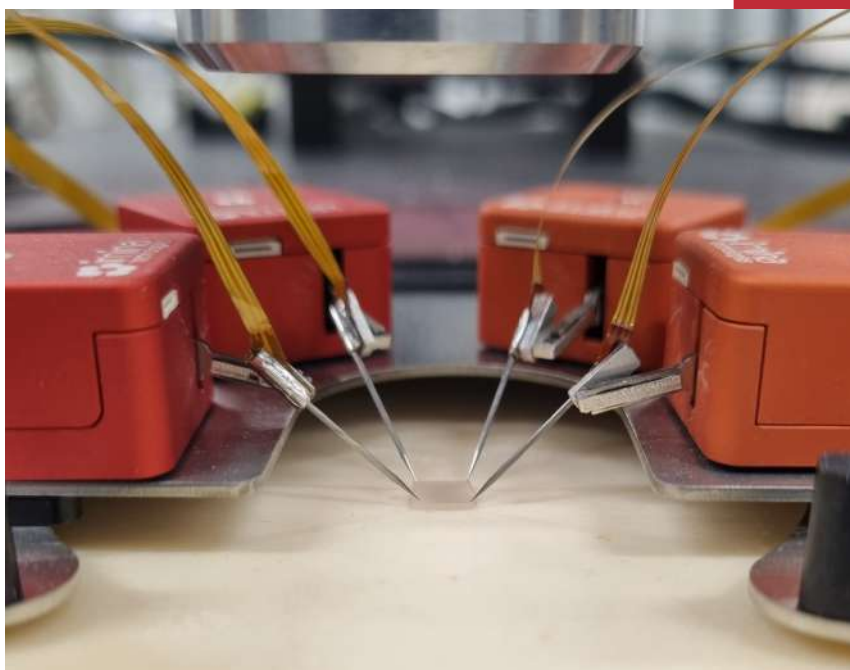
- (1) Kum, H.; Lee, D.; Kong, W.; Kim, H.; Park, Y.; Kim, Y.; Baek, Y.; Bae, S.-H.; Lee, K.; Kim, J. Epitaxial Growth and Layer-Transfer Techniques for Heterogeneous Integration of Materials for Electronic and Photonic Devices. *Nature Electronics* **2019**, *2*, 439–450.
- (2) Gao, W.; Zhu, Y.; Wang, Y.; Yuan, G.; Liu, J.-M. A Review of Flexible Perovskite Oxide Ferroelectric Films and Their Application. *Journal of Materiomics* **2020**, *6*, 1–16.
- (3) Bakaul, S. R.; Serrao, C. R.; Lee, O.; Lu, Z.; Yadav, A.; Carraro, C.; Maboudian, R.; Ramesh, R.; Salahuddin, S. High Speed Epitaxial Perovskite Memory on Flexible Substrates. *Adv. Mater.* **2017**, *29*, 1605699.
- (4) Shen, L.; Wu, L.; Sheng, Q.; Ma, C.; Zhang, Y.; Lu, L.; Ma, J.; Ma, J.; Bian, J.; Yang, Y.; Chen, A.; Lu, X.; Liu, M.; Wang, H.; Jia, C.-L. Epitaxial Lift-Off of Centimeter-Scaled Spinel Ferrite Oxide Thin Films for Flexible Electronics. *Adv. Mater.* **2017**, *29*, 1702411.
- (5) Lu, D.; Crossley, S.; Xu, R.; Hikita, Y.; Hwang, H. Y. Freestanding Oxide Ferroelectric Tunnel Junction Memories Transferred onto Silicon. *Nano Lett.* **2019**, *19*, 3999–4003.
- (6) Lu, D.; Baek, D. J.; Hong, S. S.; Kourkoutis, L. F.; Hikita, Y.; Hwang, H. Y. Synthesis of Freestanding Single-Crystal Perovskite Films and Heterostructures by Etching of Sacrificial Water-Soluble Layers. *Nat. Mater.* **2016**, *15*, 1255–1260.
- (7) Cai, S.; Lun, Y.; Ji, D.; Han, L.; Guo, C.; Zang, Y.; Gao, S.; Wei, Y.; Gu, M.; Zhang, C.; Gu, Z.; Wang, X.; Addiego, C.; Fang, D.; Nie, Y.; Hong, J.; Wang, P.; Pan, X. Giant Polarization and Abnormal Flexural Deformation in Bent Freestanding Perovskite Oxides. *arXiv* **2020**, 03177.
- (8) Hong, S. S.; Yu, J. H.; Lu, D.; Marshall, A. F.; Hikita, Y.; Cui, Y.; Hwang, H. Y. Two-Dimensional Limit of Crystalline Order in Perovskite Membrane Films. *Science Advances* **2017**, *3*, No. eaao5173.
- (9) Ji, D.; Cai, S.; Paudel, T. R.; Sun, H.; Zhang, C.; Han, L.; Wei, Y.; Zang, Y.; Gu, M.; Zhang, Y.; Gao, W.; Huyan, H.; Guo, W.; Wu, D.; Gu, Z.; Tsybal, E. Y.; Wang, P.; Nie, Y.; Pan, X. Freestanding Crystalline Oxide Perovskites Down to the Monolayer Limit. *Nature* **2019**, *570*, 87–90.
- (10) Sambri, A.; Scuderi, M.; Guarino, A.; Gennaro, E. D.; Erlandsen, R.; Dahm, R. T.; Bjorlig, A. V.; Christensen, D. V.; Capua, R. D.; Ventura, B. D.; Uccio, U. S. d.; Mirabella, S.; Nicotra, G.; Spinella, C.; Jespersen, T. S.; Granozio, F. M. Self-Formed, Conducting LaAlO₃/SrTiO₃ Micro-Membranes. *Adv. Funct. Mater.* **2020**, *30*, 1909964.
- (11) Bakaul, S. R.; Serrao, C. R.; Lee, M.; Yeung, C. W.; Sarker, A.; Hsu, S.-L.; Yadav, A. K.; Dedon, L.; You, L.; Khan, A. I.; Clarkson, J. D.; Hu, C.; Ramesh, R.; Salahuddin, S. Single Crystal Functional Oxides on Silicon. *Nat. Commun.* **2016**, *7*, 10547.
- (12) Ohtomo, A.; Hwang, H. Y. A High-Mobility Electron Gas at the LaAlO₃/SrTiO₃ Heterointerface. *Nature* **2004**, *427*, 423–426.

- (13) Pai, Y.-Y.; Tylan-Tyler, A.; Irvin, P.; Levy, J. Physics of SrTiO₃-Based Heterostructures and Nanostructures: a Review. *Rep. Prog. Phys.* **2018**, *81*, 036503.
- (14) Christensen, D. V.; Trier, F.; Niu, W.; Gan, Y.; Zhang, Y.; Jespersen, T. S.; Chen, Y.; Pryds, N. Stimulating Oxide Heterostructures: A Review on Controlling SrTiO₃-Based Heterointerfaces with External Stimuli. *Adv. Mater. Interfaces* **2019**, *6*, 1900772.
- (15) Bedell, S. W.; Fogel, K.; Lauro, P.; Shahrjerdi, D.; Ott, J. A.; Sadana, D. Layer Transfer by Controlled Spalling. *J. Phys. D: Appl. Phys.* **2013**, *46*, 152002.
- (16) Bedell, S. W.; Lauro, P.; Ott, J. A.; Fogel, K.; Sadana, D. K. Layer Transfer of Bulk Gallium Nitride by Controlled Spalling. *J. Appl. Phys.* **2017**, *122*, 025103.
- (17) Shahrjerdi, D.; Bedell, S. W. Extremely Flexible Nanoscale Ultrathin Body Silicon Integrated Circuits on Plastic. *Nano Lett.* **2013**, *13*, 315–320.
- (18) Hutchinson, J.; Suo, Z. Mixed Mode Cracking in Layered Materials. *Adv. Appl. Mech.* **1991**, *29*, 63–191.
- (19) Drory, M.; Thouless, M.; Evans, A. On the Decohesion of Residually Stressed Thin Films. *Acta Metall.* **1988**, *36*, 2019–2028.
- (20) Hu, M.; Thouless, M.; Evans, A. The Decohesion of Thin Films from Brittle Substrates. *Acta Metall.* **1988**, *36*, 1301–1307.

R. Erlandsen, **R. T. Dahm**, *et al.*

A Two-Dimensional Superconducting Electron Gas in Freestanding
 $\text{LaAlO}_3/\text{SrTiO}_3$ Micromembranes

Nano Letters **22**, 4758-4764 (2022)



Imaging station

A Two-Dimensional Superconducting Electron Gas in Freestanding LaAlO₃/SrTiO₃ Micromembranes

Ricci Erlandsen, Rasmus Tindal Dahm, Felix Trier, Mario Scuderi, Emiliano Di Gennaro, Alessia Sambri, Charline Kaisa Reffeldt Kirchert, Nini Pryds, Fabio Miletto Granozio, and Thomas Sand Jespersen*



Cite This: <https://doi.org/10.1021/acs.nanolett.2c00992>



Read Online

ACCESS |



Metrics & More



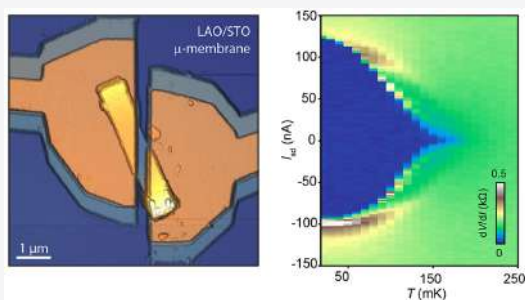
Article Recommendations



Supporting Information

ABSTRACT: Freestanding oxide membranes constitute an intriguing material platform for new functionalities and allow integration of oxide electronics with technologically important platforms such as silicon. Sambri et al. recently reported a method to fabricate freestanding LaAlO₃/SrTiO₃ (LAO/STO) membranes by spalling of strained heterostructures. Here, we first develop a scheme for the high-yield fabrication of membrane devices on silicon. Second, we show that the membranes exhibit metallic conductivity and a superconducting phase below ~ 200 mK. Using anisotropic magnetotransport we extract the superconducting phase coherence length $\xi \approx 36$ – 80 nm and establish an upper bound on the thickness of the superconducting electron gas $d \approx 17$ – 33 nm, thus confirming its two-dimensional character. Finally, we show that the critical current can be modulated using a silicon-based backgate. The ability to form superconducting nanostructures of LAO/STO membranes, with electronic properties similar to those of the bulk counterpart, opens opportunities for integrating oxide nanoelectronics with silicon-based architectures.

KEYWORDS: LAO/STO heterostructure, freestanding membrane, superconductivity, strain



and has served as a motivation for significant theoretical and experimental efforts. State of the art techniques for fabricating freestanding oxide membranes employ a sacrificial layer and epitaxial liftoff^{1–3} but have so far not allowed the realization of freestanding and conducting LAO/STO membranes. However, we recently reported an alternative method based on strain-induced spalling that consistently produces freestanding LAO/STO heterostructure membranes featuring metallic conductivity.^{22,23} The lateral size of the membranes are in the micrometer range and can be controlled by pregrowth substrate preparation, and individual membranes can be transferred to other substrates for device purposes.^{22,24} The spalled micromembranes differ significantly from the conventional bulk LAO/STO heterostructure counterpart. First, the much thicker LAO top layer (~ 70 nm) will effectively screen the conducting interface from scattering associated with fluctuations of the chemical and electrical potential due to

Freestanding membranes of complex oxides have attracted a great deal of interest in recent years^{1–3} due to the potential of integrating oxides with technologically important platforms such as silicon, flexible polyethylene terephthalate, and biocompatible polyimide, a goal which has proven a considerable challenge by conventional means of epitaxial growth. Additionally, in comparison to conventional bulk heterostructures, membranes may accommodate much larger strain and enhanced properties that are tied to mechanical degrees of freedom.^{1,4–6}

Studies of electron transport in oxide heterostructures remain an active field of research.^{7–9} The canonical system for oxide electronics is the two-dimensional electron gas (2DEG) appearing at the heterointerface between the two perovskites SrTiO₃ (STO) and LaAlO₃ (LAO).^{10–12} STO-based 2DEGs can attain high electron mobilities,¹³ allow gate tunability, and have been shown to host unique combinations of properties, including a large spin–orbit coupling¹⁴ enabling significant spin/charge interconversion efficiencies,^{15–17} room-temperature in-plane ferromagnetic ordering,¹⁸ and a gate-tunable superconducting phase at low temperature. The phase diagram of the two-dimensional superconducting state resembles that of doped bulk STO with a dome-shaped dependence of the transition temperature on carrier density.^{19–21} This closely resembles high- T_c superconductors

Received: March 11, 2022
Revised: June 2, 2022

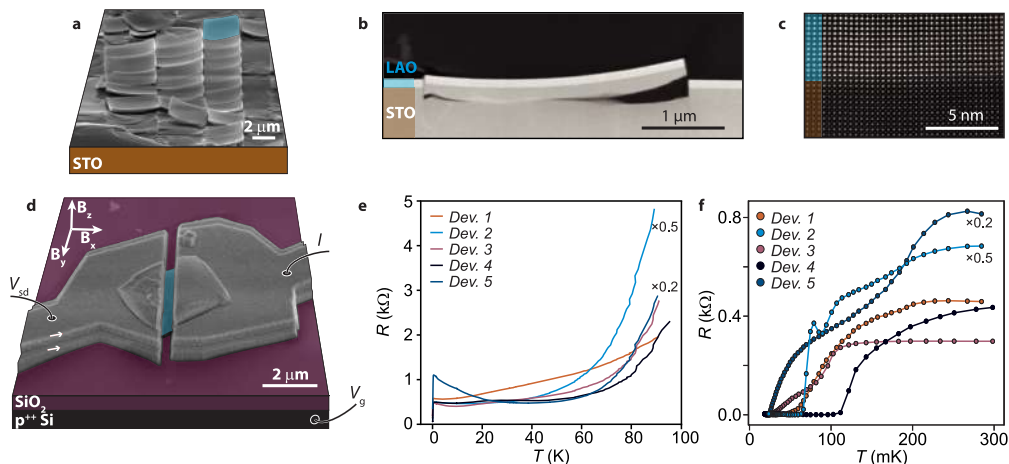


Figure 1. (a) Tilt-view scanning electron microscope (SEM) image of the as-grown LAO/STO micromembranes. (b) Low-magnification scanning transmission electron microscope (TEM) image of a cross section of the growth substrate. The LAO layer (blue) appears with a lighter contrast in comparison to the STO (brown). A partially released LAO/STO micromembrane is apparent with curving due to a LAO/STO lattice mismatch. (c) High-resolution image of the epitaxial LAO/STO interface. (d) Artificially colored SEM of a finished LAO/STO membrane device fabricated on a p^{++} Si/SiO₂ substrate. The degenerately doped substrate acts as a backgate electrode in the measurements. (e) Two-terminal resistance vs temperature for five devices showing metallic behavior. (f) Low-temperature regime of (e) showing superconducting transitions. In (e) and (f), the resistance of the cryostat filters and the membrane/metal interface have been subtracted (see text) and results for Dev. 2 and 5 have been scaled by factors of 0.5 and 0.2, respectively, for clarity.

surface defects and adsorbates. Second, strain and strain gradients are known to strongly influence the mobility and superconducting properties of the LAO/STO films^{25,26} and the interface 2DEG.²⁷ For example in ref 26, a 0.3% strain was shown to increase the mobility of STO by 300% and in ref 27 a strain gradient of 0.2 m⁻¹ was found to increase (decrease) the mobility (density) by ~10%. In comparison, the strain at the interface of the membranes is ~2% and the strain gradient is ~10⁵ m⁻¹ measured directly by a geometric phase analysis of cross-sectional TEM.²² The aim of the present study is to establish the low-temperature electrical properties of this novel system by measurements of individual membranes incorporated into devices on a Si/SiO₂ substrate. Here we demonstrate the presence of a superconducting phase with a transition temperature of ~120–250 mK, similar to typical values for bulk LAO/STO.^{19,20} From anisotropic magnetotransport we extract the in-plane phase coherence length and set an upper bound on the effective thickness of the interface electron gas, confirming its two-dimensional character. Finally, using the doped Si substrate as a gate electrode, we achieve electrostatic tunability of the normal state resistance and of the critical current of the freestanding membranes.

Devices were fabricated from freestanding LAO/STO membranes produced by spalling of a LAO/STO heterostructure with a 70 nm LAO top layer.²² The spalling technology has been developed for semiconductors^{28,29} and can occur for a tensile strained top layer with sufficient stress and bonding. For brittle crystals the interplay of the shear and opening stress at the tip of a fracture front may direct the propagation parallel to the surface at a stable depth.³⁰ The depth depends on the mechanical properties of the materials, and for LAO/STO the thicknesses are approximately 1:1. The details of the growth are given in ref 22 and in Section 1 in the Supporting Information. Figure 1a shows a scanning electron microscope (SEM) image of a spalled surface, and Figure 1b,c

shows cross sectional Z-contrast scanning transmission electron microscopy images confirming the perfect epitaxial LAO/STO interface. The images clearly show the strain-induced curvature of membranes due to the LAO/STO lattice mismatch driving the spalling process. A detailed analysis of the strain in the membranes by a geometric phase analysis of the TEM is presented in ref 22. The individual membranes are approximately square, are fractured laterally along the (100) and (010) crystal planes, and have lateral dimensions of 2–4 μm and a total thickness of ~140 nm (~70 nm LAO + ~70 nm STO).²² This thickness was chosen as a compromise of thicker membranes requiring special fabrication methods and very thick metal layers and thinner membranes which exhibit a smaller radius of curvature and thus a weaker van der Waals bonding to the substrate and risk of moving during device processing. Individual membranes were transferred from the STO growth substrate to a degenerately doped Si substrate capped with 100 nm of SiO₂ and prepatterned with a grid of gold markers for alignment of electrodes to the membranes.²⁴ Electrical contact to the membrane interface was achieved by a combination of gentle Ar⁺-ion milling followed by Ti/Au evaporation. To properly wet the interface, the contacting procedure was repeated twice using a grazing incident angle and an in-plane orientation parallel/antiparallel to the device axis (see the Supporting Information for fabrication details). This procedure is crucial for achieving a high yield of low-resistance devices and also mechanically fixes the membranes to the silicon oxide surface. A finished device is shown in Figure 1d. The steps seen in the contact profile (white arrows) are a consequence of the two-step contact procedure. The membranes remain curved also after transfer to silicon and deposition of contacts, as shown by AFM and tilt-view SEM in Figure S1 in the Supporting Information. The samples were mounted in a sample holder with conducting silver paste providing contact to the conducting p^{++} Si substrate, which

acted as an electrostatic backgate. A total of 50 two-terminal devices were fabricated, out of which 23 showed room-temperature conductivity. The remaining devices showed immeasurably high resistance presumably due to poor contact characteristics. Five conducting devices were selected for further investigation at low temperature (referred to, in the following, as Dev. 1–5). Measurements were performed in a dilution refrigerator with a base temperature of ~ 15 mK and equipped with a 6/1/1 T vector magnet. Due to the two-terminal device configuration, resistance from contacts and filtering in the cryostat contribute in series to the membrane resistance. This 6–10 k Ω constant series resistance is estimated as the baseline in the superconducting regime and is subtracted in the following.

The two-point resistance as a function of temperature is shown in Figure 1e. All devices show metallic behavior with a decreasing resistance upon lowering of the temperature. A pronounced resistance drop is observed in the sub-Kelvin regime, as emphasized in Figure 1f, consistent with the emergence of a superconducting phase. The apparent different critical temperatures between devices and the nonmonotonous transitions are similar to previous studies of superconductivity in bulk LAO/STO interfaces.^{14,19} This has been attributed to inhomogeneity at the interface leading to superconducting puddles with different individual transition temperatures embedded in a metallic background^{31–34}—a scenario which also seems to describe the membranes. Given that the 2DEG in the membranes is buried 70 nm from the surface, much deeper than that in bulk samples of < 6 nm,^{19,32,33} this result suggests that the origin of the inhomogeneity is intrinsic^{35,36} and is not associated with surface adsorbates. Also, strain in LAO/STO can modulate the interface density²⁷ and a nonhomogeneous strain profile in the membranes could lead to spatial variations.

The spatial extent of the superconducting state was probed by measuring the effect of a magnetic field applied along the principal axes of the device: the out-of-plane perpendicular direction (B_z) and the in-plane direction perpendicular (B_y) and parallel (B_x) to the current direction, respectively (see Figure 1d for the definition of the coordinate system). Figure 2a–c shows $R(T)$ values for Dev. 4 at different fields. The nonmonotonicity is pronounced at finite fields and shows regions of decreasing R with increasing T . Such behavior has been previously discussed for mesoscopic superconductors³⁷ and supports the scenario of a spatially inhomogeneous superconducting phase. The corresponding critical fields, $H_c(T)$, are shown in Figure 2d, defined such that $R(H_c) = 0.95 \times R_N$, where R_N is the normal state resistance at 300 mK. Clearly, the in-plane critical field H_c^{xy} is much larger than H_c^z , consistent with results from bulk LAO/STO samples,^{34,38,39} and shows that the superconducting coherence length, ξ , exceeds the thickness of the superconductor. The remaining devices were measured in a similar way and showed similar characteristics (see Figure S4 in the Supporting Information).

Fitting the values for H_c in Figure 2d to the Ginzburg–Landau relation $H_c(T)/H_c(0) = 1 - (T/T_c(0))^2$, we estimate the $T = 0$ critical magnetic field $H_c(0)$ along the x , y , and z directions for each device. Here $T_c(0)$ is the critical temperature for $B = 0$. The fitted values are collected in Table 1. We note that the difference in the critical fields H_c^x and H_c^y for B parallel to the substrate is consistent with the curvature of the micromembranes (Figure 1), which results in a larger projected area depending on the in-plane orientation.

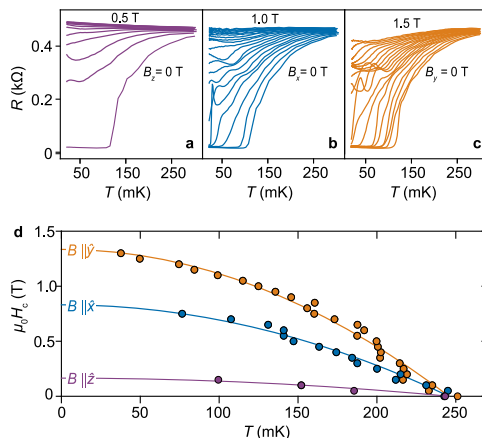


Figure 2. (a–c) Resistance of Dev. 4 as a function of temperature and fixed values of magnetic fields applied perpendicular to the substrate (B_z), in-plane parallel to the current direction (B_x), and in-plane perpendicular to the current direction (B_y), respectively. The field was increased in steps of 50 mT. (d) Critical magnetic field ($\mu_0 H_c$) as a function of temperature. Solid lines show fits to Ginzburg–Landau theory, allowing extraction of the zero temperature critical magnetic field.

We also speculate that this unavoidable field component perpendicular to the membrane is responsible for the finite slope of $H_c^z(T)$ near T_c , which for a 2D superconductor in a perfect parallel field is expected to go to zero with a vertical tangent.³⁸ In the following, we take the largest of the in-plane values as the closest estimate of the parallel in-plane critical field, $H_c^{\parallel}(0)$. On the other hand, the critical field extracted along z perpendicular to the substrate, $H_c^z(0)$, is not expected to be significantly affected by the membrane curvature and this value is thus assumed to be equal to the upper out-of-plane critical field, $H_c^z(0)$. With these values we calculate the coherence length $\xi = \sqrt{\Phi_0 / (2\pi\mu_0 H_c^{\parallel}(0))}$ and the effective thickness of the superconducting system $d = \sqrt{3} \Phi_0 / (\pi\xi\mu_0 H_c^{\parallel}(0))$, where Φ_0 is the flux quantum and μ_0 is the vacuum permeability.³⁸ The values are collected in Table 1. The thickness, d , falls in the range $d \approx 17$ – 33 nm, and for all samples $d \ll \xi$ which confirms the two-dimensional character of the superconducting phase in the membranes. This value is consistent with results from conventional planar LAO/STO extracted using the same method.^{38,40,41} We note, however, that due to the membrane curvature the extracted B_c^{\parallel} is likely underestimated and the extracted values of d should be considered an upper bound. Further, the value does not depend significantly on the specific definition of T_c . For instance, taking a 10% threshold ($R(T_c) = 0.9R_N$) results in T_c and H_c values for e.g. Dev. 5 of $T_c(0) = 196$ mK, $H_c^{z/y/z}(0) = 648/1815/191$ mT, respectively, and $d = 15$ nm. For the common 50% threshold, a rough estimate gives $B_c^{\perp} = 150$ mT and $B_c^{\parallel} = 1.1$ T leading to 50 and 25 nm for the coherence length and thickness; however, the rapid increase of R with B^{\perp} and the finite field step size prevent such analyses for most devices. In all cases, the qualitative conclusion remains unchanged.

We now consider the critical currents. Figure 3a shows the V – I curves for Dev. 4 measured at 14 mK, where the voltage

Table 1. Collected Parameters for the Five Devices^a

Dev. no.	R_S (Ω/\square)	$T_c(0)$ (mK)	$H_c^z(0)$ (mT)	$H_c^x(0)$ (mT)	$H_c^y(0)$ (mT)	ξ (nm)	d (nm)	J_c (nA/ μm)
1	1000	186	638	335				*
2	900	214	660	908	119	53	24	*
3	900	119	325	249	52	80	33	20
4	900	246	831	1335	165	45	19	60
5	2000	225	803	1922	256	36	17	1.5–4

^aThe sheet resistance R_S is estimated from the measured normal state resistances (e.g. Figure 2) in combination with a finite-element simulation of the device geometry (see text). The transition temperature at zero field, $T_c(0)$, is extrapolating $H_c(T)$ to zero (Figure 2d). Note that T_c is defined such that $R(T_c) = 0.95R_N$ and devices 1 and 2 thus have values for T_c even if they do not develop a zero-resistance state (marked with an asterisk). $H_c^{z/y/x}(0)$ denote the values of the zero temperature critical magnet field along each orientation studied extrapolated from the fits in Figure 2. ξ and d denote the corresponding in-plane coherence length and extracted superfluid thickness based on the largest in-plane critical fields, respectively. J_c denotes the measured critical supercurrent density.

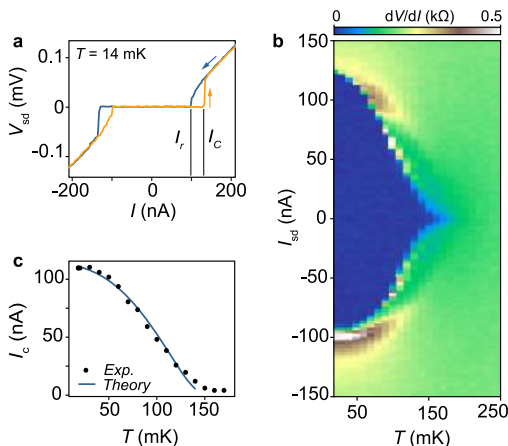


Figure 3. (a) DC bias voltage (V_{sd}) for Dev. 4 as a function of current (I), where the orange and blue traces correspond to up and down sweeping directions, respectively. The critical current for the superconducting transition (I_c) is clearly observable, as is the retrapping current. (b) Two-dimensional plot of the resistance as function of temperature and current. The zero-voltage state vanishes at around 200 mK. (c) Extracted critical current as a function of temperature. The solid line is a fit to the Ginzburg–Landau theory.

was measured in response to the applied current. Contributions to V from the resistance of cryostat wiring and contacts were identified from the superconducting state and subtracted. A clear supercurrent branch is observed at low currents with an abrupt transition to a resistive state upon increasing the current from 0 to the critical current $I_c \approx 125$ nA (orange arrow). Upon sweeping from high currents $I > I_c$ toward zero (blue curve), the device returns to the superconducting state at $I_R \approx 100$ nA. We attribute the difference between I_c and I_R to an effect of Joule heating in the normal state or to a superconducting phase consisting of an array of underdamped Josephson weak links, as previously discussed in the context of LAO/STO.^{34,42}

The magnitude of the critical current is related to the size of the sample and the carrier density of the 2DEG or the normal state resistance of possible intrinsic weak links. To allow a comparison of the measured I_c values of the membranes with those of conventional bulk heterostructures, we performed a finite element simulation of the resistance of a device consisting of a 2DEG of sheet resistance R_S contacted in the geometry of Figure 1d (see Figure S3 in the Supporting

Information). The simulation gives $R \approx 0.5R_S$, and from the measured normal state resistance $R_N \approx 0.45$ k Ω in Figure 2 we estimate the sheet resistance of the membrane 2DEG to be $R_S \approx 900$ Ω . On normalization to the width of the device $W \approx 2$ μm (see Figure 1), the critical current densities (1.5–60 nA/ μm) are given in Table 1 for each device. For Dev. 4 $J_c = 60$ nA/ μm , which is similar to the corresponding values of 10–150 nA/ μm reported in the literature for LAO/STO heterostructures^{19,34,43} and nanoscale devices^{44,45} based on bulk LAO/STO heterostructures of similar normal state resistance/resistivity. For bulk LAO/STO, J_c varies significantly between samples, and this trend is enhanced further for the membranes. We attribute this again to the increased importance of spatial inhomogeneity, as was also seen in the enhanced nonmonotonicity of $R(T)$ in Figure 2. We thus conclude that also in this respect the membrane 2DEG serves as a microscale model system for the bulk heterostructures.

Figure 3b shows a contour map of the differential resistance vs I and T . The zero-resistance state extends up to ~ 200 mK, and in Figure 3c the extracted temperature dependence of the critical current is shown along with a fit to the GL mean field result $I_c^{GL}(t) = I_c(0)(1 - t^2)^{3/2}(1 + t^2)^{1/2}$ where $t = T/T_c^{GL}$, $T_c^{GL} = 145$ mK, and $I_c(0) = 108$ nA. The fit captures the trend reasonably well but drops to zero more abruptly than in the experiment; the reason for this discrepancy is unknown.

From both scientific and application viewpoints, a key aspect of the LAO/STO system is the susceptibility to electrostatic gating, which merges the functionality of strong correlations with the tunability of semiconductors. For bulk LAO/STO heterostructures the tuning of the carrier density by backgating⁴⁶ and topgating⁴⁷ has been well established, allowing the tuning of the superconducting transition temperature.^{20,43,48} In conventional backgated devices, the bulk STO substrate acts as the gate dielectric and the large dielectric constant at low temperature ($\epsilon_{STO} \approx 2 \times 10^4$ at $T = 2$ K) ensures a significant electrostatic coupling to the electron gas, while for topgates, this is achieved by a thin gate dielectric. In the case of the membrane devices it is instead the highly doped Si substrate which acts as a conducting plane separated from the membrane by 100 nm of SiO₂.

For the measurement of Dev. 3 and 4 the backgate was not connected and instead Figure 4a shows dV/dI vs V_g and I for Dev. 5 measured in a separate cooldown. The zero-resistance region (dark blue) widens with increasing V_g and Figure 4b,c shows the corresponding extracted gate dependence of the critical current $I_c(V_g)$ and normal state resistance $R_N(V_g)$, respectively. Here R_N was extracted at a high bias of $V_{sd} = 1$ mV outside the superconducting region. R_N decreases from 5.5

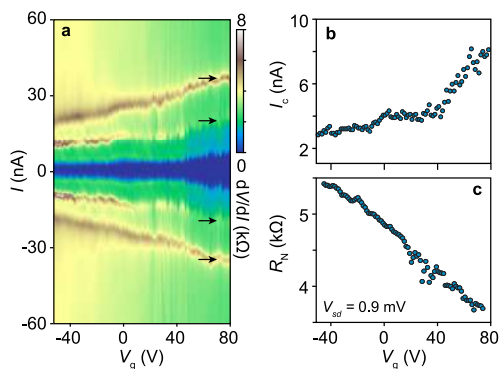


Figure 4. (a) Differential resistance as a function of applied current and gate voltage for Dev. 5. (b) Extracted critical current as a function of V_g extracted from (a). (c) Normal state resistance R_N as a function of V_g extracted at high bias outside the superconducting region. The overall trend is consistent with gate-induced carrier accumulation in the 2DEG and a superconducting phase in the underdoped side of the dome-shaped phase diagram.

to 3.5 k Ω upon inducing carriers, while the critical current increases from 3 to 8 nA. This qualitative behavior is consistent with a superconducting 2DEG following the trend of conventional LAO/STO in the underdoped regime. In Figure 4a, a series of steps in dV/dI is seen at currents higher than I_c , as indicated by arrows. The origin of these features remain unknown; however, we speculate that they may be associated with transitions of local superconducting regions of an inhomogeneous 2DEG or to interactions with resonant microwave modes in the sample holder similar to Fiske steps of conventional Josephson junctions.⁴⁹

The two-terminal configuration of the devices does not allow a Hall measurement to separately determine the mobility and density of the interfacial 2DEG. However, our results indicate a superconducting state very similar to that of conventional LAO/STO, and the values of T_c and the gate dependence place the devices as being slightly underdoped with respect to the maximum of the dome-shaped superconducting phase diagram that occurs at $n_s \approx (1.5\text{--}2) \times 10^{13} \text{ cm}^{-2}$.^{20,50} Thus, we estimate a density of $n_s \approx 1 \times 10^{13} \text{ cm}^{-2}$ for the membrane 2DEG with the extracted sheet resistance $R_s \approx 1 \text{ k}\Omega/\square$ (Table 1); the typical mobility is $\mu \sim 1000 \text{ cm}^2/(\text{V s})$, which again is a typical value of conventional LAO/STO 2DEGs.⁵⁰ We stress that this estimate is based on unknown assumptions regarding T_c , doping, etc. in the membranes and should be considered only as confirmation that, assuming a behavior similar to conventional LAO/STO, the data also support a mobility in the expected order of magnitude. In general, the analysis used here both for extracting characteristic length scales and in our simulation of R_s is based on a homogeneous superconductor, although signatures of spatial inhomogeneity are observed in the temperature dependence and presumably play a role in the sample variations. Thus, we stress that the analysis should be considered only for qualitative insights, for comparison with conventional LAO/STO, and for order of magnitude estimates.

The fact that both the quantitative parameters (T_c , d , n_s , μ , J_c , H_c , and ξ) and the qualitative behavior (shape of multistep transition) are identical with what can be found in conventional planar LAO/STO 2DEGs is surprising, given the very

large strain ($\sim 2\%$) and strain gradients ($\sim 10^5 \text{ m}^{-1}$) in the membranes.²² Detailed studies of conventional LAO/STO have indeed shown that applying strain gradients as small as 0.2 m^{-1} (6 orders below that present in the membranes) led to an increase (decrease) of the carrier mobility (density) by $\sim 10\%$.²⁷ Also, for a STO thin film a 0.3% strain (1 order below that of the membranes) increased the mobility of STO by 300%.²⁶ Also, the tetragonal domain structure of STO occurring below 105 K is expected to be aligned by the strain²² rather than form a random domain landscape as in planar STO.^{51,52} Although the domain structure has been extensively demonstrated to affect the transport properties of the 2DEG,^{51,52} no apparent influence is detected in the membranes for either the metallic conductivity or the superconducting phase. This apparent insensitivity is indeed remarkable, and the mechanisms for compensating the effects of the mechanical deformation deserve further investigation. We note, that previous studies of high- T_c perovskite membranes fabricated by epitaxial liftoff and transferred to silicon also showed properties nearly identical with those of their bulk counterparts.⁵³

In summary, using Si/SiO₂ as a substrate, we have fabricated electrical devices based on LAO/STO freestanding micro-membranes. We report measurements of the low-temperature characteristics, demonstrating the presence of a superconducting phase. From the anisotropy of the in-plane and out-of-plane critical magnetic fields we extracted a phase coherence length of $\xi \approx 36\text{--}80 \text{ nm}$ and an upper bound on the thickness of the superconducting layer of $d \approx 17\text{--}33 \text{ nm}$. This shows the two-dimensional character of the electron system in the freestanding heterostructure membranes. The critical supercurrent density and the temperature dependence are found to be similar to values reported for macroscopic LAO/STO samples. Finally, we demonstrate the tunability of the normal state resistance and the critical current using the conducting silicon back-plane as a gate electrode. The results establish the spalled heterostructure membranes as freestanding microscale models of the LAO/STO system. We demonstrate a high yield of integrating individual membranes into electrical circuitry on standard silicon substrates. The system thus provides a promising backbone for oxide-based quantum devices, mesoscopic superconductivity utilizing the unique tunability of the LAO/STO heterostructure, and investigations of mechanical degrees of freedom in suspended devices. The approach appears to be clearly feasible, and experiments can directly adapt established and optimized techniques and protocols from the field of semiconductor nanowire devices. Further, in contrast to devices based on conventional LAO/STO samples, each spalled growth produces millions of individual membranes that may be harvested for multiple device generations and thus enables rapid prototyping and optimization of devices.

■ ASSOCIATED CONTENT

SI Supporting Information

The Supporting Information is available free of charge at <https://pubs.acs.org/doi/10.1021/acs.nanolett.2c00992>.

Additional details on the synthesis of membranes, fabrication of devices, and simulations and additional data (PDF)

AUTHOR INFORMATION

Corresponding Author

Thomas Sand Jespersen – Center for Quantum Devices, Niels Bohr Institute, University of Copenhagen, 2100 Copenhagen, Denmark; orcid.org/0000-0002-7879-976X; Email: tsaje@dtu.dk

Authors

Ricci Erlandsen – Department of Energy Conversion and Storage, Technical University of Denmark, 2800 Kgs. Lyngby, Denmark

Rasmus Tindal Dahm – Department of Energy Conversion and Storage, Technical University of Denmark, 2800 Kgs. Lyngby, Denmark

Felix Trier – Department of Energy Conversion and Storage, Technical University of Denmark, 2800 Kgs. Lyngby, Denmark; orcid.org/0000-0003-0228-0635

Mario Scuderi – Institute for Microelectronics and Microsystems (CNR-IMM), I-95121 Catania, Italy; orcid.org/0000-0001-9026-5317

Emiliano Di Gennaro – Dipartimento di Fisica "Ettore Pancini", Università degli Studi di Napoli Federico II, Complesso Universitario di Monte S. Angelo, I-80126 Napoli, Italy; orcid.org/0000-0003-4231-9776

Alessia Sambri – CNR-SPIN, Complesso Universitario di Monte Sant'Angelo, I-80126 Napoli, Italy; orcid.org/0000-0003-1228-4226

Charline Kaisa Reffeldt Kirchert – Department of Energy Conversion and Storage, Technical University of Denmark, 2800 Kgs. Lyngby, Denmark

Nini Pryds – Department of Energy Conversion and Storage, Technical University of Denmark, 2800 Kgs. Lyngby, Denmark; orcid.org/0000-0002-5718-7924

Fabio Miletto Granozio – CNR-SPIN, Complesso Universitario di Monte Sant'Angelo, I-80126 Napoli, Italy; orcid.org/0000-0002-9417-7848

Complete contact information is available at:

<https://pubs.acs.org/10.1021/acs.nanolett.2c00992>

Notes

The authors declare no competing financial interest.

ACKNOWLEDGMENTS

This research was supported by the Danish National Research Foundation. T.S.J. acknowledges support by Research Grant 00013157 from VILLUM FONDEN and DFF-7014-00132 from the Danish Council for Independent Research. F.T. acknowledges support by research grant 37338 (SANSIT) from Villum Fonden. E.D.G., A.G., and F.M.G. acknowledge funding from the project QUANTOX (QUANTum Technologies with 2D-OXides) of QuantERA ERA-NET Confund in Quantum Technologies (Grant Agreement No. 731473) implemented within the 10th European Union's Horizon 2020 Programme and MIUR PRIN 2017 (Grant Nos. 20177SL7HC "TOPSPIN" and 2017YCTB59 "TWEET"). M.S. acknowledges support by the Italian Ministry of Education and Research (MIUR) under the project Beyond-Nano (PON a3-00363). N.P. acknowledges funding from Villum Fonden grant 00027993 (NEED) and the Independent Research Fund Denmark grant 0217-00069B (PiloT) and the support from the Novo Nordisk Foundation Grant No. NNF21OC0066526. .

REFERENCES

- (1) Ji, D.; et al. Freestanding crystalline oxide perovskites down to the monolayer limit. *Nature* **2019**, *570*, 87–90.
- (2) Lu, D.; Baek, D. J.; Hong, S. S.; Kourkoutis, L. F.; Hikita, Y.; Hwang, H. Synthesis of freestanding single-crystal perovskite films and heterostructures by etching of sacrificial water-soluble layers. *Nat. Mater.* **2016**, *15*, 1255–1260.
- (3) Eom, K.; Yu, M.; Seo, J.; Yang, D.; Lee, H.; Lee, J.-W.; Irvin, P.; Oh, S. H.; Levy, J.; Eom, C.-B. Electronically Reconfigurable Complex Oxide Heterostructure Freestanding Membranes. *Sci. Adv.* **2021**, *7*, No. eabh1284.
- (4) Kum, H.; Lee, D.; Kong, W.; Kim, H.; Park, Y.; Kim, Y.; Baek, Y.; Bae, S.-H.; Lee, K.; Kim, J. Epitaxial growth and layer-transfer techniques for heterogeneous integration of materials for electronic and photonic devices. *Nature Electronics* **2019**, *2*, 439–450.
- (5) Gao, W.; Zhu, Y.; Wang, Y.; Yuan, G.; Liu, J.-M. A review of flexible perovskite oxide ferroelectric films and their application. *Journal of Materiomics* **2020**, *6*, 1–16.
- (6) Hong, S. S.; Yu, J. H.; Lu, D.; Marshall, A. F.; Hikita, Y.; Cui, Y.; Hwang, H. Y. Two-dimensional limit of crystalline order in perovskite membrane films. *Science Advances* **2017**, *3*, No. eaao5173.
- (7) Mannhart, J.; Schlom, D. G. Oxide Interfaces—An Opportunity for Electronics. *Science* **2010**, *327*, 1607–1611.
- (8) Coll, M.; et al. Towards Oxide Electronics: a Roadmap. *Appl. Surf. Sci.* **2019**, *482*, 1–93.
- (9) Jouan, A.; Singh, G.; Lesne, E.; Vaz, D. C.; Bibes, M.; Barthélémy, A.; Ulysse, C.; Stormaiuolo, D.; Salluzzo, M.; Hurand, S.; Lesueur, J.; Feuillet-Palma, C.; Bergeal, N. Quantized Conductance in a One-Dimensional Ballistic Oxide Nanodevice. *Nat. Electron* **2020**, *3*, 201–206.
- (10) Ohtomo, A.; Hwang, H. Y. A high-mobility electron gas at the LaAlO₃/SrTiO₃ heterointerface. *Nature* **2004**, *427*, 423–426.
- (11) Pai, Y.-Y.; Tylan-Tyler, A.; Irvin, P.; Levy, J. Physics of SrTiO₃-based heterostructures and nanostructures: a review. *Rep. Prog. Phys.* **2018**, *81*, 036503.
- (12) Christensen, D. V.; Trier, F.; Niu, W.; Gan, Y.; Zhang, Y.; Jespersen, T. S.; Chen, Y.; Pryds, N. Stimulating Oxide Heterostructures: A Review on Controlling SrTiO₃-Based Heterointerfaces with External Stimuli. *Advanced Materials Interfaces* **2019**, *6*, 1900772.
- (13) Chen, Y. Z.; et al. A high-mobility two-dimensional electron gas at the spinel/perovskite interface of γ -Al₂O₃/SrTiO₃. *Nat. Commun.* **2013**, *4*, 1371.
- (14) Cavaglia, A. D.; Gabay, M.; Gariglio, S.; Reyren, N.; Cancellieri, C.; Triscone, J.-M. Tunable Rashba Spin-Orbit Interaction at Oxide Interfaces. *Phys. Rev. Lett.* **2010**, *104*, 126803.
- (15) Vaz, D. C.; et al. Mapping spin-charge conversion to the band structure in a topological oxide two-dimensional electron gas. *Nat. Mater.* **2019**, *18*, 1187–1193.
- (16) Trier, F.; Vaz, D. C.; Bruneel, P.; Noël, P.; Fert, A.; Vila, L.; Attané, J.-P.; Barthélémy, A.; Gabay, M.; Jaffrès, H.; Bibes, M. Electric-Field Control of Spin Current Generation and Detection in Ferromagnet-Free SrTiO₃-Based Nanodevices. *Nano Lett.* **2020**, *20*, 395–401.
- (17) Noël, P.; Trier, F.; Vicente Arche, L. M.; Bréhin, J.; Vaz, D. C.; Garcia, V.; Fusil, S.; Barthélémy, A.; Vila, L.; Bibes, M.; Attané, J.-P. Non-volatile electric control of spin-charge conversion in a SrTiO₃ Rashba system. *Nature* **2020**, *580*, 483–486.
- (18) Bi, F.; Huang, M.; Ryu, S.; Lee, H.; Bark, C.-W.; Eom, C.-B.; Irvin, P.; Levy, J. Room-temperature electrically-controlled ferromagnetism at the LaAlO₃/SrTiO₃ interface. *Nat. Commun.* **2014**, *5*, 5019.
- (19) Reyren, N.; Thiel, S.; Cavaglia, A. D.; Kourkoutis, L. F.; Hammerl, G.; Richter, C.; Schneider, C. W.; Kopp, T.; Ruetschi, A.-S.; Jaccard, D.; Gabay, M.; Müller, D. A.; Triscone, J.-M.; Mannhart, J. Superconducting Interfaces Between Insulating Oxides. *Science* **2007**, *317*, 1196–1199.
- (20) Cavaglia, A. D.; Gariglio, S.; Reyren, N.; Jaccard, D.; Schneider, T.; Gabay, M.; Thiel, S.; Hammerl, G.; Mannhart, J.; Triscone, J.-M.

Electric field control of the LaAlO₃/SrTiO₃ interface ground state. *Nature* **2008**, *456*, 624–627.

(21) Singh, G.; Venditti, G.; Saiz, G.; Herranz, G.; Sánchez, F.; Jouan, A.; Feuillet-Palma, C.; Lesueur, J.; Grilli, M.; Caprara, S.; Bergeal, N. Two-Gap s_w-Wave Superconductivity at an Oxide Interface. *Phys. Rev. B* **2022**, *105*, 064512.

(22) Sambri, A.; et al. Self-Formed, Conducting LaAlO₃/SrTiO₃ Micro-Membranes. *Adv. Funct. Mater.* **2020**, *30*, 1909964.

(23) Granozio, F. M.; Sambri, A. *Heterostructure membranes and process for fabricating heterostructure membranes*. European Patent application no. EP21190418.0, 2020; priority no. 10202000020317.

(24) Dahm, R. T.; Erlandsen, R.; Trier, F.; Sambri, A.; Gennaro, E. D.; Guarino, A.; Stampfer, L.; Christensen, D. V.; Granozio, F. M.; Jespersen, T. S. Size-Controlled Spalling of LaAlO₃/SrTiO₃ Micromembranes. *ACS Appl. Mater. Interfaces* **2021**, *13*, 12341–12346.

(25) Ahadi, K.; Galletti, L.; Li, Y.; Salmani-Rezaie, S.; Wu, W.; Stemmer, S. Enhancing superconductivity in SrTiO₃ films with strain. *Science Advances* **2019**, *5*, No. eaaw0120.

(26) Jalan, B.; Allen, S. J.; Beltz, G. E.; Moetakef, P.; Stemmer, S. Enhancing the electron mobility of SrTiO₃ with strain. *Appl. Phys. Lett.* **2011**, *98*, 132102.

(27) Zhang, F.; Lv, P.; Zhang, Y.; Huang, S.; Wong, C.-M.; Yau, H.-M.; Chen, X.; Wen, Z.; Jiang, X.; Zeng, C.; Hong, J.; Dai, J.-y. Modulating the Electrical Transport in the Two-Dimensional Electron Gas at LaAlO₃/SrTiO₃ Heterostructures by Interfacial Flexoelectricity. *Phys. Rev. Lett.* **2019**, *122*, 257601.

(28) Bedell, S. W.; Shahrjerdi, D.; Hekmatshoar, B.; Fogel, K.; Lauro, P. A.; Ott, J. A.; Sosa, N.; Sadana, D. Kerf-Less Removal of Si, Ge, and III–V Layers by Controlled Spalling to Enable Low-Cost PV Technologies. *IEEE J. Photovolt.* **2012**, *2*, 141–147.

(29) Dross, F.; Robbelein, J.; Vandeveld, B.; Van Kerschaver, E.; Gordon, I.; Beaucarne, G.; Poortmans, J. Stress-Induced Large-Area Lift-off of Crystalline Si Films. *Appl. Phys. A: Mater. Sci. Process.* **2007**, *89*, 149–152.

(30) Hutchinson, J. W.; Suo, Z. Mixed Mode Cracking in Layered Materials. *Advances in Applied Mechanics* **1991**, *29*, 63–191.

(31) Caprara, S.; Grilli, M.; Benfatto, L.; Castellani, C. Effective medium theory for superconducting layers: A systematic analysis including space correlation effects. *Phys. Rev. B* **2011**, *84*, 014514.

(32) Caprara, S.; Biscaras, J.; Bergeal, N.; Bucheli, D.; Hurand, S.; Feuillet-Palma, C.; Rastogi, A.; Budhani, R. C.; Lesueur, J.; Grilli, M. Multiband superconductivity and nanoscale inhomogeneity at oxide interfaces. *Phys. Rev. B* **2013**, *88*, 020504.

(33) Biscaras, J.; Bergeal, N.; Hurand, S.; Feuillet-Palma, C.; Rastogi, A.; Budhani, R. C.; Grilli, M.; Caprara, S.; Lesueur, J. Multiple quantum criticality in a two-dimensional superconductor. *Nat. Mater.* **2013**, *12*, 542–548.

(34) Prawiroatmodjo, G. E. D. K.; Trier, F.; Christensen, D. V.; Chen, Y.; Pryds, N.; Jespersen, T. S. Evidence of weak superconductivity at the room-temperature grown LaAlO₃/SrTiO₃ interface. *Phys. Rev. B* **2016**, *93*, 184504.

(35) Zhu, G.-z.; Radtke, G.; Botton, G. A. Bonding and structure of a reconstructed (001) surface of SrTiO₃ from TEM. *Nature* **2012**, *490*, 384–387.

(36) Frenkel, Y.; Haham, N.; Shperber, Y.; Bell, C.; Xie, Y.; Chen, Z.; Hikita, Y.; Hwang, H. Y.; Kalisky, B. Anisotropic Transport at the LaAlO₃/SrTiO₃ Interface Explained by Microscopic Imaging of Channel-Flow over SrTiO₃ Domains. *ACS Appl. Mater. Interfaces* **2016**, *8*, 12514–12519.

(37) Morelle, M.; Bruynseraede, Y.; Moshchalkov, V. V. Effect of Current and Voltage Leads on the Superconducting Properties of Mesoscopic Triangles. *Phys. Status Solidi B* **2003**, *237*, 365–373.

(38) Reyren, N.; Gariglio, S.; Caviglia, A. D.; Jaccard, D.; Schneider, T.; Triscone, J.-M. Anisotropy of the superconducting transport properties of the LaAlO₃/SrTiO₃ interface. *Appl. Phys. Lett.* **2009**, *94*, 112506.

(39) Ben Shalom, M.; Sachs, M.; Rakhmievitch, D.; Palevski, A.; Dagan, Y. Tuning Spin-Orbit Coupling and Superconductivity at the

SrTiO₃/LaAlO₃ Interface: A Magnetotransport Study. *Phys. Rev. Lett.* **2010**, *104*, 126802.

(40) Ben Shalom, M.; Tai, C. W.; Lereah, Y.; Sachs, M.; Levy, E.; Rakhmievitch, D.; Palevski, A.; Dagan, Y. Anisotropic magnetotransport at the SrTiO₃/LaAlO₃ interface. *Phys. Rev. B* **2009**, *80*, 140403.

(41) Li, D.; Lemal, S.; Gariglio, S.; Wu, Z.; Fête, A.; Boselli, M.; Ghosez, P.; Triscone, J.-M. Probing Quantum Confinement and Electronic Structure at Polar Oxide Interfaces. *Adv. Sci.* **2018**, *5*, 1800242.

(42) Hurand, S.; Jouan, A.; Lesne, E.; Singh, G.; Feuillet-Palma, C.; Bibes, M.; Barthélémy, A.; Lesueur, J.; Bergeal, N. Josephson-like dynamics of the superconducting LaAlO₃/SrTiO₃ interface. *Phys. Rev. B* **2019**, *99*, 104515.

(43) Hurand, S.; et al. Field-effect control of superconductivity and Rashba spin-orbit coupling in top-gated LaAlO₃/SrTiO₃ devices. *Sci. Rep.* **2015**, *5*, 12751.

(44) Pai, Y.-Y.; Lee, H.; Lee, J.-W.; Annadi, A.; Cheng, G.; Lu, S.; Tomczyk, M.; Huang, M.; Eom, C.-B.; Irvin, P.; Levy, J. One-Dimensional Nature of Pairing and Superconductivity at the SrTiO₃/LaAlO₃ Interface. *Phys. Rev. Lett.* **2018**, *120*, 147001.

(45) Kalaboukhov, A.; Aurino, P. P.; Galletti, L.; Bauch, T.; Lombardi, F.; Winkler, D.; Claeson, T.; Golubev, D. Homogeneous Superconductivity at the LaAlO₃/SrTiO₃ Interface Probed by Nanoscale Transport. *Phys. Rev. B* **2017**, *96*, 184525.

(46) Thiel, S.; Hammerl, G.; Schmehl, A.; Schneider, C. W.; Mannhart, J. Tunable quasi-two-dimensional electron gases in oxide heterostructures. *Science* **2006**, *313*, 1942–1945.

(47) Förg, B.; Richter, C.; Mannhart, J. Field-effect devices utilizing LaAlO₃/SrTiO₃ interfaces. *Appl. Phys. Lett.* **2012**, *100*, 053506.

(48) Eerkes, P. D.; van der Wiel, W. G.; Hilgenkamp, H. Modulation of conductance and superconductivity by top-gating in LaAlO₃/SrTiO₃ 2-dimensional electron systems. *Appl. Phys. Lett.* **2013**, *103*, 201603.

(49) Coon, D. D.; Fiske, M. D. Josephson ac and Step Structure in the Supercurrent Tunneling Characteristic. *Phys. Rev.* **1965**, *138*, A744.

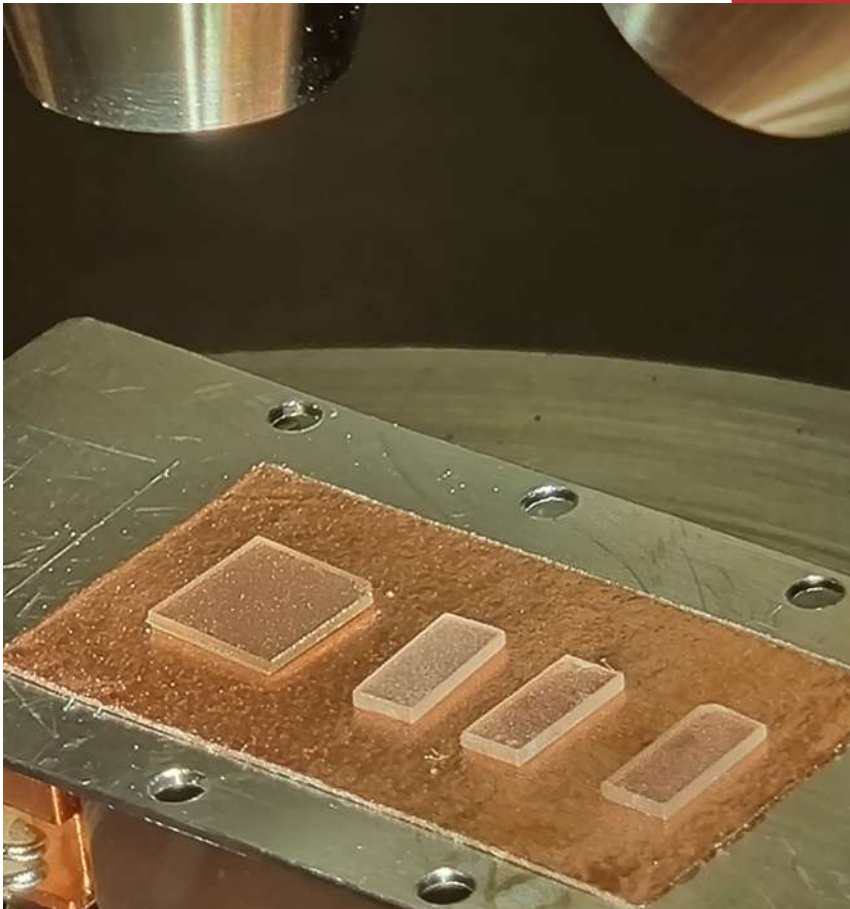
(50) Joshua, A.; Pecker, S.; Ruhman, J.; Altman, E.; Ilani, S. A universal critical density underlying the physics of electrons at the LaAlO₃/SrTiO₃ interface. *Nat. Commun.* **2012**, *3*, 1129.

(51) Kalisky, B.; et al. Locally enhanced conductivity due to the tetragonal domain structure in LaAlO₃/SrTiO₃ heterointerfaces. *Nat. Mater.* **2013**, *12*, 1091–1095.

(52) Honig, M.; Sulpizio, J. A.; Drori, J.; Joshua, A.; Zeldov, E.; Ilani, S. Local electrostatic imaging of striped domain order in LaAlO₃/SrTiO₃. *Nat. Mater.* **2013**, *12*, 1112–1118.

(53) Chen, Z.; Wang, B. Y.; Goode, B. H.; Lu, D.; Hong, S. S.; Li, D.; Kourkoutis, L. F.; Hikita, Y.; Hwang, H. Y. Freestanding Crystalline YB a 2 C u 3 O 7 - x Heterostructure Membranes. *Phys. Rev. Materials* **2019**, *3*, 060801.

A. D. Rata, J. Herrero-Martin, I. V. Maznichenko, F. M. Chiabrera,
R. T. Dahm, *et al.*
Defect-induced magnetism in homoepitaxial SrTiO₃
APL materials **10**, 091108 (2022)



X-ray photoemission spectroscopy in action

Defect-induced magnetism in homoepitaxial SrTiO₃

Cite as: APL Mater. 10, 091108 (2022); doi: 10.1063/5.0101411

Submitted: 31 May 2022 • Accepted: 23 August 2022 •

Published Online: 20 September 2022



A. D. Rata,¹ J. Herrero-Martin,² I. V. Maznichenko,¹ F. M. Chiabrera,³ R. T. Dahm,³ S. Ostanin,¹ D. Lee,⁴ B. Jalan,⁴ P. Buczek,⁵ I. Mertig,¹ A. Ernst,^{6,7} A. M. Ionescu,⁸ K. Dörr,¹ N. Pryds,^{3,a)} and D.-S. Park^{8,a)}

AFFILIATIONS

¹Institut für Physik, Martin-Luther-Universität Halle-Wittenberg, 06120 Halle, Germany

²ALBA Synchrotron Light Source, Cerdanyola del Vallès, 08290 Barcelona, Spain

³Department of Energy Conversion and Storage, Technical University of Denmark, DK-2800 Kgs Lyngby, Denmark

⁴Department of Chemical Engineering and Materials Science, University of Minnesota-Twin Cities, Minneapolis, Minnesota 55455, USA

⁵Department of Engineering and Computer Sciences, Hamburg University of Applied Sciences, 20099 Hamburg, Germany

⁶Max-Planck-Institut für Mikrostrukturphysik, 06120 Halle, Germany

⁷Institute of Theoretical Physics, Johannes Kepler University, 4040 Linz, Austria

⁸Laboratory for Nanoelectronic Devices, Swiss Federal Institute of Technology-EPFL, 1015 Lausanne, Switzerland

Note: This paper is part of the Special Topic on Materials Challenges and Synthesis Science of Emerging Quantum Materials.

a) Authors to whom correspondence should be addressed: nipr@dtu.dk and dspark1980@gmail.com

ABSTRACT

Along with recent advancements in thin-film technologies, the engineering of complex transition metal oxide heterostructures offers the possibility of creating novel and tunable multifunctionalities. A representative complex oxide is the perovskite strontium titanate (STO), whose bulk form is nominally a centrosymmetric paraelectric band insulator. By tuning the electron doping, chemical stoichiometry, strain, and charge defects of STO, it is possible to control the electrical, magnetic, and thermal properties of such structures. Here, we demonstrate tunable magnetism in atomically engineered STO thin films grown on STO (001) substrates by controlling the atomic charge defects of titanium (V_{Ti}) and oxygen (V_O) vacancies. Our results show that the magnetism can be tuned by altering the growth conditions. We provide deep insights into its association to the following defect types: (i) V_{Ti} , resulting in a charge rearrangement and local spin polarization, (ii) V_O , leading to weak magnetization, and (iii) $V_{Ti}-V_O$ pairs, which lead to the appearance of a sizable magnetic signal. Our results suggest that controlling charged defects is critical for inducing a net magnetization in STO films. This work provides a crucial step for designing magnetic STO films via defect engineering for magnetic and spin-based electronic applications.

© 2022 Author(s). All article content, except where otherwise noted, is licensed under a Creative Commons Attribution (CC BY) license (<http://creativecommons.org/licenses/by/4.0/>). <https://doi.org/10.1063/5.0101411>

INTRODUCTION

Strontium titanate (SrTiO₃, STO) has a cubic ABO₃ perovskite structure (space group: $Pm-3m$, a lattice constant of $a = 3.905$ Å) at room temperature (RT). It is a nonmagnetic band insulator with an indirect bandgap of 3.25 eV separating the valence band O $2p$ states and the lowest unoccupied Ti $3d t_{2g}$ states of the conduction band.^{1,2} STO has a large dielectric constant of about 300 at room temperature in a low electric field and exhibits a quantum paraelectric behavior at very low temperatures, i.e., a

suppression (in the ~20–100 K range) of the ferroelectric transition by quantum fluctuations.^{2,3} The electrically insulating phases of STO can be made conductive (i) by replacing oxygen atoms with oxygen vacancies, which then act as donor-type dopants or (ii) by subtle chemical doping, e.g., Nb (0.1%)-doped STO. Both undoped and Nb-doped STO single crystals have been widely used as substrates for the growth of oxide films. STO-based structures have shown a rich diversity of remarkable properties including low-temperature high ($\sim 10^4$ cm²V⁻¹s⁻¹) electron mobility,^{4–6} superconductivity below 300–500 mK,^{7,8} room-temperature ferroelectricity,^{9,10} large

dielectric constants ($\epsilon_r \sim 10^3$ at RT),^{9,11} room-temperature ferromagnetism,¹² and nonvolatile resistive switching.¹³ These interesting properties of STO can be obtained through delicate control of the electron doping (via chemical dopants such as La or Nb), variations in the stoichiometry, strain-induced symmetry breaking, and defect engineering. As a result of this panoply of material properties, for more than half a century, engineered perovskite STO materials and STO-based homo-/heterostructures have attracted considerable scientific interest and become integral materials for oxide-based electronic device applications.

In particular, inducing magnetism in STO thin films can be accomplished through modifications to the lattice strain by employing lattice-mismatched single crystalline oxide substrates (e.g., biaxial strain = -1.16% and $+1.29\%$ for NdGaO₃ and TbScO₃, respectively) and/or by controlling cation stoichiometry (Sr or Ti deficiency) and oxygen vacancy (V_O) concentrations.^{14–18} Defects typically result in lattice expansion and a charge rearrangement in STO. This can lead to lattice symmetry breaking (electric polarization), followed by an electronic reconstruction and crystal field splitting (e.g., splitting of degenerate Ti $3d_{xy, x^2-y^2}$ orbitals into a relative energy scheme that follows $d_{xz}/d_{yz} < d_{xy} < d_{3z^2-r^2} < d_{x^2-y^2}$).^{19,20} The origin of magnetism in STO has remained a long-standing problem, and the presence of V_O defects has been widely regarded as one of the main contributors to magnetization: Oxygen vacancies allow the partial reduction of Ti^{4+} into magnetically active Ti^{3+} . A few examples of some of the proposed mechanisms are listed here: Coey *et al.* suggested that the origin of ferromagnetism in reduced STO is either due to direct exchange interactions between V_O and the molecular orbitals of valence electrons of surrounding Ti ions or due to a Stoner-type spin-splitting of the Ti $3d$ band for ferromagnetically coupled electrons.¹² However, Brovko and Tosatti²¹ reported theoretical results suggesting that an isolated V_O defect in STO only stabilizes states with low or zero total magnetization since the two Ti spins facing each other across the V_O are antiferromagnetically coupled via strong direct exchange interaction. Doenning and Pentcheva²² demonstrated that in LaAlO₃ (LAO)/STO heterostructures, Ti d_{xy} bands could be dominantly magnetized via magnetic double-exchange interactions between Ti^{3+} and Ti^{4+} when a tensile in-plane strain is induced in TiO₆ octahedra and the electron doping level is below $7 \times 10^{14} \text{ cm}^{-2}$. However, this electron doping level (0.5e per Ti) per STO monolayer is hard to achieve practically when considering that Ti d_{xy} orbital polarization in a c -axis compressed STO is purely induced by a high V_O concentration of $\sim 25 \text{ at.}\%$ as a V_O sublattice. Note that it was found that the perovskite lattice of SrTiO_{3-x} retains a V_O concentration of $\leq 5.6 \text{ at.}\%$.²³ Similar V_O -mediated Ti magnetization levels have been observed experimentally in reduced STO ceramics,^{12,24} STO thin films,²⁵ STO-based heterostructures (e.g., LAO/STO interfaces),²⁶ and reduced TiO_{2-x}.²⁷ However, these examples show very weak magnetic responses, which do not appear robust enough to be employed practically. Importantly, it was also found that in the absence of V_O defects, magnetism can still occur in these systems by controlling cation off-stoichiometry (e.g. Ti vacancies).^{28–30} The above observations indicate that magnetism in the STO system might be induced by contributions of both cation and anion defects. Hence, understanding the role of these defects is of critical importance for creating and controlling the associated magnetism in STO.

In this work, we demonstrate tunable magnetic properties of homoepitaxial STO thin films by controlling both cation off-stoichiometry (V_{Ti}) and V_O contents using pulsed laser deposition (PLD). Our results show that oxygen partial pressure (P_O) strongly influences the growth dynamics and the magnetization of the films. We found incorporating both V_{Ti} and V_O defects into the lattice structure can enhance magnetism up to a threshold concentration at which a strong charge compensation occurs. We have used first-principles calculations to classify the effects of individual defects and complex defect pairs on the development of a magnetic response in STO, conclusions which are supported by x-ray magnetic circular dichroism (XMCD) measurements. Our results show that manipulating the oppositely charged atomic defects in STO is the key to creating and tuning magnetism in STO thin films.

RESULTS AND DISCUSSION

Epitaxial STO films were grown on TiO₂-terminated STO(001) substrates [Fig. 1(a)] using a pulsed laser deposition (PLD) system equipped with reflection high-energy electron diffraction (RHEED), which was used to control the thickness of the deposited films. The substrate temperature was kept at 700 °C and a laser repetition rate of 1 Hz was employed for the film growth. The laser-beam spot size on the STO target was $\sim 4.5 \text{ mm}^2$. To obtain the growth of B-site cation deficient STO films, we employed a consistent low laser fluence (e.g., $\sim 0.6 \text{ J/cm}^2$) during film growth, based on our previous work.²⁹ Meanwhile, the background oxygen partial pressure was varied from $P_O = 5 \times 10^{-2} \text{ mbar}$ to $5 \times 10^{-6} \text{ mbar}$. In addition, in order to examine the effect of V_O concentration on the magnetism of the films, we used different cooling processes after film growth: (i) in a high oxygen atmosphere (200 mbar O₂) or (ii) in the same atmosphere that was used during film growth.

In PLD, laser fluence strongly influences the kinetic energy of the ablated species, which, in turn, affects the adatom mobility at the substrate surface, thereby also affecting the ablation rate and film thickness.³¹ Especially, when considering the growth of complex compound materials, an inadequate fluence can preferentially ablate certain elements over others, which results in the formation of cation nonstoichiometric films.^{29–33} It should be noted that preferential ablation happens above a threshold ablation rate. Due to its impact on the ablation rates of various elements, laser fluence has been used in literature to control the stoichiometry of STO films.^{29,32,33} In the case of STO, a preferential ablation of Ti (Sr) can be induced by increasing (decreasing) laser fluence, leading to the formation of Sr-(Ti-) deficient STO films. Since the kinetic energy of the arriving species is affected also by the background pressure in the chamber, P_O , during the PLD process, a suitable balance between the laser fluence and background gas is essential.^{31,34} Thus, controlling the relation between the laser fluence and P_O is an effective way to induce and control atomic defects in the films.

Figure 1(b) shows RHEED intensity oscillations for STO film growth at different P_O : $5 \times 10^{-2} \text{ mbar}$, $5 \times 10^{-4} \text{ mbar}$, and $5 \times 10^{-6} \text{ mbar}$. The overall thickness of the films was kept around 25–26 nm. The appearance of persistent RHEED oscillations indicates that the growth of STO films occurred in layer-by-layer growth mode. However, it was found that the RHEED intensity dampened faster when P_O was decreased. P_O influences the growth rate (pulses

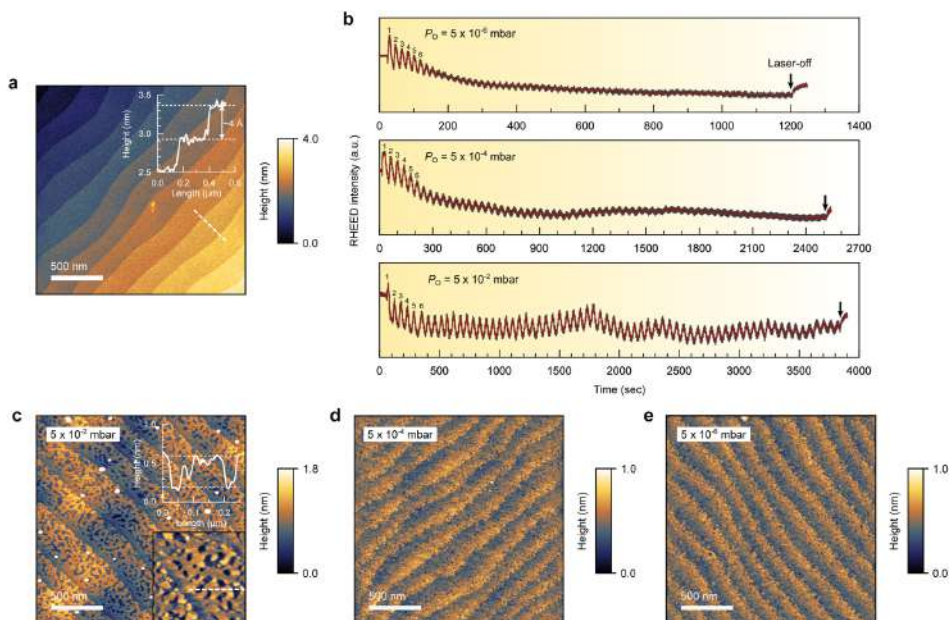


FIG. 1. (a) A topography AFM image ($3 \times 3 \mu\text{m}^2$) of atomically terminated TiO_2 -terminated STO(001) substrate, used for this work. (b) RHEED intensity oscillations for the layer-by-layer STO film growth with different P_{O} . [(c)–(e)] Topography AFM images ($3 \times 3 \mu\text{m}^2$) for the grown films in $P_{\text{O}} = 5 \times 10^{-2}$ mbar (c), 5×10^{-4} mbar (d), and 5×10^{-6} mbar (e). The insets in (c) show a height profile for an incomplete STO monolayer at the step-terrace surface.

needed per unit cell, pls/uc) of the films, which for our experiments was found to be ~ 57 pls/uc at 5×10^{-2} mbar, ~ 37 pls/uc at 5×10^{-4} mbar, and ~ 18 pls/uc at 5×10^{-6} mbar. This P_{O} -dependent growth rate variation can be attributed to the change of plasma plume dynamics during film growth, i.e., the higher the P_{O} , the more confined the plume expansion. In addition, the stoichiometric composition was found to scale with background P_{O} .³⁴ When the background pressure is high, transport occurs in a diffusion-like regime and Ti and Sr atoms can be fully oxidized in the plasma plume. In contrast, under low background pressures, the interactions between the ablated species and the background gas in the plume are minor and the species in the plume have high kinetic energies and travel following ballistic-like motion. It is particularly in this low pressure regime where preferential elemental ablation can be effectively driven by applying an inadequate laser fluence, thus intentionally controlling the cation off-stoichiometry of STO thin films. This is due to relatively large weight ratios of Ti/Sr (0.56), compared to that of TiO_2/SrO (0.77).³⁴ At low P_{O} values, around 5×10^{-6} mbar, cation off-stoichiometry is observed in the rapid damping of the RHEED intensity during the STO film growth [Fig. 1(b)]. The film variation as a function of P_{O} is reflected also in the surface morphology of the grown films as shown in Figs. 1(c)–1(e). For $P_{\text{O}} = 5 \times 10^{-2}$, an atomically flat morphology was found with a terrace step height of $\sim 4 \text{ \AA}$ [Fig. 1(c)], similar to the vicinal step-structure of the TiO_2 -terminated STO surface. Note

that the atomic force microscopy (AFM) image [Fig. 1(c)] shows an incomplete STO monolayer at the step-terrace surface—the height difference within the terrace is around 4 \AA . In contrast, at $P_{\text{O}} \leq 5 \times 10^{-4}$, the film surface is faceted due to the ballistic motion of the arriving species to the substrates. These results provide a solid indication that the growth dynamics and chemical plasma composition of the STO films can be effectively tuned by P_{O} , while the laser fluence is kept constant at a low value.

Figure 2(a) shows the high-resolution x-ray diffraction (XRD) 2θ - ω patterns of oxidized STO films, grown on STO(001), as a function of P_{O} . Note that all of the measured films were cooled down to RT in an O_2 atmosphere (200 mbar). The XRD spectra show that the oxidized films were grown epitaxially and possess thickness fringes. The STO film grown at $P_{\text{O}} = 5 \times 10^{-2}$ mbar shows almost identical 2θ (00 l) peak positions to those of the STO homo-substrate with well-defined thickness fringes. This indicates low out-of-plane strain ($x_z = +0.19\%$) in the film and an excellent crystal quality. When P_{O} was decreased to $P_{\text{O}} = 5 \times 10^{-4}$ mbar, a continuous shift of the out-of-plane STO(00 l) peaks toward lower 2θ values was found. This reveals an increase in the c -axis lattice parameter to a value of $c = 3.95 \text{ \AA}$ ($x_z = +1.15\%$), as shown in Fig. 2(c). To get further information about the strain distribution of the STO films, we performed reciprocal space mappings (RSMs) around the STO103 reflection for the two films (with $P_{\text{O}} = 5 \times 10^{-2}$ and 5×10^{-4} mbar) [Fig. 2(b)]. The results show that the in-plane lattice spacing for both films is

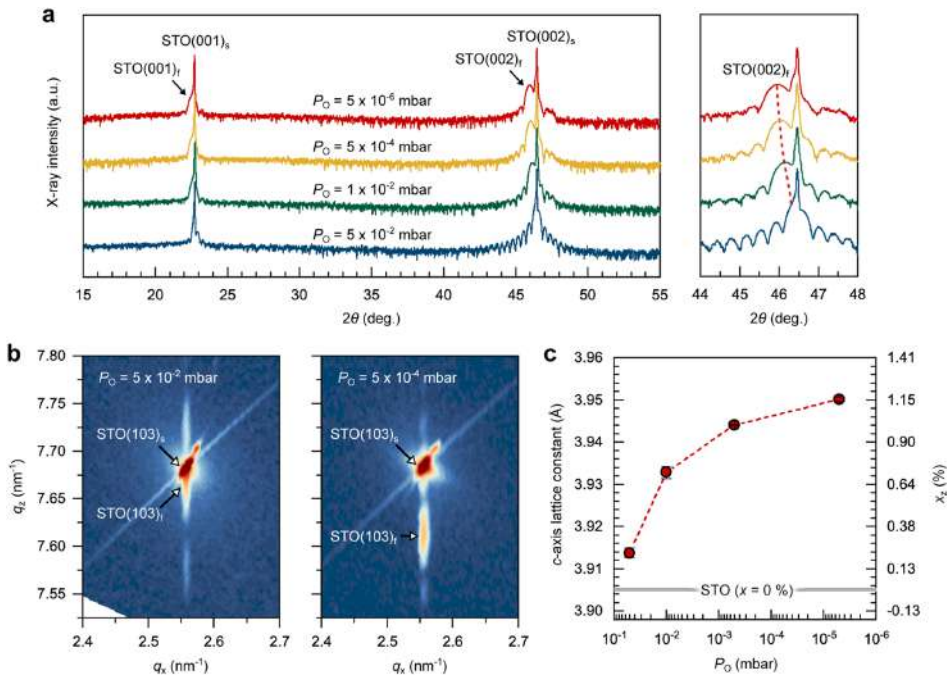


FIG. 2. (a) XRD 2θ scans for the STO films, grown on STO(001) substrates, as a function of P_O . The right panel shows the XRD (002) peaks for the STO films and substrates. (b) RSM near STO103 reflection for the STO films grown at $P_O = 5 \times 10^{-2}$ and 5×10^{-4} mbar. (c) Variations in the c-axis lattice parameter (left) and strain (right) of the films with different P_O .

coherently aligned with the in-plane spacing of the underlying STO substrates ($a = 3.905 \text{ \AA}$), while the c -axis lattice parameter was found to increase with P_O [Fig. 2(c)].

We investigated the magnetic properties of the oxidized STO films using a superconducting quantum interference device (SQUID) magnetometer. Prior to the sample measurement, external magnetic effects {e.g., sample holders, low-temperature glue, instrumental accessories, and annealed TiO₂-STO substrates [see Fig. 5(a)]} were carefully eliminated.²⁹ Figure 3(a) shows the in-plane magnetic hysteresis loops of the STO films, measured at 5 K, as a function of P_O . The results show a notable increase in the magnetization with decreasing P_O . The saturation magnetic moment of the films continuously increases up to $14 \mu\text{emu}$ ($56 \mu\text{emu}/\text{cm}^2$) as the growth pressure is decreased to a value of $P_O = 5 \times 10^{-4}$ mbar. The enhanced magnetism at low P_O can be understood through the rise of cation off-stoichiometry (Ti deficiency) in the films. We can rule out that the increase in magnetization results from external magnetic impurities that may have been present in the target materials or in the PLD growth chamber since our results show the opposite trend from what would be expected if this was the case. Lower P_O values (up to 5×10^{-4} mbar) yield higher film growth rates and, thus, require a shorter total film growth time (decreasing the time that the films are exposed to external impurities) [Fig. 1(b)]; nonetheless,

they produce larger magnetic moments. Another important observation is the steep magnetic degradation ($\leq 10 \mu\text{emu}$) seen in the STO film grown at $P_O = 5 \times 10^{-6}$ mbar. To confirm this, we repeated the film growth with the same growth conditions and observed the same weak magnetic response as compared to the results obtained using $P_O = 5 \times 10^{-4}$ mbar. We postulate that this magnetic degradation could be associated with a strong charge compensation between positively and negatively charged V_O and V_{Ti} defects as the oxidized film sample, grown at $P_O = 5 \times 10^{-6}$ mbar, shows a pale gray color. Further oxidation (200 mbar O₂ annealing at 500 °C for 2 h) will eventually cause the formation of a secondary phase (see the [supplementary material](#), Fig. S1).

To understand atomic charge defect-mediated magnetism in STO, we performed first-principles calculations on STO with atomic vacancy defects. Density functional theory (DFT) simulations using VASP code³⁵ were performed to calculate the electronic, structural, and magnetic properties of ABO₃-perovskite STO by incorporating all possible atomic vacancy defects (V_{Ti} , V_{Sr} , and V_O). The structural relaxation simulation was performed using a $4 \times 4 \times 4$ k-mesh and the conjugate-gradient algorithm until the Hellmann-Feynman forces became less than 5×10^{-3} eV/Å. The density of states (DOS) was then obtained using the Γ -centered and compacted k-mesh with minor smearing of 10 meV. The

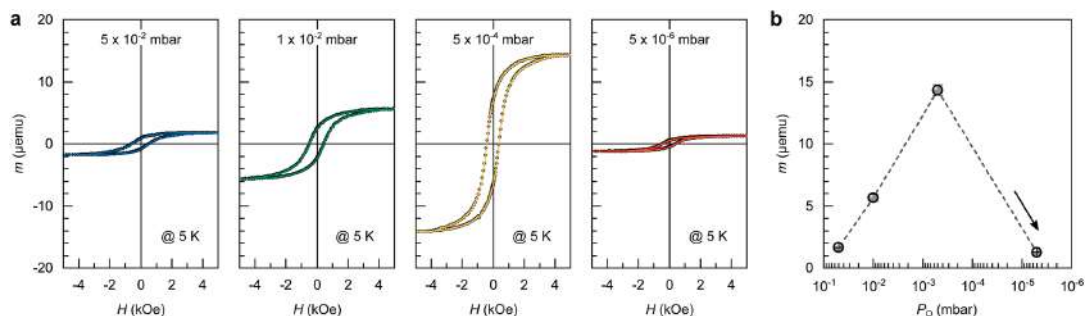


FIG. 3. (a) The 5 K magnetic hysteresis loops of the STO films, grown at different P_{O_2} ($=5 \times 10^{-2}$, 1×10^{-2} , 5×10^{-4} , and 5×10^{-6} mbar). (b) Variations in the magnetic moment of the films as a function of P_{O_2} .

Perdew–Burke–Ernzerhof (PBE) generalized-gradient approximation (GGA)³⁶ was applied to the exchange-correlation potential. The use of GGA-PBE and its reliability were discussed previously for simulations of the STO structures. Detailed calculation methods are presented elsewhere.^{29,37}

Figure 4(a) illustrates a STO model structure with a Ti vacancy (V_{Ti}) defect (~ 2 at. %) separated by a regular distance of $4a$ (where

a is the lattice constant). Together with the atomic rearrangement (which produces a local lattice expansion of $\sim 1.1\%$) of the six oxygen neighbors surrounding the V_{Ti} , a visible magnetic response in the model structure was found: The O and Ti ions neighboring a V_{Ti} site became spin-polarized through charge rearrangement, yielding a $\mu_{\text{B}}/V_{\text{Ti}}$ of 0.48. It should be noted that the V_{Ti} site itself has no magnetic moment. The cation vacancy-induced magnetic moments

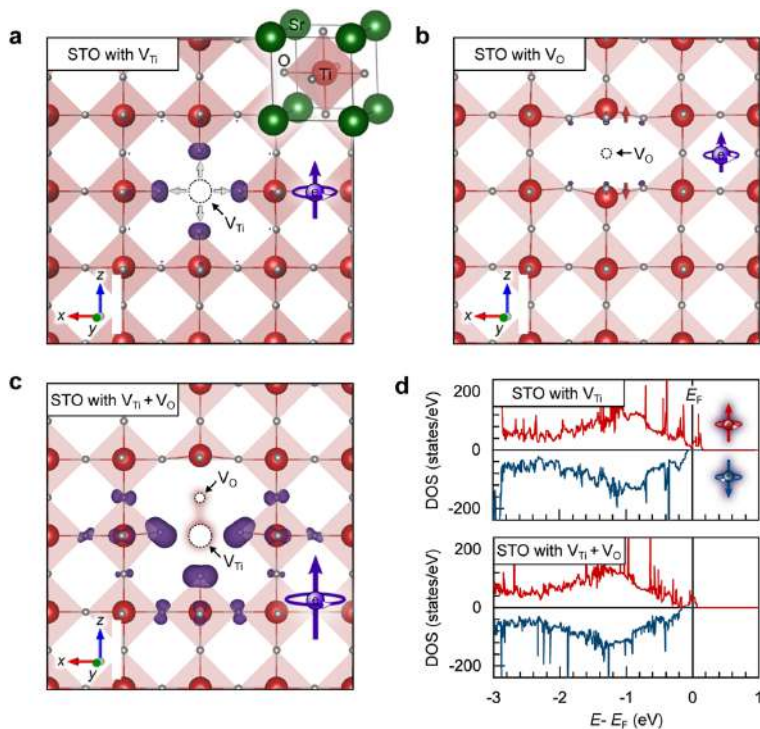


FIG. 4. [(a)–(c)] Magnetization density of the ABO_3 -perovskite STO structures, induced by different atomic vacant defects, a V_{Ti} (a), a V_{O} (b), and a $V_{\text{Ti}}-V_{\text{O}}$ pair (c). (d) Spin-polarized density of states of the STO with a V_{Ti} (upper panel) and with a $V_{\text{Ti}}-V_{\text{O}}$ pair (lower panel).

show a dome-shaped dispersive magnetic nature over the surrounding lattices, mostly on the nearest oxygen atoms. The calculated spin-polarized density of states (DOS) of the system further indicates that the negatively charged V_{Ti} in STO behaves as a p -type like acceptor locally and leads to the effective spin-polarization of the six nearest oxygen atoms due to unsaturated valence electrons, O $2p$ electrons (about 70% of the induced magnetization). In this case, a relatively weak Ti magnetization occurs via spin-polarized charge transfer through a p - d band hybridization. Furthermore, we considered the effect of A-site Sr ($2+$) vacancies on the magnetism of STO. An A-site vacancy defect contributes to a relatively weak magnetization of $m < 0.07 \mu_B/V_{Sr}$ in STO due to its much less effective charge rearrangement.²⁹ (i) Only two electrons can contribute to the oxygen atoms adjacent to a Sr vacancy site and (ii) a Sr vacant site has a relatively large distance (2.76 Å) to the 12 nearest oxygens as compared to that (1.95 Å) of a Ti vacant site. In a STO model structure with V_O defects (~1 at. %), separated by a $4a$ distance [Fig. 4(b)], the positively charged V_O acts like an n -type donor in the system and the local lattice expansion occurs primarily by moving the two neighboring Ti atoms upward. Our calculations show that an isolated V_O when stabilized in STO produces a very weak magnetism ($0.003 \mu_B/V_O$) without significant exchange interaction with the neighboring Ti atoms (e.g., a magnetization of Ti d_{xy} bands). This is consistent with previous reports.²¹ When the V_O concentration increases up to ~8 at. %, the defects are placed in STO with a separating distance of $\sqrt{2}a$ (in an orthorhombic $\sqrt{2} \times \sqrt{2} \times 2$ supercell) and the Ti d_{xy} bands become magnetized with a total moment of $0.41 \mu_B/V_O$. However, such a defect sublattice in STO with high V_O concentration is highly unrealistic as an artificial magnetic array since it is hard to retain an ABO₃-perovskite structure practically.¹⁷

Next, we examined a STO model structure incorporating both cation and anion vacancy defects. Our results show that a V_O defect energetically tends to be paired with a V_{Ti} in STO after relaxation [Fig. 4(c)]. The results of the model indicate that the atomic configuration in which the vacancies are $1/2a$ apart is much more energetically favorable than pairing at a distance of $3/2a$ by an energetic difference of ~1 eV. We found that in an unrelaxed model structure, the complex defect pair creates a magnetic spin-moment of $2 \mu_B$ /pair in the system due to an incomplete charge compensation and the relaxation of the oppositely charged V_{Ti} ($4+$) and V_O ($2-$) vacancies. After atomic relaxation with charge screening, the system has a total magnetization of $0.7 \mu_B$ /pair. The calculated DOS clearly shows a spin-polarized moment distribution near the Fermi level of the system [Fig. 4(d)]. Interestingly, the magnetization of STO induced by the defect pair is higher than the moments for individual cation defects, despite the fact that the defect charge state of V_{Ti} ($4+$) is higher than that of $V_{Ti}-V_O$ ($2+$). Our calculations clarify that the large measured magnetization is produced by the $V_{Ti}-V_O$ pair due to (i) a more energetically stable formation (smaller charge screening effect) in the STO system with a tendency of pairing the oppositely charged defects [when comparing the charge screening effect of STO with a singular V_{Ti} through relaxation and the largely varied magnetization ($4 \mu_B/V_{Ti} \rightarrow 0.48 \mu_B/V_{Ti}$)], (ii) a higher dispersive nature of the induced magnetic moment over the lattice atoms, and (iii) an effective magnetic coupling with a shorter distance ($3.5a$) between the vacant defect pairs. However, it should be noted

that an excessive concentration of V_O defects in the system can compensate for the charge state of the defect pair. This mechanism could produce a significant degradation in the defect-induced magnetism of STO as can be seen in our experimental results [Fig. 3(b)].

To examine the effect of the $V_{Ti}-V_O$ defect pair on the magnetism of STO, we prepared B-site cation deficient STO films with different V_O concentrations. To achieve this, different cooling processes were applied after film growth, i.e., cooling to room temperature in a high O₂ atmosphere (200 mbar) and under the same P_O as used during growth. Figure 5(a) shows the magnetic hysteresis loops of the STO films measured at 5 K. These two samples were grown using the same laser fluence of ~0.6 J/cm² at a pressure of $P_O = 5 \times 10^{-4}$ mbar, using the two cooling procedures described above. Notably, the magnetic moment of the STO film cooled down in the same P_O increases by a factor of ~3.5 when compared to that of the film cooled in an O₂ atmosphere. This magnetic enhancement is indicative of an increase in the formation of $V_{Ti}-V_O$ defect pairs in STO driven by the P_O cooling process. Furthermore, to examine magnetic effects of a reduced STO substrate and possible impurities in the PLD chamber, we annealed a TiO₂-terminated STO substrate by using the same heating rate (to 700 °C) and P_O cooling process in the PLD vacuum chamber that was used for film growth. The annealed STO substrate shows no magnetic response [Fig. 5(a)], confirming that the P_O cooling process at 5×10^{-4} mbar (V_O) cannot solely create the observed magnetism of the B-site cation deficient STO films. These results indicate either that the employed P_O does not create a sufficient number of V_O sites for achieving ferromagnetic ordering in STO or that the number of V_O sites plays a minor role in creating the magnetism. Moreover, both B-site cation deficient films show a similar temperature-independent magnetic response in the range of 5–300 K. Such temperature-independent magnetizations for materials with high Curie temperatures of >>300 K were also attributed to defect-induced magnetism (e.g., ZnO, MgO, TiO₂, and HfO₂).^{12,28,30,38} These are most likely explained by a spin-splitting of the defect-related impurity bands near the conduction band/valence band edge of the systems, as these are the source for ferromagnetically coupled electrons.¹² Our experimental results confirm that the magnetism of STO can be controlled by incorporating both V_{Ti} and V_O defects, which probably promotes the formation of $V_{Ti}-V_O$ pairs. However, the replacement of B-site cation with V_O defects in STO should be limited (by using $P_O \sim 5 \times 10^{-4}$ mbar in our case) in order to obtain such a magnetic enhancement and to prevent a strong atomic charge compensation, e.g., $1V_{Ti} (4+) + 2V_O (2-)$.

We further verified the magnetic nature of the B-site cation deficient STO film by x-ray magnetic circular dichroism (XMCD). The Ti $L_{2,3}$ -edge x-ray absorption (XAS) spectra were collected by using circular polarized light with parallel (μ_+) and antiparallel (μ_-) photon spin while applying a constant magnetic field of +1 T perpendicular to the sample surface, with the probing depth being around 4 nm. The spectra were collected with the beam in normal incidence. The total electron yield method was used to record the spectra (by measuring the sample drain current) in a chamber with a vacuum base pressure of 2×10^{-10} mbar. Figure 5(c) shows the Ti $L_{2,3}$ -edge XAS and XMCD spectra of the B-site cation deficient STO film sample that was cooled down to RT at the

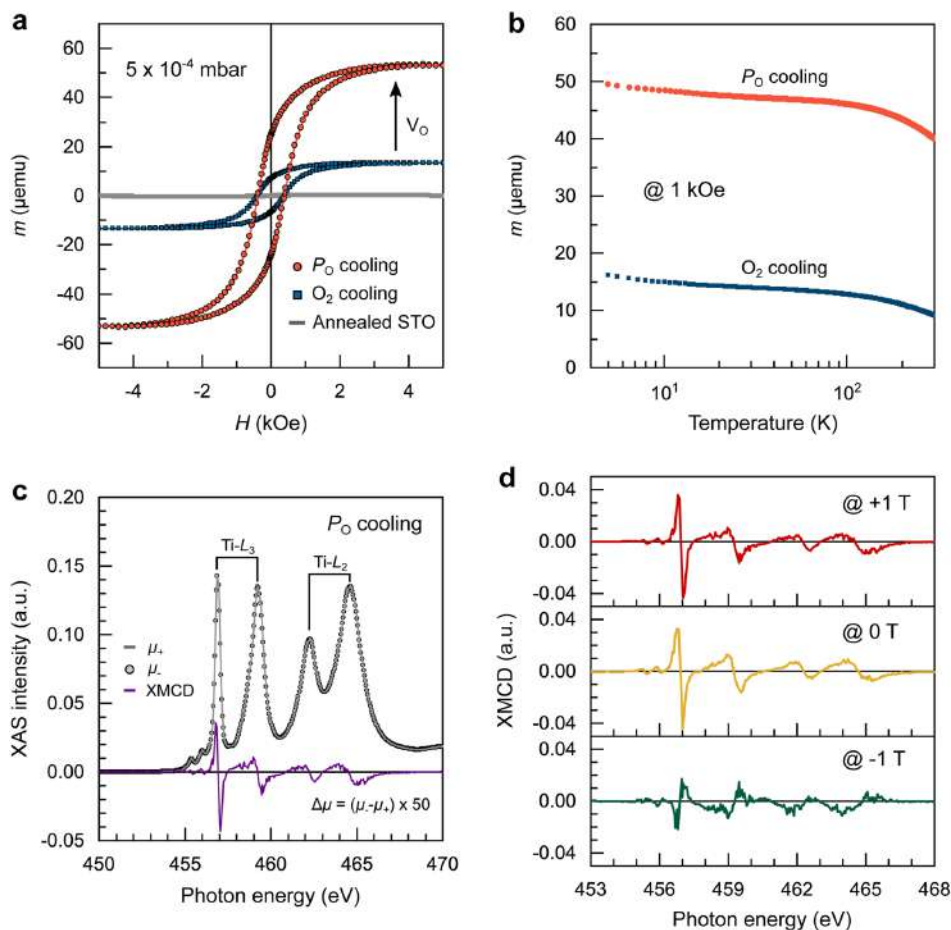


FIG. 5. (a) Comparison of the 5 K magnetic hysteresis loops of the B-site cation deficient STO films, grown at $P_{\text{O}} = 5 \times 10^{-4}$ mbar, with different cooling processes, i.e., after film growth, the two samples were cooled in a high O_2 atmosphere (blue circle, O_2 cooling) and in the same growth pressure (red circle, P_{O} cooling) separately. The hysteretic magnetic responses of the two STO/STO samples are compared with a non-magnetic annealed TiO_2 -STO(001) substrate. (b) Variable temperature magnetic moments of the samples, prepared by different cooling processes. A constant magnetic field of 1 kOe was applied to the samples during the temperature measurements. (c) XAS and XMCD across the $\text{Ti } L_{2,3}$ -edges of the B-site cation deficient STO film sample with P_{O} cooling as measured at 4 K. (d) $\text{Ti } L_{2,3}$ XMCD of the same STO thin film as measured by sweeping the applied magnetic fields (+1 T \rightarrow 0 T \rightarrow -1 T).

same P_{O} as the deposition pressure. First, we discard the possibility of the magnetic signal being due to the presence of Ti (3+) states since the spectral shape is typical of pure Ti (4+) as reported previously.^{39–41} This indicates that the $\text{Ti } L_{2,3}$ XMCD signal probably stems from the excitation between the $\text{Ti}^{4+} 3d^0$ and $\text{O } 2p$ orbitals: the $\text{Ti}^{4+} (3d^0)$ ions are related to the magnetic environment sensitivity of the electrons excited to the $2P^5 3d^1$ state. The increased number of defect pairs in the STO film should enhance the magnetization of

the surrounding Ti atoms. Furthermore, the reversible XMCD signal under applied field inversion confirms the true magnetic nature of the STO films [see Fig. 5(d)]. As a result, the XMCD analysis suggested that the defect-induced magnetism in the engineered STO films is due to the contribution of p -type like defects that spread magnetic moments over the surrounding ions. The magnetism of the engineered STO films is unlikely to be due to an accumulation of magnetic Ti^{3+} ions or any associated magnetic order.

CONCLUSION

In this work, we have demonstrated that the magnetic properties of engineered STO thin films can be effectively tuned by PLD film growth parameters (interdependent parameters of laser fluence and P_{O}) by controlling the concentration of cation vacancies, anion vacancies, and their complex defects. Our results show that B-site cation vacancies, V_{Ti} , not only contribute to the magnetization of STO but also promote the incorporation of oppositely charged V_{O} into the B-site cation deficient STO for the formation of the $V_{\text{Ti}}-V_{\text{O}}$ pairs. This greatly increases the magnetization and stability of the system and has been demonstrated both experimentally and theoretically. We further show that a strong charge compensation between oppositely charged defects significantly reduces the magnetism of STO, suggesting that under these process conditions, oxygen vacancies are not the main magnetic source for the defect-mediated magnetism of STO since we have not detected the presence of magnetic Ti^{3+} . Therefore, such a design allowing for tunable magnetism in STO films via atomic defect engineering offers important insights into the possible routes for designing magnetic STO films and related oxide heterosystems.

SUPPLEMENTARY MATERIAL

See the [supplementary material](#) for XRD 2θ patterns of the as-grown and O_2 -annealed B-site cation deficient STO film samples, grown at 5×10^{-6} mbar (Fig. S1).

ACKNOWLEDGMENTS

D.-S. Park and N. Pryds acknowledge the support provided by the European Commission through the project Biowings H2020 FET-OPEN 2018–2022 (Grant No. 80127). N. Pryds acknowledges funding from Villum Fonden for the NEED project (Grant No. 00027993) and the Danish Council for Independent Research Technology and Production Sciences for the DFF-Research Project 3 (Grant No. 00069 B). D. Lee and B. Jalan acknowledge support from the Air Force Office of Scientific Research (AFOSR) through Grant Nos. FA9550-21-1-0025 and FA9550-21-0460. We thank Thierry Désiré Pomar for reading the manuscript.

AUTHOR DECLARATIONS

Conflict of Interest

The authors have no conflicts to disclose.

Author Contributions

A. D. Rata: Investigation (equal); Writing – review & editing (equal). **I. Mertig:** Investigation (equal); Writing – review & editing (equal). **A. Ernst:** Investigation (equal); Writing – review & editing (equal). **A. M. Ionescu:** Investigation (equal); Writing – review & editing (equal). **K. Dörr:** Investigation (equal); Writing – review & editing (equal). **N. Pryds:** Conceptualization (equal); Funding acquisition (equal); Supervision (equal); Writing – original draft (equal); Writing – review & editing (equal). **D.-S. Park:** Conceptualization (equal); Data curation (equal); Formal

analysis (equal); Funding acquisition (equal); Investigation (equal); Methodology (equal); Project administration (equal); Resources (equal); Supervision (equal); Validation (equal); Visualization (equal); Writing – original draft (equal); Writing – review & editing (equal). **J. Herrero-Martin:** Investigation (equal); Writing – review & editing (equal). **I. V. Maznichenko:** Investigation (equal); Writing – review & editing (equal). **F. M. Chiabrera:** Investigation (equal); Writing – review & editing (equal). **R. T. Dahm:** Investigation (equal); Writing – review & editing (equal). **S. Ostanin:** Investigation (equal); Writing – review & editing (equal). **D. Lee:** Investigation (equal); Writing – review & editing (equal). **B. Jalan:** Investigation (equal); Writing – review & editing (equal). **P. Buczek:** Investigation (equal); Writing – review & editing (equal).

DATA AVAILABILITY

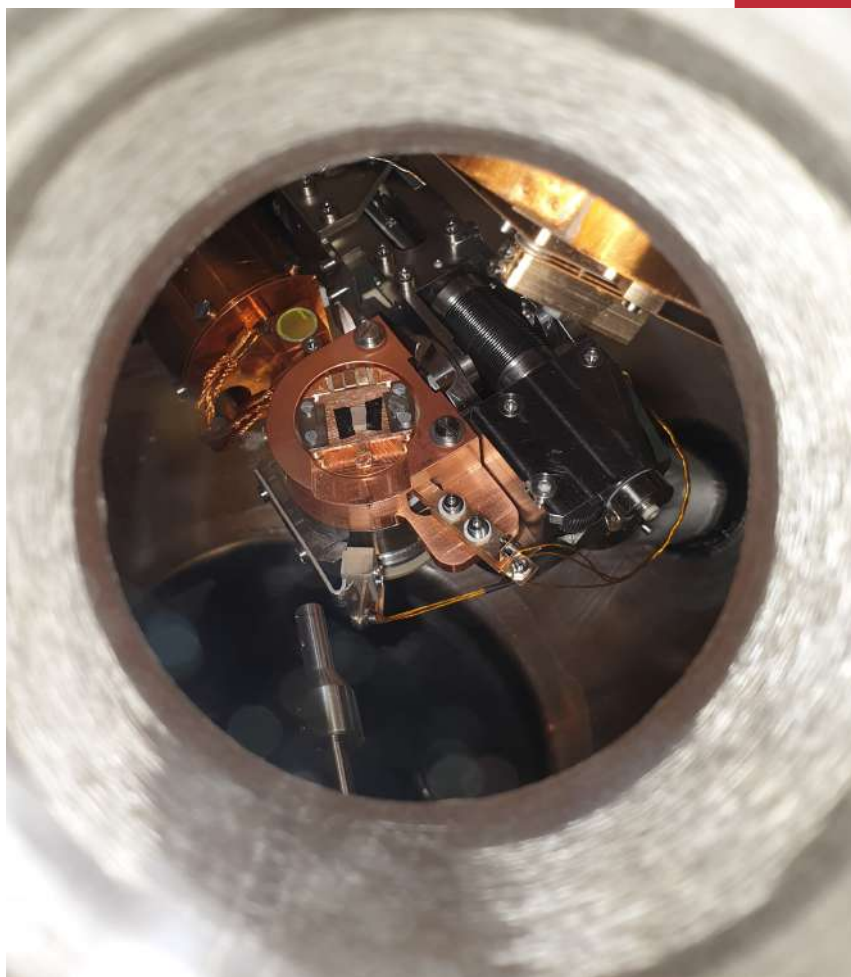
The data that support the findings of this study are available within the article.

REFERENCES

- A. S. Bhalla, R. Guo, and R. Roy, *Mater. Res. Innovations* **4**, 3 (2000).
- Y.-Y. Pai, A. Tylan-Tyler, P. Irvin, and J. Levy, *Rep. Prog. Phys.* **81**, 036503 (2018).
- R. A. Cowley, *Phys. Rev.* **134**, A981–A997 (1964).
- H. P. R. Frederikse and W. R. Hosler, *Phys. Rev.* **161**, 822–827 (1967).
- J. Son, P. Moetakef, B. Jalan, O. Bierwagen, N. J. Wright, R. Engel-Herbert, and S. Stemmer, *Nat. Mater.* **9**, 482–484 (2010).
- J. Yue, Y. Ayino, T. K. Truttman, M. N. Gastiasoro, E. Persky, A. Khanukov, D. Lee, L. R. Thoutam, B. Kalisky, R. M. Fernandes, V. S. Pribiag, and B. Jalan, *Sci. Adv.* **8**, eabl5668 (2022).
- J. F. Schooley, W. R. Hosler, and M. L. Cohen, *Phys. Rev. Lett.* **12**, 474 (1964).
- K. Ahadi, L. Galletti, Y. Li, S. Salmani-Rezaie, W. Wu, and S. Stemmer, *Sci. Adv.* **5**, eaaw0120 (2019).
- H. Haeni, P. Irvin, W. Chang, R. Uecker, P. Reiche, Y. L. Li, S. Choudhury, W. Tian, M. E. Hawley, B. Craigo, A. K. Tagantsev, X. Q. Pan, S. K. Streiffer, L. Q. Chen, S. W. Kirchoefer, J. Levy, and D. G. Schlom, *Nature* **430**, 758 (2004).
- D. Lee, H. Lu, Y. Gu, S.-Y. Choi, S.-D. Li, S. Ryu, T. R. Paudel, K. Song, E. Mikheev, S. Lee, S. Stemmer, D. A. Tenne, S. H. Oh, E. Y. Tsybal, X. Wu, L.-Q. Chen, A. Gruverman, and C. B. Eom, *Science* **349**, 1314 (2015).
- M. Lippmaa, N. Nakagawa, M. Kawasaki, S. Ohashi, Y. Inaguma, M. Itoh, and H. Koinuma, *Appl. Phys. Lett.* **74**, 3543 (1999).
- J. M. D. Coey, M. Venkatesan, and P. Stamenov, *J. Phys.: Condens. Matter* **28**, 485001 (2016).
- M. Janousch, G. I. Meijer, U. Staub, B. Delley, S. F. Karg, and B. P. Andreasson, *Adv. Mater.* **19**, 2232 (2007).
- K. T. Kang, H. I. Seo, O. Kwon, K. Lee, J.-S. Bae, M.-W. Chu, S. C. Chae, Y. Kim, and W. S. Choi, *Appl. Surf. Sci.* **499**, 143930 (2020).
- E. Breckenfeld, R. Wilson, J. Karthik, A. R. Damodaran, D. G. Cahill, and L. W. Martin, *Chem. Mater.* **24**, 331 (2012).
- G. Z. Liu, Q. Y. Lei, and X. X. Xi, *Appl. Phys. Lett.* **100**, 202902 (2012).
- A. Ohtomo and H. Y. Hwang, *J. Appl. Phys.* **102**, 083704 (2007).
- H. N. Lee, S. S. A. Seo, W. S. Choi, and C. M. Rouleau, *Sci. Rep.* **6**, 19941 (2016).
- T. Li, S. Deng, H. Liu, S. Sun, H. Li, S. Hu, S. Liu, X. Xing, and J. Chen, *Adv. Mater.* **33**, 2008316 (2021).
- Y. Cao, X. Liu, P. Shafer, S. Middey, D. Meyers, M. Kareev, Z. Zhong, J.-W. Kim, P. J. Ryan, E. Arenholz, and J. Chakhalian, *npj Quant. Mater.* **1**, 16009 (2016).
- O. Brovko and E. Tosatti, *Phys. Rev. Mater.* **1**, 044405 (2017).
- D. Doenning and R. Pentcheva, *Sci. Rep.* **5**, 7909 (2015).
- W. Gong, H. Yun, Y. B. Ning, J. E. Greedan, W. R. Datars, and C. V. Stager, *J. Solid State Chem.* **90**, 320 (1991).

- ²⁴D. A. Crandles, B. DesRoches, and F. S. Razavi, *J. Appl. Phys.* **108**, 053908 (2010).
- ²⁵W. Xu, J. Yang, W. Bai, K. Tang, Y. Zhang, and X. Tang, *J. Appl. Phys.* **114**, 154106 (2013).
- ²⁶M. Salluzzo, S. Gariglio, D. Stornaiuolo, V. Sessi, S. Rusponi, C. Piamonteze, G. M. De Luca, M. Minola, D. Marre', A. Gadaleta, H. Brune, F. Nolting, N. B. Brookes, and G. Ghiringhelli, *Phys. Rev. Lett.* **111**, 087204 (2013).
- ²⁷S. D. Yoon, Y. Chen, A. Yang, T. L. Goodrich, X. Zuo, D. A. Arena, K. Ziemer, C. Vittoria, and V. G. Harris, *J. Phys.: Condens. Matter* **18**, L355 (2006).
- ²⁸K. Potzger, J. Osten, A. A. Levin, A. Shalimov, G. Talut, H. Reuther, S. Arpaci, D. Bürger, H. Schmidt, T. Nestler, and D. C. Meyer, *J. Magn. Magn. Mater.* **323**, 1551 (2011).
- ²⁹D.-S. Park, A. D. Rata, I. V. Maznichenko, Y. Gan, S. Ostanin, S. Agrestini, M. Walker, G. J. Rees, Y. Chen, P. Murali, I. Mertig, K. Dörr, A. Ernst, and N. Pryds, *Nat. Commun.* **11**, 3650 (2020).
- ³⁰S. Wang, L. Pan, J.-J. Song, W. Mi, J.-J. Zou, L. Wang, and X. Zhang, *J. Am. Chem. Soc.* **137**, 2975 (2015).
- ³¹A. Ojeda-G-P, M. Döbeli, and T. Lippert, *Adv. Mater. Interfaces* **5**, 1701062 (2018).
- ³²T. Ohnishi, M. Lippmaa, T. Yamamoto, S. Meguro, and H. Koinuma, *Appl. Phys. Lett.* **87**, 241919 (2005).
- ³³D. J. Keeble, S. Wicklein, R. Dittmann, L. Ravelli, R. A. Mackie, and W. Egger, *Phys. Rev. Lett.* **105**, 226102 (2010).
- ³⁴K. Orsel, R. Groenen, B. Bastiaens, G. Koster, G. Rijnders, and K.-J. Boller, *APL Mater.* **3**, 106103 (2015).
- ³⁵G. Kresse and J. Furthmüller, *Phys. Rev. B* **54**, 11169 (1996).
- ³⁶J. P. Perdew, K. Burke, and M. Ernzerhof, *Phys. Rev. Lett.* **77**, 3865 (1996).
- ³⁷I. Maznichenko, S. Ostanin, A. Ernst, and I. Mertig, *Phys. Rev. Mater.* **3**, 074006 (2019).
- ³⁸P. Esquinazi, W. Hergert, D. Spemann, A. Setzer, and A. Ernst, *IEEE Trans. Magn.* **49**, 4668 (2013).
- ³⁹J. R. L. Mardegan, D. V. Christensen, Y. Z. Chen, S. Parchenko, S. R. V. Avula, N. Ortiz-Hernandez, M. Decker, C. Piamonteze, N. Pryds, and U. Staub, *Phys. Rev. B* **99**, 134423 (2019).
- ⁴⁰J.-S. Lee, Y. W. Xie, H. K. Sato, C. Bell, Y. Hikita, H. Y. Hwang, and C.-C. Kao, *Nat. Mater.* **12**, 703 (2013).
- ⁴¹N. Ortiz Hernández, Z. Salman, T. Prokscha, A. Suter, J. R. L. Mardegan, S. Moser, A. Zakharova, C. Piamonteze, and U. Staub, *Phys. Rev. B* **103**, 224429 (2021).

H. Li, Y. Gan, M. A. Husanu, **R. T. Dahm**, *et al.*
Robust Electronic Structure of Manganite-Buffered Oxide Interfaces
with Extreme Mobility Enhancement
ACS Nano **16**, 6437-6443 (2022)



SrTiO₃ sample in ADDRESS beamline at PSI

Robust Electronic Structure of Manganite-Buffered Oxide Interfaces with Extreme Mobility Enhancement

Hang Li, Yulin Gan, Marius-Adrian Husanu, Rasmus Tindal Dahm, Dennis Valbjørn Christensen, Milan Radovic, Jirong Sun, Ming Shi, Baogen Shen, Nini Pryds,* and Yunzhong Chen*



Cite This: <https://doi.org/10.1021/acsnano.2c00609>



Read Online

ACCESS |



Metrics & More



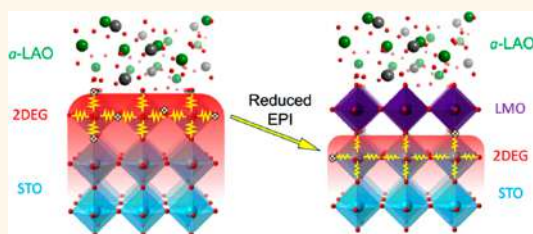
Article Recommendations



Supporting Information

ABSTRACT: The electronic structure as well as the mechanism underlying the high-mobility two-dimensional electron gases (2DEGs) at complex oxide interfaces remain elusive. Herein, using soft X-ray angle-resolved photoemission spectroscopy (ARPES), we present the band dispersion of metallic states at buffered $\text{LaAlO}_3/\text{SrTiO}_3$ (LAO/STO) heterointerfaces where a single-unit-cell LaMnO_3 (LMO) spacer not only enhances the electron mobility but also renders the electronic structure robust toward X-ray radiation. By tracing the evolution of band dispersion, orbital occupation, and electron–phonon interaction of the interfacial 2DEG, we find unambiguous evidence that the insertion of the LMO buffer strongly suppresses both the formation of oxygen vacancies as well as the electron–phonon interaction on the STO side. The latter effect makes the buffered sample different from any other STO-based interfaces and may explain the maximum mobility enhancement achieved at buffered oxide interfaces.

KEYWORDS: oxide interfaces, high mobility 2DEG, electronic structure, electron–phonon interaction, resonant angle-resolved photoemission spectroscopy



INTRODUCTION

The two-dimensional electron gas (2DEG) formed at the interface between two oxide band insulators, $\text{LaAlO}_3/\text{SrTiO}_3$ (LAO/STO), in particular,¹ exhibits exotic physical properties such as superconductivity,^{2–6} magnetism,^{7–10} Rashba-type spin–orbit coupling,^{11,12} and the quantum Hall effect.^{13,14} However, the origin of the conduction as well as the role of as-grown defects such as oxygen vacancies (OVs) on the conduction have often been topics of hot debate. In addition to the polar discontinuity-induced electronic and ionic reconstructions,^{1,15–17} OVs resulting from vacuum annealing,^{16–19} light irradiation,^{20–24} or interfacial redox reaction^{25–27} could also generate electrons, giving a large or even dominating contribution to the conduction. Regardless of the exact origin of the conduction, for most 2DEG systems related to STO, bare STO surface, or STO-based interfaces, the itinerant charges occupy the conduction band of STO with lower energy, which consists of exclusively Ti t_{2g} (d_{xy} and d_{xz}/d_{yz}) orbitals (Figure 1a).^{28–31} The electrons of the d_{xy} orbitals, contributing to the most carrier concentration, are strongly confined near the surface/interface of STO, forming quasi-2D subbands (Figure 1a), known as the light band with low

effective mass. Meanwhile, the d_{xz}/d_{yz} orbitals construct heavy bands with large effective mass while their wave functions extend deep into the bulk STO resulting in quasi-3D character (Figure 1a).³² As for the band character of each t_{2g} band, d_{xy} orbitals construct the circular electron pocket at the Fermi surface (FS), and the other two elliptical pockets are constructed by d_{xz} and d_{yz} orbitals, as revealed in Figure 1d. Compared with heavy d_{xz}/d_{yz} bands, the light d_{xy} band hosts larger bandwidth and smaller Fermi momenta (k_F) (Figure 1d).

Despite the intensive research, to date, one of the key challenges of STO 2DEGs is increasing the carrier mobility and revealing the underlying mechanism. The d_{xy} electrons, residing in closer proximity to the interface, have a smaller effective mass compared to the d_{xz}/d_{yz} ones, but their mobility

Received: January 18, 2022

Accepted: March 16, 2022

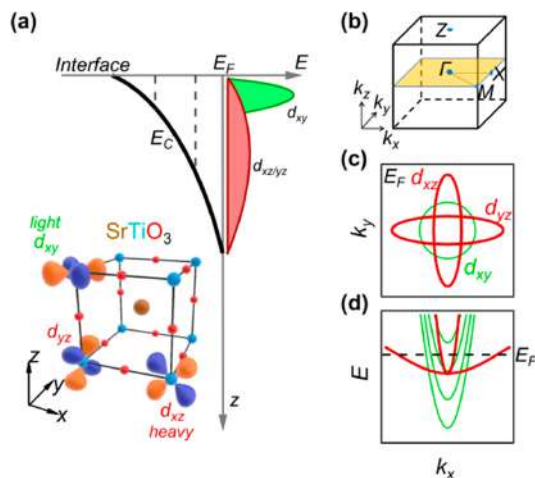


Figure 1. (a) Quantum-well states of 2DEG formed by wedgelike potential near the surface/interface of STO. Bold black curve shows the conduction band profile (E_C). The insert panel shows the unit cell and $d_{xy}/d_{xz}/d_{yz}$ orbitals of STO. The positive and negative lobes of the orbitals are shown in orange and blue, respectively. (b) 3D Brillouin zone (BZ) of STO-based systems. (c,d) Typical FS pattern and electronic structure of a STO 2DEG system, respectively.

is often lower probably due to a large defect concentration at the interface.³³ For most STO-based 2DEGs, the typical carrier mobility is around $1000 \text{ cm}^2 \text{ V}^{-1} \text{ s}^{-1}$ at low temperatures. This is expected to be further decreased under light irradiation in

high vacuum as significant oxygen-deficiency develops during light exposure.^{22,32–34} Notably, recent studies show that the carrier mobility can be significantly enhanced by deliberate surface or interface engineering.^{35–41} One significant example is the insertion of a single unit cell of epitaxial LaMnO_3 (LMO) at the interface between amorphous- LaAlO_3 and STO substrate ($a\text{-LAO/LMO/STO}$),³⁹ where an electron sink of Mn^{3+} in the perovskite structure was used to decrease the carrier density of 2DEG on the STO side through interfacial charge transfer.³⁹ The introduction of the manganite buffer layer decreases the carrier density by approximately 1 order of magnitude, whereas the carrier mobility is increased 10–100 times compared to the unbuffered $a\text{-LAO/STO}$.³⁹ It also leads to the observation of a clear quantum Hall effect at complex oxide interfaces.¹³ However, the electronic structure of these buffered oxide interfaces with enhanced carrier mobility remains to be determined. Identifying the electronic structure as well as the orbital configuration becomes even more interesting upon the recent finding that the high mobility 2DEG at $\gamma\text{-Al}_2\text{O}_3/\text{STO}$ (GAO/STO) interface shows an anomaly in orbital ordering as well as a weak electron–phonon interaction (EPI) strength of the carriers.^{42,43}

In this paper, we identify the electronic band structure of the buried oxide interfaces by soft X-ray angle-resolved photoemission spectroscopy (ARPES) for both bare and LMO-buffered $a\text{-LAO/STO}$. Besides a slight decrease in the k_F and carrier density as well as a strong suppression in the concentration of OVs,³⁹ the buffered interface exhibits two significant properties: (1) an unexpected irradiation-robust band structure, which reflects the detection of FS of intrinsic interface states, and (2) a significantly reduced EPI strength, which is absent in the nonbuffered^{42,43} as well as the diluted crystalline LAO/STO interfaces. The combined effect of the

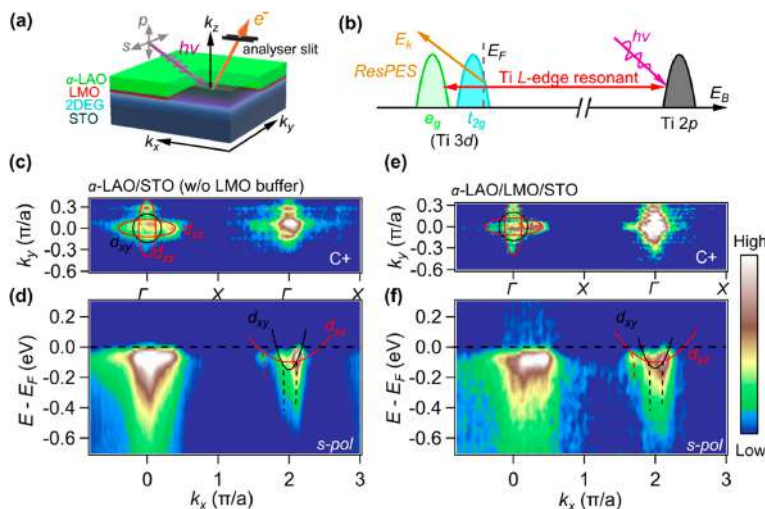


Figure 2. (a) Sketches of the modulation-doped $a\text{-LAO/LMO/STO}$ with the experimental geometry for the ARPES measurement. The gray arrows represent the s - and p -polarization of X-rays. (b) Sketches of resonant photoemission process in STO-based 2DEG systems. (c,e) FS maps and band dispersions measured at $C+$ polarization of $a\text{-LAO/STO}$ and $a\text{-LAO/LMO/STO}$ ($t = 1 \text{ uc}$) at E_F in $k_z = 0$ plane, respectively. The black circles and red ellipses indicate the FS of d_{xy} and d_{xz}/d_{yz} orbitals, respectively. (d,f) Electronic structures along k_x measured with s -polarization of $a\text{-LAO/STO}$ and $a\text{-LAO/LMO/STO}$, respectively. Black and red curves mark the band structure of d_{xy} and d_{yz} orbitals, respectively. Black and red dashed curves mark the pronounced tail of polarons induced by EPI. All data are recorded at Ti L -edge resonant energy, which corresponds to the $k_z = 7 \times 2 \pi/a$ plane in the BZ of STO (Figure S1).

reduction in the carrier density, the suppression of defect concentration of OVs, as well as the decrease in the EPI strength on the STO side could account for the extreme mobility of the buffered oxide heterostructures.

RESULTS AND DISCUSSION

The interfacial 2DEG locates on the STO side in close proximity to the interface underneath the capping layer, which is generally thicker than 1.6 nm. To investigate the band structures of these heterostructures, we used soft X-ray ARPES, where the photoelectrons have an escape depth sufficiently large to probe buried interfaces,^{42–47} as illustrated in Figure 2a for *a*-LAO/LMO/STO.

First, we identified the FS maps and band dispersions for *a*-LAO/STO heterointerfaces with and without LMO buffer. The resonant photon energies are determined by $h\nu$ -dependent ARPES intensity map at E_F (see Figure S1). As revealed in Figure 2c,e, the experimental FS map consists of one circular electron pocket located at the center of Brillouin zone (BZ) and two other intersecting elliptical electron pockets aligned along the k_x and k_y directions (the two Γ - X directions in the BZ). This is a typical FS pattern of the STO-based 2DEG systems (Figure 1c).^{31,32,42,43}

The band dispersions of *a*-LAO/STO and *a*-LAO/LMO/STO ($t = 1$ uc) along the k_x direction were measured with linear *s*-polarized light (Figure 2a), which probe mostly the antisymmetric d_{xy} and d_{yz} orbitals, whereas the symmetric d_{xz} ones can be probed by the *p*-polarized light.^{44,45} As shown in Figure 2d,f, we can clearly identify the light d_{xy} band and heavy d_{yz} bands near the second Γ -point for *a*-LAO/STO and *a*-LAO/LMO/STO ($t = 1$ uc), respectively. Similar to most other STO-based systems, the Ti t_{2g} bands are reconstructed at the interface to form deep d_{xy} subbands and shallow d_{xz}/d_{yz} bands (Figure 1d). This is due to the confined quantum well states with the banded band profiles near the surface region, which can be estimated by the binding energies of Ti 2p orbitals. However, our result (Figure S2) shows a similar value compared with pristine STO,⁴⁸ probably due to the limited energy resolutions. The pronounced intensity tail of these bands extending to higher binding energy is a sign of the strong polaronic coupling of charge carriers in these systems,^{42,43} which results in the discontinuity of band structures.

It has been found that STO-based 2DEG is often sensitive to the X-ray irradiation^{22,32,34,46} during ARPES measurements, where the photogenerated extra carriers could be used to tune the interface states, but it also makes the detection of the intrinsic electronic structure of interfacial 2DEGs challenging. Such an X-ray irradiation effect is demonstrated by the monotonous growth in the intensity of the 2DEG with respect to the X-ray exposure time as observed in *a*-LAO/STO (Figure 3a,c). On the contrary, we find that the intensity of the 2DEG in buffered sample shows a negligible increase during X-ray exposure (Figure 3b,c). The X-ray irradiation generated 2DEG is generally due to the formation of oxygen vacancies. We thus investigated the evolution of the in-gap states of OVs, which are located $E_B \sim 1.2$ eV below the Fermi energy level (E_F) (Figure S3). As shown in Figure 3d, the intensity of IGS for both buffered and unbuffered *a*-LAO/STO increases with respect to irradiation time. Notably, the intensity of the in-gap states increases at a rate much faster than that of the 2DEG for both samples, indicating that the photogenerated OVs not only contribute to the extra mobile carriers but also localized

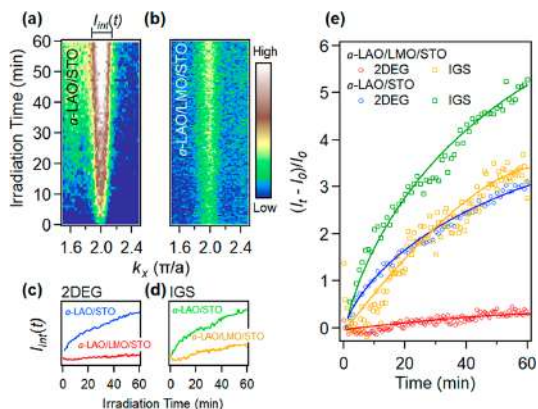


Figure 3. k -resolved intensity maps as a function of irradiation time at E_F of *a*-LAO/STO (a) and *a*-LAO/LMO/STO ($t = 1$ uc) (b), respectively. (c,d) Integrated intensities of 2DEG and OVs in-gap states (IGS) of *a*-LAO/STO and *a*-LAO/LMO/STO, respectively, as a function of irradiation time. (e) Time-dependent intensity change $[(I_t - I_0)/I_0]$ of 2DEG and OVs IGS for both *a*-LAO/STO and *a*-LAO/LMO/STO.

carriers. As far as *a*-LAO/LMO/STO is concerned, because of the nearly constant intensity of 2DEG with respect to X-ray irradiation, the difference in the intensity between the in-gap state of OVs and the 2DEG increases with respect to irradiation time although it has a slower rate compared to the unbuffered sample. This indicates two effects: first, the introduction of the LMO spacer suppresses the formation of OVs in the buffered sample; second, even though there are irradiation-induced in-gap states in buffered samples, the photogenerated extra carriers are most likely transferred to the manganite buffer layer instead of 2DEG conduction layer. This is consistent with the electron sink role of LMO buffer layer. As a consequence, the LMO buffer layer renders the intrinsic electronic structure robust toward X-ray irradiation.

Another feature of the buffered oxide interface is the strongly suppressed EPI. Besides electron–electron interactions, EPI is an important factor in STO affecting the charge transport and carrier mobility whereby the electrons drag behind a local perturbation of the crystal lattice as described by the concept of polarons.⁴⁴ Their signature in the experimental spectral function $A(\mathbf{k},\omega)$ is observed from the energy distribution curves (EDCs) as a peak-dip-hump structure, where the hump below the quasiparticle (QP) peak is formed by the EPI with the peak-to-hump distance reflecting the energy of the involved phonon modes. Figure 4c shows the EDCs of *a*-LAO/STO and *a*-LAO/LMO/STO, where the corresponding integration range is marked by the white box in Figure 4a,b for zoom-in band structures measured along k_x with *s*-polarized light. Both EDCs show clear QP peaks near E_F followed by an intensity tail at higher binding energy, consistent with previous observations in nonbuffered STO-based systems.^{42,44,45} The characteristic EPI-induced polaronic tail extends down to $E_b = -1$ eV. Notably, unlike stoichiometric crystalline LAO/STO⁴⁴ or GAO/STO,⁴² which exhibit clear satellite peaks for the LO_3 phonon mode, the hump lineshapes for these materials are structureless and extend over a wide energy range, suggesting that multiple phonon modes are involved in the EPI. The EPI strength is

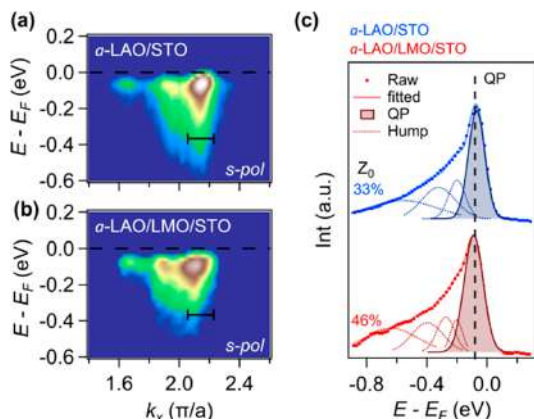


Figure 4. (a,b) Zoom-in band structures of *a*-LAO/STO and modulation-doped *a*-LAO/LMO/STO ($t = 1$ uc) measured along k_x with *s*-polarized light, respectively. (c) Integrated EDCs of d_{xy} orbitals (marked a and b). Red and blue dots show the raw integrated EDCs of *a*-LAO/LMO/STO and *a*-LAO/STO, respectively. Filled dark red and blue curves show the fitted corresponding QP peaks. Dashed curves show the fitted hump peaks. Red and blue curves show the fitted EDCs combined by QP peaks and hump peaks.

related to the QP residual weight, Z_0 ,^{44,45} which is calculated as $Z_0 = I_{QP}/(I_{QP} + I_{hump})$, with I_{QP} and I_{hump} representing the integrated spectral weight of QP and residuals from EDCs, respectively. Larger Z_0 values identify heavier QP spectral weight thus smaller EPI. Our quantitative analyses show that Z_0 increases from 33% in *a*-LAO/STO to 46% in *a*-LAO/LMO/STO (Figure 4c). Since these two systems host a similar band structure and bandwidth (~ 80 meV in *a*-LAO/STO and ~ 90 meV in *a*-LAO/LMO/STO, see the Supporting Information Figure.S4), the increase in Z_0 suggests a significant decrease of EPI strength upon the introduction of the single unit cell LMO buffer, which can fundamentally enhance the carrier mobility as discussed below.⁴¹

In STO 2DEGs, the carrier mobility is limited by several crucial ingredients including defect concentration, strong EPI, and to a lesser extent, electron–electron correlations. The EPI will result in the polaronic nature of the interfacial charge carriers that increases their effective mass,⁴⁰ whereas defects at the interface will increase the impurity scattering of carriers. Both effects will decrease the carrier mobility. For the unbuffered *a*-LAO/STO, its concentration of OV is high as expressed by the high intensity of in-gap states (Figure 3). The buffered sample shows much reduced in-gap states thus low OVs, which could explain partially the mobility enhancement. Notably, the Z_0 of the LMO-buffered sample increases to 46% in comparison to $\sim 33\%$ for *a*-LAO/STO. Previous studies on the temperature-dependent EPI effect of LAO/STO reveal that when Z_0 is increased from $\sim 30\%$ to $\sim 40\%$ the carrier mobility of 2DEG could be enhanced around 10 times.⁴⁴ It is noteworthy that a similar large Z_0 value of buffered sample is also obtained in GAO/STO,⁴² the carrier mobility of which can be up to $140000 \text{ cm}^2 \text{ V}^{-1} \text{ s}^{-1}$. Therefore, the nontrivial significant increase in Z_0 and, thus, the strong decrease in EPI of buffered oxide interfaces, on top of the suppression of the OVs, may be the main ingredient dominating the extreme mobility enhancement in buffered oxide interfaces. Addition-

ally, as the EPI is often associated with superconductivity in STO-based systems, the strong suppression of the EPI in *a*-LAO/LMO/STO could well explain its absence of superconductivity.¹³

CONCLUSIONS

In summary, we have studied in detail the electronic structure by soft X-ray ARPES of buffered oxide interfaces with enhanced electron mobility. The ARPES results reveal a nontrivial feature of weakened EPI strength concomitant with decreased formation of oxygen vacancies. The combination of these effects could explain the mobility enhancement and provide crucial insights in boosting the carrier mobility of engineered oxide heterostructures as well as the design of quantum oxide devices.

METHODS

Sample Fabrication. All heterostructures, *a*-LAO (~ 1.6 nm)/LMO/STO with different thicknesses of LMO buffer layer ($t = 0, 1$ and 2 uc) were grown on TiO_2 -terminated STO substrates by pulse laser deposition (PLD) in an O_2 atmosphere of 10^{-4} mbar. A KrF pulse laser (248 nm in wavelength, 1 Hz repetition frequency, $4.0 \text{ J}/\text{cm}^2$ laser fluence) was adopted. For buffered/unbuffered *a*-LAO/STO, amorphous LAO deposited at room temperature under 10^{-4} mbar with single crystalline LAO as target. For the buffer layer, sintered LMO ceramics were used as targets and the growth temperature of LMO was fixed at 600°C . After the epitaxial growth of monolayer LMO buffer layer, the sample was cooled under the deposition pressure at a nominal rate of $15^\circ\text{C}/\text{min}$ to room temperature (below 30°C , in 5–6 h) before the subsequent *a*-LAO film deposition *in situ*.

Angle-Resolved Photoemission Spectroscopy (ARPES). The soft-X-ray ARPES measurements were performed at the ADDRESS beamline^{49,50} of the Swiss Light Source at Paul Scherrer Institute, Switzerland. The ARPES maps were recorded with a PHOIBOS-150 analyzer at an energy resolution of 60 meV and angular resolution of 0.1° . The samples were transferred *ex situ* and measured in the ARPES setup without annealing. All measurements are acquired at 12 K in a base pressure of better than 5×10^{-11} Torr.

ASSOCIATED CONTENT

Supporting Information

The Supporting Information is available free of charge at <https://pubs.acs.org/doi/10.1021/acsnano.2c00609>.

Additional data, including summary of EPI strength (Z_0), concentration of the oxygen vacancies (n_{OV}), Fermi momenta (k_F) of d_{xy} and d_{yz} bands, carrier density (n_s), and carrier mobility (μ) of the studied samples; photon-energy-dependent result; XPS of Ti 2*p* orbitals of *a*-LAO/STO and *a*-LAO/LMO/STO; irradiation-dependent OV-states in *a*-LAO/LMO/STO and *a*-LAO/STO; extraction of k_F ; ARPES result of *a*-LAO/LMO/STO with 2 uc LMO buffer layer (PDF)

AUTHOR INFORMATION

Corresponding Authors

Yunzhong Chen – Beijing National Laboratory for Condensed Matter Physics and Institute of Physics, Chinese Academy of Sciences, 100190 Beijing, China; orcid.org/0000-0001-8368-5823; Email: yzchen@iphy.ac.cn

Nini Pryds – Department of Energy Conversion and Storage, Technical University of Denmark, 2800 Kgs. Lyngby, Denmark; orcid.org/0000-0002-5718-7924; Email: nipr@dtu.dk

Authors

Hang Li – Department of Energy Conversion and Storage, Technical University of Denmark, 2800 Kgs. Lyngby, Denmark; Swiss Light Source, Paul Scherrer Institute, 5232 Villigen, PSI, Switzerland

Yulin Gan – Beijing National Laboratory for Condensed Matter Physics and Institute of Physics, Chinese Academy of Sciences, 100190 Beijing, China

Marius-Adrian Husanu – National Institute of Materials Physics, 077125 Magurele, Romania; orcid.org/0000-0003-4510-6653

Rasmus Tindal Dahm – Department of Energy Conversion and Storage, Technical University of Denmark, 2800 Kgs. Lyngby, Denmark

Dennis Valbjørn Christensen – Department of Energy Conversion and Storage, Technical University of Denmark, 2800 Kgs. Lyngby, Denmark; orcid.org/0000-0003-0048-7595

Milan Radovic – Swiss Light Source, Paul Scherrer Institute, 5232 Villigen, PSI, Switzerland

Jirong Sun – Beijing National Laboratory for Condensed Matter Physics and Institute of Physics, Chinese Academy of Sciences, 100190 Beijing, China

Ming Shi – Swiss Light Source, Paul Scherrer Institute, 5232 Villigen, PSI, Switzerland

Baogen Shen – Beijing National Laboratory for Condensed Matter Physics and Institute of Physics, Chinese Academy of Sciences, 100190 Beijing, China

Complete contact information is available at: <https://pubs.acs.org/10.1021/acsnano.2c00609>

Author Contributions

The manuscript was written through contributions of all authors. All authors have given approval to the final version of the manuscript. Y.Z.C. designed the concept and experiments with N.P.; H.L., Y.L.G., M.A.H., and R.T.D. performed the ARPES experiment; Y.L.G. and Y.Z.C. fabricated the samples and performed their transport characterization; H.L. and M.A.H. processed the ARPES data. All authors discussed the results and interpretations and wrote the manuscript.

Notes

The authors declare no competing financial interest.

ACKNOWLEDGMENTS

The authors thank V. N. Strocov for supporting the ARPES experiments and valuable advice at all stages of the work and T. Schmitt for supporting the beamline operation. B.G.S., J.R.S., and Y.Z.C. were supported by the Science Center of the National Science Foundation of China (52088101) and the National Key Research and Development Program of China (2021YFA1400300). Y.Z.C. also acknowledges support from the Independent Research Fund Denmark (Grant No. 9041-00034B). M.A.H. was supported by a grant from the Ministry of Research, Innovation and Digitization, CNCS/CCCDI-UEFISCDI, Project No. PCE 96, within PNCDI III. N.P. and D.V.C. acknowledge funding from the Villum Fonden (00027993) and Independent Research Fund Denmark (Grant No. 00069B).

REFERENCES

(1) Ohtomo, A.; Hwang, H. Y. A High-Mobility Electron Gas at the $\text{LaAlO}_3/\text{SrTiO}_3$ Heterointerface. *Nature* **2004**, *427*, 423–426.

(2) Reyren, N.; Thiel, S.; Caviglia, A. D.; Fitting Kourkoutis, L.; Hammerl, G.; Richter, C.; Schneider, C. W.; Kopp, T.; Ruetschi, A.-S.; Jaccard, D.; Gabay, M.; Muller, D. A.; Triscone, J.-M.; Mannhart, J. Superconducting Interfaces Between Insulating Oxides. *Science* **2007**, *317*, 1196–1199.

(3) Caviglia, A. D.; Gariglio, S.; Reyren, N.; Jaccard, D.; Schneider, T.; Gabay, M.; Thiel, S.; Hammerl, G.; Mannhart, J.; Triscone, J. M. Electric Field Control of the $\text{LaAlO}_3/\text{SrTiO}_3$ Interface Ground State. *Nature* **2008**, *456*, 624–627.

(4) Joshua, A.; Pecker, S.; Ruhman, J.; Altman, E.; Ilani, S. A Universal Critical Density Underlying the Physics of Electrons at the $\text{LaAlO}_3/\text{SrTiO}_3$ Interface. *Nat. Commun.* **2012**, *3*, 1129.

(5) Prawiroatmodjo, G. E. D. K.; Trier, F.; Christensen, D. V.; Chen, Y.; Pryds, N.; Jespersen, T. S. Evidence of Weak Superconductivity at the Room-Temperature Grown $\text{LaAlO}_3/\text{SrTiO}_3$ Interface. *Phys. Rev. B* **2016**, *93*, 184504.

(6) Herranz, G.; Singh, G.; Bergeal, N.; Jouan, A.; Lesueur, J.; Gazquez, J.; Varela, M.; Scigaj, M.; Dix, N.; Sanchez, F.; Fontcuberta, J. Engineering Two-Dimensional Superconductivity and Rashba Spin–Orbit Coupling in $\text{LaAlO}_3/\text{SrTiO}_3$ Quantum Wells by Selective Orbital Occupancy. *Nat. Commun.* **2015**, *6*, 6028.

(7) Brinkman, A.; Huijben, M.; Van Zalk, M.; Huijben, J.; Zeitler, U.; Maan, J. C.; Van der Wiel, W. G.; Rijnders, G.; Blank, D. H. A.; Hilgenkamp, H. Magnetic Effects at the Interface Between Non-Magnetic Oxides. *Nat. Mater.* **2007**, *6*, 493–496.

(8) Kalisky, B.; Bert, J. A.; Klopfer, B. B.; Bell, C.; Sato, H. K.; Hosoda, M.; Hikita, Y.; Hwang, H. Y.; Moler, K. A. Critical Thickness for Ferromagnetism in $\text{LaAlO}_3/\text{SrTiO}_3$ Heterostructures. *Nat. Commun.* **2012**, *3*, 922.

(9) Bi, F.; Huang, M.; Ryu, S.; Lee, H.; Bark, C. W.; Eom, C. B.; Irvin, P.; Levy, J. Room-Temperature Electrically-Controlled Ferromagnetism at the $\text{LaAlO}_3/\text{SrTiO}_3$ Interface. *Nat. Commun.* **2014**, *5*, 5019.

(10) Christensen, D. V.; Frenkel, Y.; Chen, Y. Z.; Xie, Y. W.; Chen, Z. Y.; Hikita, Y.; Smith, A.; Klein, L.; Hwang, H. Y.; Pryds, N.; Kalisky, B. Strain-Tunable Magnetism at Oxide Domain Walls. *Nat. Phys.* **2019**, *15*, 269–274.

(11) Caviglia, A. D.; Gabay, M.; Gariglio, S.; Reyren, N.; Cancellieri, C.; Triscone, J.-M. Tunable Rashba Spin-Orbit Interaction at Oxide Interfaces. *Phys. Rev. Lett.* **2010**, *104*, 126803.

(12) Gan, Y.; Zhang, Y.; Christensen, D. V.; Pryds, N.; Chen, Y. Z. Gate-Tunable Rashba Spin-Orbit Coupling and Spin Polarization at Diluted Oxide Interfaces. *Phys. Rev. B* **2019**, *100*, 125134.

(13) Trier, F.; Prawiroatmodjo, G. E. D. K.; Zhong, Z.; Christensen, D. V.; Soosten, M.; Bhowmik, A.; Lastra, J. M. G.; Chen, Y.; Jespersen, T. S.; Pryds, N. Quantization of Hall Resistance at the Metallic Interface between an Oxide Insulator and SrTiO_3 . *Phys. Rev. Lett.* **2016**, *117*, 096804.

(14) Matsubara, Y.; Takahashi, K. S.; Bahramy, M. S.; Kozuka, Y.; Maryenko, D.; Falson, J.; Tsukazaki, A.; Tokura, Y.; Kawasaki, M. Observation of the Quantum Hall Effect in δ -Doped SrTiO_3 . *Nat. Commun.* **2016**, *7*, 11631.

(15) Nakagawa, N.; Hwang, H. Y.; Muller, D. A. Why Some Interfaces Cannot Be Sharp. *Nat. Mater.* **2006**, *5*, 204–209.

(16) Jang, H. W.; Felker, D. A.; Bark, C. W.; Wang, Y.; Niranjan, M. K.; Nelson, C. T.; Zhang, Y.; Su, D.; Folkman, C. M.; Baek, S. H.; Lee, S.; Janicka, K.; Zhu, Y.; Pan, X. Q.; Fong, D. D.; Tsymbal, E. Y.; Rzhchowski, M. S.; Eom, C. B. Metallic and Insulating Oxide Interfaces Controlled by Electronic Correlations. *Science* **2011**, *331*, 886–889.

(17) Rose, M. A.; Šmíd, B.; Vorokhta, M.; Slipukhina, I.; Andrä, M.; Bluhm, H.; Duchoň, T.; Ležaić, M.; Chambers, S. A.; Dittmann, R.; Mueller, D. N.; Gunkel, F. Identifying Ionic and Electronic Charge Transfer at Oxide Heterointerfaces. *Adv. Mater.* **2021**, *33*, 2004132.

(18) Thiel, S.; Hammerl, G.; Schmehl, A.; Schneider, C. W.; Mannhart, J. Tunable Quasi-Two-Dimensional Electron Gases in Oxide Heterostructures. *Science* **2006**, *313*, 1942–1945.

(19) Kalabukhov, A.; Gunnarsson, R.; Börjesson, J.; Olsson, E.; Claesson, T.; Winkler, D. Effect of Oxygen Vacancies in the SrTiO_3

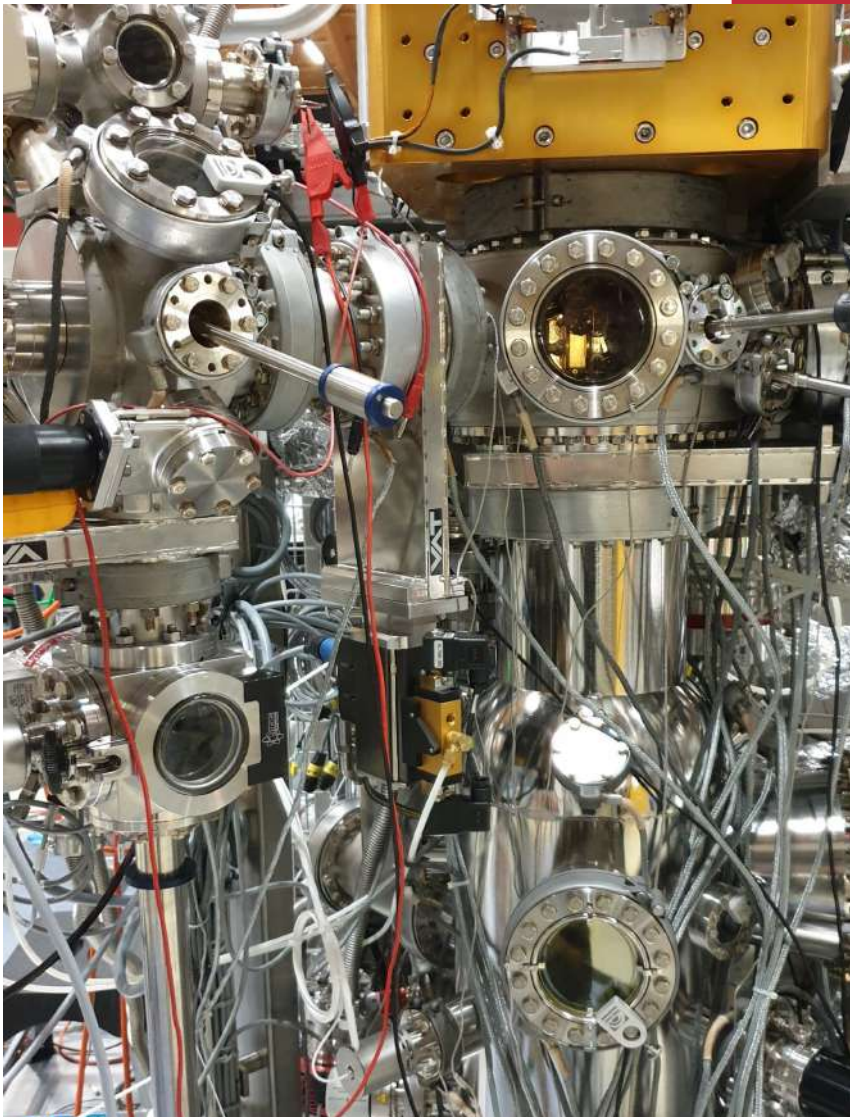
Substrate on the Electrical Properties of the $\text{LaAlO}_3/\text{SrTiO}_3$ Interface. *Phys. Rev. B* **2007**, *75*, No. 121404(R).

- (20) Gabel, J.; Zapf, M.; Scheiderer, P.; Schütz, P.; Dudy, L.; Stübinger, M.; Schlueter, C.; Lee, T. L.; Sing, M.; Claessen, R. Disentangling Specific Versus Generic Doping Mechanisms in Oxide Heterointerfaces. *Phys. Rev. B* **2017**, *95*, 195109.
- (21) Chikina, A.; Caputo, M.; Naamneh, M.; Christensen, D. V.; Schmitt, T.; Radovic, M.; Strocov, V. N. X-Ray Writing of Metallic Conductivity and Oxygen Vacancies at Silicon/ SrTiO_3 Interfaces. *Adv. Funct. Mater.* **2019**, *29*, 1900645.
- (22) Strocov, V. N.; Chikina, A.; Caputo, M.; Husanu, M. A.; Bisti, F.; Bracher, D.; Schmitt, T.; Granozio, F. M.; Vaz, C. A. F.; Lechermann, F. Electronic Phase Separation at $\text{LaAlO}_3/\text{SrTiO}_3$ Interfaces Tunable by Oxygen Deficiency. *Phys. Rev. Mater.* **2019**, *3*, 106001.
- (23) Walker, S. M.; Bruno, F. Y.; Wang, Z.; Torre, A.; Riccò, S.; Tamai, A.; Kim, T. K.; Hoesch, M.; Shi, M.; Bahramy, M. S.; King, P. D. C.; Baumberger, F. Carrier-Density Control of the SrTiO_3 (001) Surface 2D Electron Gas Studied by ARPES. *Adv. Mater.* **2015**, *27*, 3894–3899.
- (24) Schütz, P.; Christensen, D. V.; Borisov, V.; Pfaff, F.; Scheiderer, P.; Dudy, L.; Zapf, M.; Gabel, J.; Chen, Y. Z.; Pryds, N.; Rogalev, V. A.; Strocov, V. N.; Lee, T. L.; Jeschke, H. O.; Valentí, R.; Sing, M.; Claessen, R. Microscopic Origin of the Mobility Enhancement at A Spinel/Perovskite Oxide Heterointerface Revealed by Photoemission Spectroscopy. *Phys. Rev. B* **2017**, *96*, 161409.
- (25) Chen, Y. Z.; Pryds, N.; Kleibecker, J. E.; Sun, J. R.; Stamate, E.; Koster, G.; Shen, B. G.; Rijnders, G.; Linderth, S. Metallic and Insulating Interfaces of Amorphous SrTiO_3 -Based Oxide Heterostructures. *Nano Lett.* **2011**, *11*, 3774–3778.
- (26) Christensen, D. V.; Trier, F.; Soosten, M.; Prawiroatmodjo, G. E. D. K.; Jespersen, T. S.; Chen, Y. Z.; Pryds, N. Controlling Interfacial States in Amorphous/Crystalline $\text{LaAlO}_3/\text{SrTiO}_3$ Heterostructures by Electric Fields. *Appl. Phys. Lett.* **2013**, *102*, 021602.
- (27) Chen, Y. Z.; Pryds, N.; Sun, J. R.; Shen, B. G.; Linderth, S. High-Mobility Two-Dimensional Electron Gases at Oxide Interfaces: Origins and Opportunities. *Chin. Phys. B* **2013**, *22*, 116803.
- (28) Gabay, M.; Triscone, J. M. Oxide Heterostructures: Hund Rules with a Twist. *Nat. Phys.* **2013**, *9*, 610–611.
- (29) Delugas, P.; Filippetti, A.; Fiorentini, V.; Bilc, D. I.; Fontaine, D.; Ghosez, P. Spontaneous 2-Dimensional Carrier Confinement at the n-Type $\text{SrTiO}_3/\text{LaAlO}_3$ Interface. *Phys. Rev. Lett.* **2011**, *106*, 166807.
- (30) Son, W. J.; Cho, E.; Lee, B.; Lee, J.; Han, S. Density and Spatial Distribution of Charge Carriers in the Intrinsic n-Type $\text{LaAlO}_3/\text{SrTiO}_3$ Interface. *Phys. Rev. B* **2009**, *79*, 245411.
- (31) Berner, G.; Sing, M.; Guejwaara, H.; Yasui, A.; Saitoh, Y.; Yamasaki, A.; Nishitani, Y.; Sekiyama, A.; Pavlenko, N.; Kopp, T.; Richter, C.; Mannhart, J.; Suga, S.; Claessen, R. Direct k-Space Mapping of the Electronic Structure in an Oxide–Oxide Interface. *Phys. Rev. Lett.* **2013**, *110*, 247601.
- (32) Plumb, N. C.; Salluzzo, M.; Razzoli, E.; Månsson, M.; Falub, M.; Krempasky, J.; Matt, C. E.; Chang, J.; Schulte, M.; Braun, J.; Ebert, H.; Minár, J.; Delley, B.; Zhou, K. J.; Schmitt, T.; Shi, M.; Mesot, J.; Patthey, L.; Radović, M. Mixed Dimensionality of Confined Conducting Electrons in the Surface Region of SrTiO_3 . *Phys. Rev. Lett.* **2014**, *113*, 086801.
- (33) Santander-Syro, A. F.; Copie, O.; Kondo, T.; Fortuna, F.; Pailhès, S.; Weht, R.; Qiu, X. G.; Bertran, F.; Nicolou, A.; Taleb-Ibrahimi, A.; Fève, P.; Herranz, G.; Bibes, M.; Reyren, N.; Apertet, Y.; Lecoœur, P.; Barthélémy, A.; Rozenberg, M. *J. Nature* **2011**, *469*, 189–193.
- (34) Meevasana, W.; King, P. D. C.; He, R. H.; Mo, S. K.; Hashimoto, M.; Tamai, A.; Songsirithigul, P.; Baumberger, F.; Shen, Z. X. Creation and Control of a Two-Dimensional Electron Liquid at the Bare SrTiO_3 Surface. *Nat. Mater.* **2011**, *10*, 114–118.
- (35) Huijben, M.; Koster, G.; Kruize, M. K.; Wenderich, S.; Verbeeck, J.; Bals, S.; Slooten, E.; Shi, B.; Molegraaf, H. J. A.; Kleibecker, J. E.; van Aert, S.; Goedkoop, J. B.; Brinkman, A.; Blank, D. H. A.; Golden, M. S.; van Tendeloo, G.; Hilgenkamp, H.; Rijnders, G. Defect Engineering in Oxide Heterostructures by Enhanced Oxygen Surface Exchange. *Adv. Funct. Mater.* **2013**, *23*, S240–S248.
- (36) Xie, Y. W.; Bell, C.; Hikita, Y.; Harashima, S.; Hwang, H. Y. Enhancing Electron Mobility at the $\text{LaAlO}_3/\text{SrTiO}_3$ Interface by Surface Control. *Adv. Mater.* **2013**, *25*, 4735–4738.
- (37) Chen, Y. Z.; Bovet, N.; Trier, F.; Christensen, D. V.; Qu, F. M.; Andersen, N. H.; Kasama, T.; Zhang, W.; Giraud, R.; Dufouleur, J.; Jespersen, T. S.; Sun, J. R.; Smith, A.; Nygård, J.; Lu, L.; Büchner, B.; Shen, B. G.; Linderth, S.; Pryds, N. A High-Mobility Two-Dimensional Electron Gas at the Spinel/Perovskite Interface of $\gamma\text{-Al}_2\text{O}_3/\text{SrTiO}_3$. *Nat. Commun.* **2013**, *4*, 1371.
- (38) Chen, Y. Z.; Bovet, N.; Kasama, T.; Gao, W. W.; Yazdi, S.; Ma, C.; Pryds, N.; Linderth, S. Room Temperature Formation of High-Mobility Two-Dimensional Electron Gases at Crystalline Complex Oxide Interfaces. *Adv. Mater.* **2014**, *26*, 1462–1467.
- (39) Chen, Y. Z.; Trier, F.; Wijnands, T.; Green, R. J.; Gauquelin, N.; Egoavil, R.; Christensen, D. V.; Koster, G.; Huijben, M.; Bovet, N.; Macke, S.; He, F.; Sutarto, R.; Andersen, N. H.; Sulpizio, J. A.; Honig, M.; Prawiroatmodjo, G. E. D. K.; Jespersen, T. S.; Linderth, S.; Ilani, S.; Verbeeck, J.; Van Tendeloo, G.; Rijnders, G.; Sawatzky, G. A.; Pryds, N. Extreme Mobility Enhancement of Two-Dimensional Electron Gases at Oxide Interfaces by Charge-Transfer-Induced Modulation Doping. *Nat. Mater.* **2015**, *14*, 801–806.
- (40) Gan, Y. L.; Christensen, D. V.; Zhang, Y.; Zhang, H.; Krishnan, D.; Zhong, Z.; Niu, W.; Carrad, D. J.; Norrman, K.; Soosten, M.; Jespersen, T. S.; Shen, B. G.; Gauquelin, N.; Verbeeck, J.; Sun, J. R.; Pryds, N.; Chen, Y. Z. Diluted Oxide Interfaces with Tunable Ground States. *Adv. Mater.* **2019**, *31*, 1805970.
- (41) Chen, Y. Z.; Green, R. J.; Sutarto, R.; He, F.; Linderth, S.; Sawatzky, G. A.; Pryds, N. Tuning the Two-Dimensional Electron Liquid at Oxide Interfaces by Buffer-Layer-Engineered Redox Reactions. *Nano Lett.* **2017**, *17*, 7062–7066.
- (42) Chikina, A.; Christensen, D. V.; Borisov, V.; Husanu, M. A.; Chen, Y. Z.; Wang, X. Q.; Schmitt, T.; Radovic, M.; Nagaosa, N.; Mishchenko, A. S.; Valentí, R.; Pryds, N.; Strocov, V. N. Band-Order Anomaly at the $\gamma\text{-Al}_2\text{O}_3/\text{SrTiO}_3$ Interface Drives the Electron-Mobility Boost. *ACS Nano* **2021**, *15*, 4347–4356.
- (43) Cao, Y. W.; Liu, X. R.; Shafer, P.; Middey, S.; Meyers, D.; Kareev, M.; Zhong, Z. C.; Kim, J. W.; Ryan, P. J.; Arenholz, E.; Chakhalian, J. Anomalous Orbital Structure in a Spinel–Perovskite Interface. *npj. quantum materials* **2016**, *1*, 16009.
- (44) Cancellieri, C.; Mishchenko, A. S.; Aschauer, U.; Filippetti, A.; Faber, C.; Barišić, O. S.; Rogalev, V. A.; Schmitt, T.; Nagaosa, N.; Strocov, V. N. Polaronic Metal State at the $\text{LaAlO}_3/\text{SrTiO}_3$ Interface. *Nat. Commun.* **2016**, *7*, 10386.
- (45) Strocov, V. N.; Cancellieri, C.; Mishchenko, A. S. Electrons and Polarons at Oxide Interfaces Explored by Soft-X-Ray ARPES. *Spectroscopy of Complex Oxide Interfaces*, Springer **2018**, *266*, 107–151.
- (46) Strocov, V. N. Photoemission Response of 2D Electron States. *J. Electron Spectrosc. Relat. Phenom.* **2018**, *229*, 100–107.
- (47) Cancellieri, C.; Reinle-Schmitt, M. L.; Kobayashi, M.; Strocov, V. N.; Willmott, P. R.; Fontaine, D.; Ghosez, P.; Filippetti, A.; Delugas, P.; Fiorentini, V. Doping-Dependent Band Structure of $\text{LaAlO}_3/\text{SrTiO}_3$ Interfaces by Soft X-Ray Polarization-Controlled Resonant Angle-Resolved Photoemission. *Phys. Rev. B* **2014**, *89*, No. 121412(R).
- (48) Chambers, S. A.; Sushko, P. V. Influence of Crystalline Order and Defects on the Absolute Work Functions and Electron Affinities of TiO_2 - and SrO -Terminated n- SrTiO_3 (001). *Phys. Rev. Mater.* **2019**, *3*, 125803.
- (49) Strocov, V. N.; Wang, X.; Shi, M.; Kobayashi, M.; Krempasky, J.; Hess, C.; Schmitt, T.; Patthey, L. Soft-X-ray ARPES Facility at the ADDRESS Beamline of the SLS: Concepts, Technical Realisation and Scientific Applications. *J. Synchrotron Rad.* **2014**, *21*, 32–44.
- (50) Strocov, V. N.; Schmitt, T.; Flechsig, U.; Schmidt, T.; Imhof, A.; Chen, Q.; Raabe, J.; Betemts, R.; Zimoch, D.; Krempasky, J.; Wang, X.; Groni, M.; Piazzalunga, A.; Patthey, L. High-Resolution

Soft X-ray Beamline ADDRESS at the Swiss Light Source for Resonant Inelastic X-ray Scattering and Angle-Resolved Photoelectron Spectroscopies. *J. Synchrotron Rad.* **2010**, *17*, 631–643.

E. B. Guedes, T. W. Jensen, M. Naamneh, A. Chikina,
R. T. Dahm, *et al.*

Disclosing the response of the surface electronic structure in
 SrTiO_3 (001) to strain
JVST A **40**, 013213 (2022)



Angle-resolved photoemission spectroscopy setup at SIS, PSI

Disclosing the response of the surface electronic structure in SrTiO₃ (001) to strain

Cite as: J. Vac. Sci. Technol. A 40, 013213 (2022); doi: 10.1116/6.0001480

Submitted: 20 September 2021 · Accepted: 23 November 2021 ·

Published Online: 21 December 2021



Eduardo Bonini Guedes,¹ Tobias Willemoes Jensen,² Muntaser Naamneh,^{1,3} Alla Chikina,¹ Ramus T. Dahm,² Shinhee Yun,² Francesco M. Chiabrera,² Nicholas C. Plumb,¹ J. Hugo Dil,^{1,4} Ming Shi,¹ Dennis Valbjørn Christensen,² Walber Hugo Brito,⁵ Nini Pryds,² and Milan Radović¹

AFFILIATIONS

¹Photon Science Division, Paul Scherrer Institut, CH-5232 Villigen, Switzerland

²Department of Energy Conversion and Storage, Technical University of Denmark, Fysikvej, 2800 Kgs. Lyngby, Denmark

³Department of Physics, Ben-Gurion University of the Negev, Beer-Sheva 84105, Israel

⁴Institut de Physique, École Polytechnique Fédérale de Lausanne, CH-1015 Lausanne, Switzerland

⁵Departamento de Física, Universidade Federal de Minas Gerais, C.P. 702, 30123-970 Belo Horizonte, Minas Gerais, Brazil

Note: This paper is a part of the Special Collection Honoring Dr. Scott Chambers' 70th Birthday and His Leadership in the Science and Technology of Oxide Thin Films.

ABSTRACT

Combining angle-resolved photoemission spectroscopy and density functional theory calculations, we addressed the surface electronic structure of bent SrTiO₃ (STO) (001) wafers. Using a custom-made device, we observe that the low-dimensional states that emerge at the STO (001) surface are robust to an external tensile strain of about 0.1%. Our results show that this value of strain is too small to sensibly alter the surface conduction band of STO, but, surprisingly, it is enough to shift the energy of the in-gap states. In order to access higher strain values of around 2%, standard for STO-based heterostructures, we performed density functional theory calculations of STO slabs under different strain configurations. The simulations predict that such levels of both compressive and tensile strain significantly alter the orbital splitting of the surface conduction band. Our study indicates that the strain generated in STO can tailor the electronic properties of its bare surface and of STO-based interfaces.

Published under an exclusive license by the AVS. <https://doi.org/10.1116/6.0001480>

I. INTRODUCTION

Transition metal oxides (TMOs) exhibit a wide variety of exotic and very promising properties, such as high-temperature superconductivity,¹ colossal magnetoresistance,² wide-ranging magnetically ordered states,³ metal-insulator transitions (MITs),⁴ ferroelectricity,⁵ and multiferroicity.⁶ The interplay between the electronic and lattice degrees of freedom in the TMO compound, distinguished by a partially filled *d* orbital, opens a possibility to further tune the emerging physical properties. In addition, surfaces and interfaces present an additional playground⁷ where physical properties can be altered mostly due to heteroepitaxy and defects. Indeed, it was demonstrated that external pressure and epitaxial strain affect the physical properties of TMO, such as MIT⁸ or ferroelectricity.⁹ For instance, by combining thin film growth and angle-resolved photoemission (ARPES), it was shown that epitaxial

strain engineering affects the Fermi surface topology and many-body interactions in two-dimensional ruthenates.¹⁰

The low-dimensional electronic system (LDES) at the interface between SrTiO₃ (STO) and LaAlO₃ (LAO)¹¹ motivates extensive research to understand its origin and to develop methods for tuning physical parameters.¹² However, it is challenging to disentangle and study the impact of different effects (strain, charge transfer, polar discontinuity, defects, surface termination, etc.) on the physical properties at the usual LAO/STO interface individually. Favorably, the finding of the low-dimensional electronic state (LDES) on a surface of the STO wafer,^{13–15} grants us with an unadulterated playground for studying this marvel using very susceptible methods such as scanning tunneling spectroscopy (STM)¹⁶ and angle-resolved photoemission spectroscopy (ARPES).^{13–15,17}

A recent study reports that a relatively standard annealing temperature of 550 °C in an oxygen-rich atmosphere leads to a

Sr-rich surface,¹⁸ consequently favoring the formation of 2DEG at the surface, similar to findings related to SrO-terminated STO films.¹⁹ STO used as a substrate undergoes extreme annealing procedures during the film growth, which must also be considered. However, STO films grown on STO²⁰ or NdGaO₃ (110)²¹ show a tendency to end with Sr-rich surfaces. One of the important features of the LDES is a relatively large splitting between d_{xy} and d_{xz}/d_{yz} bands,^{15,18} suggesting that deviations from the cubic (or slightly tetragonal when at low temperatures) structure occurs at the surface region. The enhancement of the electron mobility of over 300% observed in La-doped STO films under uniaxial stress²² confirmed that the strain could be effectively used for altering the STO bulk properties. Furthermore, it was shown by ARPES measurements that *in situ* strain modifies the electronic structure of doped bulk 2D ruthenates.²³ Hence, altering the surface crystal structure can presumably tune the electronic properties of the LDES at the STO surface.

In this work, combining ARPES with DFT simulations, we investigated the response of the STO (001) surface electronic structure to an externally applied structural perturbation by mechanically bending the crystal.

II. METHODS AND MATERIALS

Commercially available STO (001) wafers (SurfaceNET GmbH) were mounted on a custom-made device, referred to as a bender, as shown in Fig. 1. The screw pushes a cylindrical part of the bender that subsequently induces strain on the substrate, as shown schematically in Figs. 1(a) and 1(d). The cylinder displacement is controlled by turning a screw with a conical tip, which serves as a wedge. By rotating the screw, the cylinder's displacement forces the STO wafer to bend, thereby creating strains in the sample.²² The actual profile of a bent 500 μm thick STO ($5 \times 10 \text{ mm}^2$) wafer was measured at different displacements with a Cyberscan Vantage optical profilometer. The resulting data, as shown in figure Fig. 1(b), are fitted to parabolas of the form $y = ax^2 + bx + c$, where $C = 2a$ is the maximum curvature. The profilometry data show that the STO wafer bends around its shorter symmetry axes. We have estimated a generated strain by multiplying curvatures (C) by half the thickness of the wafer $S = C \cdot t/2$.²² The produced strain vs displacement is presented in Fig. 1(c). The error bars are the standard deviations of the calculated strain across all lines in a single profilometry measurement.

Using the COMSOL Multiphysics® software²⁴, we calculated a generated strain for the bent slab of 500 μm STO with the edges fixed. We have assumed that displacements in the middle of the wafer form a straight line. With this assumption, COMSOL Multiphysics® was used to simulate the bending of the wafer, mimicking the one that occurs using the cylinder in the bender. The simulations generated intuitively expected results: the bent STO wafer is expanded in the long direction, i.e., in the sample plane perpendicular to the cylinder axis, which we assign as x-direction, while it is compressed in the direction perpendicular to the sample surface, assigned as x-direction. In contrast, along with the cylinder axis, identified as the sample y-direction, the sample is negligibly affected compared to the previous two directions. The calculated strains in all three directions are plotted in Fig. 1(c), as a function

of the displacements at the middle of the wafer, along with the strain estimated from the profilometry data. The 2D map of calculated strains for 30 μm displacement is shown in Figs. 1(e)–1(g).

The electronic band structures of two STO wafers strained with a progressive force have been investigated using ARPES at the SIS beamline of the Swiss Light Source. The same bender, previously characterized with profilometry measurements, was specially designed to serve also as a sample holder compatible with our ARPES setup. The bender device is designed based on a standard mushroom-like sample holder [see Fig. 1(d)] in such a way that the applied force can be adjusted *in situ* using a screwdriver installed on the wobble stick.

The experimental data were compared with the aid of DFT calculations performed within the Perdew–Burke–Ernzerhof generalized gradient approximation (GGA-PBE),²⁵ using projector augmented-wave (PAW) potentials,²⁶ as implemented in the Vienna *Ab initio* Simulation Package (VASP).^{27,28} In addition, we employed the DFT+U functional of Liechtenstein,²⁹ which takes into account the electronic interactions at a mean-field level by means of a partially screened Coulomb interaction $U = 5.0 \text{ eV}$ and $J = 0.64 \text{ eV}$. The structural optimizations were done until the forces on each atom were less than $0.01 \text{ eV}/\text{\AA}$. An energy cutoff of 500 eV was used for our plane-wave basis set. A k -mesh grid of $10 \times 10 \times 2$ was employed in the evaluation of the band structures.

III. RESULTS

The ARPES measurements were carried out on two differently treated 2 wt. % Nb-doped STO (001) wafers, both nominally TiO₂ terminated. In order to understand how natural adsorbents (arising from exposure to air) impact the 2DEG, the first sample was measured “as received” (without any additional treatment), serving as a reference to examine the bent STO crystal's electronic structure, and it is referred to as *nonannealed* (N-A). The second sample, referred as *annealed* (A), was annealed at 500 °C in 100 mbar of O₂ for 1 h to remove surface contamination and then *in situ* transferred to the ARPES instrument. The ARPES data were acquired at different bending levels, always with the synchrotron beam positioned at the center of the sample, mapping the electron structure of the conduction and the valence band at 20 K. The strain generated in STO samples was estimated as explained in the Methods section above.

At first exposure of the sample to synchrotron light of 85 eV, the ARPES spectrum shows no indication of states at the Fermi level (E_F). During the measurements, states with parabolic dispersion develop, showing the intensity increase and finally saturate. All the data shown in Figs. 2 and 3 were obtained at the saturated state.

The photo-induced 2DEG formed on the STO surface at this temperature exhibits a well-known band structure arising from the three orbitals with t_{2g} symmetry in the conduction band. Figure 2 shows the ARPES data obtained with 85 eV, circularly polarized light. Panels (a)–(f) display the data of the N-A sample, while panels (g)–(l) show the band structure of the A sample. Panels (b), (e), (h), and (k) show band dispersion maps of samples without any applied force, while panels (c), (f), (i), and (l) show the equivalent data of samples with maximum applied force (just before sample breaks). The maximum strain was estimated to be 0.1%.

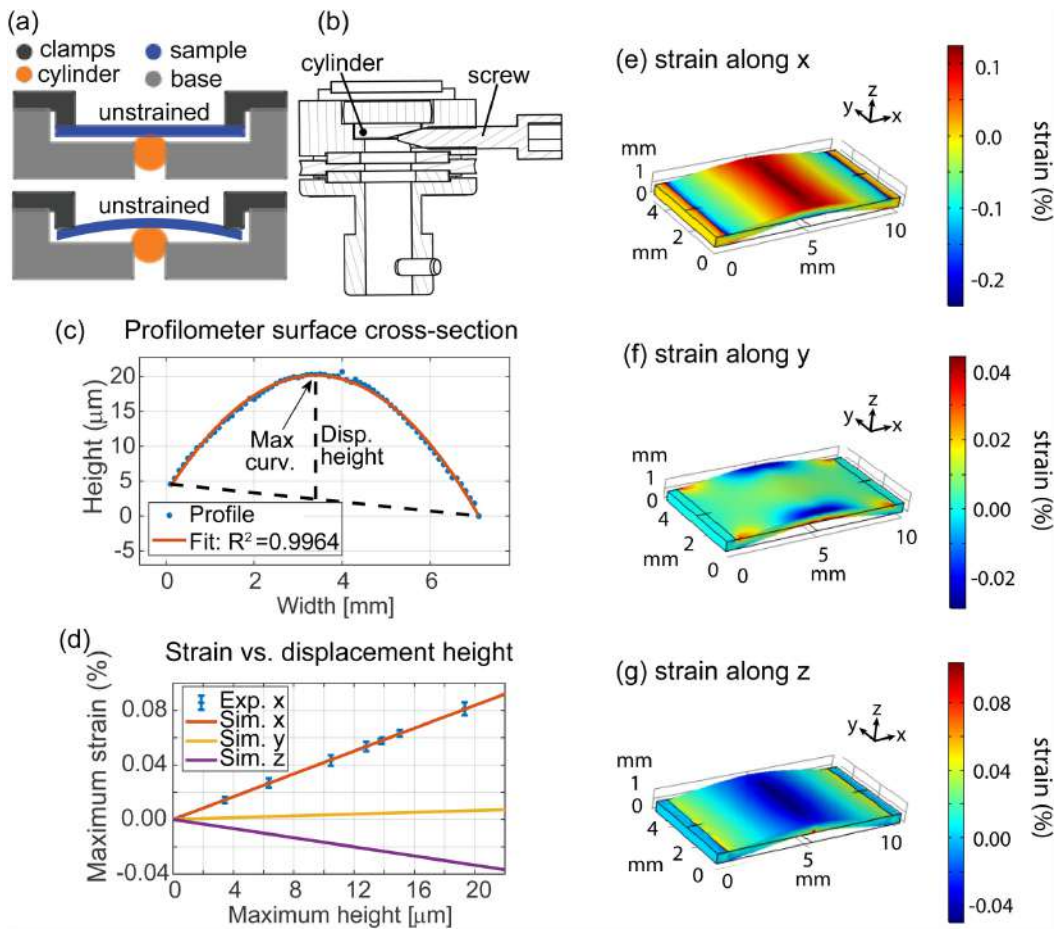


FIG. 1. (a) Schematic of the strain device, showing how a centered cylinder can force a sample to bend. (b) Cross section of a measured bend profile, fitted to a parabola, from which the curvature and strain can be calculated. (c) Experimental strain data along with the simulated strain in the center of the slabs shown in (e)–(g), as a function of displacement height. (d) Schematic of the strain device, where the cylinder from (a) is shown along with the screw which forces it up against the sample. (e)–(g) The x, y, and z strains, respectively, simulated in COMSOL Multiphysics[®], at 30 μm deflection.

The used photon energy was chosen such that it is possible to measure the band structure that corresponds to the bulk Γ point, while C+ polarization enables to capture the contributions from all orbitals of the t_{2g} manifold.¹⁵

Matrix element effects, i.e., modulations of the spectral intensity caused by the dependence of the ARPES data on photon energy and experimental geometry,³⁰ are known to greatly impact the observation of the 2DEG on STO.^{14,15,18} In particular, the bottom of the d_{yz} band and the outer d_{xy} band are easily seen around $\bar{\Gamma}_{00}$, while the bottom of the $d_{xy,xz}$ bands are very clear

around $\bar{\Gamma}_{10}$.¹⁵ Thus, the measurements were performed around both the $\bar{\Gamma}_{00}$ and $\bar{\Gamma}_{10}$ points, which allowed us to identify all the features in the spectra necessary for the reliable analysis of the data. The respective band dispersion maps in Fig. 2 were obtained along ΓX at $k_y = 0$, represented by the horizontal line in Fermi surface (FS) maps on Figs. 2(a), 2(d), 2(g), and 2(j).

The $d_{xz,yz}$ (out-of-plane) orbitals form heavy bands (along either k_x or k_y) with a mixed 2D/3D character, while a light band with 2D character arises from the in-plane d_{xy} orbital.¹⁵ The d_{xy} -, d_{xz} -, and d_{yz} -derived bands remain degenerate for the N-A sample,

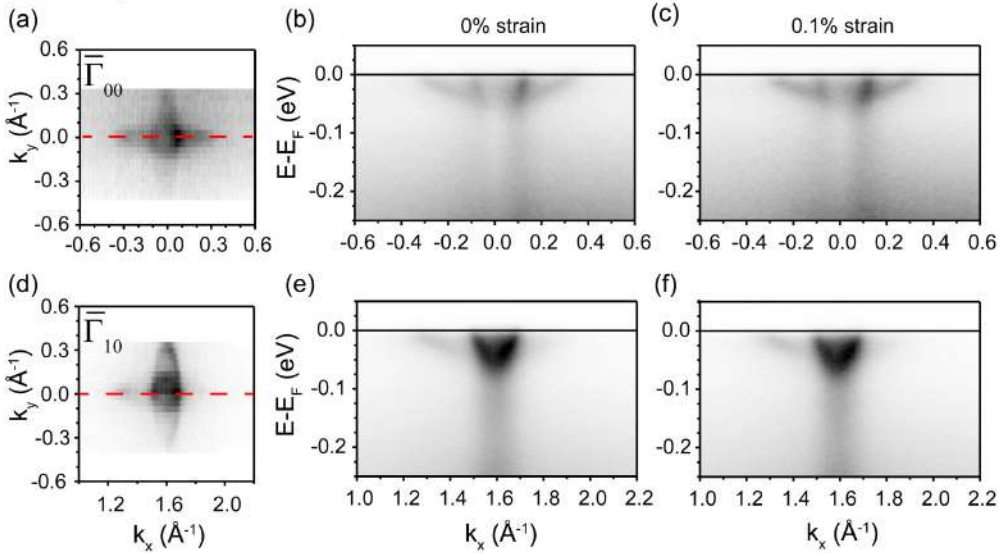
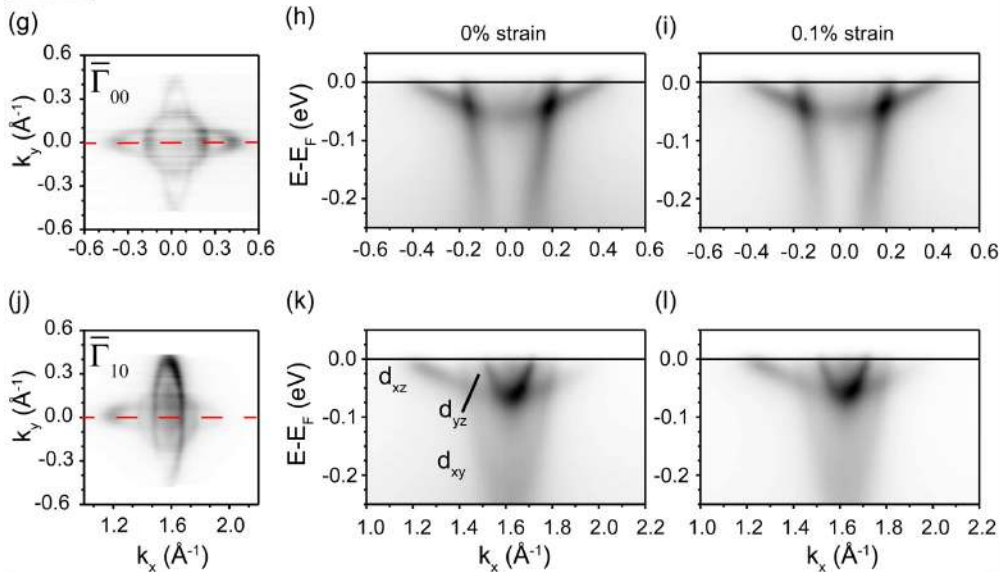
STO N-A**STO A**

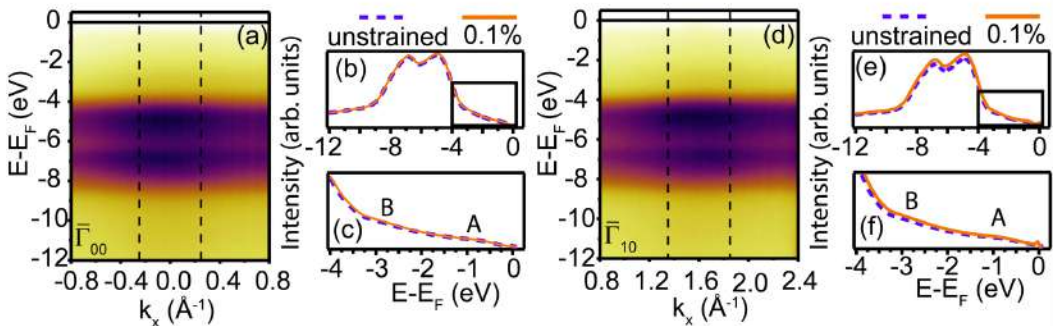
FIG. 2. ARPES data of the nonannealed (N-A) and annealed (A) STO (001) samples collected around the $\bar{\Gamma}_{00}$ and $\bar{\Gamma}_{01}$ points along the ΓX direction. Fermi surfaces (FSs) of N-A sample (a) and (d) and A sample (g) and (j). The conduction bands corresponding to the band dispersion map along the red line in the Fermi surfaces for both no strained, N-A sample (b) and (e), and A sample (h) and (k). The same maps for strained N-A (c) and (f) and A samples (i) and (l).

resembling the bulk conduction band, while, for the A sample, the bottom of the d_{xy} band shifts around 180 meV to lower binding energies. This increases the separation between the light and heavy bands, indicating a change in the surface structure.¹⁸ The light band was previously observed to further split into lower and upper branches with opposite spin winding,³¹ although the two branches are not well resolved using $h\nu = 85$ eV.²⁰ The very distinct band structure found in the N-A and A samples indicate that the adsorbents passivate the surface and prevent the formation of the 2DEG, whereas it can be fully developed at the clean surface. Careful analysis of the Fermi wave vector k_F and of the splitting value between d_{xy} and d_{yz} bands can only confirm that no change in the conduction band is observed within the experimental resolution (around 10 meV) for either the N-A or the A samples upon bending. This finding suggests that the maximum strain generated by our bender ($\approx 0.1\%$) is too small to distinctly alter the conduction band of STO.

Along with the conduction band, the valence band has also been examined. Figures 3(a), 3(d), 3(g), and 3(j) display the valence band, measured along the X Γ X high-symmetry direction, of both N-A and a samples, around $\bar{\Gamma}_{00}$ and $\bar{\Gamma}_{10}$. The energy distribution curves (EDCs) in Figs. 3(b), 3(c), 3(e), 3(f), 3(h), 3(i), 3(k), and 3(l) were integrated and indicated by dashed lines in panels (a), (d), (g), and (j).

First, we observe that annealing causes a noticeable spectral weight redistribution from the peak at -5 to the one at -7 eV. Somewhat surprisingly, already at a low applied strain of about 0.1%, the in-gap states undergo noticeable spectroscopic changes, even though the surface conduction band is stable as seen in Fig. 2. While the N-A sample is essentially unaffected, the A sample shows a broadening of the O 2p band and a further increase in the intensity of the peak at -7 eV. Zooming in the in-gap state's region, spanning from the onset of the valence band to E_F (represented by the black rectangles), exposes additional changes. While

STO N-A



STO A

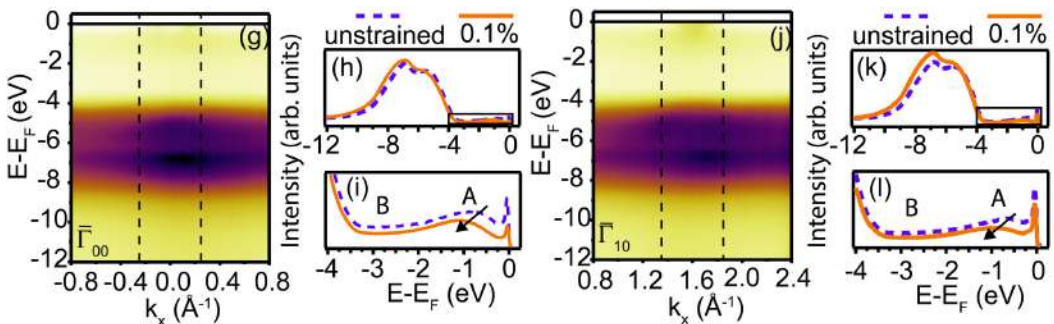


FIG. 3. Valence bands of the 0.1% strained nonannealed (N-A, top row) and the annealed (A, bottom row) samples around the $\bar{\Gamma}_{00}$ - (a) and (g) and $\bar{\Gamma}_{10}$ -points (d) and (j). The measured valence bands correspond to the cut indicated by the line in the Fermi surfaces presented in Fig. 2 for both strained, N-A, and A samples. The energy distribution cuts (EDCs) in panels (b), (e), (h), and (k) are integrated within the region indicated by dotted lines. Panels (c), (f), (i), and (l) display zoom of the EDC, which enhances the region of in-gap states, which is indicated by the dotted box on the EDCs.

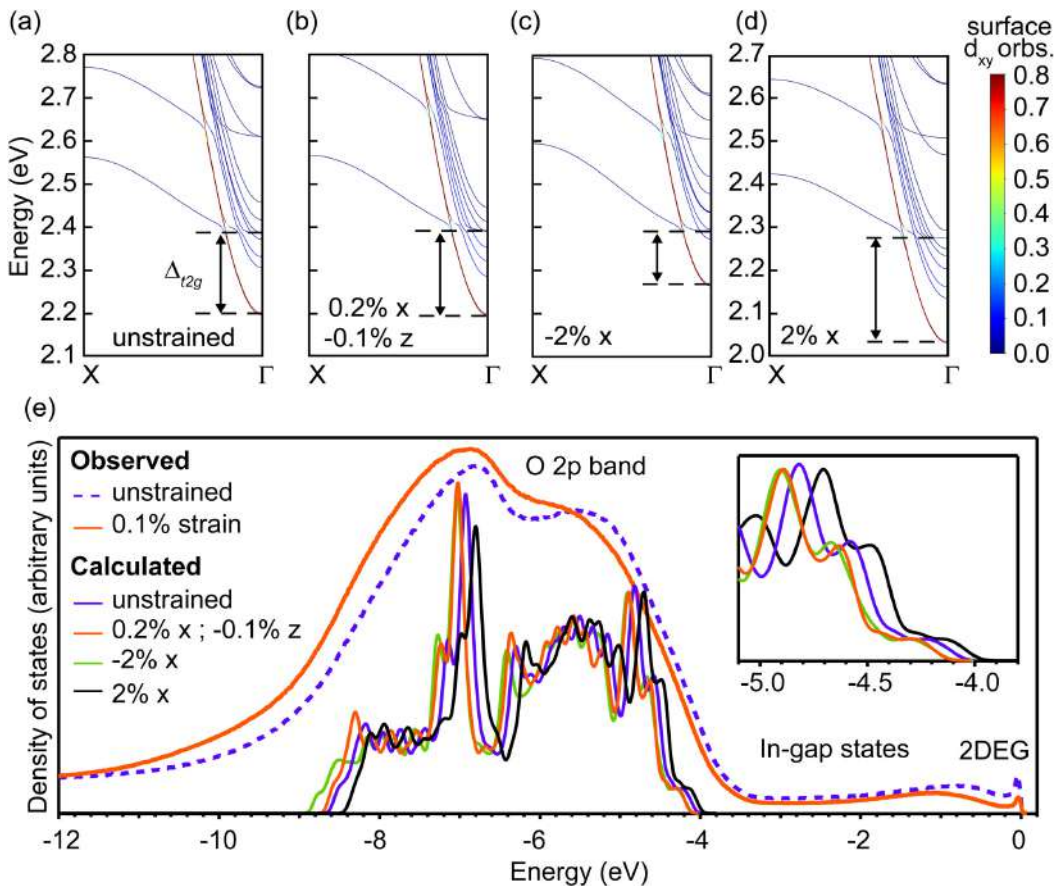


FIG. 4. Calculated band structures of the STO slab with and without strain. The color map indicates the contribution from Ti-3d_{xy} states of atoms within the TiO₂ layer just below the SrO surface termination. (a) 0% strain, (b) 0.2% strain along x and -0.1% strain along z, (c) -2% strain along x, and (d) 2% strain along x. Panel (e) shows a comparison between the measured valence bands and the ones calculated for the same strain configurations as in (a)–(d).

the in-gap state (IGS) of the N-A sample clearly shows two local maxima around 1 and 2.8 eV, the A sample shows spectral weight only around 1 eV. With applied strain, the IGSs shift to higher binding energies and lose intensity.

The IGSs have been associated with the existence of a variety of point defects in the crystal,^{32–35} which give rise to localized electronic states such as in doped semiconductors or, more intricately, induce the formation of small polarons, quasiparticles arising due to strong, short-range electron-phonon interaction, which show a typical binding energy of 1 eV.^{36–39} Temperature-dependent ARPES data show that the high-binding energy IGS (peak B indicated by arrows around -2.8 eV in the zoom panels) is robust

under the irradiation and temperature cycling during photoemission experiments, while the peak at lower binding energies (peak A indicated by arrows on the zoom panels, around 1 eV) underwent an energy shift and yet vanished with increasing temperature.¹⁸ Because of their distinct temperature evolution, the IGSs A were associated with the formation of small polarons while the IGSs B to simple defects. Accordingly, the energy shift and intensity depletion of peak A for strained STO can be attributed to a mutation in the crystal lattice of the surface region, which might influence the interplay between the conduction electrons and the lattice.

In order to conjecture and examine how strain alters the conduction band and controls the electronic properties of the STO

TABLE I. Calculated splitting between d_{xy} and d_{yz} bands (Δ_{t2g}) under different strain configurations.

x (%)	z (%)	Δ_{t2g} (eV)
0	0	0.188
-2	0	0.124
2	0	0.244
0	-2	0.244
0	2	0.138
0.2	-0.1	0.195
2	-2	0.281
2	2	0.179
x (%)	y (%)	Δ_{t2g} (eV)
2	2	0.117
-2	-2	0.248

surface, we performed density functional theory (DFT) simulations of STO slabs under distinct strain configurations defined by a $-a_0/a_0$, where a_0 is the bulk lattice parameter, as shown in Fig. 4. Our previous study reveals that only the SrO-terminated slab band structure is distinguished with the surface state with d_{xy} character, which is significantly lower than d_{xz} and d_{yz} bands.¹⁸ Therefore, we also used the SrO-terminated slab as the model system and focussed on the surface band structure response to various strains. Also, for simplicity, we did not include oxygen vacancies or other possible defects in our calculations. We have calculated the band structure applying different strain values up to 2%, which is reasonable since this value befalls in the range of those found at interfaces between STO and other oxides (LAO, for instance).

The calculations indicate that the energy splitting between the Ti $3d_{xy}$ and Ti $3d_{yz}$ states (Δ_{t2g}) can be efficiently ruled by a complex interplay between applied strain along x- (in-plane) and z-directions (out-of-plane). As shown in Table I and in Fig. 4(a), for no applied strain, a Δ_{t2g} of 188 meV is generated by the intrinsic surface relaxation of a SrO-terminated slab, which is in good agreement with the experimentally observed splitting (see Fig. 2) for the A sample. We denote tensile (compressive) strain with positive (negative) values.

According to the results in Table I, uniaxial tensile strain up to 2% along the x-direction, as shown in Table I and Fig. 4(c), causes Δ_{t2g} to monotonically increase up to 0.244 eV. In turn, for the same values of compressive strain, Δ_{t2g} is monotonically reduced to 0.124 eV [Fig. 4(d)]. The situation is reversed in the case of uniaxial strain along the z-direction, as shown in Table I, for which tensile strain decreases Δ_{t2g} down to 0.138 eV, while compressive strain enhances it up to 0.244 eV. Interestingly, applying 2% in the x-direction has the same effect of applying -2% along the z-direction, which evidences the strong role of intrinsic (out-of-plane) relaxation of the slab surface. Finally, applying tensile strain of 2% in both x- and z- directions leads to a small reduction of Δ_{t2g} to 0.179 eV, while reversing the sign of the strain along the z-direction dramatically increases the splitting to 0.281 eV.

The sample with the maximum applied strain can be represented by the calculation with 0.2% along the x-direction and

-0.1% along the z-direction, which shows a slightly increased Δ_{t2g} of 0.195 eV. The conduction band of such a slab is displayed in Fig. 4(b). From the theoretically obtained band structure, a strain level of 0.2% increases the splitting in less than 7 meV, consistent with the results from Fig. 2. Increasing the strain levels to 2% x and -1% results in a Δ_{t2g} of 0.256 eV, while inverting the direction of the strain along z leads to a Δ_{t2g} of 0.201 eV. Finally, we have also calculated structures with applied biaxial in-plane strain, since this configuration is more easily achieved with the growth of heterostructures. A tensile strain of 2% reduces the splitting to 0.117 eV, while the same value of compressive strain increases it to 0.248 eV.

Furthermore, in Fig. 4(e), we study the changes caused by strain in the VB comparing the measured one of the A sample with the calculated density of states (DOS) from the simulations shown in (a)-(d). The calculated valence bands are aligned by their vacuum levels and were rigidly shifted by -4 eV to match the experimental spectra. For simplicity, the calculated conduction band is not shown, since it would appear below the experimental E_F due to the well-known underestimation of the bandgap in calculations using GGA functionals.

The calculated VB is mostly composed of O 2p states. The results reveal that the valence band responds sensibly even to a small strain of 0.2% along the x-direction and -0.1% along the z-direction, overall shifting to higher binding energies. The inset shows the VB leading edge, for which a shift of -0.06 eV is seen. The main panel shows that the peak around -7 eV shifts by -0.09 eV, and the tail of the VB becomes more intense and move by -0.12 eV. These changes with small applied strain are in agreement with the measured VB. For comparison, we also plot the corresponding VB of the structures calculated in Figs. 4(c) and 4(d).

IV. CONCLUSION

By combining the DFT calculation and ARPES, we examined the consequence of the application of strain (uniaxial and biaxial) on the electronic structure of the STO (001) surface. We used a custom-made device to bend and, consequently, generate a strain of around 0.1% on an STO wafer before it cracks. While this level of in-plane tensile strain shows no influence on the electronic structure of the low-dimensional states, it is enough to sensibly alter the in-gap states. Nevertheless, our extensive calculations predict that either compressive or tensile strain levels around 2%, such as the ones achieved with the growth of heterostructures¹¹ and flexible membranes,⁴⁰ induce sizable changes in the 2DEG.

Moreover, by showing that in-gap states are tunable with strain, while band structure modifications require heteroepitaxial growth, our findings offer practical guideposts for engineering the optical properties of STO via the application of strain.

AUTHORS CONTRIBUTIONS

E.B.G. and T.W.J. contributed equally to this work.

ACKNOWLEDGMENTS

M.R. and E.B.G. acknowledge the support of SNF Project No. 200021_182695. E.B.G. was partially supported by the Sino-Swiss Science and Technology Cooperation grant No. IZLCZ2_170075.

M.N. received support from the Swiss National Science Foundation grant no. 200021_59678 and from the European Union's Horizon 2020 research and innovation programme under the Marie Skłodowska-Curie grant agreement no. 701647. N.P. and D.V.C. acknowledge the funding from Villum Fonden for the NEED project (00027993) and Danish Council for Independent Research Technology and Production Sciences for the DFF- Research Project 3 (Grant No. 00069B). W.H.B. acknowledges the Pró-Reitoria de Pesquisa of Universidade Federal de Minas Gerais, and the National Laboratory for Scientific Computing (LNCC/MCTI, Brazil) for providing HPC resources of the SDumont supercomputer, which have contributed to the research results, URL: <http://sdumont.lncc.br>.

DATA AVAILABILITY

The data that support the findings of this study are available from the corresponding author upon reasonable request.

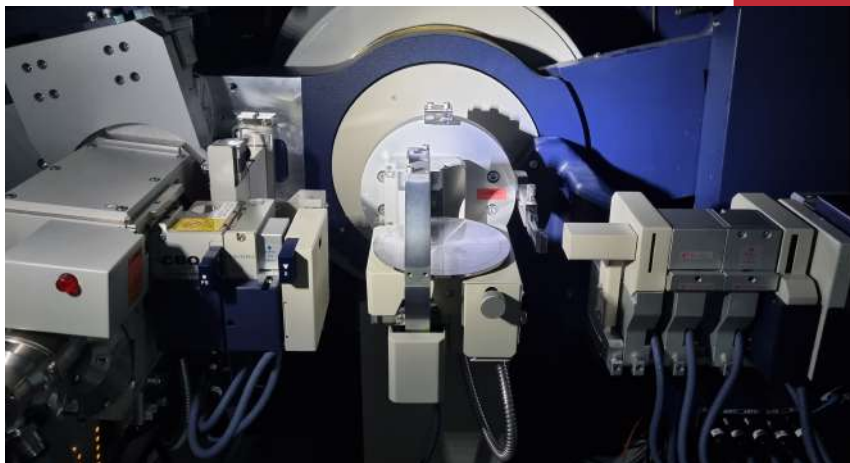
REFERENCES

- ¹J. G. Bednorz and K. A. Müller, *Z. Phys. B: Condens. Matter* **64**, 189 (1986).
- ²R. von Helmolt, J. Wecker, B. Holzapfel, L. Schultz, and K. Samwer, *Phys. Rev. Lett.* **71**, 2331 (1993).
- ³H. Fujishiro, T. Fukase, and M. Ikebe, *J. Phys. Soc. Jpn.* **67**, 2582 (1998).
- ⁴F. J. Morin, *Phys. Rev. Lett.* **3**, 34 (1959).
- ⁵B. H. Park, B. S. Kang, S. D. Bu, T. W. Noh, J. Lee, and W. Jo, *Nature* **401**, 682 (1999).
- ⁶C. Lu, W. Hu, Y. Tian, and T. Wu, *Appl. Phys. Rev.* **2**, 021304 (2015).
- ⁷S. R. Spurgeon, P. V. Sushko, S. A. Chambers, and R. B. Comes, *Phys. Rev. Mater.* **1**, 063401 (2017).
- ⁸M. Imada, A. Fujimori, and Y. Tokura, *Rev. Mod. Phys.* **70**, 1039 (1998).
- ⁹D. G. Schlom, L.-Q. Chen, C.-B. Eom, K. M. Rabe, S. K. Streiffer, and J.-M. Triscone, *Ann. Rev. Mater. Res.* **37**, 589 (2007).
- ¹⁰B. Burganov *et al.*, *Phys. Rev. Lett.* **116**, 197003 (2016).
- ¹¹A. Ohtomo and H. Hwang, *Nature* **427**, 423 (2004).
- ¹²T. C. Kaspar, P. V. Sushko, S. R. Spurgeon, M. E. Bowden, D. J. Keavney, R. B. Comes, S. Saremi, L. Martin, and S. A. Chambers, *Adv. Mater. Interfaces* **6**, 1801428 (2019).
- ¹³A. F. Santander-Syro *et al.*, *Nature* **469**, 189 (2011).
- ¹⁴W. Meevasana, P. D. C. King, R. H. He, S.-K. Mo, M. Hashimoto, A. Tamai, P. Songsiririthigul, F. Baumberger, and Z.-X. Shen, *Nat. Mater.* **10**, 114 (2011).
- ¹⁵N. C. Plumb *et al.*, *Phys. Rev. Lett.* **113**, 086801 (2014).
- ¹⁶R. Di Capua *et al.*, *Phys. Rev. B* **86**, 155425 (2012).
- ¹⁷P. D. C. King *et al.*, *Nat. Commun.* **5**, 3414 (2014).
- ¹⁸E. B. Guedes, S. Muff, W. H. Brito, M. Caputo, H. Li, N. C. Plumb, J. H. Dil, and M. Radović, *Adv. Sci.* **8**, 2100602 (2021).
- ¹⁹S. N. Rebec, T. Jia, H. M. Sohail, M. Hashimoto, D. Lu, Z.-X. Shen, and R. G. Moore, *Proc. Natl. Acad. Sci. U.S.A.* **116**, 16687 (2019).
- ²⁰E. B. Guedes, S. Muff, M. Fanciulli, A. P. Weber, M. Caputo, Z. Wang, N. C. Plumb, M. Radović, and J. H. Dil, *Phys. Rev. Res.* **2**, 033173 (2020).
- ²¹M. Radović, N. Lampis, F. M. Granozio, P. Perna, Z. Ristic, M. Salluzzo, C. M. Schlepütz, and U. Scotti di Uccio, *Appl. Phys. Lett.* **94**, 022901 (2009).
- ²²B. Jalan, S. J. Allen, G. E. Beltz, P. Moetakef, and S. Stemmer, *Appl. Phys. Lett.* **98**, 132102 (2011).
- ²³S. Riccò *et al.*, *Nat. Commun.* **9**, 4535 (2018).
- ²⁴"COMSOL multiphysics® v. 5.6.," COMSOL AB, Stockholm, Sweden, 2020.
- ²⁵J. P. Perdew, K. Burke, and M. Ernzerhof, *Phys. Rev. Lett.* **77**, 3865 (1996).
- ²⁶P. E. Blüchl, *Phys. Rev. B* **50**, 17953 (1994).
- ²⁷G. Kresse and J. Furthmüller, *Comput. Mater. Sci.* **6**, 15 (1996).
- ²⁸G. Kresse and J. Furthmüller, *Phys. Rev. B* **54**, 11169 (1996).
- ²⁹A. I. Liechtenstein, V. I. Anisimov, and J. Zaanen, *Phys. Rev. B* **52**, R5467 (1995).
- ³⁰A. Damascelli, Z. Hussain, and Z.-X. Shen, *Rev. Mod. Phys.* **75**, 473 (2003).
- ³¹A. F. Santander-Syro, F. Fortuna, C. Bareille, T. C. Rödel, G. Landolt, N. C. Plumb, J. Dil, and M. Radović, *Nat. Mater.* **13**, 1085 (2014).
- ³²M. Choi, F. Oba, and I. Tanaka, *Phys. Rev. Lett.* **103**, 185502 (2009).
- ³³Y. S. Kim, J. Kim, S. J. Moon, W. S. Choi, Y. J. Chang, J.-G. Yoon, J. Yu, J.-S. Chung, and T. W. Noh, *Appl. Phys. Lett.* **94**, 202906 (2009).
- ³⁴S. A. Chambers *et al.*, *Phys. Rev. B* **97**, 245204 (2018).
- ³⁵A. Al-Zubi, G. Bihlmayer, and S. Blügel, *Crystals* **9**, 580 (2019).
- ³⁶A. Fujimori, A. Bocquet, K. Morikawa, K. Kobayashi, T. Saitoh, Y. Tokura, I. Hase, and M. Onoda, *J. Phys. Chem. Solids* **57**, 1379 (1996).
- ³⁷H. O. Jeschke, J. Shen, and R. Valentí, *New J. Phys.* **17**, 023034 (2015).
- ³⁸A. Janotti, J. B. Varley, M. Choi, and C. G. Van de Walle, *Phys. Rev. B* **90**, 085202 (2014).
- ³⁹X. Hao, Z. Wang, M. Schmid, U. Diebold, and C. Franchini, *Phys. Rev. B* **91**, 085204 (2015).
- ⁴⁰R. Xu *et al.*, *Nat. Commun.* **11**, 3141 (2020).

D.-S. Park, A. D. Rata, **R. T. Dahm**, *et al.*

Controlled Electronic and Magnetic Landscape in Self-Assembled
Complex Oxide HeterostructuresSelf-Assembled
Complex Oxide Heterostructures

Submitted for *ADV. Materials*



Rigaku X-ray diffractometer

Main Manuscript for

Self-Assembled Complex Oxide Heterostructures: A playground for electronic and magnetic phenomena

D.-S. Park^{1,2*}, A. D. Rata³, R. T. Dahm⁴, K. Chu¹, Y. L. Gan⁵, I. V. Maznichenko³, S. Ostanin³, F. Trier⁴, H. Baek⁶, W. S. Choi⁷, C.-J. Choi⁸, Y. H. Kim⁹, G. J. Rees¹⁰, H. P. Gíslason¹¹, P. Buczek¹², I. Mertig³, M. A. Ionescu², A. Ernst¹³, K. Dörr³, P. Murali¹, N. Pryds⁴

1. Institute of Materials, Swiss Federal Institute of Technology–EPFL, 1015 Lausanne, Switzerland.
2. Institute of Electrical and Micro Engineering, Swiss Federal Institute of Technology–EPFL, 1015 Lausanne, Switzerland.
3. Institut für Physik, Martin-Luther-Universität Halle-Wittenberg, 06120 Halle, Germany.
4. Department of Energy Conversion and Storage, Technical University of Denmark, DK-2800 Kgs Lyngby, Denmark.
5. Institute of Physics, Chinese Academy of Sciences, 100190 Beijing, P. R. China.
6. Korea Basic Science Institute, 02841 Seoul, Republic of Korea.
7. Department of Physics, Sungkyunkwan University, 16419 Suwon, Republic of Korea.
8. School of Semiconductor and Chemical Engineering, Chonbuk National University, 54596 Jeonju, Republic of Korea.
9. Chungnam National University, 34134 Daejeon, Republic of Korea.
10. Department of Materials, University of Oxford, OX1 3PH Oxford, UK.
11. Science institute, University of Iceland, IS-104 Reykjavik, Iceland.
12. Department of Engineering and Computer Sciences, Hamburg University of Applied Sciences, D-20099 Hamburg, Germany.
13. Max-Planck-Institut für Mikrostrukturphysik 06120 Halle, Germany.

Email: dspark1980@gmail.com

Author Contributions: D.-S.P. conceived research idea and managed the entire project. D.-S.P. performed material synthesis and thin film growth for this project with support of K.D., W. S.C., P.M., M.A.I. and N.P. D.-S.P. and A.D.R. collected and analyzed XRD and magnetic data. D.-S.P. and H.P.G. acquired and analyzed PL data. H. B., Y.-H.K., C.-J.C. and K.C. measured samples in TEM and analyzed data. G.J.R. acquired and evaluated the NMR data. I.V.M, S.O., P.B., I.M. and A.E. carried out and analysed the DFT calculations. Y.G., D.-S.P., R.T.D., F.T. and N.P. carried out electrical measurements and analyzed the collected data. All authors discussed the results and interpretations. D.-S.P. and N.P. wrote the manuscript.

Competing Interest Statement: Authors declare no competing interests.

Classification: Applied Physical Science

Keywords: Functional oxides, thin film growth, self-assembly, 2DEGs, magnetism.

This PDF file includes:

Main Text
Figures 1 to 5
References 1 to 44

Abstract

Complex oxide heterointerfaces contain a rich playground of novel physical properties and functionalities, giving rise to emerging technologies. The electronic states at the interface include strongly correlated interactions, governed by distortions of crystal symmetry, lattice strains, electronic reconstruction, and defect orders. Here, we demonstrate that self-assembly approach from 2D to 3D growth mode provides electronic and magnetic landscape in the same heterostructure. An initial two-dimensional (2D) layer-by-layer growth on SrTiO₃(001) yields atomically abrupt interfaces where vertically aligned magnetic (3D) structures are subsequently formed in the LaAlO₃(1-x):LaBO₃(x) (LABO)/SrTiO₃ heterostructures. The transient structural assembly is primarily driven by the composition ratio, leading to the coexistence of low-dimensional electron gas and anisotropic magnetic ordering. The origin of the confined electron gas and magnetism in the multi-dimensional heterostructure was theoretically understood. Our work paves the way for designing oxide nanocomposite heterostructures with multifunctional phenomena via a self-assembly approach.

Significance Statement

Vertically aligned nanostructure (VAN) films using a self-assembling bottom-up deposition method present great promise in terms of structural flexibility and property tunability. In this work, we have extended the bottom-up self-assembly to a new approach using a mixture of matrix containing a 2D layer-by-layer growth mode, followed by a 3D growth mode of vertically aligned two-phase nanocomposite oxides. Here, the two-phase nanocomposite thin films are based on LaAlO₃:LaBO₃, grown on lattice-mismatched SrTiO₃. The transition in the growth mode from 2D to 3D is characterized with unique strain orderings, which are strongly coupled with the observed multiple properties, 2D electron gas and magnetic anisotropy. This approach provides unique film heterostructures which enrich emergent phenomena in a single film for multifunctional applications.

Main Text

Introduction

Over the last three decades, the rapid and continued development of thin film growth technologies of strongly correlated complex oxides (e.g., those composed of transition metals with the variable occupancy of *d*-/*f*-band electrons and/or with orbital orderings) provide rich and emerging

functionalities such as high-mobility two-dimensional electron gases (2DEGs) (1), ionic conduction (2), topological states (3), ferroelectricity (4), ferromagnetism with high Curie temperatures (5), and multiferroicity (4,6,7). These functionalities represent properties different from their bulk counterparts. The prototypical heterostructure, $\text{LaAlO}_3(\text{LAO})/\text{SrTiO}_3(\text{STO})$, is an excellent example which exhibits a wealth of intriguing properties at the interface such as low-temperature superconductivity (below ~ 200 mK) and unconventional magnetism (8,9). The low-dimensional conduction stems from the confined charge carriers at the polar/non-polar complex oxide interface and appears when ≥ 4 unit cells (UCs) of LAO are grown on singly terminated TiO_2 -STO substrates (10). Despite the continuous debate to the underlying mechanism on the enhanced electron mobility at the interfaces, these interfaces turn out to be a central way to realize high electron mobility ($\mu \approx 1000 - 10,000 \text{ cm}^2\cdot\text{V}^{-1}\cdot\text{s}^{-1}$ at 2 K). It is widely believed that realizing interfaces with high mobility requires delicate growth control to achieve the interfacial electron and/or orbital reconstruction, control of oxygen vacancy content, cation stoichiometry, and sufficiency of charge carrier sources (11-14). The electronic and magnetic interactions at the 2DEGs have been exploited via electrical gating (15,16), inserting δ -doping layers (17), and assembly of magnetic and ferroelectric layers (18,19) to trigger tunable functionalities for nanoscale electronic applications such as spin valves and non-volatile electrical switching devices.

Another approach for controlling the functional properties of complex oxide heterostructures is to utilize self-assembled three-dimensional (3D) vertical arrays of heterointerfaces by composing largely mismatched oxides under strain-mediated and/or thermodynamically equilibrium film growth modes (20,21). The main advantages of this approach are (i) a self-assembly of vertical interfaces of two/more phase materials and (ii) circumventing the length-scale and number limits of conventional planar epitaxial thin film heterointerfaces (e.g. superlattice-type heterostructures) for mesoscale-film materials. Thus, it can enrich the interfacial effects in terms of lattice strain, defect, charge, and spin. The main difference between the horizontal and vertical interfaces is their different stress configuration. The horizontal interfaces have often zero vertical stress, whereas in the plane the misfit stress is in general non-zero (22). In a layered structure, the elastic energy increases with increasing the number of monolayers, leading to the formation of misfit dislocations and the following stress reduction along the film. In contrast, the strain at the vertical interfaces is often accomplished by embedding a secondary oxide phase into the host matrix. Vertically aligned interfaces have shown fascinating multifunctional properties such as high ionic conductivity (23), extraordinary ferroelectric orderings (24), and magnetic anisotropy (25). For example, high ionic conduction is preferentially formed near or at the vertical interfaces due to the formation of charged cation/anion point defects, e.g. oxygen vacancies at these interfaces (21). Despite a large diversity of the functional properties, the formation of self-assembled vertical interfaces is still relied on the 3D growth mode of vertically aligned nanostructures which significantly limits the long-range electronic interactions due to the lack of long-range atomic precision between the two phases and the detrimental distribution of structural/atomic defects. In self-assembly approach, a mixture of matrix containing a 2D layer-by-layer growth mode for horizontal interface and a 3D growth mode for vertical interface is still not realized yet. Achieving this can lead to the coexistence of multiple properties in two different orientations.

In this work, we demonstrate a new design of self-assembly multi-dimensional growth of 2D and 3D complex oxide nanocomposite thin films. The nanocomposite films are formed via a selection of two distinct oxide materials, rhombohedral LaAlO_3 [$\text{LAO}(1-x)$] and orthorhombic LaBO_3 [$\text{LBO}(x)$], outlined in Fig. 1a. The composition of LAO:LBO (hereafter is referred to as LABO) is varied over the range of LBO composition, $x = 0 - 10$ %. Our results show a structural transition from a 2D

(LAO/STO) layered film to a 3D (LAO/LBO) vertical aligned nanopillar, which takes place at the composition above $x = 8\%$. The formation of these two distinct orientations of interfaces (horizontal and vertical interfaces) is achieved via a composition-assistant transition which is complementary with strain matching. This gives rise to simultaneous multiple properties such as 2DEG and magnetic anisotropy in the multi-dimensional nanocomposite heterostructure.

Results

Structural Evolution of Epitaxial LABO Nanocomposite Films on STO.

LABO composite thin films with composition of $0 \leq x \leq 10\%$ were simultaneously grown on TiO₂-terminated SrTiO₃(001) substrates by pulsed laser deposition (PLD) as schematically shown in Fig. 1A. For a systematic comparison, the total thickness was kept constant at $t \sim 22 - 25$ nm. The composition of the grown films was determined by x-ray photoelectron spectroscopy (Fig. S1). Details of the film growth are given in the [Materials and Methods](#).

To gain insights into the film growth characteristics of the LABO films, reciprocal space mappings (RSM) were performed around the STO(113) reflections. Figure 1B shows the results of the RSM. The RSM shows that the in-plane LAO($hh0$) for the undoped LAO film (~ 25 nm thick) is constrained along the STO($hh0$) yielding a positive strain of approximately $+3.0\%$. The out-of-plane ($00l$) of the film shows a negative strain of approximately -0.8% following the Poisson ratio, partially relaxing back towards the value of bulk LAO. In contrast, the RSM of the LABO nanocomposite films ($22 - 25$ nm thick) on STO(001) exhibits the development of two reflections of the films that vary significantly with the composition, x . These two reflections are assigned to: (I) a film region that is coherently constrained to the in-plane STO and (II) a region that moves away from the in-plane STO. The nanocomposite films with lower compositions ($x \leq 5\%$) indicate partial in-plane strain relaxation of the region-I with respect to STO while the region-II is gradually developed with higher compositions, x . When the composition increases above $x \geq 8\%$, the reflections of the $(113)_{pc}$ plane of the nanocomposite films separate into two regions, streak and broad peaks. The streak peak reflects the strain gradient of a 2D coherent film layer which is perfectly aligned along with the in-plane STO. The resulting c -lattice constant of the coherent layers in the films increases with x , while aligning along the in-plane of the underlying STO substrate, as shown in Fig. 1C. Thus, the c -lattice strain distribution of the coherent layer (lined up along the in-plane of STO in reciprocal space in Fig. 1B) is different, compared to the case of the elastic deformation of a coherent LAO layer which is completely imposed by STO substrate with a Poisson ratio of LAO (0.24) (26). For example, a pure elastic deformation ($\varepsilon_x = +3.03\%$ and $\varepsilon_z = -1.92\%$, where ε_x and ε_z are the in-plane and the out-of-plane strain, respectively) of the LAO layer on STO undergoes a reduced thickness (≤ 20 UCs) due to the misfit strain (26). However, in this work, we observed that the in-plane and out-of-plane strain of the coherent layer (I) in the nanocomposite ($x \geq 8\%$) films are $\varepsilon_x = +3.0\%$ and $\varepsilon_z = +0.1\%$ as compared with the bulk LAO value, respectively. This means that the out-of-plane of the continuously developed coherent layer is oppositely constrained (c -axis lattice elongation) in the LABO nanocomposite films maintaining the in-plane matching with the underlying STO substrate.

A clear increase in the reflection area and the intensity of the broad reflection region-II is observed with higher compositions (see dashed line in Fig. 1B). This is believed to be due to a strain relaxation process of the LAO phase, which is extended after the development of the region-I. Importantly, the position of the region II in RSM seems to shift away from the value of the bulk LAO (see Fig. 1B). We further confirmed that the lattice of the region-II is distorted tetragonally. This was

verified by RSM reflections for different crystallographic orientations of the films (Fig. S2). These results indicate a two-step structural development, i.e., an initial growth of coherent 2D layer and a following relaxed layer. When the composition of LBO reaches $x \geq 8\%$, the strain distribution of the LABO nanocomposite films is manifested. To confirm this structural assembly of the LABO films on the STO(001), scanning transmission electron microscopy (STEM) measurements were performed. Figure 1D illustrates a cross-sectional high-angle annular dark field (HAADF) STEM image of the undoped LAO(001) film grown on STO(001). As expected, for the undoped LAO ($x = 0$) (001) film grown on STO(001), only a layer-by-layer epitaxial growth was observed. Significant structural disorder was found in the LBO composition of $x \leq 5\%$ (Fig. S3). In contrast, we found that the LABO film ($x = 8\%$) shows well defined vertically aligned nanostructures (1.5 – 2 nm width) with visible contrast (atomic z-contrast) as shown in the HAADF-STEM images in Fig. 1E. The ratio of the relatively dark to bright areas in the nanocomposite film layer is around $\sim 0.91 \pm 0.03$, similar to what observed in the composition of the nanocomposite film ($x = 8\%$). Interestingly, the vertically aligned structure is not directly formed on STO(001) substrate, but they developed after the initial 2D layer was formed (see Fig. 1E). The TEM results verify the spontaneous occurrence of a two-step growth of the 2D layer and the subsequent 3D vertical array in the epitaxial LABO nanocomposite film, which is consistent with the XRD results.

Growth Mechanism of Self-assembled 2D-3D LABO Nanocomposite Film Structure.

To understand the compositional characteristics of the self-assembled LABO nanocomposite film, we carried out 2D elementary mappings for B, Al, La, and O for the 2D-3D LABO film ($x = 10\%$) using the electron energy loss spectroscopy (EELS) as shown in Figs. 2A and Fig. S4. Figures 2B and 2C demonstrate the integrated EELS intensities of Al, B, and La for the 2D and 3D film areas, respectively. The results indicate that the 2D layer is mainly composed of the Al and La contents with indistinguishable intensity of the B K-edge EELS signal. However, in the 3D film layer, B signals were found, also confirmed by a secondary ion mass spectroscopy (see Fig. S5). The intensity of B is alternated in the lateral direction with the Al intensity distribution. The intensity signal of the La is kept almost uniform in the lateral (x) and vertical (z) directions. The periodic distribution of B directly corresponds to the positions of vertical nanostructures in the 3D layer as denoted in Fig. 2A. An abrupt lateral interface is formed between the self-assembled 2D-LAO and STO (see Fig. 2D). In the upper 3D nanocomposite film layer, the two vertically aligned LAO and LBO structures are tightly coupled through the vertical interfaces. We found that the lattice match between LAO and LBO phases occur via aligning the LAO $[100]_{pc}$ /LBO $[010]_{pc}$ (or LBO $[-101]_o$) and LAO $[001]_{pc}$ /LBO $[100]_{pc}$ as schematically illustrated in Figs. 2E,F. Note that the $[101]_o$ and $[010]_o$ crystallographic orientations of orthorhombic LBO (space group: $Pnam$, $a_o = 5.106 \text{ \AA}$, $b_o = 8.257 \text{ \AA}$, and $c_o = 5.873 \text{ \AA}$) correspond to pseudocubic $[100]_{pc}$ and $[001]_{pc}$ directions, respectively (27,28). Consequently, our results directly show that the consecutive formation of coherent 2D film layer and vertically arrayed 3D film is spontaneously formed in the LABO/STO(001) heterostructures (Fig. 2G).

In general, the nucleation-and-growth process on a substrate relies on island formation which is controlled by temperature, the surface concentration of adatoms or molecular, ionic species, nucleation sites (e.g. substrate treatment, surface defects, dislocations), and growth rate (22). When the concentration of boron in the LBO is low, the nucleation and the subsequent growth process (coalescence) are limited by a low probability of boron atoms to diffuse and form a critical nucleus (a critical nucleus is one that has the potential to grow), causing a random distribution of atomic point defects (solid solution). Alternatively, when the adatom concentration of boron is

sufficiently high, *i.e.*, when the LBO compositions of $x \geq 8\%$, a supersaturation condition is achieved (22), leading to the nucleation of LBO crystals. This means that the nucleation and growth of LBO islands are promoted by a high diffusivity/low capture rate of boron atoms on the LAO surface. The change of the film growth mode from 2D to 3D is accompanied by a relaxation process of the elastic energy that minimizes the misfit strain between LAO and STO for LBO formation in the nanocomposite film following the *Stranski-Krastnov* growth mode (22). Overall, the growth processes can be described in the following way: (i) the initial growth of 2D LAO on STO(001) under 3% biaxial strain with less boron accommodation, (ii) strain relaxation after a critical thickness of ~ 10 UC by overcoming the *Matthews-Blakeslee barrier* (29) resulting in excessive boron diffusion towards the growing surface, and (iii) accumulated concentration of boron distributed as islands on the 2D LAO surface which acts as the seed for the formation of 3D vertically aligned LAO:LBO nanostructures. This transient growth behavior was directly monitored by *in-situ* reflection high energy electron diffraction during the LABO film growth process when compared to the 2D growth feature of undoped LAO on STO (Fig. S6).

Epitaxial strain distribution in multi-dimensional LABO/STO(001) heterostructure.

In order to understand the strain distribution of the 2D-3D LABO/STO(001) heterostructure, we performed the peak-pair analysis and associated strain analysis from the STEM images. Details of the image processing (including noise filtering, intensity detection and refinement) are given in [SI Appendix, Fig. S7](#). Figure 3A shows the refined HAADF-STEM image for a self-assembled 2D-3D LABO ($x = 10\%$) film layer on STO(001). Based on the statistical determination of La cage with atomic precisions of ~ 20 pm, lattice displacements and the associated epitaxial strain taken by the STEM image were elaborated using the lattice parameter (3.905 \AA) of cubic bulk STO. Figures 3B and 3C exhibit strain maps for the relative biaxial (ϵ_{xx}) and uniaxial (ϵ_{zz}) strain of the 2D-3D LABO/STO heterostructure, revealing the strain characteristics along the x - and z -axis. The ϵ_{xx} mapping (Fig. 3B) shows that the in-plane spacing of the 2D LAO layer is perfectly matched, as expected, with that of the underlying STO. In the 3D LABO layer, we observe an alternating strain characteristic along the lateral direction with the repetition of tensile (average $\epsilon_{xx} \sim +3.5\%$ with respect to a of bulk STO) and compressive (average $\epsilon_{xx} \sim -1\%$) strain. A displacement vector mapping for a transient LAO-to-LABO area presented in Fig. 3D directly visualizes the opposite directions $[100]$ and $[-100]$ of the compressive strain of the two LAO columns across an LBO column. The aligned nanostructures (R1) with tensile strain correspond to the $(010)_{pc}$ -oriented LBO crystals in the LABO composite film layer, while the areas (R2) with compressive strain correspond to the $(001)_{pc}$ -oriented LAO columns. We found further that the out-of-plane compressive strain (ϵ_{zz}) of the LABO composite layer in the z -direction saturates starting from $\epsilon_{zz} \sim -4\%$ towards an average $\epsilon_{zz} \sim -1.8\%$. Notably, the ϵ_{zz} strain becomes uniform along the lateral x -direction (see Figs. 3C). This reveals that the vertical alignment of the LAO:LBO nanocomposite film layer is energetically stabilized via a lateral period of alternating tensile and compressive ϵ_{xx} strain components as a complementary in-plane strain matching.

Another interesting observation is the ϵ_{zz} distribution at the self-assembled LAO/STO interface (Fig. 3F). A large interfacial strain of $\epsilon_{zz} \sim +4\%$ appears at the topmost area (< 2 nm) of STO. In contrast, an opposite strain of max. $\epsilon_{zz} \sim -4\%$ at the initial growth of the 2D LAO layer (5 nm-thick) gradually decreases towards the interface with the LABO. Such unique reversal lattice distortions (the pseudomorphically c -contracted LAO and c -elongated STO) across the interface is driven by the

energy cost of the epitaxially contracted LAO. This can lead to the emergence of an epitaxial strain-mediated head-to-head ferroelectric-like polarization and thus interfacial conductivity (similar to the formation of charged domain walls in the head-to-head (or tail-to-tail) domain configuration of insulating ferroelectrics) (30). Together with such reversal *c*-lattice distortions of LAO and topmost STO, 2DEG formation have been also observed in the STO of conductive LAO/STO heterosystems with a critical thickness of LAO (> 3 unit cells) (31,32). Our striking observation is that such reversal lattice distortions across the interface are preserved in conjunction with the self-assembly of 2D-3D LABO film structure on STO(001).

Formation of 2DEGs and Magnetism in the LABO/STO Heterostructures.

Based on the above results, it is clear that two types of interfaces with different orientations (*i.e.* lateral and vertical interfaces) are formed. To probe the characteristics of the self-assembled 2D layer on the STO(001), photoluminescence (PL) measurements were performed using an excitation photon energy He-Cd laser ($\lambda = 325$ nm, 3.9 eV, a penetration depth of ~ 20 nm). Figure 4A shows the PL spectra, measured at 12 K, of a treated TiO₂-STO(001) substrate and the LABO ($0 \leq x \leq 10$)/TiO₂-STO samples. The PL emission of the samples were found with the near band-edge emission (BE) at ~ 3.2 eV (close to the bandgap energy of STO, ~ 3.2 eV). This is dominated by the recombination processes between the excited electrons and excited holes (conduction band minimum or subbands near the conduction band edges to valence band minimum) (33). The indirect bandgap STO substrate shows two weak BEs, commonly generated by the band-to-band optical transitions involving optical phonon absorption (BE-I at ~ 3.27 eV) and excitation (BE-II at ~ 3.22 eV). In contrast, for all the undoped LAO/STO and LABO/STO samples, additional BE emission pairs were found at lower energies, 3.18 - 3.20 eV (2DE-I) and 3.25 - 3.26 eV (2DE-II), compared to the BE-I and -II. Such a BE emission corresponds to the existence of 2D electron gases (2DEGs) at the heterointerfaces, consistent with an earlier work (34). Thus, the energy and intensity of the 2DEG-associated BE directly reflects the band bending of the STO surface and the subsequent charge carrier confinement at the LABO/STO interfaces. A low-temperature PL feature of 2DEG is observed in the 25 nm-thick LAO/STO heterostructure. However, the 2DEs of the LABO ($x \leq 5$ %)/STO heterostructures move towards lower energies with significant suppression. These degradations reflect the distorted/non-abrupt interfaces for the formation of 2DEGs. Clearly, the enhancement of the phonon-assisted 2DE-emission pair was observed in the LABO ($x \geq 8$ %)/STO heterostructures at the same emission energies that appear in the undoped LAO/STO interface. This directly indicates the formation of a 2DEG LAO/STO interface in the 2D-3D LABO ($x \geq 8$ %) film structures. Furthermore, variable temperature BE emissions of the LABO ($x = 8$ %) / STO shows a typical temperature-dependent characteristic of 2DEG formation (Fig. 4B). To further identify and characterize the presence of a 2DEG at the LAO/STO interface in the heterostructures, electrical measurements with variable temperatures were performed. The undoped LAO/STO shows an insulating behavior at low temperatures (Fig. 4D), although a signature of 2DEG was observed in PL. This could be due to the fact that the carriers at the interface are localized and/or the absence of long-range conducting channel along the interface (11,12). Moreover, the LABO/STO heterostructures with $x \leq 5$ % were insulating due to the structural disorder and the lack of the 2D-LAO/STO interfaces, consistent with largely suppressed 2DEG emissions in PL. When the composition increases to $x = 8$ and 10 %, both of the LABO/STO heterostructures exhibit metallic behaviors with decreasing the sheet resistance (R_{xx}) upon cooling (Fig. 4C). This confirms the formation of 2DEGs at their LAO(001)_{pc}/STO(001) interfaces as illustrated in Fig. 4D.

Another intriguing observation is the appearance of magnetism with its anisotropic nature, which is accompanied with the development of the 2D-3D LABO/STO heterostructures. In this work, all the measured magnetic hysteresis loops were carefully evaluated (see the section of Materials and Methods, and Fig. S8). No ferromagnetic response was found in an annealed TiO₂-STO substrate used for film growth (see Fig. 4E and Fig. S8). The undoped LAO/STO heterostructure shows a typical weak magnetic response with saturation magnetization (M_s) of $M = 4 - 7 \mu\text{emu}/\text{cm}^2$, measured along both the in-plane [IP, $H//\langle 100 \rangle$] and out-of-plane [OOP, $H//\langle 001 \rangle$] directions at 5 K. Figure 4E illustrates the 5 K IP and OOP magnetic hysteresis loops of the LABO/STO sample with the LBO composition of $x = 1.5\%$ (like a solid solution). Clear ferromagnetic hysteresis loops of the sample were found with no variation in the IP and OOP saturation magnetization of $\sim 37 \mu\text{emu}/\text{cm}^2$. In contrast, a large difference was observed for $x \geq 8\%$, i.e., the OOP M_s of the LABO($x = 8\%$)/STO was found to be $\sim 30 \mu\text{emu}/\text{cm}^2$ in comparison with about $6 \mu\text{emu}/\text{cm}^2$ for the IP magnetization (Fig. 4F). The OOP saturation magnetization of the 2D-3D LABO/STO samples ($x \geq 8\%$) was found to be about 5 times stronger than the IP magnetization. These results clearly reveal that the magnetic anisotropy is accompanied by the formation of vertically aligned LABO structure. The overall measurements of the IP and the OOP M_s are listed in Fig. 4G.

Origin of Magnetism and Magnetic Ordering in the LABO/STO Heterostructures. The strong preferential magnetization observed in the OOP of vertically aligned LABO structure is different from the weak magnetism nature of the LAO/STO interfaces (e.g., oxygen defect-mediated magnetic ordering and/or localized unpaired Ti d -band electron spins through exchange coupling of itinerant carriers), which is typically expected to show an in-plane ordering of the magnetic domains (16). The magnetic responses of the nanocomposite correspond to an OOP magnetic density of $\sim 3 \times 10^{13} \mu_B/\text{mm}^2$ for the $5 \times 5 \text{ mm}^2$ -sized LABO sample ($x \geq 8\%$) and the in-plane density of $\sim 8 \times 10^{12} \mu_B/\text{mm}^2$, similar to typical moment density ($\sim 10^{12} \mu_B/\text{mm}^2$) of LAO/STO interfaces reported in the literature (35). Our results indicate that the magnetization of the LABO/STO heterostructures does not increase with increasing x , implying that there is no direct contribution of LBO on the magnetism of the nanocomposite films. Hence, we suggest that the origin of magnetism in the LABO nanocomposite system is associated with the boron interstitials (B_i) (28). Interstitial doping can transform the non-magnetic host oxide into a high-temperature ferromagnetism as an impurity band-associated Stoner ferromagnetism (36). Additionally, theoretical calculations carried out in this work show that the effective B_i doping in the host LAO lattices is limited to 3.2 at.% due to the tendency of dimerization/clustering, while we confirmed that the effect of oxygen vacancies on the boron interstitial-induced ferromagnetism is negligible. We therefore postulate that the distribution/orderings of B_i in the host LAO lattices could be located near the vertical LAO/LBO interfaces although a precise atomic identification of B_i position is still challenging using electron microscopy. Nonetheless, it was possible to confirm the presence of metallic B_i in the local area of a 3D LABO nanocomposite layer by STEM-EELS (Figs. 5A and B) and NMR (Fig. S9).

To understand the above magnetic nature in the LABO films, we performed first principles calculations on realistic model structures, strained LAO supercells with B_i . A more detailed information is given in the Methods Section. First, there is no effect of substitutional B doping on the development of magnetism in a tetragonally distorted LAO (by replacing B-site Al cation with B) and no magnetism in a tetragonally deformed LBO structure. Next, to study a preferential magnetic structure, we simulated boron impurities in a 3%-biaxial strained LAO (Fig. 5C). This model mimics the lattice mismatch between LAO and STO and the initial growth of LAO overlayer which is tetragonally compressed, so that the La-B-La chains are not equivalent. The in-plane (IP) chains expand in this regime, however, together with a significant relaxation of the four nearest

oxygen to Bi, it shows a relatively very weak total magnetization (m_B and $m_{La} < 0.02 \mu_B$) (Fig. 5D). In contrast, when a Bi is energetically relaxed in the middle of two La atoms along the OOP direction of the LAO, the total magnetic moment arises up to $1 \mu_B$ (e.g. $m_B = 0.4 \mu_B$ for Bi and $m_{La} = 0.2 \mu_B$ for La) (Fig. 5E). Thus, the OOP La- Bi-La chains form as magnetic species in the Bi-doped LAO. Figure 5F clearly shows that the Bi induces three impurity bands: two spin-up and one spin-down peaks which are located just below the Fermi level (E_F) in the bandgap of the LAO. The calculated spin imbalance is +1 that enables the magnetization of $1 \mu_B$ in the system. It should be noted that the total magnetic moment of LAO induced by a Bi cannot exceed $1 \mu_B$ because it is induced by n -doping with one extra electron of Bi. The above *ab-initio* calculations further suggest that in the finite film thickness range (up to 10 UC) the Bi is energetically located along the horizontal direction with a weak magnetic contribution. As the thickness increases, the structure evolves into vertically aligned structure and the Bi is accumulated at the LAO/LBO vertical interfaces, resulting in a strong magnetic moment along the OOP direction.

Discussion

In this work, we demonstrate a self-assembly of combined 2D and 3D nanocomposite heterostructure, which can be evoked by the composition of two constituent oxide phases. To obtain this structural transition, it is essential to control the ratio between two distinct crystal components, LAO and LBO. In order to achieve the initial 2D LAO layer and the subsequent 3D LABO layer, it is required that the host LAO composition should be higher than that of the LBO. Choosing an equal composition (e.g. ratio of the LAO:LBO = 50:50) would lead to only the formation of vertically aligned nanopillar structure (20,21). Thus, finding an appropriate composition of LBO is a key parameter for driving the spontaneous transition from 2D to 3D structure - in this work, the structural transition happened at composition of $x \geq 8\%$. The formation of atomically defined horizontal 2D-LAO/STO and vertical 3D-LAO/LBO interfaces leads to the coexistence of a 2DEG and a tunable magnetic ordering. Our work offers new perspectives for designing and controlling magnetic and electric properties at the interfaces of complex oxide nanocomposite thin film heterostructures via a self-assembly approach. This self-assembly approach is a powerful means not only for nanoscale investigation of emerging physics phenomena, but also it could extend engineering of thin film materials beyond the current limits of atomically delicate interface engineering.

Materials and Methods

Sample preparation. PLD LABO(x) ceramic targets were fabricated by standard solid-state synthesis techniques by mixing three different metal oxide powders (highly pure 99.99% – 99.999% La_2O_3 , Al_2O_3 , and B_2O_3 powders). The mixed and pressed targets were sintered at 1400 °C for 4 hours in air (28). LABO films ($x = 0 - 10\%$) were grown on TiO_2 - $SrTiO_3(001)$ using PLD (KrF excimer laser: $\lambda = 248$ nm). The growth temperature was kept constant at 700 °C and the films were grown under oxygen partial pressure of $5 \times 10^{-4} - 1 \times 10^{-3}$ mbar. After film growth, all the samples were cooled down to room temperature at the same growth pressure with a ramping-down rate of 10 °C/min. The films were grown by a laser fluence of ~ 1.6 J/cm² with a repetition rate of 1 Hz. The growth characteristics and thickness of all the films were monitored and controlled by reflection of high energy electron diffraction (RHEED). All the film preparations were carried out in different PLD laboratories in UK, South Korea, and Germany.

Sample characterizations. Structural properties of all the grown films were examined by a high-resolution Bruker D8 Discover diffractometer with monochromatic Cu K α 1 radiation ($\lambda = 1.54056$ Å). The magnetic measurements were performed by Quantum Design SQUID Magnetometer with the samples mounted at different orientations to measure the in-plane [100] and out-of-plane [001] crystallographic directions. To evaluate the magnetic properties of the films, external magnetic contributions were eliminated by measuring the sample holders and accessories (low-temperature glues). The substrate contribution was subtracted from the field-dependent magnetization data by removing a field-linear diamagnetic term fitted to the high-field data (Fig. S8). Microstructural properties of the LABO films were determined by performing scanning electron microscopy (a FEI double Cs-aberration corrected Titan3 G2 60-300 S/TEM instrument with Chemi-STEM technology). For ^{11}B NMR, The LABO-STO thin films were sliced into sub-mm pieces and packed into rotors. No grinding was performed on the samples, to ensure that degradation of the samples did not take place. To make the samples spin stably, PTFE tape was inserted into each rotor to fill the void space left by such inefficient packing. There is possible evidence of preferential alignment features in the solid-state NMR results achieved, this suggests the boron has a preferred alignment in the thin film. All ^{11}B ($I = 3/2$) MAS (12 kHz) solid state NMR spectra were achieved using a 11.7T Bruker Avance III 500 MHz spectrometer operating at a Larmor frequency of 160.45 MHz. A Varian-Chemagnetics 4 mm probe was utilized to achieve spinning frequencies of 12 kHz and to prevent a boron background being visible. The single pulse experiment consisted of a 'non-selective' (solid) $\pi/6$ pulse of 1.0 μs pulse. The spectra were calibrated to the secondary reference NaBH_4 ($\delta_{\text{iso}} = -42.09$ ppm w.r.t $\text{BF}_3 \cdot \text{Et}_2\text{O}$ in CDCl_3 at 0 ppm) (39). The T_1 data was simulated to a single exponential, $f(t) = I_0[1 - \exp(-t/T_1)]$, and no statistically significant improvements were achieved with stretched or multiple exponential simulations. As the T_1 relaxation of the B_i environment was measured at 0.522 seconds, all experiments were taken with a 60° nutation tip angle and $3 \times T_1$ to achieved maximum efficiency of the experiment. All spectral simulations were completed using the in-house developed Quadfit programme (40). Photoluminescence data for the samples were collected at variable temperatures (5 K – 300 K) using an excitation energy of HeCd laser ($\lambda = 325$ nm). A complementary long-pass optical filter with a cut-off wavelength of 420 nm was used to increase the dynamic range of deep level emissions in the samples and remove the laser line and its second order diffraction. All the PL measurements were performed using a constant optimized exposure for the absolute comparison of the luminescence intensity from the samples. For the electrical measurements, the measured sample sizes are $5 \times 5 \text{ mm}^2$ and $2.5 \times 5 \text{ mm}^2$. and contracts are achieved by Ohmic Al wire bonding on all the edge corners of the sample. The transport measurements were carried out in a CRYOGENIC cryogen-free measurement system with the temperature ranging from RT to 4 K. The temperature was controlled utilizing a Lakeshore 340. Measurements was done utilizing a SR830 lock-in amplifier with a 300 M Ω load resistor at a frequency of 77.39 Hz and a voltage excitation of 3 V for 10 nA driving current.

Theoretical calculations. The density functional theory (DFT) package VASP (41) was used to calculate the electronic, structural and magnetic properties of LAO doped by boron. The code has a plane-wave basis set that provides the reliable structural optimizations and accurate energetics. Electron-ion interactions within VASP calculations were described by projector-augmented wave pseudopotentials and electronic wave functions were represented by plane waves with an energy cutoff of 450 eV. We used here the Perdew-Burke-Ernzerhof (PBE) generalized-gradient approximation (GGA) (42) to the exchange-correlation potential. The use of GGA-PBE and its reliability were discussed previously for simulations of the LAO overlayers on $\text{SrTiO}_3(001)$ (11,43) and boron-doped material (28). The equilibrium lattice parameter of LAO, which was obtained

within the GGA-PBE, is 3.79 Å. Here, by adding one boron into the 135-atom LAO supercell, we simulated an isolated B impurity in cubic and tetragonally distorted LAO and tetragonally distorted LBO. In all cases, the positions of boron and its nearest cations and oxygens were allowed to relax. The structural relaxation was performed using the $4 \times 4 \times 4$ \mathbf{k} -mesh and the conjugate-gradient algorithm until the Hellmann-Feynman forces became less than 5×10^{-3} eV/Å. The density of states (DOS) was obtained then using the Γ -centered and compacted \mathbf{k} -mesh with minor smearing of 10 meV. The DOS calculations were performed also in the presence of the spin-orbital coupling (SOC), within the non-collinear option of VASP (44).

Acknowledgments

Authors thank E. B. Þorsteinsson in the University of Iceland, Iceland, for his technical support for this work. Dr. K. Kaufmann in Fraunhofer Center for Silicon Photovoltaics, Germany, is thanked for his support on the elementary analysis of samples. Authors thank Dr. M. Walker in the University of Warwick for XPS measurements. Dr. A. Bhatnagar in Zentrum für Innovationskompetenz SiLi-nano®, Germany, is thanked for useful discussion on this work. D.-S.P. and N.P. acknowledge the support from the European commission through project Biowings H2020 FET-OPEN 2018-2022 (grant No 80127). Y.L.G. acknowledges the support from China Postdoctoral Science Foundation (grant No 2020M680726, YJ20200325). N.P. acknowledges funding from Villum Fonden for the NEED project (grant No 00027993), the Danish Council for Independent Research Technology and Production Sciences for the DFF- Research Project 3 (grant No 00069B) and the support from the "Challenge Programme 2021 - Smart Nanomaterials for Applications in Life-Science" Grant No. NNF21OC0066526. W.S.C. was supported by the National Research Foundation of Korea (grant No NRF-2021R1A2C2011340). F.T. acknowledge support by research grant 37338 (SANSIT) from Villum Fonden.

References

- Ohtomo A, Hwang HY (2004) A high-mobility electron gas at the $\text{LaAlO}_3/\text{SrTiO}_3$ heterointerface. *Nature* 427:423.
- Zhou Y, et al. (2016) Strongly correlated perovskite fuel cells. *Nature* 534:231-234.
- Chakhalian J, Liu X, Fiete GA (2020) Strongly correlated and topological states in [111] grown transition metal oxide thin films and heterostructures. *APL Mater* 8:050904.
- Efremov DV, Brink JVD, Khomskii DI (2004) Bond- versus site-centred ordering and possible ferroelectricity in manganites. *Nat Mater* 3:853-856.
- Taniuchi T, et al. (2016) Imaging of room-temperature ferromagnetic nano-domains at the surface of a non-magnetic oxide. *Nat Commun* 7:11781.
- Ederer C, Spaldin, NA (2004) A new route to magnetic ferroelectrics. *Nat Mater* 3:849-851 (2004).
- Zheng H, et al. (2004) Multiferroic $\text{BaTiO}_3\text{-CoFe}_2\text{O}_4$ nanostructures. *Science* 303:661.
- Reyren N, et al. (2007) Superconducting interfaces between insulating oxides. *Science* 317:1196-1199.
- Li L, Mannhart J, Aschoori RC (2011) Coexistence of magnetic order and two-dimensional superconductivity at $\text{LaAlO}_3/\text{SrTiO}_3$ interfaces. *Nat Phys* 7:762-766.
- Park JW, et al. (2010) Creation of a two-dimensional electron gas at an oxide interface on Silicon. *Nat Commun* 1:94.
- Park D-S, et al. (2020) The emergence of magnetic ordering at complex oxide interfaces tuned by defects. *Nat Commun* 11:3650.
- Chen Y, et al. (2011) Metallic and insulating interfaces of amorphous SrTiO_3 -based oxide heterostructures. *Nano Lett* 11:3774-3778.

13. Warusawithana MP, et al. (2013) LaAlO₃ stoichiometry is key to electron liquid formation at LaAlO₃/SrTiO₃ interfaces. *Nat Commun* 4:2351.
14. Salluzzo M, et al. (2013) Structural and electronic reconstructions at LaAlO₃/SrTiO₃ interface. *Adv Mater* 25:2333-2338.
15. Zeng S, et al. (2016) Liquid-gated high mobility and quantum oscillation of the two-dimensional electron gas at an oxide interface. *ACS Nano* 10:4532-5437.
16. Bi F, et al. (2014) Room-temperature electronically controlled ferromagnetism at the LaAlO₃/SrTiO₃ interface. *Nat Commun* 5:5019.
17. Stornaiuolo D, et al. (2015) Tunable spin polarization and superconductivity in engineered oxide interfaces. *Nat Mater* 15:278-283.
18. Ngo TDN, et al. (2015) Polarity-tunable magnetic tunnel junctions based on ferromagnetism at oxide heterointerfaces. *Nat Commun* 6:8035.
19. Tra VT, et al. (2013) Ferroelectric control of the conduction at the LaAlO₃/SrTiO₃ heterointerface. *Adv Mater* 25:3357-3364.
20. MacManus-Driscoll JL, et al. (2008) Strain control and spontaneous phase ordering in vertical nanocomposite heteroepitaxial thin films. *Nat Mater* 7:314.
21. MacManus-Driscoll JL, Suwardi A, Wang H (2015) Composite epitaxial thin films: A new platform for tuning, probing, and exploiting mesoscale oxides. *MRS Bull* 40:933-942.
22. Ohring M. (2002) *Materials Science of Thin Films*, Academic Press.
23. Yang SM, et al. (2015) Strongly enhanced oxygen ion transport through samarium-doped CeO₂ nanopillars in nanocomposite films. *Nat Commun* 6:8588.
24. Harrington SA, et al. (2011) Thick lead-free ferroelectric films with high Curie temperatures through nanocomposite-induced strain. *Nat Nanotechnol* 6:491-495.
25. Zheng H, et al. (2004) Multiferroic BaTiO₃-CoFe₂O₄ Nanostructures. *Science* 303:661-663.
26. Cancellieri C, et al. (2011) Electrostriction at the LaAlO₃/SrTiO₃ interface. *Phys Rev Lett* 107:056102.
27. Levin EM, Roth RS, Martin JB (1961) Polymorphism of ABO₃ Type Rare Earth Borates. *Am Mineral* 46:1030.
28. Park D-S, et al. (2018) Electromagnetic functionalization of wide-bandgap dielectric oxides by boron interstitial doping. *Adv Mater* 30:1802025.
29. Matthews JW, Blakeslee AE (1974) Defects in epitaxial multilayers. *J Cryst Growth* 27:118-125.
30. Sluka T, et al. (2013) Free-electron gas at charged domain walls in insulating BaTiO₃. *Nat Commun* 4:1808.
31. Lee PW, et al. (2016) Hidden lattice instabilities as origin of the conductive interface between insulating LaAlO₃ and SrTiO₃. *Nat Commun* 7:12773.
32. Stengel M (2011) First-principles modeling of electrostatically doped perovskite systems. *Phys Rev Lett* 106:136803.
33. Kan D, et al. (2005) Blue-light emission at room temperature from Ar⁺-irradiated SrTiO₃. *Nat Mater* 4:816-819.
34. Islam MA, et al. (2016) Surface chemically switchable ultraviolet luminescence from interfacial two-dimensional electron Gas. *Nano Lett* 16:681-687.
35. Kalisky B, et al. (2012) Critical thickness for ferromagnetism in LaAlO₃/SrTiO₃ heterostructures. *Nat Commun* 3:922.
36. Ackland K, Venkatesan M, Coey JMD (2012) Magnetism of BaB₆ thin films synthesized by pulsed laser deposition. *J Appl Phys* 111:07A322.

37. Lee SK, et al. (2018) Amorphous boron oxide at megabar pressures via inelastic X-ray scattering. *PNAS* 115:5855-5860.
38. Cretu O, et al. (2015) Structural and local chemical properties of boron-terminated tetravacancies in hexagonal boron nitride. *Phys Rev Lett* 114:075502.
39. Harris RK, Becker EDA (2002) NMR nomenclature: Nuclear spin properties and conventions for Chemical Shifts. IUPAC Recommendations 2001. International union of pure and applied chemistry. Physical Chemistry Division. Commission on molecular structure and spectroscopy. *Magn Reson Chem* 40:489-505.
40. Kemp TF, Smith ME (2009) QuadFit-A new cross-platform computer program for simulation of NMR line shapes from solids with distributions of interaction parameters. *Solid State Nucl Magn Reson* 35:243-252.
41. Kresse G, Furthmüller J (1996) Efficient iterative schemes for *ab initio* total-energy calculations using a plane-wave basis set. *Phys Rev B* 54:11169.
42. Perdew JP, Burke K, Ernzerhof M (1996) Generalized gradient approximation made simple. *Phys Rev Lett* 77:3865.
43. Maznichenko I, Ostanin S, Ernst A, Mertig I (2019) Tunable 2D electron gas at the LaAlO₃/SrTiO₃(001) interface. *Phys Rev Mater* 3:074006.
44. Hobbs D, Kresse G, Hafner J (2000) Fully unconstrained noncollinear magnetism within the projector augmented-wave method. *Phys Rev B* 62:11556.

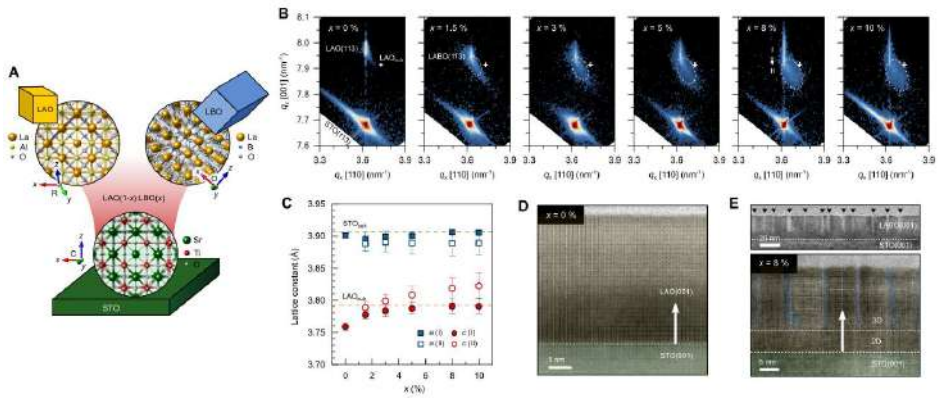


Figure 1. The growth of LABO nanocomposite films on STO(001) substrates with different x . (A) A schematic for the formation of LABO nanocomposite films, consisting of a rhombohedral LAO(1-x) and an orthorhombic LBO(x), grown on a cubic STO(001). (B) RSM (113)_{pc} reflections of the nanocomposite films as a function of x , measured around the (113) reflection of STO substrates. The cross mark indicates the (113)_{pc} reflection position of bulk LAO ($a_{pc} = 3.79 \text{ \AA}$). A streak and broad peak for the RSM(113)_{pc} reflections of the nanocomposite films gradually develop with increasing x . (C) The a- and c-axis lattice constants of the nanocomposite films with different x . The lattice parameters of the (I) and (II) layers are separately presented. (D) A cross-sectional HR-STEM image projected along <100> direction for the 25 nm-thick epitaxial LAO film grown on STO (001). (E) Cross-sectional TEM (upper panel) and HR-STEM (lower panel) images of the LABO ($x = 8 \%$) nanocomposite film on STO (001). The results indicate the formation of a mixed LABO film structure, consisting of an initial epitaxial 2D layer and subsequent 3D vertically aligned nanocomposite layer, grown on STO (001).

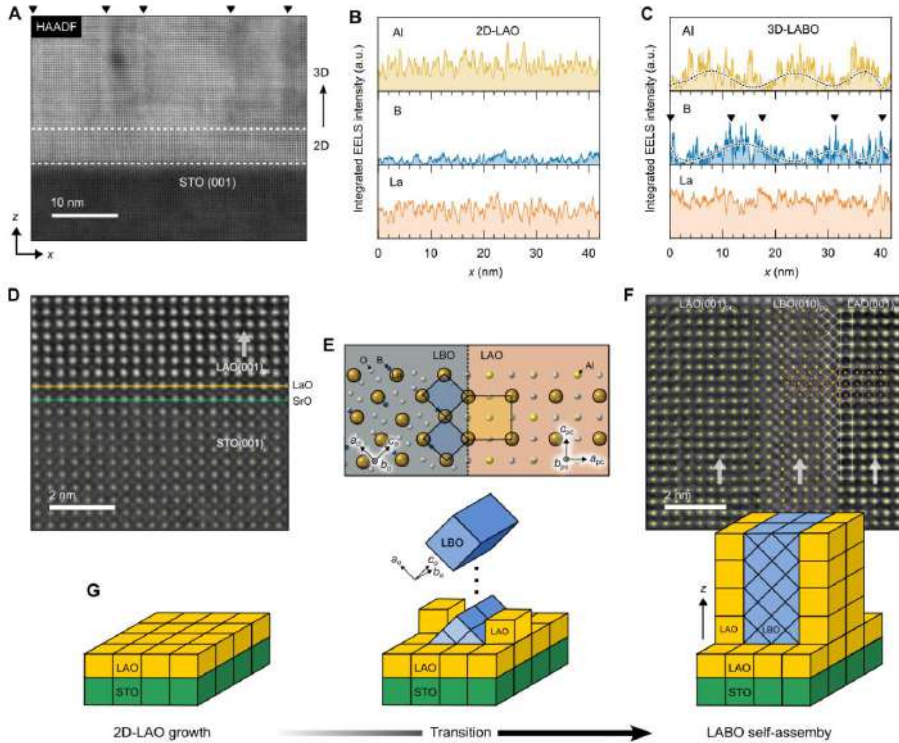


Figure 2. Formation of 2D-3D LABO film layers on STO(001). (A) A cross-sectional HAADF-STEM image for a 2D-3D LABO($x = 10\%$)/STO(001) sample. The positions of vertical stripes in the 3D area are marked along the x -direction by triangles. (B,C) Integrated EELS intensity profiles of Al, B, and La elements for the 2D (B) and 3D (C) areas corresponding to the film areas in (A). (D) An atomic resolution HAADF-STEM image for the atomically abrupt 2D-LAO/STO interface in the LABO/STO heterostructure. (E,F) Schematics for the crystallographic alignment of pseudocubic LAO and orthorhombic LBO crystals (E). The corresponding atomic resolution HAADF-STEM image for the vertically aligned LAO:LBO nanocomposite film layer (F). (G) Schematic illustrations for the transient growth sequence of 2D-3D LABO nanocomposite film on STO.

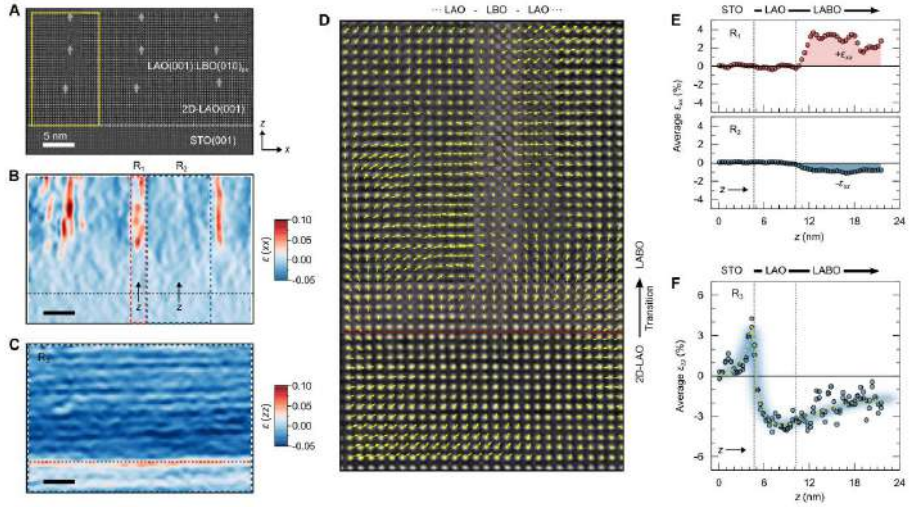


Figure 3. Strain distribution of the LABO/STO(001) heterostructure. (A) The atomically refined STEM image for the 2D-3D LABO film on STO(001). **(B)** The corresponding in-plane strain (ϵ_{xx}) map. **(C)** The corresponding out-of-plane (ϵ_{zz}) map. **(D)** Displacement vector map for the area where a structural transition starts from the topmost 2D layer, denoted by a red dash line. This selected area corresponds to the marked area in (A). In the intuitive quiver map, the reference mean lattice defines the starting point of individual arrows. **(E)** The averaged ϵ_{xx} profiles along the z-direction for the LBO (R1 in (B)) and LAO (R2 in (B)) columns in the 3D LABO film layer. **(F)** The averaged ϵ_{zz} profile along the z-direction of **(A)**.

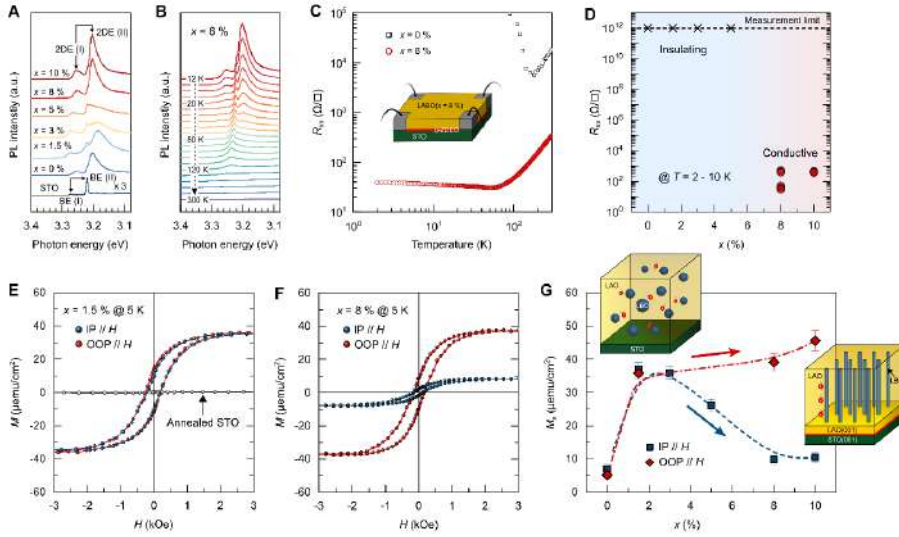


Figure 4. The co-existence of 2DEG and out-of-plane magnetic ordering in the 2D-3D LABO/STO(001) heterostructure. (A) Near BE PL spectra of the LABO($x = 1.5\%$, 3% , 5% , 8% , and 10%) nanocomposite films grown on STO, measured at 12 K . The BE of the undoped LAO/STO and LABO/STO samples show additional emission besides the BE (I & II) peaks of STO, which are assigned to the emission peaks of the 2DEG (2DE I & II). (B) Variable temperature ($12\text{ K} - 300\text{ K}$) near BE spectra of the LABO ($x = 8\%$) / STO sample. (C) Temperature-dependent sheet dc-resistance (R_{xx}) of $\sim 25\text{ nm}$ -thick undoped LAO/STO and $\sim 24\text{ nm}$ -thick LABO ($x = 8\%$) / STO samples, measured in the Van der Pauw geometry. (D) Low temperature ($2 - 10\text{ K}$) R_{xx} of the LABO/STO samples as a function of x ($= 0\% - 10\%$). (E) 5 K IP and OOP magnetic hysteresis loops of the LABO ($x = 1.5\%$) / STO sample. (F) 5 K IP and OOP magnetic hysteresis loops of the LABO ($x = 8\%$) / STO sample. (G) Variations in the IP and OOP M_s of the LABO/STO samples as a function of x ($= 0\% - 10\%$). The identical IP and OOP magnetic responses respond to randomly distributed magnets in the film as schematically illustrated in the inset. While, larger ($x \sim 4.5$) OOP M_s of the samples was found compared to the IP ones, corresponding to preferential OOP magnetic orderings in the vertically aligned LABO film structure.

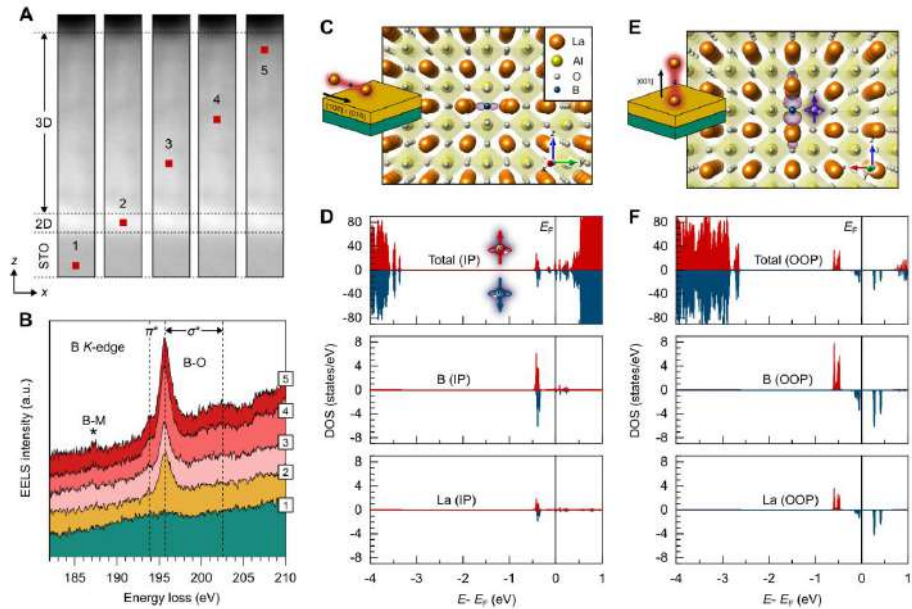
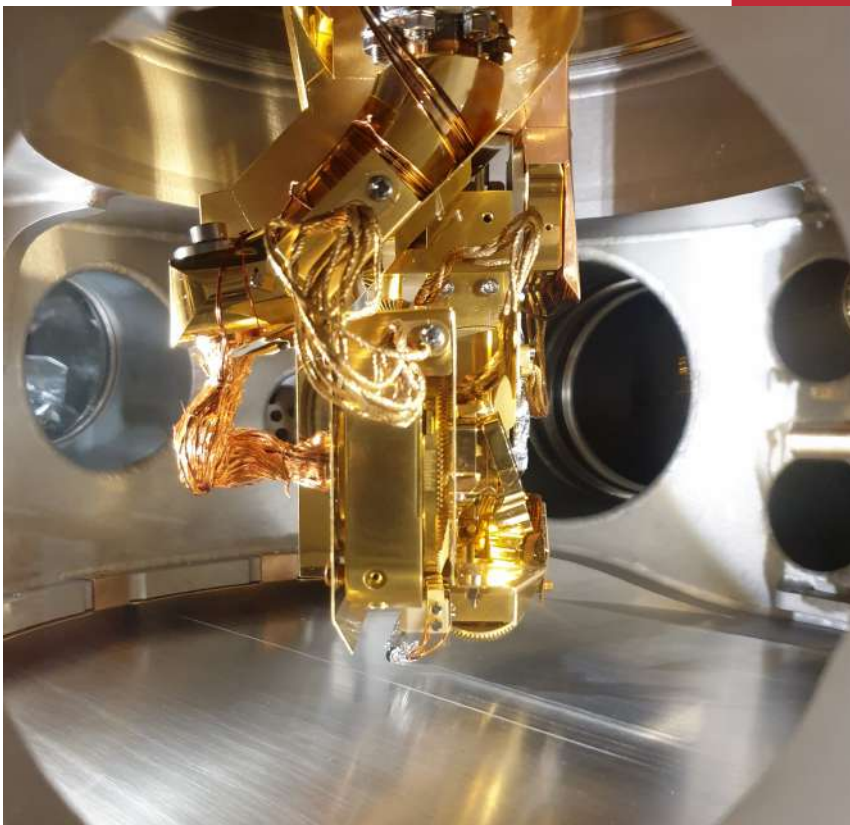


Figure 5. The B-associated magnetism in the LABO system. (A) Selected points (1 – 5) in the same local area of a LABO ($x = 10\%$)/STO heterostructure for B K-edge EELS spectra acquisition. (B) The corresponding experimental EELS spectra from a top area of STO [P1] to a top area of the 3D LABO layer [P5]. Two weak energy loss peaks were seen at ~ 194 eV and ~ 202.5 eV for B_2O_3 , typically resulting from the transition of a $1s$ electron to unoccupied B-O π^* and σ^* antibonding orbitals, respectively (37). In the upper 3D film layer, an anomalous peak between the π^* and σ^* peaks is dominated at ~ 195.8 eV, which could be associated with the lowered energy of σ^* peak due to the loss of LBO symmetry in the 3D-LABO strain network (37,38). Besides these, in the 3D film layer, a peak at ~ 187 eV visibly appears, which reflects the existence of metallic B_i (28). (C) Magnetization density of the 3%-strained LAO induced by an IP La-B-La chain. (D) Spin-polarized density of states (DOS) of the B-doped LAO with the IP La-B-La chain: the top panel is the total DOS, the middle one is the B-projected DOS, the bottom panel is the partial DOS of the nearest La neighbor. (E) Magnetization density of the strained LAO induced by an OOP La-B-La chain. (F) Spin-polarized density of states (DOS) of the B-doped LAO with the OOP La-B-La chain.

H. Li, W. H. Brito, E. B. Guedes, A. Chikina,

R. T. Dahm, *et al.*

Reconstruction of low dimensional electronic states by altering the chemical arrangement at the SrTiO₃ surface



Angle-resolved photoemission spectroscopy sample holder

Reconstruction of low dimensional electronic states by altering the chemical arrangement at the SrTiO₃ surface

Hang Li^{1,2*}, Walber H. Brito³, Eduardo B. Guedes², Alla Chikina², Rasmus T. Dahm¹, Dennis V. Christensen¹, Shinhee Yun¹, Francesco M. Chiabrera¹, Nicholas C. Plumb², Ming Shi², Nini Pryds¹ and Milan Radovic^{1,2 #}

¹*Department of Energy Conversion and Storage, Technical University of Denmark, 2800 Kgs. Lyngby, Denmark*

²*Photon Science Division, Paul Scherrer Institute, 5232 Villigen-PSI, Switzerland*

³*Departamento de Física, Universidade Federal de Minas Gerais, C. P. 702, 30123-970 Belo Horizonte, Minas Gerais, Brazil*

Email: * hang.li@psi.ch, # milan.radovic@psi.ch

Abstract

Developing reliable methods for modulating the electronic structure of the two-dimensional electron gas (2DEG) in SrTiO₃ is crucial for utilizing its full potential and inducing novel properties. Here, we show that relatively simple surface preparation reconstructs the 2DEG of SrTiO₃ (STO) surface, leading to a Lifshitz-like transition. Combining experimental methods, such as angle-resolved photoemission spectroscopy (ARPES) and X-ray photoemission spectroscopy (XPS) with *ab initio* calculations, we find that the modulation of the surface band structures is primarily attributed to the reorganization of the chemical composition. In addition, ARPES experiments demonstrate that vacuum ultraviolet (VUV) light can be efficiently employed to alter the band renormalization of the 2DEG system and control the electron-phonon interaction (EPI). Our study provides a robust and straightforward route to stabilize and tune the low-dimensional electronic structure via the chemical degeneracy of the STO surface.

Introduction

Transition metal oxide-based interfaces and surfaces, in particular those based on STO, exhibit a plethora of properties such as superconductivity [1-5], magnetism [6-9], Rashba-type spin-orbital coupling [10,11], and quantum Hall effect [12,13]. SrTiO₃, with a cubic perovskite structure, is a typical choice as a substrate for epitaxial growth

of many oxides. In cubic STO, the octahedral crystal field splits the Ti $3d$ orbitals in the well-known t_{2g} and e_g subbands, with degenerate t_{2g} states at the Γ point and the e_g states lying at higher energies. Structural relaxation and reconstructions at the STO surface and interface regions can lift the degeneracy and lower the dimensionality of the electronic bands [14]. The evolution of the electronic phases in STO-based systems and its relation to the properties have been intensively investigated: e.g., high mobility in γ -Al₂O₃/STO [15,16], anomalous Hall effect induced by Lifshitz transition [17], and quantum Hall effect [12,13], Rashba-like spin structure [18, 19]. The mentioned complex phenomena, which often coincide, demonstrate that understanding the electronic structure and the low degeneracy surface is crucial to understanding the causes of these behaviors and achieving control over them. Because of its simplicity, studies on the bare SrTiO₃ surface are essential to shed light on the fundamental mechanisms leading to the observed band order and predicting new ways for their manipulation.

The band modulations in bare STO can be modified by temperature change [20-23], stress [24-26], and surface termination [27-29]. Angle-resolved photoemission spectroscopy (ARPES) studies on nominally TiO₂-terminated STO single crystal [14, 30-32] display the typical electronic structures of STO consisting of shallow d_{xz}/d_{yz} bands and deep d_{xy} subbands – a fingerprint of most STO-based systems. Interestingly, a single band was observed in epitaxial-grown SrO layer on TiO₂-terminated STO [27]. These studies suggest that the surface termination and its chemical composition plays a crucial role in determining the properties of the underlying 2DEG.

Figure 1 shows a schematic illustration of two possible surfaces terminations of STO (001) (TiO₂ and SrO) and their combination (panel 1a) as well as their electronic structures (panel 1c) [14,18,26,27,30,31]. If the octahedral symmetry of the 001-oriented STO is preserved at the surface, it protects the degeneracy of the t_{2g} (d_{xy} , d_{xz} and d_{yz}) bands. Lowering the symmetry from octahedral to tetragonal leads to splitting of the d_{xy} and the d_{xz}/d_{yz} bands (Figure 1b), characterized by the energy difference, Δt_{2g} . We have used this parameter to evaluate the lowering of dimensionality and the degeneracy of Nb-doped STO wafers through surface engineering. Furthermore, it was shown that increasing temperature causes a depletion of the 2DEG of STO [23] while reducing the orbital splitting, which can be further controlled by strain [26].

By combining Ar sputtering and vacuum annealing, we establish a vigorous

procedure to tune the 2DEG of STO (Fig.1c). Importantly, we report that the 2D d_{xy} subband emerges at a Sr-enriched surface, leading to a pure single-orbital 2DEG system. This electronic phase is found to be air-stable, offering an advantage for applications. Meanwhile, the band splitting between d_{xy} and d_{xz}/d_{yz} caused by ultraviolet (VUV) irradiations demonstrates that light can be used as a knob for tuning the band splitting (Δt_{2g}) and Lifshitz-like transition in the 2DEG system.

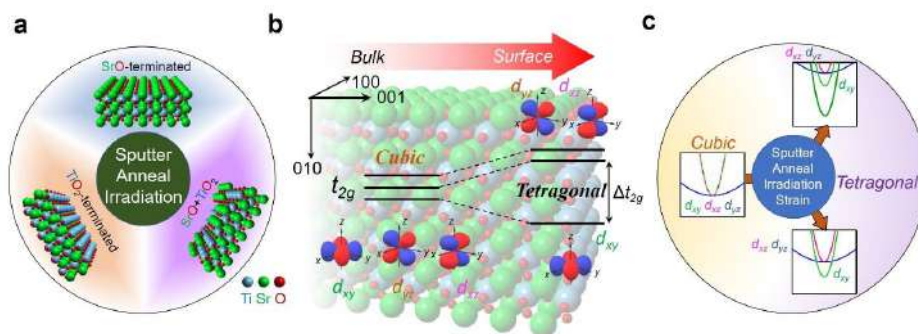


Figure 1. **a**, Schematic illustration of SrTiO₃ surfaces with three types of terminations, SrO-termination, TiO₂-termination and SrO+TiO₂-termination, respectively. **b**, Tetragonal crystal field splitting between d_{xy} and d_{xz}/d_{yz} bands, where Δt_{2g} marks the energy difference. **c**, Schematic illustration of the electronic structures of STO surfaces observed in our study.

Results and discussion

Band structures of surface-engineered STO

Figure 2 displays the electronic structures of STO single crystal (001) surfaces measured by ARPES after various preparation processes. The as-received STO samples are nominally TiO₂-terminated with 0.5% Nb doping (SurfaceNet GmbH). The characterizations of the “as-received” sample (stage #1) were performed by ARPES and XPS and used as reference. Subsequently, the sample was treated by Ar sputtering and annealing (stage #2: 5 minutes of Ar sputtering followed by annealing in ultra-high vacuum (UHV) at 700 °C for one hour). Afterward, we annealed the sample at 800 °C for 2 hours in UHV (stage #3). Both stages (#2 and #3) were studied by XPS and ARPES. The detailed surface preparation procedure is presented in the Methods section and in figure S1.

The ARPES data in Figure 2 were obtained using circular polarized (C+) light.

With such light polarization, both in-plane d_{xy} and out-of-plane d_{xz}/d_{yz} orbitals at the STO surface are probed [20-22], showing the evolution of the electronic structure during irradiation. Figures 2a-c display the electronic structures of STO in stages #1, #2, and #3 after 100 minutes of irradiation along the Γ - X crystal direction. Similar to previous ARPES studies on STO surfaces [14, 30-32], the electronic structures of as-received STO (#1) and high-temperature annealed STO (#3) after irradiation of $t_f \sim 1.6$ h show degenerate d_{xz} and d_{yz} bands and down-shifted d_{xy} subbands (Figure 2a,c). The band structure measurement of stage #2 (Figure 2b) shows that only one d_{xy} subband near the Γ point is occupied. This indicates an electronic transition from a multi-band (#1) to a single-band system (#2) and back (#3).

The band character of stages #1 to #3 is depicted by in-plane Fermi surfaces maps and k_z maps (Figure 2j-l). For stages #1 and #3 (Figure 2j,l), the in-plane Fermi surfaces (FSs) consist of one circular electron pocket and two intersecting ellipsoidal electron pockets centered at Γ , which are typical for the STO (001) surface [14, 30, 31]. The d_{yz} and d_{xz} bands for stages #1 and #3 exhibit quasi-3D characters, while the d_{xy} band shows two-dimensional (2D) character (Figure 2j,l). In contrast, stage #2 is characterized only by a single circular electron pocket around Γ (Figure 2k) with 2D character – i.e., without dispersion in the k_z direction (Figure 2k). The occupation of a single band was earlier reported in the LAO/STO [17] and STO systems [19, 27]. However, in the following section, we will discuss the origin and properties of the single d_{xy} band with pure 2D character found in stage #2.

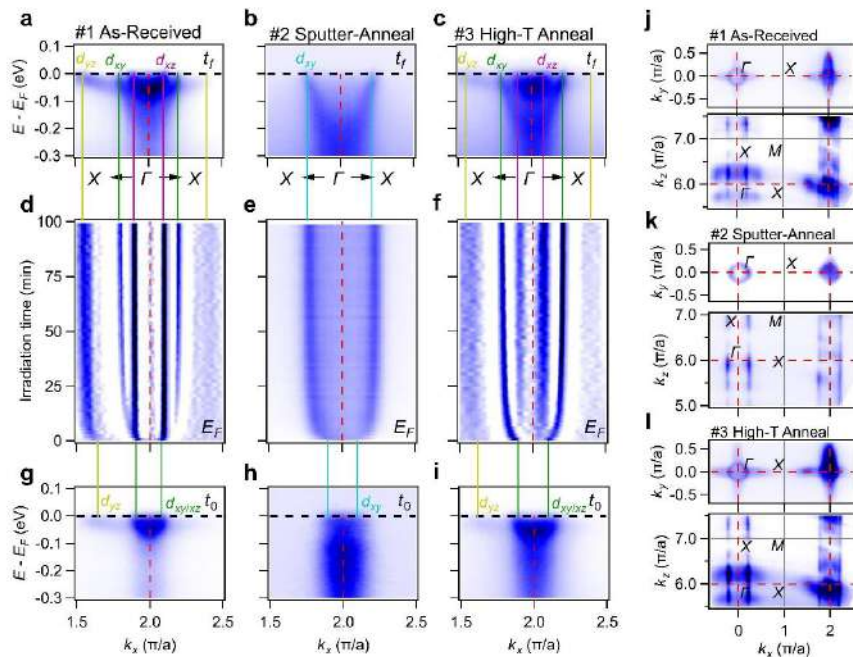


Figure 2. **a-c**, ARPES intensity cuts of as-received (stage #1), sputter-annealed (stage #2), and high temperature annealed (stage #3) STO wafers, respectively, after saturating the carrier density by irradiation (t_f). **d-f**, k -resolved ARPES maps at E_F of stages #1 to #3, respectively, as a function of VUV irradiation time. **e** is an intensity map, and **d,f** are horizontal 2nd derivative maps. **g-i**, ARPES intensity cuts of stages #1 to #3 measured at a fresh spot and acquired within 2 minutes of VUV-irradiation (t_0), respectively. Green, pink, cyan and yellow lines mark the k_F of d_{xy} , d_{xz} , d_{xy} in #2, and d_{yz} bands, respectively. **j-l**, Fermi surface maps of the ΓXY plane (upper) by in-plane mapping and the ΓXZ plane (lower) by $h\nu$ -dependent mapping of stage #1 to #3, respectively. Grey solid lines mark the BZ boundary and red dashed lines show the high-symmetry lines. Figure **a-i** and the upper panel of **j-l** are measured at 85 eV. All figures are measured with circular polarized (C+) light.

Reorganization of surface chemical composition and theoretical analyses

Figures 3a and 3b present XPS spectra of the STO sample in the three stages by measuring the Sr 3d and Ti 3p and Ti 2p core levels with photon energies in the VUV (170eV; surface sensitive) and soft X-ray (750 eV; more bulk sensitive) ranges. In the regions of the spectra where core-levels of Ti are situated, the peaks at $E_B \sim 38$ eV (3p) (Figure 3a) and at $E_B \sim 459$ eV (2p) (Figure 3b) are due to Ti^{4+} ions, while the peaks at

$E_B \sim 35$ eV and at $E_B \sim 457$ eV belong to the Ti^{3+} ions. The overall shape of Ti^{4+} is similar for all stages, while in stage #3 we have observed a minor amount of Ti^{3+} as compared to the other two (Figure 3b). Yet a remarkable transformation happens with Sr 3d core level of STO surface after sputtering and annealing (#2). While the data acquired by soft X-rays (Figure 3b) do not show the effect of the heat treatment, the VUV-XPS data reveals that the spectral weight of Sr at the surface is significantly raised (Figure 3a). Moreover, the same data show that the additional annealing (in #3) transforms the doublet peaks of the Sr 3d core level into a multippeak (at least two doublets) structure, indicating the presence of chemically distinct Sr species after surface rearrangement.

By comparing the spectral weight of Sr 3d and Ti 3p core levels using VUV light (surface sensitive) for stages #1 and #2, it is evident that surface treatment yields an increased Sr content. Interestingly, with additional annealing (stage #3), the opposite trend was observed: the spectral weight of Sr 3d decreases while the weight of Ti 3p increases. To quantify this effect, we use the ratio of Sr and Ti ($I_{\text{Sr}}/I_{\text{Ti}}$) spectral weight (integral one) of the three stages obtained from the VUV and soft X-ray data, as shown in Figure 3c. We set the Sr/Ti ratio of as-received STO (stage #1) to unity and normalized the other values to it. As a result, the ratio $I_{\text{Sr}}/I_{\text{Ti}}$ of the surface region (VUV-extracted) increases by about 50% from stage #1 to stage #2 and decreases in stage #3. In contrast, the ratio $I_{\text{Sr}}/I_{\text{Ti}}$ of the bulk-like region (soft X-ray extracted) remains nearly unchanged. The obtained results suggest that the surface preparation alters the surface chemical composition from a nominally TiO_2 -terminated surface (#1) to one with increased Sr content (#2). Additional annealing seems to restore the TiO_2 termination. S. N. Rebec et al. reported that the SrO layer deposited on TiO_2 -terminated STO yields a similar one-band electronic feature [27]. Furthermore, the same study showed that the $I_{\text{Sr}}/I_{\text{Ti}}$ ratio also increases around 50% for the SrO-capped sample [27], similar to our result presented in Figure 3c. All of these outcomes indicate that the surface chemical composition is crucial for modulating the electronic structures of STO surface.

To resolve the link between the STO surface composition and the band reconstruction, we employ theoretical calculations of TiO_2 - and SrO- terminated STO to emulate the two possible final derivatives of surface preparation (Figure 3d,e). For the TiO_2 -terminated STO slab, the calculation shows that the band splitting (Δt_{2g}) between d_{xy} band bottom and d_{yz}/d_{xz} band bottom is negligible (Figure 3f). This outcome is, indeed, in good agreement with band structures observed in stage #1 at t_0 (Figure

3h), indicating that the cubic symmetry is mostly preserved. In contrast, the calculations for SrO-terminated slabs show that the d_{xy} band (derived from the first TiO₂ layer under SrO surface layer, which is highlighted in Figure 3g) shifts downward with ~ 150 meV, generating the splitting of t_{2g} bands with tetragonal symmetry. Indeed, the ARPES data for stage #2 (t_0) reveals this type of 2D band, which is slightly shallower than the calculated one (Figure 3i). A possible explanation of this deviation is the larger effective mass of the observed band (t_0) caused by the strong EPI, which was not considered in the theoretical calculations. When the E_F is set according to the experimental k_F (Figure 3h, i), only the surface d_{xy} band crosses E_F for #2, while the other t_{2g} bands remain unoccupied, hence showing that a single-band state arises in stage #2.

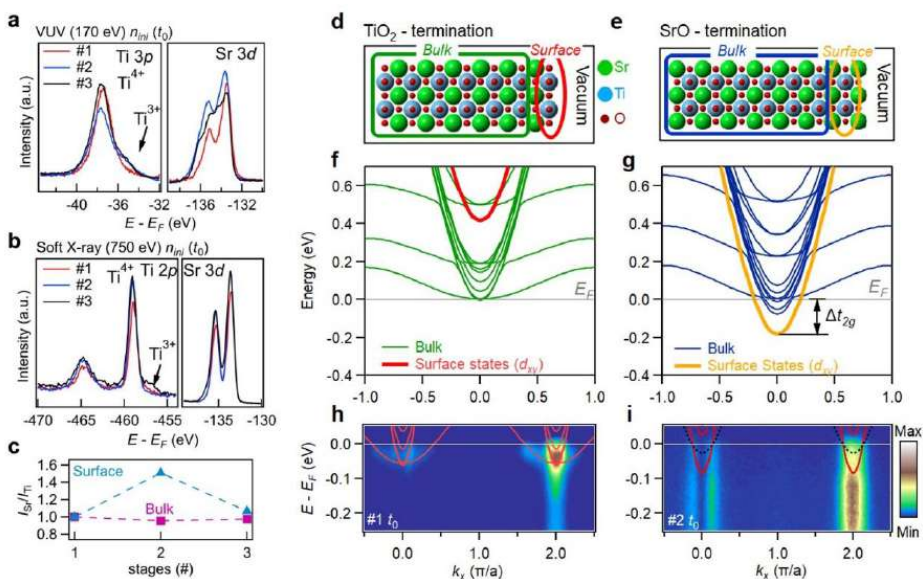


Figure 3. **a,b** Core-level of Ti 3*p* and Sr 3*d* orbitals measured at $h\nu=170$ eV at the initial carrier density of the three stages (t_0). **b**, Core-level of Ti 2*p* and Sr 3*d* orbitals measured at 750 eV at the initial carrier densities of the three stages (t_0). **c**, Calculated spectral weight ratio of Sr/Ti extracted from **a** and **b**, and normalized to the ratio of the as-received STO wafer (#1). **d-e**, Relaxed $2 \times 2 \times 7$ STO slabs of TiO₂-termination and SrO-termination, respectively. Red/orange ellipses and dark green/blue squares mark the superficial TiO₂ layer and the bulk of two models, respectively. Green, blue, and red spheres represent the Sr, Ti, and O atoms, respectively. **f,g**, Calculated electronic band structures of TiO₂- and SrO- terminated STO models as presented in **a** and **b**,

respectively. The red and orange curve in **f** and **g** highlights the d_{xy} band from the first TiO₂ layer. **h,i**, ARPES intensity cuts of as-received (#1) and sputter-annealed (#2) STO wafer at t_0 , plotted with calculated band structures in **f** and **g**, respectively. The dashed black curves in **f** show the fitted d_{xy} bands.

Intriguingly, a recent study of SrO-capped STO systems exhibits the absence of electronic states near E_F [33]. This lack can arise due to the surface insensitive nature of soft X-ray incident light used for this study, which is unfavorable to detecting the d_{xy} surface band in Sr-enriched STO. However, our ARPES and DFT data validate that the formed Sr-enriched STO (001) surface is characterized by the intrinsic splitting of the t_{2g} states and the surface state, causing a pure 2D electronic structure. Therefore, the surface state with d_{xy} character, which is first occupied when the system is doped, should be considered the main component of the 2DEG system [27,28,34].

Wedge-potential in STO

One of the key parameters of the STO band structures, shown in Figure 2, is the splitting of the d_{xy} and d_{xz}/d_{yz} bands (Δt_{2g}). E. B. Guedes et al., by combining DFT calculation and ARPES, established the link between atomic displacements of STO surface layers and Δt_{2g} [23]. However, the trapped photo-generated electrons during APRES experiments can cause lattice distortion while free ones yield the electric field. Indeed, Δt_{2g} alters during beam irradiation (Figure 2d,f) and directly correlates to carrier density.

Starting as a degenerate system (Figures 2g,i), the d_{xy} and d_{xz}/d_{yz} bands separate (Figure 2d, f) later during irradiation, resulting in 3D d_{xz}/d_{yz} bands and 2D d_{xy} subbands (Figure 2a and Figure 2c). The extracted Fermi momenta (k_F) and the energy splitting between d_{xy} and d_{xz}/d_{yz} bands (Δt_{2g}) as a function of irradiation time illustrate this process more clearly (see also Figure S3f). It has been extensively discussed in the literature that the STO-based 2DEG system experiences a wedge-like potential within the surface region [30, 35, 36]. This potential at the STO surface can be described using a quantum well model with the form, $V(z)=V_0+eFz$, where F is the strength of the electric field in the direction perpendicular to the sample surface, and e is the charge of the electron (Figure 4a). The quantized eigenenergies (E_n) of subbands at the surface region can be described by the equation 1[30, 36]:

$$E_n = V_0 + \left(\frac{\hbar}{2m_z^*}\right)^{1/3} \left[\left(\frac{3\pi}{2}\right)\left(n - \frac{1}{4}\right)eF\right]^{2/3} \quad \text{Eq. 1}$$

where m_z^* is the effective mass along the field direction (perpendicular to the surface).

The band splitting of t_{2g} bands, Δt_{2g} , can be calculated by the difference between the $n=1$ eigenenergies of d_{xy} and d_{xz}/d_{yz} bands as $\Delta t_{2g} = E_{1^{xy}} - E_{1^{xz/yz}}$ in the following way:

$$\Delta t_{2g} = 7.5 \times 10^{-7} \left[\left(\frac{m_e}{m_z^{*xz/yz}}\right)^{1/3} - \left(\frac{m_e}{m_z^{*xy}}\right)^{1/3} \right] F^{2/3} \quad \text{Eq. 2}$$

The relationship between F and the carrier density (n_{2D}) can be describe in the following way [36]:

$$\frac{e}{2} n_{2D} = \int_0^F \varepsilon_0 \varepsilon_r(F') dF' \quad \text{Eq. 3}$$

(ε_0 : the vacuum dielectric constant; $\varepsilon_r(F)$: is field-dependent dielectric constant of STO) From Eq. 3 it is possible to extract the electric field by using the carrier densities of each band taken from the ARPES data (See Figure S3 f,g, and Supplementary Sec. III). The effective mass m_z^* of d_{xy} and d_{xz}/d_{yz} bands can also be estimated by ARPES.

Figure 4b shows the calculated and experimental values of Δt_{2g} of stages #1 and #3 as a function of the carrier density, n_{2D} . The agreement between the observed and calculated values of Δt_{2g} indicates that the electric field (F or $\varepsilon_r(F)$) is caused by the accumulation of charges at the surface during the irradiation process.

All outcomes above and the results reported by E.B. Guedes [23], imply that the lattice distortion (stabilized by trapped electrons) cooperates vigorously with the field (generated by free electrons), conducting to the common properties of the 2DEG at the STO surface.

EPI and effective mass

The waterfall-like feature identified as an incoherent part of the band dispersion (see Figure 2g-h) is usually attributed to the polaronic electron-phonon interaction (EPI) in STO, which plays an essential role in modulating the physical properties of the 2DEG [37-39]. The EPI can be quantified by the quasi-particle (QP) residue, $Z_0 = I_{QP} / (I_{QP} + I_{hump})$, where the $I_{QP/hump}$ represents the integrated spectral weight of QP/hump of corresponding energy distribution curves (EDCs) [39,40].

Figure 4c displays the background-subtracted EDCs of stages #1-3 taken at the k_F of the d_{xy} bands for different carrier densities, $n(t)$, normalized by the QP peak's intensity. The peak-dip-hump line shape, which extends to higher binding energy (Figure 4c), relates to the multiple phonon modes interacting with electrons [39,40]. However, the EPI at t_0 (red curves in Figure 4c), related to intrinsic transport properties, exhibits a significant increase for stage #2 (a reduction of Z_0 from 0.55 in #1 to 0.15 in #2) and partially recovers after the sample has been additionally annealed ($Z_0 \sim 0.35$ in #3). Therefore, besides changes in the band topology (see Figure 2), surface engineering also modifies the EPI strength, affecting the carrier properties such as the effective mass, m^* (from $0.6m_e$ in #1 to $1.8m_e$ in #2, and $0.8m_e$ in #3, See Figure S5). Figure 4d shows the EPI strength (through Z_0) as a function of the carrier densities of d_{xy} bands. The positive (negative) Z_0 (EPI) behavior for different carrier densities is probably due to the screening suppressing the long-range Fröhlich polaron interaction [37,39]. It is important to note that the spectral weight of the peak-dip-hump structures undergoes a continuous decrease during irradiation, indicating a weakening of the EPI for all stages (#1 to #3).

In weak coupling and long-range electron-phonon interactions, the relationship between effective mass and quasiparticle residue (Z_0) is defined by the Fröhlich model, where the effective mass of the electrons is enhanced due to EPI: $m^*/m_0 = 1/(1-\alpha/6)$, m_0 is the bare band mass, and α is the coupling strength [41,42], which can be estimated from Z_0 by a diagrammatic quantum Monte Carlo study (presented in Figure 4d with gradient background and the right axis) [43]. In Figure 4e, we plot both effective mass fitted from band dispersion (fitting details are presented in Supplementary Section III and IV) and calculated one from Z_0 by weak-coupling Fröhlich model of stages #1 as a function of carrier density. Our data show good agreement between the fitted m^* and calculated values for stages #1 and #3 for all observed carrier densities. However, for stage #2 this concurrence is valid only for the high doping regime, which is consistent with the weak coupling regime (See Figure 4d, and more details are shown in Figure S6). For the low-doping regime of stage #2, with $Z_0 < 0.3$ and $\alpha > 3$ (Figure 4d), a strong coupling model we used for the approximation established by R. P. Feynman [44], $m^*/m_0 = 0.0232\alpha^4$, which reproduces the effective mass more appropriately, as shown in Figure 4e.

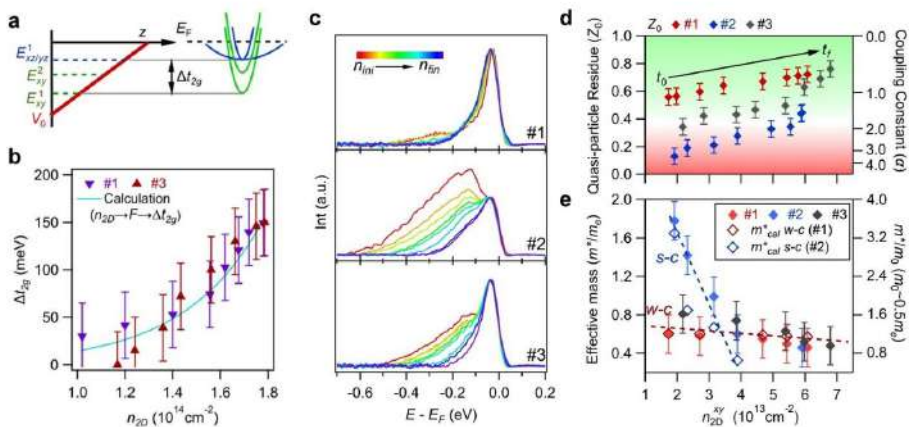


Figure 4. **a**, Wedge potential and band structure at the surface of STO. **b**, Calculated energy differences between d_{xy} and d_{xz}/d_{yz} bands (Δt_{2g}) as a function of carrier density, and experimental Δt_{2g} extracted from ARPES data of stage #1 and #3. **c**, Energy distribution curves of stage #1 to #3 at different carrier densities at $k=k_F^{xy}$. **d**, Calculated quasiparticle residue (Z_0) from the EDCs (presented in panel **a**) as a function of carrier density of d_{xy} bands, n_{2D}^{xy} . The gradient background and right axis indicate the transition between weak (light green) to strong (light red) coupling strength (reproduced from ref. 42). **e**, Fitted effective masses of d_{xy} bands of all three stages as a function of n_{2D}^{xy} . The empty marks represent the calculated effective mass from coupling strength (α) by weak-coupling, $m^*/m_0=1/(1-\alpha/6)$, and strong coupling, $m^*/m_0=0.0232\alpha^4$, of Fröhlich polarons, respectively.

Our data and analyses in Figures 4e and 4d show that the EPI transit from the weak-coupling (stage #1) to the strong-coupling regime (stage #2). Further, the verified inverse relation between the EPI strength and the effective mass of all three stages shows the softening of polarons caused by increasing carrier densities [37].

Summary and Outlook

Employing systematic XPS measurements, we show that combining Ar sputtering and UHV annealing modifies the STO chemical composition, transforming nominally TiO_2 -terminated to SrO-enriched surface. Utilizing ARPES and DFT calculations validates that the formed Sr-enriched STO (001) surface is characterized by the intrinsic splitting of the t_{2g} states while the d_{xy} surface state yields a pure 2D electronic structure.

The observed single-band electronic phase is air-stable (Supplementary, Sec.II), showing the potential to service in designing novel devices.

The additional UHV annealing at moderate temperature eradicates Sr from the surface and partially recovers the nominally TiO₂-terminated character, leading to the Lifshitz-like transition in STO (from one band to three bands metallicity).

Our work describes a straightforward method for varying the surface chemical composition, which, combined with VUV-irradiation, efficiently modulates the electronic structures of the t_{2g} band, doping, and electron-phonon interaction in STO.

METHODS

Sample Preparation

In this study, as-received commercially available 0.5% Nb doped nominally TiO₂-terminated SrTiO₃ wafers (SurfaceNet GmbH) are used with a miscut within 0.2° to the nominal (001) surface.

During ARPES measurements, multiple surface engineering procedures are applied to the as-received STO wafer, including sputtering and annealing. The sputtering process is conducted under an argon atmosphere with a pressure of 2×10^{-6} mbar. The voltage is set as 1kV and the STO wafers are 45° facing the ion beam. The vacuum annealing process is conducted under an ultra-high vacuum better than 2×10^{-8} mbar. The annealing temperatures are read through an infrared thermometer. The detailed sample treatment routes are shown in Supplementary, Sec. I. In our studies, we reproduce similar results of band modulation in at least another three samples, which are shown in Supplementary Sec. V.

Angle-resolved photoemission spectroscopy

All the ARPES and XPS data presented were measured at the ULTRA endstation at the Surface/Interface Spectroscopy (SIS) beamline of the Swiss Light Source. The data were acquired with a Scienta Omicron DA30L hemispherical analyzer. The energy and angular resolution are better than 20 meV and 0.1°. The measurements were performed at a temperature of 20 K in a base pressure better than 1×10^{-10} Torr. The un-irradiated results are measured by moving the samples to un-irradiated areas.

DFT calculation

The density functional theory calculations were performed within the Perdew–Burke–Ernzerhof generalized gradient approximation (PBE-GGA) [45], using projector augmented wave (PAW) potentials [46], as implemented in the Vienna *ab initio* Simulation Package (VASP) [47,48]. In addition, the DFT+U functional of Liechtenstein et al. [49] was employed with $U = 5$ eV and $J = 0.64$ eV, as similarly performed in ref. [50]. A basis set of 500 eV were used, and the structures were relaxed until the forces on atoms were less than $0.01 \text{ eV}\text{\AA}^{-1}$. The relaxation of the atomic positions was done using a $4 \times 4 \times 1$ k-mesh, whereas the band structures were evaluated using an $8 \times 8 \times 2$ k-points set.

Acknowledgements

This work was supported by the Swiss National Science Foundation (SNF), No. 200021_182695 and No. 200021_188413. W.H.B acknowledges the support from the Brazilian agencies CNPq, FAPEMIG, and CAPES, as well as the CENAPAD-SP, CESUP (UFRGS), and the National Laboratory for Scientific Computing (LNCC/MCTI, Brazil) for providing HPC resources of the SDumont supercomputer, which have contributed to the research results, URL: <http://sdumont.lncc.br>.

Author contributions

M.R. designed the concept and experiments with N.P. and H.L. H.L., E.B.G. A.C. and M.R. performed the ARPES experiment with the help from R.T.D., N.C.P. and M.S. W.H.B. performed the DFT calculations. H. L. processed the ARPES data. H.L. and M.R. wrote the manuscript assisted by E.B.G and A.C and with the help and useful discussions with all other authors.

Competing interests: The authors declare that they have no competing interests.

Data and materials availability: All data needed to evaluate the conclusions in the paper are present in the paper and/or the Supplementary Materials. Materials and additional data related to this paper may be requested from the authors.

References

- [1] N. Reyren, S. Thiel, A. D. Caviglia, L. Fitting Kourkoutis, G. Hammerl, C. Richter, C. W. Schneider, T. Kopp, A.-S. Rüetschi, D. Jaccard, M. Gabay, D. A. Müller, J. M. Triscone, J. Mannhart, Superconducting interfaces between insulating oxides, *Science* **317**, 1196 (2007).
- [2] A. D. Caviglia, S. Gariglio, N. Reyren, D. Jaccard, T. Schneider, M. Gabay, S. Thiel, G. Hammerl, J. Mannhart, J. M. Triscone, Electric field control of the LaAlO₃/SrTiO₃ interface ground state, *Nature* **456**, 624 (2008).
- [3] A. Joshua, S. Pecker, J. Ruhman, E. Altman, S. Ilani, A universal critical density underlying the physics of electrons at the LaAlO₃/SrTiO₃ interface, *Nat. Commun.* **3**, 1129 (2012).
- [4] G. E. D. K. Prawiroatmodjo, F. Trier, D. V. Christensen, Y. Chen, N. Pryds, T. S. Jespersen, Evidence of weak superconductivity at the room-temperature grown LaAlO₃/SrTiO₃ interface, *Phys. Rev. B* **93**, 184504 (2016).
- [5] G. Herranz, G. Singh, N. Bergeal, A. Jouan, J. Lesueur, J. Gazquez, M. Varela, M. Scigaj, N. Dix, F. Sanchez, J. Fontcuberta, Engineering two-dimensional superconductivity and Rashba spin-orbit coupling in LaAlO₃/SrTiO₃ quantum wells by selective orbital occupancy, *Nat. Commun.* **6**, 6028 (2015).
- [6] A. Brinkman, M. Huijben, M. van Zalk, J. Huijben, U. Zeitler, J. C. Maan, W. G. van der Wiel, G. Rijnders, D. H. Blank, H. Hilgenkamp, Magnetic effects at the interface between non-magnetic oxides, *Nat. Mater.* **6**, 493 (2007).
- [7] B. Kalisky, J. A. Bert, B. B. Klopfer, C. Bell, H. K. Sato, M. Hosoda, Y. Hikita, H. Y. Hwang, K. A. Moler, Critical thickness for ferromagnetism in LaAlO₃/SrTiO₃ heterostructures, *Nat. Commun.* **3**, 922 (2012).
- [8] F. Bi, M. Huang, S. Ryu, H. Lee, C. W. Bark, C. B. Eom, P. Irvin, J. Levy, Room-temperature electronically-controlled ferromagnetism at the LaAlO₃/SrTiO₃ interface, *Nat. Commun.* **5**, 5019 (2014).
- [9] D. V. Christensen, Y. Frenkel, Y. Z. Chen, Y. W. Xie, Z. Y. Chen, Y. Hikita, A. Smith, L. Klein, H. Y. Hwang, N. Pryds, and B. Kalisky, Strain-tunable magnetism at oxide domain walls, *Nat. Phys.* **15**, 269 (2019).
- [10] A. D. Caviglia, M. Gabay, S. Gariglio, N. Reyren, C. Cancellieri, J.-M. Triscone, Tunable Rashba Spin-Orbit Interaction at Oxide Interfaces. *Phys. Rev. Lett.* **104**, 126803 (2010).

- [11] Yulin Gan, Yu Zhang, Dennis Valbjørn Christensen, Nini Pryds, and Yunzhong Chen, Gate-tunable Rashba spin-orbit coupling and spin polarization at diluted oxide interfaces, *Phys. Rev. B* **100**, 125134 (2019).
- [12] Felix Trier, Guenevere E. D. K. Prawiroatmodjo, Zhicheng Zhong, Dennis Valbjørn Christensen, Merlin von Soosten, Arghya Bhowmik, Juan Maria García Lastra, Yunzhong Chen, Thomas Sand Jespersen, and Nini Pryds, Quantization of Hall Resistance at the Metallic Interface between an Oxide Insulator and SrTiO₃, *Phys. Rev. Lett.* **117**, 096804 (2016).
- [13] Y. Matsubara, K. S. Takahashi, M. S. Bahramy, Y. Kozuka, D. Maryenko, J. Falson, A. Tsukazaki, Y. Tokura & M. Kawasaki, Observation of the quantum Hall effect in δ -doped SrTiO₃, *Nat. Commun.* **7**, 11631 (2016).
- [14] N. C. Plumb, M. Salluzzo, E. Razzoli, M. Månsson, M. Falub, J. Krempasky, C. E. Matt, J. Chang, M. Schulte, J. Braun, H. Ebert, J. Minár, B. Delley, K.-J. Zhou, T. Schmitt, M. Shi, J. Mesot, L. Patthey, and M. Radović, Mixed Dimensionality of Confined Conducting Electrons in the Surface Region of SrTiO₃, *Phys. Rev. Lett.* **113** 086801 (2014).
- [15] Y. Z. Chen, N. Bovet, F. Trier, D. V. Christensen, F. M. Qu, N. H. Andersen, T. Kasama, W. Zhang, R. Giraud, J. Dufouleur, T. S. Jespersen, J. R. Sun, A. Smith, J. Nygård, L. Lu, B. Büchner, B. G. Shen, S. Linderoth, and N. Pryds, A high-mobility two-dimensional electron gas at the spinel/perovskite interface of γ -Al₂O₃/SrTiO₃, *Nat. Commun.* **4**, 1371 (2013).
- [16] Alla Chikina, Dennis V. Christensen, Vladislav Borisov, Marius-Adrian Husanu, Yunzhong Chen, Xiaoqiang Wang, Thorsten Schmitt, Milan Radovic, Naoto Nagaosa, Andrey S. Mishchenko, Roser Valentí, Nini Pryds, and Vladimir N. Strocov, Band-Order Anomaly at the γ -Al₂O₃/SrTiO₃ Interface Drives the Electron-Mobility Boost, *ACS Nano* **15**, 4347-4356 (2021).
- [17] Yulin Gan, Dennis Valbjørn Christensen, Yu Zhang, Hongrui Zhang, Dileep Krishnan, Zhicheng Zhong, Wei Niu, Damon James Carrad, Kion Norrman, Merlin von Soosten, Thomas Sand Jespersen, Baogen Shen, Nicolas Gauquelin, Johan Verbeeck, Jirong Sun, Nini Pryds, Yunzhong Chen, Diluted Oxide Interfaces with Tunable Ground States, *Adv. Mater.* **31**, 1805970 (2019).
- [18] A. F. Santander-Syro, F. Fortuna, C. Bareille, T. C. Rödel, G. Landolt, N. C. Plumb, J. H. Dil & M. Radović, Giant spin splitting of the two-dimensional electron gas at the surface of SrTiO₃, *Nat. Mater.* **13** 1085 (2014).

- [19] Eduardo B. Guedes, Stefan Muff, Mauro Fanciulli, Andrew P. Weber, Marco Caputo, Zhiming Wang, Nicholas C. Plumb, Milan Radovic, and J. Hugo Dil, Single spin-polarized Fermi surface in SrTiO₃ thin films, *Phys. Rev. Research*, **3**, 033173 (2020).
- [20] Z. Salman, R. F. Kiefl, K. H. Chow, M. D. Hossain, T. A. Keeler, S. R. Kreitzman, C. D. P. Levy, R. I. Miller, T. J. Parolin, M. R. Pearson, H. Saadaoui, J. D. Schultz, M. Smadella, D. Wang, W. A. MacFarlane, Near-Surface Structural Phase Transition of SrTiO₃ Studied with Zero-Field β -Detected Nuclear Spin Relaxation and Resonance, *Phys. Rev. Lett.* **96**, 147601 (2006).
- [21] M. Smadella, Z. Salman, K. Chow, M. Egilmez, I. Fan, M. Hossain, R. Kiefl, S. Kreitzman, C. Levy, W. MacFarlane, A. Mansour, G. Morris, T. Parolin, M. Pearson, H. Saadaoui, Q. Song, D. Wang, Surface dependent structural phase transition in SrTiO₃ observed with spin relaxation of ⁸Li, *Phys. B: Cond. Matter* **404**, 924 (2009).
- [22] Z. Salman, M. Smadella, W. A. MacFarlane, B. D. Patterson, P. R. Willmott, K. H. Chow, M. D. Hossain, H. Saadaoui, D. Wang, R. F. Kiefl, Depth dependence of the structural phase transition of SrTiO₃ studied with β -NMR and grazing incidence x-ray diffraction, *Phys. Rev. B* **83**, 224112 (2011).
- [23] Eduardo B. Guedes, Stefan Muff, Walber H. Brito, Marco Caputo, Hang Li, Nicholas C. Plumb, J. Hugo Dil, Milan Radović, Universal Structural Influence on the 2D Electron Gas at SrTiO₃ Surfaces, *Adv. Sci.* 2021, 8, 2100602 (2021).
- [24] B. Burganov, C. Adamo, A. Mulder, M. Uchida, P. D. C. King, J. W. Harter, D. E. Shai, A. S. Gibbs, A. P. Mackenzie, R. Uecker, M. Bruetzam, M. R. Beasley, C. J. Fennie, D. G. Schlom, and K. M. Shen, Strain Control of Fermiology and Many-Body Interactions in Two-Dimensional Ruthenates, *Phys. Rev. Lett.* **116**, 197003 (2016).
- [25] B. Jalan, S. J. Allen, G. E. Beltz, P. Moetakef, and S. Stemmer, Enhancing the electron mobility of SrTiO₃ with strain, *Appl. Phys. Lett.* **98**, 132102 (2011).
- [26] Eduardo Bonini Guedes, Tobias Willemoes Jensen, Muntaser Naamneh, Alla Chikina, Ramus T. Dahm, Shinhee Yun, Francesco M. Chiabrera, Nicholas C. Plumb, J. Hugo Dil, Ming Shi, Dennis Valbjørn Christensen, Walber Hugo Brito, Nini Pryds, and Milan Radović, Disclosing the response of the surface electronic structure in SrTiO₃ (001) to strain, *J. Vac. Sci. Technol. A* **40**, 013213 (2022).
- [27] S. N. Rebec, T. Jia, H. M. Sohail, M. Hashimoto, D. Lu, Z.-X. Shen, and R. G. Moore, Dichotomy of the photo-induced 2-dimensional electron gas on

- SrTiO₃ surface terminations, *Proc. Natl. Acad. Sci. U.S.A.* **116**, 16687 (2019).
- [28] E. B. Guedes, S. Muff, M. Fanciulli, A. P. Weber, M. Caputo, Z. Wang, N. C. Plumb, M. Radović, and J. H. Dil, Single spin-polarized Fermi surface in SrTiO₃ thin films, *Phys. Rev. Res.* **2**, 033173 (2020).
- [29] M. Radović, N. Lampis, F. M. Granozio, P. Perna, Z. Ristic, M. Salluzzo, C. M. Schlepütz, and U. Scotti di Uccio, Growth and characterization of stable SrO-terminated SrTiO₃ surfaces, *Appl. Phys. Lett.* **94**, 022901 (2009).
- [30] A. F. Santander-Syro, O. Copie, T. Kondo, F. Fortuna, S. Pailhès, R. Weht, X. G. Qiu, F. Bertran, A. Nicolaou, A. Taleb-Ibrahimi, P. L. Fèvre, G. Herranz, M. Bibes, N. Reyren, Y. Apertet, P. Lecoeur, A. Barthélémy, M. J. Rozenberg, Two-dimensional electron gas with universal subbands at the surface of SrTiO₃, *Nature* **469**, 189 (2011).
- [31] W. Meevasana, P. D. C. King, R. H. He, S.-K. Mo, M. Hashimoto, A. Tamai, P. Songsirithigul, F. Baumberger, Z.-X. Shen, Creation and control of a two-dimensional electron liquid at the bare SrTiO₃ surface, *Nat. Mater.* **10**, 114 (2011).
- [32] N. C. Plumb, M. Kobayashi, M. Salluzzo, E. Razzoli, C. E. Matt, V. N. Strocov, K. J. Zhou, M. Shi, J. Mesot, T. Schmitt, L. Patthey, M. Radović, Evolution of the SrTiO₃ surface electronic state as a function of LaAlO₃ overlayer thickness, *Appl. Surf. Sci.* **412** 271–8 (2017).
- [33] Xi Yan, Friederike Wrobel, I-Cheng Tung, Hua Zhou, Hawoong Hong, Fanny Rodolakis, Anand Bhattacharya, Jessica L. McChesney, Dillon D. Fong, Origin of the 2D Electron Gas at the SrTiO₃ Surface, *Adv. Mater.* 2200866 (2022).
- [34] P. Delugas, V. Fiorentini, A. Mattoni, A. Filippetti, Intrinsic origin of two-dimensional electron gas at the (001) surface of SrTiO₃, *Phys. Rev. B* **91**, 115315 (2015).
- [35] Ando, T., Fowler, A. B. & Stern, F. Electronic properties of two-dimensional systems. *Rev. Mod. Phys.* **54**, 437-672 (1982).
- [36] K. Ueno, S. Nakamura, H. Shimotani, A. Ohtomo, N. Kimura, T. Nojima, H. Aoki, Y. Iwasa, and M. Kawasaki, Electric-field-induced superconductivity in an insulator, *Nat. Mater.* **7**, 855 (2008).
- [37] D. V. Christensen, Y. Frenkel, P. Schütz, F. Trier, S. Wissberg, Claessen, Kalisky, Smith, Y. Z. Chen, and N. Pryds, Electron Mobility in γ -Al₂O₃/SrTiO₃, *Phys. Rev. Appl.* **9**, 054004 (2018).
- [38] Chaoyu Chen, Jose Avila, Emmanouil Frantzeskakis, Anna Levy & Maria C.

- Asensio, Observation of a two-dimensional liquid of Fröhlich polarons at the bare SrTiO₃ surface, *Nat. Commun.* **6**, 8585 (2014).
- [39] Z. Wang, S. McKeown Walker, A. Tamai, Y. Wang, Z. Ristic, F. Y. Bruno, A. de la Torre, S. Riccò, N. C. Plumb, M. Shi, P. Hlawenka, J. Sánchez-Barriga, A. Varykhalov, T. K. Kim, M. Hoesch, P. D. C. King, W. Meevasana, U. Diebold, J. Mesot, B. Moritz, T. P. Devereaux, M. Radovic and F. Baumberger, Tailoring the nature and strength of electron–phonon interactions in the SrTiO₃ (001) 2D electron liquid, *Nat. Mater.* **15** 835–9 (2016).
- [40] C. Cancellieri, A. S. Mishchenko, U. Aschauer, A. Filippetti, C. Faber, O. S. Barišić, V. A. Rogalev, T. Schmitt, N. Nagaosa, V. N. Strocov, Polaronic Metal State at the LaAlO₃/SrTiO₃ Interface. *Nat. Commun.* **7**, 10386 (2016).
- [41] H. Fröhlich, H. Pelzer & S. Zienau, Properties of slow electrons in polar materials, *Phil. Mag.* **41**, 221 (1950).
- [42] Jozef T Devreese and Alexandre S Alexandrov, Fröhlich polaron and bipolaron: recent developments *Rep. Prog. Phys.* **72**, 066501 (2009).
- [43] A. S. Mishchenko, N. V. Prokof'ev, A. Sakamoto, and B. V. Svistunov, Diagrammatic quantum Monte Carlo study of the Fröhlich polaron, *Phys. Rev. B* **62**, 6317 (2000).
- [44] R. P. Feynman, Slow electron in a polar crystal, *Phys. Rev.* **92**, 660 (1955).
- [45] J. P. Perdew, K. Burke, M. Ernzerhof, Generalized Gradient Approximation Made Simple, *Phys. Rev. Lett.* **77**, 3865 (1996).
- [46] P. E. Blüchl, Projector augmented-wave method, *Phys. Rev. B* **50**, 17953 (1994).
- [47] G. Kresse, J. Furthmüller, Efficiency of ab-initio total energy calculations for metals and semiconductors using a plane-wave basis set, *Comput. Mater. Sci.* **6**, 15 (1996).
- [48] G. Kresse, J. Furthmüller, Efficient iterative schemes for *ab initio* total-energy calculations using a plane-wave basis set, *Phys. Rev. B* **54**, 11169 (1996).
- [49] A. I. Liechtenstein, V. I. Anisimov, J. Zaanen, Density-functional theory and strong interactions: Orbital ordering in Mott-Hubbard insulators, *Phys. Rev. B* **52**, R5467 (R) (1995).
- [50] J. Shen, H. Lee, R. Valentí, H. O. Jeschke, Ab initio study of the two-dimensional metallic state at the surface of SrTiO₃: Importance of oxygen vacancies, *Phys. Rev. B* **86**, 195119 (2012).

Bibliography

1. Haeni, J. H. *et al.* Room-temperature ferroelectricity in strained SrTiO₃. *Nature* **430**, 758–761 (2004).
2. Klyukin, K. & Alexandrov, V. Effect of intrinsic point defects on ferroelectric polarization behavior of SrTiO₃. *Phys Rev B* **95**, 35301 (2017).
3. Yang, F. *et al.* Room-temperature ferroelectricity of SrTiO₃ films modulated by cation concentration. *Appl Phys Lett* **107**, 82904 (2015).
4. Kim, Y. S. *et al.* Defect-related room-temperature ferroelectricity in tensile-strained SrTiO₃ thin films on GdScO₃ (110) substrates. *Appl Phys Lett* **97**, 242907 (2010).
5. Rice, W. D. *et al.* Persistent optically induced magnetism in oxygen-deficient strontium titanate. *Nat Mater* **13**, 481–487 (2014).
6. Christensen, D. v *et al.* Strain-tunable magnetism at oxide domain walls. *Nat Phys* **15**, 269–274 (2019).
7. Kalisky, B. *et al.* Scanning probe manipulation of magnetism at the LaAlO₃/SrTiO₃ heterointerface. *Nano Lett* **12**, 4055–4059 (2012).
8. Park, D.-S. *et al.* The emergence of magnetic ordering at complex oxide interfaces tuned by defects. *Nat Commun* **11**, 1–9 (2020).
9. Brinkman, A. *et al.* Magnetic effects at the interface between non-magnetic oxides. *Nat Mater* **6**, 493–496 (2007).
10. Zhang, H. H. *et al.* Magnetic two-dimensional electron gases with high Curie temperatures at LaAlO₃/SrTiO₃: Fe interfaces. *Phys Rev B* **97**, 155150 (2018).
11. Mardegan, J. R. L. *et al.* Magnetic and electronic properties at the γ -Al₂O₃/SrTiO₃ interface. *Phys Rev B* **99**, 134423 (2019).
12. Ederer, C. & Spaldin, N. A. A new route to magnetic ferroelectrics. *Nat Mater* **3**, 849–851 (2004).
13. Efremov, D. v, van den Brink, J. & Khomskii, D. I. Bond-versus site-centred ordering and possible ferroelectricity in manganites. *Nat Mater* **3**, 853–856 (2004).
14. Zheng, H. *et al.* Multiferroic BaTiO₃-CoFe₂O₄ nanostructures. *Science (1979)* **303**, 661–663 (2004).
15. Schilling, A., Cantoni, M., Guo, J. D. & Ott, H. R. Superconductivity above 130 K in the Hg-Ba-Ca-Cu-O system. *Nature* **363**, 56–58 (1993).
16. Seri, S. & Klein, L. Antisymmetric magnetoresistance of the SrTiO₃/LaAlO₃ interface. *Phys Rev B* **80**, 180410 (2009).
17. Wang, X. *et al.* Magnetoresistance of two-dimensional and three-dimensional electron gas in LaAlO₃/SrTiO₃ heterostructures: Influence of magnetic ordering, interface scattering, and dimensionality. *Phys Rev B* **84**, 75312 (2011).

18. Dagotto, E., Hotta, T. & Moreo, A. Colossal magnetoresistant materials: the key role of phase separation. *Phys Rep* **344**, 1–153 (2001).
19. Uehara, M., Mori, S., Chen, C. H. & Cheong, S.-W. Percolative phase separation underlies colossal magnetoresistance in mixed-valent manganites. *Nature* **399**, 560–563 (1999).
20. Thiel, S., Hammerl, G., Schmehl, A., Schneider, C. W. & Mannhart, J. Tunable quasi-two-dimensional electron gases in oxide heterostructures. *Science (1979)* **313**, 1942–1945 (2006).
21. Liu, H.-J. *et al.* A metal-insulator transition of the buried MnO₂ monolayer in complex oxide heterostructure. *Advanced Materials* **28**, 9142–9151 (2016).
22. Tokura, Y. Correlated-Electron Physics in Transition-Metal Oxides. *Phys Today* **56**, 50–55 (2003).
23. Dagotto, E. Complexity in strongly correlated electronic systems. *Science (1979)* **309**, 257–262 (2005).
24. Ramirez, A. P. Oxide electronics emerge. *Science (1979)* **315**, 1377–1378 (2007).
25. Anderson, P. W. More is different: broken symmetry and the nature of the hierarchical structure of science. *Science (1979)* **177**, 393–396 (1972).
26. Goldenfeld, N. & Kadanoff, L. P. Simple lessons from complexity. *Science (1979)* **284**, 87–89 (1999).
27. Li, W., Shi, J., Zhang, K. H. L. & MacManus-Driscoll, J. L. Defects in complex oxide thin films for electronics and energy applications: challenges and opportunities. *Mater Horiz* **7**, 2832–2859 (2020).
28. Wang, K. F., Liu, J.-M. & Ren, Z. F. Multiferroicity: the coupling between magnetic and polarization orders. *Adv Phys* **58**, 321–448 (2009).
29. Erlandsen, R. Enhancing the extraordinary magnetoresistance by variations in geometry and material properties. (Technical University of Denmark, 2022).
30. Maduraiveeran, G., Sasidharan, M. & Jin, W. Earth-abundant transition metal and metal oxide nanomaterials: Synthesis and electrochemical applications. *Prog Mater Sci* **106**, 100574 (2019).
31. Burns, R. G. & Burns, R. G. *Mineralogical applications of crystal field theory*. (Cambridge university press, 1993).
32. Pai, Y. Y., Tylan-Tyler, A., Irvin, P. & Levy, J. Physics of SrTiO₃-based heterostructures and nanostructures: A review. *Reports on Progress in Physics* **81** 036503, (2018).
33. Tilley, R. J. D. *Perovskites: structure-property relationships*. (John Wiley & Sons, 2016).
34. Rijnders, G. & Blank, D. H. A. Build your own superlattice. *Nature* **433**, 369–370 (2005).

-
35. Park, D.-S. *et al.* Electromagnetic Functionalization of Wide-Bandgap Dielectric Oxides by Boron Interstitial Doping. *Advanced Materials* **30**, 1802025 (2018).
 36. Qazi, U., Mehmood, S., Ali, Z., Khan, I. & Ahmad, I. Electronic structure and magnetic properties of the perovskites SrTMO₃ (TM= Mn, Fe, Co, Tc, Ru, Rh, Re, Os and Ir). *Physica B Condens Matter* **624**, 413361 (2022).
 37. Jalan, B., Allen, S. J., Beltz, G. E., Moetakef, P. & Stemmer, S. Enhancing the electron mobility of SrTiO₃ with strain. *Appl Phys Lett* **98**, 132102 (2011).
 38. Catalano, S. *et al.* Rare-earth nickelates RNiO₃: thin films and heterostructures. *Reports on Progress in Physics* **81**, 46501 (2018).
 39. Shojaei, F. & Yin, W.-J. Stability Trend of Tilted Perovskites. *The Journal of Physical Chemistry C* **122**, 15214–15219 (2018).
 40. Goldschmidt, V. M. Die gesetze der krystallochemie. *Naturwissenschaften* **14**, 477–485 (1926).
 41. Whangbo, M.-H., Gordon, E. E., Bettis Jr, J. L., Busmann-Holder, A. & Köhler, J. Tolerance factor and cation--anion orbital interactions differentiating the polar and antiferrodistortive structures of perovskite oxides ABO₃. *Z Anorg Allg Chem* **641**, 1043–1052 (2015).
 42. Woodward, P. M. Octahedral tilting in perovskites. I. Geometrical considerations. *Acta Crystallogr B* **53**, 32–43 (1997).
 43. Filip, M. R. & Giustino, F. The geometric blueprint of perovskites. *Proceedings of the National Academy of Sciences* **115**, 5397–5402 (2018).
 44. Reaney, I. M., Colla, E. L. C. E. L. & Setter, N. S. N. Dielectric and structural characteristics of Ba-and Sr-based complex perovskites as a function of tolerance factor. *Jpn J Appl Phys* **33**, 3984 (1994).
 45. Alvarez, G., Mayr, M., Moreo, A. & Dagotto, E. Areas of superconductivity and giant proximity effects in underdoped cuprates. *Phys Rev B* **71**, 14514 (2005).
 46. Tebano, A. *et al.* Preferential occupation of interface bands in La_{2/3}Sr_{1/3}MnO₃ films as seen via angle-resolved photoemission. *Phys Rev B* **82**, 214407 (2010).
 47. Shirane, G. & Yamada, Y. Lattice-dynamical study of the 110 K phase transition in SrTiO₃. *Physical Review* **177**, 858 (1969).
 48. Lytle, F. W. X-ray diffractometry of low-temperature phase transformations in strontium titanate. *J Appl Phys* **35**, 2212–2215 (1964).
 49. Buckley, A., Rivera, J.-P. & Salje, E. K. H. Twin structures in tetragonal SrTiO₃: The ferroelastic phase transition and the formation of needle domains. *J Appl Phys* **86**, 1653–1656 (1999).
 50. Hayward, S. A. & Salje, E. K. H. Cubic-tetragonal phase transition in SrTiO₃ revisited: Landau theory and transition mechanism. *Phase Transitions* **68**, 501–522 (1999).

51. Müller, K. A., Berlinger, W. & Tosatti, E. Indication for a novel phase in the quantum paraelectric regime of SrTiO₃. *Zeitschrift für Physik B Condensed Matter* **84**, 277–283 (1991).
52. Müller, K. A. & Burkard, H. SrTiO₃: An intrinsic quantum paraelectric below 4 K. *Phys Rev B* **19**, 3593 (1979).
53. Trybuła, Z., Miga, S., Łoś, S., Trybuła, M. & Dec, J. Evidence of polar nanoregions in quantum paraelectric KTaO₃. *Solid State Commun* **209**, 23–26 (2015).
54. Lemanov, V. v, Sotnikov, A. v, Smirnova, E. P., Weihnacht, M. & Kunze, R. Perovskite CaTiO₃ as an incipient ferroelectric. *Solid State Commun* **110**, 611–614 (1999).
55. Shin, D. *et al.* Quantum paraelectric phase of SrTiO₃ from first principles. *Phys Rev B* **104**, L060103 (2021).
56. Koonce, C. S., Cohen, M. L., Schooley, J. F., Hosler, W. R. & Pfeiffer, E. R. Superconducting transition temperatures of semiconducting SrTiO₃. *Physical Review* **163**, 380 (1967).
57. Stucky, A. *et al.* Isotope effect in superconducting n-doped SrTiO₃. *Sci Rep* **6**, 1–9 (2016).
58. Aruta, C. *et al.* Pulsed laser deposition of SrTiO₃/LaGaO₃ and SrTiO₃/LaAlO₃: Plasma plume effects. *Appl Phys Lett* **97**, 252105 (2010).
59. Rata, A. D. *et al.* Defect-induced magnetism in homoepitaxial SrTiO₃. *APL Mater* **10**, 91108 (2022).
60. Reibold, M. *et al.* Evidence of SrO (SrTiO₃) n Ruddlesden-Popper Phases by High Resolution Electron Microscopy and Holography. in *EMC 2008 14th European Microscopy Congress 1--5 September 2008, Aachen, Germany* 569–570 (2008).
61. Gunkel, F. *et al.* Thermodynamic ground states of complex oxide heterointerfaces. *ACS Appl Mater Interfaces* **9**, 1086–1092 (2017).
62. Pavlenko, N., Kopp, T., Tsymbal, E. Y., Sawatzky, G. A. & Mannhart, J. Magnetic and superconducting phases at the LaAlO₃/SrTiO₃ interface: The role of interfacial Ti 3d electrons. *Phys Rev B* **85**, 20407 (2012).
63. Salluzzo, M. *et al.* Origin of interface magnetism in BiMnO₃/SrTiO₃ and LaAlO₃/SrTiO₃ heterostructures. *Phys Rev Lett* **111**, 87204 (2013).
64. Pavlenko, N., Kopp, T., Tsymbal, E. Y., Mannhart, J. & Sawatzky, G. A. Oxygen vacancies at titanate interfaces: Two-dimensional magnetism and orbital reconstruction. *Phys Rev B* **86**, 64431 (2012).
65. Xu, C. *et al.* Disentanglement of growth dynamic and thermodynamic effects in LaAlO₃/SrTiO₃ heterostructures. *Sci Rep* **6**, 1–9 (2016).
66. Szot, K. & Speier, W. Surfaces of reduced and oxidized SrTiO₃ from atomic force microscopy. *Phys Rev B* **60**, 5909 (1999).

-
67. Kröger, F. A. & Vink, H. J. Solid state physics, Vol. 3. *Edited by F. Seitz and D. Turnbull Academic Press, New York* 307 (1956).
 68. Coey, J. M. D., Venkatesan, M. & Stamenov, P. Surface magnetism of strontium titanate. *Journal of Physics: Condensed Matter* **28**, 485001 (2016).
 69. Eror, N. G. & Balachandran, U. High-temperature defect structure of acceptor-doped strontium titanate. *Journal of the American Ceramic Society* **65**, 426–431 (1982).
 70. Hanzig, J. *et al.* Migration-induced field-stabilized polar phase in strontium titanate single crystals at room temperature. *Phys Rev B* **88**, 24104 (2013).
 71. Merkle, R., de Souza, R. A. & Maier, J. Optically Tuning the Rate of Stoichiometry Changes: Surface-Controlled Oxygen Incorporation into Oxides under UV Irradiation. *Angewandte Chemie* **113**, 2184–2187 (2001).
 72. Santander-Syro, A. F. *et al.* Two-dimensional electron gas with universal subbands at the surface of SrTiO₃. *Nature* **469**, 189–193 (2011).
 73. Lin, C. & Demkov, A. A. Electron correlation in oxygen vacancy in SrTiO₃. *Phys Rev Lett* **111**, 217601 (2013).
 74. Blanc, J. & Staebler, D. L. Electrocoloration in SrTiO₃: Vacancy drift and oxidation-reduction of transition metals. *Phys Rev B* **4**, 3548 (1971).
 75. Wells, F. S., Pan, A. v, Wang, X. R., Fedoseev, S. A. & Hilgenkamp, H. Analysis of low-field isotropic vortex glass containing vortex groups in YBa₂Cu₃O_{7-x} thin films visualized by scanning SQUID microscopy. *Sci Rep* **5**, 1–5 (2015).
 76. Tinkham, M. *Introduction to superconductivity*. (Courier Corporation, 2004).
 77. Gariglio, S., Reyren, N., Caviglia, A. D. & Triscone, J.-M. Superconductivity at the LaAlO₃/SrTiO₃ interface. *Journal of Physics: Condensed Matter* **21**, 164213 (2009).
 78. Reyren, N. *et al.* Superconducting interfaces between insulating oxides. *Science (1979)* **317**, 1196–1199 (2007).
 79. Caviglia, A. D. *et al.* Tunable Rashba spin-orbit interaction at oxide interfaces. *Phys Rev Lett* **104**, 126803 (2010).
 80. Kawasaki, M. *et al.* Atomic control of the SrTiO₃ crystal surface. *Science (1979)* **266**, 1540–1542 (1994).
 81. Kareev, M. *et al.* Atomic control and characterization of surface defect states of TiO₂ terminated SrTiO₃ single crystals. *Appl Phys Lett* **93**, 61909 (2008).
 82. Schlom, D. G., Chen, L.-Q., Pan, X., Schmehl, A. & Zurbuchen, M. A. A thin film approach to engineering functionality into oxides. *Journal of the American Ceramic Society* **91**, 2429–2454 (2008).
 83. Jalan, B., Moetakef, P. & Stemmer, S. Molecular beam epitaxy of SrTiO₃ with a growth window. *Appl Phys Lett* **95**, 32906 (2009).

84. Jalan, B., Engel-Herbert, R., Wright, N. J. & Stemmer, S. Growth of high-quality SrTiO₃ films using a hybrid molecular beam epitaxy approach. *Journal of Vacuum Science & Technology A: Vacuum, Surfaces, and Films* **27**, 461–464 (2009).
85. Sbrockey, N. M. *et al.* LaAlO₃/SrTiO₃ epitaxial heterostructures by atomic layer deposition. *J Electron Mater* **41**, 819–823 (2012).
86. Ohtomo, A. & Hwang, H. Y. A high-mobility electron gas at the LaAlO₃/SrTiO₃ heterointerface. *Nature* **427**, 423–426 (2004).
87. Christensen, D. V. *et al.* Stimulating Oxide Heterostructures: A Review on Controlling SrTiO₃-Based Heterointerfaces with External Stimuli. *Adv Mater Interfaces* **6**, 1900772 (2019).
88. Mannhar, J. & Herrnberger, A. The interface is still the device. *Nat Mater* **11**, 91–91 (2012).
89. Sing, M. *et al.* Profiling the interface electron gas of LaAlO₃/SrTiO₃ heterostructures with hard X-ray photoelectron spectroscopy. *Phys Rev Lett* **102**, 176805 (2009).
90. Song, K. *et al.* Direct imaging of the electron liquid at oxide interfaces. *Nat Nanotechnol* **13**, 198–203 (2018).
91. Sulpizio, J. A., Ilani, S., Irvin, P. & Levy, J. Nanoscale phenomena in oxide heterostructures. *Annu Rev Mater Res* **44**, 117–149 (2014).
92. Salluzzo, M. *et al.* Orbital reconstruction and the two-dimensional electron gas at the LaAlO₃/SrTiO₃ interface. *Phys Rev Lett* **102**, 166804 (2009).
93. Nakagawa, N., Hwang, H. Y. & Muller, D. A. Why some interfaces cannot be sharp. *Nat Mater* **5**, 204–209 (2006).
94. Doennig, D. & Pentcheva, R. Control of orbital reconstruction in (LaAlO₃)_M/(SrTiO₃)_N (001) quantum wells by strain and confinement. *Sci Rep* **5**, 1–6 (2015).
95. Chen, Y. *et al.* Metallic and insulating interfaces of amorphous SrTiO₃-based oxide heterostructures. *Nano Lett* **11**, 3774–3778 (2011).
96. Kalabukhov, A. *et al.* Effect of oxygen vacancies in the SrTiO₃ substrate on the electrical properties of the LaAlO₃/SrTiO₃ interface. *Phys Rev B* **75**, 121404 (2007).
97. Yamamoto, R. *et al.* Structural comparison of n-type and p-type LaAlO₃/SrTiO₃ interfaces. *Phys Rev Lett* **107**, 36104 (2011).
98. Yu, L. & Zunger, A. A polarity-induced defect mechanism for conductivity and magnetism at polar–nonpolar oxide interfaces. *Nat Commun* **5**, 1–9 (2014).
99. Lee, J. S. *et al.* Titanium dxy ferromagnetism at the LaAlO₃/SrTiO₃ interface. *Nat Mater* **12**, 703–706 (2013).
100. Cen, C., Thiel, S., Mannhart, J. & Levy, J. Oxide nanoelectronics on demand. *Science (1979)* **323**, 1026–1030 (2009).

-
101. Dahm, R. T. *et al.* Size-controlled spalling of LaAlO₃/SrTiO₃ micromembranes. *ACS Appl Mater Interfaces* **13**, 12341–12346 (2021).
 102. Joshua, A., Pecker, S., Ruhman, J., Altman, E. & Ilani, S. A universal critical density underlying the physics of electrons at the LaAlO₃/SrTiO₃ interface. *Nat Commun* **3**, 1–7 (2012).
 103. Smink, A. E. M. *et al.* Gate-Tunable Band Structure of the LaAlO₃/SrTiO₃ Interface. *Phys Rev Lett* **118**, 106401 (2017).
 104. Han, Y.-L. *et al.* Two-dimensional superconductivity at (110) LaAlO₃/SrTiO₃ interfaces. *Appl Phys Lett* **105**, 192603 (2014).
 105. Reyren, N. *et al.* Anisotropy of the superconducting transport properties of the LaAlO₃/SrTiO₃ interface. *Appl Phys Lett* **94**, 112506 (2009).
 106. Li, L., Richter, C., Mannhart, J. & Ashoori, R. C. Coexistence of magnetic order and two-dimensional superconductivity at LaAlO₃/SrTiO₃ interfaces. *Nat Phys* **7**, 762–766 (2011).
 107. Caviglia, A. D. *et al.* Electric field control of the LaAlO₃/SrTiO₃ interface ground state. *Nature* **456**, 624–627 (2008).
 108. Gunkel, F. *et al.* Defect control of conventional and anomalous electron transport at complex oxide interfaces. *Phys Rev X* **6**, 1–15 (2016).
 109. Ariando, A. *et al.* Electronic phase separation at the LaAlO₃/SrTiO₃ interface. *Nat Commun* **2**, 188 (2011).
 110. Salluzzo, M. Electronic Reconstruction at the Interface Between Band Insulating Oxides: The LaAlO₃/SrTiO₃ System. in *Oxide Thin Films, Multilayers, and Nanocomposites* 181–211 (Springer, 2015).
 111. Kalisky, B. *et al.* Critical thickness for ferromagnetism in LaAlO₃/SrTiO₃ heterostructures. *Nat Commun* **3**, 1–7 (2012).
 112. Pavlenko, N., Kopp, T., Tsymbal, E. Y., Sawatzky, G. A. & Mannhart, J. Magnetic and superconducting phases at the LaAlO₃/SrTiO₃ interface: The role of interfacial Ti 3d electrons. *Phys Rev B* **85**, 20407 (2012).
 113. Bi, F. *et al.* Room-temperature electronically-controlled ferromagnetism at the LaAlO₃/SrTiO₃ interface. *Nat Commun* **5**, 1–7 (2014).
 114. Ko, E. K. *et al.* Oxygen vacancy engineering for highly tunable ferromagnetic properties: a case of SrRuO₃ ultrathin film with a SrTiO₃ capping layer. *Adv Funct Mater* **30**, 2001486 (2020).
 115. Hu, H.-L. *et al.* Oxygen vacancy dependence of magnetic behavior in the LaAlO₃/SrTiO₃ heterostructures. *Adv Mater Interfaces* **3**, 1600547 (2016).
 116. Park, D.-S. *et al.* The emergence of magnetic ordering at complex oxide interfaces tuned by defects. *Nat Commun* **11**, 1–9 (2020).

117. Stornaiuolo, D. *et al.* Tunable spin polarization and superconductivity in engineered oxide interfaces. *Nat Mater* **15**, 278–283 (2016).
118. de Luca, G. M. *et al.* Transport properties of a quasi-two-dimensional electron system formed in LaAlO₃/EuTiO₃/SrTiO₃ heterostructures. *Phys Rev B* **89**, 224413 (2014).
119. Kormondy, K. J. *et al.* Large positive linear magnetoresistance in the two-dimensional t_{2g} electron gas at the EuO/SrTiO₃ interface. *Sci Rep* **8**, 1–9 (2018).
120. Fix, T., MacManus-Driscoll, J. L. & Blamire, M. G. Delta-doped LaAlO₃/SrTiO₃ interfaces. *Appl Phys Lett* **94**, 172101 (2009).
121. Christensen, D. v *et al.* Strain-tunable magnetism at oxide domain walls. *Nat Phys* **15**, 269–274 (2019).
122. Shalom, M. ben *et al.* Anisotropic magnetotransport at the SrTiO₃/LaAlO₃ interface. *Phys Rev B* **80**, 140403 (2009).
123. Liang, H. *et al.* Nonmonotonically tunable Rashba spin-orbit coupling by multiple-band filling control in SrTiO₃-based interfacial d-electron gases. *Phys Rev B* **92**, 75309 (2015).
124. Kane, M. J., Apsley, N., Anderson, D. A., Taylor, L. L. & Kerr, T. Parallel conduction in GaAs/Al_xGa_{1-x}As modulation doped heterojunctions. *Journal of Physics C: Solid State Physics* **18**, 5629 (1985).
125. Inoue, J. & Ohno, H. Taking the Hall effect for a spin. *Science (1979)* **309**, 2004–2005 (2005).
126. Witt, H. *et al.* Patterning of superconducting two-dimensional electron gases based on AlO_x/KTaO₃ (111) interfaces. *arXiv preprint arXiv:2210.14591* (2022).
127. Niu, W. *et al.* Giant tunability of the two-dimensional electron gas at the interface of γ-Al₂O₃/SrTiO₃. *Nano Lett* **17**, 6878–6885 (2017).
128. Bjørlig, A. v *et al.* Nanoscale patterning of electronic devices at the amorphous LaAlO₃/SrTiO₃ oxide interface using an electron sensitive polymer mask. *Appl Phys Lett* **112**, 171606 (2018).
129. Velasco-Davalos, I., Thomas, R. & Ruediger, A. Realization of single-termination SrTiO₃ (100) surfaces by a microwave-induced hydrothermal process. *Appl Phys Lett* **103**, 202905 (2013).
130. Matsumoto, T., Tanaka, H., Kawai, T. & Kawai, S. STM-imaging of a SrTiO₃ (100) surface with atomic-scale resolution. *Surface Science Letters* **278**, L153–L158 (1992).
131. Zhang, J. *et al.* Depth-resolved subsurface defects in chemically etched SrTiO₃. *Appl Phys Lett* **94**, 92904 (2009).
132. Ohnishi, T. *et al.* Preparation of thermally stable TiO₂-terminated SrTiO₃ (100) substrate surfaces. *Appl Phys Lett* **85**, 272–274 (2004).

-
133. Liang, Y., Rothman, J. B. & Bonnell, D. A. Effect of annealing on the stoichiometry of SrTiO₃ (001). *Journal of Vacuum Science & Technology A: Vacuum, Surfaces, and Films* **12**, 2276–2280 (1994).
 134. Radovic, M. *et al.* Growth and characterization of stable SrO-terminated SrTiO₃ surfaces. *Appl Phys Lett* **94**, 22901 (2009).
 135. Bachelet, R., Sánchez, F., Palomares, F. J., Ocal, C. & Fontcuberta, J. Atomically flat SrO-terminated SrTiO₃ (001) substrate. *Appl Phys Lett* **95**, 141915 (2009).
 136. Eom, C.-B. & Lee, J. Metal-organic pulsed laser deposition for stoichiometric complex oxide thin films.
 137. Ojeda-G-P, A., Döbeli, M. & Lippert, T. Influence of plume properties on thin film composition in pulsed laser deposition. *Adv Mater Interfaces* **5**, 1701062 (2018).
 138. Wang, S. *et al.* Titanium-defected undoped anatase TiO₂ with *p*-type conductivity, room-temperature ferromagnetism, and remarkable photocatalytic performance. *J Am Chem Soc* **137**, 2975–2983 (2015).
 139. Ohnishi, T., Lippmaa, M., Yamamoto, T., Meguro, S. & Koinuma, H. Improved stoichiometry and misfit control in perovskite thin film formation at a critical fluence by pulsed laser deposition. *Appl Phys Lett* **87**, 241919 (2005).
 140. Keeble, D. J. *et al.* Identification of A- and B-site cation vacancy defects in perovskite oxide thin films. *Phys Rev Lett* **105**, 226102 (2010).
 141. Lee, H. N., Ambrose Seo, S. S., Choi, W. S. & Rouleau, C. M. Growth control of oxygen stoichiometry in homoepitaxial SrTiO₃ films by pulsed laser epitaxy in high vacuum. *Sci Rep* **6**, 1–7 (2016).
 142. Trier, F. *et al.* Controlling the conductivity of amorphous LaAlO₃/SrTiO₃ interfaces by in-situ application of an electric field during fabrication. *Appl Phys Lett* **103**, 31607 (2013).
 143. Sambri, A. *et al.* Plasma plume effects on the conductivity of amorphous-LaAlO₃/SrTiO₃ interfaces grown by pulsed laser deposition in O₂ and Ar. *Appl Phys Lett* **100**, 231605 (2012).
 144. Yao, X., Schneider, C. W., Wokaun, A. & Lippert, T. New Insight into the Gas Phase Reaction Dynamics in Pulsed Laser Deposition of Multi-Elemental Oxides. *Materials* **15**, 4862 (2022).
 145. Amoruso, S., Toftmann, B. & Schou, J. Thermalization of a UV laser ablation plume in a background gas: From a directed to a diffusionlike flow. *Phys Rev E* **69**, 56403 (2004).
 146. Koster, G., Huijben, M. & Rijnders, G. *Epitaxial growth of complex metal oxides.* (Elsevier, 2015).
 147. Frank, F. C. & van der Merwe, J. H. One-dimensional dislocations. I. Static theory. *Proc R Soc Lond A Math Phys Sci* **198**, 205–216 (1949).

148. Volmer, M. Nucleus formation in supersaturated systems. *Z. phys. Chem.* **119**, 277–301 (1926).
149. Stranski, I. N. & Krastanov, L. Theory of orientation separation of ionic crystals. *Ber. Akad. Wiss. Wien* **146**, 797 (1938).
150. Huijben, M. *et al.* Structure-Property Relation of SrTiO₃/LaAlO₃ Interfaces. *Advanced Materials* **21**, 1665–1677 (2009).
151. Adeyeye, A. O. & Shimon, G. Growth and characterization of magnetic thin film and nanostructures. in *Handbook of Surface Science* vol. 5 1–41 (Elsevier, 2015).
152. Kraft, A., Rupprecht, C. & Yam, Y.-C. Superconducting Quantum Interference Device (SQUID). *UBC Phys* (2017).
153. Hertz, H. Ueber einen Einfluss des ultravioletten Lichtes auf die electrische Entladung. *Ann Phys* **267**, 983–1000 (1887).
154. Einstein, A. Über einen die Erzeugung und Verwandlung des Lichtes betreffenden heuristischen Gesichtspunkt [AdP 17, 132 (1905)]. *Ann Phys* **14**, 164–181 (2005).
155. Hüfner, S. *Photoelectron spectroscopy: principles and applications*. (Springer Science & Business Media, 2013).
156. Damascelli, A. Probing the electronic structure of complex systems by ARPES. *Phys Scr* **2004**, 61 (2004).
157. Grioni, M. Photoelectron spectroscopy. in *Neutron and X-ray Spectroscopy* 189–237 (Springer, 2006).
158. Chambers, S. A. Understanding the mechanism of conductivity at the LaAlO₃/SrTiO₃ (001) interface. *Surf Sci* **605**, 1133–1140 (2011).
159. Chaves, A. *et al.* Bandgap engineering of two-dimensional semiconductor materials. *NPJ 2D Mater Appl* **4**, 1–21 (2020).
160. Zeng, M., Xiao, Y., Liu, J., Yang, K. & Fu, L. Exploring two-dimensional materials toward the next-generation circuits: from monomer design to assembly control. *Chem Rev* **118**, 6236–6296 (2018).
161. Lu, D. *et al.* Synthesis of freestanding single-crystal perovskite films and heterostructures by etching of sacrificial water-soluble layers. *Nat Mater* **15**, 1255–1260 (2016).
162. Lu, D., Crossley, S., Xu, R., Hikita, Y. & Hwang, H. Y. Freestanding oxide ferroelectric tunnel junction memories transferred onto silicon. *Nano Lett* **19**, 3999–4003 (2019).
163. Kum, H. S. *et al.* Heterogeneous integration of single-crystalline complex-oxide membranes. *Nature* **578**, 75–81 (2020).
164. Sambri, A. *et al.* Self-Formed, Conducting LaAlO₃/SrTiO₃ Micro-Membranes. *Adv Funct Mater* **30**, 1909964 (2020).

-
165. Erlandsen, R. *et al.* A Two-Dimensional Superconducting Electron Gas in Freestanding LaAlO₃/SrTiO₃ Micromembranes. *Nano Lett* (2022).
 166. Prodjosantoso, A. K., Kennedy, B. J. & Hunter, B. A. Synthesis and structural studies of strontium-substituted tricalcium aluminate Ca_{3-x}Sr_xAl₂O₆. *Aust J Chem* **53**, 195–202 (2000).
 167. Baek, D. J., Lu, D., Hikita, Y., Hwang, H. Y. & Kourkoutis, L. F. Mapping cation diffusion through lattice defects in epitaxial oxide thin films on the water-soluble buffer layer Sr₃Al₂O₆ using atomic resolution electron microscopy. *APL Mater* **5**, 0–8 (2017).
 168. Baek, D. J., Lu, D., Hikita, Y., Hwang, H. Y. & Kourkoutis, L. F. Ultrathin epitaxial barrier layer to avoid thermally induced phase transformation in oxide heterostructures. *ACS Appl Mater Interfaces* **9**, 54–59 (2017).
 169. Shin, J. *et al.* Atomistic screening mechanism of ferroelectric surfaces: An in situ study of the polar phase in ultrathin BaTiO₃ films exposed to H₂O. *Nano Lett* **9**, 3720–3725 (2009).
 170. Li, X., Bai, Y., Wang, B. C. & Su, Y. J. Water adsorption induced in-plane domain switching on BaTiO₃ surface. *J Appl Phys* **118**, 094104 (2015).
 171. Yang, C., Wang, Y., Sigle, W. & van Aken, P. A. Determination of Grain-Boundary Structure and Electrostatic Characteristics in a SrTiO₃ Bicrystal by Four-Dimensional Electron Microscopy. *Nano Lett* **21**, 9138–9145 (2021).
 172. Singh, P. *et al.* Large-area crystalline BaSnO₃ membranes with high electron mobilities. *ACS Appl Electron Mater* **1**, 1269–1274 (2019).
 173. Hughes, L. A. & van Benthem, K. Low-angle twist grain boundary in SrTiO₃ fabricated by spark plasma sintering techniques. *Journal of the American Ceramic Society* **102**, 578–586 (2019).
 174. Bedell, S. W., Lauro, P., Ott, J. A., Fogel, K. & Sadana, D. K. Layer transfer of bulk gallium nitride by controlled spalling. *J Appl Phys* **122**, 25103 (2017).
 175. Shahrjerdi, D. & Bedell, S. W. Extremely flexible nanoscale ultrathin body silicon integrated circuits on plastic. *Nano Lett* **13**, 315–320 (2013).
 176. Bedell, S. W. *et al.* Layer transfer by controlled spalling. *J Phys D Appl Phys* **46**, 152002 (2013).
 177. Hutchinson, J. W. & Suo, Z. Mixed mode cracking in layered materials. *Advances in applied mechanics* **29**, 63–191 (1991).
 178. Reagor, D. W. & Butko, V. Y. Highly conductive nanolayers on strontium titanate produced by preferential ion-beam etching. *Nat Mater* **4**, 593–596 (2005).
 179. Caprara, S., Grilli, M., Benfatto, L. & Castellani, C. Effective medium theory for superconducting layers: A systematic analysis including space correlation effects. *Phys Rev B* **84**, 14514 (2011).

180. Huijben, M. *et al.* Defect engineering in oxide heterostructures by enhanced oxygen surface exchange. *Adv Funct Mater* **23**, 5240–5248 (2013).
181. Caprara, S. *et al.* Multiband superconductivity and nanoscale inhomogeneity at oxide interfaces. *Phys Rev B* **88**, 20504 (2013).
182. Biscaras, J. *et al.* Multiple quantum criticality in a two-dimensional superconductor. *Nat Mater* **12**, 542–548 (2013).
183. Zhu, G., Radtke, G. & Botton, G. A. Bonding and structure of a reconstructed (001) surface of SrTiO₃ from TEM. *Nature* **490**, 384–387 (2012).
184. Frenkel, Y. *et al.* Anisotropic transport at the LaAlO₃/SrTiO₃ interface explained by microscopic imaging of channel-flow over SrTiO₃ domains. *ACS Appl Mater Interfaces* **8**, 12514–12519 (2016).
185. Zhang, F. *et al.* Modulating the electrical transport in the two-dimensional electron gas at LaAlO₃/SrTiO₃ heterostructures by interfacial flexoelectricity. *Phys Rev Lett* **122**, 257601 (2019).
186. Morelle, M., Bruynseraede, Y. & Moshchalkov, V. v. Effect of current and voltage leads on the superconducting properties of mesoscopic triangles. *physica status solidi (b)* **237**, 365–373 (2003).
187. Förg, B., Richter, C. & Mannhart, J. Field-effect devices utilizing LaAlO₃/SrTiO₃ interfaces. *Appl Phys Lett* **100**, 53506 (2012).
188. Hurand, S. *et al.* Field-effect control of superconductivity and Rashba spin-orbit coupling in top-gated LaAlO₃/SrTiO₃ devices. *Sci Rep* **5**, 1–9 (2015).
189. Eerkes, P. D., van der Wiel, W. G. & Hilgenkamp, H. Modulation of conductance and superconductivity by top-gating in LaAlO₃/SrTiO₃ 2-dimensional electron systems. *Appl Phys Lett* **103**, 201603 (2013).
190. Brovko, O. O. & Tosatti, E. Controlling the magnetism of oxygen surface vacancies in SrTiO₃ through charging. *Phys Rev Mater* **1**, 44405 (2017).
191. Orsel, K. *et al.* Influence of the oxidation state of SrTiO₃ plasmas for stoichiometric growth of pulsed laser deposition films identified by laser induced fluorescence. *APL Mater* **3**, 106103 (2015).
192. Li, T. *et al.* Strong Room-Temperature Ferroelectricity in Strained SrTiO₃ Homoepitaxial Film. *Advanced Materials* **33**, 2008316 (2021).
193. Cao, Y. *et al.* Anomalous orbital structure in a spinel-perovskite interface. *NPJ Quantum Mater* **1**, 1–6 (2016).
194. Mannhart, J. & Schlom, D. G. Oxide interfaces—an opportunity for electronics. *Science (1979)* **327**, 1607–1611 (2010).
195. Inaba, J. & Katsufuji, T. Large magnetoresistance in spin-and carrier-doped SrTiO₃. *Phys Rev B* **72**, 52408 (2005).

-
196. Goto, T. *et al.* Magnetism and Faraday rotation in oxygen-deficient polycrystalline and single-crystal iron-substituted strontium titanate. *Phys Rev Appl* **7**, 24006 (2017).
 197. Tang, A. S., Onbasli, M. C., Sun, X. & Ross, C. A. Thickness-Dependent Double-Epitaxial Growth in Strained SrTi_{0.7}Co_{0.3}O_{3-δ} Films. *ACS Appl Mater Interfaces* **10**, 7469–7475 (2018).
 198. Elfimov, I. S., Yunoki, S. & Sawatzky, G. A. Possible path to a new class of ferromagnetic and half-metallic ferromagnetic materials. *Phys Rev Lett* **89**, 216403 (2002).
 199. Joshua, A., Ruhman, J., Pecker, S., Altman, E. & Ilani, S. Gate-tunable polarized phase of two-dimensional electrons at the LaAlO₃/SrTiO₃ interface. *Proceedings of the National Academy of Sciences* **110**, 9633–9638 (2013).
 200. Cancellieri, C. *et al.* Electrostriction at the LaAlO₃/SrTiO₃ interface. *Phys Rev Lett* **107**, 56102 (2011).
 201. Plumb, N. C. *et al.* Mixed dimensionality of confined conducting electrons in the surface region of SrTiO₃. *Phys Rev Lett* **113**, 86801 (2014).
 202. Salman, Z. *et al.* Near-surface structural phase transition of SrTiO₃ studied with zero-field β -detected nuclear spin relaxation and resonance. *Phys Rev Lett* **96**, 147601 (2006).
 203. Smadella, M. *et al.* Surface dependent structural phase transition in SrTiO₃ observed with spin relaxation of ⁸Li. *Physica B Condens Matter* **404**, 924–926 (2009).
 204. Guedes, E. B. *et al.* Universal Structural Influence on the 2D Electron Gas at SrTiO₃ Surfaces. *Advanced Science* **8**, 2100602 (2021).
 205. Salman, Z. *et al.* Depth dependence of the structural phase transition of SrTiO₃ studied with β -NMR and grazing incidence x-ray diffraction. *Phys Rev B* **83**, 224112 (2011).
 206. Rebec, S. N. *et al.* Dichotomy of the photo-induced 2-dimensional electron gas on SrTiO₃ surface terminations. *Proceedings of the National Academy of Sciences* **116**, 16687–16691 (2019).
 207. Guedes, E. B. *et al.* Single spin-polarized Fermi surface in SrTiO₃ thin films. *Phys. Rev. Res.* **2**, 33173 (2020).
 208. Meevasana, W. *et al.* Creation and control of a two-dimensional electron liquid at the bare SrTiO₃ surface. *Nat Mater* **10**, 114–118 (2011).
 209. Plumb, N. C. *et al.* Evolution of the SrTiO₃ surface electronic state as a function of LaAlO₃ overlayer thickness. *Appl Surf Sci* **412**, 271–278 (2017).
 210. Yan, X. *et al.* Origin of the 2D Electron Gas at the SrTiO₃ Surface. *Advanced Materials* **34**, 2200866 (2022).
 211. Delugas, P., Fiorentini, V., Mattoni, A. & Filippetti, A. Intrinsic origin of two-dimensional electron gas at the (001) surface of SrTiO₃. *Phys Rev B* **91**, 115315 (2015).

212. Hensling, F. V. E., Baeumer, C., Rose, M.-A., Gunkel, F. & Dittmann, R. SrTiO₃ termination control: a method to tailor the oxygen exchange kinetics. *Mater Res Lett* **8**, 31–40 (2020).
213. Chen, Y. Z. *et al.* A high-mobility two-dimensional electron gas at the spinel/perovskite interface of γ -Al₂O₃/SrTiO₃. *Nat Commun* **4**, 1–6 (2013).
214. Anh, L. D. *et al.* High-Mobility 2D Hole Gas at a SrTiO₃ Interface. *Advanced Materials* **32**, 1906003 (2020).
215. Xie, Y., Bell, C., Hikita, Y., Harashima, S. & Hwang, H. Y. Enhancing electron mobility at the LaAlO₃/SrTiO₃ interface by surface control. *Advanced Materials* **25**, 4735–4738 (2013).
216. Chen, Y. Z. *et al.* Room Temperature Formation of High-Mobility Two-Dimensional Electron Gases at Crystalline Complex Oxide Interfaces. *Advanced Materials* **26**, 1462–1467 (2014).
217. Chen, Y. Z. *et al.* Extreme mobility enhancement of two-dimensional electron gases at oxide interfaces by charge-transfer-induced modulation doping. *Nat Mater* **14**, 801–806 (2015).
218. Gan, Y. *et al.* Diluted oxide interfaces with tunable ground states. *Advanced Materials* **31**, 1805970 (2019).
219. Chen, Y. *et al.* Tuning the two-dimensional electron liquid at oxide interfaces by buffer-layer-engineered redox reactions. *Nano Lett* **17**, 7062–7066 (2017).
220. Chikina, A. *et al.* Band-order anomaly at the γ -Al₂O₃/SrTiO₃ interface drives the electron-mobility boost. *ACS Nano* **15**, 4347–4356 (2021).
221. Cancellieri, C. *et al.* Polaronic metal state at the LaAlO₃/SrTiO₃ interface. *Nat Commun* **7**, 1–8 (2016).
222. Cancellieri, C. & Strocov, V. N. *Spectroscopy of Complex Oxide Interfaces*. (Springer, 2018).
223. Strocov, V. N. Photoemission response of 2D electron states. *J Electron Spectros Relat Phenomena* **229**, 100–107 (2018).
224. Cancellieri, C. *et al.* Doping-dependent band structure of LaAlO₃/SrTiO₃ interfaces by soft x-ray polarization-controlled resonant angle-resolved photoemission. *Phys Rev B* **89**, 121412 (2014).
225. Strocov, V. N. *et al.* Three-dimensionality of mobile electrons at X-ray-irradiated LaAlO₃/SrTiO₃ interfaces. *arXiv preprint arXiv:1909.04106* (2019).
226. Straub, T. *et al.* Many-body definition of a Fermi surface: application to angle-resolved photoemission. *Phys Rev B* **55**, 13473 (1997).
227. Yukawa, R. *et al.* Control of two-dimensional electronic states at anatase TiO₂(001) surface by K adsorption. *Phys Rev B* **97**, 165428 (2018).

-
228. Choi, M., Oba, F. & Tanaka, I. Role of Ti antisitelike defects in SrTiO₃. *Phys Rev Lett* **103**, 185502 (2009).
 229. Kim, Y. S. *et al.* Localized electronic states induced by defects and possible origin of ferroelectricity in strontium titanate thin films. *Appl Phys Lett* **94**, 202906 (2009).
 230. Chambers, S. A. *et al.* Interconversion of intrinsic defects in SrTiO₃ (001). *Phys Rev B* **97**, 245204 (2018).
 231. Al-Zubi, A., Bihlmayer, G. & Blügel, S. Electronic structure of oxygen-deficient SrTiO₃ and Sr₂TiO₄. *Crystals (Basel)* **9**, 580 (2019).
 232. Fujimori, A. *et al.* Electronic structure and electron-phonon interaction in transition metal oxides with d⁰ configuration and lightly doped compounds. *Journal of Physics and Chemistry of Solids* **57**, 1379–1384 (1996).
 233. Jeschke, H. O., Shen, J. & Valentí, R. Localized versus itinerant states created by multiple oxygen vacancies in SrTiO₃. *New J Phys* **17**, 23034 (2015).
 234. Janotti, A., Varley, J. B., Choi, M. & de Walle, C. G. Vacancies and small polarons in SrTiO₃. *Phys Rev B* **90**, 85202 (2014).
 235. Hao, X., Wang, Z., Schmid, M., Diebold, U. & Franchini, C. Coexistence of trapped and free excess electrons in SrTiO₃. *Phys Rev B* **91**, 85204 (2015).
 236. Zubko, P., Gariglio, S., Gabay, M., Ghosez, P. & Triscone, J.-M. Interface physics in complex oxide heterostructures. *Annu. Rev. Condens. Matter Phys.* **2**, 141–165 (2011).
 237. 19.3 Spectroscopic and Magnetic Properties of Coordination Compounds - Chemistry 2e. Preprint at <https://openstax.org/books/chemistry-2e/pages/19-3-spectroscopic-and-magnetic-properties-of-coordination-compounds>.
 238. Loetzsch, R. *et al.* The cubic to tetragonal phase transition in SrTiO₃ single crystals near its surface under internal and external strains. *Appl Phys Lett* **96**, 71901 (2010).
 239. He, R. *et al.* Structural phase transitions in SrTiO₃ from deep potential molecular dynamics. *Phys Rev B* **105**, 64104 (2022).
 240. Chen, Y.-Z., Pryds, N., Sun, J.-R., Shen, B.-G. & Linderöth, S. High-mobility two-dimensional electron gases at oxide interfaces: Origin and opportunities. *Chinese Physics B* **22**, 116803 (2013).
 241. Goble, N. J. *et al.* Anisotropic electrical resistance in mesoscopic LaAlO₃/SrTiO₃ devices with individual domain walls. *Sci Rep* **7**, 1–9 (2017).
 242. Chusuei, C. C. & Goodman, D. W. X-ray photoelectron spectroscopy. in *Encyclopedia of physical science and technology* 17:921–938 (2002).

$$\sqrt{17} + \int \delta e^{i\pi} = -1$$

$\{2.7182818284\}$ ο αριθμός του ευσταθίου

$\chi^2 \sum \gg \approx \lambda$